Title
Analytical and Experimental Assessment of Seismic Vulnerability of Beam-Column Joints without Transverse Reinforcement in Concrete Buildings

Author
Hassan, Wael M.

Publication Date
2011

Peer reviewed|Thesis/dissertation

Analytical and Experimental Assessment of Seismic Vulnerability of Beam-Column Joints without Transverse Reinforcement in Concrete Buildings

By

Wael Mohammed Hassan

A dissertation submitted in partial satisfaction of the

requirements for the degree of

Doctor of Philosophy

in

Engineering - Civil and Environmental Engineering

in the

GRADUATE DIVISION

of the

UNIVERSITY Of CALIFORNIA, BERKELEY

Committee in charge:

Professor Jack Moehle, Chair

Professor Bozidar Stojadinovic

Professor Douglas Dreger

Spring 2011

Analytical and Experimental Assessment of Seismic Vulnerability of Beam-Column Joints without Transverse Reinforcement in Concrete Buildings

By

Wael Mohammed Hassan

ABSTRACT

Analytical and Experimental Assessment of Seismic Vulnerability of Beam-Column Joints without Transverse Reinforcement in Concrete Buildings

by

Wael Mohamed Hassan

Doctor of Philosophy in Engineering – Civil and Environmental Engineering

University of California, Berkeley

Professor Jack P. Moehle, Chair

Beam-column joints in concrete buildings are key components to ensure structural integrity of building performance under seismic loading. Earthquake reconnaissance has reported the substantial damage that can result from inadequate beam-column joints. In some cases, failure of older-type corner joints appears to have led to building collapse.

Since the 1960s, many advances have been made to improve seismic performance of building components, including beam-column joints. New design and detailing approaches are expected to produce new construction that will perform satisfactorily during strong earthquake shaking. Much less attention has been focused on beam-column joints of older construction that may be seismically vulnerable. Concrete buildings constructed prior to developing details for ductility in the 1970s normally lack joint transverse reinforcement. The available literature concerning the performance of such joints is relatively limited, but concerns about performance exist.

The current study aimed to improve understanding and assessment of seismic performance of unconfined exterior and corner beam-column joints in existing buildings. An extensive literature survey was performed, leading to development of a database of about a hundred tests. Study of the data enabled identification of the most important parameters and the effect of each parameter on the seismic performance.

The available analytical models and guidelines for strength and deformability assessment of unconfined joints were surveyed and evaluated. In particular, The ASCE 41 existing building document proved to be substantially conservative in joint shear strength estimation. Upon identifying deficiencies in these models, two new joint shear strength models, a bond capacity model, and two axial capacity models designed and tailored specifically for unconfined beam-column joints were developed. The proposed models strongly correlated with previous test results.

In the laboratory testing phase of the current study, four full-scale corner beam-column joint subassemblies, with slab included, were designed, built, instrumented, tested, and analyzed. The specimens were tested under unidirectional and bidirectional displacement-controlled quasi-static loading that incorporated varying axial loads that simulated overturning seismic moment effects. The axial loads varied between tension and high compression loads reaching about 50% of the column axial capacity. The test parameters were axial load level, loading history, joint aspect ratio, and beam reinforcement ratio. The test results proved that high axial load increases joint shear strength and decreases the deformability of joints failing in pure shear failure mode without beam yielding. On the contrary, high axial load did not affect the strength of joints failing in shear after significant beam yielding; however, it substantially increased their displacement ductility. Joint aspect ratio proved to be instrumental in deciding joint shear strength; that is the deeper the joint the lower the shear strength. Bidirectional loading reduced the apparent strength of the joint in the uniaxial principal axes. However, circular shear strength interaction is an appropriate approximation to predict the biaxial strength. The developed shear strength models predicted successfully the strength of test specimens.

Based on the literature database investigation, the shear and axial capacity models developed and the test results of the current study, an analytical finite element component model based on a proposed joint shear stress-rotation backbone constitutive curve was developed to represent the behavior of unconfined beam-column joints in computer numerical simulations of concrete frame buildings. The proposed finite element model included the effect of axial load, mode of joint failure, joint aspect ratio and axial capacity of joint. The proposed backbone curve along with the developed joint element exhibited high accuracy in simulating the test response of the current test specimens as well as previous test joints.

Finally, a parametric study was conducted to assess the axial failure vulnerability of unconfined beam-column joints based on the developed shear and axial capacity models. This parametric study compared the axial failure potential of unconfined beam-column joint with that of shear critical columns to provide a preliminary insight into the axial collapse vulnerability of older-type buildings during intense ground shaking.

TO MY PARENTS,

MY GRANDMOTHER

AND

MY LOVELY DAUGHTER

MAY ALLAH BLESS THEM ALL

ACKNOWLEDGEMENTS

First, I would like to praise Allah for His bounty He blessed me with; that He gave me the ambition, ideas, strength and endurance to go through all difficulties and achieve this work. I hope He blesses this work as an ongoing charity and a beneficial knowledge for Humanity to save precious lives during future earthquakes.

My warmest appreciation and deepest gratitude are due for my research advisor and dissertation committee chair Prof. Jack P. Moehle. He provided invaluable advising throughout the years of this study. His deep yet very broad knowledge, continuous encouragement and support, inspiring ideas, keen supervision and meticulous revisions tremendously helped me achieve this work. I learned a lot through my rich experience with him on the academic, professional and personal levels.

Special thanks are also due for other members of the dissertation committee; Professor Bozidar Stojadinovic and Professor Douglas Dreger. Thanks are also extended to Professor James Kelly and Professor Stephen Mahin; members of my qualifying examination committee.

I would like also to express my gratitude to National Science Foundation that provided financial and facility support for this investigation through Network for Earthquake Engineering Simulation (NEES).

Truly grateful to the *Great Egyptian People*, that provided generous financial support for four years through a full Fellowship of the Department of Education.

I would like also to extend my deep thanks to the Pacific Earthquake Engineering Research Center staff for providing technical and administrative services and to *nees@berkeley* laboratory staff that provided professional technical quality service to accommodate the challenging test setup and loading protocol of the experimental phase of this study.

My sincere appreciation is due for Prof. Khalid Mosalam who provided valuable input through our fruitful discussions in this project. Thanks are also extended to Prof. Anil Chopra, my academic advisor, for providing valuable advising to assemble a useful matrix of courses at Berkeley that maximized my benefit and reflected positively on my research work.

I want also to extend my thanks to undergraduate student research assistants Steven Wong and Jeffery Zhang whose help in the experimental part of this study is much appreciated.

Special thanks are due for *Erico* Company that donated and machined the headed bars for the tension assembly of the test setup.

I would like to extend my special thanks to all my friends and colleagues at UC Berkeley and the Bay Area for their support and assistance throughout the years. Thanks to Mohamed Aly for his friendship and his assistance in the test preparation, to Juan Carlos Reyes for our friendship and great technical discussions, and to Tarek Radwan and Ziad Mustafa for their moral support and valuable friendship. Special Thanks are due for Ramon Smith and Jennifer Mattheson for their brotherhood and continuous prayers for me.

Finally, I would like to express my sincere love and warmest gratitude to my beloved family; my great parents Prof. Mohamed Hassan and Prof. Zeinab El-Awamry, my grandmother Mrs. Fatemah El-Sanafawy, my daughter Ms. Mariam, my brother Dr. Hythem and my sister Dr. Rasha. Their continuous support, encouragement and prayers greatly helped me achieve this work. I am especially grateful for Mariam's love, patience and accommodation of a very busy father throughout the years of demanding studies at Berkeley.

TABLE OF CONTENTS

ABSTRACT **1**
ACKNOWLEDGMENTS ..... **iii**
TABLE OF CONTENTS ..... **iv**
LIST OF FIGURES ..... **x**
LIST OF TABLES ..... **xxiii**

CHAPTER 1: INTRODUCTION **1**
1.1 Background 1
1.2 Problem Statement 1
1.3 Research Program Objectives 2
1.4 Research Program Scope 2
1.5 Manuscript Organization 3

CHAPTER 2: UNCONFINED BEAM-COLUMN JOINTS: BACKGROUND **6**
2.1 Introduction 6
2.2 Beam-Column Joint Failures in Past Earthquakes 6
2.3 Geometry of Exterior and Corner Joints 12
2.4 Older-Type Beam-Column Joint Seismic Deficiencies 13
2.5 Mechanics of Exterior and Corner Unconfined Joints 15
2.5.1 Shear force transfer mechanisms 15
2.5.2 Joint Shear Strength Calculation 17
2.5.3 Joint Principal Tension Stress 17

CHAPTER 3: UNCONFINED BEAM-COLUMN JOINTS: LITERATURE REVIEW **19**
3.1 Introduction 19
3.2 Geometry of Joint Test Sub-assemblages 19
3.3 Unconfined Beam-Column Joint Failure Modes 22
3.4 Exterior Beam-Column Joint Tests 24
3.5 Corner Beam-Column Joint Tests 34
3.6 Beam-Column Joint Analytical Models 45
3.6.1 Strut-And-Tie Models 45
3.6.1.1 Fixed Angle Softened Strut and Tie Model (SSTM) 45
3.6.1.2 Modified Rotated Angle Strut and Tie Model (MRA- STM) 50
3.6.1.3 General Multi-Strut-and-Tie Model 51
3.6.1.4 Generalized Monotonic Strut-and-Tie Model 52
3.6.2 Empirical Joint Shear Strength Models 53
3.6.2.1 Bakir and Boduroğlu Empirical Model 53
3.6.2.2 Fixed Angle Strut Monotonic Empirical Model 53
3.6.2.3 Sarsam and Phipps Empirical Strength Model 54
3.6.3 Panel Zone Principal Stress-Strain Models 55
3.6.4 Shear Strength Degradation Models 56

3.6.4.1 Curvature Ductility-Based Shear Strength Degradation Model 56
3.6.4.2 Joint Rotation-Based Principal Tension Degradation Model 56
3.6.4.3 Story Drift-Based Principal Tension Degradation Model 57
3.6.5 Panel Zone Spring Models for Computer Simulation of RC Frames.....58
3.6.5.1 Single Rotational Spring Model, Pampanin et al 58
3.6.5.2 Single Rotational Spring With Rigid Links Model (Scissors Model) 59
3.6.5.3 Rotational Spring Model, Favvata et al 62
3.6.6 Finite Element Continuum Models.....64
3.6.7 Performance-Based and Shear Deformation Backbone Models 65
3.7 Summary of the Influence of Design Parameters on Joint Behavior 69
3.7.1 Effect of Axial Load.....69
3.7.2 Effect of Concrete Slab 70
3.7.3 Effect of Loading History.....70
3.7.4 Effect of Transverse Spandrel Confinement 71
3.7.5 Effect of Longitudinal Beam Reinforcement Detail inside Joint 73
3.7.6 Effect of Presence of Column Intermediate Vertical Reinforcement.....75
3.7.7 Effect of Presence of Column Lap Splices.....76
3.7.8 Common Design Parameters for Unconfined Joints in Older Construction ..76
3.7.9 Joint Contribution to Total Interstory Drift 77

CHAPTER 4: PARAMETERS AFFECTING SEISMIC PERFORMANCE OF JOINTS..78
4.1 Introduction 78
4.2 Effects of Various Parameters 78
4.2.1 General.....78
4.2.2 Unconfined Joint Database.....82
4.2.3 Effect of Joint Aspect Ratio 83
4.2.4 Effect of Column Axial Load 89
4.2.5 Effect of Beam Reinforcement Ratio 95
4.3 Observed Strength-Ductility Trends of Exterior and Corner Joints 96
4.3.1 Shear Strength-Drift Ratio Observations of Exterior and Corner Joints.....96
4.3.2 Relation between Shear Strength and Displacement Ductility.....97
4.3.3 Relation between Principal Tension Stress and Displacement Ductility.....99

CHAPTER 5 : PROPOSED STRENGTH MODELS FOR UNCONFINED JOINTS 102
5.1 Introduction 102
5.2 Database Used for Model Assessment 102
5.3 Assessment of ASCE/SEI 41-06 Joint Shear Strength Provisions 103
5.4 Evaluation of Existing Analytical Joint Shear Strength Models 105
5.4.1 Strut-and-Tie Models.....105
5.4.1.1 Fixed Angle Softened Strut-and-Tie Model 105
5.4.1.2 Monotonic Fixed Angle Softened Strut-and-Tie Model 108
5.4.1.3 Generalized Monotonic Fixed Angle Softened Strut-and-Tie

Model....109
5.4.2 Empirical Shear Strength Models....111
5.4.2.1 Sarsam and Phipps Empirical Strength Model....111
5.4.2.2 Bakir and Boduroğlu Empirical Model....112
5.4.3 Panel Zone Principal Strain Model....114
5.4.4 Probabilistic Shear Strength Model....115
5.5 Evaluation of Available Bond Strength Models....118
5.6 Proposed Strength Models....122
5.6.1 J-Failure Modified ACI 318-08 Strut-and-Tie Analytical Model....122
5.6.2 J-Failure Empirical Shear Strength Model....126
5.6.3 J-Failure Shear Strength Degradation Model....127
5.6.4 BJ-Failure Mode Shear Strength....129
5.6.5 CJ-Failure Mode Shear Strength....130
5.6.6 S-Failure Empirical Bond Strength Model....130
5.6.7 Verification of Proposed Models....132
5.6.7.1 J-Failure Modified ACI 318-08 Strut-and-Tie Analytical Model....132
5.6.7.2 J-Failure Empirical Model....134
5.6.7.3 J-Failure Strength Degradation Model....134
5.6.7.4 S-Failure Empirical Bond Model....136
5.6.8 Practical Criterion to Determine Joint Strength Limit State....136
5.6.9 Strength Reduction Factors (ϕ-Factor)....137
5.6.10 Model Limitations....137

CHAPTER 6: EXPERIMENTAL PROGRAM....138
6.1 Introduction....138
6.2 Program Objectives....138
6.3 Shortcomings of Previous Tests....139
6.4 Test Parameters....139
6.4.1 Beam Reinforcement Ratio....140
6.4.2 Joint Aspect Ratio....140
6.4.3 Axial Load Ratio....140
6.4.4 Loading History....141
6.5 Specimens Design and Construction....141
6.5.1 Test Specimens' Design Criteria....141
6.5.1.1 Prototype Building....141
6.5.1.2 Lateral Load-Axial Load Relationship....142
6.5.1.3 Effective Slab Width....142
6.5.1.4 Failure Modes and Design Criteria....143
6.5.2 Test Matrix and Specimen Design....143
6.5.2.1 Beam Design....144
6.5.2.2 Column Design....144
6.5.2.3 Slab Design....145
6.5.2.4 Beam-Column Joint Design....145
6.5.3 Specimen Construction....150

6.5.4 Material Properties 158
6.5.4.1 Concrete 158
6.5.4.2 Reinforcing Steel 161
6.5.5 Predicted Strength and Deformations of Test Specimens 164
6.5.5.1 Beam and Column Flexural Strength 164
6.5.5.2 Joint Shear Strength 164
6.5.5.3 Yield Displacement 165
6.6 Instrumentation 178
6.6.1 Overview 178
6.6.2 Internal Instrumentation: Steel Strain Gages 178
6.6.3 External Instrumentation 180
6.6.3.1 Joint Shear Strains 183
6.6.3.2 Joint Global Rotation in Space 185
6.6.3.3 Beam Relative Rotation with Respect to Joint 186
6.6.3.4 Beam Torsional Rotation 187
6.7 Design of Test Setup 188
6.8 Testing Protocol 196
6.8.1 Gravity Loading 196
6.8.2 Displacement History 196
6.8.3 Axial Load Protocol 200
6.9 Data Acquisition 204
6.10 Photography and Laser Scanning 204

CHAPTER 7: EXPERIMENTAL RESULTS AND DISCUSSION 207
7.1 Introduction 207
7.2 Seismic Performance Measures 207
7.3 General Seismic Behavior of Test Specimens 208
7.3.1 Specimen U-J-1 208
7.3.2 Specimen U-J-2 230
7.3.3 Specimen B-J-1 248
7.3.4 Specimen U-BJ-1 267
7.4 Effect of Test Parameters on Performance Measures 291
7.4.1 Effect of Axial Load Level 291
7.4.1.1 Joint Shear Strength 291
7.4.1.2 Interstory Drift Ratio and Displacement Ductility 298
7.4.1.3 Stiffness and Stiffness Degradation 299
7.4.1.4 Joint Shear Deformations 300
7.4.2 Effect of Joint Aspect Ratio 311
7.4.2.1 Joint Shear Strength 311
7.4.2.2 Interstory Drift Ratio and Displacement Ductility 312
7.4.2.3 Stiffness and Stiffness Degradation 312
7.4.2.4 Joint Shear Deformations 313
7.4.3 Effect of Loading History 319
7.4.3.1 Joint Shear Strength 319
7.4.3.2 Interstory Drift Ratio and Displacement Ductility 320

7.4.3.3 Stiffness and Stiffness Degradation 321
7.4.3.4 Joint Shear Deformations 322
7.4.4 Effect of Beam Reinforcement Ratio 329
7.4.3.1 Joint Shear Strength....329
7.4.3.2 Interstory Drift Ratio and Displacement Ductility 330
7.4.3.3 Stiffness and Cyclic Performance 330
7.4.3.4 Joint Shear Deformations 331
7.4.5 Effect of Concrete Slab....336
7.4.5.1 Effective Slab Width 336
7.4.5.2 Twisting Effect 338
7.4.6 Effect of Intermediate Column Reinforcement 352
7.4.7 Effect of Joint Geometry 353

CHAPTER 8: AXIAL CAPACITY MODELS FOR UNCONFINED BEAM-COLUMN JOINTS....354
8.1 Introduction 354
8.2 Background....354
8.3 Modes and Mechanics of Joint Axial Failure....355
8.4 Observed Axial Capacity of Unconfined Beam-Column Joints....362
8.5 Axial Capacity Model for Columns 370
8.6 Proposed Axial Capacity Model for Unconfined Joints....371
8.6.1 Analytical Shear-Friction Capacity Model....372
8.6.1.1 Assumptions and Equilibrium Equations 372
8.6.1.2 Effective Coefficient of Friction....373
8.6.2 Empirical Shear-Friction Capacity Model....376
8.6.3 Proposed Models Evaluation 380
8.7 Axial Collapse Vulnerability of Shear Deficient Buildings 382
8.7.1 Axial Failure Vulnerability: Parametric Study....382
8.7.2 Analysis Results of the Parametric Study....384

CHAPTER 9: ANALYTICAL BEAM-COLUMN JOINT MODEL FOR FINITE ELEMENT BUILDING SIMULATION 388
9.1 Introduction 388
9.2 Modeling Joint Behavior in Finite Element Models 388
9.2.1 Existing Panel Zone Modeling Techniques....388
9.2.1.1 Conventional Centerline Frame Analysis....388
9.2.1.2 ASCE/SEI 41-06 Joint Model 389
9.2.1.3 ASCE/SEI 41-06 Supplement-ACI 369-R11 Joint Model 393
9.2.1.4 Rotational Spring with Rigid Links Joint Model (Scissors Model) 394
9.2.2 Proposed Joint Spring Model 396
9.2.2.1 Proposed Shear Stress-Strain Backbone Curves 397
9.2.2.2 Bond-Slip Modeling 405
9.2.2.3 Joint Rotational Spring Hysteretic Material Model....410
9.2.2.4 Bond-Slip Rotational Spring Material Model 413

9.3 Simulation of Beam-Column Joint Subassemblages....414
9.3.1 Model Geometry....414
9.3.2 Material Simulation Parameters....415
9.3.3 Beam and Column Simulation Parameters....416
9.3.4 Comparison of Slip Rotation Simulation Options A and B....417
9.3.5 Simulation Results using Proposed Joint Model....418
9.3.6 Simulation Response using Conventional Rigid Joint....422
9.3.7 Simulation Response using ASCE 41 Nonlinear Modeling Provisions....422
9.3.8 Model Validation and Calibration....422

CHAPTER 10: CONCLUSIONS....428
10.1 Summary....428
10.2 Conclusions and Recommendations....429
10.2.1 Joint Shear Strength Assessment....429
10.2.2 Existing Buildings Assessment Documents ASCE/SEI 41-10 and ACI 369-11....430
10.2.3 Effect of Key Test Parameters on Joint Performance Measures....431
10.2.3.1 Axial Load Level....431
10.2.3.2 Bidirectional Loading History....432
10.2.3.3 Joint Aspect Ratio....433
10.2.3.4 Beam Reinforcement Ratio / Mode of Joint Shear Failure..434
10.2.4 Effect of Other Design Parameters on Joint Performance Measures....434
10.2.5 Joint Numerical Modeling for Finite Element Simulation....435
10.2.6 Axial Capacity of Unconfined Beam-Column Joints....435
10.3 Future Research Work....437

REFERENCES....438

APPENDICES....452

LIST OF FIGURES

Figure 2.1.a Structure collapse due to failure of deficient beam-column joints, Kaiser Permanente Building, Northridge earthquake, 1994....7
Figure 2.1.b Structure collapse due to failure of deficient beam-column joints....7
Figure 2.2.a Partial Building Collapse due to failure of beam-column joints in the Izmit, Turkey earthquake of August 17, 1999, (b) close-up of third-level joint, (c) close-up of second-level joint....8
Figure 2.3 Damage to partially collapsed 15-story building: beam-column failure in Chi-Chi, Taiwan, earthquake of Sep. 21, 1999....9
Figure 2.4 Collapsed building following Izmit, Turkey earthquake of Aug. 17, 1999....9
Figure 2.5 Corner beam-column joint damage in the Izmit, Turkey, earthquake of August 17, 1999....10
Figure 2.6 Joint failure and partial building collapse in the March 13, 1992, Erzincan, Turkey earthquake, Zahertar [158]....10
Figure 2.7.a Severe corner joint damage, Caracas, Venezuela building damage after an earthquake, Pagni [110]....11
Figure 2.7.b Severe corner joint damage, Taiwan Chi-Chi 1999 earthquake, NISEE [106].11
Figure 2.8 Severe exterior joint earthquake damage [82]....11
Figure 2.9 Exterior and corner joints in reinforced concrete frame building....12
Figure 2.10 Pre-1970 U.S. typical construction details....14
Figure 2.11 Common older-type joint construction....14
Figure 2.12 Exterior Beam Column Joint Subjected to Seismic Loading....15
Figure 2.13 Exterior confined joint force transfer mechanisms(a) Diagonal strut (b) Truss, (c) Forces, Hwang and Lee [64]....16
Figure 2.14 Exterior joint force transfer mechanism: diagonal compression strut....16
Figure 3.1.a Isolated exterior joint and exterior joint with transverse stubs....20
Figure 3.1.b Corner-simulated and corner Joints....20
Figure 3.2 Deformed shape of actual and test idealized beam-column joint subassembly 21
Figure 3.3 Modes of failure of unconfined beam-column joints....23
Figure 3.4 Details of test specimens and moment rotation hysteretic response, Hanson and Connor [53]....24
Figure 3.5 Test specimens, moment rotation hysteretic response for corner joint, Hanson and Connor [54]....25
Figure 3.6 Details of test specimens with and without beam stubs, Beres et al. [17]....26
Figure 3.7 Hysteresis response of typical exterior specimen, Beres et al. [17]....27
Figure 3.8 Hysteresis response for specimens with low and high axial loads, Clyde et al. [26]....28
Figure 3.9 Unconfined isolated exterior joint details, Pantelides et al. [116]....28
Figure 3.10 Isolated exterior joint details, Pantelides et al. [116]....29
Figure 3.11 Isolated exterior joints with intermediate column reinforcement, Wong [155] 29
Figure 3.12 Exterior specimens with and without slab, Gogkoz [50]....30
Figure 3.13 Test specimen details and loading history, Gogkoz [50]....30
Figure 3.14 Backbone curves of test specimens, Gogkoz [50]....31

Figure 3.15 Hysteretic response of test specimens, Barnes et al. [13].....31
Figure 3.16 Hysteresis response and failure modes of units O6 and O7, Hakuto et al. [51]32
Figure 3.17 Details and results of exterior joint tests, Pampanin et al. [113].....33
Figure 3.18 Alternative damage mechanisms for exterior joints.....34
Figure 3.19 "As Built" specimen details in longitudinal and transverse directions 35
Figure 3.20 Test setup for corner Joint, Priestley and Hart [129].....35
Figure 3.21 Response of longitudinal beam of corner Joint, Priestley and Hart [129].....36
Figure 3.22 Axial failure mode of "As Built" corner joint, Priestley and Hart [129] 36
Figure 3.23 Specimen geometry and details and test setup, Engindeniz [41] 37
Figure 3.24 Loading history, Engindeniz [41].....38
Figure 3.25 Hysteresis responses of test specimens and failure mode, Engindeniz [41] 38
Figure 3.26 Contribution of different components to overall drift, Engindeniz [41] 39
Figure 3.27 Specimens US3-C-Control and US3-CS-Control, Topcu [143] 39
Figure 3.28 Specimens US3-C-Control and US3-CS-Control failure modes, Topcu [143].39
Figure 3.29 Backbone curves of different test specimens, Topcu [143] 40
Figure 3.30 Corner-simulated test specimen and hysteric response, Sanchez et al. [132] ...41
Figure 3.31 Test setup and loading sequence of corner joints, Kishida and Kotaro [74].....41
Figure 3.32 Setup of corner joint tests, Pampanin et al. [111].....42
Figure 3.33 Effect of loading History, Pampanin et al. [111] 42
Figure 3.34 SSTM force transfer mechanisms, Hwang and Lee [64] 45
Figure 3.35 SSTM forces of different mechanisms, Hwang and Lee [64].....46
Figure 3.36 Contribution of SSTM force transfer mechanisms to joint shear strenght 47
Figure 3.37 Constitutive models of concrete and steel, Hwang and Lee [64].....49
Figure 3.38 Compatibility relations, Hwang and Lee [64].....49
Figure 3.39 Global truss model and strut-and-tie model for exterior joints, Pantelides et al. [116].....51
Figure 3.40 Generalized monotonic strut and-tie model, Parker and Bullman [45].....52
Figure 3.41 Vertical equilibrium of strut and-tie model, Vollum and Newman [153].....54
Figure 3.42 Diagonal strut and truss mechanism for panel zone model, Tsonos [145].....55
Figure 3.43 Shear strength degradation model with curvature ductility, Park [119].....56
Figure 3.44 Principal tension strength degradation models with drift ratio, Priestley [127]57
Figure 3.45 Principal tension strength degradation models, Pamapanin et al. [112].....57
Figure 3.46 Interstory displacement/drift contributions of joint, column and beam deformations Pampanin et al. [112].....58
Figure 3.47 Contributions to interstory drift: exterior specimen T1 behavior (numerical), Pampanin et al. [112] 58
Figure 3.48 Proposed analytical model for joint behavior: rotational spring, Pampanin et al. [112].....59
Figure 3.49 Analytical-experimental comparison of exterior joint behavior, Pampanin et al. [112].....59
Figure 3.50 Existing beam-column joint models: (a) Alath and Kunnath [5], (b) Biddah and Ghobarah [18], (c) Youssef and Ghobarah [157], (d) Lowes and Altoontash [87], (e) Altoontash [8], and (f) Shin and LaFave [140]. After Celik and Ellingwood [23] …….....59

Figure 3.51 Beam-column joint spring models implemented, Celik and Ellingwood [23] ..61
Figure 3.52 Unconfined joint model verification against Pantelides experimental results, Celik and Ellingwood [23] ..61
Figure 3.53 Proposed model for the simulation of the exterior RC beam–column joints, Favvata et al. [42] ..62
Figure 3.54 Verification of rotational spring model applicability for unconfined joints seismic response predication, Favvata et al. [42] ..63
Figure 3.55 Dynamic analysis results for 8 story RC frame using rigid zone and rotational spring model, Favvata et al. [42] ..63
Figure 3.56 Basic assumptions of the bond model implemented FEM, Eligehausen et al. [34] ..64
Figure 3.57 Model of test specimen, Eligehausen et al. [34] ..64
Figure 3.58 Comparison of cracking during cycling, Eligehausen et al. [34] ..65
Figure 3.59 Limit state performance levels suggested by Clyde et al. [26] ..66
Figure 3.60 Limit states performance levels suggested by Pantelides et al. [9] ..67
Figure 3.61 Experimental backbone curves for exterior joints, Pantelides et al. [116] ..67
Figure 3.62 Proposed backbone curves for exterior joints, Pantelides et al. [116] ..68
Figure 3.63 Bidirectional loading shear strength interaction for interior joints, Kurose et al. [77] ..71
Figure 3.64 Limited capacity of bent-out bars and secondary strut mechanism in exterior-column joints ..73
Figure 3.65 Insufficient beam-bar embedment in beam-column joints ..74
Figure 3.66 Effect of intermediate column reinforcement on unconfined joint shear strength, Wong [155] ..75
Figure 3.67 Contribution of different components of deformation to overall story drifts, Walker [154] ..77
Figure 4.1 Statics of beam-column joint subassembly ..79
Figure 4.2 Yield deformation definition based on reduced (secant) stiffness elasto-plastic yield ..80
Figure 4.3 Ultimate deformation definition: (a) Peak load deformation (b) significant (85%) load capacity after peak load ..81
Figure 4.4 Effect of joint aspect ratio on joint shear strength ..84
Figure 4.5 Linear trends of the effect of joint aspect ratio on exterior joint shear strength84
Figure 4.6 Effect of joint aspect ratio on joint subassembly drift ratio ..85
Figure 4.7 Effect of joint aspect ratio on displacement ductility factor ..86
Figure 4.8 Effect of joint aspect ratio on principal tension stress ..87
Figure 4.9 Effect of joint aspect ratio on post peak deformability ..88
Figure 4.10 Overall effect of axial load on joint shear strength ..90
Figure 4.11 Effect of axial load on joint shear strength ..90
Figure 4.12 Effect of axial load on joint subassembly drift ratio ..91
Figure 4.13 Effect of axial load on joint subassembly displacement ductility facto ..92
Figure 4.14 Effect of axial load on joint principal tension stress at joint shear strength peak …. ..94
Figure 4.15 Effect of beam reinforcement on joint shear strength coefficient ..95

Figure 4.16 Joint shear strength-drift relationship 96
Figure 4.17 Joint shear strength-displacement ductility relationship 98
Figure 4.18 Relation between displacement ductility-joint shear strength normalized by aspect ratio and axial load ratio for J-Failure joints 98
Figure 4.19 Principal tension stress-drift ratio relationship 99
Figure 4.20 Principal tension stress-displacement ductility relationships 100
Figure 4.21 Principal tension stress-displacement ductility relationships for J-Failure joints 101
Figure 5.1 Geometry and details of investigated joints 103
Figure 5.2 Evaluation of ASCE 41 exterior joint shear strength provisions 104
Figure 5.3 Experimental verification of SSTM, Hwang and Lee [40] 105
Figure 5.4 Assessment of SSTM for unconfined exterior and corner joints experiencing J-Failure 106
Figure 5.5 Assessment of SSTM for unconfined exterior and corner joints experiencing BJ-Failure 107
Figure 5.6 Assessment of Vollum and Newman [153] monotonic SSTM for unconfined exterior and corner joints with J-Failure mode 108
Figure 5.7 Assessment of Parker and Bullman [122] generalized SSTM for unconfined exterior and corner joints with J-Failure mode 109
Figure 5.8 Parker and Bullman generalized SSTM for unconfined exterior and corner joints with J-Failure mode 110
Figure 5.9 Assessment of Sarsam and Phipps [133] empirical model prediction of unconfined joint shear strength experiencing J-Failure mode 111
Figure 5.10 Assessment of Bakir and Boduroğlu [12] empirical model for unconfined exterior and corner joints with J-Failure mode 112
Figure 5.11 Assessment of the effect of beam reinforcement ratio for Bakir and Boduroğlu [12] empirical model 113
Figure 5.12 Assessment of the effect of joint aspect ratio for Bakir and Boduroğlu empirical model 114
Figure 5.13 Assessment of Tsonos [1] panel zone model for unconfined exterior and corner joints with J-Failure mode 115
Figure 5.14 Assessment of Kim and Lafave [71] probabilistic Bayesian model for unconfined exterior and corner joints with J-Failure mode 116
Figure 5.15 Joint shear coefficients based on referenced bond strength model and based on measured behavior 120
Figure 5.16 Proposed strut-and-tie model 122
Figure 5.17 Effect of axial load ratio on proposed model's shear strength prediction 124
Figure 5.18 Axial load factor for proposed empirical model 127
Figure 5.19 Proposed shear strength degradation coefficient with displacement ductility demand 128
Figure 5.20 Proposed bond-slip model for bottom beam bars in unconfined joints 131
Figure 5.21 Experimental verification of proposed J-Failure strut-and-tie shear strength model 133
Figure 5.22 Experimental verification of proposed J-Failure shear strength empirical

model....134
Figure 5.23 Assessment of the proposed strut-and-tie-based shear strength degradation model, ductility definition B....135
Figure 5.24 Assessment of the proposed empirical model-based shear strength degradation model, ductility definition B....135
Figure 5.25 Experimental verification of proposed S-Failure bond strength model....136
Figure 5.26 Proposed models strength prediction with a strength reduction factor of 0.75 (a) J-Failure strut-and-tie model (Eq. 5.28) (b) S-Failure bond strength model (Eq. 5.38)....137
Figure 6.1 Van Nuys Hotel, the prototype building model, Kranwinkler et al. [75]....142
Figure 6.2 Schematic rendering and concrete dimensions of test specimen....146
Figure 6.3.a Reinforcement details of test specimens....147
Figure 6.3.b Reinforcement details of specimen U-J-2....148
Figure 6.4 Slab reinforcement of test specimens....149
Figure 6.5 Effective depth of EW and NS beams of test specimens....151
Figure 6.6 Steel cage construction of specimen U-J-1....152
Figure 6.7 Congested beam reinforcement steel hooks inside the joint....153
Figure 6.8 Reinforcement cage of specimen U-J-2....154
Figure 6.9 Deck reinforcement and lower column headed bars of test specimens....154
Figure 6.10 Concrete casting and compaction of test specimens....155
Figure 6.11 Supervision of concrete casting and compaction....156
Figure 6.12 Cast specimens curing and finalized formwork....156
Figure 6.13 Finished test specimens after removing wood forms....157
Figure 6.14 Test date concrete compressive stress-strain relationship for specimens U-J-1 and U-J-2....159
Figure 6.15 Test date concrete compressive stress-strain relationship for specimens B-J-1 and U-BJ-1....162
Figure 6.16 EW beam moment-curvature relation prediction for specimens U-J-1 and U-J-2....171
Figure 6.17 EW beam moment-curvature relation prediction for specimens B-J-1 and U-BJ-1s....172
Figure 6.18 Column interaction diagram and predicted column forces at EW beam flexural strength for downward loading direction of test specimens....173
Figure 6.19 Column moment-curvature diagram and predicted column forces at EW beam flexural strength for upward loading direction of test specimens, specimen U-J-1 and U-J-2....174
Figure 6.20 Column moment-curvature diagram and predicted column forces at EW beam flexural strength for upward loading direction of test specimens, specimen B-J-1 and U-BJ-1....175
Figure 6.21 Force-displacement prediction for specimens U-J-1 and U-J-2....176
Figure 6.22 Force-displacement prediction for specimens B-J-1 and U-BJ-1....177
Figure 6.23 Strain gauge instrumentation....179
Figure 6.24 External instrumentations....180
Figure 6.25 3D view of external instrumentations....182

Figure 6.26 Shear strain measurement....183
Figure 6.27 Joint global rotation instrumentation....185
Figure 6.28 Beam-joint relative rotation instrumentation....186
Figure 6.29 Beam torsional rotation measurements....187
Figure 6.30 Schematic rendering of test setup....189
Figure 6.31 Test setup: vertical loading systems....190
Figure 6.32 Test Setup: Lateral Restraint Frame....191
Figure 6.33.a 3D universal hinge....192
Figure 6.33.b Transition plate design between 3D universal hinge and concrete column....193
Figure 6.34 Specimens U-J-1 and U-J-2 in the test rig....194
Figure 6.35 Specimens B-J-1and U-BJ-1 in the test rig....195
Figure 6.36 Unidirectional alternating loading history for specimens U-J-1, U-J-2 and U-BJ-1....197
Figure 6.37 Bidirectional loading history for specimen B-J-1....198
Figure 6.38 Loading sequence and sign convention....199
Figure 6.39 Displacement-based axial load protocol....202
Figure 6.40 Displacement-based protocol axial load history....203
Figure 6.41 Effective stiffness of actual axial load-beam displacement relation....204
Figure 6.42 Synchronized video clip for specimen monitoring....205
Figure 6.43 3D laser scanning machine....206
Figure 6.44 Fish-eye generated navigable 3D images for collapse inspection....206
Figure 7.1 Relation between applied force and drift for EW-beam of specimen U-J-1....209
Figure 7.2 Relation between applied force and drift for NS-beam of specimen U-J-1....209
Figure 7.3 Development of north joint cracking and distress of specimen U-J-1....210-212
Figure 7.4 Characteristic joint panel cracks....212
Figure 7.6 Axial failure of specimen U-J-1....214
Figure 7.7 Backbone curves of specimen U-J-1 beam shear forces....216
Figure 7.8 Backbone curves of specimen U-J-1 joint shear stresses....216
Figure 7.9 Upper column axial load time history of specimen U-J-1....217
Figure 7.10 Beam shear time history of specimen U-J-1....217
Figure 7.11 Joint shear stress-strain envelopes for specimen U-J-1....218
Figure 7.12 North joint shear stress-strain hysteresis performance for specimen U-J-1....219
Figure 7.13 East joint shear stress-strain hysteresis performance for specimen U-J-1....219
Figure 7.14 Peak-to-peak stiffness for specimen U-J-1....221
Figure 7.15 Peak-to-peak cumulative energy dissipation for specimen U-J-1....221
Figure 7.16 Joint shear strain contribution to total drift ratio for specimen U-J-1....222
Figure 7.17 Slab top reinforcement strain distribution for U-J-1 first negative drift peaks for EW-Beam loading....224
Figure 7.18 Slab top reinforcement strain distribution for U-J-1 first negative drift peaks for NS-beam loading....224
Figure 7.19 EW-beam top exterior longitudinal reinforcement strain for U-J-1 negative displacement peaks....225
Figure 7.20 EW-beam top interior longitudinal reinforcement strain for U-J-1 negative displacement peaks....225

Figure 7.21 EW-beam bottom exterior longitudinal reinforcement strain for U-J-1 positive displacement peaks 226
Figure 7.22 EW-beam bottom interior longitudinal reinforcement strain for U-J-1 positive displacement peaks 226
Figure 7.23 Strain development for column intermediate reinforcement CN of U-J-1 EW-beam drift peaks 227
Figure 7.24 Strain development for column intermediate reinforcement CE of U-J-1 NS-beam drift peaks 227
Figure 7.25 North joint crack development and progression during EW beam loading of specimen U-J-2 231-233
Figure 7.26 Axial failure of specimen U-J-2 234
Figure 7.28 Relation between applied force and drift for EW-beam of specimen U-J-2 ...236
Figure 7.29 Relation between applied force and drift for EW-beam of specimen U-J-2 ...236
Figure 7.30 Backbone curves of specimen U-J-2 237
Figure 7.31 Backbone curves of specimen U-J-2 237
Figure 7.32 Upper column axial load history of specimen U-J-2....238
Figure 7.33 Beam shear history of specimen U-J-2....238
Figure 7.34 North joint shear stress-strain hysteresis performance for specimen U-J-2 239
Figure 7.35 Joint shear stress-strain envelopes for specimen U-J-2....239
Figure 7.36 North Joint deformation contribution to total drift ratio of EW-beam for specimen U-J-2 240
Figure 7.37 Peak-to-peak stiffness for specimen U-J-2....241
Figure 7.38 Peak-to-peak cumulative energy dissipation for specimen U-J-2 241
Figure 7.39 Slab top reinforcement strain distribution for U-J-2 negative drift peaks for EW-Beam loading 243
Figure 7.40 Slab top reinforcement strain distribution for U-J-2 negative drift peaks for NS-Beam loading 243
Figure 7.41 EW-beam top exterior longitudinal reinforcement strain for U-J-2 negative drift peaks 244
Figure 7.42 EW-beam top interior longitudinal reinforcement strain for U-J-2 negative drift peaks 244
Figure 7.43 EW-beam bottom exterior longitudinal reinforcement strain for U-J-2 positive drift peaks....245
Figure 7.44 EW-beam bottom interior longitudinal reinforcement strain for U-J-2 positive drift peaks....245
Figure 7.45 Strain development for column intermediate reinforcement CN of U-J-2 EW-beam drift peaks....246
Figure 7.46 Strain development for column intermediate reinforcement CE of U-J-2 NS-beam drift peaks....246
Figure 7.47 Crack development and distress of Specimen B-J-1 north Joint..... 250-21
Figure 7.48 Global views of Specimen B-J-1 axial collapse....252
Figure 7.49 Evidence of 3D shear diagonal strut through the joint of specimen B-J-1.....253
Figure 7.51 Relation between applied force and drift for EW-beam of specimen B-J-1 ...254
Figure 7.52 Relation between applied force and drift for NS-beam of specimen B-J-1 254

Figure 7.53 Backbone curves of specimen B-J-1 255
Figure 7.54 Backbone curves of specimen B-J-1 255
Figure 7.55 Upper column axial load history of specimen B-J-1 256
Figure 7.56 Beam shear history of specimen B-J-1 256
Figure 7.57 North joint shear stress-strain hysteresis performance for specimen B-J-1 257
Figure 7.58 East joint shear stress-strain hysteresis performance for specimen B-J-1 257
Figure 7.59 North joint shear stress-strain envelope for specimen B-J-1 258
Figure 7.60 North Joint deformation contribution to total drift ratio of EW-beam for specimen B-J-1 259
Figure 7.61 Peak-to-peak stiffness for specimen B-J-1 259
Figure 7.62 Peak-to-peak cumulative energy dissipation for specimen B-J-1 260
Figure 7.63 Slab reinforcement strain distribution for B-J-1 during first negative drift peaks 262
Figure 7.64 Slab reinforcement strain distribution for B-J-1 during first negative drift peaks 262
Figure 7.65 EW-beam top exterior longitudinal reinforcement strain for B-J-1 negative drift peaks 263
Figure 7.66 EW-beam top interior longitudinal reinforcement strain for B-J-1 negative drift peaks 263
Figure 7.67 NS-beam bottom exterior longitudinal reinforcement strain for B-J-1 positive drift peaks....264
Figure 7.68 NS-beam bottom interior longitudinal reinforcement strain for B-J-1 positive drift peaks....264
Figure 7.69 Strain development for column intermediate reinforcement CN of B-J-1 first drift peaks....265
Figure 7.70 Strain development for column intermediate reinforcement CE of B-J-1 first drift peaks....265
Figure 7.71 North joint crack development and joint distress in specimen U-BJ-1 269
Figure 7.72 Global views of specimen U-BJ-1 after axial failure 271
Figure 7.73 East joint crack development and progression during NS beam loading of specimen U-BJ-1....272
Figure 7.74 East joint axial failure during EW beam loading of specimen U-BJ-1 273
Figure 7.75 Relation between force and drift for EW-beam of specimen U-BJ-1 275
Figure 7.76 Relation between force and drift for NS-beam of specimen U-BJ-1 275
Figure 7.77 Backbone curves of specimen U-BJ-1 276
Figure 7.78 Backbone curves of specimen U-BJ-1 276
Figure 7.79 Upper column axial load history of specimen U-BJ-1 277
Figure 7.80 Beam shear history of specimen U-BJ-1 277
Figure 7.81 North joint shear stress-strain hysteretic performance for specimen U-BJ-1..278
Figure 7.82 Shear stress-strain backbone curves for specimen U-BJ-1....279
Figure 7.83 Joint deformation contribution to total interstory drift ratio specimen U-BJ-1280
Figure 7.84 Peak-to-peak stiffness for specimen U-BJ-1 281
Figure 7.85 Peak-to-peak cumulative energy dissipation for specimen U-BJ-1 281
Figure 7.86 Slab top reinforcement strain distribution for U-BJ-1 negative drift peaks for

EW-Beam loading....283
Figure 7.87 Slab top reinforcement strain distribution for U-BJ-1 negative drift peaks for NS-Beam loading....283
Figure 7.88 EW-beam top exterior longitudinal reinforcement strain for U-BJ-1 negative drift peaks....284
Figure 7.89 EW-beam top interior longitudinal reinforcement strain for U-BJ-1 negative drift peaks....284
Figure 7.90 EW-beam bottom exterior longitudinal reinforcement strain for U-BJ-1 positive drift peaks....285
Figure 7.91 EW-beam bottom interior longitudinal reinforcement strain for U-BJ-1 positive drift peaks....285
Figure 7.92 Strain development for column intermediate reinforcement CN of U-BJ-1 EW-beam first drift peaks....286
Figure 7.93 Strain development for column intermediate reinforcement CE of U-BJ-1 NS-beam first drift peaks....286
Figure 7.94 Effect of axial load level on hysteretic performance of EW-beam for J-Failure specimens....293
Figure 7.95 Effect of axial load level on hysteretic performance of NS-beam for J-Failure specimens....293
Figure 7.96 Effect of axial load level on backbone curves for J-Failure specimens (EW-Beam/North Joint)....294
Figure 7.97 Effect of axial load level on backbone curves for J-Failure specimens (EW-Beam/North Joint)....294
Figure 7.98 Effect of axial load level on backbone curves for J-Failure specimens (NS-Beam/East Joint)....295
Figure 7.99 Effect of axial load level on backbone curves for J-Failure specimens (NS-Beam/East Joint)....295
Figure 7.100 Effect of axial load level on peak-to-peak stiffness degradation for J-Failure specimens....303
Figure 7.101 The effect of high axial load on joint shear stress-joint rotation backbone for J-Failure specimens....304
Figure 7.102 Crack pattern of north joint at peak joint shear strength of downward drift loading....304
Figure 7.103 Effect of axial load level on hysteretic performance of EW-beam for BJ-Failure specimens....305
Figure 7.104 Effect of axial load level on hysteretic performance of NS-beam for BJ-Failure specimens....305
Figure 7.105 Effect of axial load level on backbone curves for BJ-Failure specimens (EW-Beam/North Joint)....306
Figure 7.106 Effect of axial load level on backbone curves for BJ-Failure specimens (EW-Beam/North Joint)....306
Figure 7.107 Effect of axial load level on backbone curves for BJ-Failure specimens (NS-Beam/East Joint)....307
Figure 7.108 Effect of axial load level on backbone curves for BJ-Failure specimens (NS-

Beam/East Joint) 307
Figure 7.109 Effect of axial load level on peak-to-peak stiffness degradation for BJ-Failure specimens 308
Figure 7.110 Effect of axial load on joint shear stress-joint rotation hysteresis for BJ-Failure specimens 309
Figure 7.111 Crack pattern of EW beam and north joint at peak 6a (-3.6%) downward drift loading for: (a) Specimen U-BJ-1, (b) Specimen SP1, [120] 309
Figure 7.112 EW Beam steel strain distribution (a) Specimen SP1, [120], (b) Specimen U-BJ-1 310
Figure 7.113 Effect of joint aspect ratio on hysteretic performance of north joint for J-Failure specimens 314
Figure 7.114 Effect of joint aspect ratio on hysteretic performance of east joint for J-Failure specimens 314
Figure 7.115 Effect of joint aspect ratio on backbone curves for J-Failure specimens (EW-Beam/North Joint) 315
Figure 7.116 Effect of joint aspect ratio on backbone curves for J-Failure specimens (EW-Beam/North Joint) 315
Figure 7.117 Effect of joint aspect ratio on backbone curves for J-Failure specimens (NS-Beam/East Joint) 316
Figure 7.118 Effect of joint aspect ratio on backbone curves for J-Failure specimens (NS-Beam/East Joint) 316
Figure 7.119 Effect of joint aspect ratio on peak-to-peak stiffness degradation for J-Failure specimens 317
Figure 7.120 The effect of joint aspect ratio on north joint shear stress-joint rotation backbone for J-Failure specimens 318
Figure 7.121 Crack pattern of north joint at peak joint shear strength of downward drift loading 318
Figure 7.122 Experimental joint shear stress interaction counters in specimen B-J-1 322
Figure 7.123 Effect of loading history on hysteretic performance of EW-beam for J-Failure specimens 323
Figure 7.124 Effect of loading history on hysteretic performance of NS-beam for J-Failure specimens 323
Figure 7.125 Effect of loading history on backbone curves for J-Failure specimens 324
Figure 7.126 Effect of loading history on backbone curves for J-Failure specimens 324
Figure 7.127 Biaxial loading shear strength interaction for unconfined corner beam-column joints 325
Figure 7.128 Effect of loading history on joint shear stress-strain hysteresis for J-Failure specimens 325
Figure 7.129 Effect of loading history on north joint shear stress-strain envelope for J-Failure specimens 326
Figure 7.130 Effect of loading history on joint shear deformation contribution for J-Failure specimens 326
Figure 7.131 Effect of loading history on north joint face cracking for J-Failure specimens 327

Figure 7.132 Effect of joint aspect ratio on peak-to-peak stiffness degradation for J-Failure specimens 328
Figure 7.133 Effect of beam reinforcement ratio on hysteretic performance of EW-beam 332
Figure 7.134 Effect of beam reinforcement ratio on hysteretic performance of NS-beam .332
Figure 7.135 Effect of failure mode on backbone curves 333
Figure 7.136 Effect of failure mode on backbone curves 333
Figure 7.137 Effect of beam reinforcement ratio on joint shear stress-strain hysteresis 334
Figure 7.138 Effect of beam reinforcement ratio on joint shear stress-strain envelopes 334
Figure 7.139 Effect of failure mode on peak-to-peak stiffness degradation 335
Figure 7.140 Torsional cracking in specimen U-BJ-1 339
Figure 7.141 Crack pattern of slab in specimen U-BJ-1 340
Figure 7.142 Twisting angle of EW beam during its downward loading 341
Figure 7.143 Twisting angle profile along EW beam during its loading in specimen U-BJ-1 341
Figure 7.144 Twist deformation of NS beam during EW beam loading in specimen U-BJ-1 342
Figure 7.145 Twist deformation of EW beam during NS beam loading in specimen U-BJ-1 342
Figure 7.146 Torsional cracking of EW beam during NS beam(a) Downward loading (b) Upward loading in specimen U-J-2 243
Figure 7.147 Twisting angle profile along EW beam during its loading in specimen U-J-2 344
Figure 7.148 Twisting angle profile along NS beam during its loading in specimen U-J-2 344
Figure 7.149 Crack pattern of slab in specimen U-J-2 345
Figure 7.150 Twist deformation of NS beam during EW beam loading of specimen U-J-2 346
Figure 7.151 Twist deformation of EW beam during NS beam loading of specimen U-J-2 346
Figure 7.152 Torsional cracking of EW beam during NS beam downward loading in specimen U-J-1 347
Figure 7.153 Crack pattern of slab in specimen U-J-1 348
Figure 7.154 Twist deformation of EW beam for specimen B-J-1 349
Figure 7.155 Twist deformation of NS beam for specimen B-J-1 349
Figure 7.156 Torsional cracking of EW and NS beam (a) Downward loading (b) Upward loading in specimen B-J-1 350
Figure 7.157 Crack pattern of slab in specimen B-J-1 351
Figure 8.1 Joint axial failure during past earthquakes and laboratory tests: Caracas, Venezuela earthquake, Pagni [110], (b) Taiwan Chi-Chi 1999 earthquake, NISEE [106], (c) Izmit, Turkey earthquake of 1999, Engindeniz [41], (d) Izmit, Turkey earthquake of 1999, NISEE [106], (e) Exterior joint test, Pantelides et al. [116], (f) Corner joint test, Priestley and Hart [129], (g) Corner simulated joint test, Uzumeri [150] 356
Figure 8.2 (a), (b) Column bar side-sway axial failure mode in specimen U-J-1, (c) Bar

buckling axial failure mode in specimen U-J-2, (d) specimen U-BJ-1, and (e) specimen B-J-1 357
Figure 8.3 Global failures of specimens, B-J-1, U-J-1, U-BJ-1, and U-J-2 358
Figure 8.4 Deformed shape for longitudinal bars at loss of axial load capacity for column with (a) high axial load and (b) with low axial load, Sezen [137] 359
Figure 8.5 Plastic strength of longitudinal reinforcement in deformed configuration, Elwood and Moehle [39] 360
Figure 8.6 Bar axial capacity comparison for unconfined joints with axial failure 361
Figure 8.7 Axial load-drift ratio relationship at axial failure (or test termination) point for exterior and corner joints 364
Figure 8.8 Relation between axial load at axial failure and drift ratio 366
Figure 8.9 Relation between axial load at axial failure and drift at shear failure and at axial failure 367
Figure 8.10 Relations between joint shear strain and axial failure load 368
Figure 8.11 Relation between residual joint shear capacity (at axial failure) and maximum drift capacity reached prior to axial failure 369
Figure 8.12 Relation between residual joint shear capacity and axial failure load ratio 369
Figure 8.13 (a) Damaged column from 1999 Kocaeli earthquake, (b) Free body diagram of column at shear failure, (c) Model correlation to test results, Elwood and Moehle [39] 370
Figure 8.14 Development of shear-friction model for joint axial capacity based on experimental observation, (a) Proposed sliding mechanism, (b) Observed damage after axial failure, specimen U-J-1 371
Figure 8.15 Free body diagram for beam-column joint at the onset of axial failure 372
Figure 8.16 Relation between effective coefficient of friction and drift at axial failure 374
Figure 8.17 Linear trends of axial failure load-drift ratio relationship 377
Figure 8.18 Proposed empirical model (Eq. 8.21) for drift capacity at axial failure 378
Figure 8.19 Proposed empirical model (Eq. 8.24) normalized by concrete strength 379
Figure 8.20 Effect of concrete strength and column steel strength on drift capacity at axial failure 379
Figure 8.21 Correlation of the proposed axial capacity model (Eq. 8.18) to test results 380
Figure 8.22 Correlation of the proposed axial capacity empirical model (Eq. 8.21) to test results 381
Figure 8.23 Axial failure vulnerability of shear critical joints and columns 383
Figure 8.24 Fictitious frame for parametric study 383
Figure 8.25 Axial failure vulnerability, 2L/H=1.5 385
Figure 8.26 Axial failure vulnerability, 2L/H=2 386
Figure 8.27 Axial failure vulnerability, 2L/H=2.5 387
Figure 9.1 Centerline rigid joint model for concrete frame simulation 389
Figure 9.2 Recommended rigid joint model for linear concrete frame simulation, ASCE 41 [11] 390
Figure 9.3 Recommended joint strength-shear deformation backbone curve for unconfined beam-column joint nonlinear modeling, ASCE 41 [11] and ACI 369 [3] 390
Figure 9.4 Comparison between test and ASCE 41 nonlinear modeling backbone curve

parameters (heavy lines: ASCE 41 backbone curves, light lines: experimental backbone curves) 392
Figure 9.5 Rigid end zones for beam-column joint modeling. (ΣMnc, ΣMnb = sums of the nominal flexural strengths of the columns and beams, respectively, at the face of the joints.), ASCE/SEI 41[11] 393
Figure 9.6 Existing beam-column joint panel models: (a) Alath and Kunnath [5], (b) Biddah and Ghobarah [18], (c) Youssef and Ghobarah [157], (d) Lowes and Altoontash [87], (e) Altoontash [1], and (f) Shin and LaFave [140]. After Celik and Ellingwood [23] 395
Figure 9.7 Scissors joint model: (a) Model kinematics, FEMA 451 [45], (b) Drawback of missing joint translation, Theiss [142] 396
Figure 9.8 Proposed scissors model: (a) Explicit slip modeling, (b) Implicit slip modeling, (c) Slaving nodes.....397
Figure 9.9.a Proposed moment-rotation backbone curve for joint rotational spring model ..... …….....404
Figure 9.9.b Proposed shear stress-strain backbone curve for joint rotational spring model . ….....404
Figure 9.10 Lowes and Altoontash bond model [87]. 407
Figure 9.11.a Different cases of bond-slip parameters for J-Failure joints 409
Figure 9.11.b Different cases of bond-slip parameters for BJ-Failure joints.....409
Figure 9.12 Pinching4 OpenSees model, Lowes et al [1], after Theiss [88]. 410
Figure 9.13 Hysteretic material model, OpenSees [108]. 413
Figure 9.14.a NEES GC beam-column joint test simulation model, Option A 414
Figure 9.14.b NEES GC beam-column joint test simulation model, Option B 415
Figure 9.15 Simulation results for specimen U-J-2 using explicit and implicit slip rotation models 417
Figure 9.16 Simulation results of specimen U-J-2.....419
Figure 9.17 Simulation results of specimen U-J-1.....420
Figure 9.18 Simulation results of specimen U-BJ-1 421
Figure 9.19 Simulation results of Park [120] specimen SP4 424
Figure 9.20 Simulation results of Wong [155] specimen BS-L.....425
Figure 9.21 Simulation results of Wong [155] specimen B-S-L600 426
Figure 9.22 Simulation results of Park [120] specimen SP2 426
Figure 9.23 Simulation results of Pantelides et al. [116] specimens, (a) Unit 5, (b) Unit 6 427

LIST OF TABLES

Table 3.1 Design details and loading data for beam-column joint test database 43
Table 3.2 Limit state performance levels of exterior unconfined beam-column joint Clyde et al. [26] 65
Table 3.3 Limit states for isolated exterior joint based on joint shear deformation, Pampanin et al., [112] 68
Table 3.4 Average parameters for pre-1967 buildings, Moisre [104] 76
Table 5.1 Database of J-Failure exterior and corner unconfined joints 117
Table 5.2 Joint database for S-Failure exterior and corner joints and proposed bond model evaluation 121
Table 6.1 Test Parameters 139
Table 6.2 Test matrix and specimen design 143
Table 6.3.a Concrete mix design 158
Table 6.3.b Concrete strength of test specimens 158
Table 6.4 Steel reinforcement tensile test results 161
Table 6.5 Predicated joint shear strength for coefficients γj (psi0.5) for EW beam downward loading 165
Table 6.6 Speculated joint shear strains γs (rad.) for test specimens 166
Table 6.7 Predicted beam-tip displacements, in inches, for EW beam of test specimens .168
Table 6.8.a Predicted strength of test specimens for EW-beam downward loading 169
Table 6.8.b Predicted strength of test specimens for EW-beam upward loading direction .170
Table 6.9.a Displacement history amplitudes 199
Table 6.9.b Elastic" displacement cycles amplitudes 199
Table 7.1.a Summary of performance parameters of specimen U-J-1, EW direction, downward loading 228
Table 7.1.b Summary of performance parameters of specimen U-J-1, NS direction, downward loading 228
Table 7.1.c Summary of performance parameters of specimen U-J-1, EW direction, upward loading 229
Table 7.1.d Summary of performance parameters of specimen U-J-1, NS direction, upward loading 229
Table 7.2.a Summary of performance parameters of specimen U-J-2, EW direction, downward loading 247
Table 7.2.b Summary of performance parameters of specimen U-J-2, NS direction, downward loading 247
Table 7.2.c Summary of performance parameters of specimen U-J-2, EW direction, upward loading 247
Table 7.2.d Summary of performance parameters of specimen U-J-2, NS direction, upward loading 247
Table 7.3.a Summary of performance parameters of specimen B-J-1, EW direction, downward loading 266

Table 7.3.b Summary of performance parameters of specimen B-J-1, NS direction, downward loading....266
Table 7.3.c Summary of performance parameters of specimen B-J-1, EW direction, upward loading....266
Table 7.3.d Summary of performance parameters of specimen B-J-1, NS direction, upward loading....266
Table 7.4.a Summary of performance parameters of specimen U-BJ-1, EW direction, downward loading....287
Table 7.4.b Summary of performance parameters of specimen U-BJ-1, NS direction, downward loading....287
Table 7.4.c Summary of performance parameters of specimen U-BJ-1, EW direction, upward loading....288
Table 7.4.d Summary of performance parameters of specimen U-BJ-1, NS direction, upward loading....288
Table 7.5 Characteristic response measures for tested corner beam-column joints....289
Table 7.6 Displacement ductility factors for tested corner beam-column joints....290
Table 7.7.a Slab contribution to joint shear stress demand (bottom slab bar considered) ...337
Table 7.7.b Slab contribution to joint shear stress demand (bottom slab bar excluded) 337
Table 8.1 Database of unconfined beam-column joints with axial failure....365
Table 8.2 Parametric study matrix....382
Table 9.1 Nonlinear joint modeling parameters, ASCE 41 and ACI 369....391
Table 9.2 Pinching4 material model parameter definitions and Tcl command....411
Table 9.3 Pinching4 material model parameter....412
Table 9.4 Backbone curve parameters for simulated specimens, Option A....413

CHAPTER 1

INTRODUCTION

1.1 BACKGROUND

Beam-column joints in concrete buildings are key components to ensure structural integrity of building performance under seismic loading. Earthquake reconnaissance has shown the substantial vulnerability and structural damage that can result from inadequacy of beam-column joints. In some cases, failure of older-type corner joints appears to have led to building collapse.

Since the 1960s, tremendous research efforts have been devoted to develop tools to fulfill adequate seismic performance of components of concrete structures, including beam-column joints. These efforts included developing new design concepts along with new ductile details to provide sufficient deformability and satisfactory performance during earthquake excitations.

However, much less research attention has been paid to understanding the performance of existing substandard buildings not designed as seismically resistant, although they constitute the vast majority of building inventory in many countries. Concrete buildings constructed prior to developing ductile details in the 1970s normally lack joint transverse reinforcement. The available literature concerning the performance of beam-column joints without transverse reinforcement, denoted "unconfined" joints in this manuscript, is relatively limited. Most researchers focused on testing and modeling unconfined interior and exterior beam-column joints. There is very scarce available published test data concerning the seismic performance of unconfined corner beam-column joints.

1.2 PROBLEM STATEMENT

Most of the available literature on the seismic behavior of unconfined beam-column joints was dedicated to testing interior and exterior joints. However, most tests lacked the accuracy of representing the actual structure's realistic conditions, including the effect of slab presence, bidirectional seismic loading, axial load variation due to overturning moment during test, and realistic axial load level. Until today, scarce research efforts were directed to testing bi-directionally loaded corner joints in their realistic conditions, due to the associated testing difficulties. The effect of high axial loads on shear strength of unconfined joints is a very controversial topic. In addition, the axial capacity and potential to axial failure of unconfined

beam-column joints is still highly unknown. Moreover, shear strength models designed particularly for unconfined joints are not available in the literature. Finally, the available documents for assessment of existing buildings are believed to be quite conservative. These topics need thorough analytical and experimental investigation to be addressed and quantified.

1.3 RESEARCH PROGRAM OBJECTIVES

The current study aims to fill crucial unresolved gaps in the understanding and assessment of seismic performance and vulnerability of unconfined exterior and corner joints in existing reinforced concrete buildings. As such, the following objectives are targeted:

1. Conducting an extensive literature investigation on the available tests and analytical models concerned with seismic performance of exterior and corner unconfined beam-column joints.
2. Establishing a database for available unconfined exterior and corner beam-column joint tests.
3. Identifying and quantifying the key influence parameters and important failure modes in seismic performance of unconfined joints.
4. Experimental quantification of the effect of high axial loads on strength and deformability of unconfined corner joints through realistically designed tests.
5. Experimental investigation of the effect of bidirectional loading on seismic performance of unconfined corner joints.
6. Experimental verification of the effect of joint aspect ratio and beam reinforcement ratio on seismic performance of unconfined corner joints.
7. Experimentally exploring the effects of concrete slab and column intermediate reinforcement bars on seismic performance of unconfined corner joints.
8. Evaluating the accuracy of existing joint shear strength models when implemented to unconfined joints.
9. Evaluating joint seismic performance provisions in existing building assessment document ASCE/SEI 41-06
10. Developing simplified analytical tools (models) to estimate unconfined joint shear strength.
11. Introducing an expression for bond capacity of beam reinforcement in unconfined joints.
12. Experimental assessment of axial capacity of shear-damaged unconfined joints.
13. Introducing analytical means to quantify axial failure and drift capacity of shear-damaged unconfined joints.
14. Evaluation of collapse vulnerability due to axial failure of unconfined joints.
15. Developing a robust analytical finite element and constitutive models to resemble unconfined joint behavior in numerical simulations of reinforced concrete buildings

1.4 RESEARCH PROGRAM SCOPE

The current research is a part of National Science Foundation major research project through the Network for Earthquake Engineering Simulation (NEES). The project is called "*NEES Grand*

Challenge Project: Mitigation of Collapse Risk of Older Concrete Buildings". This project aims to develop loss estimates, through fragility functions, to inform policy makers about the seismic vulnerability of existing concrete buildings constructed before enforcing ductile detials (pre 1970s). Many of these buildings are believed to be at severe damage or collapse hazards during even moderate seismic actions. The scope of the current study fits within developing the necessary tools to understand, quantify and model the seismic behavior of unconfined exterior and corner joints for the ultimate purpose of estimating the seismic collapse risk of older buildings through nonlinear dynamic analysis simulations that lead to sound fragility functions (Appendix B).

Four major building blocks of the current research efforts to achieve the proposed objectives were conducted. The first block is performing an extensive literature investigation of the published research on unconfined beam-column joint tests and models leading to establishing a database of more than a hundred tests. Observations of the database's joint strength and deformability trends led to qualitatively, and quantitatively when possible, identifying the most important parameters and the effect of each parameter on the seismic performance of unconfined exterior and corner joints.

The second building block in the current research is surveying the available analytical models for strength and deformability assessment of unconfined joints, and upon identifying deficiencies in these models, developing new joint shear strength models, a bond capacity model and an axial capacity model designed and tailored specifically for unconfined beam-column joints.

The third block of this research is the experimental phase where four full-scale corner beam-column joint subassemblies, with slab included, resembling a corner bay of a prototype concrete building were built, instrumented, tested and analyzed. The specimens were tested under displacement controlled quasi-static regime that incorporated varying axial loads that resembled overturning seismic moments. The axial loads varied between tension and high compression loads reaching 50% of the column axial capacity.

Based on the experimental and analytical results of the above three blocks, the fourth building block of the current investigation comprises developing an analytical finite element component model to represent the behavior of unconfined beam-column joints in computer numerical simulations of concrete frames. In addition, the fourth block also includes a parametric study to assess the axial failure vulnerability of unconfined beam-column joints based on the developed shear and axial capacity models.

1.5 MANUSCRIPT ORGANIZATION

This research manuscript is organized in ten chapters. Chapter 2 presents an overview of the current state of knowledge on the behavior of unconfined joints including joint failures during past earthquakes, deficient joint details in older-type construction, mechanisms of joint shear resistance and theoretical considerations of joint seismic performance.

Chapter 3 explores, describes and criticizes the literature body to highlight the key experimental and analytical research efforts conducted worldwide over the last half century to assess the seismic performance of exterior and corner unconfined beam-column joints. Different joint failure modes are identified and presented in Chapter 3. The chapter paves the way to establishing a useful database of unconfined beam-column joints that experienced different failure modes. It also sets the stage to select the analytical models claimed by their authors to be applicable for unconfined joints for further investigation.

Chapter 4 is concerned with identifying and developing an understanding of the effect of key parameters influencing the seismic performance of unconfined exterior and corner beam-column joints. This task is performed through establishing a large joint test database and investigating, and quantifying when possible, the trends of joint strength and deformability measures under the collective and isolated effects of different design and test parameters.

In Chapter 5, different existing analytical and empirical shear and bond strength models are thoroughly investigated, criticized and evaluated for accuracy and suitability for unconfined joints. In addition, joint strength provisions of existing building assessment document ASCE/SEI 41-06 are evaluated in Chapter 5. As a result of shortcomings of the existing models when implemented to evaluate unconfined joints, two new joint shear strength models are developed. The first is a simplified analytical strut-and-tie model and the second is an empirical shear strength models. Moreover, a shear strength degradation model with ductility parameters is developed and integrated with the proposed shear strength models. In addition, an empirical bond model for pullout strength for exterior and corner deficient joints is proposed. Finally, existing unconfined exterior and corner joint limit state evaluation criteria are presented based on the proposed models.

Chapter 6 presents the details of the experimental program carried out at the *nees@berkeley* laboratories at the University of California, Berkeley to address the seismic performance of unconfined corner beam-column joints. The primary goal of the program was to provide a thorough understanding of unconfined corner beam-column joint seismic performance and vulnerability to shear and axial failures.

The test results and discussion of the current experimental investigation are presented in Chapter 7. The test results are represented by various seismic performance measures that are defined in this chapter. The test results and the effect s of test parameters on the seismic performance of corner beam column joints are also discussed in Chapter 7. Further evaluation of joint strength provisions of existing building assessment document ASCE/SEI 41-06 is conducted in Chapter 7 in the light of test results.

Chapter 8 deals with the problem of axial failure and axial capacity of unconfined exterior and corner joints. It presents a background about the state of knowledge and the importance of axial capacity estimation for unconfined joints. The chapter explores the observed axial failure modes during past earthquakes and laboratory tests, along with observed trends of drift ratio-axial load ratio relations. Two axial capacity models for unconfined joints based on theoretical and empirical bases and experimental observations are developed in Chapter 8. A parametric

study to assess the vulnerability of axial failure of unconfined joints in older-type buildings is also performed.

In Chapter 9, a review of the different methods currently in use for modeling shear deformations of unconfined beam-column joints in finite element numerical simulation of concrete frames is presented. A new constitutive model and finite element component model particularly designed to resemble unconfined exterior and corner joints are developed in Chapter 9. Finally, an evaluation of the accuracy of the existing and proposed joint simulation models in capturing the response of the current and literature joint test specimens.

Chapter 10 presents summary of the conducted research as well as concluding remarks drawn based on the experimental and analytical work performed in this research. Suggestions for future research are also presented in Chapter 10.

CHAPTER 2

UNCONFINED BEAM-COLUMN JOINTS: BACKGROUND

2.1 INTRODUCTION

This chapter presents an overview of the current state of knowledge on behavior of older-type beam-column joints lacking joint transverse reinforcement, which will be denoted as unconfined joints throughout this manuscript. This overview will include beam-column joint failures during past earthquakes as well as older-type details thought to contribute to such collapses. Mechanisms of shear resistance in beam-column joints are presented. Theoretical considerations of joint strength and deformation capacity are also included.

2.2 BEAM-COLUMN JOINT FAILURES IN PAST EARTHQUAKES

Past earthquake reconnaissance has identified distress and failure in beam-column joints with inadequate transverse reinforcement, including, in some cases, the appearance that the joint contributed to partial or total building collapse (Moehle and Mahin [103]). Examples of earthquakes that involved beam-column joint damage are El-Ansam, Algeria, 1980; Northridge, California, 1994; Tehuacan, Mexico, 1999; Izmit, Turkey, 1999; Athens, Greece, 1999; Chi-Chi Taiwan, 1999; and Haiti, 2010.

One example of partial building collapse due to beam-column joint failure is the Kaiser Permanente building, a pre-1970 moment frame building with anchored infill walls that collapsed during the 1994 Northridge earthquake. Photographs of the collapsed building (Fig. 2.1 through 2.3) show multiple corner beam-column joint failures with other framing elements intact, suggesting that failure of the beam-column joints may have triggered the building collapse (Hassan et al. [57]).

Figure 2.1(a) Structure collapse due to failure of deficient beam-column joints, Kaiser Permanente Building, Northridge earthquake, 1994 (photo credit, G. Edstrom)

Figure 2.1(b) Structure collapse due to failure of deficient beam-column joints, Moehle [96]

Figure 2.2(a) Partial Building Collapse due to failure of beam-column joints in the Izmit, Turkey earthquake of August 17, 1999, (b) close-up of third-level joint, (c) close-up of second-level joint, (Courtesy of NISEE, University of California, Berkeley [106])

In other cases, the role of joint failure in building collapse is less certain, as beam-column joint failures coexist with failures in other members. For example, the partial collapse of a concrete frame building (Fig. 2.1) during the 1999 Izmit, Turkey earthquake involved joints and columns. Similarly, the partial building collapse of a building (Fig. 2.3) during the 1999 Chi-Chi, Taiwan earthquake involved both column and joint failure. Determining whether failure occurred simultaneously in multiple component types, or whether failure in one component type initiated the collapse and led to failure of the other components, can only be determined through detailed study and, in some cases can never be determined with certainty.

Figure 2.3 Damage to partially collapsed 15-story building: beam-column failure in Chi-Chi, Taiwan, earthquake of Sep. 21, 1999, Uang et al. [149]

Other examples of joint distress and partial building collapses during past earthquakes are shown in Fig. 2.4 through 2.8. It is clear from these examples that joint distress and failure have been observed in several buildings following past earthquakes.

Figure 2.4 Collapsed building following Izmit, Turkey earthquake of Aug. 17, 1999, Said and Nehdi [130]

Figure 2.5 Corner beam-column joint damage in the Izmit, Turkey, earthquake of August 17, 1999, photo credit: Güney Özcebe, Engindeniz [41]

Figure 2.6 Joint failure and partial building collapse in the March 13, 1992, Erzincan, Turkey earthquake, Zahertar [158]

(a)

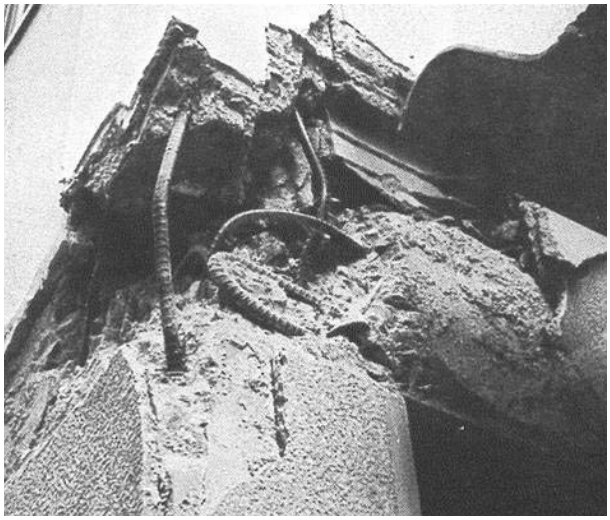

(b)

Figure 2.7 Severe corner joint damage,
(a) Caracas, Venezuela building damage after an earthquake, Pagni [110]
(b) Taiwan Chi-Chi 1999 earthquake, NISEE, UC Berkeley [106]

Figure 2.8 Severe exterior joint earthquake damage, Lehman [82]

2.3 GEOMETRY OF EXTERIOR AND CORNER JOINTS

Beam-column joints exist in buildings in different geometries and locations. The current study is concerned with typical floor exterior and corner joints (Fig. 2.9).

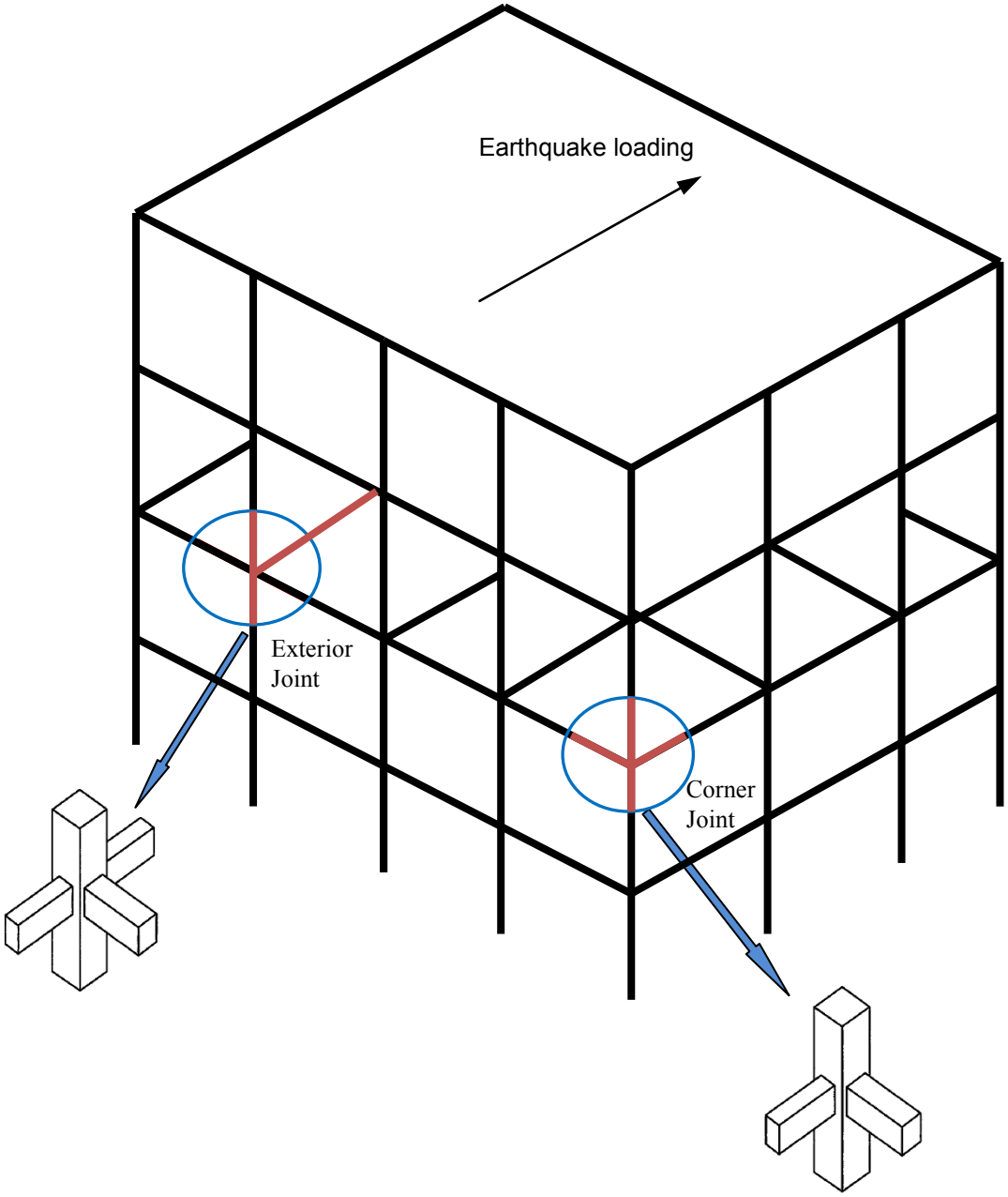

Figure 2.9 Exterior and corner joints in reinforced concrete frame building

2.4 OLDER-TYPE BEAM-COLUMN JOINT SEISMIC DEFICIENCIES

Ductile details for seismic resistance were first introduced in California in the 1960s. SEAOC Blue Book 1963 and 1965 presented the first ductile frame requirements including joint shear strength calculation and joint transverse reinforcement. However, these provisions were required only for buildings above 160 ft. (13 story) height, (Moehle [98]). As a result of the damage observed following 1967 Caracas earthquake and the 1971 San Fernando earthquake, the SEAOC Blue Book 1971 extended the ductile details requirement to buildings under 160 ft. height. SEAOC continued improving ductile detailing requirements throughout the 1970s paving the way to the development of the benchmark Uniform Building Code 1976 that marks the era of modern seismic ductile details. The UBC 1976 is formally taken as defining the change from non-ductile to ductile reinforced concrete construction, (Moehle [98]).

Since Blue Book 1960s and 1970s recommendations were not legally mandated before 1976, it is reasonable to consider most buildings built before the 1980s susceptible for deficient seismic details, particularly those built before 1971. The consciousness of the need for ductile details and capacity design concepts to mitigate seismic collapse risk has been much stronger in the western U.S. The rest of the U.S. construction lagged behind the 1976 UBC seismic requirements although there are many regions in the U.S. other than the west coast that are posing seismic risk.

According to data compiled by the Concrete Coalition [27], the number of pre-1980 concrete buildings in California is about 12000-15000 buildings. Most of these were built without ductile detailing as is commonly used in regions of high seismicity today. In regions of lower seismicity in the U.S. and elsewhere, buildings without ductile detailing continue to be built today. These buildings pose a threat to public safety and economic security in future earthquakes. Effective programs to mitigate this seismic risk currently are lacking. Research to better understand the risks posed by older-type concrete buildings can contribute to the development of effective risk mitigation programs.

The main deficiencies in older-type concrete buildings are inelastic mechanisms that are not suitable for ductile response and inadequate detailing of yielding components, including beam-column joints. The specific joint details and resulting deficiencies vary depending on the local construction practices. One of the most common deficiencies is absence of transverse hoops within the joint. Other common deficiencies include splicing longitudinal reinforcement within or adjacent to joints, insufficient anchorage of beam reinforcement within joints, use of plain reinforcing bars, and beam reinforcement bent away from the joint. Figures 2.10 and 2.11 show some of the deficiencies in older joints.

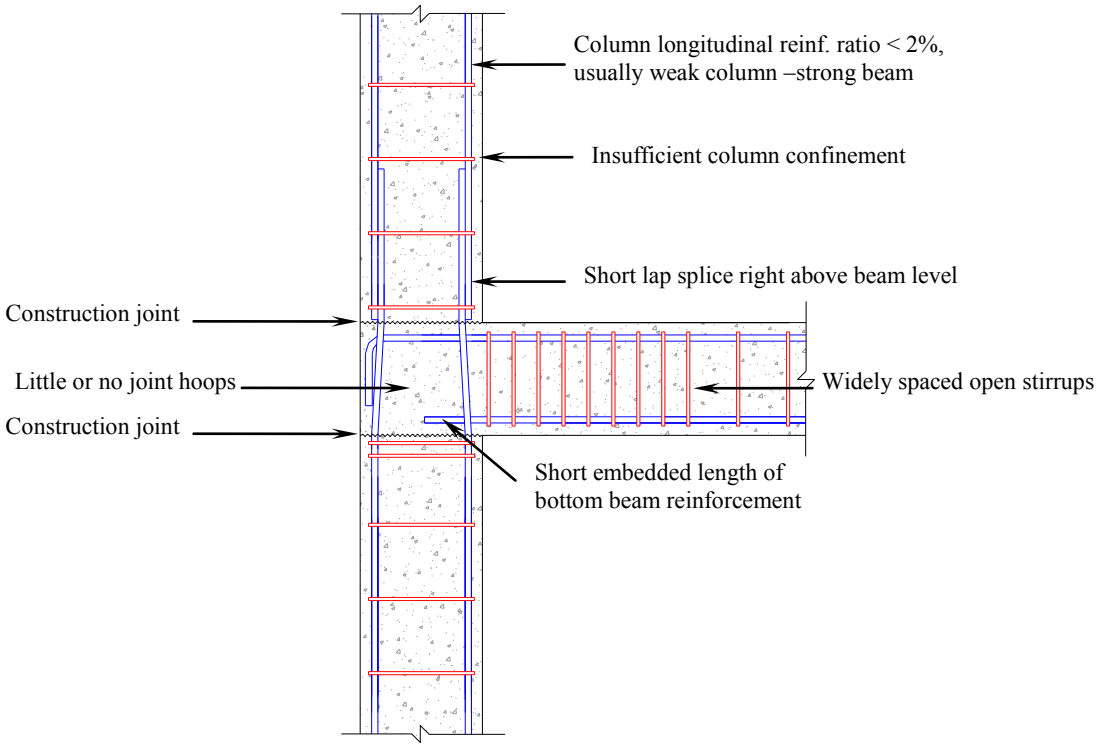

Figure 2.10 Pre-1970 U.S. typical construction details

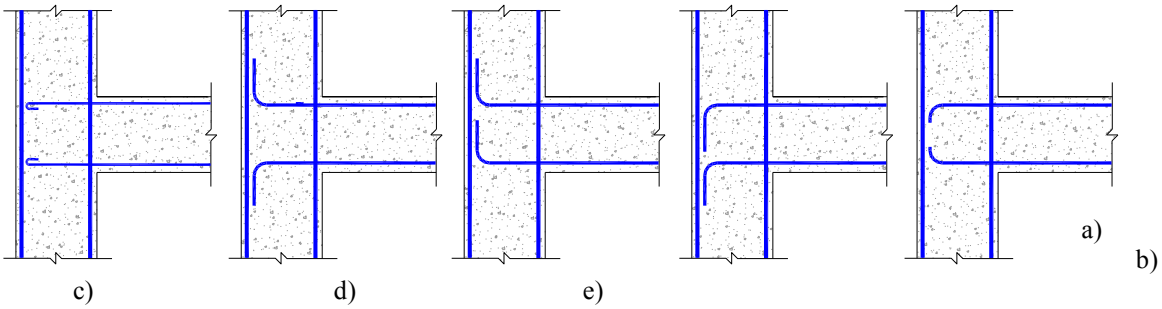

Figure 2.11 Common older-type joint construction. (a) plain unbent reinforcement, (b), (c), (d) bent-out beam reinforcement, (e) insufficient anchorage length

Several research studies have been conducted with the aim of better understanding behavior and design requirements for beam-column joints. As a result, new design concepts have been developed aimed at ensuring the soundness of the joint while developing the full inelastic capacity of members connected to the joint. These design concepts are commonly employed in the design of new earthquake-resistant concrete buildings. Fewer studies have emphasized behavior of older-type joints in existing buildings, especially in exterior joints and corner joints, which have suffered the most significant damage in past earthquakes.

2.5 MECHANICS OF EXTERIOR AND CORNER UNCONFINED JOINTS

2.5.1 Shear Strength Transfer Mechanisms

Under seismic excitation, beam-column joints are subjected to shear forces whose magnitudes typically are substantially higher than those within the adjacent framing beams and columns, [118]. If the demand exceeds the capacity, the joint may become the weak link that limits strength and deformation capacity of the structure.

Figure 2.12 displays the forces acting at the boundary of an exterior beam-column joint subjected to earthquake-type loading, along with its crack pattern and force transmission mechanisms. In exterior joints without transverse reinforcement, the forces are initially transmitted by bond bearing through secondary struts generated between beam and column reinforcement. Those struts are represented by the minor diagonal cracks in Fig. 2.12. After diagonal cracking in the joint core, the beam and column forces are transferred across the joint core primarily by a diagonal compression strut, (Park and Paulay [118]). At the exterior face of the joint, the strut is anchored in a node formed by the inside of the standard hook of the beam longitudinal reinforcement, which establishes the requirement that the hook be bent into the joint core as indicated in the figure. If the beam reinforcement are bent away from joint, a common practice in older construction, the required diagonal compression strut will not be stabilized by a node within, potentially leading to premature joint failure.

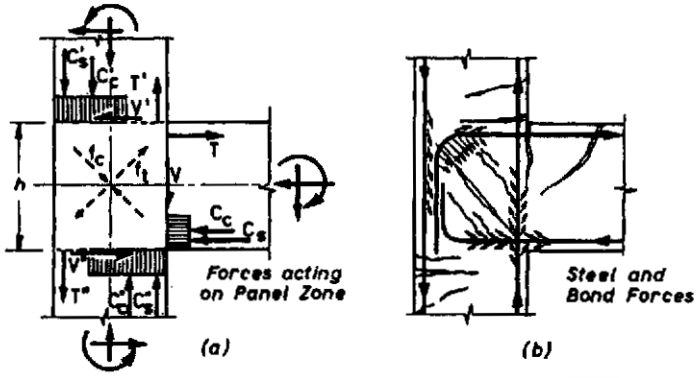

Figure 2.12 Exterior Beam Column Joint Subjected to Seismic Loading**,** Park and Paulay [4]

In a joint with bent-in beam reinforcement and transverse hoops, the two shear-resisting mechanisms are the truss mechanism and the strut mechanism shown in Fig. 2.13, where the joint hoops act as tension members for the truss mechanism. The truss mechanism is initially engaged along the straight segments of beam and column reinforcement due to the bearing of reinforcement ribs or in other words through bond strength. If bond strength is secured between beam's and column's reinforcement and concrete until reaching shear capacity of the joint, both strut and truss mechanisms could contribute to the strength. If bond strength deteriorates early, a very common case in joints due to the limited joint depth that does not allow full development length of beam reinforcement at their straight segment within the joint, the truss mechanism contribution to shear strength is nullified, giving the full shear resistance to the strut mechanism.

Since joint hoops are necessary to develop such truss mechanism, only secondary struts can be developed prior to bond strength deterioration in their absence.

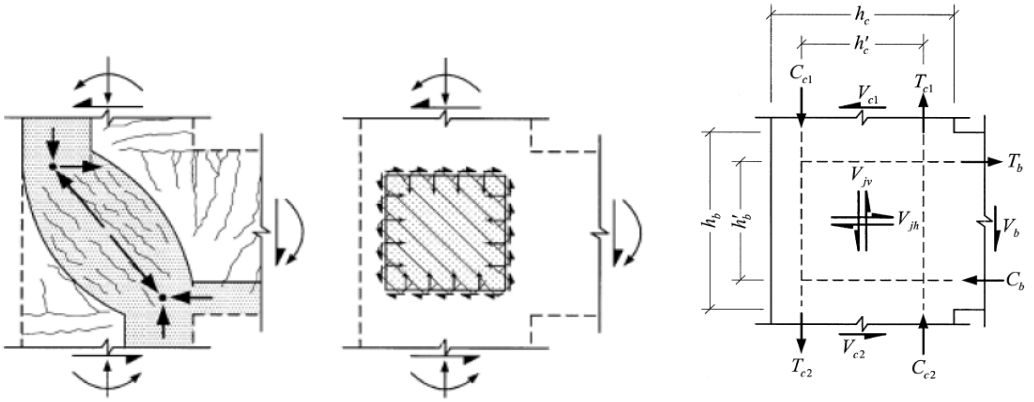

Figure 2.13 Exterior confined joint force transfer mechanisms (a) Diagonal strut (b) Truss, (c) Forces, Hwang and Lee [64]

Secondary struts have a "temporary role" in shear resistance until delivering the beam reinforcement tension force to be pivoted at the main diagonal joint strut. One argument to support this observation is the case when the straight segment of beam reinforcement within the joint has sufficient length to develop the full tension force to concrete through bond stress; this is likely if beam reinforcement size is relatively small. In this case, the main strut mechanism is "not needed"; hence, the joint could survive to high shear stresses with straight unhooked reinforcement. This contradicts past experimental results. Thus, the opinion of relying solely on the main strut mechanism, Fig. 2.14, to provide joint shear strength is adopted throughout this manuscript.

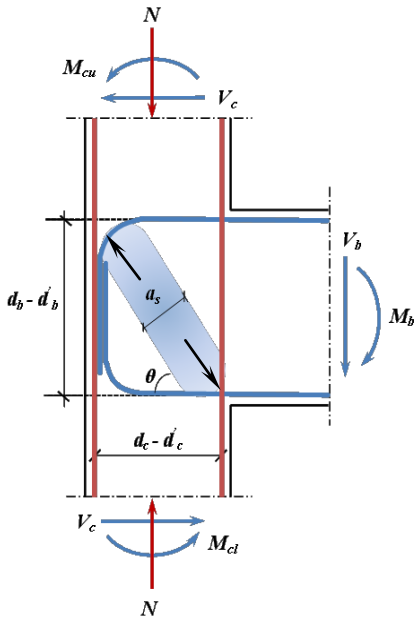

Figure 2.14 Exterior joint force transfer mechanism: diagonal compression strut

The diagonal strut within the joint exists in a region of transverse tension. Consequently, the effective compressive strength of the strut is less than the concrete compression strength as measured in uniaxial compression. Extensive diagonal cracking that leads to joint shear failure can result from high principal tension stresses associated with developing the capacity of the beam and columns connected to the joint. Cyclic loading in cracked concrete leads to repeated opening and closing of cracks, as well as movements parallel to open cracks. Grinding and progressive splitting due to uneven concrete bearing may lead to further disintegration of core concrete and subsequent loss of strength.

The key aspect in ensuring the safety and survival of the building during strong shaking, is to maintain joint shear strength until developing full plastic capacity of beams and columns. This can be done through designing the joint strength to be greater than the plastic capacity of any member it connects. In addition, it is necessary to maintain bond strength by proper detailing to ensure integrity and full anchorage in the joints. Special care has to be given to the bond of top beam reinforcement which is much more affected by concrete bleeding and segregation.

2.5.2 Joint Shear Strength Calculation

The joint shear stress is expressed by the concrete strength normalized coefficient γ:

$$\gamma = \frac{v_j}{\sqrt{f_c'}} \tag{2.1}$$

where the v_j is the nominal joint shear stress in each direction defined as:

$$v_j = \frac{V_j}{A_j} \tag{2.2}$$

where the V_j is the joint shear force in the direction considered and A_j is the effective joint area calculated per ACI 352-02 [2]. Chapters 4 and 5 present detailed derivation of joint shear strength parameters and calculations. Joint shear strength coefficient γ will be used throughout this manuscript to reflect joint shear strength.

2.5.3 Joint Principal Tension Stress

Some researchers, (Priestley and Hart [129], among others) used the principal tension stress as a measure of joint shear strength. The principal tension stress is given by:

$$p_t = \frac{-f_a}{2} + \sqrt{\left(\frac{f_a}{2}\right)^2 + v_{jh}^2} \tag{2.3}$$

$$f_a = \frac{N}{A_j} \tag{2.4}$$

and N is the column axial load with positive sign for compression, from which the principal tension is related to joint shear stress through:

$$v_j = p_t \sqrt{1 + \frac{f_a}{p_t}} \tag{2.5}$$

The appropriateness of using principal tension as an indicator for joint shear strength will be investigated in the subsequent chapters.

CHAPTER 3

LITERATURE REVIEW

UNCONFINED BEAM-COLUMN JOINT TESTS AND ANALYTICAL MODELS

3.1 INTRODUCTION

This chapter reviews past experimental and analytical research on seismic performance of exterior and corner beam-column joints without joint transverse reinforcement. Past tests include isolated exterior joints, exterior joints with transverse spandrels, and corner joints. Test details, test results, and discussion of the results are presented.

Several analytical models also are reviewed. Models for ductile connections include joint idealization models for computer simulation, finite element models, empirical models, strut-and-tie models, shear strength models, bond strength models, and shear and principal tension strength degradation models. Relatively fewer models apply to unconfined beam-column joints.

3.2 GEOMETRY OF JOINT TEST SUB-ASSEMBLAGES

The beam-column joint tests and analytical models presented in this chapter are concerned with exterior and corner joints. Figure 3.1 displays the test subassemblies used in the literature to model exterior and corner beam-column joints. The first type of exterior joints is the exterior joint with no transverse spandrels, denoted as isolated exterior joint. The second type is the exterior joint with two transverse spandrel beams (or just unloaded concrete transverse stubs) on both sides of the joint. The corner joint has obviously one transverse spandrel beam, while the corner-simulated joint has one transverse unloaded stub. In some cases, concrete slab is included.

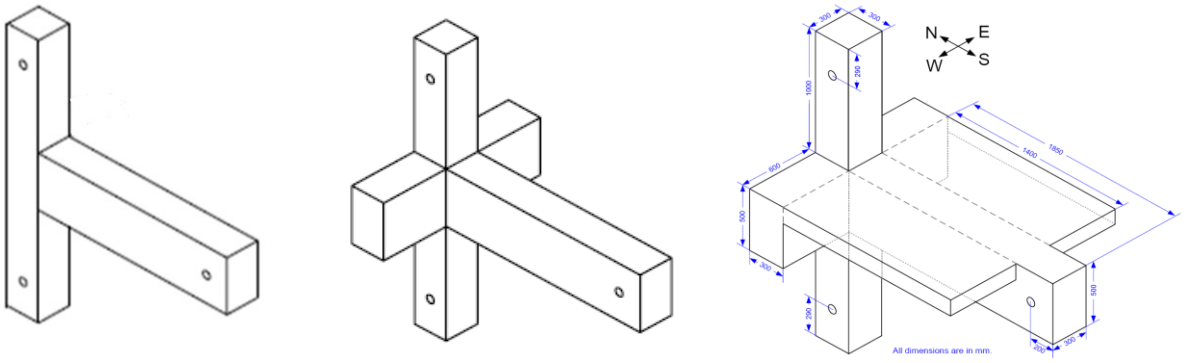

Figure 3.1(a) Isolated exterior joint and exterior joint with transverse stubs, Gogkoz [50]

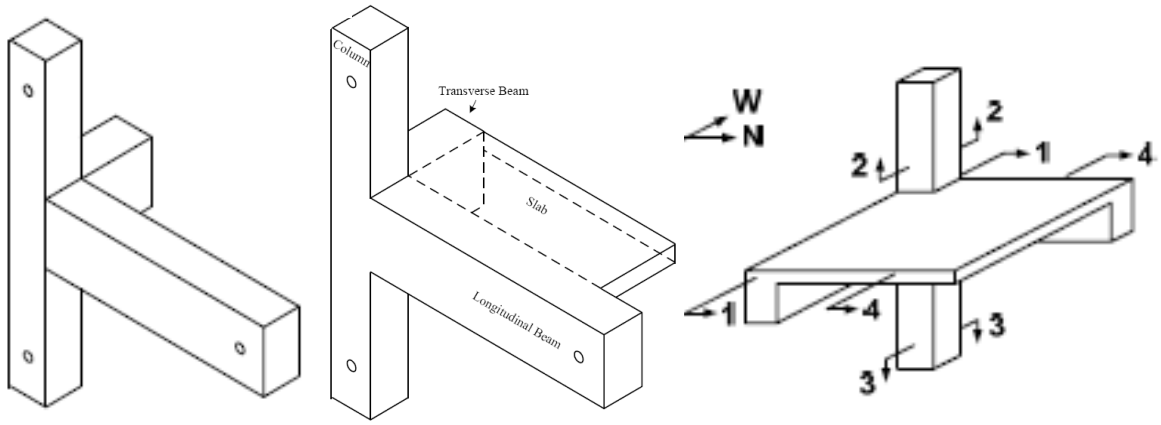

Figure 3.1(b) Corner-simulated and corner Joints, Topcu [143] and Engindeniz [41]

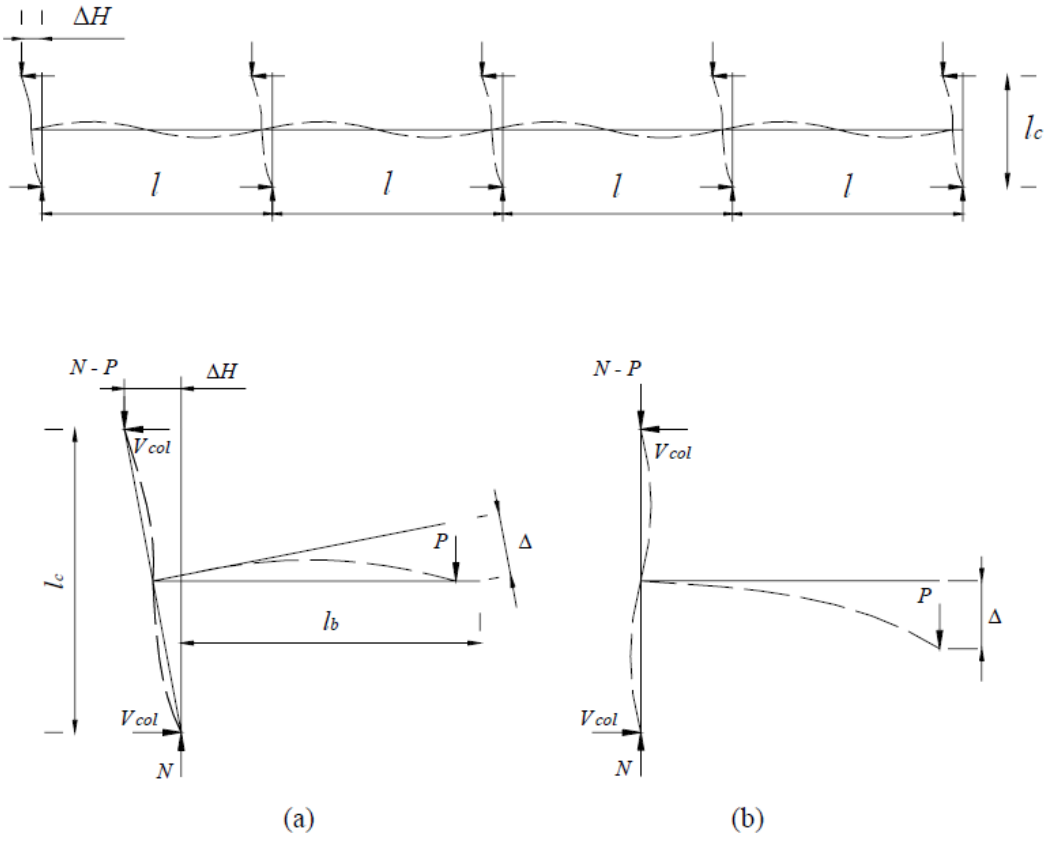

Figure 3.2 Deformed shape of actual and test idealized beam-column joint subassembly, [91]

Figure 3.2 depicts the deformed shape of a single story under the effect of seismic lateral load along with the beam-column joint subassembly's forces and deformations. Due to the practical difficulty associated with directly applying lateral loading to the column in the test laboratory and releasing its top end to sway (Fig. 3.2(a)), an idealized loading scheme is usually used instead to mimic lateral loading by applying the displacement reversals to the beam while pin restraining both column ends (Fig. 3.2(b)). This test configuration closely represents the realistic subassembly performance except for the P-Δ effect on column, which is not a concern in beam-column joint performance.

3.3 UNCONFINED BEAM-COLUMN JOINT FAILURE MODES

After a thorough investigation of the available literature on unconfined beam-column joint tests, presented in this chapter, the following modes of failure were identified:

J-FAILURE

In this failure mode, beams and columns are adequately reinforced to resist the seismic forces hence the unconfined joint becomes the weak link. Thus, joint fails in pure shear with no yielding of beam or column reinforcement. This type of failure is the most representative of the actual shear strength of unconfined joints. Hence, it is noteworthy to mention that the J-Failure is less ductile and is associated with relatively lower displacement ductility capacity.

BJ-FAILURE

The BJ-Failure is initiated by yielding of top or bottom beam reinforcement. Shortly after beam yielding, the joint experience severe shear cracking and subsequently joint shear failure. Compared to the above J-Failure, the BJ-Failure is more ductile since it involves beam yielding. As will be discussed later, joint shear strength is directly related to beam flexural capacity in this type of failure. The column experiences no yielding and the connection acts as a strong column-weak beam one.

CJ-FAILURE

In CJ-Failure, the connection is strong beam-weak column. This is a very common case in older non-seismic resistant construction. Thus, the failure is initiated by column yielding that penetrates joint core and triggers shear failure. The joint shear capacity is expected to be less than that of J-Failure due to softening of joint concrete strut due to column reinforcement yield penetration. This failure mode however needs more test results to be confirmed, [132]. It is likely to have global instability due to excessive column deformation after yielding before final joint shear failure.

BCJ-FAILURE

This mixed failure mode combines CJ and BJ, in which beam and column experience simultaneous yielding followed shortly by joint shear failure. Similar to BJ and CJ failure modes, the joint shear strength is less than that of direct J-Failure counterpart. Some previous tests reported this failure mode, [16].

S-FAILURE (ANCHORAGE FAILURE)

This failure mode is resulted from the bond slip failure (pullout) of beam bottom reinforcement, which has a short unhooked embedment length indicted in Fig. 2.10. This failure mode jeopardizes the strength of the connection since the full joint shear capacity is not engaged. The bottom beam reinforcement is insufficiently embedded within the joint; hence, the joint strut is not formed in one loading direction resulting premature failure of the whole connection. There could be global instability without actual shear failure in the joint in case of excessive beam rotation resulting from pullout deformation.

B-FAILURE AND C-FAILURE

These two failure modes involve flexural yielding of beam or column undergoing large inelastic deformation until ultimate rotational capacity of beam or column without joint shear failure. This mode is likely when beam or column flexural capacity is very poor compared to joint shear strength. This mode of failure is out of the scope of this study.

AXIAL FAILURE

It is evident from previous tests ([129] and [150]) that axial failure can occur after joint shear failure. Few tests have continued to the point of axial failure of the joint. From these tests, it appears that exterior and corner joints may be susceptible to axial failure under very large drifts or under high axial loads. However, additional experimental data is needed to draw definitive conclusions about axial joint failure and axial residual capacity after shear failure in exterior and corner unconfined joints.

Figure 3.3 depicts a speculated representation of exterior unconfined beam-column joint failure modes and the relative shear strength and ductility associated with each mode. The figure shows a backbone representation of joint shear strength parameter and engineering demand parameter (EDP), such as drift or ductility. More details about the influence of different design parameters on the failure modes are presented subsequently in this chapter and in Chapter 4.

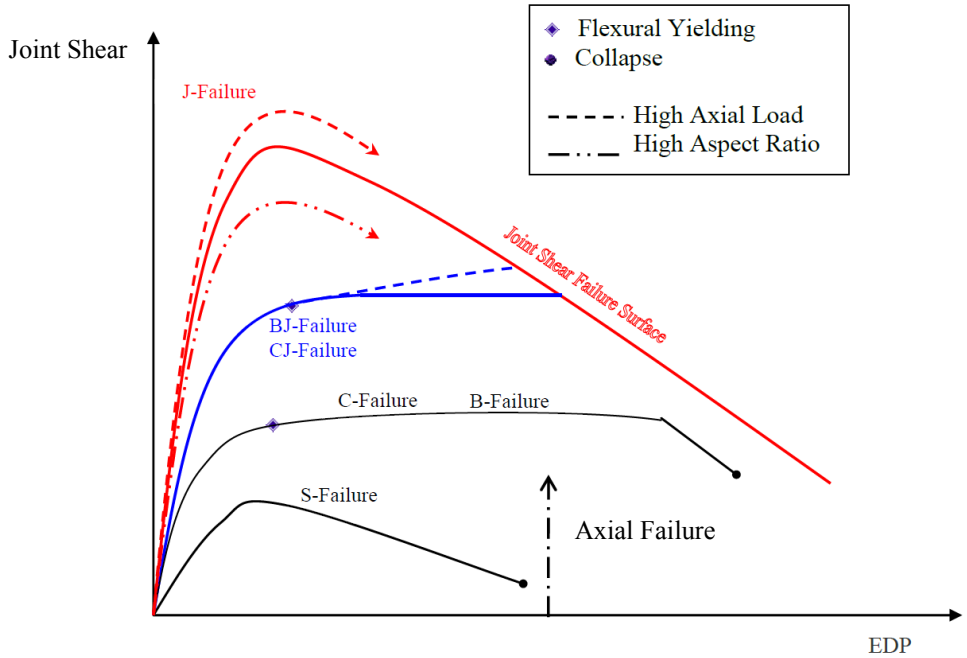

Figure 3.3 Modes of failure of unconfined beam-column joints

3.4 EXTERIOR BEAM-COLUMN JOINT TESTS

Among the limited number of past studies on seismic performance of unconfined beam-column joints, those on interior and exterior joints are the most numerous.

The earliest study was reported in Hanson and Conner [53] in 1965. They tested seven exterior beam-column joints. Five specimens contained transverse reinforcement in various amounts, while two specimens (V and V-A) had no joint transverse reinforcement. The principal variables of their study were column size, column load, and amount of joint transverse reinforcement. Figure 3.4 shows test specimen details, while Table 3.1 lists test design parameters and details.

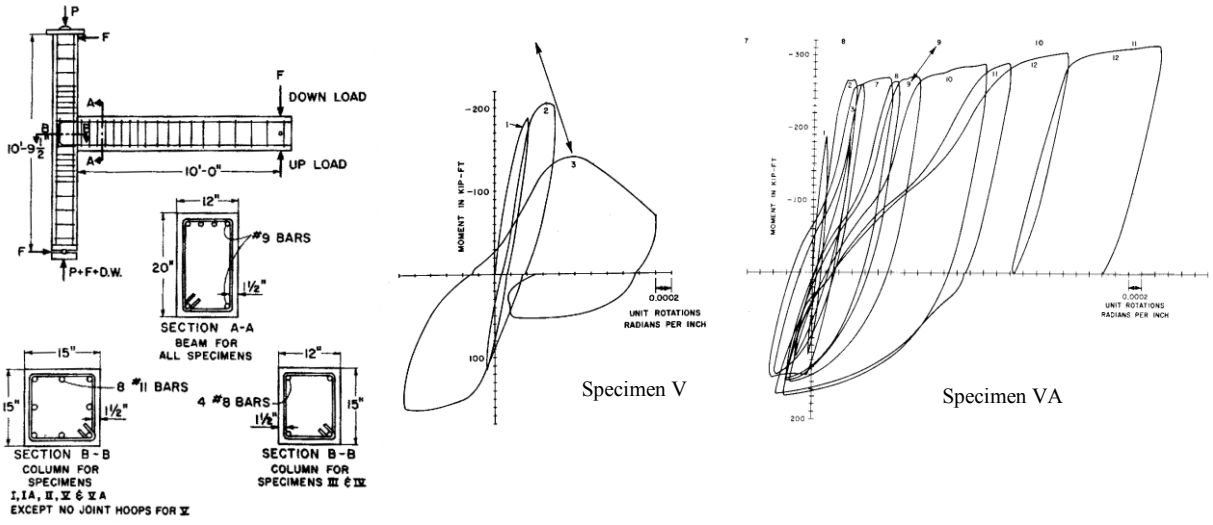

Figure 3.4 Details of test specimens and moment rotation hysteretic response, Hanson and Connor [53]

For the two unconfined joints, it is noted that the joint concrete strength was similar to beam concrete strength (3300 psi) in specimen V, whereas it was similar to column concrete strength (5420 psi) in specimen V-A. In addition, specimen V was constructed without transverse beam stubs whereas specimen V-A had unloaded transverse concrete stubs on both sides of the joint to simulate the confining effect of transverse beams. The loading sequence was uniaxial in both specimens. The axial load level was $0.86 f_c' A_g$ for specimen V and $0.54 f'_c A_g$ for specimen V-A. The axial load is relatively high for an exterior connection in a real structure. Furthermore, axial load did not vary significantly during testing as it might in a real building during earthquake shaking.

Test specimen V performed relatively poorly, reaching only 89% of the computed ultimate moment strength, with failure occurring during the third cycle of moderate loading (Figure 3.4). In contrast, specimen V-A developed the computed beam moment strength and survived numerous cycles to relatively large deformation with only minor cracks in the joint. The test was

terminated when displacements reached displacement capacity of the test setup. Obviously, the failure modes of joints V and V-A were J and BJ, respectively.

The authors recommended using joint hoops in isolated exterior beam-column joints. They also stated that hoops are not required for exterior joints having sufficient concrete strength and having at least three sides confined by beams of equal depth. They recommended the use of joint hoops in corner joints until further tests determine the need for them. We here note that the lack of load on the transverse beams may have influenced the observed beneficial effect of the beam stubs.

Hanson and Conner [54] reported additional tests on unconfined joints, including exterior joints loaded in the plane of the spandrel beam and one test on a corner joint. The test specimens included a transverse stub on one side of the joint (Figure 3.5).The axial load level of all specimens was $0.86 f_c' A_g$ constantly applied throughout the test.

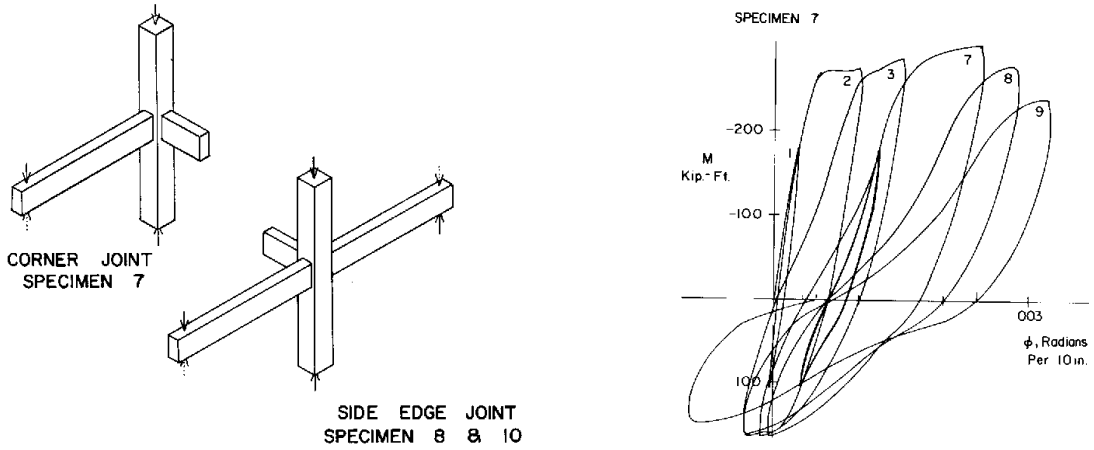

Figure 3.5 Test specimens, moment rotation hysteretic response for corner joint, Hanson and Connor [54]

The authors pre-loaded the concrete stub of specimen 7 beyond the cracking limit but prior to beam reinforcement yielding to simulate a cracked stub-joint interface section in a building. The aforementioned cracking load was removed before lateral-load testing. The quasi-static loading protocol subjected the test specimens to 9 cycles, 5 of which drove the beam into inelastic range. They measured beam plastic hinge rotation, joint shear distortion, beam deflection, strains in all reinforcement, joint shear strength, and beam moments.

Specimen 7 was able to develop beam flexural strength with diagonal cracking through the joint appearing in the first load cycle. The joint withstood cycles to around 2.5 times the yield rotation, followed by extensive joint cracking and degrading strength in subsequent cycles (Figure 3.5). This result suggests the potential inadequacy of unconfined beam-column corner joints to withstand severe inelastic loading cycles.

Uzumeri [150] reported tests on two corner joints with transverse stubs on one side and one isolated exterior joint loaded in the plane of the spandrel. Transverse stubs were loaded continuously during the test. The column axial load ratio was $0.51f'_cA_g$ throughout the test. The test protocol was unidirectional, with details of the history determined subjectively as the test proceeded. The report states that loading history has no effect on strength of different specimens, but significant effect on stiffness.

In contrast with the finding of Hanson and Conner [53], Uzumeri [150] reports that the three unconfined joints (one exterior and two corner joints) behaved similarly. No confinement effect of transverse stubs in corner joints was observed except for increasing slightly the anchorage capacity of beam reinforcement. All three specimens sustained joint failure without yielding in the columns and with slight yielding in the beams. This can be interpreted as BJ-Failure mode. The author concludes that axial load is helpful in the early loading stages and detrimental in the later stages of loading. Furthermore, the assumption of rigid beam-column connections in structural analysis is invalid. It was recommended to measure the anchorage length of beam reinforcement into column starting from the column longitudinal reinforcement rather than from column face because of ineffectiveness of the cover concrete.

National Center for Earthquake Engineering Research (NCEER) sponsored an initiative in 1988 to better understand seismic performance of older concrete frames, including tests of thirty four full-scale beam-column joints. Fourteen of these specimens were exterior ones tested by Beres et al. [16, 17]. The specimens were designed to represent pre-1971 construction in the eastern U.S. Characteristics were: no joint hoops, short embedded length of bottom beam reinforcement, column lap splice just above joint in the maximum moment region, and construction joints above and below joints. Transverse stubs on both sides were included in some specimens, with stubs prestressed to represent the confining effect of compression zone in spandrel beams. Two of the 14 joints had light transverse reinforcement (volumetric ratio of 0.37), while the rest were unconfined. Table 3.1 lists the design parameters and Fig. 3.6 shows joint details. Key test variables were column axial force, transverse confinement, spandrel beam confinement effect, and amount of reinforcement in the columns. Column axial load was constant at $0.11f_c'A_g$ in some specimens and $0.39f_c'A_g$ in others. The loading was a uniaxial quasi-static displacement-controlled scheme. Beams were preloaded with gravity load and loading history started from that load as an initial value.

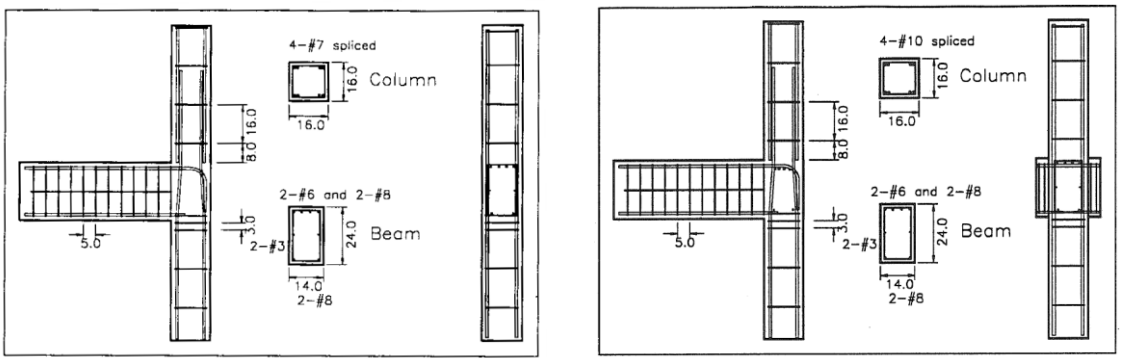

Figure 3.6 Details of test specimens with and without beam stubs, Beres et al. [17]

Failure of test specimens was mainly attributed to pulling out of bottom beam reinforcement combined with diagonal shear cracking followed by splice failure in the top column, spalling of joint concrete cover due to the prying action of hook anchoring the beam top reinforcement. Lower columns were intact while some upper columns experienced shear failure. Specimens with stubs and those without stubs showed similar failure mechanism, although the ones with stubs degraded less rapidly and were less severely cracked. Applying higher axial loads resulted in strength increase of 15-25% and more gradual strength degradation. However, the specimens with higher axial load experienced a very sudden failure at a relatively low rotation value. Peak strength for exterior specimens was reached at interstory drifts of 1.5-2.7%. The authors noted that the transverse beams did not increase joint strength, in contrast to the increase indicated by ACI-352 (1976). They suggested that this may have been because occurrence of other failure mechanisms pre-empted possible influence of transverse confinement. Figure 3.7 indicates hysteresis loops for a typical exterior specimen.

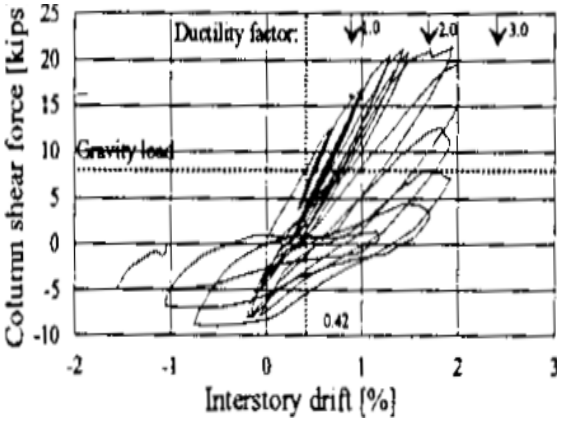

Figure 3.7 Hysteresis response of typical exterior specimen, Beres et al. [17]

Clyde et al. [26] report tests of four half-scale exterior beam-column joints without transverse reinforcement and without transverse beams/stubs. Table 3.1 lists test details. Beams and columns had sufficient flexural strength such that failure was initiated in the joint. Test parameters included column axial load ($0.10f_c'A_g$ and $0.25f_c'A_g$). Loading history was applied uni-directionally.

The joints sustained shear failure after initially yielding the beam longitudinal reinforcement. The higher axial load resulted in 8% increase in joint shear strength. The average displacement ductility of the specimens with $0.1f_c'A_g$ column axial load was 2.7 as compared with 1.6 for the specimens with $0.25f_c'A_g$ column axial load. Figure 3.8 shows hysteresis measured at different axial load levels.

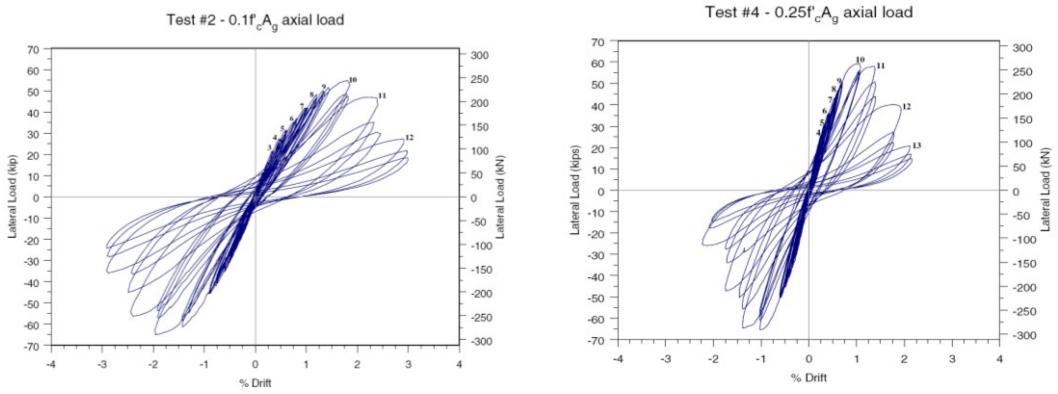

Figure 3.8 Hysteresis response for specimens with low and high axial loads, Clyde et al. [26]

Pantelides et al. [116] subsequently reported an additional six tests of full-scale exterior beam-column joints without transverse reinforcement and without transverse stubs/beams. Test variables were axial load and anchorage details of beam bottom reinforcement. Two axial load levels were investigated: $0.10f_c'A_g$ and $0.25f_c'A_g$. Although intended to maintain axial load constant through the test, some variation occurred. Three anchorage details were tested: straight beam bottom bars with short embedded length into the joint, straight beam bottom bars continuing to the far side of the joint, and bent up beam bottom bars (Fig. 3.9). Table 3.1 lists design parameters. Beam and column reinforcement ratios were relatively high to force shear failure in the joint.

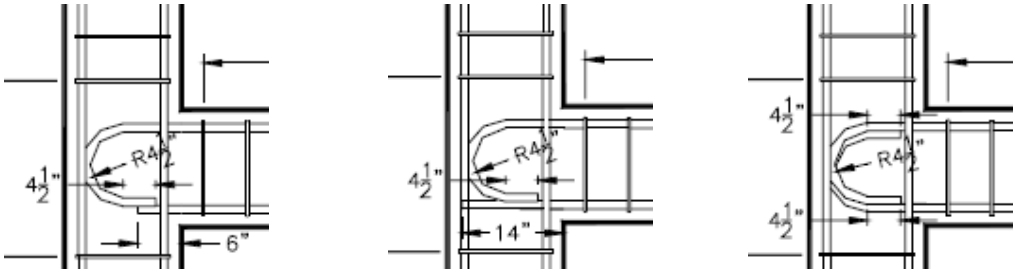

Figure 3.9 Unconfined isolated exterior joint details, Pantelides et al. [116]

Three primary failure modes were observed. These are bond-slip failure in the joints with short embedded length of beam bottom bars, joint failure following beam yielding in three other specimens, and joint failure without beam yielding in one specimen. The specimen with short embedded bottom beam bars sustained bond-slip failure, precluding development of the joint shear strength for loading in one direction (Figure 3.10). Increasing the axial load increased the strength by 35% for specimens with insufficient beam bar length inside the joint. It enhanced joint shear strength by about 15% for joints with hooked or sufficiently embedded beam bar within the joint. However, higher axial load resulted in reduced deformation capacity. Specimens

sustaining joint shear failure had notably lower deformation capacity than specimens with bond-slip failure. Loading of the four joints with the joint shear failure mode was continued until axial failure, which was at drift levels beyond 5%. The two joints with the bond-slip failure mode failed due to loss of lateral load capacity.

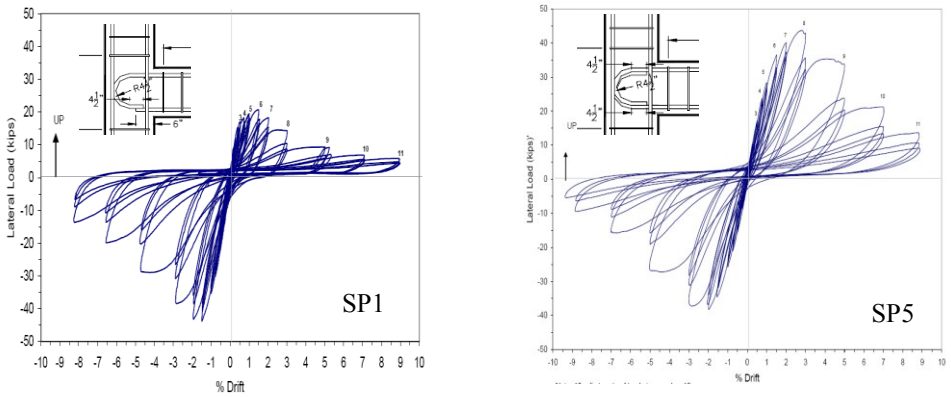

Figure 3.10 Isolated exterior joint details, Pantelides et al. [116]

Wong [155] reports tests of 11 isolated exterior unconfined beam-column joints (Fig. 3.11). The main test parameters were: axial load, column intermediate longitudinal reinforcement, beam reinforcement anchorage detail, presence of column lap splice, and joint aspect ratio (beam-to-column depth ratio).

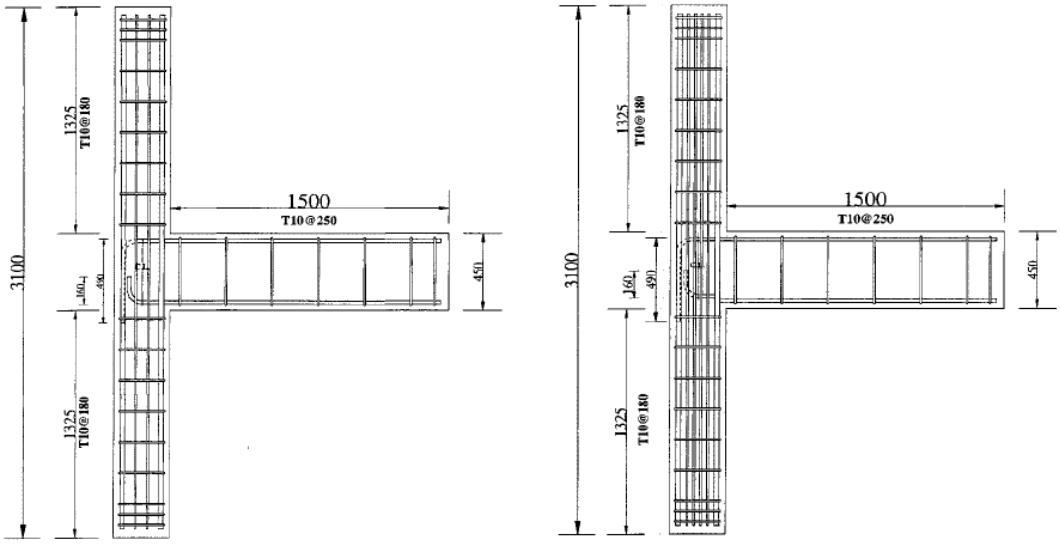

Figure 3.11 Isolated exterior joints with intermediate column reinforcement, Wong [155]

Increasing axial load from $0.03f_c'A_g$ to $0.15f_c'A_g$ resulted in slight increase of joint shear strength. Two failure mechanisms were observed: joint failure before beam yielding (J-Failure) or after beam yielding (BJ-Failure). Increasing the joint aspect ratio by increasing beam depth resulted in decreased joint shear strength. Specimens with intermediate column longitudinal reinforcement were stronger than those without intermediate bars (24% increase in shear strength). However, further increasing the amount of intermediate column bars had only a slight effect, implying a threshold limit. The column lap splice had no effect in these tests, as the columns were sufficiently strong to preclude flexural yielding.

Gogkoz [50] tested two exterior joint subassemblies with transverse stubs on both sides. One specimen included a slab. Reinforcement details were typical of pre-1970 U.S. details (Fig. 3.12).

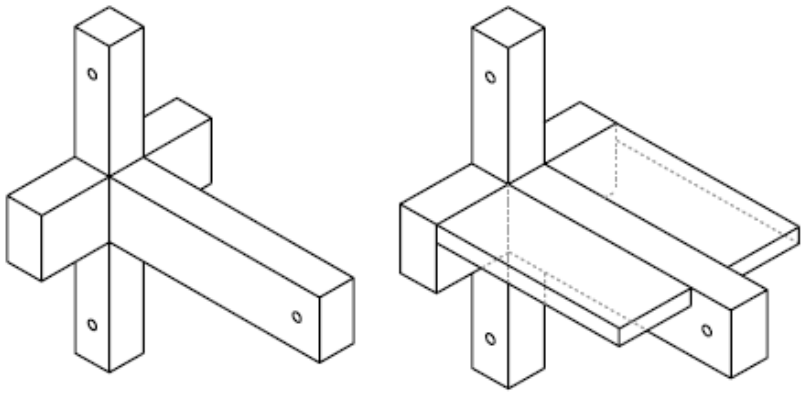

Figure 3.12 Exterior specimens with and without slab, Gogkoz [50]

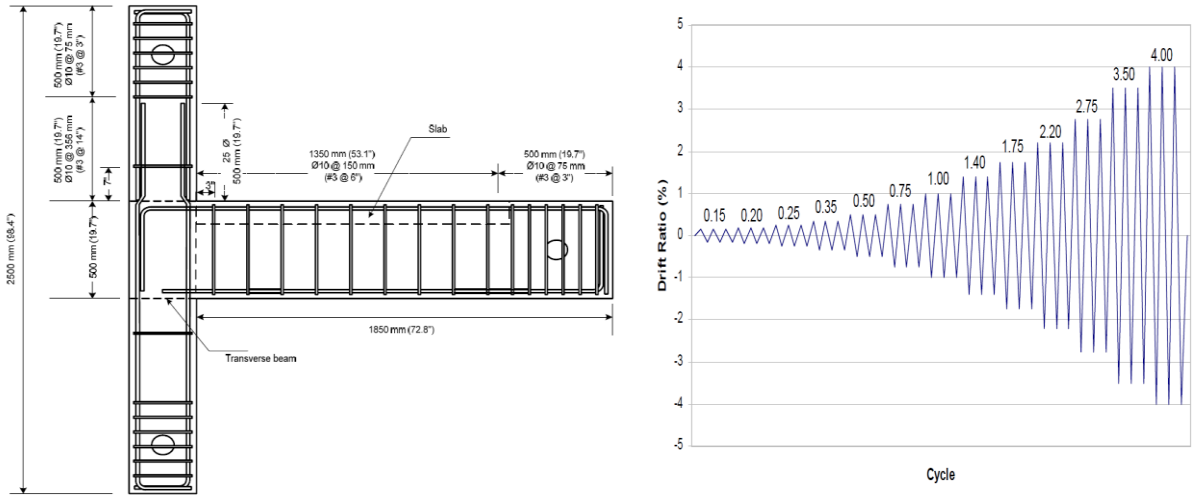

Figure 3.13 Test specimen details and loading history, Gogkoz [50]

Results were compared with results of previously reported companion specimens without transverse beam stubs; a specimen with stubs (US-E-Control) has similar stiffness but higher strength and deformation capacity than a specimen without stubs (US-C-Control) (Fig 3.14). Introducing the slab (US-ES-Control) significantly increased stiffness and strength.

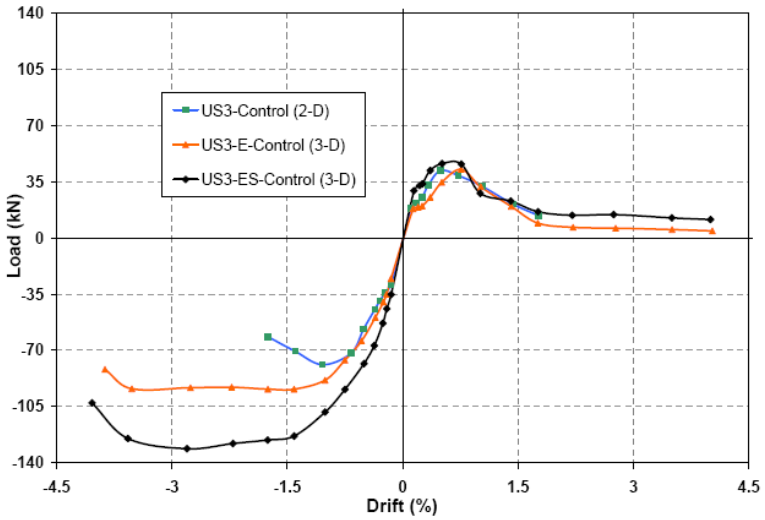

Figure 3.14 Backbone curves of test specimens, Gogkoz [50]

Barnes and Jigorel [13] reports two exterior beam-column joints without transverse reinforcement but with two sided transverse stubs and slab. The intended mechanism was column yielding, simulating a common condition in older buildings. Column axial load was $0.40f_c'A_g$ for Test 1 and $0.20f_c'A_g$ for Test 2. Figure 3.15 displays the load-displacement response. The nominal joint shear stress coefficient reached 18.9 and 21 for smaller and higher axial load specimens, respectively. The test specimen with higher axial load degraded somewhat more rapidly.

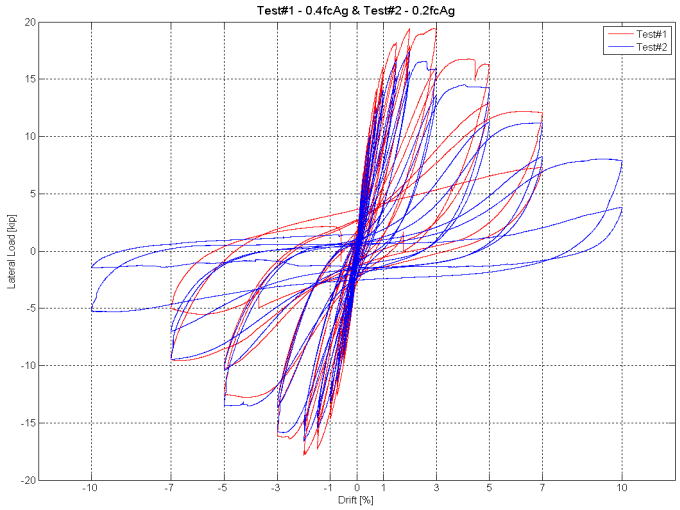

Figure 3.15 Hysteretic response of test specimens, Barnes et al. [13]

Hakuto et al. [51] reports tests of two exterior beam-column joints without transverse stubs/beams. Unit O6 had one joint hoop with beam longitudinal bars hooked into joint, while unit O7 had one joint hoop with beam longitudinal bars hooked outside the joint. Table 3.1 lists design parameters. The column had no axial load. Figure 3.16 illustrates the hysteresis response and failure modes. The early degradation of joint O7 with bent-out hooks is evident. Apparently, the joint could not develop an effective joint diagonal strut to resist joint shear. Instead, an apparent strut pushed against the column longitudinal reinforcement developing splitting cracks along the column reinforcement, later connected to diagonal joint cracks. The flexural strength of beam was not reached because of premature joint failure. In contrast, unit O6 demonstrated stable and ductile response (ductility factor of 12) with very little degradation in flexural and shear strength. This suggests the importance of bending the beam longitudinal reinforcement into the joint rather than away from the joint.

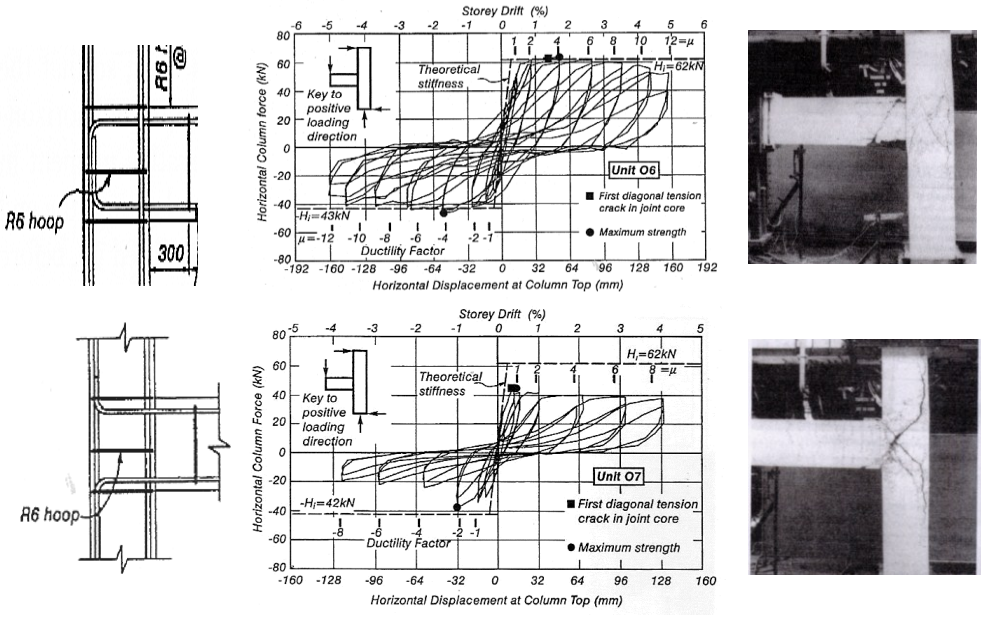

Figure 3.16 Hysteresis response and failure modes of units O6 and O7, Hakuto et al. [51]

Ghobarah and Said [48] carried out an experimental investigation into the behavior of FRP retrofitted exterior seismically substandard beam-column joints. Their control specimen was isolated bare exterior joint without transverse reinforcement. The behavior of their control specimen emphasized the previous results of high vulnerability of unconfined exterior beam-column joint, as it failed in a classical shear failure manner experiencing significant strength degradation at displacement ductility factor of 2 and almost lost its gravity load capacity at ductility factor of 2.5.

Pampanin et al. [113] reports tests of two 2/3-scale exterior beam-column subassemblies without transverse stubs/beams. Deficiencies included using smooth reinforcement, absence of joint hoops, and absence of adequate beam longitudinal reinforcement anchorage. Reinforcement

and concrete had lower strengths characteristic of older construction. Longitudinal beam reinforcement ratio varied between the two specimens. Axial load varied as a function of the lateral force, starting at $0.10f_c'A_g$ and varying by 40-50% throughout the test. Figure 3.17 shows details of specimens while Table 3.1 lists design parameters.

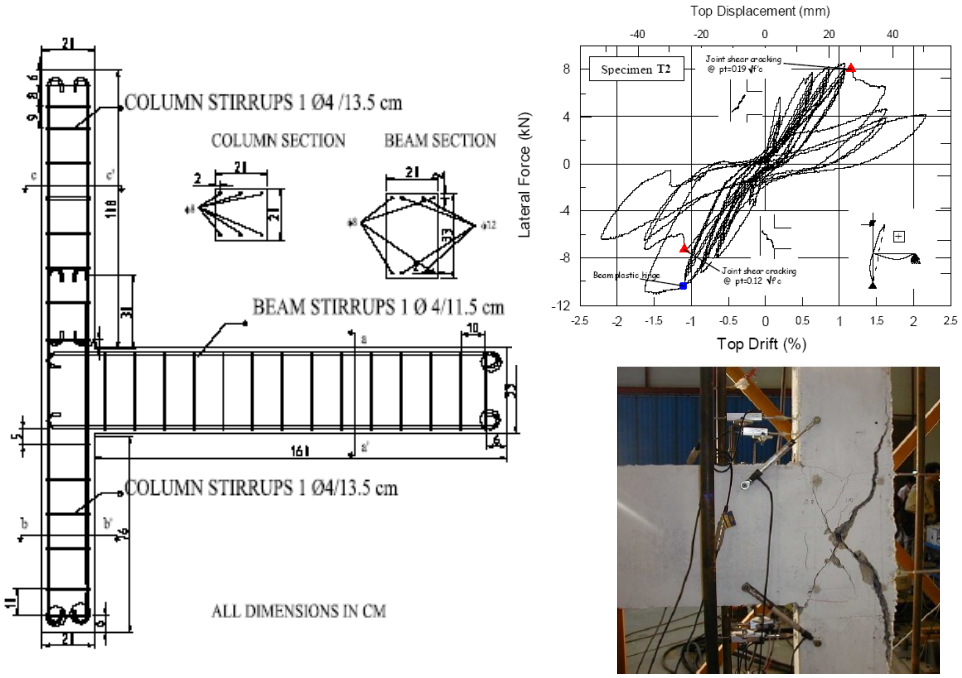

Figure 3.17 Details and results of exterior joint tests, Pampanin et al. [113]

The two specimens experienced what was termed a "brittle hybrid failure mechanism: sudden and severe joint shear damage after the first diagonal crack combined with slippage of longitudinal beam reinforcement within the joint and concentrated compressive force at the end-hook anchorage." This led to spalling of a concrete wedge causing brittle local failure and loss of bearing load capacity. This combined action inhibited any alternative source of shear transfer mechanism in the joint. Significant stiffness degradation took place during the test as seen in Fig. 3.17. Figure 3.18 illustrates development of concrete wedge and the alternative damage mechanisms in different exterior joint details. Similar to joints with bent-out longitudinal beam reinforcement, these joints could not effectively develop a diagonal joint strut as the beam longitudinal reinforcement end hook was incapable of acting as a node especially after its tendency to straighten by excessive slippage at early stages. It was evident that the performance of the joints was quite similar to the case of bent-out beam reinforcement joint since both joints failed at a principal tension stress of $.29\sqrt{f'_c}$ MPa.

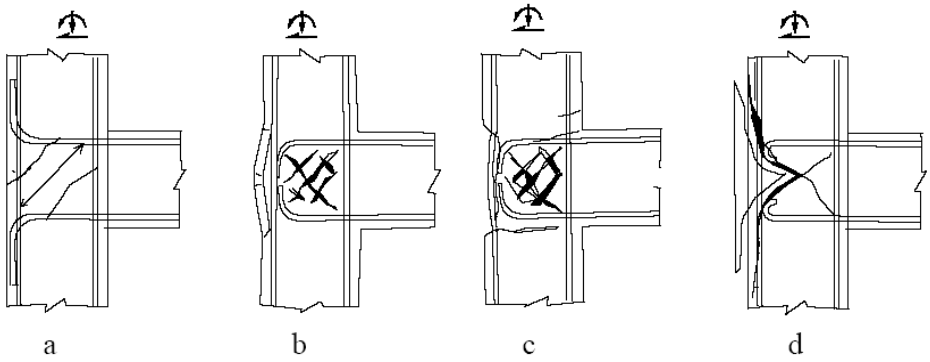

Figure 3.18 Alternative damage mechanisms for exterior joints:
(a) Beam reinforcement bent away from joint region;
(b), (c) Beam bars bent in joint region;
d) End-hook anchorage: "concrete wedge" mechanism, Pampanin et al. [113]

Several researchers have conducted monotonic tests on exterior unconfined beam-column joints. Among these studies are Sarsam and Phipps [133], Parker and Bullman [122], Vollum and Newman [153], Scott and Hamil [136], Ortiz [109], and Salim [131]. They tested the effect of joint aspect ratio, axial load ratio, beam and column reinforcement ratio and end hook configurations of beam longitudinal reinforcement. The main goal of these studies was to develop a monotonic shear strength model of exterior joints. The models developed by the above-mentioned authors are presented and evaluated in a subsequent section. The details of these tests are not included for brevity. The reader is referred to the above references for more details about test specimens.

3.5 CORNER BEAM-COLUMN JOINT TESTS

Relatively fewer tests on corner beam-column joints have been reported in the literature. This brief review covers most tests for which information is available.

Priestley and Hart [129] investigated the failure of a specific prototype structure that was thought to have collapsed due to corner beam-column joint failure. Tests of two corner beam-column joints were reported. The first ¨As built¨ specimen represented a joint lacking transverse reinforcement, while the other ¨As designed¨ joint was identical except for the presence of joint transverse reinforcement with a volumetric ratio of 1.2%. Transverse and longitudinal beams were different in length, depth, reinforcement, and, consequently, in flexural strength. Furthermore, each beam had a spandrel wall extending beneath the beam. The test specimen had no slab. Also, the base of the column was fixed to a footing. Axial load varied as a function of lateral load. The lateral loading history had three stages - the first was uniaxial loading in the longitudinal direction, followed by uniaxial loading in the transverse direction and finally a diagonal loading scheme. Figures 3.19 and 3.20 show the details of the specimens and test setup while Table 3.1 lists design parameters.

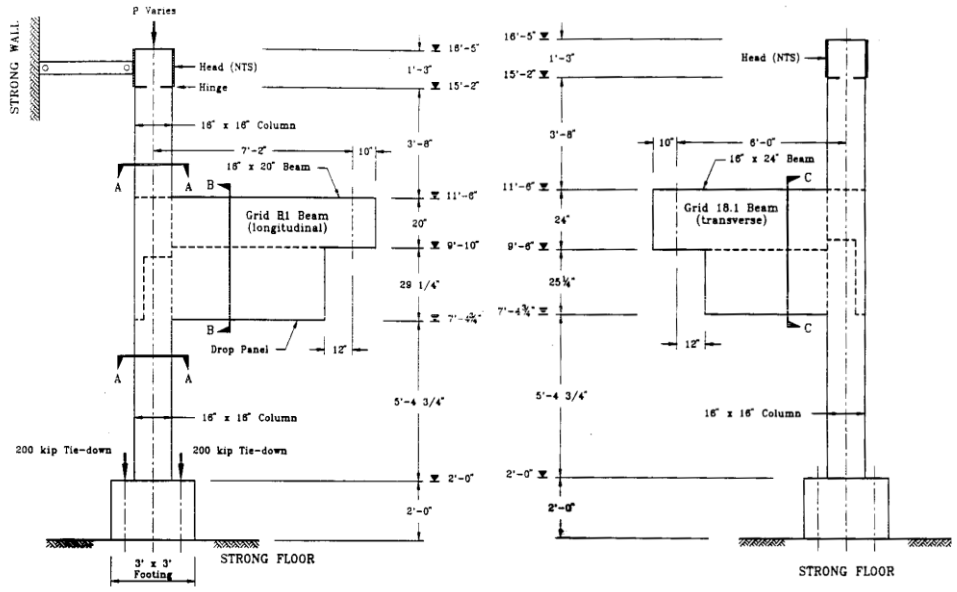

Figure 3.19 "As Built" specimen details in longitudinal and transverse directions, Priestley and Hart [129]

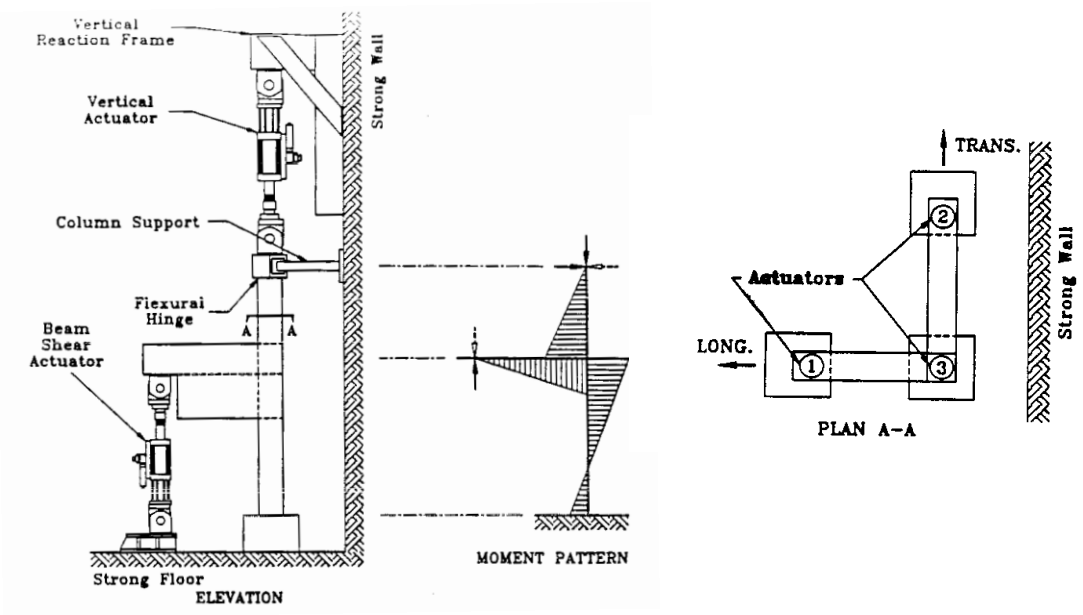

Figure 3.20 Test setup for corner Joint, Priestley and Hart [129]

The mode of failure of the ¨As built¨ specimen involved beam yielding followed by joint shear failure. The failure mode included concrete cover spalling and core crushing, straightening of beam reinforcement, and eventual loss of axial load capacity leading to axial collapse at 3.3%

drift angle and axial load of $0.23f_c'A_g$. In contrast, the well-detailed joint sustained the loading successfully and provided a residual capacity sufficient to maintain structural integrity and prevent total collapse leaving the joint in an easily repaired condition. The response histories of the ¨As built¨ specimen showing the joint degradation in longitudinal directions by general loading and diagonal loading are presented in Figure 3.21.

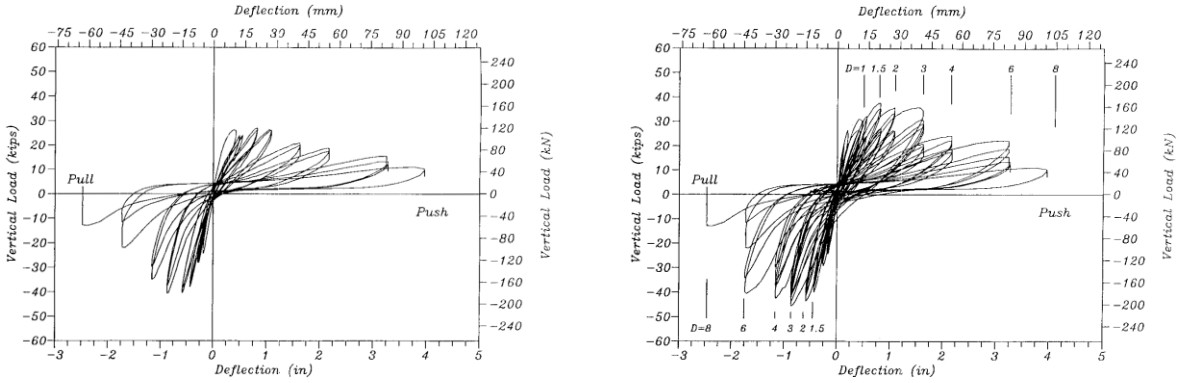

Figure 3.21 Response of longitudinal beam of corner Joint to (a) General and (b) Diagonal loading, Priestley and Hart [129]

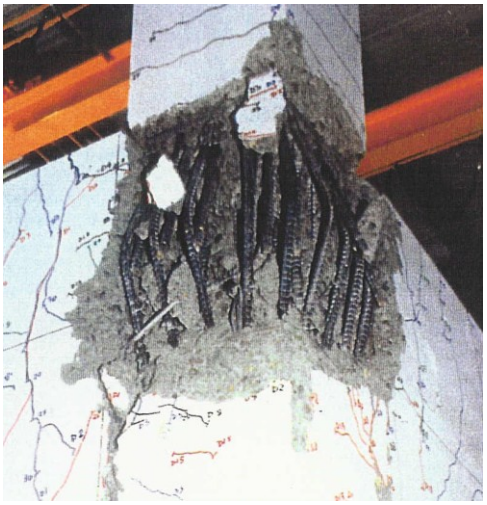

Figure 3.22 Axial failure mode of "As Built" corner joint, Priestley and Hart [129]

The ¨As built¨ joint shear strength expressed in terms of principal tension stress was $5.15\sqrt{f_c'}$ on average for uniaxial loading and $7.45\sqrt{f_c'}$ on average for diagonal loading. Those values correspond to joint shear stress coefficient γ of 5.61 and 8.11, respectively. It was concluded that joint shear strength was inherently higher for diagonal loading. Subsequent analysis, however,

suggests that the joint demands may have been controlled instead by beam flexural strength, explaining the higher joint demand (and capacity at failure) for diagonal loading.

Engindeniz [41] also reports results of a test on a corner joint without transverse reinforcement. Figure 3.23 shows the test specimen geometry and details and test setup while Fig. 3.24 shows the loading history. The details include column lap splices, light column confinement, short embedded length of beam bottom longitudinal reinforcement, and a strong beam-weak column design. Although the test specimen is representative of a class of older construction, it might not give insight into the actual joint shear strength because joint shear failure may not be triggered due to the initiation of other failure modes.

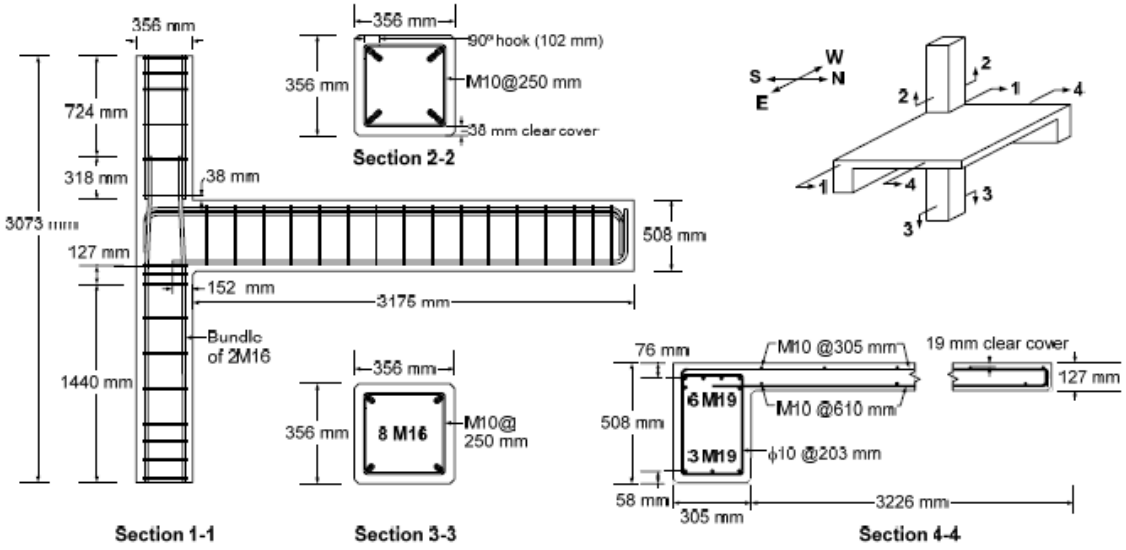

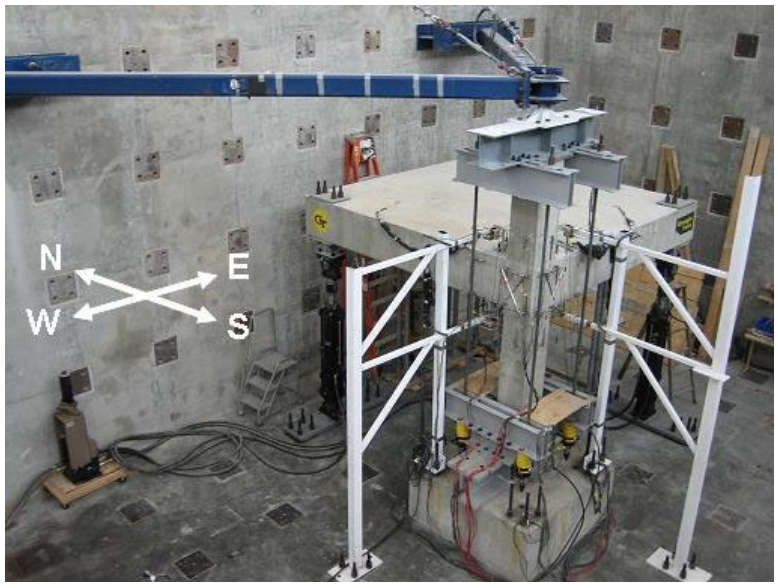

Figure 3.23 Specimen geometry and details and test setup, Engindeniz [41]

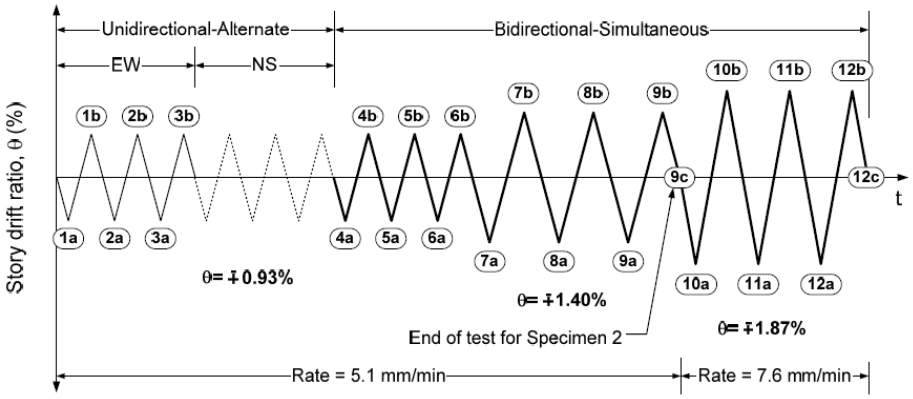

Figure 3.24 Loading history, Engindeniz [41]

Figure 3.25 presents the load-deformation relations of the two tested corner joint specimens that differ only in concrete strength. The overall lack of ductility can be observed in the figure. The mode of failure of the subassembly was column yielding followed by some joint cracking, and bond-slip failure in the beam bottom reinforcement confirming that the joint shear strength was not engaged in these tests. Figure 3.26 confirms the substantial effect of joint shear deformations to the global drift for the case of the beam loaded downward, emphasizing the importance of including this effect in analytical models. For upward loading of the beam, the joint contribution was much less apparently because of the early slip of the beam bottom reinforcement.

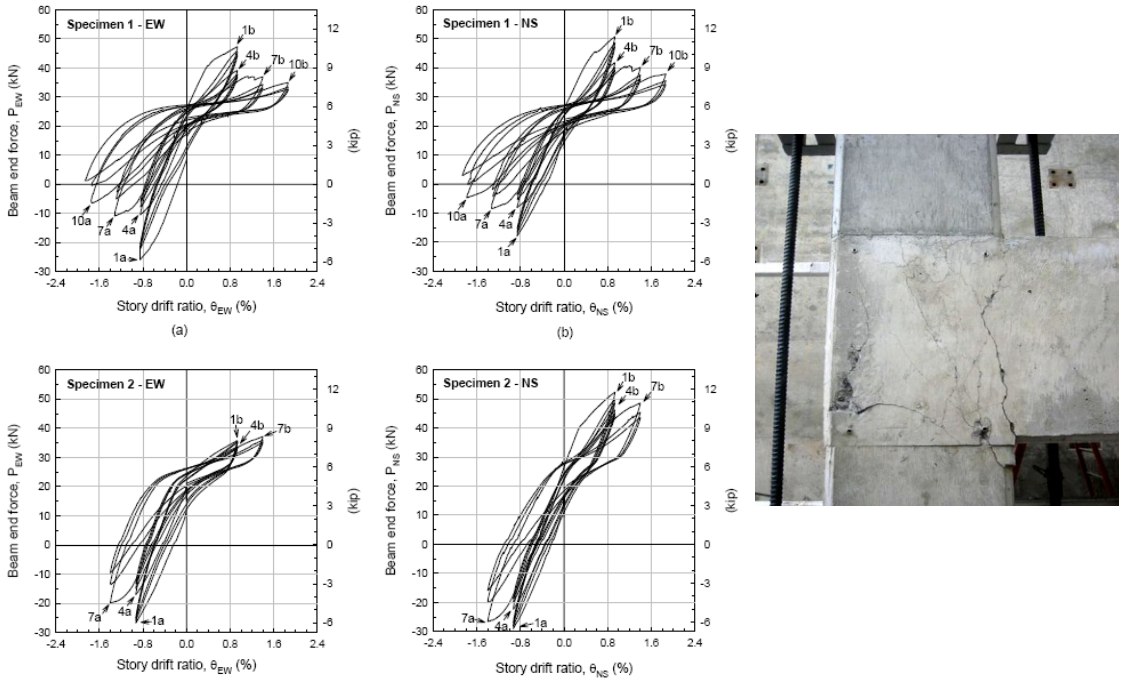

Figure 3.25 Hysteresis responses of test specimens and failure mode, Engindeniz [41]

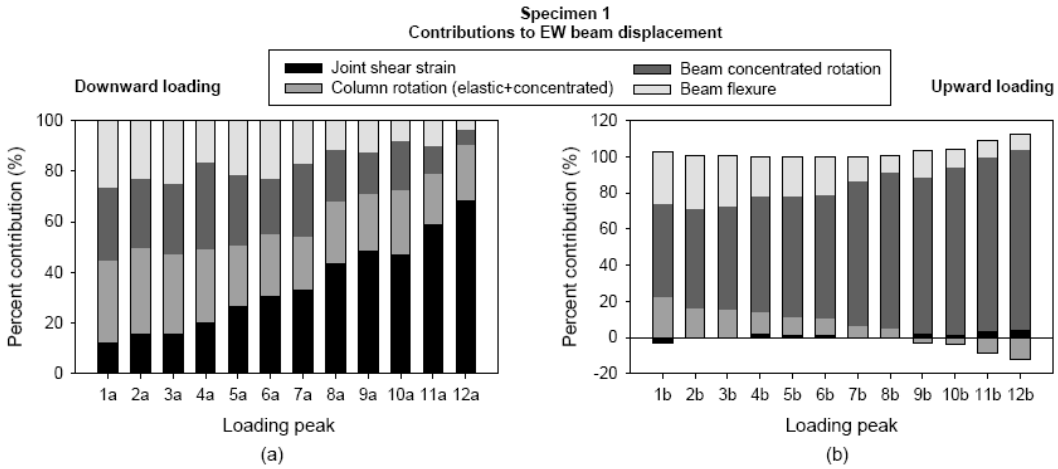

Figure 3.26 Contribution of different components to overall drift, Engindeniz [41]

Topcu [143] reports tests of corner-simulated joints having configuration shown in Fig. 3.27 and details similar to those shown in Fig. 3.13.

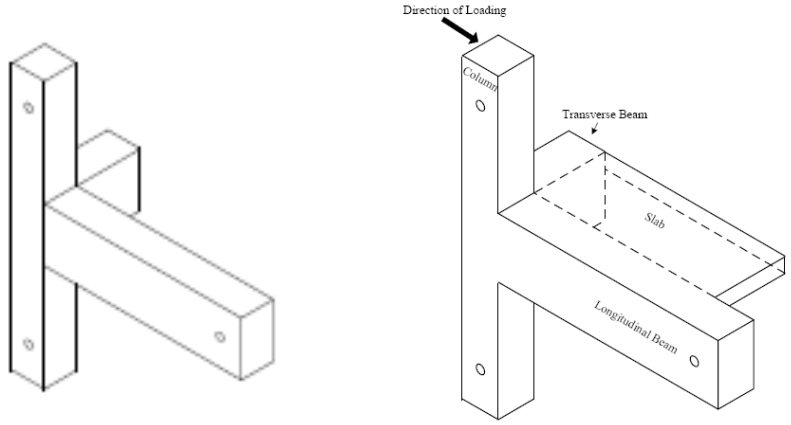

Figure 3.27 Specimens US3-C-Control and US3-CS-Control, Topcu [143]

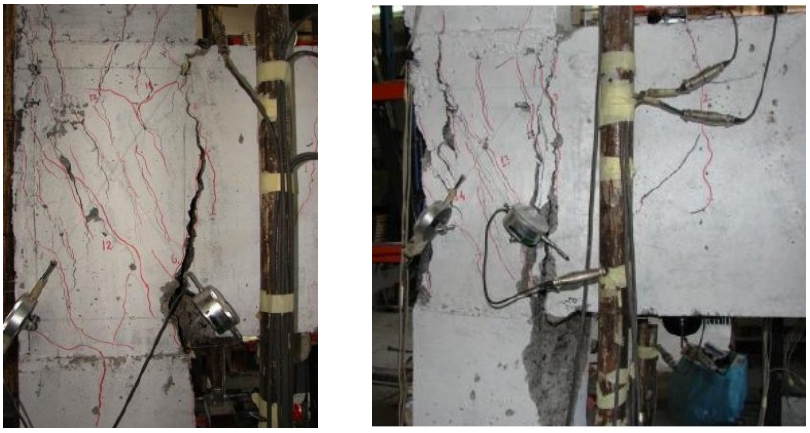

Figure 3.28 Specimens US3-C-Control and US3-CS-Control failure modes, Topcu [143]

In these tests, bond-slip failure preceded joint shear failure. The presence of a transverse beam increased the joint shear strength but did not affect the bond-slip characteristics of the bottom bars. The inclusion of slab did not change the behavior for upward loading of the beam but increased beam strength for downward loading. Slab contribution increased with the increasing drift level. Compared with a previously tested isolated exterior joint US3 with no stubs, the presence of one side stub did not affect the initial stiffness, but significantly enhanced joint shear strength and resulted in much higher ductility and less severe strength and stiffness degradation. The transverse stubs were not loaded during the test.

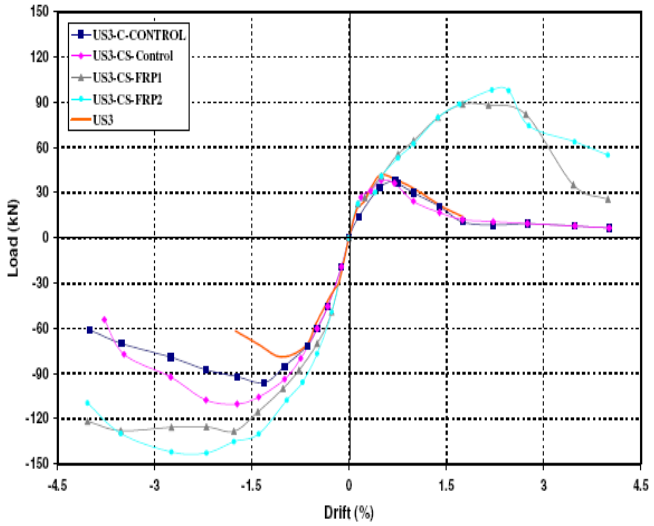

Figure 3.29 Backbone curves of different test specimens, Topcu [143]

Sanchez et al. [132] tested a strong beam-weak column unconfined corner joint subassembly including concrete slab. The aim of the test was to investigate the effect of the presence of one versus two concrete stubs. Otherwise, the test specimen was identical to those of Barnes and Jigorel [13] except for using one-sided transverse stub. The test specimen represented a subassembly from a two story non-ductile frame tested dynamically on shaking table of NCREE, Taiwan (Fig. 3.30). The test results confirmed the improved joint shear strength due to the confinement effect of unloaded single concrete stub compared to isolated exterior joints (about 40% enhancement). The strength enhancement was less pronounced than that in joints with two sided unloaded stubs (80% strength enhancement). This test also provided data for the case of column yielding prior to joint failure. Figure 3.26 presents the test specimen along with its hysteretic performance.

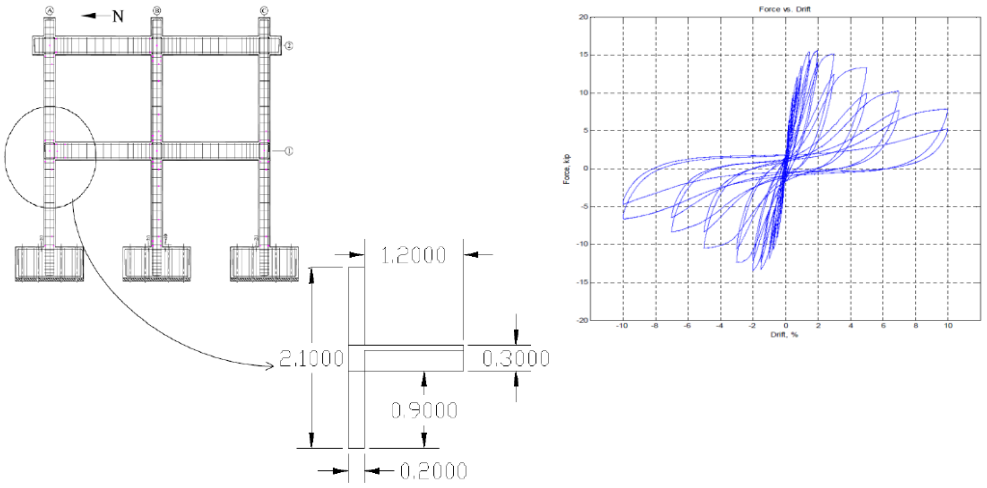

Figure 3.30 Corner-simulated test specimen and hysteric response, Sanchez et al. [132]

Although the following two tests were concerned with well-designed, ductile joints, they are included because they introduce issues associated with loading sequence and test setup similar to those considered in the present study.

Kishida and Kotaro [74] report tests of two 3-dimensional, precast, post-tensioned beam-column corner joints. The specimens did not have a slab. Constant axial load was $0.13f_c'A_g$. Figure 3.31 shows the test specimen and the applied biaxial loading protocol. Three actuators were used to load the specimens quasi-statically.

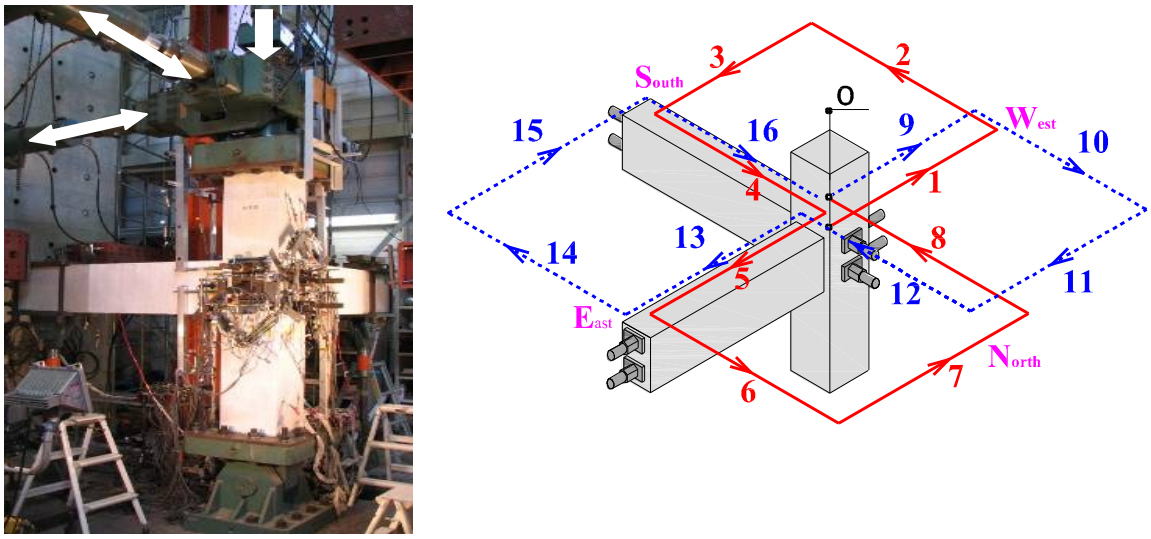

Figure 3.31 Test setup and loading sequence of corner joints, Kishida and Kotaro [74]

Pampanin [111] reports tests of corner joints with and without slabs. These subassemblies had innovative ductile post-tensioning details to mitigate the joint failure. Figure 3.32 shows the test specimens while Fig. 3.33 shows response to different deformation histories. Compared to the unidirectional loading, the bidirectional loading did not have much negative effect on joint performance in the elastic range, with a more pronounced effect on stiffness and strength degradation in the inelastic range.

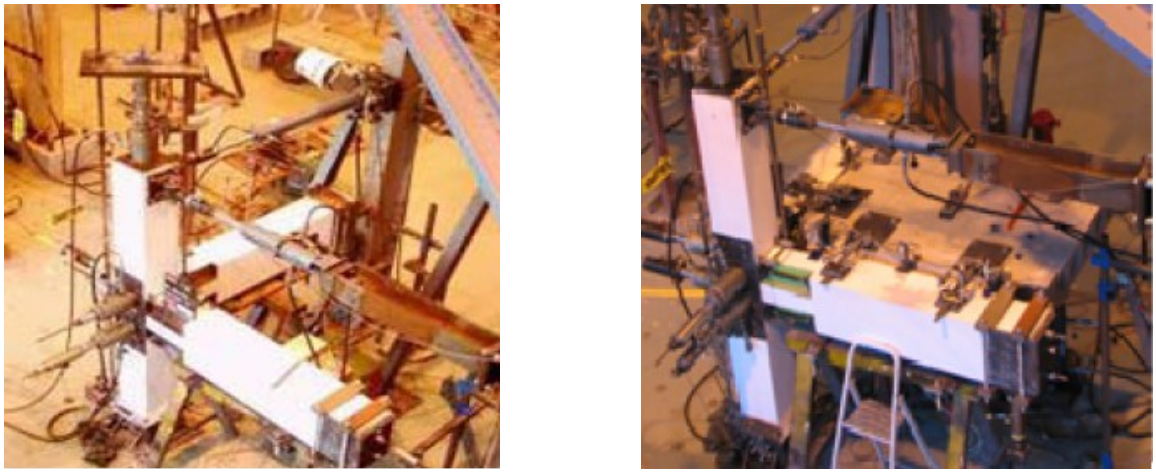

Figure 3.32 Setup of corner joint tests, Pampanin et al. [111]

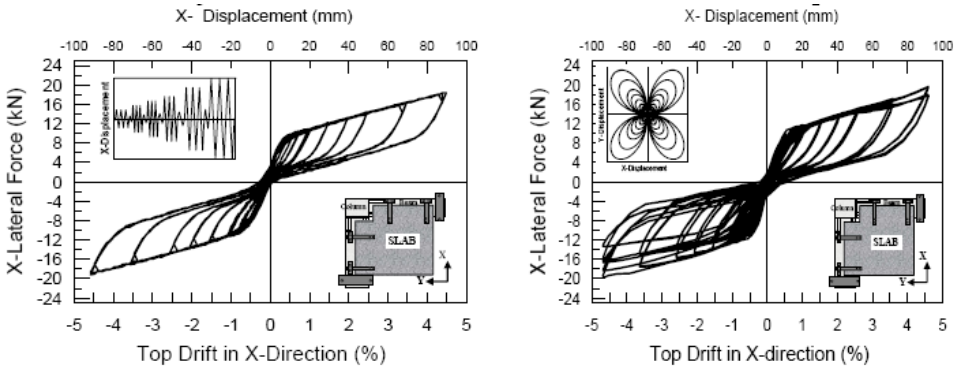

Figure 3.33 Effect of loading History, Pampanin et al. [111]

Table 3.1 Design details and loading data for beam-column joint test database

Investigator	Specimen	Joint type	f_c' (ksi)	γ psi$^{0.5}$	Axial load ratio	Variable axial load	Range of axial load ratio variation	Loading history	Joint aspect ratio α_j	Bot/top beam reinf. ratio%	f_{yb} (ksi)	Column reinf. ratio%	f_{yc} (ksi)
Beres[17]	E-01	Iso. exterior	3.79	6.18	0.11	No	NA	U	1.50	0.5/0.8	77.1	2.00	60.0
	E-02	Ext 2-stubs	3.89	7.62	0.11	No	NA	U	1.50	0.5/0.8	77.1	2.00	60.0
	E-05	Iso. exterior	4.57	6.94	0.32	No	NA	U	1.50	0.5/0.8	77.0	2.00	60.0
	E-06	Ext 2-stubs	4.50	7.95	0.32	No	NA	U	1.50	1.6/0.8	76.7	2.00	60.0
	E-07	Iso. exterior	4.25	5.35	0.10	No	NA	U	1.50	0.29/0.8	76.7	2.00	60.0
	E-08	Ext 2-Stubs	4.36	6.72	0.10	No	NA	U	1.50	0.29/0.8	76.7	2.00	60.0
	E-09	Ext 2-stubs	2.89	8.45	0.50	No	NA	U	1.50	0.5/0.8	70.0	2.00	60.0
	E-10	Iso. exterior	2.97	7.79	0.49	No	NA	U	1.50	0.5/0.8	76.6	2.00	60.0
	E-11	Ext 2-stubs	2.38	7.58	0.18	No	NA	U	1.50	0.5/0.8	70.0	1.00	60.0
	E-12	Iso. exterior	2.74	5.45	0.15	No	NA	U	1.50	0.5/0.8	70.0	1.00	60.0
	E-13	Iso. exterior	2.46	5.96	0.17	No	NA	U	1.50	0.5/0.8	70.0	1.00	60.0
	E-14	Ext 2-stubs	30.4	8.43	0.48	No	NA	U	1.50	0.5/0.8	70.0	1.00	60.0
Priestly & Hart[129]	As-Built	Corner	4.80	8.81	0.26	Yes	0.01-0.38	U and B	1.25	0.47/0.47	62.2	2.75	62.0
Pampanin et al.[113]	T1	Iso. exterior	3.42	NA	0.10	Yes	0.05-0.15	U	1.00	0.58/0.58	52.0	0.75	52.0
	T2	Iso. exterior	3.42	4.4	0.10	Yes	0.05-0.15	U	1.00	0.58/0.58	52.0	0.75	52.0
Clyde et al.[26]	SP 2	Iso. exterior	6.70	11.1	0.10	No	NA	U	0.89	2.45/2.45	65.9	2.23	68.0
	SP 6	Iso. exterior	5.94	11.8	0.10	No	NA	U	0.89	2.45/2.45	65.9	2.23	68.0
	SP 4	Iso. exterior	5.37	14.0	0.25	No	NA	U	0.89	2.45/2.45	65.9	2.23	68.0
	SP 5	Iso. exterior	5.82	13.0	0.25	No	NA	U	0.89	2.45/2.45	65.9	2.23	68.0
Pantelides et al.[116]	SP 1	Iso. exterior	4.79	11.3	0.10	No	NA	U	1.00	1.9/1.9	66.5	2.45	68.0
	SP 2	Iso. exterior	4.79	11.0	0.25	No	NA	U	1.00	1.9/1.9	66.5	2.45	68.0
	SP 3	Iso. exterior	4.93	10.5	0.10	No	NA	U	1.00	1.9/1.9	66.5	2.45	68.0
	SP 4	Iso. exterior	4.93	11.7	0.25	No	NA	U	1.00	1.9/1.9	66.5	2.45	68.0
	SP 5	Iso. exterior	4.59	11.7	0.10	No	NA	U	1.00	1.9/1.9	66.5	2.45	68.0
	SP 6	Iso. exterior	4.59	11.7	0.25	No	NA	U	1.00	1.9/1.9	66.5	2.45	68.0
Uzumeri[150]	SP 1	Corner-stub	4.46	10.7	0.52	No	NA	U	1.33	0.95/1.43	50.3	2.80	48.1
	SP 2	Iso. exterior	4.51	10.7	0.51	No	NA	U	1.33	0.95/1.43	50.6	2.80	48.6
	SP 5	Corner-stub	4.63	9.74	0.50	No	NA	U	1.33	0.95/1.43	50.4	2.80	48.7
Hanson and Conner [54]	SP 7	Corner-stub	5.70	12.9	0.50	No	NA	U	1.33	0.95/1.9	50.7	5.30	81.8
Hanson and Conner [53]	SP-V	Iso. exterior	3.30	11.6	0.86	No	NA	U	1.33	0.95/1.9	51.0	5.30	64.8
	SP-VA	Ext. w/ stub	5.42	12.1	0.54	No	NA	U	1.33	0.95/1.9	49.8	5.30	70.2

Table 3.1 (*Continued*) Design details and loading data for beam-column joint test specimens*

Investigator	Specimen	Joint type	f_c' (psi)	γ_j psi$^{0.5}$	Axial load ratio	Variable axial load	Range of axial load variation	Loading history	Joint aspect ratio α_j	Bot/top beam reinf. ratio%	f_{yb} (ksi)	Column reinf. ratio%	f_{yc} (ksi)
Hakuto et al.[51]	O7	Iso. exterior	4.50	8.13	0.00	No	NA	U	1.10	0.66/1	44.7	0.86	44.7
	O6	Iso. exterior	4.50	8.78	0.00	No	NA	U	1.10	0.66/1	44.7	0.86	44.7
Wong[155]	BS-L	Iso. exterior	4.48	8.80	0.15	No	NA	U	1.50	0.94/0.94	75.4	2.25	75.4
	BS-U	Iso. exterior	4.49	8.79	0.15	No	NA	U	1.50	0.94/0.94	75.4	2.25	75.4
	BS-LL	Iso. exterior	6.12	10.0	0.15	No	NA	U	1.50	0.94/0.94	75.4	2.25	75.4
	BS-L-LS	Iso. exterior	4.58	10.84	0.15	No	NA	U	1.50	0.94/0.94	75.4	2.25	75.4
	BS-V2T10	Iso. exterior	4.73	6.74	0.15	No	NA	U	1.50	0.94/0.94	75.4	2.25	75.4
	BS-V4T10	Iso. exterior	4.10	10.84	0.15	No	NA	U	1.50	0.94/0.94	75.4	2.25	75.4
	BS-L600	Iso. exterior	5.28	6.74	0.15	No	NA	U	2.00	0.68/0.68	75.4	2.25	75.4
	JA-NN03	Iso. exterior	6.51	6.08	0.03	No	NA	U	1.33	0.46/0.46	75.4	2.25	75.4
	JA-NN15	Iso. exterior	6.67	6.87	0.15	No	NA	U	1.33	0.46/0.46	75.4	2.25	75.4
	JB-NN03	Iso. exterior	6.87	6.81	0.03	No	NA	U	1.00	0.65/0.65	75.4	2.25	75.4
	BS-L-300	Iso. exterior	4.95	12.4	0.16	No	NA	U	1.00	1.53/1.53	75.4	2.25	75.4
Gogkoz[50]	US3-E	Ext 2-stubs	3.42	10.8	0.30	No	NA	U	1.67	0.59/0.72	52.0	2.10	64.0
	US3-ES	Ext 2-stubs	3.42	15.2	0.30	No	NA	U	1.67	0.59/1.08	52.0	2.10	64.0
Barnes[13]	Test 1	Ext 2-stubs	6.70	19.6	0.16	No	NA	U	1.50	1/1.94	65.0	3.20	68.0
	Test 2	Ext 2-stubs	5.94	21.8	0.32	No	NA	U	1.50	1/1.94	65.0	3.20	68.0
Topcu[143]	US3-C	Corner-stub	5.37	11.4	0.30	No	NA	U	1.67	0.59/0.72	63.8	2.10	64.0
	US3-CS	Corner-stub	5.82	13.3	0.30	No	NA	U	1.67	0.59/0.90	60.7	2.10	64.0
Sanchez et al.[132]	Test 1	Corner-stub	4.79	16.1	0.20	No	NA	U	1.50	1/1.81	65.0	3.20	65.0
Engindeniz[41]	SP1	Corner	4.79	8.05	0.10	Yes	0.07-0.1	U and B	1.43	0.68/1.43	71.0	3.03	66.8
	SP2	Corner	4.93	7.80	0.10	Yes	0.07-0.1	U and B	1.43	0.68/1.43	71.0	3.03	66.8

U: uniaxial loading
B: biaxial loading
α_j = beam depth/column depth
γ_j = joint shear strength coefficient
Axial load ratio: $P/f_c'A_g$
*Unconfined joints tested by Filiatraut and Lebrun [43], Hoffschild et al., [62], Hwang et al. [65], Karayannis et al. [68], Tsonos and Stylianidis [148], Le-Trung et al. [144], Salim [131], and Ortiz [109] were also used for database development and are shown in Table 5.1.

3.6 BEAM-COLUMN JOINT ANALYTICAL MODELS

Several analytical models have been proposed to represent the seismic behavior of ductile beam-column joints. These models included strut-and-tie models, mathematical simulation models, empirical models, finite element models, shear strength models, bond strength models, and strength degradation models. Relatively fewer models have been developed beam-column joints lacking transverse reinforcement. This section presents a review of models that may be suitable for unconfined exterior and corner joints.

3.6.1 Strut-and-Tie Models

3.6.1.1 FIXED ANGLE SOFTENED STRUT-AND-TIE MODEL (SSTM)

Hwang and Lee [64] proposed a softened strut-and-tie model for shear strength of exterior isolated beam-column joints. The model was intended to accommodate reinforced and unconfined joints by distinguishing three force transfer mechanisms (Fig. 3.34). The model satisfies the three basic mechanics principles: stress equilibrium, material constitutive laws, and strain compatibility. The basic assumption is that bond deterioration of beam reinforcement should be tolerated, leading to a predominance of a diagonal strut to resist joint shear. Additional struts are associated with joint hoops and column intermediate reinforcement, resulting in three force-transferring mechanisms; diagonal, vertical and horizontal. One important approximation in this model is the fixed angle of strut coinciding with the principal compression stress direction as predetermined by joint aspect ratio. Figures 3.34 and 3.35 display the basic concepts, including external and internal force transferring mechanisms.

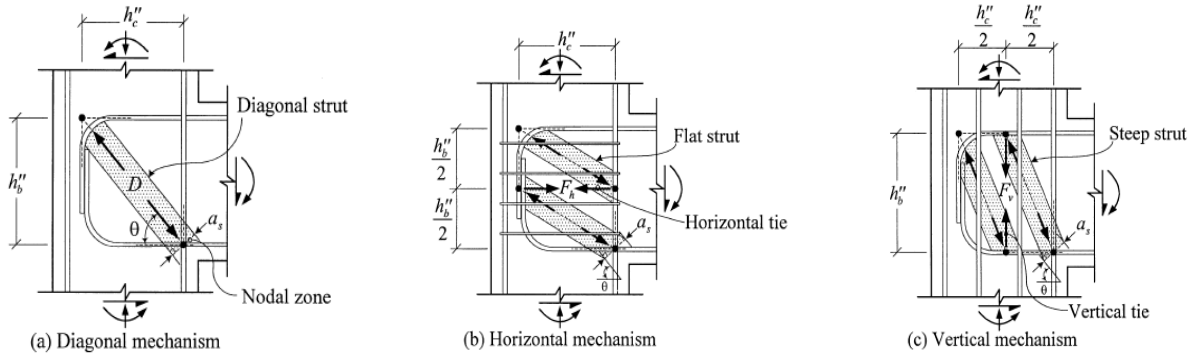

Figure 3.34 SSTM force transfer mechanisms (a) Diagonal (b) Horizontal (c) Vertical, Hwang and Lee [64]

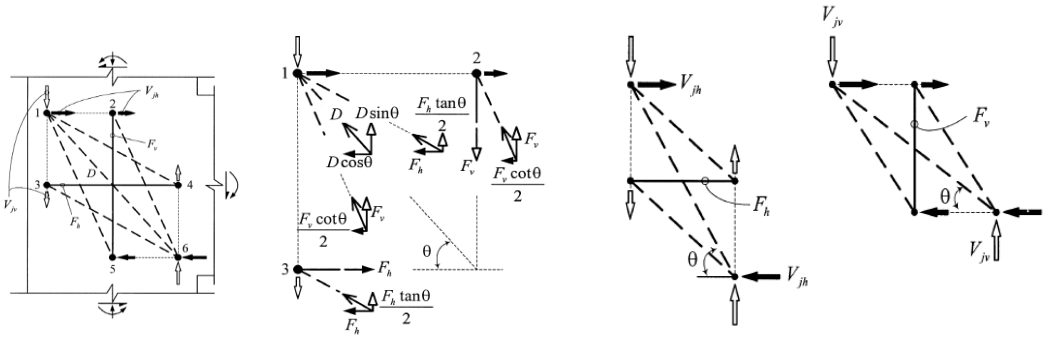

Figure 3.35 SSTM forces of different mechanisms, Hwang and Lee [64]

The diagonal strut area is

$$A_{str} = a_s b_s \tag{3.1}$$

where a_s is the strut width approximated in this model by

$$a_s = a_c \tag{3.2}$$

$$a_c = (0.25 + 0.85\frac{N}{f_c^{'} A_g})h_c \tag{3.3}$$

where a_c is the column compression zone depth. The model neglects beam compression zone depth considering its small dimension in yielding beams. However, this approximation can limit the use of the model to cases where beam yielding precedes joint failure. The strut width b_s is calculated using ACI 318-08 code provisions for effective joint width.

The horizontal joint shear force is:

$$V_{jh} = D\cos\theta + F_h + F_v \cot\theta \tag{3.4}$$

where F_h and $F_v \cot \theta$ are horizontal and vertical shear force mechanism contributions, respectively. The basic equilibrium equations the forces in the diagonal strut and vertical and horizontal mechanisms are:

$$D = \frac{1}{\cos\theta}\frac{R_d}{R_d + R_h + R_v}V_{jh} \qquad R_d = \frac{(1-\gamma_h)(1-\gamma_v)}{1-\gamma_h\gamma_v} \tag{3.5.a}$$

$$F_h = \frac{R_h}{R_d + R_h + R_v}V_{jh} \qquad R_h = \frac{\gamma_h(1-\gamma_v)}{1-\gamma_h\gamma_v} \tag{3.5.b}$$

$$F_v = \frac{1}{\cot\theta}\frac{R_v}{R_d + R_h + R_v}V_{jh} \qquad R_v = \frac{\gamma_h(1-\gamma_h)}{1-\gamma_h\gamma_v} \tag{3.5.c}$$

where R_d, R_h, R_v are the diagonal, horizontal, and vertical shear force mechanism contribution factors, respectively. γ_h is the fraction of horizontal shear transferred by the horizontal tie in the absence of vertical tie, while γ_v is the fraction of vertical shear carried by the vertical tie in the absence of horizontal tie.

$$\gamma_h = \frac{2\tan\theta - 1}{3} \quad \text{for } 0 \le \gamma_h \le 1 \qquad \gamma_v = \frac{2\cot\theta - 1}{3} \quad \text{for } 0 \le \gamma_v \le 1 \tag{3.6}$$

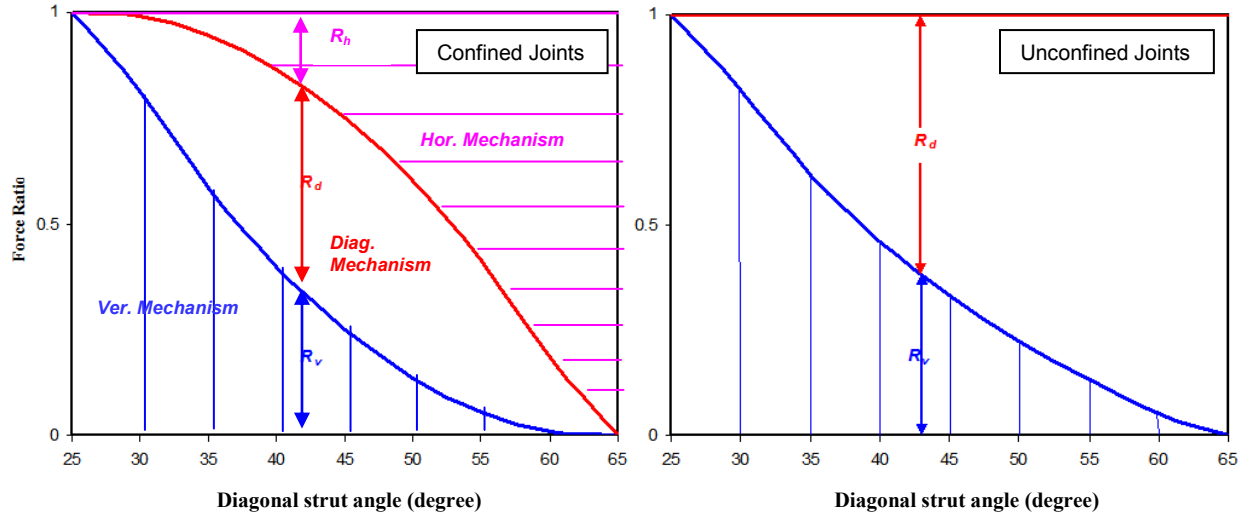

(a) (b)

Figure 3.36 Contribution of SSTM force transfer mechanisms to joint shear strength

Figure 3.36.a shows the contribution of the three mechanisms to the shear strength of the joint, when all three mechanisms exist, as a function of diagonal strut angle. If SSTM is applied to joints without transverse reinforcement, Fig. 3.36.b displays the contribution of the diagonal and vertical mechanisms as a function of diagonal strut angle (for possible application to unconfined joints). The model suggests that the importance of intermediate column reinforcement declines with an increase of strut angle. To check whether the joint strength is reached, the bearing pressure on the nodal zone is checked. The maximum compressive stress on the nodal zone is:

$$\sigma_{d,\,max} = \frac{1}{A_{str}}\left\{ D + \frac{\cos\left(\theta - \tan^{-1}\left(\frac{h_b''}{2h_c''}\right)\right)}{\cos\left(\tan^{-1}\left(\frac{h_b''}{2h_c''}\right)\right)} F_h + \frac{\cos\left(\tan^{-1}\left(\frac{2h_b''}{h_c''}\right) - \theta\right)}{\sin\left(\tan^{-1}\left(\frac{2h_b''}{h_c''}\right)\right)} F_v \right\} \tag{3.7}$$

The constitutive relations for cracked concrete recognize concrete softening and assume principal axes parallel and orthogonal to the strut. Concrete strut compressive stress-strain relation is:

$$\sigma_d = \xi f_c^{'}\left[2\left(\frac{\varepsilon_d}{\xi\varepsilon_o}\right)-\left(\frac{\varepsilon_d}{\xi\varepsilon_o}\right)^2\right] for \frac{\varepsilon_d}{\xi\varepsilon_o} \le 1 \tag{3.8}$$

where ζ is the softening coefficient

$$\xi = \frac{5.8}{\sqrt{f_c^{'}}}\frac{1}{\sqrt{1+400\varepsilon_r}} \le \frac{0.9}{\sqrt{1+400\varepsilon_r}} \tag{3.9}$$

The above expression for softening coefficient is adopted from Belarbi et al. [14]. The concrete compression stain corresponding to $f_c^{'}$ is

$$\varepsilon_o = -0.002 - 0.001\left(\frac{f_c^{'}-20}{80}\right) for 20 \le f_c^{'} \le 100 MPa \tag{3.10}$$

The joint reaches its capacity when

$$\sigma_d = \zeta . f_c^{'} \qquad \varepsilon_d = \zeta . \varepsilon_o \tag{3.11}$$

The constitutive relations for concrete and steel are depicted in Fig. 3.34. The steel is assumed elastic perfectly plastic with the following constitutive relations:

$$\begin{aligned} f_s &= E_s\varepsilon_s \quad \text{for} \quad \varepsilon_s < \varepsilon_y \\ f_s &= f_y \qquad \text{for} \quad \varepsilon_s \ge \varepsilon_y \end{aligned} \tag{3.12}$$

The relationship between forces and strains in tension ties are:

$$F_h = A_{th}E_s\varepsilon_h \le F_{yh} \tag{3.13}$$

$$F_v = A_{tv}E_s\varepsilon_v \le F_{yv} \tag{3.14}$$

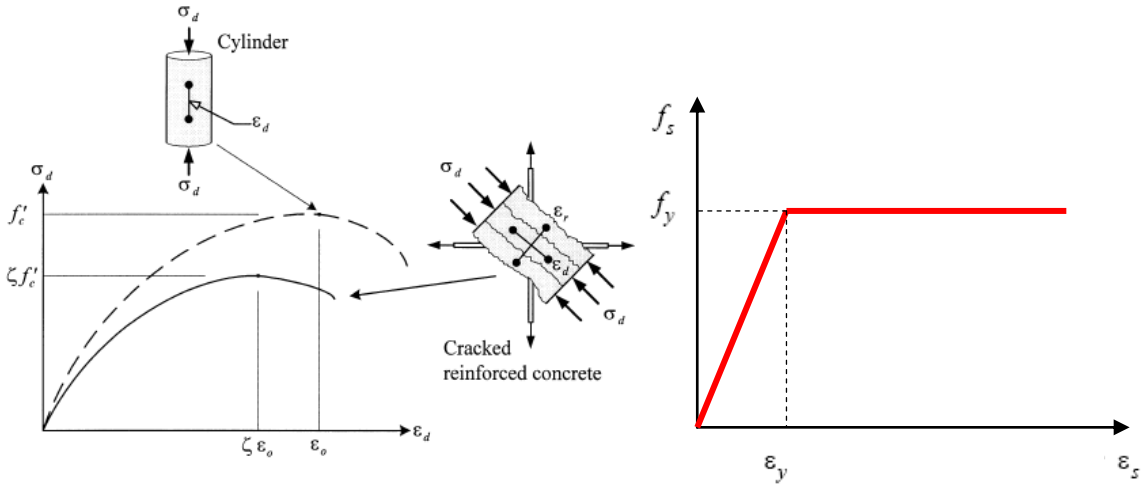

Figure 3.37 Constitutive models of concrete and steel, Hwang and Lee [64]

Two-dimensional compatibility (Fig. 3.38) involves relating the predetermined direction principal tensile strain ε_r to vertical and horizontal strains ε_v and ε_h as:

$$\varepsilon_r = \varepsilon_h + (\varepsilon_h - \varepsilon_d)\cot^2\theta$$

$$\varepsilon_r = \varepsilon_v + (\varepsilon_v - \varepsilon_d)\tan^2\theta \qquad (3.15)$$

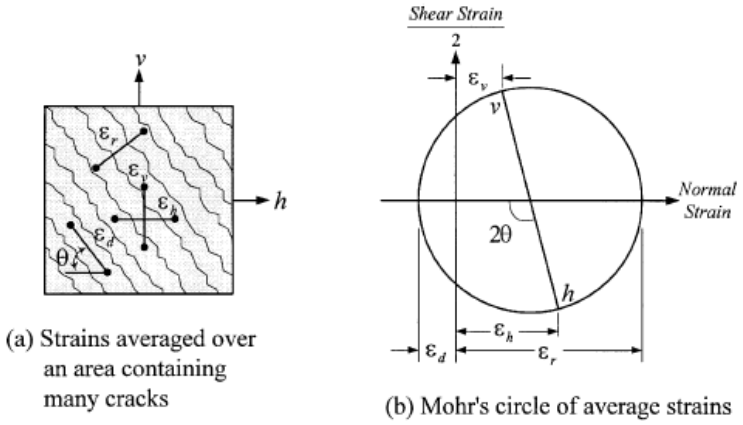

Figure 3.38 Compatibility relations, Hwang and Lee [64]

Hwang and Lee [64] present algorithms to implement the joint strength model, classifying the solution based on the state of strain in horizontal and vertical ties. They included unconfined beam-column joints in one of their algorithm categories, namely the one with yielding horizontal ties, interpreting the yielding tie as being inefficient in a manner similar to the case without ties.

3.6.1.2 MODIFIED ROTATED ANGLE STRUT-AND-TIE MODEL

Wong [155] developed a model for exterior joint shear strength based on the modified compression field theory (MCFT). The model was developed primarily for reinforced joints (by modeling a 2D membrane reinforced panel), with subsequent adjustments for unconfined joints. The model adopted a rotating angle compression strut and is called Modified Rotated Angle Strut and Tie Model (MRA-STM). Similar to the Hwang and Lee model, this model satisfies stress equilibrium, constitutive laws, and the compatibility conditions. The basic equations of the model are:

$$f_{cx} = f_{c1} - v_{cxy}\cot\theta$$
$$f_{cy} = f_{c1} - v_{cxy}\tan\theta \qquad (3.16)$$
$$v_{cxy} = \frac{f_{c1} - f_{c2}}{2}\sin 2\theta$$

where f_{cx}, f_{cy} are average concrete stresses in x and y directions, respectively, and f_{c1}, f_{c2} are average principal stresses in x and y directions, respectively. v_{cxy} is the average concrete shear stress in x-y coordinates and θ is the inclination of principal compression. The average concrete strains are:

$$\varepsilon_{cx} = \frac{\varepsilon_{c1} - \varepsilon_{c2}}{2}(1 - \cos 2\theta) + \varepsilon_{c2}$$
$$\varepsilon_{cy} = \varepsilon_{cx} + (\varepsilon_{c1} - \varepsilon_{c2})\cos 2\theta \qquad (3.17)$$
$$\gamma_{cxy} = 2(\varepsilon_{cy} - \varepsilon_{c2})\tan\theta$$

ε_{cx} , ε_{cy} are the average concrete strains in x and y directions, respectively.
ε_{c1} , ε_{c2} average principal strains in 1 and 2 directions (tension and compression), respectively.
γ_{cxy} is the average shear strain of concrete in x-y plane.

The concrete constitutive laws are

$$f_{c2} = \zeta f_c^{'}\left[1 - \left(\frac{\frac{\varepsilon_{c2}}{\zeta\varepsilon_o} - 1}{\frac{4}{\zeta} - 1}\right)^2\right] \qquad \text{for} \quad \varepsilon_{c2}/\zeta\varepsilon_o > 1 \qquad (3.18)$$

where the softening coefficient ζ is:

$$\zeta = \frac{5.8}{\sqrt{f_c^{'}}}\frac{1}{\sqrt{1 + 400\varepsilon_{c1}}}$$
$$\frac{5.8}{\sqrt{f_c^{'}}}\frac{1}{\sqrt{1 + 400\varepsilon_{c1}}} \le \frac{0.9}{\sqrt{1 + 400\varepsilon_{c1}}} \qquad (3.19)$$

The concrete tensile stress strain relationships are:

$$f_{c1} = E_c \varepsilon_{c1} \qquad \text{for } \varepsilon_{c1} \le \varepsilon_{cr}$$
$$f_{c1} = f_{cr}\left(\frac{0.00008}{\varepsilon_{c1}}\right)^{0.4} \qquad \text{for } \varepsilon_{c1} > \varepsilon_{cr} \tag{3.20}$$

where the cracking strain ε_{cr} is 0.00008 and the cracking stress is (MPa)

$$f_{cr} = 0.31\sqrt{f_c'} \tag{3.21}$$

The model implements solution algorithms incorporating the above equations to predict the shear strength of reinforced beam-column exterior joints. The model is calibrated using test results for unconfined joints.

3.6.1.3 GENERAL MULTI-STRUT-AND-TIE MODEL

Pantelides et al. [116] developed a strut-and-tie model (STM) based on their experimental results to represent the behavior of unconfined isolated exterior joints. They generated first a global truss model for the entire specimen excluding the D-Region (Fig. 3.39), and subsequently developed the D-Region STM that best matched their experimental results. The STM was characterized by the extension of struts to the nearest column hoop outside the joint and by the presence of three major compression struts within the joint. The authors evaluated the failure modes of the STM based on the methods suggested by MacGregor [90]. They confirmed that the tension ties are not likely to yield. It was found that the failure modes would be either compression strut crushing due to overlapping struts or reaching strut capacity, or node compression failure. The authors suggested specific nodes and struts to be potential weak links, a finding that was confirmed by their experimental observations. The model, although matching a specific experiment, is somewhat difficult to extend to more general cases.

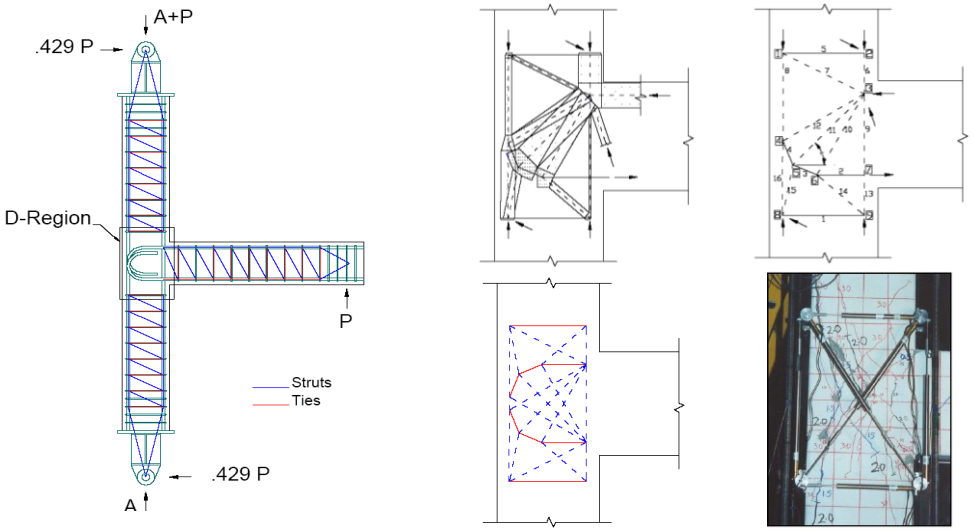

Figure 3.39 Global truss model and strut-and-tie model for exterior joints, Pantelides et al. [116]

3.6.1.4 GENERALIZED MONOTONIC STRUT-AND-TIE MODEL

Parker and Bullman [122] developed a strut-and-tie shear strength model that is dependent on shear span α_v and the critical inclination angle of the strut θ_{crit} that has the maximum stiffness in resisting shear displacements. The authors intended the model to be applicable to shear critical elements including beam-column joints.

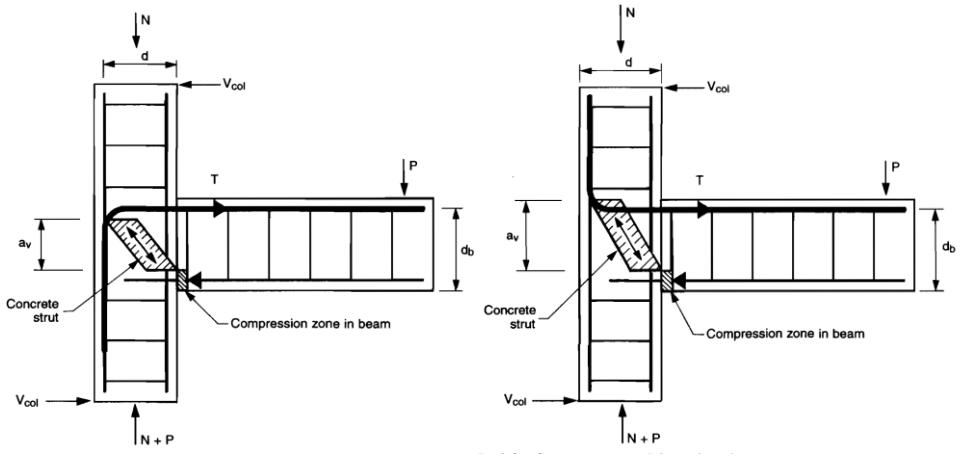

Figure 3.40 Generalized monotonic strut and-tie model, Parker and Bullman [45]

The authors suggested an empirical expression for shear span as:

$$a_v = 0.8d_b - 0.8R \tag{3.24}$$

where R is the hook radius of beam reinforcement. The shear span ratio is defined as

$$\gamma = a_v / d_c \tag{3.25}$$

The critical strut angle can be determined from:

$$\tan\theta_{crit} = 1 - \gamma/2 \qquad \text{for} \quad \gamma < 0.5 \tag{3.26.a}$$

$$\tan\theta_{crit} = 1/(2\gamma) + (\gamma^2 - 0.75)/(6\gamma^3 + 2.5\gamma) \quad \text{for} \quad \gamma > 0.5 \tag{3.26.b}$$

The shear strength of the joint is then obtained as:

$$V_j = (A_v f_y + N)\tan\theta_{crit} \quad \leq \quad V_j = 0.8\alpha.\upsilon.f_c' b_j d_c \tag{3.27}$$

$$\text{where} \ \ \alpha = (1 - \tan\theta_{crit})/(\tan\theta_{crit} + 1/\tan\theta_{crit}) \tag{3.28}$$

and υ is the concrete softening coefficient:

$$\upsilon = 0.56 - 0.004 f_c^{'} \geq 0.40 \tag{3.29}$$

This softening expression is based on Euro Code EC2 for monotonic loading.

3.6.2 Empirical Joint Shear Strength Models

3.6.2.1 BAKIR AND BODUROĞLU EMPIRICAL MODEL

Bakir and Boduroğlu [12] developed an empirical equation for shear strength of exterior joints under monotonic loading. The model is based on a parametric study carried out by the authors to quantify the effect of different parameters on joint strength, including beam reinforcement ratio, joint aspect ratio, and beam reinforcement anchorage details. The effect of each parameter was calibrated independently from other parameters based on test results. Eventually, the effects of all parameters were lumped into the following equation for unconfined joints:

$$V_c = 0.71\beta\gamma\left(\frac{100A_{sb}}{b_b d_b}\right)^{0.4289}\left(\frac{h_b}{h_c}\right)^{-0.61}\left(\frac{b_c + b_b}{2}\right)h_c\sqrt{f_c^{'}} \tag{3.29}$$

where β=1 for beam reinforcement having 90-degree standard hooks bent into the joint, and γ=1 for unconfined joints.

This model does not consider the effect of axial column load or the effect column longitudinal reinforcement. In addition, the model includes the effect of beam reinforcement ratio without recognizing whether that reinforcement yields prior to onset of joint failure.

3.6.2.2 FIXED ANGLE MONOTONIC EMPIRICAL MODEL

Vollum and Newman [153] developed a fixed angle softened strut-and-tie model based on a database of monotonic exterior beam-column joint tests. The model considered the joint aspect ratio and beam reinforcement detail as influential parameters; however, it did not include a method to explicitly evaluate the strut capacity or the mode of failure. The effect of axial load also was not accounted for as an influential parameter.

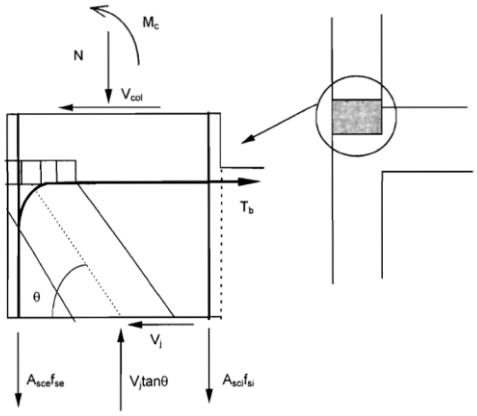

Figure 3.41 Vertical equilibrium of strut and-tie model, Vollum and Newman [153]

The model equations can be interpreted for the case of unconfined joints as:

$$V_j = 0.624\beta(1 + 0.555(2 - h_b / h_c))b_e h_c \sqrt{f_c'} \tag{3.22}$$

$$V_j \;<\; 0.97 b_e h_c \sqrt{f_c'}(1 + 0.555(2 - h_b / h_c)) \;<\; 1.33 b_e h_c \sqrt{f_c'} \tag{3.23}$$

where V_j is the joint shear strength and β is 1.0 for the case of beam reinforcement having standard 90-degree hook bent into the joint. The model suggested increasing the joint shear strength by 33% to account for the presence of transverse beams.

3.6.2.3 SARSAM AND PHIPPS EMPIRICAL MODEL

Sarsam and Phipps [133] developed a joint shear strength expression based on an empirical shear strength model for beams with low shear span ratio $a_v/d \leq 2.5$. A monotonic exterior joint test database was used to calibrate this model. The model accounted for the effect of joint aspect ratio, column axial load, and column reinforcement ratio through the expression:

$$V_j = 5.47(f_c' \rho_c)^{0.33}(\frac{d_c}{d_b})^{1.33}(1 + 0.29N / A_g)^{0.5} b_c d_c \tag{3.30}$$

where the column effective depth was used instead of joint effective depth. ρ_c is the column reinforcement ratio of the layer of steel furthest away from the maximum compression face of the column. A limit of axial load ratio of $N/(f_c' A_g) \leq 0.42$ and a limit of $\rho_c \leq 0.02$ were set due to the lack of available test results beyond these limits.

The mode of joint failure after beam flexural yielding was accounted for by setting shear strength of the joint to be equal to1.25 the shear stress corresponding to yield strength of beams.

3.6.3 Panel Zone Principal Stress-Strain Models

Tsonos [145] developed a joint shear strength model based on combining softened diagonal strut mechanism and truss mechanisms (Fig. 3.42). This model is similar to that of Hwang and Lee [64]. The model satisfies the constitutive laws by complying with Mohr's circle compressive and tensile principal stresses σ_I and σ_{II} and adopting the fifth degree parabola for concrete biaxial strength curve. This is represented as:

$$\sigma_{I,II} = \frac{\sigma}{2} \pm \frac{\sigma}{2}\sqrt{1+\frac{4\tau^2}{\sigma^2}} \tag{3.31}$$

$$-10\frac{\sigma_I}{K.f_c^{'}} + \left(\frac{\sigma_{II}}{K.f_c^{'}}\right)^5 = 1 \tag{3.32}$$

where K is the concrete confinement effectiveness coefficient which is equal to 1 in unconfined joints and τ is the joint shear stress. The joint shear strength coefficient γ_j is obtained by solving the following power equation iteratively:

$$\left[\frac{\alpha_j\gamma_j}{2\sqrt{f_c^{'}}}\left(1+\sqrt{1+\frac{4}{\alpha_j}}\right)\right]^5 + \frac{5\alpha_j\gamma_j}{\sqrt{f_c^{'}}}\left(\sqrt{1+\frac{4}{\alpha_j^2}}-1\right) = 1 \tag{3.33}$$

where α_j is the joint aspect ratio.

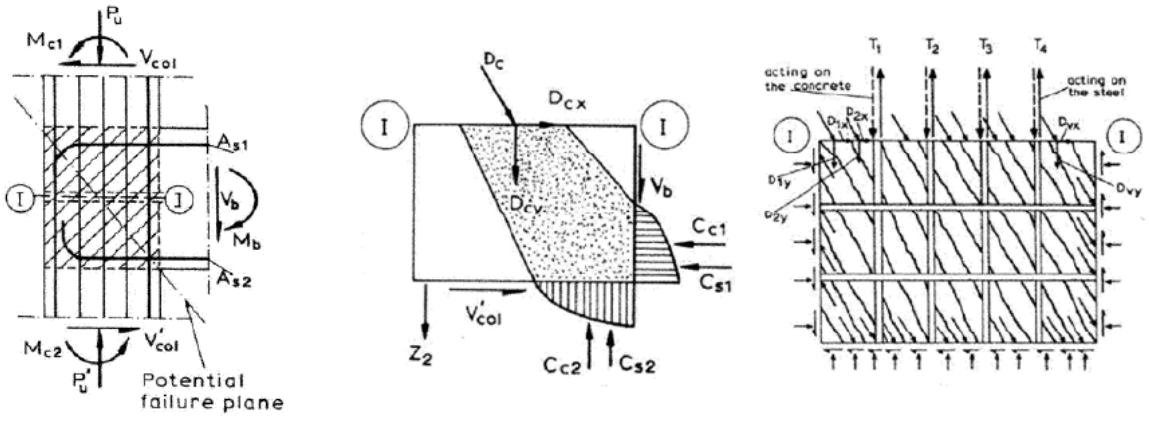

Figure 3.42 Diagonal strut and truss mechanism for panel zone model, Tsonos [145]

3.6.4 Shear Strength Degradation Models

3.6.4.1 CURVATURE DUCTILITY-BASED SHEAR STRENGTH DEGRADATION MODEL

Based on lightly reinforced joint test results of Hakuto et al. [51], Park [119] proposed nominal shear strength degradation models for exterior and interior non-ductile beam-column joints as a function of imposed curvature ductility factor. He distinguished the two cases of beam reinforcement; bent into the joint and bent away from the joint. The models are shown in Fig. 3.43.

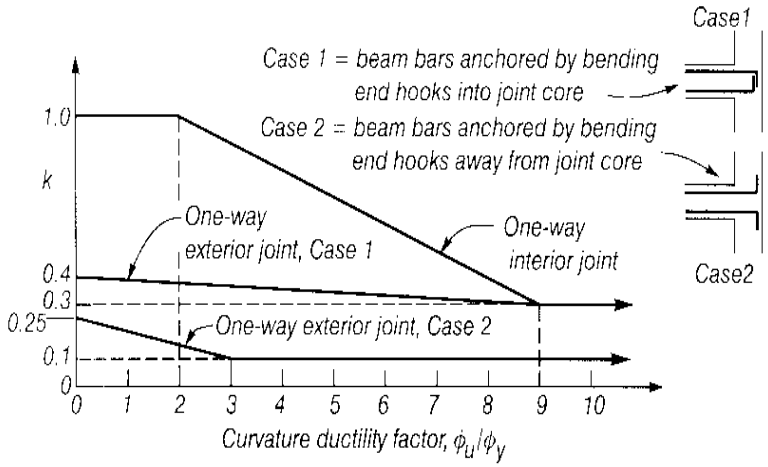

Figure 3.43 Shear strength degradation model with curvature ductility, Park [119]

The model defines shear-resisting force of joints without transverse reinforcement as:

$$V_j = k\sqrt{f_c'}\sqrt{1+\frac{N}{A_g k\sqrt{f_c'}}}\,b_j h_c \tag{3.34}$$

The model recognizes that exterior joints are weaker than interior ones, especially where beam bars are hooked away from the joint.

3.6.4.2 JOINT ROTATION-BASED PRINCIPAL TENSION DEGRADATION MODEL

Priestley [127] presented a model for principal tension strength degradation as function of drift ratio (Fig. 3.44). This model distinguishes the two cases of bent-in and bent-out beam reinforcement. The model recognizes the effect of axial force as it uses the principal tension as an indication for shear strength. The model suggests a higher strength for corner joints due to confinement of spandrel beams, compared with isolated exterior joints.

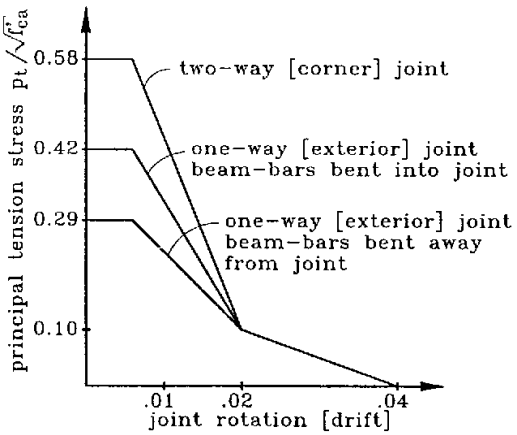

Figure 3.44 Principal tension strength degradation models with drift ratio, Priestley [127]

3.6.4.3 STORY DRIFT-BASED PRINCIPAL TENSION DEGRADATION MODEL

Based on their experimental observation, Pampanin et al. [112] developed a strength degradation curve for exterior substandard joints, with smooth beam reinforcement having a small hook within the joint and no transverse reinforcement (Fig. 3.45). This model expresses joint strength in terms of principal tension stress rather than shear strength, thereby indirectly including the effect of axial load. Principal tension stress of $0.2\sqrt{f'_c}$ MPa is considered an upper limit for first diagonal cracking, associated with the compression principal stress generated by concentrated compression force at the end of the small hook of the beam reinforcement. Immediately after reaching this limiting stress, strength reduction is expected because of absence any hardening or alternative shear transfer (strut) mechanisms.

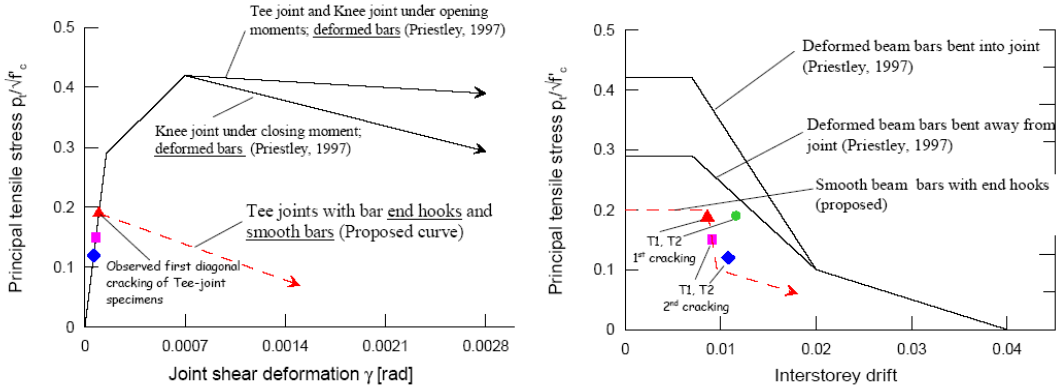

Figure 3.45 Principal tension strength degradation models, Pamapanin et al. [112]

3.6.5 Panel Zone Spring Models for Computer Simulation of RC Frames

3.6.5.1 SINGLE ROTATIONAL SPRING MODEL, PAMPANIN ET AL.

Pampanin et al. [112] introduced a simplified analytical model for exterior joints sustaining joint damage. The model recognizes various components that contribute to overall interstory drift, as shown in Fig. 3.46 and Fig. 3.47 and defined by:

$$\Delta_{tot} = \Delta_{joint} + \Delta_{column} + \Delta_{beam}$$

$$\theta_{tot} = \frac{\Delta_{tot}}{h} = \theta_{joint} + \theta_{column} + \theta_{beam} \tag{3.38}$$

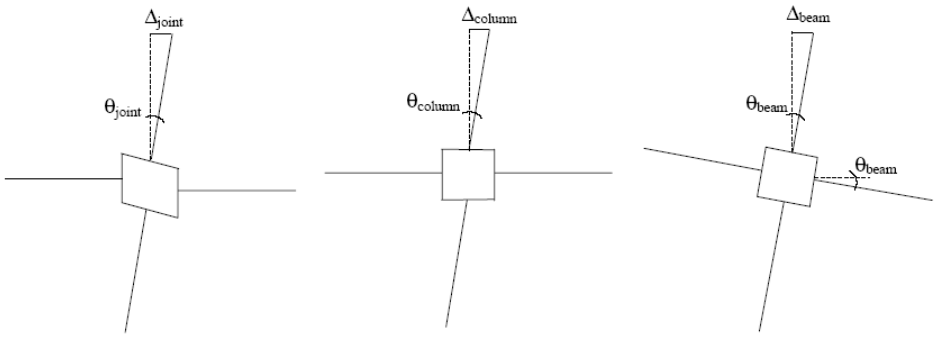

Figure 3.46 Interstory displacement/drift contributions of joint, column and beam deformations, Pampanin et al. [112]

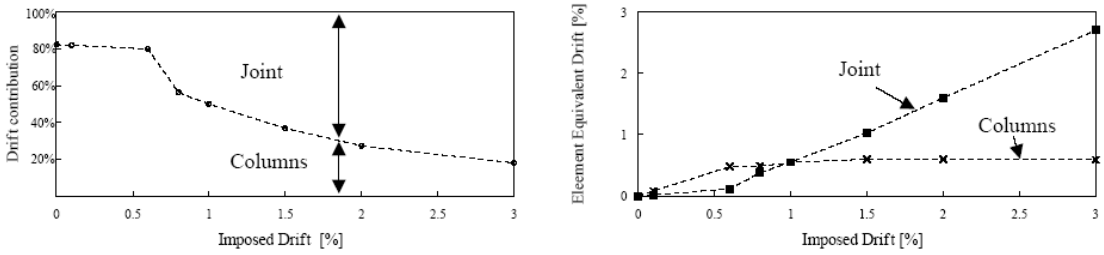

Figure 3.47 Contributions to interstory drift: exterior specimen T1 behavior (numerical), Pampanin et al. [112]

Pampanin et al. [112] propose a shear hinge mechanism that is activated by joint shear and displays significant degradation after onset of failure. The model uses an equivalent moment rotational spring governing the relative rotation of beams and columns (Fig. 3.48). The spring moment is the sum of column OR beam moments for a given joint shear stress demand, while the spring rotation corresponds to joint shear deformation. The model results are compared with their laboratory test results (Fig. 3.49).

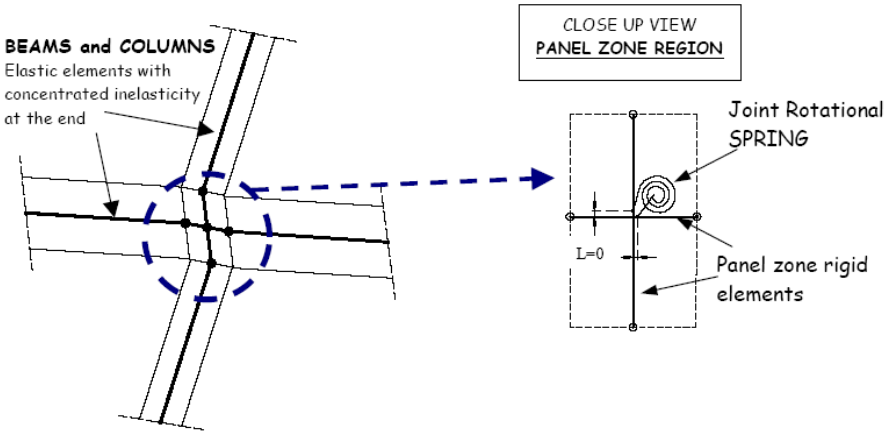

Figure 3.48 Proposed analytical model for joint behavior: rotational spring, Pampanin et al. [112]

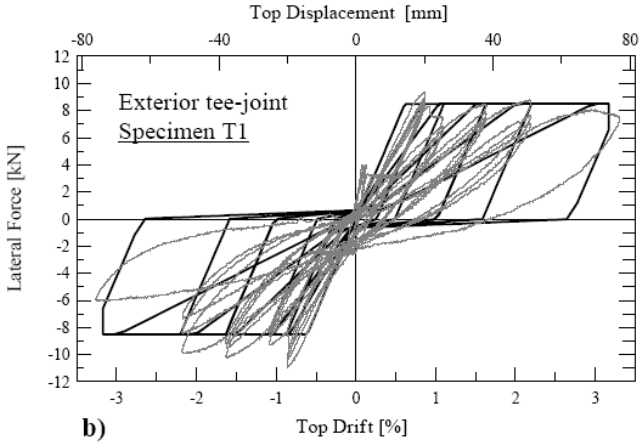

Figure 3.49 Analytical-experimental comparison of exterior joint behavior, Pampanin et al. [112]

3.6.5.2 SINGLE ROTATIONAL SPRING WITH RIGID LINKS MODEL (SCISSORS MODEL)

Celik and Ellingwood [23] presents a review of available models for computer simulation of beam-column joints in dynamic analysis of reinforced concrete frames (Figure 3.50). They implemented three of these models in OpenSees [108] finite element simulation platform to compare simulated behavior with measured behavior for exterior joint tests reported in Pantelides et al. [116]. They were a rigid joint model, a single rotational spring model (with no rigid links), a single rotational spring with rigid links model (Scissors Model, Alath and Kunnath [5]), and a model developed by Altoontash [8]. The Altoontash model is a simplification of the model in Fig. 3.50d, which was later built in OpenSees as *Joint2D* model. The other models in Fig. 3.50 are excluded due to complexity. The panel zone constitutive parameters are defined to replicate the experimental joint shear stress-strain relationships, while the effect of bond-slip is taken into account through a reduced envelope for the joint shear stress-strain relationship instead of using separate rotational springs for bond-slip modeling.

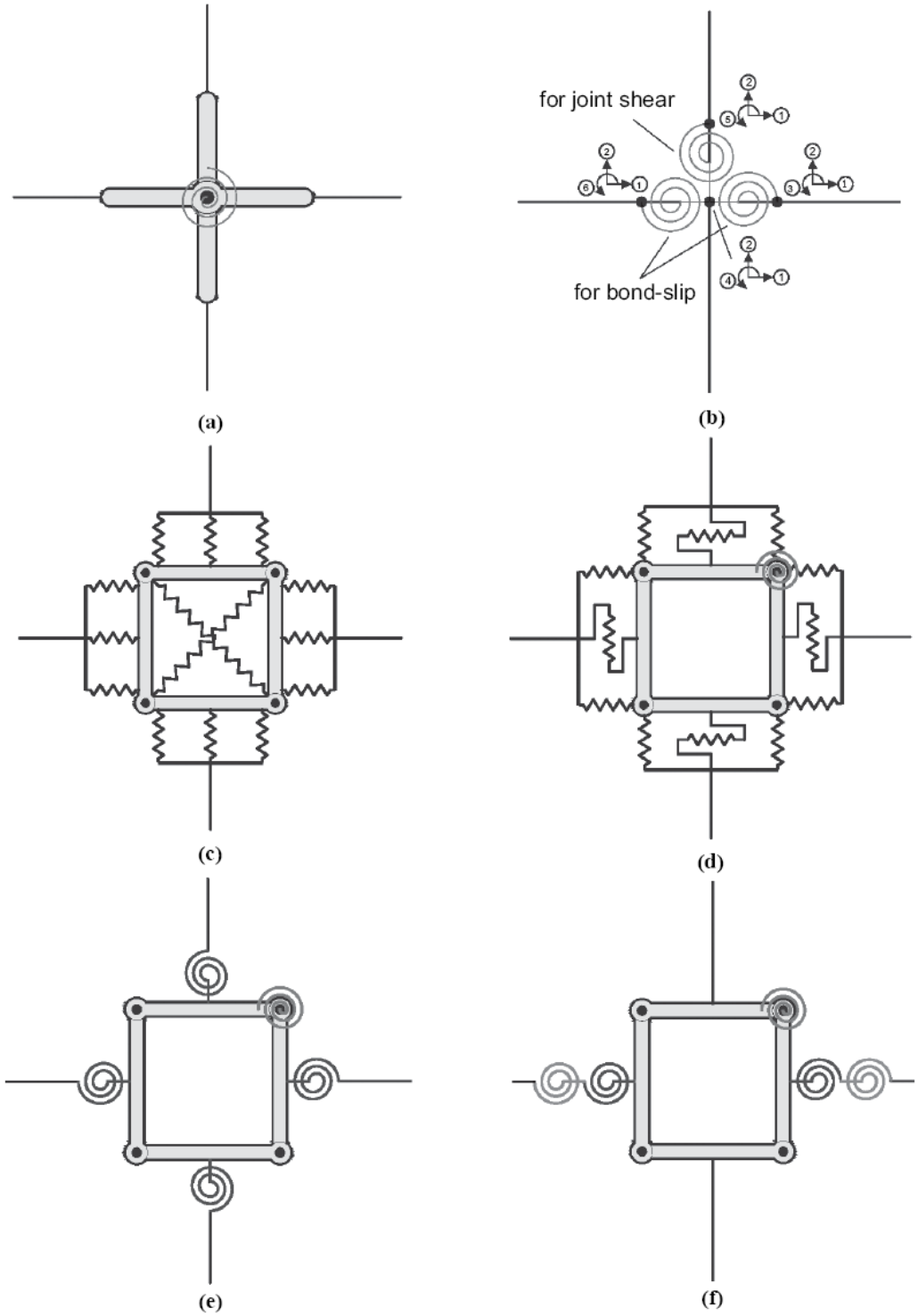

Figure 3.50 Existing beam-column joint models: (a) Alath and Kunnath [5], (b) Biddah and Ghobarah [18], (c) Youssef and Ghobarah [157], (d) Lowes and Altoontash [87], (e) Altoontash [8], and (f) Shin and LaFave [140]. After Celik and Ellingwood [23]

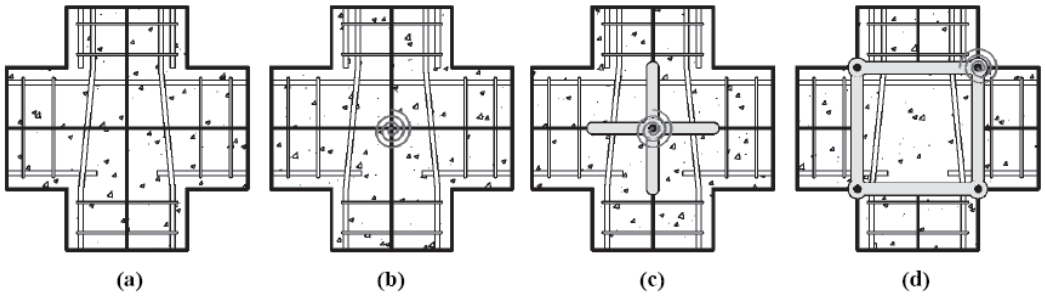

Figure 3.51 Beam-column joint spring models implemented, Celik and Ellingwood [23]

The model results were compared with test of Units1 and 3 tested by Pantelides et l. [116] (Fig. 3.52). Overall, the scissors model with rigid end zones (or single rotational spring with rigid links) was found to produce acceptably accurate results. The current implementation of the *Joint2D* model in OpenSees was found to be less accurate.

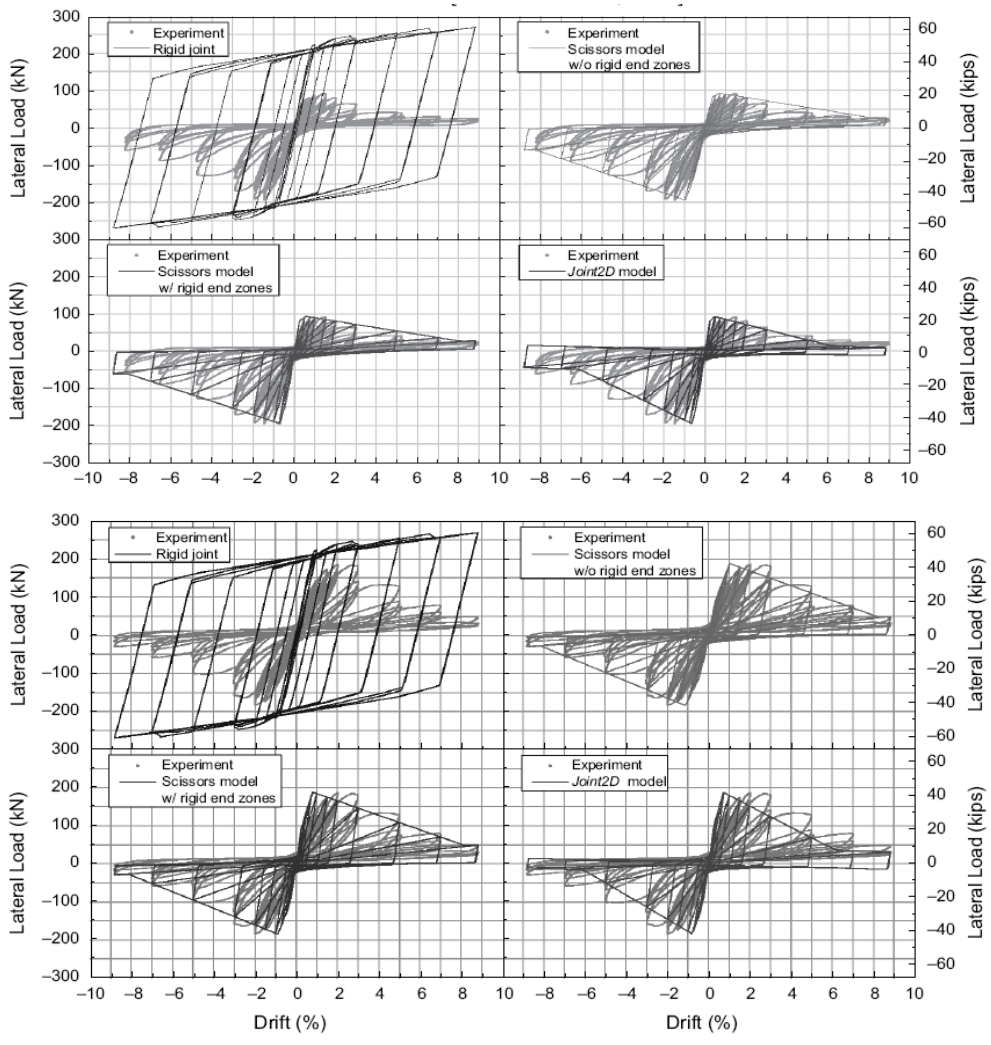

Figure 3.52 Unconfined joint model verification against Pantelides experimental results (a) Unit 1 (b) Unit 3, Celik and Ellingwood [23]

3.6.5.3 ROTATIONAL SPRING (SCISSORS) MODEL, FAVVATA ET AL

Favvata et al. [42] presents a joint rotational spring model with zero length element to represent the performance of exterior joints (Fig. 3.53). They present criteria to define the spring flexural strength M_{sp}, based on different strength limit states. These limit states include: joint shear strength for joints with beam reinforcement hooked inside joint, bond-slip limit state for pullout failure in joints with insufficiently embedded beam reinforcement, and beam flexural strength for joints where strength is limited by the beam strength.

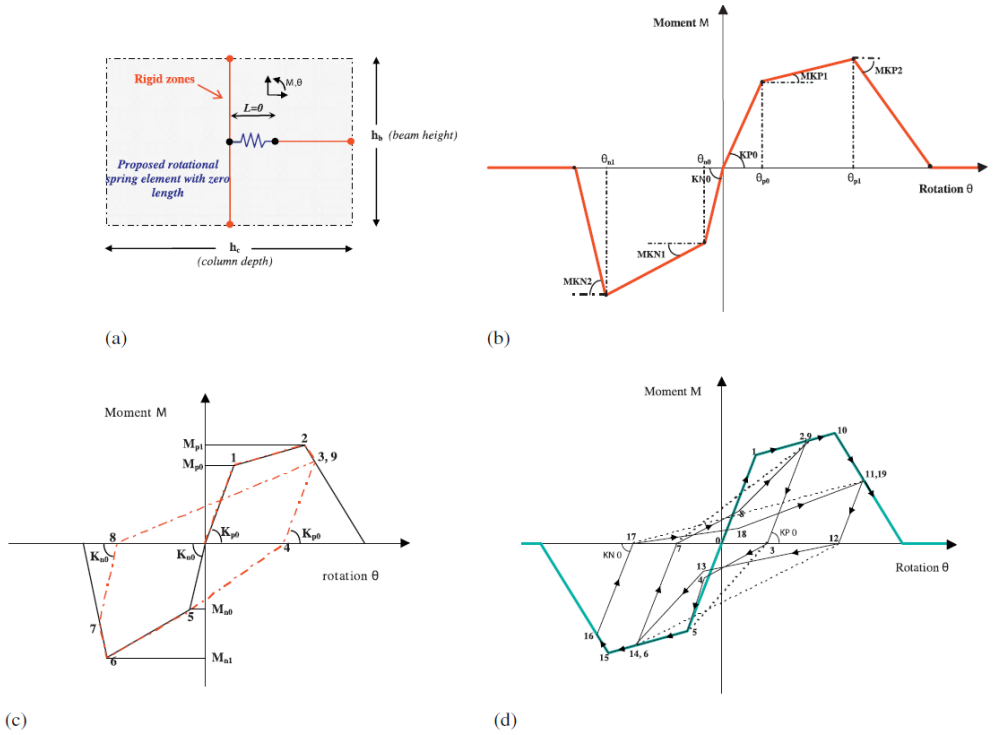

Figure 3.53 Proposed model for the simulation of the exterior RC beam–column joints: (a) Analytical model—partial elevation view of a joint region; (b) envelope curve of the proposed model; (c) response model during a typical hysteretic cycle; and (d) hysteretic response of the proposed model including pinching effect. Favvata et al. [42]

The model is used to model measured response of unconfined exterior beam-column joints (Fig. 3.54). The rotational spring model with rigid links correlates well with measured behavior. The model is used in the nonlinear dynamic analysis of an eight-story, reinforced concrete frame building with unconfined joints. The results demonstrate that including the joint response in the building model has a significant effect on the calculated dynamic response (Fig. 3.55).

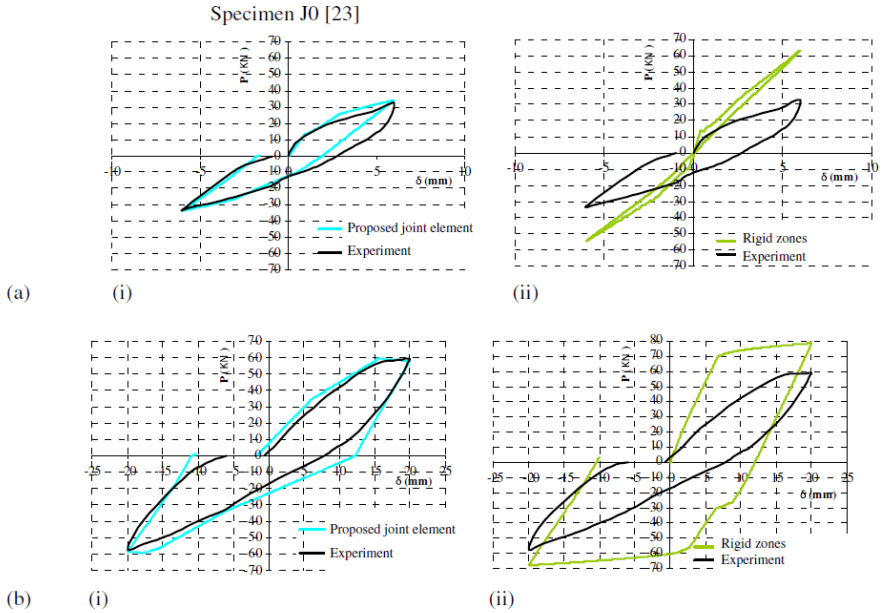

Figure 3.54 Verification of rotational spring model applicability for unconfined joints seismic response predication, Favvata et al. [42]

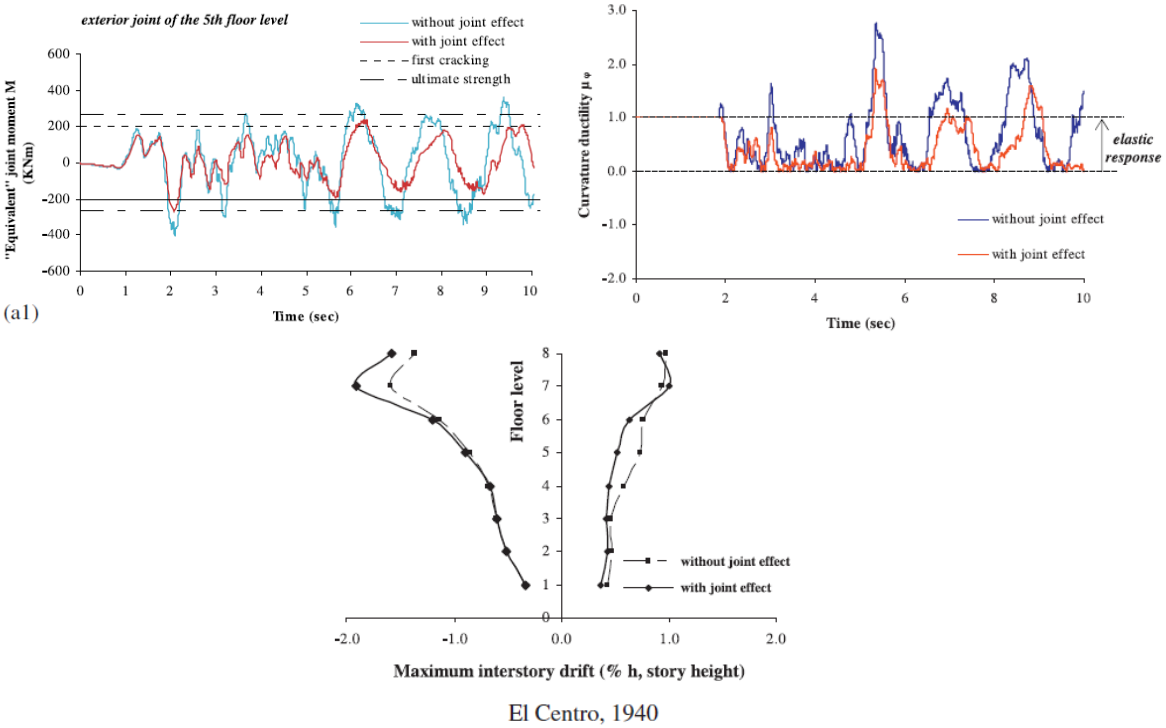

Figure 3.55 Dynamic analysis results for 8 story RC frame using rigid zone and rotational spring model, Favvata et al. [42]

3.6.6 Finite Element Continuum Models

Eligehausen et al. [34] report finite element models (FEM) using a 3-D nonlinear continuum finite element program developed specially for detailed modeling of fracture in quasi-brittle materials to simulate the behavior of unconfined beam-column exterior joints. The specimens of Pampanin et al. [113] were selected for modeling. Both monotonic and cyclic behaviors were investigated. A microplane material model for concrete and a trilinear constitutive law for reinforcement were used. The microplane model is a 3-D macroscopic model in which the material is characterized by uniaxial relations between the stress and strain components on planes of various orientations called "microplanes." Bond between steel and concrete was simulated using discrete bond elements comprising one-dimensional finite elements (Fig. 3.56) with a realistic bond-slip relationship. Due to difficulties in 3-D modeling of the 180° hooked beam reinforcement, the discrete bond model was calibrated to reproduce the stress-displacement behavior of the hook as measured from the experiments. Cyclic analyses were carried out using a relatively coarse discretization as indicated in Fig. 3.57.

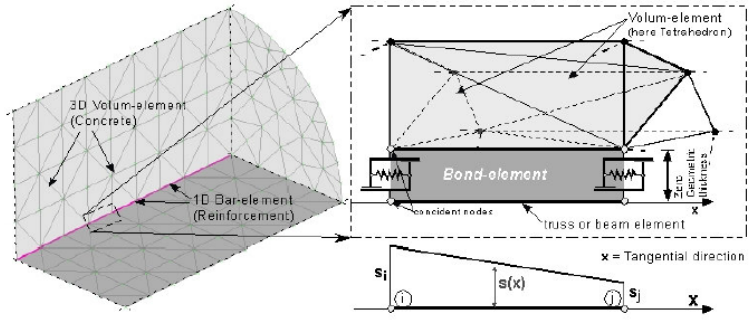

Figure 3.56 Basic assumptions of the bond model implemented FEM, Eligehausen et al. [34]

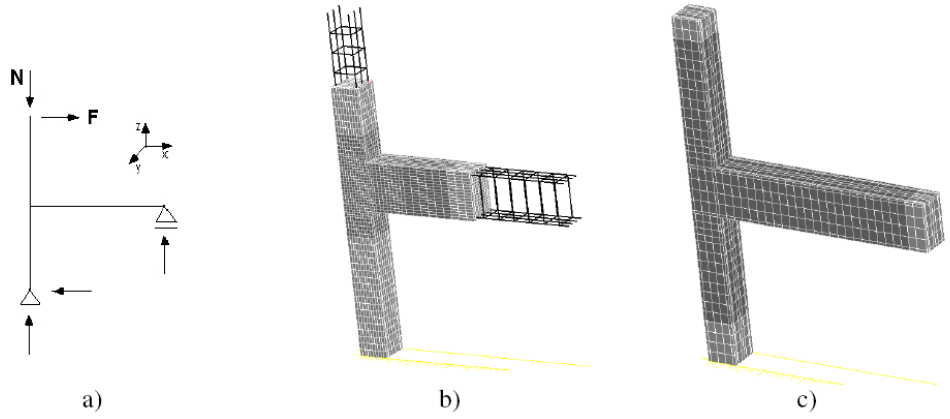

Figure 3.57 Model of test specimen: (a) static system; (b) fine 3D FE mesh used for monotonic loading; (c) coarse 3D FE mesh used for cyclic loading, Eligehausen et al. [34]

The FEM provides some detailed information about joint behavior. Figure 3.58 contrasts the crack pattern of the FEM with the observed cracks. Good agreement was obtained in the

cracking sequence (Fig. 3.58). However, the FEM failed to predict the actual strength and stiffness degradation. The authors attributed the discrepancy to an excessively coarse element mesh and to local bending stiffness of reinforcement, which in the test contributes to the resistance and prevents sudden failure typical for shear.

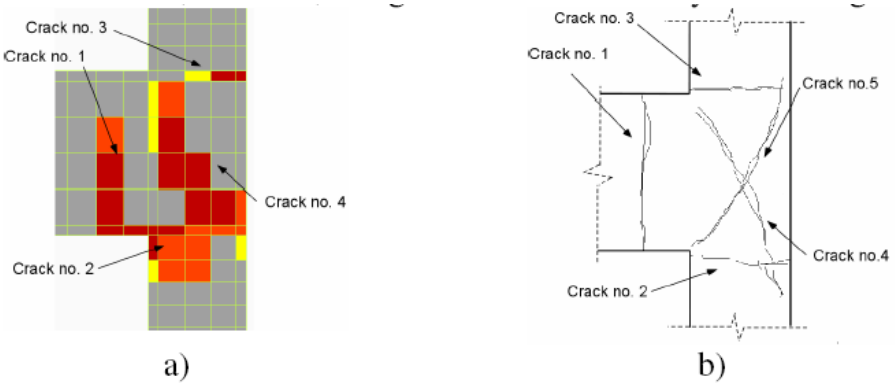

Figure 3.58 Comparison of cracking during cycling: (a) numerical model; (b) experimental results, Eligehausen et al. [34]

3.6.7 Performance-Based and Shear Deformation Backbone Models

Clyde et al. [26] developed performance-based model to evaluate joint performance based on five performance levels as indicated in Table (3.2) for one of their test specimens. These levels were decided and delineated by drift, joint crack width, the joint strength coefficient and type of damage associated with each step.

Table 3.2 Limit state performance levels of exterior unconfined beam-column joint [26]

Level	Qualitative Performance Description	Quantitative Performance Description	Load Step	Lateral Load kip (kN)	Crack Width in (mm)	Drift %	γ psi (MPa)
I	no damage	--	2	18 (80)	--	0.24	4.0 (0.33)
II	first yield in longitudinal reinforcement	onset of cracking in the joint and beam	5	31 (138)	hairline	0.56	6.7 (0.56)
III	initiation of mechanism	continued cracking in the beam and beam/column interface	7	41 (182)	0.004 (0.1)	0.88	8.8 (0.73)
IV	formation of local mechanism	extensive shear cracking in the joint, diagonal joint cracks extend into the column	9	59 (262)	0.06 (1.4)	1.90	12.7 (1.05)
V	strength degradation	spalling concrete in the joint and back of column	10	49 (218)	0.79 (20)	2.64	10.5 (0.87)

Figure 3.59 displays the five performance levels on the hysteresis loops of a typical specimen. Level I exhibited no damage to the joint and occurred at very low drift levels. Level II was characterized by barely visible, initial cracking in the joint and first yielding of longitudinal reinforcement. Level III was associated with growing diagonal cracks in the joint and the appearance of more cracks in the beam and joint. This level represents the initial stages of the failure mechanism. Level IV occurred at the peak lateral load and was characterized by extensive cracking in the joint and the extension of diagonal joint cracks into the column implying full development of the failure mechanism. Finally, level V was characterized by lateral load strength degradation and concrete spalling on the back of the column at the joint level.

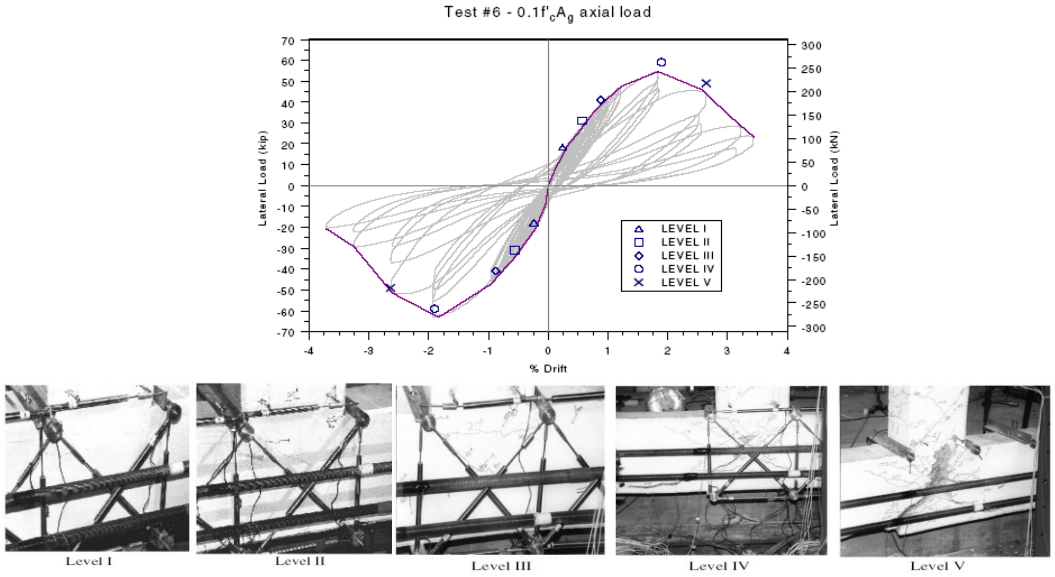

Figure 3.59 Limit state performance levels suggested by Clyde et al. [26]

Pantelides et al. [116] developed a similar performance based model comprises five performance levels whose delineating governing parameters were found to be drift, plastic rotation, joint crack width, joint strength coefficient and type and extent of damage in the joint associated with each step. Figure 3.60 shows the five damage levels for a typical exterior specimen.

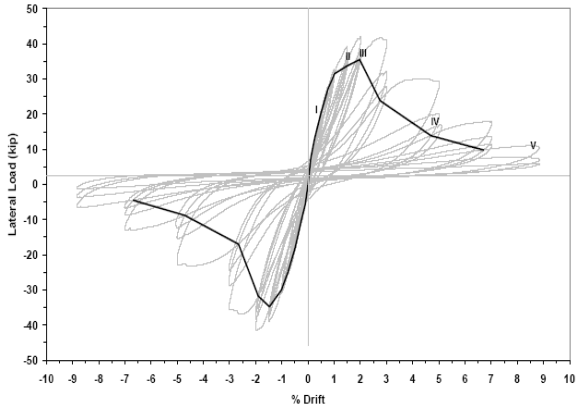

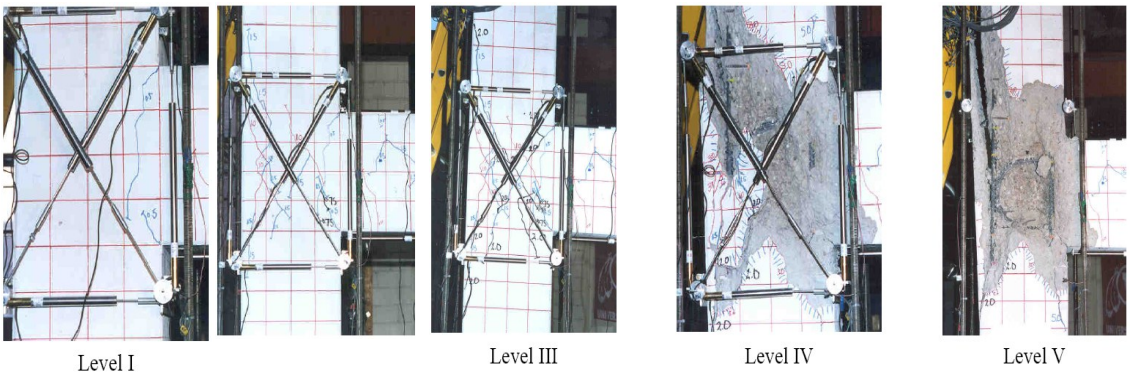

Figure 3.60 Limit states performance levels suggested by Pantelides et al. [116]

Pantelides et al. [116] also introduced a limit state model and backbone curves to be used in design and assessment purposes. This model could be used for performance evaluation after an earthquake, i.e. to determine the plastic rotation and actual joint shear strength of the collapsed joint. In addition, the proposed backbone curves can be used for developing finite element component model to represent joint shear behavior in building frame computer simulation. The authors decided that only three parameters are sufficient to describe the behavior of RC exterior joints for limit state model: plastic rotation, joint shear strength coefficient, and crack width. Figures 3.61 shows typical limit states models for the performance of exterior unconfined joints.

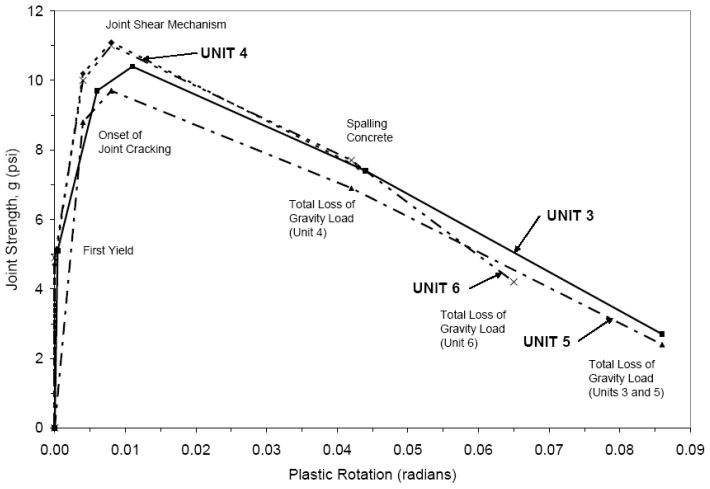

Figure 3.61 Experimental backbone curves for exterior joints, Pantelides et al. [116]

A revision to FEMA 273 generalized deformation relation for exterior joints was suggested by Pantelides et al. [116] based on their test results; and a new modeling criteria distinguishing shear failure model from bond slip failure model was presented. They used four parameters for establishing the new modeling criteria shown in Fig. 3.62.
P1 = Lateral load resistance value at yield
P2 = Peak value of lateral load resistance
P3 = Sudden reduction in lateral load resistance
P4 = Residual strength ratio

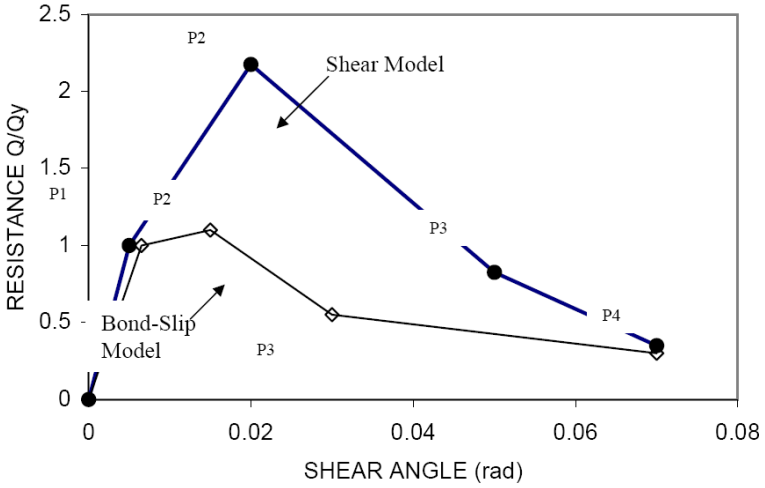

Figure 3.62 Proposed backbone curves for exterior joints, Pantelides et al. [116]

Pampanin et al. [112] presented a similar limit states performance model based on their experimental and analytical models [113] and [112]. Table 3.3 summarizes the limit states of the exterior joints. This model is restricted to buildings with smooth unhooked beam reinforcement inside the joint.

Table 3.3 Limit states for isolated exterior joint based on joint shear deformation, Pampanin et al., [112]

Limit State	Subassembly Drift (%)	Joint Shear Deformation [rad]
First diagonal cracking	0.65	0.0002
Extensive Damage	1.0	0.005
Critical Damage (reparirability issues)	1.5	0.01
Incipient Collapse	2	0.015

3.7 SUMMARY OF THE INFLUENCE DESIGN PARAMETERS ON JOINT BEHAVIOR

The surveying of the previous beam-column joint tests reveals that many parameters affect the seismic performance of unconfined joints. These parameters include joint aspect ratio, beam and column reinforcement ratios, axial load level, axial load variation, mode of failure, presence of concrete slab, loading history, presence of transverse stub or spandrel beam, column longitudinal intermediate reinforcement, presence of lap splice in column reinforcement and detail of beam longitudinal reinforcement terminated inside joints.

The effect of some of these parameters, namely joint aspect ratio, beam reinforcement ratio and axial load ratio, will be thoroughly discussed in Chapter 4 based on database analysis of previous tests. However, the literature findings regarding the effect of the influence parameters will be briefly presented in the next sections

3.7.1 Effect of Axial Load

The effect of column axial load on joint shear strength has been the subject of several studies. Some studies [116], [26] and [13] find that joint shear strength increases with increasing axial load, while other studies [152] find that joint shear strength is not affected by axial load, and still other studies [114] find that shear strength decreases with increasing axial load. Apparently, the effect is complicated by the complex mechanisms associated with joint shear resistance. Most of these studies, however, report gradual strength degradation with higher axial loads.

In joint shear failures preceded by other failure modes, namely BJ, CJ, and S, the basis for shear strength improvement by higher axial load could be different. For example, Kim and LaFave [71] reasonably suggested that for weak column-strong beam connections, the clear reason for joint shear strength enhancement due to higher axial load is the enhancement of column flexural capacity for a tension-controlled column. This enhancement means less tensile strains in column longitudinal reinforcement, which delays column yielding and column bar yield penetration into the joint. The lesser tensile strain penetration into the joint, the lesser the concrete softening effect, which in turn means higher shear strength. This explanation is experimentally verified by [13] for a weak column-strong beam connection test.

In the case of S-Failure mode, the axial load tendency to improve pullout bond strength of beam bottom insufficiently embedded reinforcement is experimentally evident [107]. This, in turn, improves the overall global lateral load capacity of the subassembly although it does not locally improve joint shear capacity that is not engaged because of the premature pullout failure.

3.7.2 Effect of Concrete Slab

There are very few available tests, [50] and [143], investigating the change in unconfined joint performance due to the presence of concrete slab versus the case of isolated joints without slab. However, there are sufficient tests reporting on the effect of slab presence on the response of confined beam-column joints. The common finding in both types of tests is that the slab presence significantly increases the beam plastic moment capacity, which in turn increases the imposed shear demand on joint, and consequently it is considered less conservative to test joints in the absence of the slab. Slab presence slightly increase loading stiffness compared to no-slab specimens, but the major increase is in the post peak strength. Including slab can also increase joint shear strength in case of BJ-Failure. This is because the specimen without slab yields earlier than that with slab included, resulting in a premature joint shear failure of the joint because of yield penetration and excessive strut softening. Another common observation is that the presence of the slab reduces the confining effect of spandrel beams and hence results in more rapid joint strength and stiffness deterioration compared to specimens without slab. This was attributed to the torsional stresses and cracking that the slab imposes on spandrels. In other words, when a three-dimensional specimen is loaded in an alternating bidirectional fashion (one beam at a time), torsional cracking develops in the unloaded beam during the loading of the other beam. Thus, during any seismic event this aspect might be important to be considered to avoid it is negative post peak effects on strength and ductility. This phenomenon was also confirmed for unconfined corner joints tested in the current study (Chapter 7) and in the tests by Park [120].

The subject of the effective slab width in tension contributing to shear stress demand to joints received great deal of research attention. Several investigators such as Zerbe and Duranni [29] and [159], Cheung et al. [24], and Pantazopoulou [114] report different effective slab widths in tension according to the level of inelastic deformation. ACI 352-02 [2] includes provisions for effective slab width. Based on the above studies, a reasonable effective width of exterior and corner joints experiencing BJ-Failure might be the width of the beam in the direction of lateral loading plus the total depth of the transverse beam. For J-Failure joints, this effective width might be lower due to the non-yielding condition of beam reinforcement. The effective width of the slab in tension will be investigated in Chapter 7 based on test results of the experimental program.

3.7.3 Effect of Loading History

It is evident from the previously discussed test results in Chapter 3 that the change in loading history has no or little effect on elastic performance or joint strength. However, using too many cycles of per each displacement step level prior to reaching joint shear strength may result in slightly lower shear strength. The typical practice in quasi-static cyclic testing is using two to three loading cycles per displacement step. Within this range, slight effect is observed on joint shear strength and deformation. However, it was observed through the experimental phase of the current study that the number of cycles could significantly affect the drift capacity before axial failure of beam-column joints. The higher number of cycles obviously reduces the post-peak

deformational capacity. The effect of loading cycle on axial load capacity will be demonstrated in more detail in Chapter 8.

Using a more sophisticated or bidirectional loading history significantly deteriorates post peak stiffness of the tested specimens, [41]. A result supporting this observation is found in [129] as the diagonal bidirectional loading of a corner joint resulted in similar shear stress and principal tension stress to those of uniaxial loading case (using elliptical interaction of orthogonal components of shear strength). This observation is particularly true in the elastic range. Some studies reported lower joint shear strength due to bidirectional loading, but this cannot be decoupled from the effect of yielding the specimen first under uniaxial loading before applying the bidirectional scheme in such studies [41]. Bidirectional loading tests for confined interior joints by Kurose et al. [77] (Fig. 3.63) proved that elliptical shear strength interaction under bidirectional loading gives a reasonably conservative estimate of joint shear strength. Further bidirectional loading tests for unconfined joints are needed to confirm the loading history effect. This topic will be readdressed in Chapter 7 in the light of test results of the experimental phase of the current study.

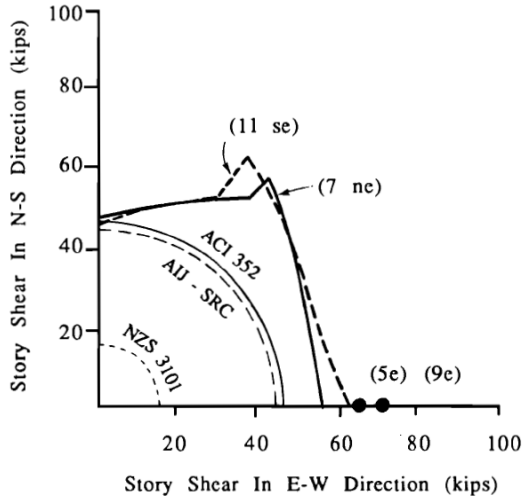

Figure 3.63 Bidirectional loading shear strength interaction for interior joints, Kurose et al. [77]

It is also evident from the literature that the quasi-static cyclic loading of beam-column subassemblies is more conservative than the shaking table dynamic testing due to the apparent increase in strength due to short time step loading in the rapid dynamic test. It is also conservative enough to assume that monotonic testing of beam-column joints results in joint shear strength less by 25%-30% than cyclic loading tests, [84].

3.7.4 Effect of Transverse Spandrel Confinement

Early researchers [53] reported a tremendous strength improvement of unconfined exterior beam-column joints by adding transverse concrete stubs simulating corner joints, suggesting that joint transverse hoops are not needed corner joints.

Similar results were reported by Megget [93]. He indicated that the transverse beams confined the joint core concrete and allowed beam hinging to occur. However, he speculated that the benefit of transverse spandrels in an actual building might not be as significant since it is likely that the transverse beams will crack along the beam-column interface during a bidirectional loading earthquake and may increase the demand on the joint.

Other researchers ([150] among others) reported no additional benefit or confinement effect of transverse stubs in corner joints except increasing slightly the anchorage capacity of beam reinforcement. However, in these tests, the concrete stub was pre-cracked by applying an equivalent gravity load using prestressing. Cheung et al. [25] proposed that the spandrel beam has no effect in enhancing the shear capacity of joint under large inelastic deformations. This confirms the above speculation of no additional benefit of concrete transverse beam in a corner joint during seismic event.

Other test results for joints with preloaded transverse stubs support the latter opinion. The authors suggested that the effect of transverse stubs is minor on the strength, reflected by similar failure mechanism and strength of both specimens with and without stubs, with more pronounced effect in decreasing the severity of cracking and strength degradation in specimens with stub. However, the mixed mode of failure in these tests reduces their reliability to draw definitive conclusions.

The most recent test on the effectiveness of stubs in older unconfined joints [50] and [143] observed that stubs increased the joint shear capacity of subassemblies by about 15-20%, but did not affect the bond-slip characteristics of inadequately anchored longitudinal beam bottom reinforcements. As noticed earlier from Fig. 3.14 and Fig. 3.29, shear strength improvement, higher ductility, and less strength and stiffness degradation are evident due to stub confinement effect. However, improvement is negligible in the elastic range.

ACI 352-02, [2] suggests that isolated exterior and corner confined joints treated similarly. In other words, it suggests that no additional confinement exists in the case of corner joints because of the spandrel beam. However, for an exterior reinforced joint with spandrel beams on both sides, ACI 352-02 suggests 25%-33% improvement in joint shear strength because of the spandrels.

Similarly, ASCE 41 [11] suggest 33% improvement of joint shear strength of exterior joints due to presence of spandrel beams on both sides. The author tends to support the opinion of beneficial nature of spandrels only if they are provided on both opposite joint sides. Presence of one-sided spandrel, the case of corner joint, might only negligibly enhance joint shear strength. A realistic bidirectional test of three-dimensional corner joint loaded simultaneously is carried out in the experimental phase of this study to determine whether there is any benefit because of the spandrel on one side of the joint.

3.7.5 Effect of Longitudinal Beam Reinforcement Detail inside Joint

The most common ways of terminating beam longitudinal reinforcement inside joint in gravity building construction were presented in Fig. 2.10. It is evident from experimental results, [51], that bending the beam reinforcement hook outside of joint (Fig. 3.64) significantly contributes to both poor joint shear strength and principal tension as well as to more strength degradation compared to the case of bent-inside-joint hook. There are two available shear transfer mechanisms in joints with hooked-out reinforcement. The first is the secondary strut mechanism generated through bond strength of beam reinforcement inside the joint, which is reflected by bearing forces of bar lugs against concrete. The strength of this virtual secondary strut is limited by bond strength of beam bars. The other is the attempt of a main diagonal strut to pin on the nearest column hoop to the joint, which is an unstable mechanism. However, it is evident that both mechanisms are not effective to transfer shear within the joint. The joint shear strength coefficient of such detail cannot exceed 4, [51] and [113].

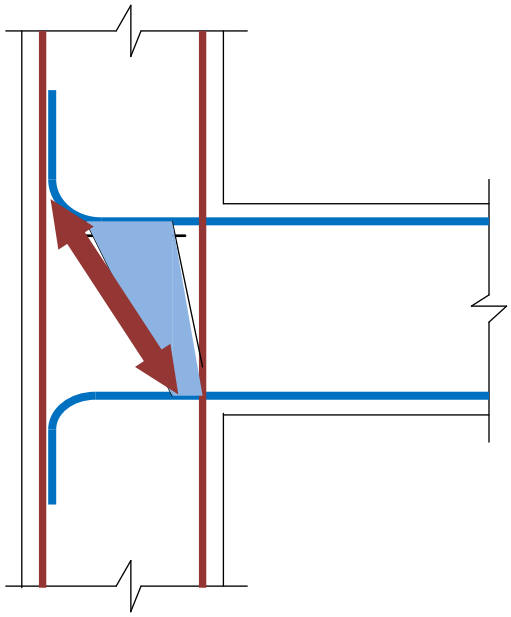

Figure 3.64 Limited capacity of bent-out bars and secondary strut mechanism in exterior beam-column joints

The detail of beam bottom reinforcement embedment in the joint has proven to be instrumental and decisive to determine joint capacity. The older construction practice of providing a short embedment of bottom beam bar inside the joint (Fig. 3.65) is confirmed to jeopardize joint shear capacity under earthquake loading due to bond-slip failure. This insufficient embedment length significantly threatens the joint capacity as at leads to a premature bond pullout failure (S-Failure) at less than 25-50% of the actual joint shear strength, depending on the length embedded. This is attributed to the absence of the main shear transfer mechanism, which is the diagonal strut since there is no hook corner the strut can be supported at. Moreover, even the secondary strut mechanism cannot be formed since the embedment length of beam reinforcement is too short to generate it. That means that the joint subassembly strength is solely a direct function of bond capacity of this insufficient bar length. This premature pullout failure

jeopardizes the joint capacity since its actual shear strength is not triggered. Moreover, the crack opening at the beam joint interface due to reinforcement slip in the beam push-up cycle hinders the development of full joint shear strength in the beam pull-down cycle. This is resulted from yielding of this bar which prevent crack closing in the downward loading direction. This effect is validated by test results, [51]. Quantitative assessment of shear strength corresponding to pull-out failure is addresses in detail in Chapter 5. In terms of displacement, the insufficient bar termination detail results in excessive displacements due to slip of beam reinforcement, which could lead to global instability of concrete frame. There is no point in addressing ductility observations for the S-Failure mode.

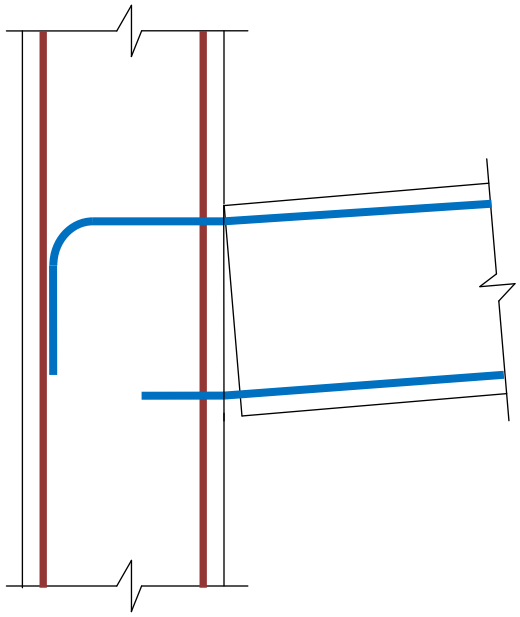

Figure 3.65 Insufficient beam-bar embedment in beam-column joints

Hook terminating smooth beam reinforcement inside joint as in Fig. 3.19.d is considered a very poor construction practice which leads to brittle hybrid failure mechanism of sudden and severe joint shear damage after the first diagonal crack combined with slippage of longitudinal beam reinforcement within the joint and concentrated compressive force at the end-hook anchorage. The strength of joints of this type of hooked ended reinforcement is similar to those of bent-out-beam-reinforcement joints.

Accordingly, it is evident the current practice of bending beam longitudinal reinforcement into the joint is the best among all other alternatives to form stable diagonal strut mechanism in both cyclic loading directions. This enables engaging the full seismic joint shear capacity in J-Failure mode.

3.7.6 Effect of Presence of Column Intermediate Vertical Reinforcement

Another controversial factor is the effect of column intermediate longitudinal reinforcement on the joint shear strength. Some researchers (Wong [155], Hwang and Lee [64], and Hwang et al. [65]) confirm the enhancement of joint shear strength due to the presence of this reinforcement.

Wong [155] reported 24% enhancement of joint shear strength due to using two layers of intermediate column reinforcement compared to bare joints. Further increase of column intermediate reinforcement (four layers) slightly improved the strength (34% enhancement compared to bare specimen). This suggests asymptotic trend approaching a threshold limit of strength enhancement due to column intermediate reinforcement (Fig. 3.66).

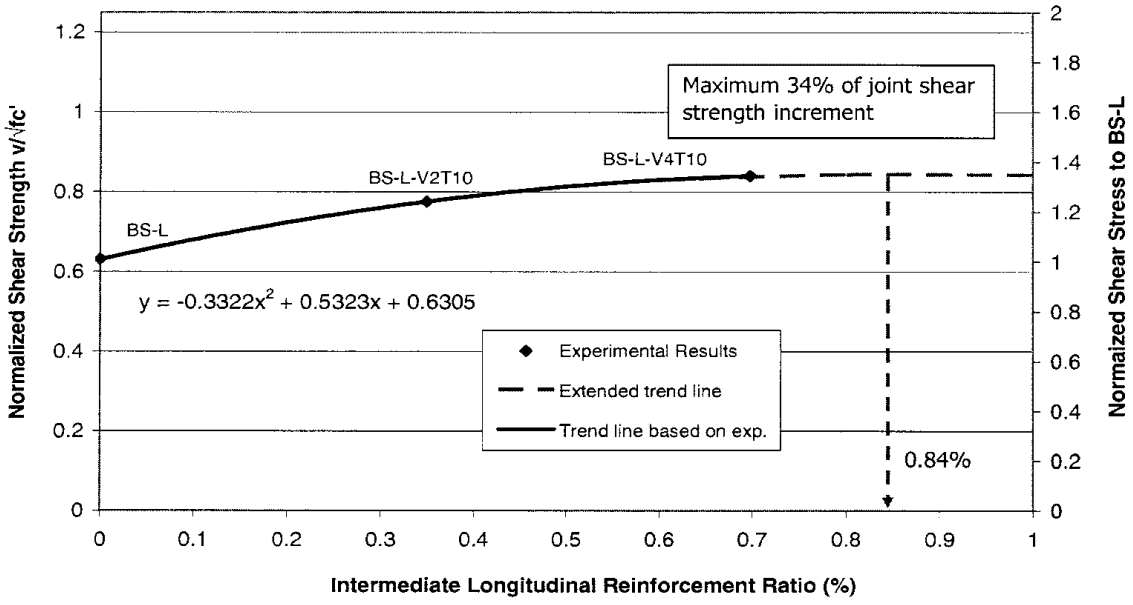

Figure 3.66 Effect of intermediate column reinforcement on unconfined joint shear strength, Wong [155]

Hwang and Lee [64] analytically suggested the contribution of column intermediate reinforcement as tension ties in his three component strut-and-tie mechanisms. However, according to that model, the contribution of intermediate column reinforcement unrealistically increases as the strut angle increases in resisting shear strength in unconfined joints (Fig. 3.1.b). This obviously contradicts mechanics and intuition. Hwang et al. [65] also confirmed yielding of column intermediate reinforcement inside the joint as it acted as tension tie improving joint shear strength. It is worth mentioning that in all the above tests, more than one central layer of column intermediate reinforcement was provided.

Park [120] reported insignificant strains of column intermediate reinforcement within the joint area, which means that they did not act as tension tie to improve shear strength. However, the important observation in these two tests that only one central layer

of column intermediate bar was used. In some tests [120], the central layer of column reinforcement reflects a reinforcement ratio of 0.76%, which is according to Fig. 3.66 corresponding to 34% improvement in shear strength. However, this did not reflect the joint shear strength of these tests since insignificant strains of column intermediate bars were recorded at mid-joint height.

This suggests that intermediate column reinforcement might be only helpful to increase joint shear strength *if more than one layer* of intermediate bars is provided. Further investigation of the effect of intermediate column bars will be provided through the discussion of test results of the experimental phase of the current study.

3.7.7 Effect of Presence of Column Lap Splices

Two main experimental observations were evident regarding the effect of column lap splice on joint shear strength, [155] and [16]. The first is that the column lap splice has no effect on joint shear strength degradation if the mechanism is strong column-weak beam. The second is that in strong beam weak column mechanism, it is evident the deterioration of bond stress and longitudinal cracking at lap splice location contributing along with the overall column yielding to the decline of joint shear capacity and lead to the premature failure of joint.

3.7.8 Common Design Parameters for Unconfined Joints in Older Construction

Table 3.4 shows the most common column to beam strength ratios found in older buildings. It can be seen from that table that both hinging scenarios, Strong Column-Weak Beam and Strong Beam-Weak Column exist in older buildings. The failure mechanism classification of unconfined joints into J, BJ, CJ and BCJ primarily exists because of the varying column to beam strength ratio, through either different beam or column reinforcement only or through changing aspect ratio (dimensions), which in turn changes flexural capacities.

Table 3.4.a Average parameters for pre-1967 buildings, (Mosier, [104])

	Axial load ratio	Column lap splice length (in.)*	v_j/f_c'	Vol. joint reinf. ratio	$\Sigma M_c/\Sigma M_b$
Average	0.12	28	0.21	0.000	2.2
Standard Deviation	0.07	8	0.09	0.000	2.8
Minimum	0.03	20	0.03	0.000	0.2
Maximum	0.28	38	0.37	0.002	9.4

*: typically spliced above floor

Table 3.4.b Average parameters for 1967-1979 buildings

	Axial load ratio	Column lap splice length (in.)*	v_j/f_c'	Vol. joint reinf. ratio	$\Sigma M_c/\Sigma M_b$
Average	0.17	Variable in location and length	0.15	0.009	2.04
Standard Deviation	0.10		0.06	0.008	1.29
Minimum	0.03		0.06	0.000	0.70
Maximum	0.33		0.29	0.021	5.18

3.7.9 Joint Contribution to Total Interstory Drift

As mentioned previously, the assumption of rigid joints in modeling inelastic frame seismic performance is no longer appropriate. It has been constantly evident from past test results that the joint flexibility is quite significant to contribute to the total frame deformations especially in the later stages of inelastic loading. The joint contribution to total deformation can reach up to 75% in the inelastic range of some cases of J-Failure joints as reported by Engindeniz [41]. The beam tip displacement (Δ_b) can be divided into seven components:

$$\Delta_b = \Delta^{be} + \Delta^{ce} + \Delta^{bj\text{-}a} + \Delta^{cj\text{-}a} + \Delta^{bj\text{-}b} + \Delta^{cj\text{-}b} + \Delta^{js} \tag{3.39}$$

where Δ^{be} and Δ^{ce} are the elastic deformations of the beam and column, respectively; $\Delta^{bj\text{-}a}$ and $\Delta^{cj\text{-}a}$ are caused by the concentrated elastic and inelastic rotations of the beam and column with respect to the joint, respectively; including plastic hinge rotation. $\Delta^{bj\text{-}b}$ and $\Delta^{cj\text{-}b}$ represent, respectively, concentrated beam joint interface's and column joint interface's rotations due to loss of anchorage of reinforcing bars (e.g. beam bar bond slip, column lap-splice slip). Δ^{js} is caused by joint shear strains.

As shown in Fig. 3.67, the contribution of joint shear deformations to the overall deformation response can be significant, especially in the inelastic range. This can lead to underestimation of global displacements if ignored and assumed a rigid joint in the process of joint performance assessment. Many experimental studies reported substantial contribution of joint shear deformations to total story drifts (Uzumeri, [150], Engindeniz, [41], Walker [154], among others).

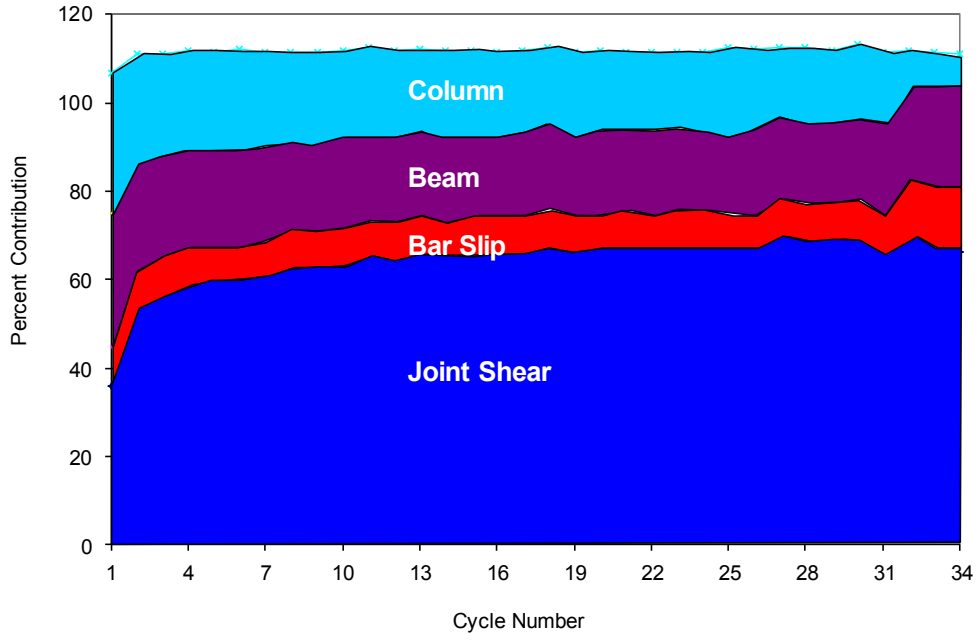

Figure 3.67 Contribution of different components of deformation to overall story drifts, Walker [154], Moehle [97]

CHAPTER 4

PARAMETERS AFFECTING SEISMIC PERFORMANCE OF UNCONFINED BEAM-COLUMN JOINTS

4.1 INTRODUCTION

This chapter is concerned with developing an understanding of the effect of key parameters influencing the seismic performance of unconfined exterior and corner beam-column joints. The main seismic performance measures used to explore these effects are joint shear strength and displacement ductility capacity. Reference also will be made to other seismic response quantities, such as joint shear strains, principal stresses, energy dissipation and strength and stiffness degradation. A database is developed from past tests reported in the literature; this database will serve as a primary source for drawing observations.

4.2 EFFECTS OF VARIOUS PARAMETERS

4.2.1 General

This section discusses the effect of various parameters on seismic performance. These parameters include joint aspect ratio, beam reinforcement ratio, axial load level, and mode of failure.

In some of the presentations, measured joint shear strength is normalized according to the expression $\gamma_j = V_j / A_j \sqrt{f_c'}$, in which V_j = maximum joint shear measured or inferred from the test, A_j = effective joint shear area defined by column depth h_c multiplied by effective joint width b_j according to ACI 352-02 [2] definition, and f_c' = measured concrete compressive strength. V_j can be related to measured beam shear force using Fig. 4.1 and Eq. 4.1 through Eq. 4.3.

$$V_j = T_b + T_s - V_c \tag{4.1}$$

where V_c is column shear force and T_b *and* T_s are tension forces in beam and effective slab reinforcement calculated using beam moment M_b lever arm as:

$$T_b + T_s = \frac{M_b}{jd_b} \tag{4.2}$$

where d_b is the effective beam depth, and j is the lever arm factor which can be calculated exactly from section analysis or approximated as 0.9 for BJ-Failure and 0.875 for J-Failure. It is worth mentioning that the beam moment is calculated at the face of column hence:

$$M_b = V_b L_b \tag{4.3}$$

where L_b is the beam length measured from the face of column to the beam inflection point approximately at beam mid-span. L is half the beam center to center span.

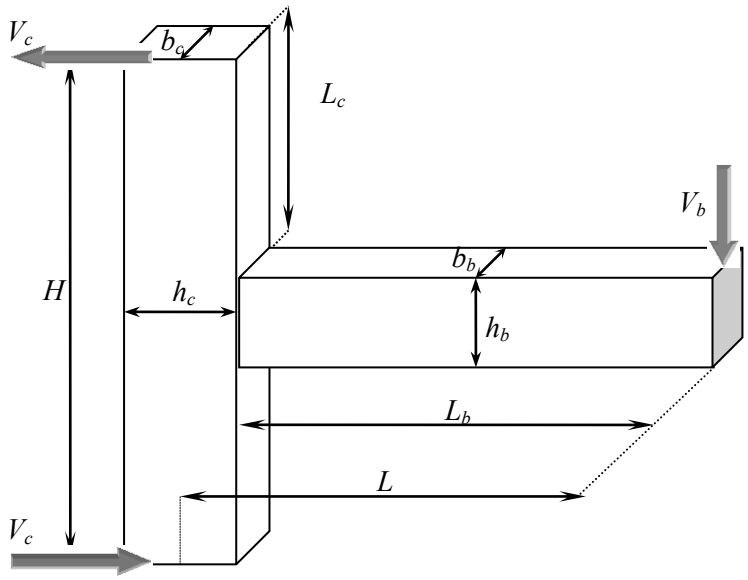

Figure 4.1 Statics of beam-column joint subassembly

In some cases, test specimen displacement is normalized relative to the yield displacement. In such cases, displacement ductility is defined as the ratio of ultimate displacement to yield displacement. In this study, two different definitions of ultimate displacement were explored.

The first defined the ultimate displacement as the displacement δ_{ua} corresponding to the peak lateral force resistance. The second defined the ultimate displacement as the displacement

δ_{ub} corresponding 15 percent reduction in the lateral force resistance. To define yield displacement, a secant was drawn through the measured force-displacement envelope at 0.75 times the maximum resistance; the intersection of that secant with a horizontal line at the maximum resistance defined the yield displacement. The procedure is illustrated in Figures 4.2 and 4.3. The resulting secant corresponds approximately to the effective "cracked" stiffness of a test specimen.

The displacement (or drift) ductility is expressed as:

$$\mu_\delta = \frac{\delta_u}{\delta_y} \tag{4.4}$$

Where δ_u and δ_y are the ultimate and yield drift ratios, respectively. A subscript "a" will be used to denote the displacement ductility corresponding to the peak lateral load deformation $\mu_{\delta,a}$ while a subscript "b" will be used for displacement ductility corresponding to 15% strength loss calculated using 85% peak load deformation in the post-peak region $\mu_{\delta,b}$.

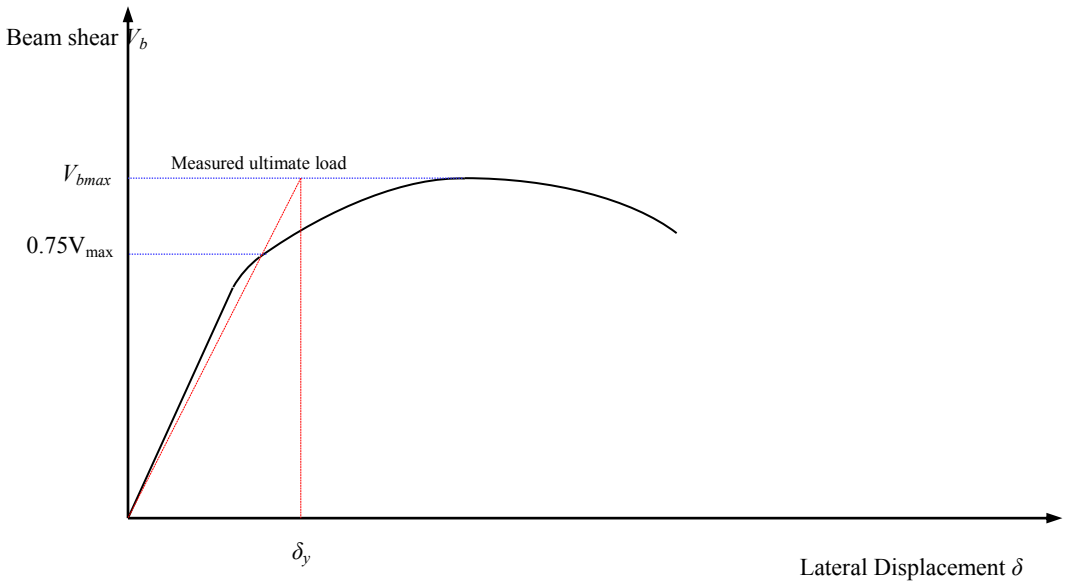

Figure 4.2 Yield deformation definition based on reduced (secant) stiffness elasto-plastic yield

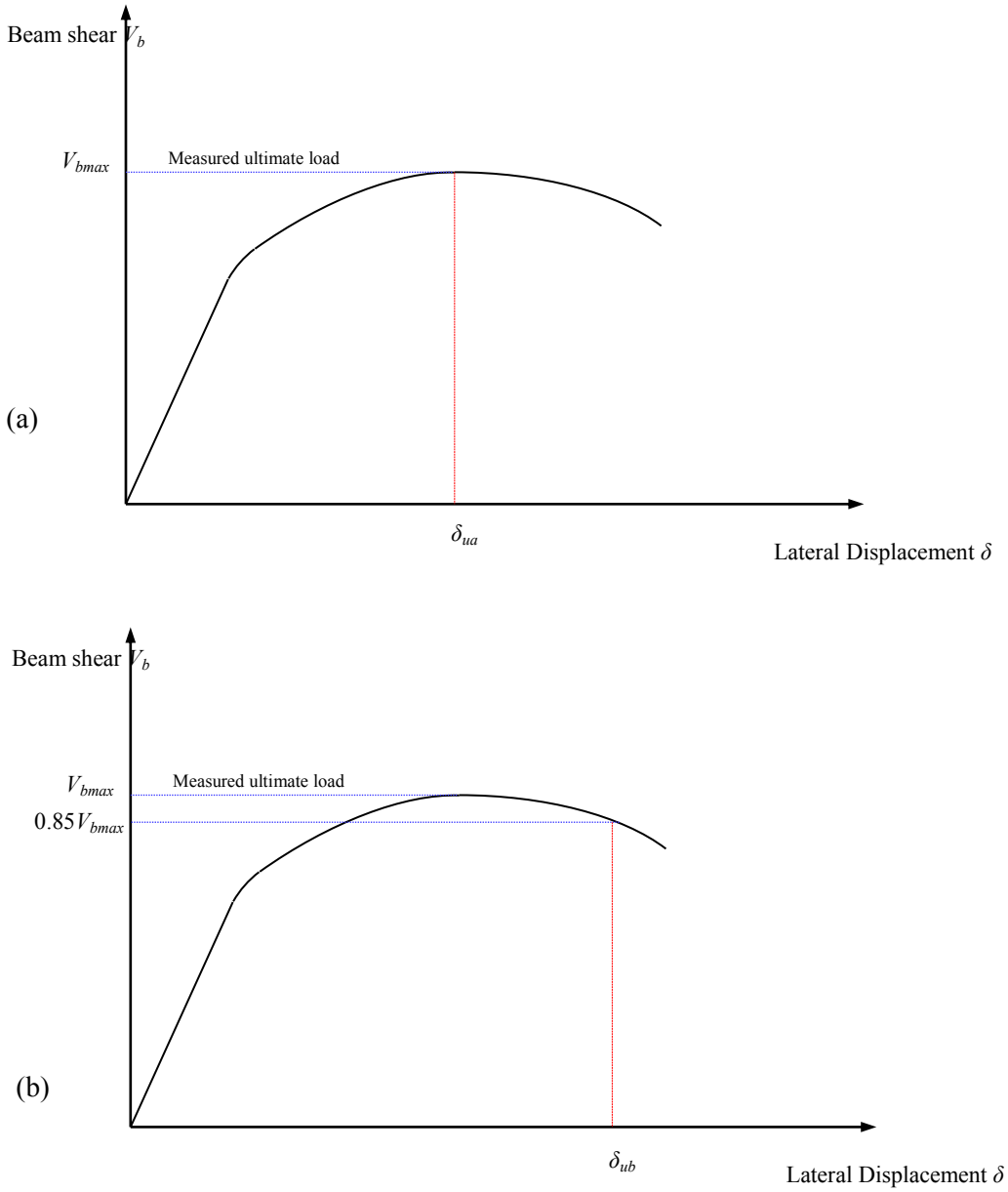

Figure 4.3 Ultimate deformation definition: (a) Peak load deformation
(b) significant (85%) load capacity after peak load

In some cases, nominal principal tension stress is used as an index. Principal tension stress was calculated:

$$p_t = \frac{-f_a}{2} + \sqrt{\left(\frac{f_a}{2}\right)^2 + v_j^2}$$

$$f_a = \frac{P}{A_j} \tag{4.5}$$

in which p_t is principal tension stress (positive in tension), f_a is normal stress on the joint calculated as the axial force divided by the gross area of the joint, and v_j = nominal joint shear stress calculated as $v_j = V_j / A_j$.

4.2.2 Unconfined Joint Database

The database used in this study comprises 100 unconfined beam-column joints tests. Tables 3.1, 5.1 and 5.2 show the details and parameters of joints considered. The database was established using consistent criteria considering the following:

1. The joints are isolated exterior joints, corner joints, corner-simulated joints, or exterior joints with transverse stubs on both sides. Stubs are pre-cracked to simulate gravity loading.
2. For the main joint response quantities considered, the detail of beam top longitudinal reinforcement termination inside the joint is the standard end hook bent into the joints.

Modes of failure considered are defined as J, BJ, and BCJ. Failure mode is designated as J if the joint failed prior to yielding of the beam or column longitudinal reinforcement, BJ if the beam longitudinal reinforcement yielded prior to joint failure, and BCJ if both beam and column longitudinal reinforcement yield prior to joint failure. Longitudinal axes of beams and columns intersect. Joints with eccentricity of framing members are excluded. For all plots in this chapter, axial load ratio less than 0.2 is denoted low axial load, and axial load ratios higher than 0.2 are denoted high axial load. The BJ-Failure joint database included unconfined joint tests by Hanson and Conner specimen VA [53], Hanson and Conner SP 7 [54], Priestley and Hart [129], Clyde et al. [26], Wong [155] specimens JA-NN03, JA-NN15, JB-NN03, BS-L-300, Filiatraut and Lebrun [43], Zahertar [158], Hwang et al. [65] specimens 0T0, 1B8, and Le-Trung et al. [144].

The seismic response parameters included in the computational code for the database reflected strength parameters such as yield strength of subassemblies, maximum joint shear strength and joint shear strength coefficient at peak load, peak load principal tension, residual strength at test termination, and axial load ratios. The parameters also included deformational Engineering Demand Parameters (EDP) such as deformations and drifts at yield, peak load drifts, maximum inelastic deformation and drift, plastic rotations of beams, and displacement and drift ductility factors. Backbone curves have been developed to envelop the hysteresis response of some of the test specimens. Careful unified yield displacement definitions have been adopted to have consistent bases for comparisons regardless the authors' used ductility and yield displacement definitions.

4.2.3 Effect of Joint Aspect Ratio

The effect of joint aspect ratio on joint shear strength is well established based on analytical and experimental observations. The joint shear strength decreases as joint aspect ratio (ratio of beam depth to column depth) increases.

As discussed in Chapters 2 and 3, the main mechanism controlling shear strength of an unconfined beam-column joint is the strut mechanism (Fig. 2.7.b). The strut angle θ relative to horizontal affects the joint strength. For a given joint area A_j, the joint has maximum strength for strut at a 45 degree angle. The larger the joint aspect ratio, the larger the angle θ and the lower the joint shear strength. Two definitions for joint aspect ratio are commonly used. The first is the ratio between beam depth h_b to column depth h_c, that is $\alpha_j = h_b/h_c$. This definition assumes the entire joint as a shear panel transferring loads through direct normal and shear stresses. The second definition visualizes the diagonal strut as being constrained within the outermost beam and column longitudinal bars. By this definition, the joint aspect ratio is defined as the ratio h''_c/h''_b. which are centerline distances between outermost column longitudinal reinforcement and beam longitudinal reinforcement, respectively.

Based on an analysis of database of monotonic joint tests, Vollum and Newman [1] and Bakir and Boduroğlu [12] suggested an inversely proportional linear relation between joint shear strength and joint aspect ratio in the range of 1 to 2.

Figures 4.4 and 4.5 display the relationship between joint aspect ratio and joint shear strength coefficient for the database of cyclically loaded joints used in the current investigation. It is clear that joint shear strength is inversely proportional to joint aspect ratio. However, other factors affect the relation. For example, the reduction in joint strength with aspect ratio is more pronounced for higher axial loads. Figure 4.2 reveals an average 20% reduction in shear strength for axial loads above $0.2\, f'_c A_g$ and 12.5% average reduction for axial loads below $0.2\, f'_c A_g$ for joints experiencing J-failure.

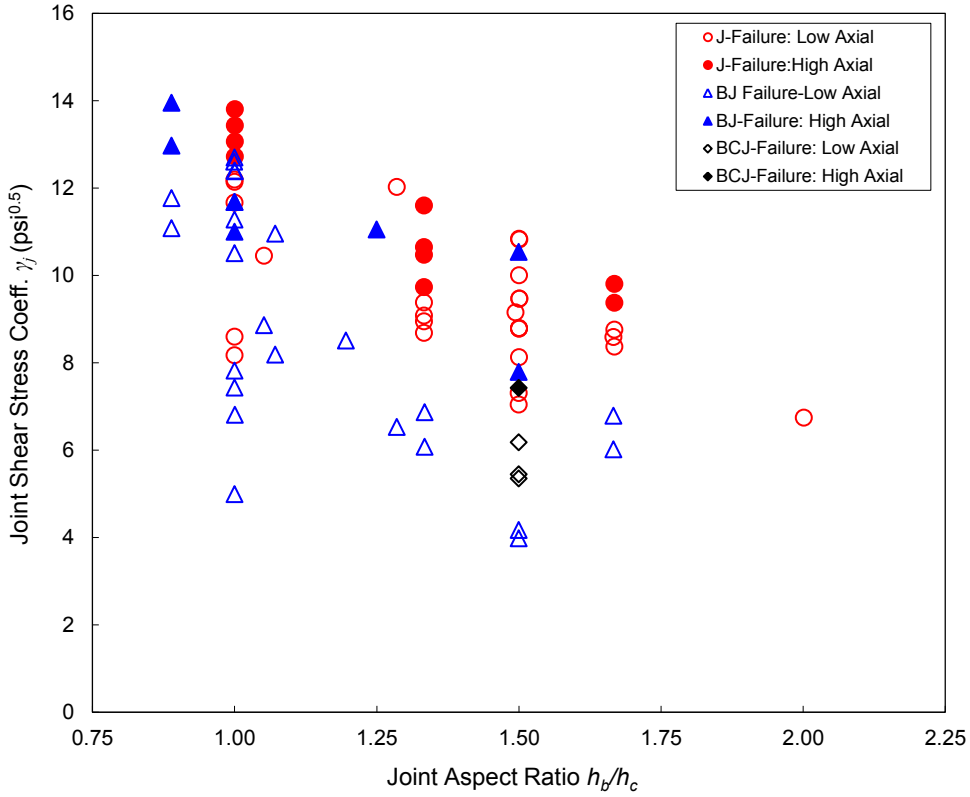

Figure 4.4 Effect of joint aspect ratio on joint shear strength

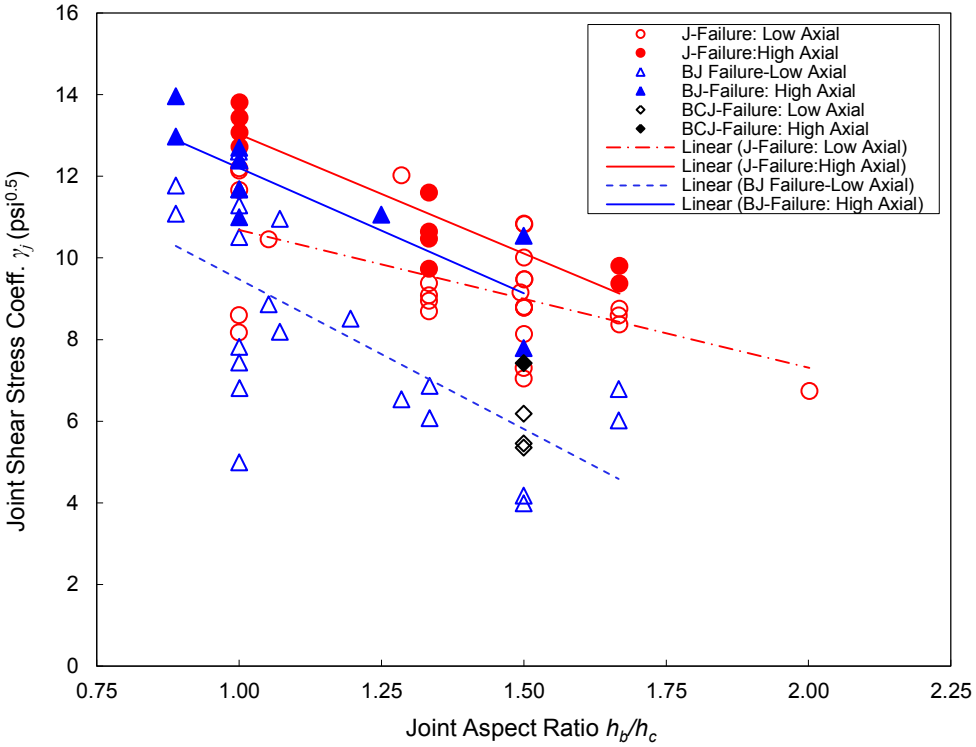

Figure 4.5 Linear trends of the effect of joint aspect ratio on exterior joint shear strength

A steeper compression strut is likely to be more flexible; hence, a joint with higher aspect ratio is likely to be more flexible than an equivalent joint with smaller aspect ratio. Consequently, joints with higher aspect ratio may be more flexible and may have greater contributions of the joint to overall deformation. However, this hypothesized effect is not apparent in the ultimate drift capacity (Figure 4.6).

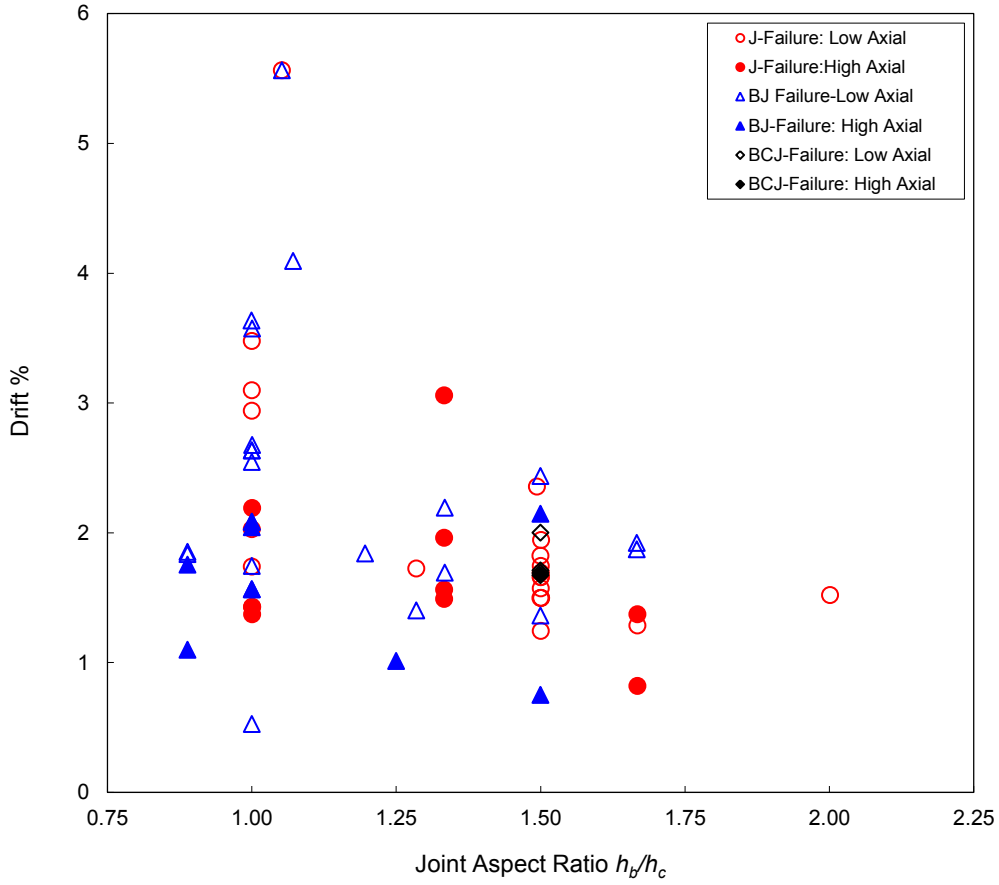

Figure 4.6 Effect of joint aspect ratio on joint subassembly drift ratio

Figure 4.7 plots the observed displacement ductility capacity as function of joint aspect ratio. As noted in Section 4.2.1, two definitions of displacement ductility are used. $\mu_{\delta,a}$ is calculated for ultimate displacement corresponding to the maximum lateral force resistance while $\mu_{\delta,b}$ is calculated for ultimate displacement corresponding to 15% loss in lateral force resistance. There is no definite trend in the plotted data for either definition, although joints with higher aspect ratio tend to have somewhat higher displacement ductility.

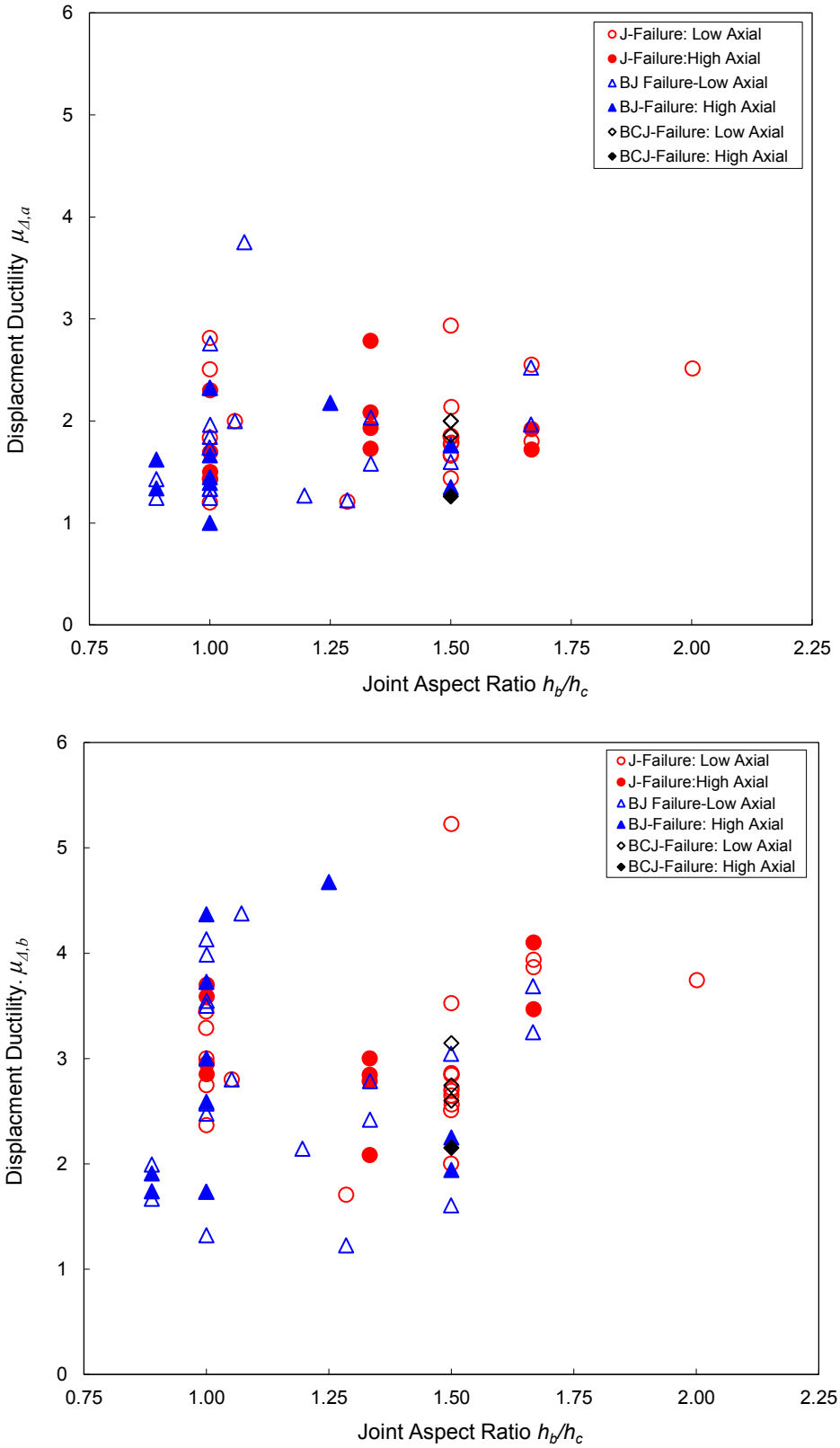

Figure 4.7 Effect of joint aspect ratio on displacement ductility factor

Joint axial load and shear stress at failure were combined using Equation 4.5 to derive nominal principal tension stress at failure. Figure 4.8 plots the relation between principal tension stress at failure and joint aspect ratio. The scatter in data suggests that principal tension stress is not a universal measure of joint strength. Interestingly, joints with higher axial load failed at lower principal tension stress, while joints at lower axial load failed at higher principal tension stress, suggesting that the principal tension stress model overstates the effect of axial load on joint shear strength.

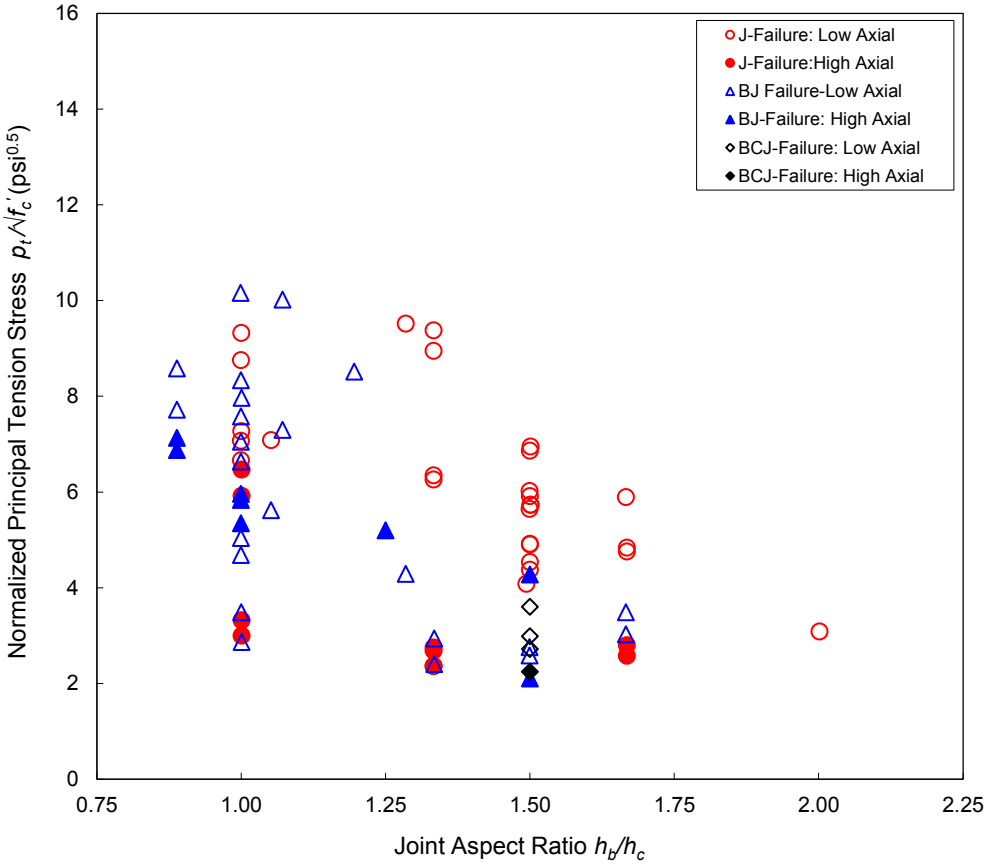

Figure 4.8 Effect of joint aspect ratio on principal tension stress

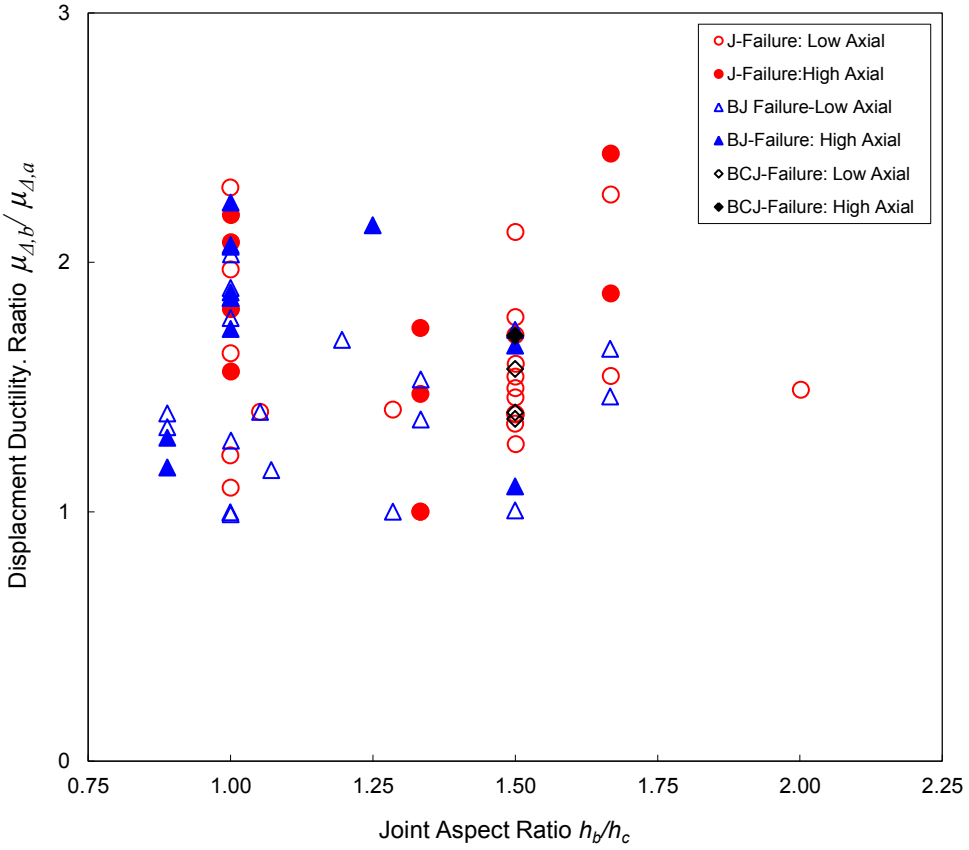

Figure 4.9 Effect of joint aspect ratio on post peak deformability

The joint post peak degradation slope is an important measure of collapse vulnerability. Figure 4.9 plots the effect of joint aspect ratio on the ratio between the two displacement ductility definitions introduced previously $\mu_{\delta,b} / \mu_{\delta,a}$. This ratio reflects how severe the post-peak strength degradation is. That is the higher this ratio the steeper the post-peak degradation slope and more severe the strength deterioration. No clear trend can be observed, although joints with higher aspect ratio tend to have somewhat post-peak strength deterioration. It seems that for a specific joint aspect ratio, higher axial loads tend to degrade post-peak strength more profoundly.

4.2.4 Effect of Column Axial Load

The effect of column axial load on joint shear strength has been the subject of several studies. Some studies [116], [26] and [13] find that joint shear strength increases with increasing axial load, while other studies [114], [152] and [77] find that joint shear strength is not affected by axial load, and still other studies [151] find that shear strength decreases with increasing axial load. Apparently, the effect is complicated by the complex mechanisms associated with joint shear resistance. Most studies that opine on the subject agree that higher axial load reduces ductility capacity and results in more rapid strength degradation after initiation of failure.

Figure 4.10 depicts the relationship between axial load ratio and joint shear strength coefficient for the database used in this study. Taken altogether, there is a slight trend for increasing strength with increasing axial load. However, investigating each separate category in the figure permits some useful observations. The beneficial effect of axial load is more pronounced when applying axial loads higher than $0.2f_c'A_g$. Within the range of 0 to $0.2f_c'A_g$, the joint shear strength enhancement due to increasing axial load is not as significant as the effect of increasing axial load beyond $0.2f_c'A_g$. The increase in shear strength with increasing axial load is especially clear for joints experiencing J type failure. For joints experiencing BJ type failure, the trends are less clear. This can be explained by the fact that beam flexural strength, which limits the joint shear at failure, is not affected by axial load. However, higher strengths for BJ type failure may occur in some cases because the higher axial load increases the joint shear strength, and the higher joint strength in turn may force the failure initiation into the beam. It is also possible that higher axial load will increase bond strength of beam bars anchored in the joint, which in turn enhances the beam flexural strength and, consequently, the joint strength at failure (Pantelides et al., [116]). Figure 4.11 also confirms the positive effect of axial compression on joint shear strength. Within the same joint aspect ratio, a 10-20% increase in joint shear strength can be observed due to increasing axial load.

Figure 4.12.a displays the effect of axial load on the drift capacity at peak joint shear strength of unconfined beam-column joints used in the current database. No clear trend is apparent in the data. However, joints with higher axial load tend to have lower drift capacity than joints with lower axial load. The tendency of higher axial load to decrease drift capacity is clearer in Fig. 4.12.b that shows the effect of axial load on drift capacity at 15% reduction of shear strength.

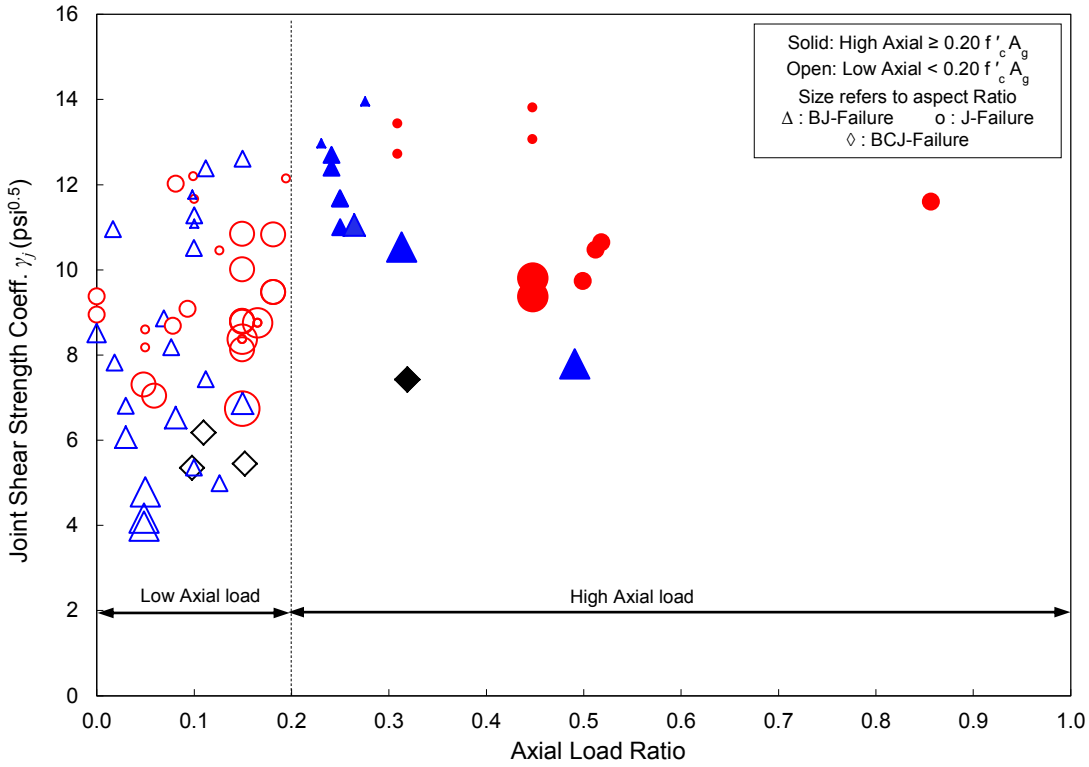

Figure 4.10 Overall effect of axial load on joint shear strength

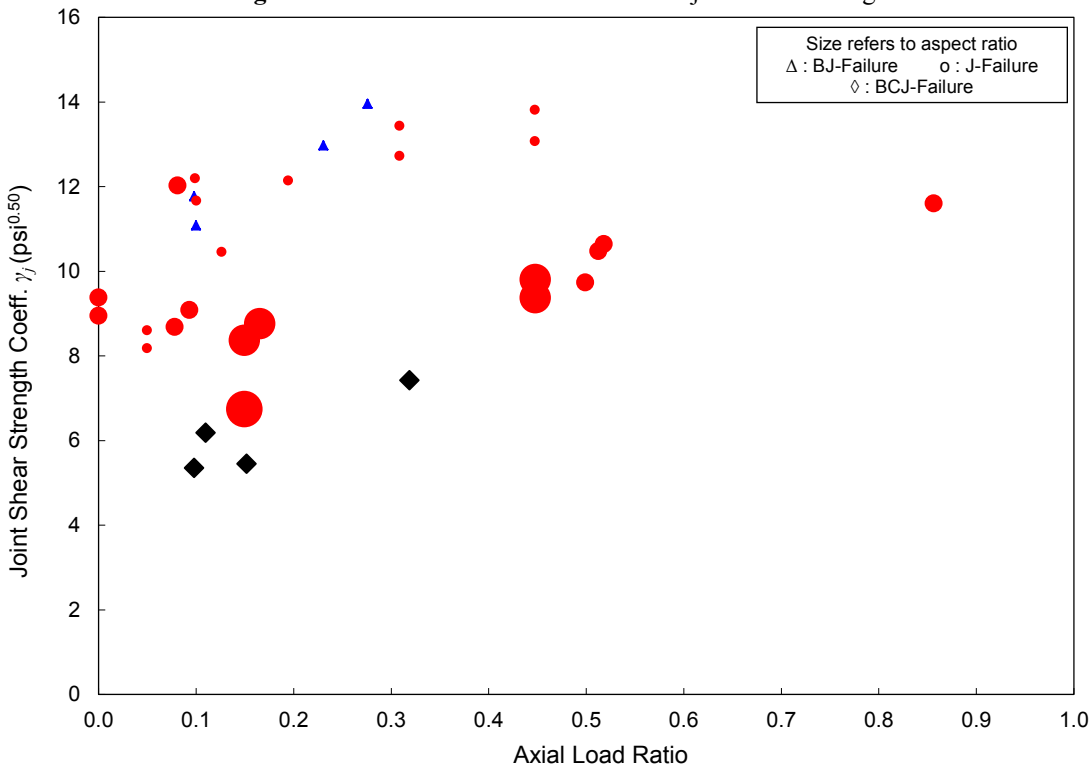

Figure 4.11 Effect of axial load on joint shear strength

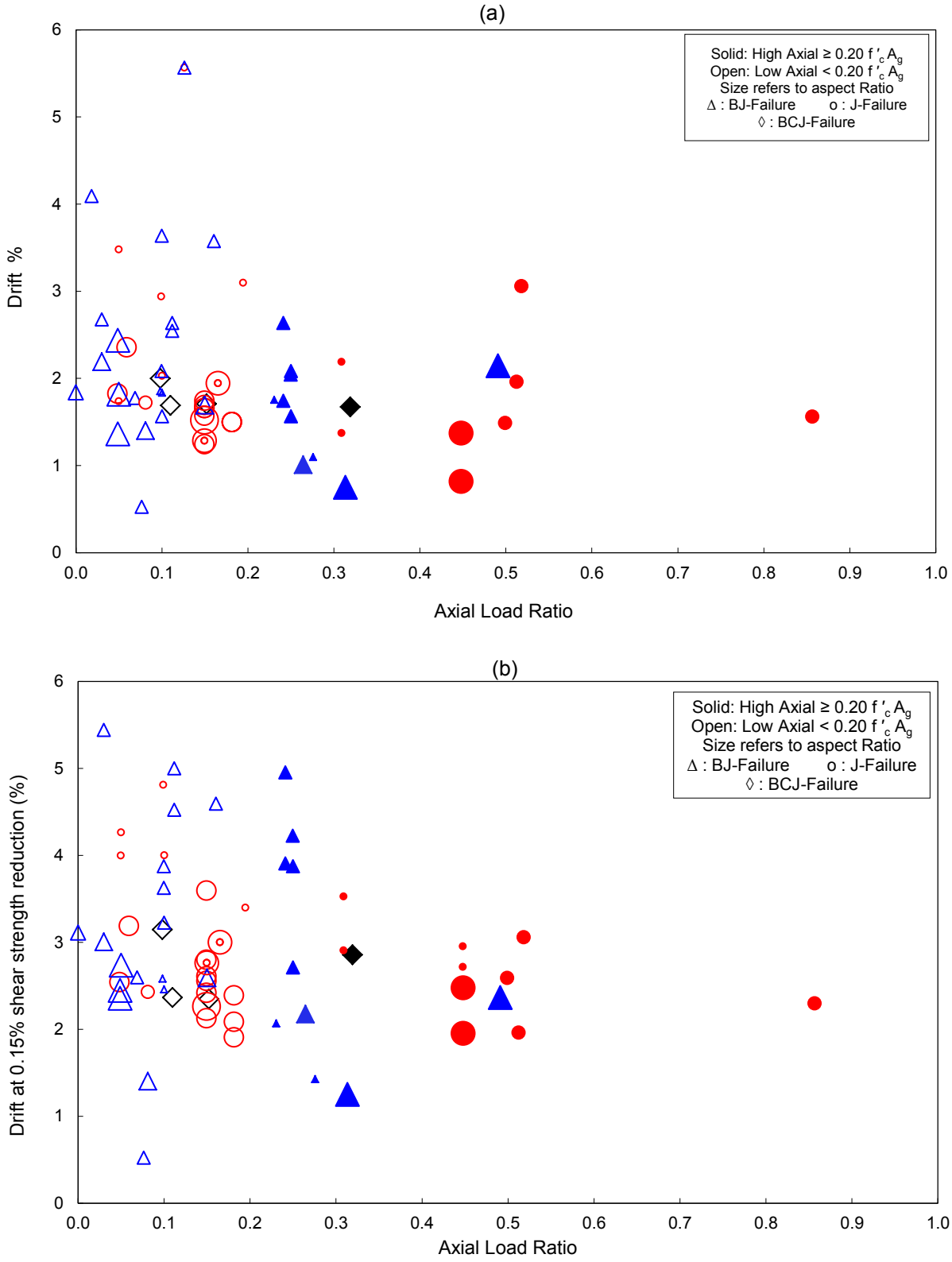

Figure 4.12 Effect of axial load on joint subassembly drift ratio

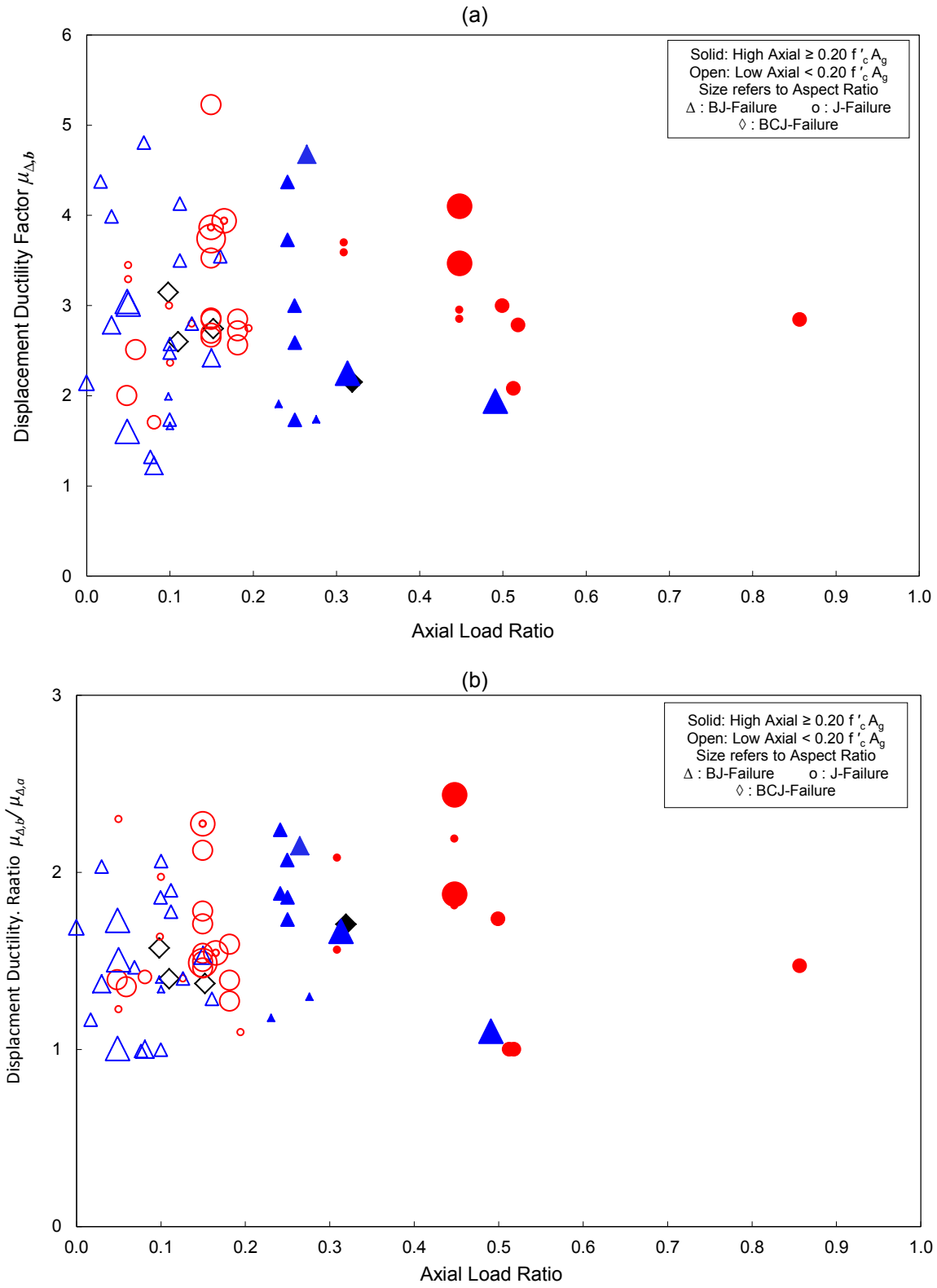

Figure 4.13 Effect of axial load on joint subassembly displacement ductility factor

Figure 4.13.a plots the effect of axial load ratio on displacement ductility capacity. No clear trend can be observed for BJ-Failure mode. However, there is some tendency for higher axial loads to decrease displacement ductility of J-Failure joints, especially for axial loads higher than $0.2f_c'A_g$. Figure 4.13.b shows the effect of axial load on the ratio of the two displacement ductility definitions, which reflects the rate of post-peak strength degradation. No general correlation is observed. However, some reduction of this ratio with high axial loads is associated with J-Failure joints.

Figure 4.14 plots the relationship between column axial load and principal tension stress at joint failure for the database. Focusing only on the J-Failure cases, it is clear that nominal principal tension stress at joint failure decreases as axial load increases. Apparently, the principal tension stress model overstates the effect of axial load on joint shear strength.

Higazy et al. [59] investigated the effect of tensile axial loads on joint shear strength and deformation capacity, and reports 12% loss in joint shear strength and 30% loss in displacement ductility capacity due to applying constant tensile axial load ratio of 5% as opposed to constant compressive axial load of $0.05(f_c'A_g + f_{yc}A_{sc})$

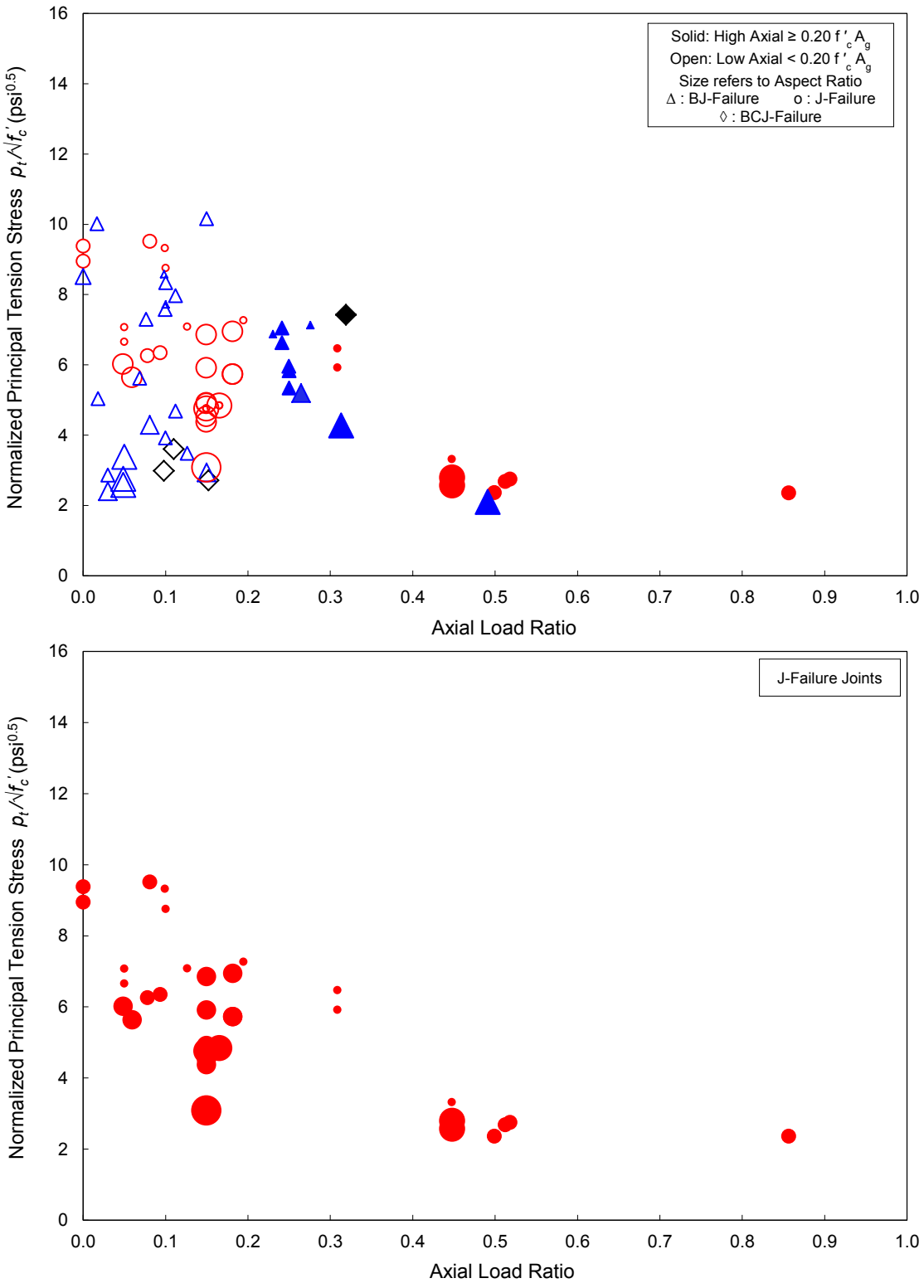

Figure 4.14 Effect of axial load on joint principal tension stress at joint shear strength peak

4.2.5 Effect of Beam Reinforcement Ratio

The effect of beam reinforcement ratio on joint shear strength has been the subject of several previous investigations. Moehle [97] suggested that the strength of unconfined exterior joints was equal to the shear stress demand from beam flexural capacity with an upper bound of $12\sqrt{f_c'}$. The upper bound corresponds to J-Failure strength.. Based on tests of interior joints, Alire [6] showed that joint shear strength is tied to beam flexural strength. Park [120] tested four corner joints and proved that the beam flexural capacity decided the mode of joint failure. If the joint shear stress demand corresponding to beam plastic moment is higher than the basic joint shear strength, relatively brittle failure occurs in the joint (J-Failure). On the other hand, if for lower beam reinforcement ratio, the beam may yield first, leading to relatively more ductile response that eventually is limited by failure of the joint at a lower joint shear stress (BJ-Failure). The maximum joint shear strength that can be reached in this case equals the shear stress demand determined from the beam flexural reinforcement. This apparently occurs because yield penetration of the beam longitudinal reinforcement into the joint leads to degradation of the joint shear resistance mechanisms.

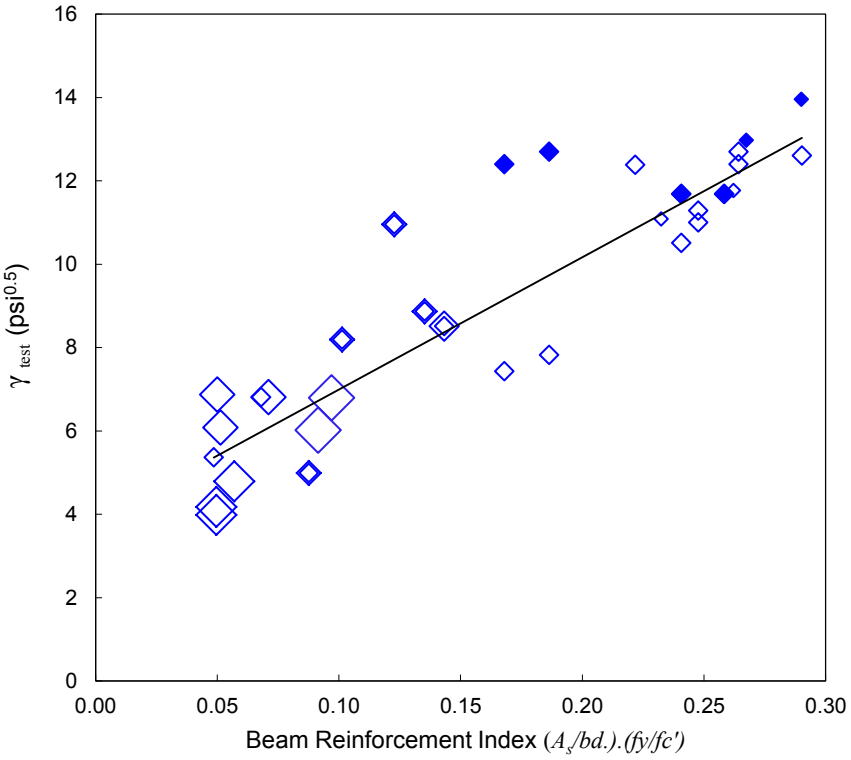

Figure 4.15 Effect of beam reinforcement on joint shear strength coefficient

Figure 4.15 shows the relationship between joint shear strength coefficient and beam reinforcement index BI defined as:

$$BI = \frac{A_s f_y}{bdf_c'} \tag{4.3}$$

Solid diamonds in Figure 4.15 refer to joints with axial load ratio higher than 0.2, while the size of diamond represent the joint aspect ratio. Only joints experiencing BJ-Failure are plotted. The increase of joint strength with increasing reinforcement index is apparent.

4.3 OBSERVED STRENGTH - DUCTILITY TRENDS OF EXTERIOR AND CORNER JOINTS

4.3.1 Shear Strength-Drift Ratio Observations of Exterior and Corner Joints

Figures 4.16 illustrates the relationship between joint shear strength coefficient γ_j and the drift capacity at peak shear strength.

A wide scatter in joint shear strength coefficient is observed. It ranges from 4 to about 14 (psi units). This variability gives a glimpse on the inaccuracy of the current assessment documents such as the ASCE /SEI 41-06 [11] that recommends a shear strength coefficient of 6 for such joints. This scattered variability of joint shear strength coefficient values for isolated exterior joints is believed to be attributed to the effect of the influence parameters discussed in this chapter and in Chapter 3. No clear shear strength-drift ratio trend can be recognized.

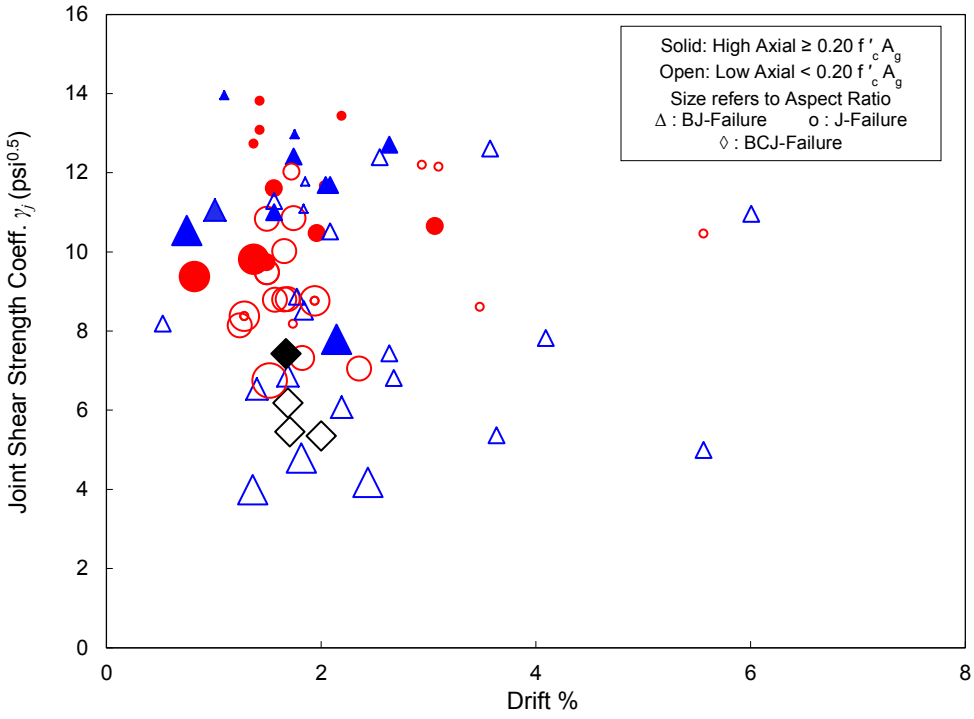

Figure 4.16 Joint shear strength-drift relationship

4.3.2 Relation between Shear Strength and Displacement Ductility

Figure 4.17 plots the relationship between the joint shear strength coefficient and displacement ductility $\mu_{\Delta,b}$. No definitive trend is recognized. However, there is some tendency to lower strength associated with large drifts for J-Failure mode. The BJ-failure mode generally is more ductile compared to J-Failure mode. Displacement ductility $\mu_{\Delta,b}$ ranges from 1.22 to 4.68 for BJ-Failure joints and 1.7 and 5.23 for J-Failure mode, while $\mu_{\Delta,a}$ ranges from 1. to 3.75 for BJ-Failure and 1.2 to 2.94 for J-Failure mode.

As mentioned, it is difficult to immediately recognize the intuitive strength degradation trend with ductility for unconfined joints reported and modeled by previous researchers. However, the effects of axial load ratio and joint aspect ratio should be isolated first to decide if there is any proportionality between displacement ductility or other EDPs and shear strength of exterior and corner joints.

Based on the observations on effect of axial load ratio and joint aspect ratio in Sec. 4.2, and backed by test results of the current study, the effect of axial load can be isolated based on the assumption that it has an uncertain (or negligible) effect within the range of axial load ratio 0-0.2 and a positive effect on shear strength for higher axial load ratios. Accordingly, a linear fitting was used to derive an axial load enhancement factor κ defined as:

$$\kappa = 1 + (0.86 - 0.31\alpha_j)\left[\frac{P}{f_c' A_g} - 0.15\right] \qquad 1 \le \kappa \le 1.35 - 0.10\alpha_j \qquad (4.6)$$

The effect of joint aspect ratio on J-Failure joint shear strength can be modeled using the empirical expression $\alpha_j^{-0.50}$ fitted from test data plots in Sec. 4.2, where α_j is the joint aspect ratio h_b/h_c. Consequently, these expressions were used to normalize the shear strength coefficient γ_j for the database subset of joints experiencing J-Failure mode, as shown in Fig. 4.18.

Better correlation can be seen after isolating the effect of axial load and joint aspect ratio between shear strength and displacement ductility. However, the scatter is still evident. It might be possible to establish a conservative inverse linear proportionality between these two parameters as basis for shear strength degradation model. It is worth mentioning that this ductility observed in J-Failure mode is an inherent ductility due to joint flexibility and independent from flexural ductility.

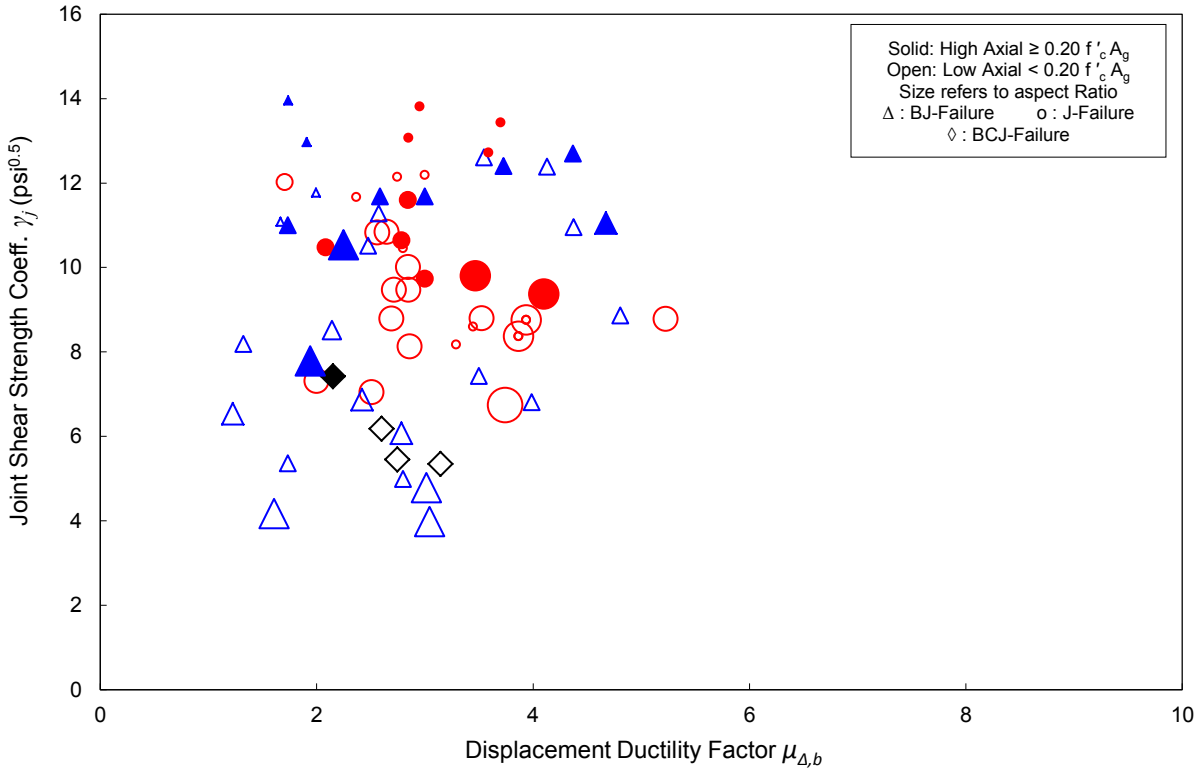

Figure 4.17 Joint shear strength-displacement ductility relationship

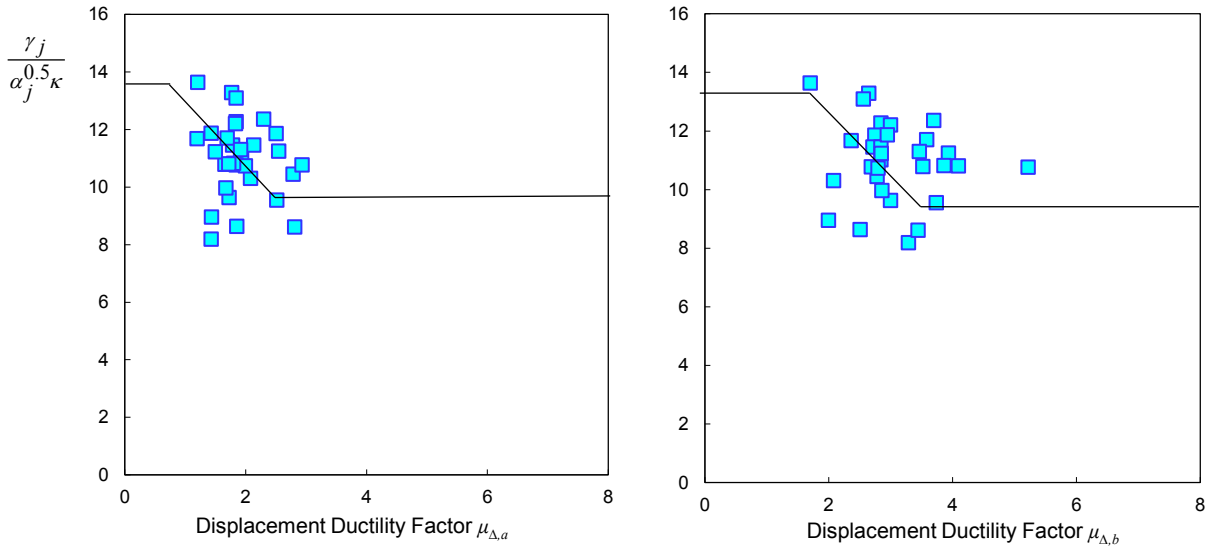

Figure 4.18: Relation between displacement ductility-joint shear strength normalized by aspect ratio and axial load ratio for J-Failure joints

4.3.3 Relation between Principal Tension Stress and Displacement Ductility

Investigating Fig. 4.19 through Fig. 4.21 gives an insight into the effect of different design parameters on the principal tension strength. No generalized clear trend between principal tension stress and drift ratio or displacement ductility can be observed. However, examining Fig. 4.21 reveals some inverse proportionality between principal tension stress and displacement ductility for J-Failure joints.

It is intended in the rest of the current study and in the experimental program to use the normalized joint shear strength coefficient to as a better indicator of joint shear strength rather than principal tension stress. The notion of visualizing the joint as a "shear panel", which is the main field of principal stresses, seems to be representative of joints with transverse reinforcement. However, this simulation might not be appropriate for unconfined joints. This aspect will be investigated in more details in the subsequent chapters.

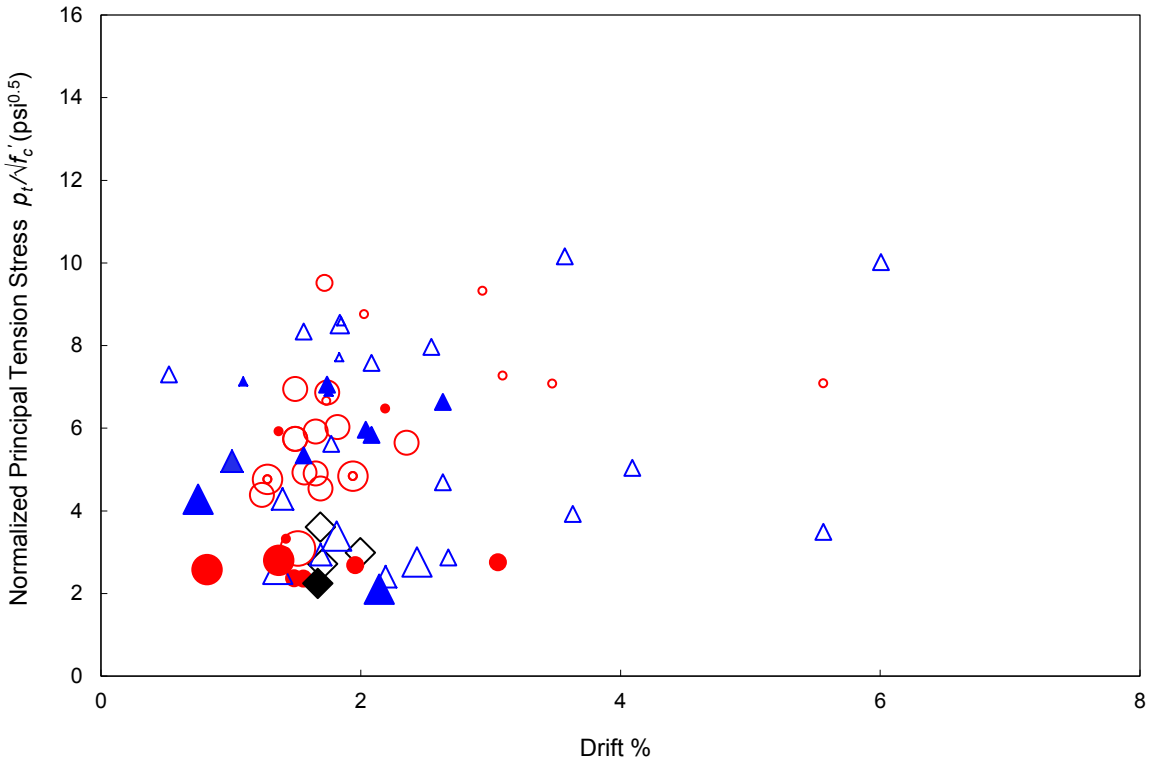

Figure 4.19 Principal tension stress-drift ratio relationship

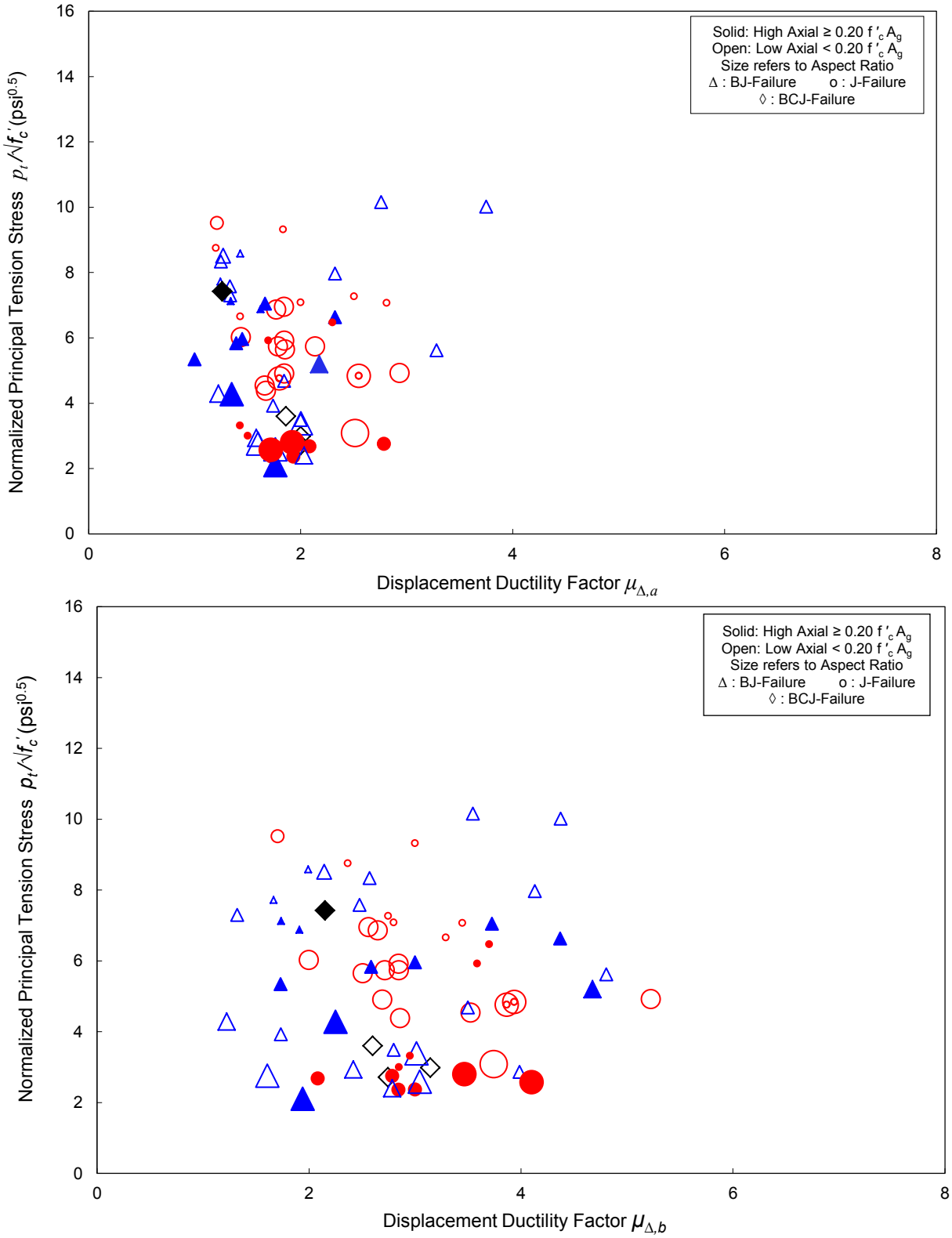

Figure 4.20 Principal tension stress-displacement ductility relationships

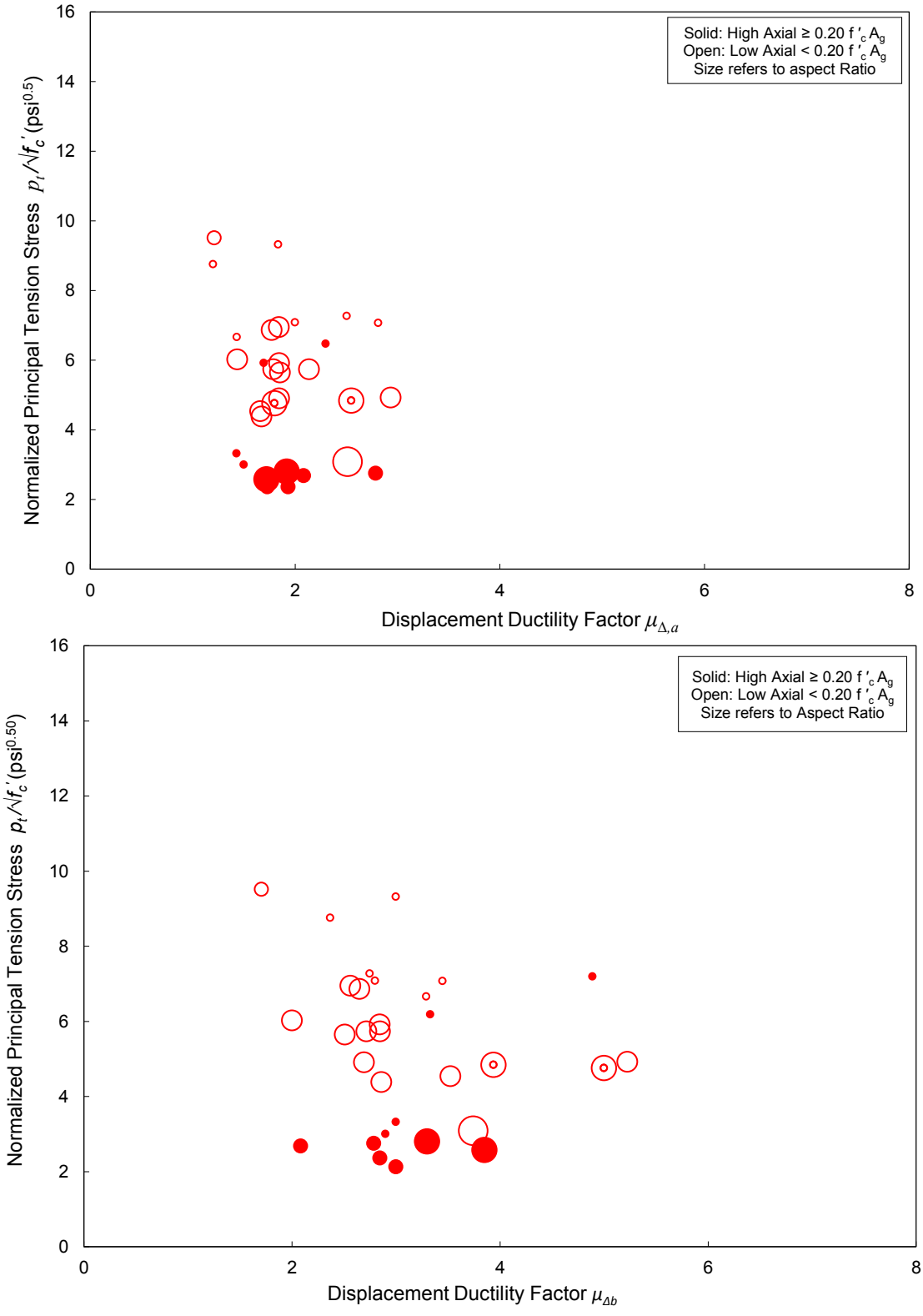

Figure 4.21 Principal tension stress-displacement ductility relationships for J-Failure joints

CHAPTER 5

PROPOSED STRENGTH MODELS FOR UNCONFINED BEAM-COLUMN JOINTS

5.1 INTRODUCTION

Most analytical joint strength models were developed and calibrated for confined beam-column joints. A few analytical models to assess shear strength of exterior joints are available, of which a smaller number are claimed to be applicable to unconfined exterior joints. This chapter presents an evaluation of some available shear and bond strength models when applied to unconfined exterior and corner joints with deficient details. Two simplified shear strength models are developed. Moreover, a shear strength degradation model with ductility parameters is developed. An empirical bond model for pullout strength for exterior and corner deficient joints also is proposed. The models are applied to evaluation of exterior joints without transverse reinforcement.

5.2 DATABASE USED FOR MODEL ASSESSMENT

The database of joint tests used in this chapter includes isolated exterior joints without slab or transverse spandrels and corner joints with or without slab in which the transverse beam (or stub) is initially loaded with gravity equivalent load or is subjected to cyclic load reversals. In all the joints used for the shear strength evaluation, the top and bottom beam longitudinal reinforcement has a standard hook bent into the joint (Fig. 5.1.a), such that bar pullout failure is excluded. A second database of joints used for bar pullout evaluation had beam bottom bars with straight embedment without a hook (Fig. 5.1.b). The databases used to establish and verify the joint strength models in this chapter consisted of 100 tests. Table 5.1 shows the database used for shear strength models while Table 5.2 shows the database used for bond strength models.

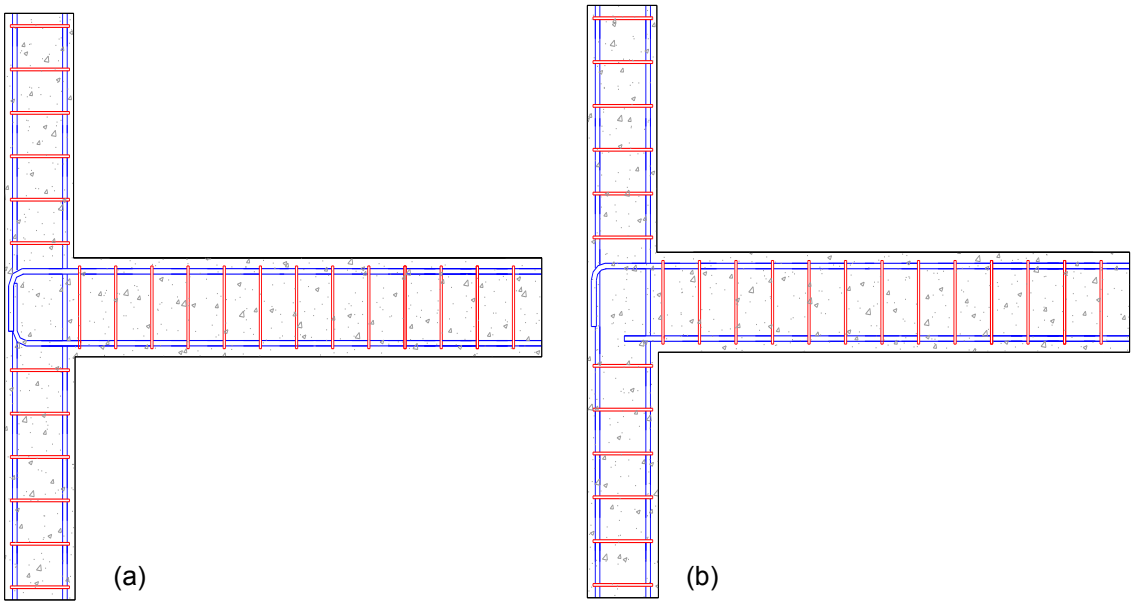

Figure 5.1 Geometry and details of investigated joints, (a) Shear strength database, (b) Bond strength database

5.3 ASSESSMENT OF ASCE/SEI 41-06 JOINT SHEAR STRENGTH PROVISIONS

Joint shear strength provisions in ASCE 41/SEI 41-06 (denoted here as ASCE 41) [11] are appealing for professional practice because they use a familiar format and simple to implement. According to ASCE 41, nominal joint shear strength in lb. units is defined as:

$$V_n = \gamma_n \sqrt{f_c'} b h_c$$

where γ_n is joint shear strength coefficient, f_c' is concrete compressive strength in psi, h_c is total column depth, and b_{eff} is effective joint width defined by either ACI 318-08 or ACI 352R-02. As mentioned in Chapter 4, the ACI 352R-02 definition of effective joint width is adopted in this investigation. The coefficient γ_n is a function of joint geometry (that is, whether it is of exterior, interior, or knee configuration, and whether there is a beam framing into the joint in the orthogonal direction). For an isolated exterior joint with geometry shown in Figure 5.1a, $\gamma_n = 6$. ASCE 41 does not differentiate between a corner joint and an exterior joint, such that the same value of $\gamma_n = 6$ applies to both geometries. It is also worthy to mention that ASCE 41 also does not differentiate joint strength for joints with different bar anchorage (Figure 5.1a versus Figure 5.1b), although there is an expression for the strength of straight embedded bars that can be used to check the strength corresponding to bar pullout.

The joint shear strength database established in the current investigation is used to assess the accuracy of the ASCE 41 joint shear strength expression. The procedures for determining joint

strength and displacement ductility were presented in Chapter 4. As a reminder, joint strength corresponds to the joint shear at time of maximum test specimen resistance. Displacement ductility corresponds to ultimate displacement at 15% post peak strength reduction divided by yield displacement calculated using secant stiffness at 75% of peak strength.

These values of γ_j inferred from the test results are compared with the ASCE 41 limit in Fig. 5.2. The measured strength coefficient γ ranges from approximately 4 to 14, compared with γ_n = 6 in ASCE 41.

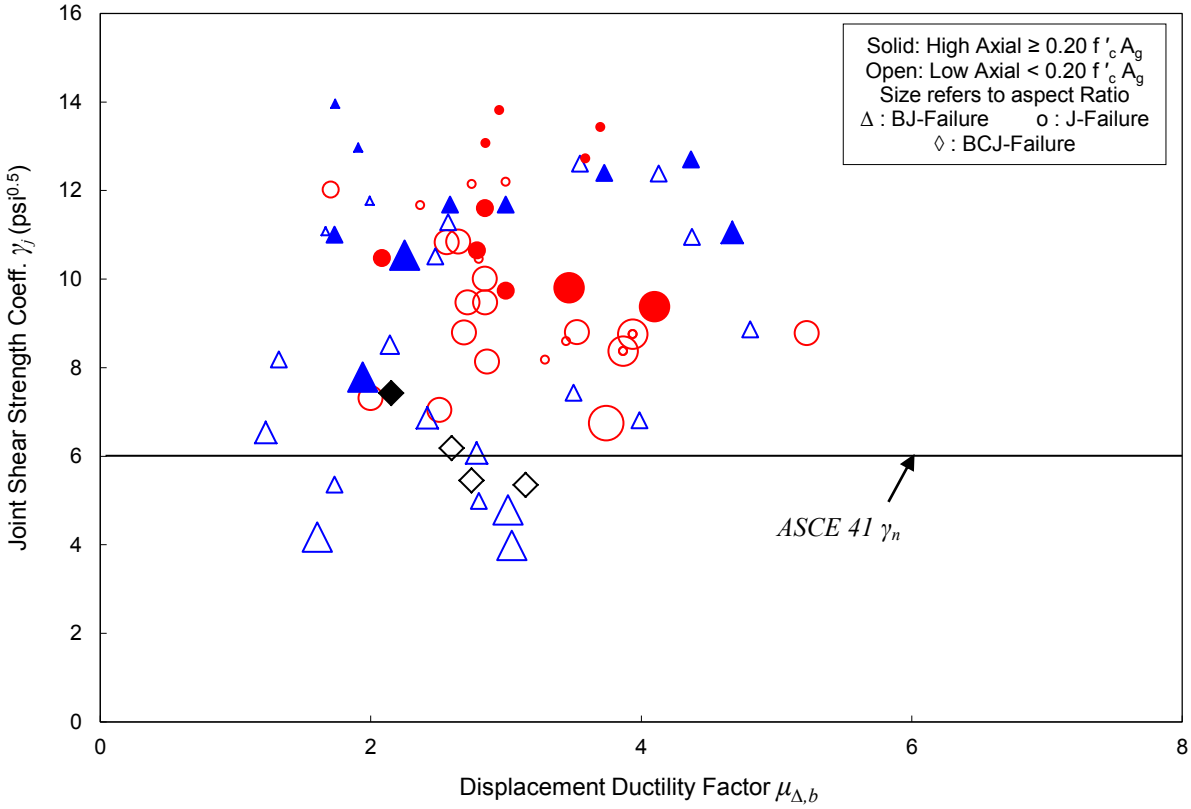

Figure 5.2 Evaluation of ASCE 41 exterior joint shear strength provisions.

From Figure 5.2 it is apparent that the joint shear strength coefficient recommended by ASCE 41 for exterior isolated joints corresponds to approximately the lower quartile of the actual strength. With measured strengths ranging from approximately two-thirds of calculated strength (that is, unconservative strength calculation) to approximately 2.3 times calculated strength (that is, over conservative). As discussed in Chapter 4, joint strength is strongly affected by joint aspect ratio and less strongly affected by joint axial load, both variables that ASCE 41 does not consider. The ASCE 41 model also overlooks the important distinction between different failure modes, that is, J-Failure, BJ-Failure, CJ-Failure and S-Failure modes.

Some additional potential shortcomings of ASCE 41 can be postulated. The effect of bi-directional loading on an exterior joint performance is not addressed in ASCE 41 shear strength values. Some tests have shown 20% decrease in shear strength due to bidirectional loading of interior joints [24], while others suggest no difference in bidirectional shear strength [78]. ASCE 41 also does not recognize the possible effect of deformation demand and cycling on shear strength degradation.

5.4 EVALUATION OF EXISTING ANALYTICAL JOINT SHEAR STRENGTH MODELS

5.4.1 Strut-and-Tie Models

5.4.1.1 FIXED ANGLE SOFTENED STRUT-AND-TIE MODEL

Hwang and Lee [64] presents a softened strut-and-tie model, described in Chapter 3, that is intended to accommodate confined and unconfined joints by distinguishing three force transfer mechanisms. The applicability of this model to unconfined joints is assessed in this section. The sophisticated iterative model satisfies the three basic mechanics principles: stress equilibrium, materials constitutive laws, and strain compatibility. A basic assumption is that the bond deterioration of beam reinforcement can be tolerated and thus the primary resistance mechanism is a primary diagonal strut without secondary struts, but allowance is made for struts to tension ties representing joint hoops and column intermediate reinforcement. The authors applied the model to unconfined beam column joints by interpreting the case of unconfined joints as being similar to the case of yielding, inefficient hoops. Model details were presented in Chapter 3.

Figure 5.2 compares measured and calculated joint shear strength as presented by Hwang and Lee [64]. Only two of the data points shown are for unconfined joints, with the remainder for confined joints. The measured and calculated strengths compare well with few exceptions. Hwang and Lee report 26% and 52% model underestimation of shear strength for the two unconfined joints.

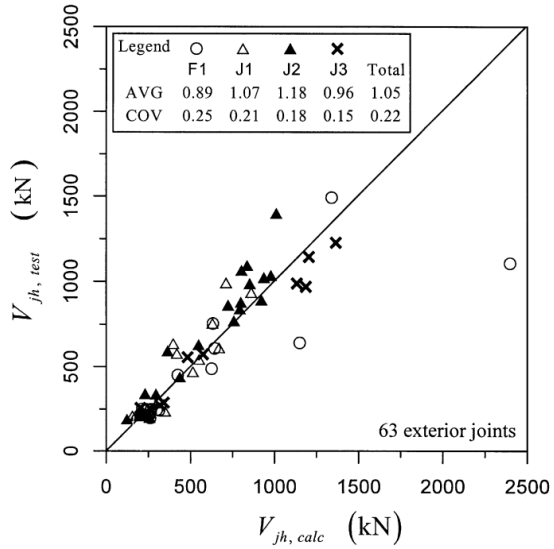

Figure 5.3 Experimental verification of SSTM, Hwang and Lee [64]

The Hwang and Lee model was applied to 37 joints from the database for which J-Failure or BJ-Failure occurred. Figures 5.4 and 5.5 compare measured and calculated strengths. (The dashed lines in all correlation curves of this chapter represent the "mean plus or minus one standard deviation from the mean" for model predicted strength.) For joints experiencing J-Failure, the model underestimates strength for low γ_j values and overestimates strength for higher γ_j values. Overall mean and coefficient of variation of ratio of test to calculated strengths are AVG $\gamma_{test}/\gamma_{model}$ = 1.52 and COV=0.33. It is noteworthy that strengths were overestimated for two tests with a very high axial load ($0.86\ f_c' A_g$ and $0.51\ f_c' A_g$), suggesting inaccuracy in strut width calculation for high axial loads.

For BJ-Failure joints, the model prediction is generally more accurate than for J-Failure (AVG $\gamma_{test}/\gamma_{model}$ = 1.06, COV=0.25) if neglecting beam compression zone depth as recommended by model developers.

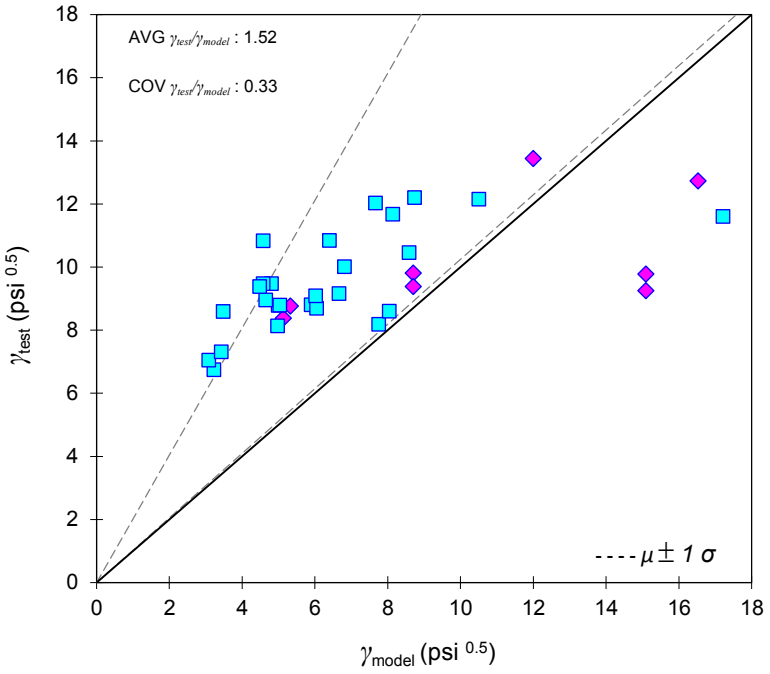

Figure 5.4 Assessment of SSTM for unconfined exterior and corner joints experiencing J-Failure

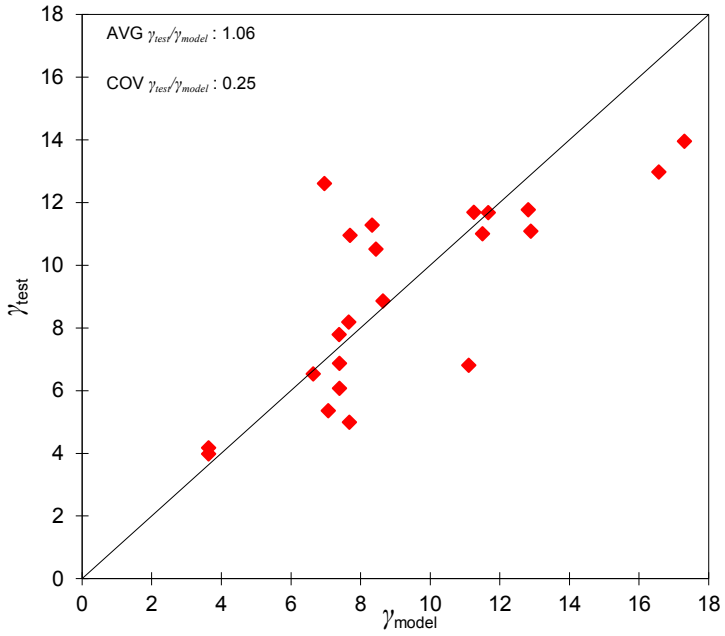

Figure 5.5 Assessment of SSTM for unconfined exterior and corner joints experiencing BJ-Failure

The SSTM developers intended the model, when first designed, to be applied to confined joints. In such joints, J-Failure is initiated by joint hoop yielding, which is represented in the model by assuming a yielding horizontal tie. Consequently, the model assumes that the horizontal hoop strain is larger than yield strain ($\varepsilon_h > \varepsilon_y$), which can be tolerated by a reinforced joint. In an unconfined joint, this assumption leads to unrealistic concrete softening of the diagonal compression strut. Unconfined joints cannot tolerate large tensile strain without significant strength degradation. This effect can be mathematically observed from equation of principal tension strain ε_r from the compatibility relations (Eq. 3.9 and Eq. 3.15). By adopting the same algorithm of yielding tie without providing a lower bound for concrete softening coefficient ζ, the model may be overestimating the degree of concrete softening, thereby leading to underestimation of the concrete strut capacity and joint shear strength.

Another possible reason for relatively poor strength estimation for J-Failure cases is that the model uses compatibility relations that were derived and calibrated for reinforced concrete panels by Hsu [63]. These may not apply to the strut-and-tie mechanism in unconfined joints.

It was noted in the model and data comparison that the model underestimates strength in the J-Failure mode for joints in which the axial load level exceeds $0.5f_c'Ag$. According to the model calculation, the strut depth is almost the same as joint depth in cases with high axial load. Consequently, a direct shear mechanism develops that does not follow the strut-and-tie theory. An alternative approach may be necessary for joints with very high axial loads.

The better correlation for BJ-Failure mode than for J-Failure mode possibly relates to the concrete softening effect. In BJ-Failure mode, yielding of beam longitudinal reinforcement

penetrates into the joint core resulting in an increased softening effect compared with J-Failure mode. The increased softening mimics the effect of yielding ties that the model uses to predict shear strength. The joint strength is thus limited indirectly by beam yielding strength.

The above analysis highlights the limited applicability of the SSTM to the J-Failure mode in non-ductile unconfined joints, and the coincidental agreement between model and some experimental results in the BJ-Failure type. In evaluating the rest of analytical and empirical models in this chapter, only the J-failure cases are considered. Strength for the BJ-mode can be more readily estimated on the basis of the beam flexural strength. This discussed more fully in Chapter 4 and in Sec. 5.6.2.

5.4.1.2 MONOTONIC FIXED ANGLE SOFTENED STRUT-AND-TIE MODEL

Vollum and Newman [153] presents a monotonic, fixed-angle, softened strut-and-tie model, as described in Chapter 3. The only two model parameters are the joint aspect ratio and beam bar detail inside the joint. The model does not include a method to explicitly evaluate the strut capacity or the mode of failure. The effect of axial load also is not accounted for in the case of unconfined joints. The model equations specialized for unconfined joints are:

$$V_j = 0.624\beta(1+0.555(2-h_b/h_c))b_e h_c\sqrt{f_c'} \tag{5.2.a}$$

$$V_j \;<\; 0.97 b_e h_c\sqrt{f_c'}(1+0.555(2-h_b/h_c)) \;<\; 1.33 b_e h_c\sqrt{f_c'} \tag{5.2.b}$$

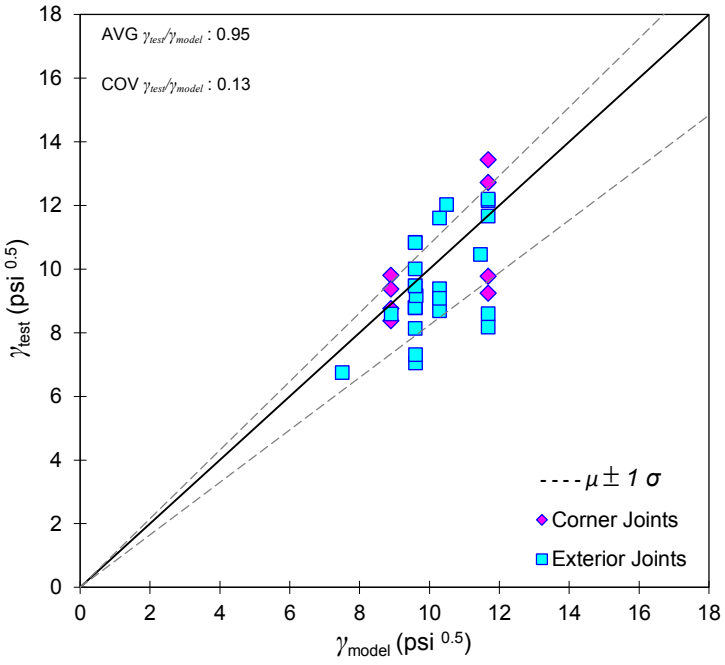

Figure 5.6 Assessment of Vollum and Newman [153] monotonic SSTM for unconfined exterior and corner joints with J-Failure mode

The upper limits set on joint shear strength (Eq. 5.2b) were imposed because of the limitations of the test database the authors used to calibrate the model. Figure 5.6 shows the correlation of shear strength predicted by the Vollum and Newman model to cyclic test results of unconfined exterior and corner joints. The average test to model strength correlation of the model is 0.95 with a COV of 0.13.

It is worth observing that the Vollum and Newman model incorporates a linear reduction of joint shear strength of 25% as the joint aspect ratio changes from 1 to 2. This relation was chosen based on the monotonic joint database the authors used to calibrate the model. However, as discussed in Chapter 4, this trend may not apply for seismically loaded joints and joints with higher axial loads. Nonetheless, the correlation with the available data is generally very good.

5.4.1.3 GENERALIZED MONOTONIC FIXED ANGLE SOFTENED STRUT-AND-TIE MODEL

The monotonic fixed angle softened strut-and-tie model by Parker and Bullman [122] was presented earlier in Chapter 3. The authors intended the model to be applicable to shear critical elements including beam-column joints. However, this model was developed originally for shear-critical beams. The empirical relationship for shear span a_v was developed originally from a static beam-column joint test database. When applied to the tests in the current database, the model significantly underestimates the unconfined joint seismic shear strength (AVG $\gamma_{test}/\gamma_{model}$ = 2.02, with COV=0.36) (Fig 5.7). Some possible reasons for model inaccuracy are discussed below.

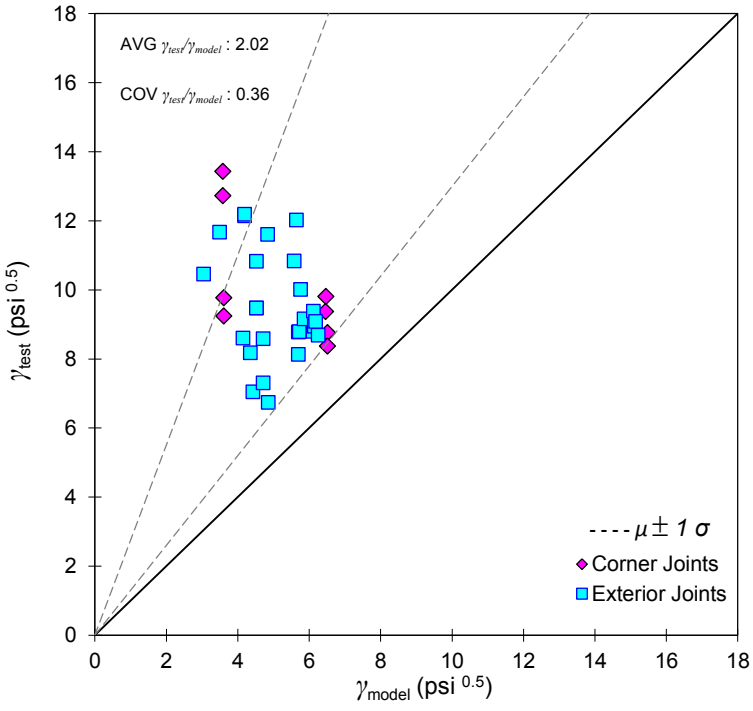

Figure 5.7 Assessment of Parker and Bullman [122] generalized SSTM for unconfined exterior and corner joints with J-Failure mode

According to the model, joint shear strength is given by the expression

$$V_j = \alpha \upsilon f_{cu} \tan\theta_{crit} \tag{5.3}$$

The fact that the critical strut angle expression was developed using beam theory at the point of contraflexure contributes to the discrepancy of the model. This critical angel θ_{crit} is obtained by maximizing the expression:

$$f(\theta) = (1 - \gamma \tan\theta)\sin^2\theta\cos^2\theta \tag{5.4}$$

The inclination of strut is then reflected into strut capacity using the factor α in Eq. 5.3:

$$\alpha = (1 - \gamma \tan\theta_{crit})/(\tan\theta_{crit} + 1/\tan\theta_{crit}) \tag{5.5}$$

Figure 5.8 depicts the relationship between shear span-column depth ratio (which is a representative of joint aspect ratio for a fixed beam reinforcement hook radius) and the factor α which is linearly proportional to joint shear strength. It is obvious that the relationship is logically inversely proportional only starting at shear critical span-to column depth ratio of 2, before which the joint strength is either insensitive or almost linearly proportional to joint aspect ratio. This relationship contradicts the experimental evidence that the joint strength decreases with increasing joint aspect ratio. The practical range of critical span-to column depth ratio is normally below 2 where the relationship is unrealistic. Another factor that contributes to shear strength underestimation is the relatively small lower bound of 0.40 for concrete softening coefficient. Finally, the model is insensitive to column axial load ratio, whereas axial load is known to affect strength.

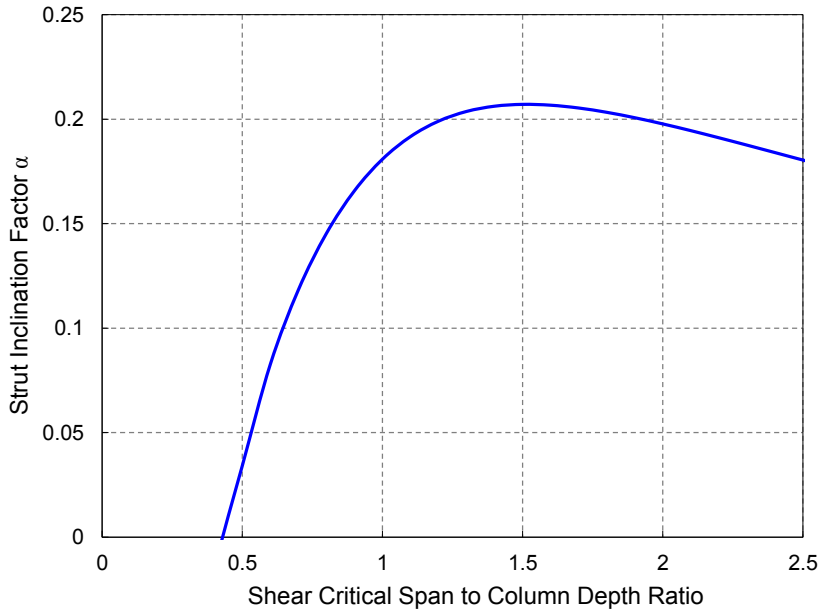

Figure 5.8 Parker and Bullman generalized SSTM for unconfined exterior and corner joints with J-Failure mode

5.4.2 Empirical Shear Strength Models

5.4.2.1 SARSAM AND PHIPPS EMPIRICAL STRENGTH MODEL

The empirical model by Sarsam and Phipps [133] is presented in Chapter 3. The controlling model equation, represented by Eq. 5.6, was derived based on shear strength of shear critical beams with low shear span ratio, $a_v/d_b \leq 2.5$.

$$V_j = 5.47(f_c^{'}\rho_c)^{0.33}(\frac{d_c}{d_b})^{1.33}(1+0.29N/A_g)^{0.5}b_c d_c \tag{5.6}$$

A monotonic beam-column joint test database was used to derive the empirical coefficients. The model accounted for the effect of joint aspect ratio, column axial load, and column reinforcement ratio. It implicitly accounted for mode of failure by setting the shear strength to be the minimum of 1.25 times the shear stress demand from beam yielding and the shear strength provided by the empirical expression. Thus, it can be deduced that this model is basically for J-failure joints although some BJ-Failure specimens may have been used to derive the empirical expression.

Figure 5.9 depicts the evaluation of this model against experimental results of the seismic test database used in this chapter. The model correlation to test results (AVG $\gamma_{test}/\gamma_{model} = 1.41$, with COV=0.32) indicates general underestimation of seismic shear strength of unconfined exterior beam column joints.

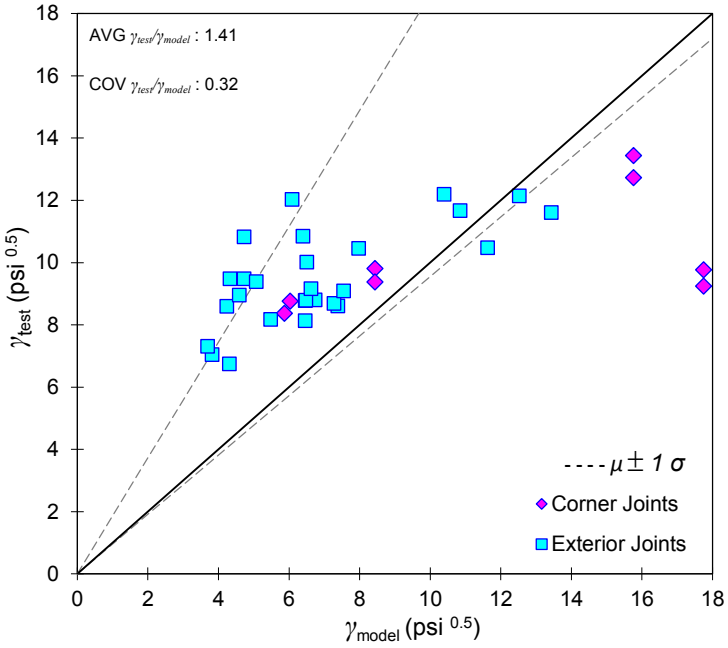

Figure 5.9 Assessment of Sarsam and Phipps [133] empirical model prediction of unconfined joint shear strength experiencing J-Failure mode

5.4.2.2 BAKIR AND BODUROĞLU EMPIRICAL MODEL

The Bakir and Boduroğlu [12] empirical model for joint shear strength of exterior joints is expressed in Eq. 5.7. The model is based upon a parametric study to quantify the effect of different parameters on joint strength such as beam reinforcement ratio, joint aspect ratio, and beam reinforcement anchorage details. The effect of parameters was calibrated independently and collectively based on test results of a monotonic exterior joint database. The model does not explicitly account for the effect of axial column load on joint shear strength.

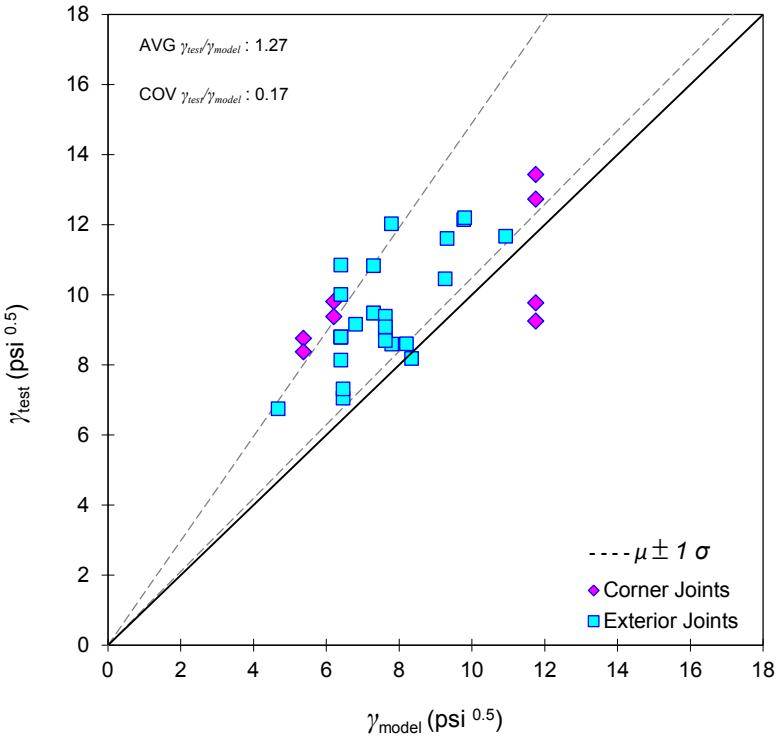

Figure 5.10 Assessment of Bakir and Boduroğlu [12] empirical model for unconfined exterior and corner joints with J-Failure mode

$$V_c = 0.71\beta\gamma\left(\frac{100A_{sb}}{b_b d_b}\right)^{0.4289}\left(\frac{h_b}{h_c}\right)^{-0.61}\left(\frac{b_c + b_b}{2}\right)h_c\sqrt{f_c'} \qquad (5.7)$$

Figure 5.10 displays the correlation of this model to test results of seismically loaded exterior and corner unconfined beam-column joints. The model prediction (AVG $\gamma_{test}/\gamma_{model}$ = 1.27, and COV=0.17) indicates moderate underestimation of the seismic joint shear strength. One drawback of the model that contributed to its inaccuracy is the inclusion of the effect of beam reinforcement ratio without recognizing the distinction between different failure modes (J-failure and BJ-failure). In other words, the model assumes that the joint shear strength is proportional to

beam reinforcement ratio with no boundaries on this proportionality. However, as indicated in Chapter 4, this proportionality is only valid as long as the joint shear stress demand from yielding beam reinforcement is less than the J-Failure mode direct shear strength. When beam reinforcement is relatively high, the joint shear capacity is less that the shear stress demand from beam reinforcement at yield, which in turn, makes the joint shear capacity relatively insensitive to the amount of beam reinforcement after this J-failure threshold strength. Figure 5.11 indicates the shear strength-beam reinforcement ratio relationship for a fixed joint aspect ratio and dimensions. It is clear that the model's nearly bilinear profile keeps predicting the joint shear strength as a function of beam reinforcement ratio even after reaching the J-Failure threshold strength.

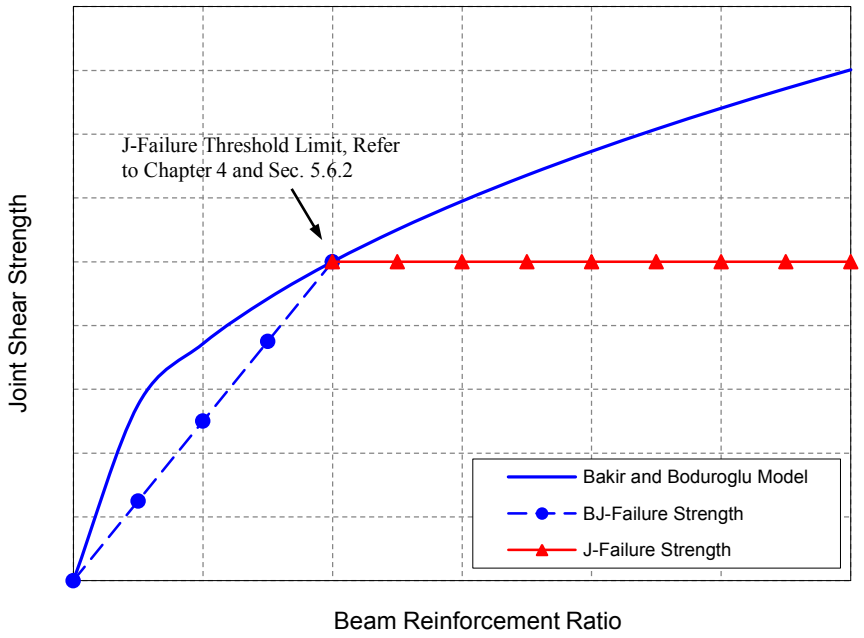

Figure 5.11 Assessment of the effect of beam reinforcement ratio for Bakir and Boduroğlu [12] empirical model

Figure 5.12 depicts a comparison of the effect of aspect ratio on joint shear strength for a constant beam reinforcement ratio within the J-Failure region. The joint aspect ratio coefficient is defined as $(h_b/h_c)^{-0.61}$ in the Bakir and Boduroğlu empirical model and $cos[tan^{-1}(h_b/h_c)]$ in the strut-and-tie models. It is clear that the empirical model prediction of the trend of joint shear strength matches that of the theoretical strut-and-tie model, except for the offset corrected by the empirical factors in the model. This confirms the empirical model sensitivity to joint aspect ratio that makes it one of the least dispersed empirical models in accounting for the effect of joint aspect ratio.

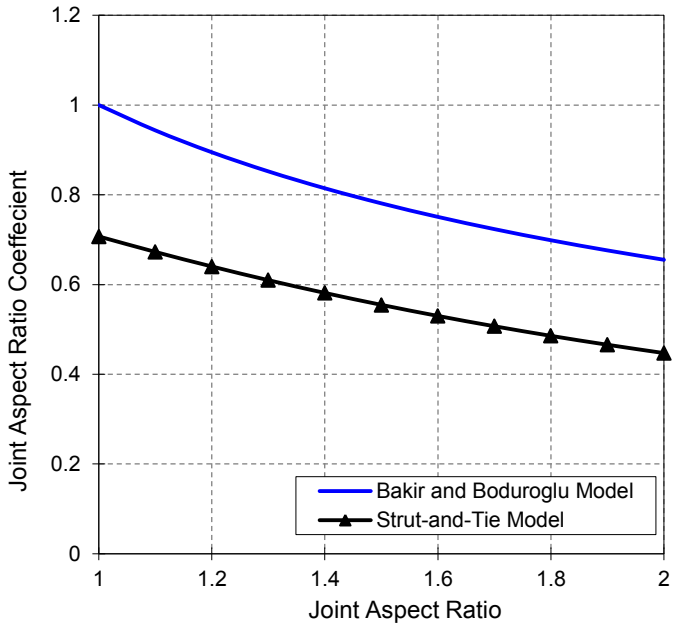

Figure 5.12 Assessment of the effect of joint aspect ratio for Bakir and Boduroğlu empirical model

5.4.3 Panel Zone Principal Strain Model

The Tsonos [145] joint shear strength model was developed based on principal stress-strain relations for reinforced panels combining both strut and truss mechanisms. The model satisfies the constitutive laws by complying with Mohr's circle compressive and tensile principal stresses σ_I and σ_{II} (Eq. 3.31) and adopting the fifth degree parabola for concrete biaxial strength curve. The model equations were presented earlier in Chapter 3.

Figure 5.13 compares results of the Tsonos [145] model and tests for the database used in the current study. The model generally overestimates shear strength (AVG $\gamma_{test}/\gamma_{model} = 0.80$, with COV=0.26). The discrepancy is believed to result in part because the model uses compatibility relations and principal stress expressions developed and calibrated for reinforced panels, whereas the joints lack transverse reinforcement.

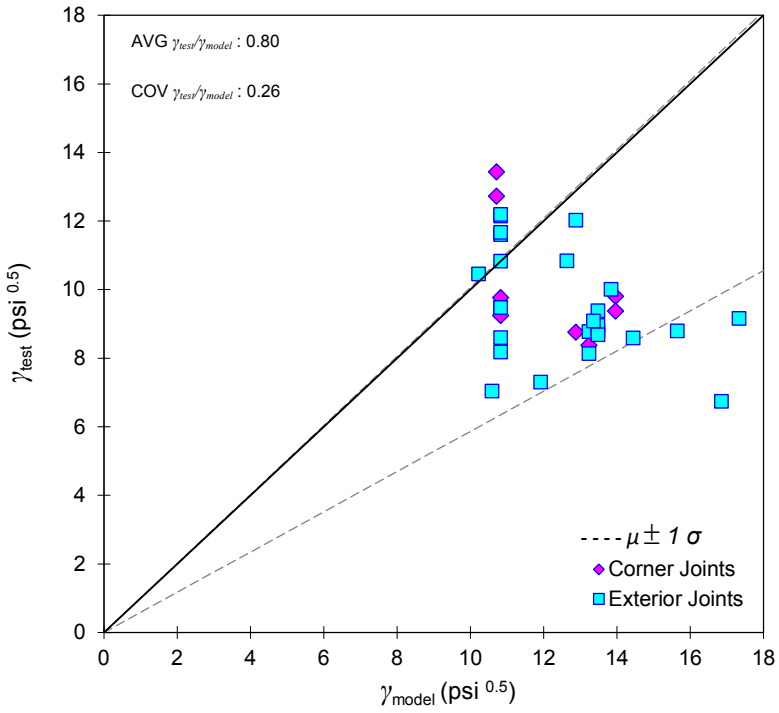

Figure 5.13 Assessment of Tsonos [145] panel zone model for unconfined exterior and corner joints with J-Failure mode

5.4.4 Probabilistic Shear Strength Model

The Bayesian probabilistic joint shear strength model by Kim and LaFave [71] is:

$$V_j(MPa) = \alpha_b \lambda_b (JI)^{0.07} (BI)^{0.25} (f_c')^{0.75} \tag{5.8}$$

where α_b is a parameter describing in-plane geometry: 1.0 for interior connections, 0.7 for exterior connections, and 0.4 for knee connections; λ_b is calibration factor: 1.02, JI is joint transverse reinforcement index defined as $\rho'' f_{yj}/f_c'$ and BI is beam reinforcement index defined as $\rho f_y/f_c'$.

The database used to construct this model had few unconfined joints (8 out of 182 joints). Nonetheless, the model results compare well with test results for the current database (Fig. 5.14). However, the insensitively of this model to the effect of axial load is clear. The model also does not distinguish the different joint failure modes. The model also downplayed the importance of the effect of joint aspect ratio and joint transverse reinforcement. This contradicts well-established test results. Therefore, it is suggested to extend this model to unconfined beam-column joints database taking into account the joint aspect ratio and axial load ratio effects.

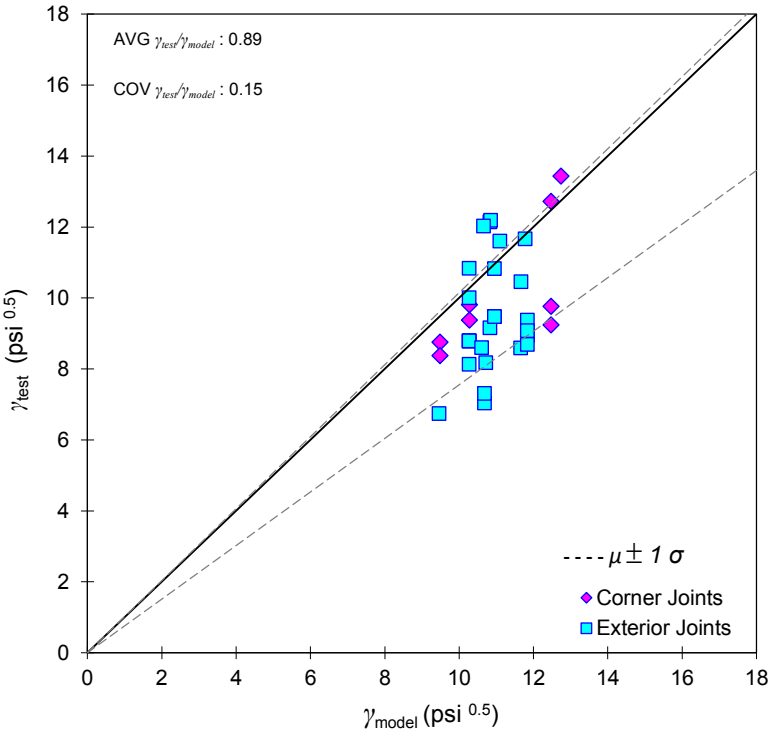

Figure 5.14 Assessment of Kim and Lafave [71] probabilistic Bayesian model for unconfined exterior and corner joints with J-Failure mode

Table 5.1 Database of J-Failure exterior and corner unconfined joints

Investigator	Specimen	Materials				Joint				Loading			Shear Strength				
		f'_c (ksi)	f_{yc} (ksi)	f_{yb} (ksi)	n	a_s (in)	A_{str} (in^2)	α_j	θ	P/f'_cA_g	Variable Axial	μ_Δ	D_{model} (kips)	γ_{jtest}	γ_{jmodel}	$\gamma_{jtest}/\gamma_{j\,model}$	Dispersion*
Hanson & Conner[53]	V	3.30	64.8	51.0	8.86	9.30	125.5	1.33	55.8	0.86	constant	2.84	211	11.6	10.2	1.14	0.01
Pantelides et al.[116] (minor yield before J-failure)	Unit 3	4.9	68.1	66.5	7.24	6.65	107	1.00	44.4	0.10	constant	2.48	268	10.5	8.44	1.24	0.04
	Unit 4	4.9	68.1	66.5	7.24	8.39	134	1.00	44.4	0.25	constant	2.59	338	11.7	11.7	1.00	0.00
	Unit 6	4.6	68.1	66.5	7.5	8.54	136	1.00	44.4	0.25	constant	3.00	320	11.7	11.3	1.04	0.00
	Unit 5	4.60	68.1	66.5	7.50	7.27	116	1.00	44.4	0.10	constant	2.37	264	11.7	10.9	1.07	0.00
Wong[155]	BS-L	4.48	75.6	75.40	7.60	6.30	69.5	1.50	59.5	0.15	constant	2.86	155	8.13	8.98	0.90	0.01
	BS-U	4.50	75.6	75.40	7.59	6.30	69.5	1.50	59.5	0.15	constant	5.23	155	8.78	9.00	0.98	0.00
	BS-LL	6.12	75.6	75.40	6.51	6.14	67.7	1.50	59.5	0.15	constant	3.53	189	8.80	9.37	0.94	0.01
	BS-L-LS	4.58	75.6	75.40	7.52	6.29	69.4	1.50	59.5	0.15	constant	2.69	157	8.79	9.02	0.97	0.00
	BS-L-V2T10	4.73	75.6	75.40	7.40	6.28	69.2	1.50	59.5	0.15	constant	2.85	161	10.0	9.07	1.10	0.01
	BS-L-V4T10	4.10	75.6	75.40	7.94	6.35	70	1.50	59.5	0.15	constant	2.65	146	10.8	8.83	1.23	0.04
	BS-L-600	5.28	0.00	75.40	7.00	6.86	75.6	2.00	67.7	0.15	constant	3.74	190	6.74	7.63	0.88	0.02
Ghobarah and Said[49]	T1	4.48	61.7	61.6	7.61	7.74	76.2	1.00	44	0.19	constant	2.75	170	12.1	11.7	1.03	0.00
	T2	4.48	61.7	61.6	7.61	6.93	68.2	1.00	44	0.10	constant	3.00	152	12.2	10.5	1.16	0.02
Karayannis et al[68]	B0	4.59	84.3	84.3	7.51	4.55	35.8	1.00	42	0.05	constant	3.29	81.0	8.18	9.58	0.85	0.03
	C0	4.59	84.3	84.3	7.51	4.53	35.6	1.00	42.8	0.05	constant	3.45	81.0	8.60	9.41	0.91	0.01
Tsonos and Stylianidis[148]	L1	3.00	66.8	70.5	9.29	4.67	36.8	1.50	58.8	0.18	constant	2.72	59.0	10.2	8.98	1.19	0.04
	L2	3.00	66.8	70.5	9.29	4.67	36.8	1.50	59.7	0.18	constant	2.56	59.0	10.6	8.76	1.39	0.05
	O1	3.00	66.8	70.5	9.29	4.67	36.8	1.50	59.7	0.18	constant	2.85	59.0	10.2	8.76	1.22	0.04
Antonopoulos and Triantafillou[10]	C1	2.82	66.8	84.8	9.58	3.97	31.2	1.50	59.6	0.06	constant	2.51	45.0	7.04	6.88	1.02	0.00
	C2	3.44	66.8	84.8	8.67	3.85	30.3	1.50	59.6	0.05	constant	2.00	53.0	7.31	7.37	0.99	0.00
Sarsam and Phipps[133]	EX2	7.50	61.6	80	5.87	4.34	26.4	1.49	59.8	0.19	constant	NA	83.0	9.15	9.87	0.93	0.01
Filiatrault and Lebrun[43]	S1	4.93	69.	69	7.25	6.66	91.5	1.29	52.8	0.08	constant	1.70	219	12.0	9.95	1.21	0.04
Hoffschild et al[62]	-	3.82	65.4	83.2	8.23	3.48	24.3	1.05	41.7	0.13	constant	2.80	47.0	10.5	10.9	0.96	0.00
Park[120]	SP4-EW	3.96	68.1	72.2	8.08	9.87	167.8	1.67	59.9	0.17	variable	3.94	339	8.70	8.80	1.00	0.00
	SP4-NS	3.96	68.1	72.2	8.08	9.89	168.2	1.67	60.1	0.15	variable	3.87	339	7.40	8.78	0.85	0.00
NEES Joints (Current Test) Hassan, W.M.	UJ1-EW	4.30	70.00	71	7.76	9.32	158.4	1.00	45.6	0.31	variable	3.70	342	14.3	13.0	1.10	0.01
	UJ1-NS	4.30	70.00	71	7.76	9.37	159.3	1.00	45.6	0.31	variable	3.59	344	12.7	13.0	0.98	0.00
	UJ2-EW	4.43	70.00	71	7.64	10.5	179.3	1.67	59.9	0.45	variable	3.47	396	9.98	9.77	1.02	0.00
	UJ2-NS	4.43	70.00	71	7.64	10.8	182.9	1.67	59.9	0.45	variable	4.10	404	9.45	9.77	0.97	0.01
	BJ1-EW	4.41	70.00	71	7.66	9.42	120.6	1.00	41.8	0.45	variable	2.95	266	11.7	9.90	1.14	0.02
	BJ1-NS	4.41	70.00	71	7.66	9.42	120.6	1.00	42.1	0.45	variable	2.85	266	10.8	10.0	1.08	0.01
Salim[131]	S1	4.39	68.2	66.8	7.68	4.35	28.3	1.67	63.1	0.09	constant	NA	62.0	8.59	9.17	0.94	0.01
Ortiz[109]	BCJ1	4.93	66.8	104.4	7.25	5.35	42.1	1.33	54.9	0.00	constant	NA	101	8.95	8.86	1.01	0.00
	BCJ2	4.78	66.8	104.4	7.36	5.37	42.2	1.33	55.3	0.00	constant	NA	99.0	9.38	8.74	1.07	0.00
	BCJ3	5.51	66.8	104.4	6.85	5.75	45.2	1.33	55.7	0.08	constant	NA	117	8.69	9.58	0.91	0.01
	BCJ3	5.07	66.8	104.4	7.15	5.90	46.4	1.33	55.7	0.09	constant	NA	114	9.08	9.66	0.94	0.01

*: Dispersion $=[(\gamma_{jtest}/\gamma_{j\,model})_i-(\gamma_{jtest}/\gamma_{j\,model})_{mean}]^2$

5.5 EVALUATION OF EXISTING BOND STRENGTH MODELS

If bottom beam longitudinal reinforcement is hooked into the joint with sufficient anchorage length, joint failure by reinforcement pullout is unlikely, such that joint shear strength is likely to be limited by joint failure. In the case of insufficient embedment length l_{sp} of unhooked beam bottom reinforcement, Fig. 5.1.b, a typical detailing practice for many buildings not designed for seismic resistance, pullout failure of the beam bottom reinforcement should be considered as a possible failure mode. This failure mode is referred to here as S-Failure mode.

The key factor in assessing strength of joints experiencing this S-Failure mode is the bond strength τ_{max} between concrete and the short embedded length of beam bottom reinforcement. Bond strength may be affected by many factors, including concrete strength, bar diameter, column axial load, yielding of beam or column reinforcement, and presence of confining elements such as transverse reinforcement or transverse beams orthogonal to joint [87] and [107].

Several models have been developed for bond strength and bond-slip relations for reinforced concrete components. This includes both monotonic and cyclic models for columns, beams, interior beam-column joints, and exterior beam column joints with standard embedded hooked beam reinforcement. The author is unaware of bond model dedicated to deficient beam column joints with short embedded beam reinforcement (Fig. 5.1.b).

The following paragraphs introduce some existing bond models, and compares results of these models with measured response of exterior and corner joints having short embedded bottom bars as in Fig. 5.1.b. The database used to evaluate the models (Table 5.2) included isolated exterior joints, exterior joints with one or two loaded or unloaded stubs, with or without slab, and corner joints with two cyclically loaded transverse beams and concrete slab. Models of Lehman [81], Elwood and Eberhard [38], Lowes and Altoontash [87], Kurose [76], and NZS 3101 [107] are briefly assessed.

The expressions of the average bond strength of these models are presented below:

Lehman [81],

$$\tau_{max} = 6\sqrt{f_c'} \qquad \text{for} \quad f_s > f_y \tag{5.8.a}$$

$$\tau_{max} = 12\sqrt{f_c'} \qquad \text{for} \quad f_s < f_y \tag{5.8.b}$$

Elwood and Eberhard [38],

$$\tau_{max} = 6\sqrt{f_c'} \tag{5.9}$$

Lowes and Altoontash [87],

$$\tau_{\max} = 0.6\sqrt{f_c'} \text{ to } 4.8\sqrt{f_c'} \quad \text{for} \quad f_s > f_y \tag{5.10}$$

$$\tau_{max} = 21\sqrt{f_c'} \quad \text{for} \quad f_s < f_y \tag{5.11}$$

Kurose [76],

$$\tau_{max} = 15.63\sqrt{f_c'} \tag{5.12}$$

NZS 3101 [107],

$$\tau_{\max} = 1.2\sqrt{f_c'} \quad \text{(SI units)} \quad \text{For zero axial load} \tag{5.13}$$

$$\tau_{\max} = 1.2\sqrt{f_c'}\left(\frac{P}{2f_c'A_g} + 0.95\right) \quad \text{(SI units)} \tag{5.14}$$

The bond stress τ_{exp} is defined as the average uniform bond stress at peak tension force in the reinforcement during a test, that is, the peak tension force divided by the product of the nominal circumference and the embedded length. Values of τ_{exp} were calculated using test results from the database of joints experiencing S-Failure, as summarized in Table 5.2. The parameters presented in Table 5.2 include bar embedment length l_{sp}, reinforcement tensile force at the onset of bond failure T_s, bar diameter ϕ_b, and steel stress at bond failure f_s. In addition, the joint shear stress coefficient γ_{sj} at the onset of bond failure also was determined. Bond strength also was calculated according to each of the models identified above. The corresponding bar pullout force was used to calculate an associated joint shear strength coefficient corresponding to bar pullout. Figure 5.15 compares measured and calculated joint shear stress coefficients at bond failure. It can be observed that the Lowes and Altoontash model is the most accurate among the evaluated models, with mean ratio of test to model strength equal to 0.96 with a COV of 0.22.

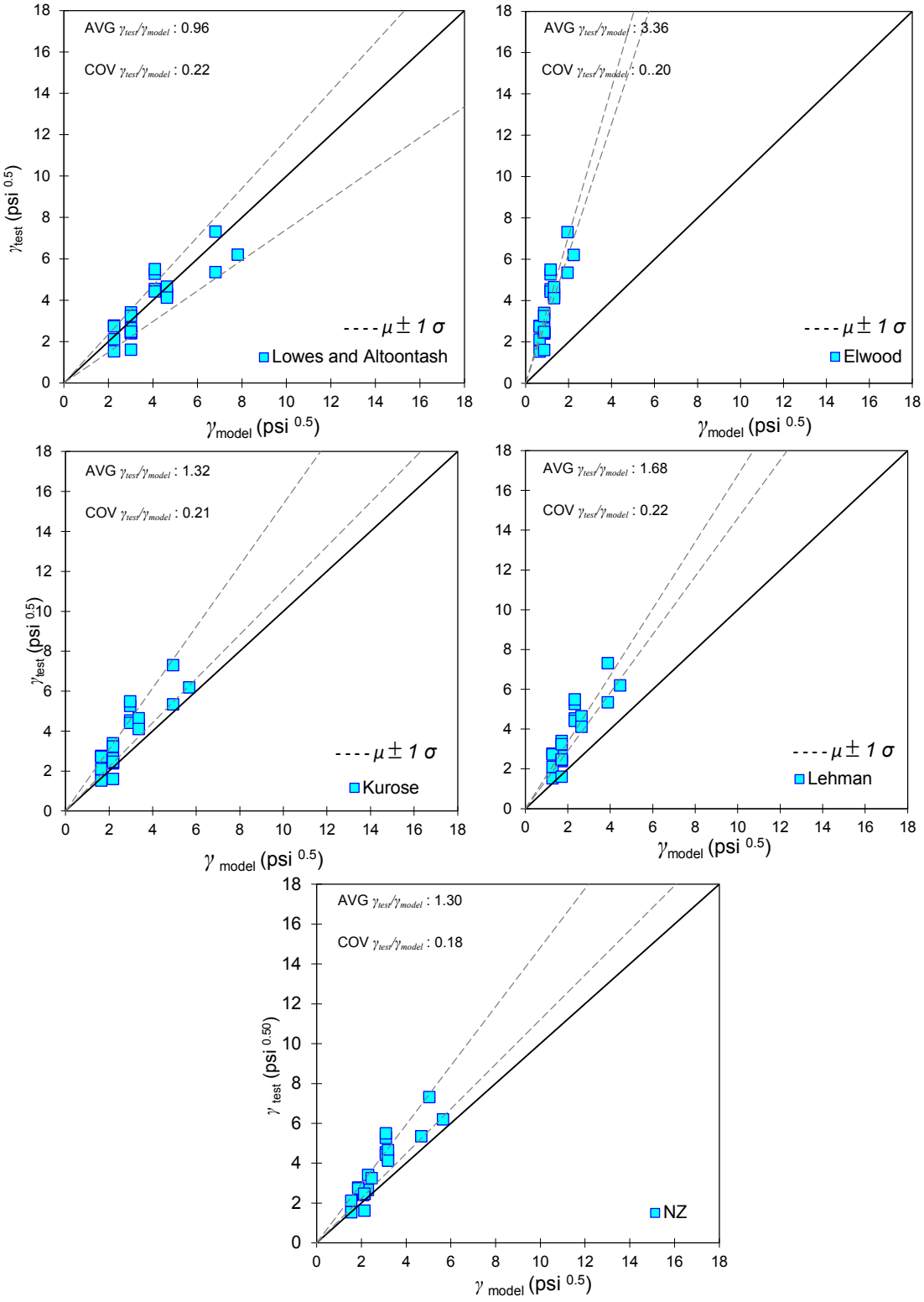

Figure 5.15 Joint shear coefficients based on referenced bond strength model and based on measured behavior.

Table 5.2 Joint database for S-Failure exterior and corner joints and proposed bond model evaluation

Investigator	ID	Materials		Beam				Column					Bond Parameters								Equivalent shear strength	
		f'_c (ksi)	f_{yb} (ksi)	L_b (in.)	h_b (in.)	b_b (in.)	a_b (in.)	L_c (in.)	h_c (in.)	b_c (in.)	a_c (in.)	P/f'_cA_g	l_{sp} (in.)	ϕ_b (in.)	f_s/f_y	T_s (kip)	c/d	$\tau_{exp}/\sqrt{f'_c}$	$\tau_{model}/\sqrt{f'_c}$	τ_{exp}/τ_{model}	γ_{jtest}	$\gamma_{test}/\gamma_{model}$
Pantelides et al.[116]	SP1	4.79	66.5	63.0	16.0	16.0	1.80	166	16.0	16.0	5.36	0.10	6	1.13	0.39	23.6	2.17	18.7	16.1	1.16	5.34	1.09
	SP2	4.79	66.5	63.0	16.0	16.0	1.80	166	16.0	16.0	7.40	0.25	6	1.13	0.53	29.71	2.17	25.6	20.2	1.26	7.30	1.18
Beres et al.[17]	E-01	3.79	77.1	47.0	24.0	14.0	3.40	133	16.0	16.0	5.40	0.11	6	1.00	0.23	21.0	2.38	19.4	18.1	1.08	2.41	1.02
	E-02	3.89	77.1	47.0	24.0	14.0	5.10	133	16.0	16.0	5.36	0.11	6	1.00	0.23	25.3	2.38	19.2	21.5	0.89	2.38	0.84
	E-05	4.57	77.0	47.0	24.0	14.0	3.40	133	16.0	16.0	8.06	0.32	6	1.00	0.27	30.0	2.38	21.2	23.6	0.90	2.63	0.85
	E-06	4.50	76.7	47.0	24.0	14.0	3.40	133	16.0	16.0	8.13	0.32	6	1.00	0.35	35.9	2.38	27.3	28.4	0.96	3.39	0.91
	E-07	4.25	76.7	47.0	24.0	14.0	3.40	133	16.0	16.0	5.25	0.10	6	0.75	0.15	17.0	2.50	16.2	18.5	0.88	1.52	0.84
	E-08	4.36	76.7	47.0	24.0	14.0	3.40	133	16.0	16.0	5.22	0.10	6	0.75	0.21	20.6	2.50	22.4	22.0	1.02	2.10	0.97
	E-09	2.89	77.0	47.0	24.0	14.0	3.40	133	16.0	16.0	10.4	0.50	6	0.75	0.23	25.4	2.50	29.5	33.4	0.88	2.76	0.84
	E-10	2.97	76.6	47.0	24.0	14.0	3.40	133	16.0	16.0	10.3	0.49	6	0.75	0.23	21.3	2.50	29.1	27.6	1.05	2.72	1.00
	E-11	2.38	70.0	47.0	24.0	14.0	3.40	133	16.0	16.0	6.23	0.18	6	1.00	0.20	22.4	2.38	19.6	24.3	0.81	2.43	0.76
	E-12	2.74	70.0	47.0	24.0	14.0	3.40	133	16.0	16.0	5.94	0.15	6	1.00	0.22	19.3	2.38	19.8	19.6	1.01	2.45	0.96
	E-13	2.46	70.0	47.0	24.0	14.0	5.10	133	16.0	16.0	6.16	0.17	6	1.00	0.13	18.8	2.38	12.9	20.1	0.64	1.59	0.61
	E-14	3.04	70.0	47.0	24.0	14.0	3.40	133	16.0	16.0	10.1	0.48	6	1.00	0.30	32.6	2.38	26.0	31.3	0.83	3.23	0.79
Ghobarah and ElAmoury[47]	T0	4.45	61.8	65.8	15.8	9.84	-	112	15.8	9.84	5.55	0.20	6	0.79	0.64	21.9	2.50	19.3	22.1	0.87	6.19	0.83
Gokgoz[50]	US3-E	4.23	63.8	72.8	19.7	11.8	2.54	98.4	11.8	11.8	5.96	0.30	6	0.79	0.62	28.4	2.50	31.2	29.3	1.06	5.26	1.01
	US3-ES	4.23	60.7	72.8	19.7	11.8	2.54	98.4	11.8	11.8	5.96	0.30	6	0.79	0.45	28.4	2.50	32.5	29.3	1.11	5.48	1.05
Topcu[143]	US3-C	4.23	63.8	72.8	19.7	11.8	3.81	98.4	11.8	11.8	5.96	0.30	6	0.79	0.53	26.5	2.50	26.8	27.4	0.98	4.53	0.93
	US3-CS	4.23	60.7	72.8	19.7	11.8	3.81	98.4	11.8	11.8	5.96	0.30	6	0.79	0.44	26.6	2.50	26.1	27.4	0.96	4.41	0.91
Engindeniz[41]	SP1-EW	3.74	46.7	125	20.0	12.0	3.90	121	14.0	14.0	4.69	0.10	6	0.75	0.40	17.9	2.50	22.4	20.8	1.08	4.28	1.03
	SP1-NS	3.74	46.7	125	20.0	12.0	3.90	121	14.0	14.0	4.69	0.10	6	0.75	0.43	17.9	2.50	24.3	20.8	1.17	4.63	1.11

5.6 PROPOSED STRENGTH MODELS

5.6.1 J-Failure Modified Strut-and-Tie Analytical Model (ACI 318-08)

The major problem encountered when applying strain-based strut-and-tie models to unconfined beam-column joints is the uncertainty in the expressions for computing principal tensile strains as they are strongly affected by crack width from early loading stages. This problem is more pronounced in plain concrete in unconfined joints. Hillerberg et al. [60] recognized this uncertainly in tensile strain calculation in development of nonlinear fracture mechanics model for plain concrete. They used crack width instead as a means of computing stress intensity factor. Crack width was not reported in most of the available unconfined joint tests in the literature, and it is not a practical variable to use for design. It was then decided in this study not to rely on explicit expressions for tensile strains or crack width in estimating softening of the concrete strut in developing shear strength models for unconfined beam-column joints. Instead, a global softening coefficient value based on regression analysis of previous joint test results was sought.

The shortcomings of the available SSTM in shear strength prediction of J-Failure modes motivated the search for a simpler model that accommodates the force transfer mechanism in unconfined joints exterior joints. The controversial assessment of softening strut coefficient based on principal strains led to revisiting the simple concept of a direct strut that incorporates a softening coefficient suitable for each individual case, namely the ACI 318-08 [1] strut and tie model approach. Figure 5.16 depicts the proposed model

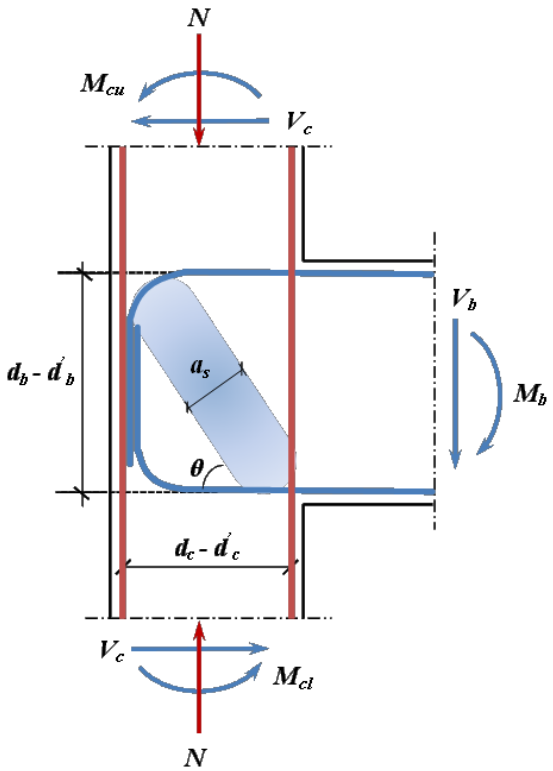

Figure 5.16 Proposed strut-and-tie model

The effective strut compressive strength f_{cu} and diagonal strut capacity D are

$$f_{cu} = 0.85\beta_s f_c^{'} \tag{5.15}$$

$$D = f_{cu} A_{str} \tag{5.16}$$

where β_s is concrete softening coefficient, which varies according to section A.3.2, ACI 318-08. For the case of a bottle-shaped strut with no crack control reinforcement, β_s = 0.6. A_{str} is the concrete strut area calculated by

$$A_{str} = a_s b_j \tag{5.17}$$

where b_j is the effective joint width defined by ACI 352R-02 and a_s is the strut depth defined as

$$a_s = \beta_1 \sqrt{a_b^2 + a_c^2} \tag{5.18}$$

a_b and a_c are the compression zone depths of the beam and column, respectively. β_1 is a factor to account for the further reduction in beam and column stress block height associated with concrete strengths greater than 4 ksi.

$$\beta_1 = 1 - 0.05(f_c^{'} - 4) \qquad f_c^{'}: \text{ksi} \tag{5.19}$$

a_b can be estimated by locating the neutral axis of transformed cracked linear beam section:

$$a_b = k d_b \tag{5.20}$$

$$k = [(\rho + \rho')^2 n^2 + 2(\rho + \rho' \frac{d_b^{'}}{d_b}) n]^{1/2} - (\rho + \rho') n \tag{5.21}$$

where d_b and $d_b^{'}$ are depths from extreme compression fiber to centroids of beam tension and compression longitudinal reinforcement, respectively, n is the modular ratio, and ρ and ρ' are beam tension and compression reinforcement ratios, respectively. The quantity a_c can be estimated by Paulay and Priestley [127]:

$$a_c = (0.25 + 0.85 \frac{P}{f_c^{'} A_g}) h_c \qquad \leq \ 0.4\, h_c \tag{5.22}$$

where P is column axial load and A_g is gross section area. The above calculation of a_b is based on the assumption that the beam is not yielding before the joint reaches the shear capacity in J-Failure mode. Review of previous tests with J-Failure shows that the tensile strain of the beam

reinforcement, corresponding to joint shear capacity, typically is about 0.002 in isolated exterior unconfined joints, i.e., the beam is usually at the onset of yielding when the joint reaches its shear capacity (in those particular tests). However, in theory, this strain should be directly dependent on the amount of beam longitudinal reinforcement.

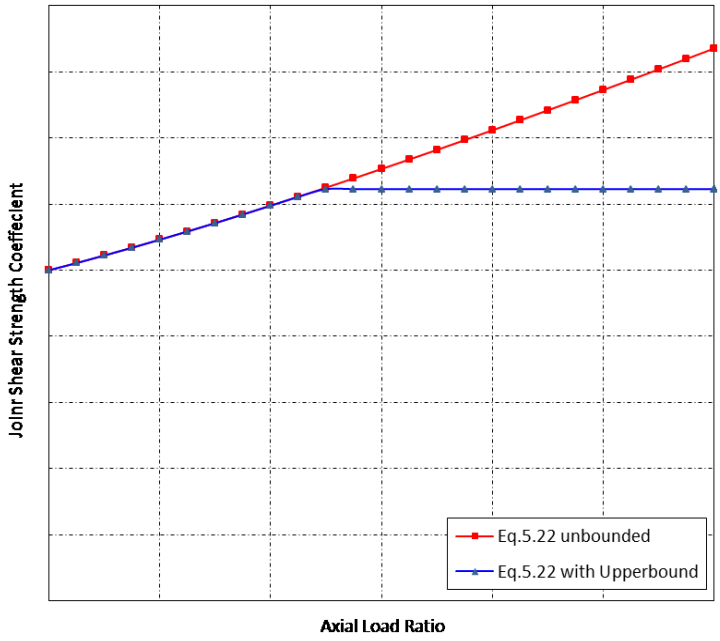

Figure 5.17 Effect of axial load ratio on proposed model's shear strength prediction

The SSTM of Hwang and Lee [64] assumes that depth of the beam flexural compression zone a_b can be ignored because it is small in the case of a yielding beam. This assumption may be invalid for J-Failure because a_b is relatively larger for an elastic beam. The expression for a_c accommodates the effect of column axial load on joint shear strength. Past tests indicate that increasing axial load can result in a 10% - 20% increase in shear strength [116], [26], [13]. The limit on $a_c = 0.4h_c$ is proposed so that the calculated strength increase due to axial load is limited accordingly. Close agreement with this choice of a_c limit can be found in [161].

The choice of a softening coefficient β_s of 0.6 for a bottle shaped strut with no crack control reinforcement is an interpretation of ACI 318-08 code provisions for unconfined joints. Accordingly, joint shear strength based on diagonal strut capacity without including the effect of intermediate column reinforcement is:

$$V_j = D\cos\theta \tag{5.23}$$

$$\theta = \tan^{-1}\left(\frac{d_b - d_b'}{d_c - d_c'}\right) \tag{5.24}$$

where d_c and $d_c^{'}$ are depths from extreme compression fiber to centroids of tension and compression longitudinal reinforcement in the column, respectively. The joint shear strength coefficient for joints experiencing J-Failure mode is:

$$\gamma_j = \frac{V_j}{h_c b_j \sqrt{f_c^{'}}} \tag{5.25}$$

The shear strength calculated from Eq. 5.25 is for a unidirectional loading within the plane of the frame. Therefore, this shear strength expression is applicable to exterior joints or corner joints under unidirectional loading. For a corner joint undergoing bidirectional framing, an elliptical biaxial shear strength interaction diagram suggested by ACI 353R-02, Fig. 3.63, is adopted to determine the shear strength coefficient for each orthogonal joint direction. The most critical case of bidirectional loading is diagonal loading on a 45^0 angle to the plane of each beam of a corner connection subassembly. As discussed in Chapter 3, for square joint section the interaction surface becomes circular. Thus, the shear strength coefficient for each orthogonal direction of a corner joint or exterior joints with two transverse spandrel beams can be expressed as;

$$\gamma_{jx} = \gamma_j \cos(\lambda) \tag{5.26.a}$$

$$\gamma_{jy} = \gamma_j \sin(\lambda) \tag{5.26.b}$$

where λ is the angle between the resultant of the two horizontal components of the shear force demand on column resulted from bidirectional ground motion analysis and the local x-direction of the column considered. In the case of equal components of shear force demand in both directions, the angle λ tends to 45^o and the shear strength coefficient in each orthogonal direction is:

$$\gamma_{jx} = \gamma_{jy} = \frac{\gamma_j}{\sqrt{2}} \tag{5.27}$$

In the presence of intermediate column reinforcement, the vertical mechanism of Hwang and Lee [64] suggests that the contribution of vertical reinforcement increases unboundedly as the diagonal strut angle becomes steeper (Fig 3.5). Test results by Wong [1] indicate also an asymptotic trend of shear strength gain due to the presence of intermediate column reinforcement, reflecting that increasing column intermediate reinforcement becomes less significant after a certain limit, for a fixed strut angle. Other researchers report no beneficial effect for intermediate column reinforcement [120]. As discussed in Chapter 4, it seems that only if heavy amount of column intermediate column reinforcement is provided, marginal enhancement to joint shear strength is gained. More research is needed on this aspect to arrive at quantified solid conclusions. Accordingly, it was decided to ignore the contribution of intermediate column reinforcement in developing this model.

It is noteworthy to mention that the model adopts the hydrostatic node assumption, whereby equal pressure is sustained by the three edges of the node and, hence, the strut strength controls the failure.

5.6.2 J-Failure Empirical Shear Strength Model

In Chapter 4, the effects of the major parameters influencing joint shear strength were studied. This enabled establishing empirical expressions for the effect of the most important parameters on shear strength of J-Failure mode joints, namely joint aspect ratio and axial load ratio. The empirical factors were derived first for each individual parameter based on the observed trend of the effect of the parameters considered on joint shear strength. Consequently, an empirical shear strength expression (Eq. 5.28) was developed to take into account collectively the effects of both axial load ratio and joint aspect ratio. The empirical constant was used to adjust the overall shear strength expression to best fit the trend of model-to-test shear strength. This empirical model can serve as a preliminary means for quick estimation of joint shear strength with sufficient accuracy, without the need to perform strut capacity calculations. The empirical joint shear strength expression is given by:

$$V_j = 11.25\alpha_j^{-0.50}\kappa b_j h_c \sqrt{f_c'} \tag{5.28}$$

where the joint aspect ratio α_j is:

$$\alpha_j = \frac{h_b}{h_c} \tag{5.29}$$

The effect of axial load is reflected through the factor κ as indicated in Fig. 5.18 and Eq. 5.30. As indicated earlier, the effect of axial load enhancement of joint shear strength is more pronounced with smaller aspect ratio. Thus, a linear interpolation is suggested to obtain the axial load factor κ between the two boundary aspect ratios α_j=1 and α_j=2.

$$\kappa = 1 + (0.86 - 0.31\alpha_j)\left[\frac{P}{f_c' A_g} - 0.15\right] \qquad 1 \le \kappa \le 1.35 - 0.10\alpha_j \tag{5.30}$$

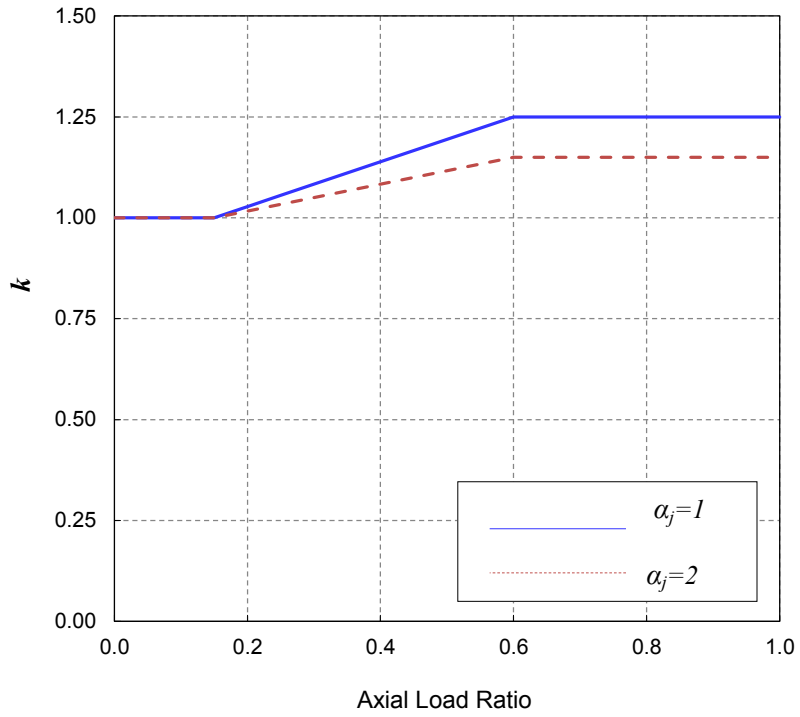

Figure 5.18 Axial load factor for proposed empirical model

Finally, the shear strength coefficient is calculated:

$$\gamma_j = \frac{V_j}{h_c b_j \sqrt{f_c'}} \tag{5.31}$$

5.6.3 J-Failure Shear Strength Degradation Model

A strength degradation coefficient k_Δ is proposed to represent the observed experimental degradation of joint shear strength associated with J-Failure mode with displacement ductility demand indicated previously in Chapter 4, Fig. 4.18. k_Δ relationships with displacement ductility factor based on ductility definition B defined in Chapter 4 is shown in Fig. 5.19.

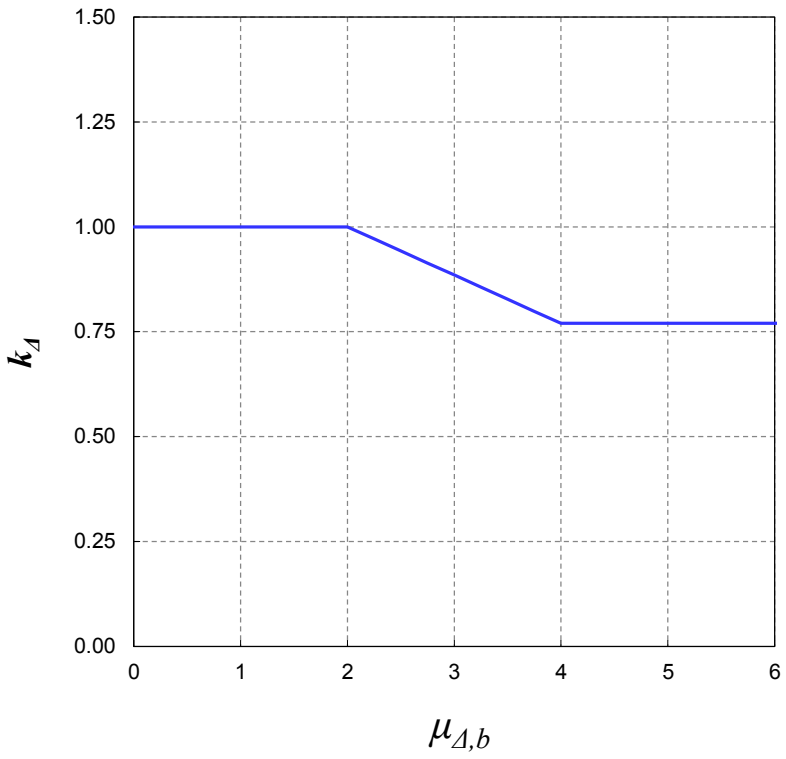

Figure 5.19 Proposed shear strength degradation coefficient with displacement ductility demand

The degradation factor k_Δ is supposed to modify the joint shear strength obtained using the proposed analytical strut-and-tie model (Eq. 5.23) or the empirical strength model (Eq. 5.28) to account for strength deterioration with increased ductility demand μ_Δ. The k_Δ-μ_Δ relationship can be mathematically represented as:

$$0.77 \le k_\Delta = 1.23 - 0.115\mu_\Delta \le 1.00 \quad \text{for Ductility Definition B} \tag{5.33}$$

Accordingly, the expression of joint shear strength coefficient after accounting for strength degradation becomes:

$$\gamma_{j\Delta} = k_\Delta \gamma_j \tag{5.34}$$

It is worth mentioning that this ductility degradation factor is not stemming from flexural ductility since the beam has not yielded. Instead, it rather represents the inherent ductility of J-Failure mode resulted from joint flexibility.

5.6.4 BJ-Failure Mode Shear Strength

As presented in Chapter 4, previous tests on unconfined beam-column joints experiencing beam yielding before joint shear failure suggest an inherent relationship between joint shear strength and the flexural capacity of yielding beam. Specifically, the flexural resistance of a yielding beam decides the limiting joint shear demands and, as yielding progresses, joint strength degrades until joint shear failure occurs, usually shortly after onset of beam yielding. Hence, the joint shear strength is the shear corresponding to development of beam flexural strength. In some tests, there is some minor joint shear strength gain after flexural beam yielding. This is basically attributed to strain hardening of beam reinforcement. Since the strength overshot is slight and uncertain, it is recommended to limit joint shear strength to the joint shear corresponding to beam flexural yielding strength. This observation and recommendation are in line with those found in Alire [6] for interior joints.

An exception to the above phenomenon is the B-Failure case when the flexural capacity of the beam is very small relative to the joint capacity. In this case, a beam plastic hinge is formed and ultimate failure corresponds to exhausting the beam plastic hinge rotation capacity while the joint is still in the elastic range. The special case is out of the scope of this study and should be dealt with as a beam plastic rotation capacity problem rather than joint capacity problem.

The following criterion is suggested to determine the joint shear stress demand corresponding to the case of BJ-Failure mode, which may or may not be the final joint shear strength depending on its relationship to J-Failure mode strength from Eq. 5.25:

1. Calculate beam yielding capacity M_{ny} which is approximately 1.13 the flexural capacity M_n obtained using standard procedures taking slab reinforcement in tension within b_b+h_{bt} effective width into account.

2. Compute tension force in beam (and effective slab width) reinforcement at yielding capacity:

$$T_{by} + T_{sy} = \frac{M_{ny}}{0.9d_b} \tag{5.35.a}$$

or more accurately from section equilibrium taking into account slab reinforcement and compression reinforcement effects on effective depth and moment lever arm.

3. Obtain column shear force corresponding to beam yielding V_{cy} by joint equilibrium

$$V_c = \left(\frac{L_b + 0.5h_c}{H} \right) \left[\frac{M_{ny}}{L_b} \right] \tag{5.35.b}$$

4. Calculate joint shear force corresponding to beam yielding as:

$$V_{bj} = T_{by} + T_{sy} - V_{cy} \tag{5.36}$$

5. Compute joint shear stress coefficient γ_{bj} at a level corresponding to beam flexural capacity (BJ-Failure shear strength capacity):

$$\gamma_{bj} = \frac{V_{bj}}{h_c b_j \sqrt{f_c'}} \tag{5.37}$$

5.6.5 CJ-Failure Mode Shear Strength

Few laboratory tests have suggested the presence of this failure mode initiated by column yielding and followed shortly by joint shear failure [132], [13]. Additional experimental evidence is needed to draw a definitive conclusion about the amount of overshot above column yielding before onset of joint shear failure. For assessment purposes, it is recommended to consider column yield strength as a threshold limit for joint shear strength until more test data are available to test this hypothesis. More importantly, once the column reaches moment strength, weak-story behavior and possibly P-Δ effects may govern the response and may lead to column shear and axial failure before joint final failure. Accordingly, joint shear strength corresponding to column yielding γ_{cj} should be calculated using similar approach to that of BJ-Failure mode and then compared to those of other failure modes.

5.6.6 S-Failure Empirical Bond Strength Model

The present study was motivated to explore whether improvements could be achieved in empirical equations to estimate the bond strength of short embedded bars by including influential parameters such as axial load, beam bar diameter, cover to bar diameter ratio, and presence of transverse beams orthogonal to joint. After exploration of the relevant quantities and algebraic expressions, the following expression was developed to represent the concrete average bond stress capacity of beam bottom reinforcement with insufficient bonded length:

$$\tau_{\max} = 13.2\left(\frac{P}{f_c' A_g}\right)^{0.25} \sqrt{f_c'}\, \Psi_s \Omega \left(\frac{c}{d}\right) \qquad \geq 6\sqrt{f_c'} \tag{5.38}$$

where P is column axial load, Ψ is bar diameter factor, and Ω is transverse beam confinement factor defined as follows:

$\Psi_s = 1$ for bar diameter $\geq$ 0.75 in. (5.39)
$\Psi_s = 1.25$ for bar diameter < 0.75 in.

$\Omega = 1$ for exterior isolated joints (5.40)
$\Omega = 1.12$ for joints with transverse beam on one side

$\Omega = 1.20$ for joints with transverse beam on both sides

(c/d) is the minimum of bottom and side concrete cover-to-bar diameter ratio measuring cover to bar centroid, which is not to exceed 2.5. The power term in the above expression is intended to account for axial load level and is calibrated from test results of the S-Failure database. For consistency with the presentation method of the current chapter and for comparison to other failure modes, this model is presented in terms of joint shear stress coefficient γ_{sj}, corresponding to pullout failure, although joint shear strength in this case is not fully engaged. In all tests of the database used, pullout failure occurred before bar yielding. Thus, expression 5.38 is only applicable for this case with no bar yield, which is very likely in bond-slip failure of short embedded bar. However, it is recommended to develop a future extension of this expression to cases with bar yield (Fig. 5.20) for more generality.

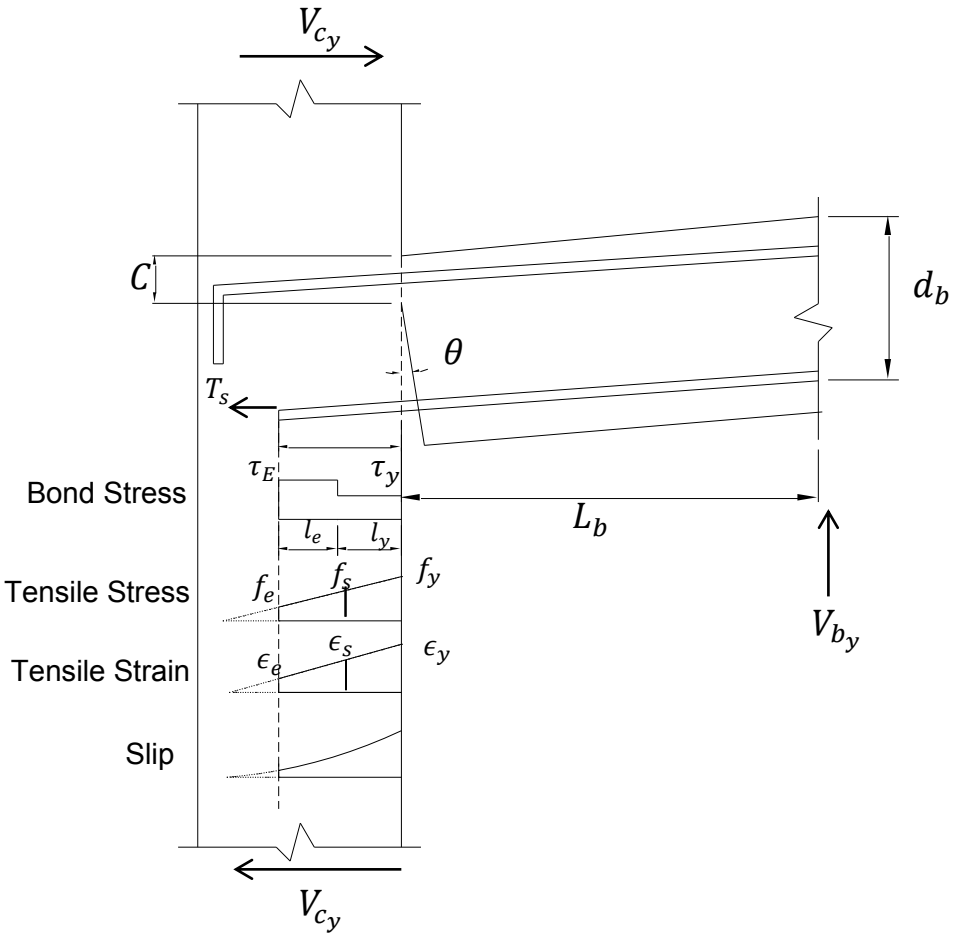

Figure 5.20 Proposed extension of bond-slip model for bottom beam bars in unconfined joints for yielding bar condition

The procedure to assess exterior and corner unconfined joint pullout strength of insufficiently embedded beam reinforcement is summarized in the following steps:

Determine joint shear stress coefficient corresponding to pullout failure γ_{sj} as follows:
1. Calculate tension force in beam longitudinal bar corresponding to bond capacity as:

$$T_s = l_{sp}\pi\phi_b\tau_{\max} \tag{5.41}$$

where l_{sp} is the length of the horizontal embedded part of longitudinal beam reinforcement, ϕ_b is beam bar diameter and τ_{max} is the allowable average bond stress given by Eq. 5.38.

2. Determine the corresponding beam shear force and moment

$$V_{bs} = 0.875\frac{d_b}{L_b}T_s \qquad M_{bs} = L_b.V_{bs} \tag{5.42}$$

where L_b is the clear distance between beam inflection point and column face and d_b is the effective beam depth.

3. From joint equilibrium, Eq. 5.35.b, determine column shear corresponding to pullout failure of beam reinforcement V_{cs}

4. Calculate joint shear force at the onset of bond slip of beam reinforcement

$$V_{sj} = T_s - V_{cs} \tag{5.43}$$

5. Determine joint shear stress coefficient corresponding to bond slip failure:

$$\gamma_{sj} = \frac{V_{sj}}{h_c b_j \sqrt{f_c'}} \tag{5.44}$$

5.6.7 Verification of Proposed Models

5.6.7.1 J-FAILURE MODIFIED ACI 318-08 STRUT-AND-TIE ANALYTICAL MODEL

A database of fifty-two previous exterior and corner joint tests were used to test the accuracy of shear strength prediction of the proposed modified ACI 318-08 strut-and-tie model for joints experiencing J-failure mode. The details of these tests were presented earlier in Chapter 3. Tables 3.1 and 5.1 depict test parameters and observed and calculated shear strengths. Table 5.1 only includes those specimens with a confirmed J-failure mode, while Table 3.1 shows also specimens with other failure modes. To confirm J-failure mode in a published test, it was not only relied on the authors' interpretation of failure mode. This interpretation could be frequently

subjective and in some older investigations, the distinction between the different modes of failure was not fully understood. Thus, a procedure to verify J-failure mode was followed. This procedure included:

1. Checking authors' observation of failure mode
2. Tracking beam longitudinal reinforcement strains if provided
3. Calculating beam longitudinal reinforcement strains if not provided
4. Investigating cracking pattern at the joint peak lateral load
5. Comparing theoretical beam flexural capacity to that observed at peak strength.
6. Checking the hysteretic loops' backbone curve for sharp softening, flat or hardening plateau after peak strength.
7. If the author reported beam yielding, specimens was considered a BJ-Failure specimen. If this information was not available, the beam flexural strength was calculated and if the strength matched beam strength the joint was considered in BJ-Failure mode.

Figure 5.21 displays the correlation between joint shear strength coefficients calculated by the proposed modified ACI 318-08 strut-and-tie model for J-Failure joints. The accuracy of the model is reflected in the average test to model shear strength ratio of 1.03 with coefficient of variation of 0.11. As shown in Table 5.1, the average dispersion coefficient is .02 ranging from 0.01 to 0.05. The figure shows the mean plus and minus standard deviation lines.

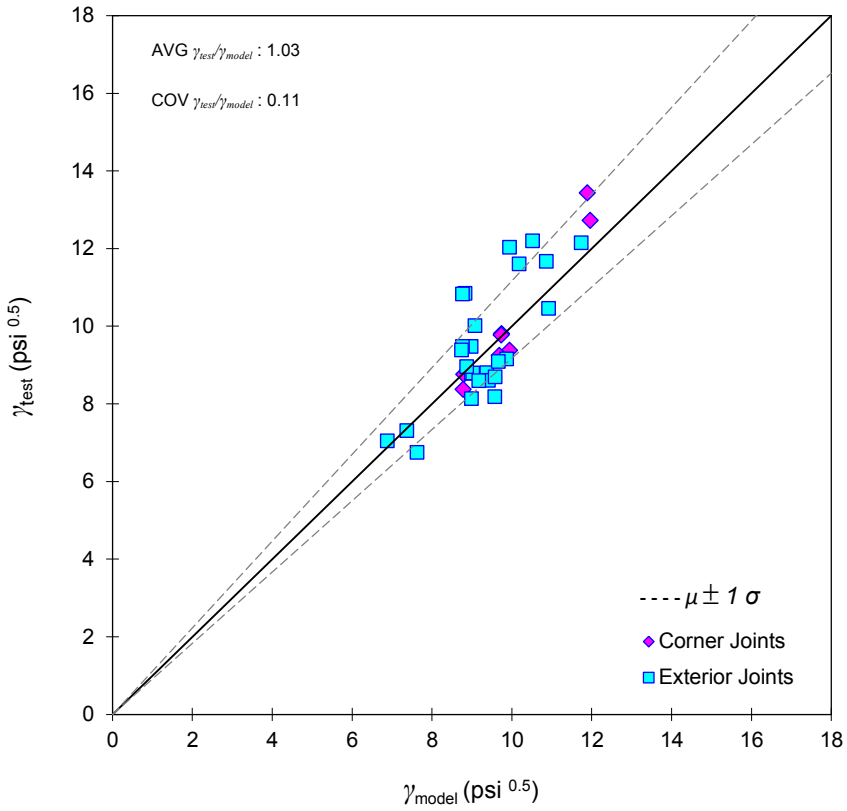

Figure 5.21 Experimental verification of proposed J-Failure strut-and-tie shear strength model

5.6.7.2 J-FAILURE EMPIRICAL MODEL

Figure 5.22 displays the correlation of test results to joint shear strength calculated using the proposed empirical shear strength expression Eq. 5.28. Average test-to-model joint shear strength coefficient is 0.99 while the COV is 0.13. This reveals the accuracy of the proposed empirical expression for quick estimation of unconfined exterior and corner joint shear strength for preliminary assessment purposes.

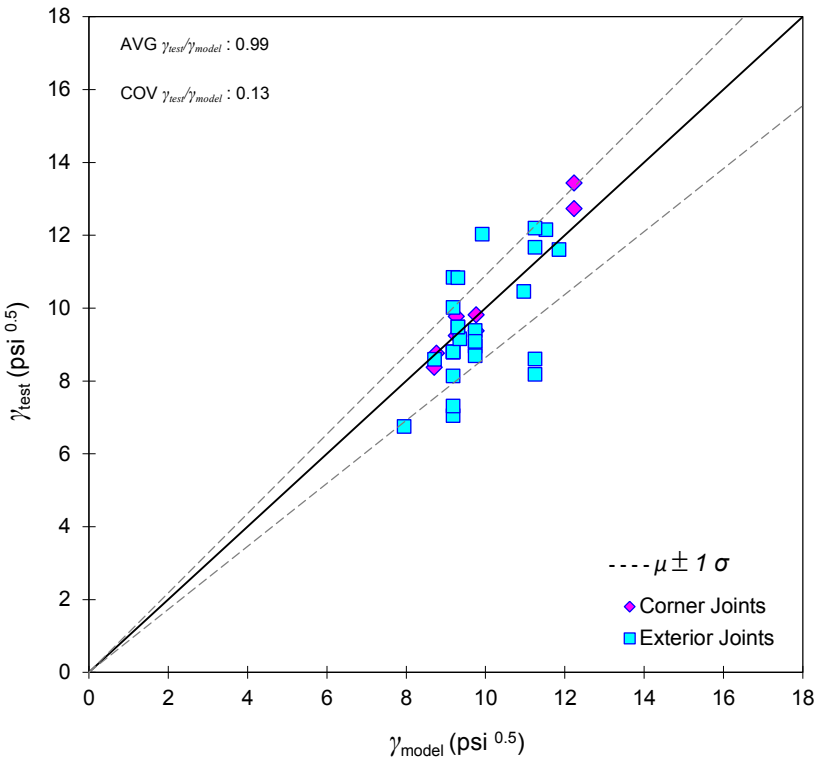

Figure 5.22 Experimental verification of proposed J-Failure shear strength empirical model

5.6.7.3 J-FAILURE STRENGTH DEGRADATION MODEL

Figures 5.23 and 5.24 displays the correlation of test results to joint shear strength calculated using the proposed shear strength degradation model for both analytical strut-and-tie and empirical models, respectively. It can be observed that including a ductility parameter in the shear strength model slightly shifts the correlation of the model to the more conservative side. This shift is the result of the conservative choice of the ductility parameter expression k_{Δ} to reflect the uncertainty and variability of ductility calculations.

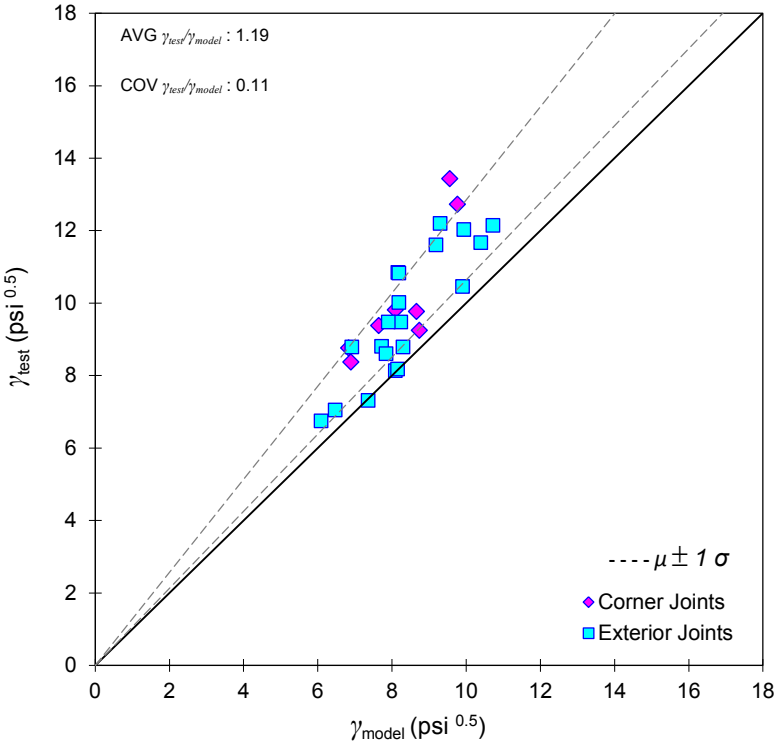

Figure 5.23 Assessment of the proposed strut-and-tie-based shear strength degradation model, ductility definition B

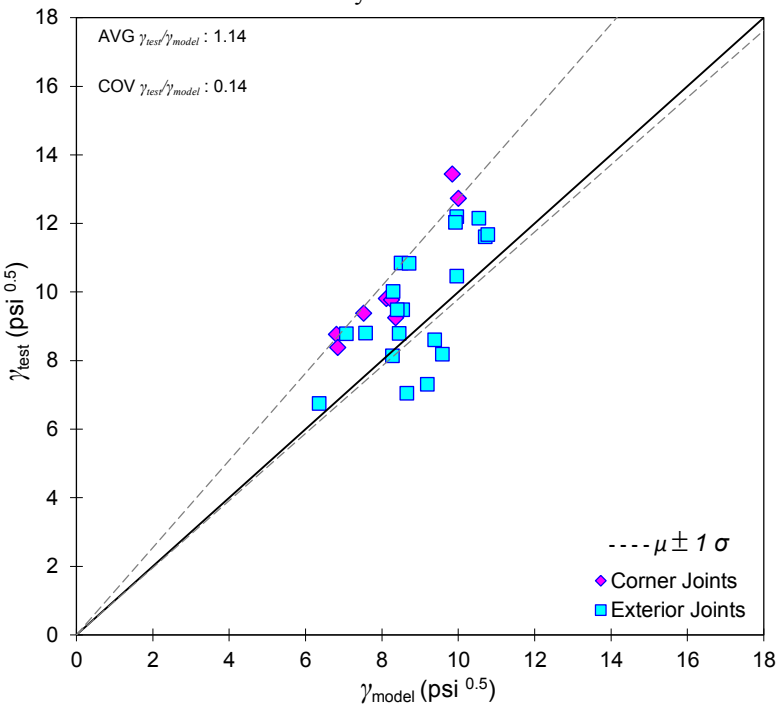

Figure 5.24 Assessment of the proposed empirical model-based shear strength degradation model, ductility definition B

5.6.7.4 S-FAILURE EMPIRICAL BOND MODEL

A database of twenty-five previous exterior and corner joint tests was used to test the accuracy of the proposed empirical bond strength model for joints experiencing pullout S-failure mode. The details of these tests were presented earlier in Chapter 3. Tables 3.1 and 5.2 list test parameters and observed and calculated bond and corresponding shear strengths of these tests. Table 5.1 only includes those specimens with a confirmed S-failure mode. The distinction between S-failure and other failure modes in previous tests was evident from the reported test specimen behavior.

Figure 5.25 exhibits joint shear stress coefficient corresponding to experimental and calculated empirical model bond capacities. Correlation parameters reflect 0.94 mean test-to-model strength ratio associated with a 0.14 coefficient of variation. These values indicate the relative accuracy of the proposed empirical bond model. More tests would be useful to further verify and refine this empirical model.

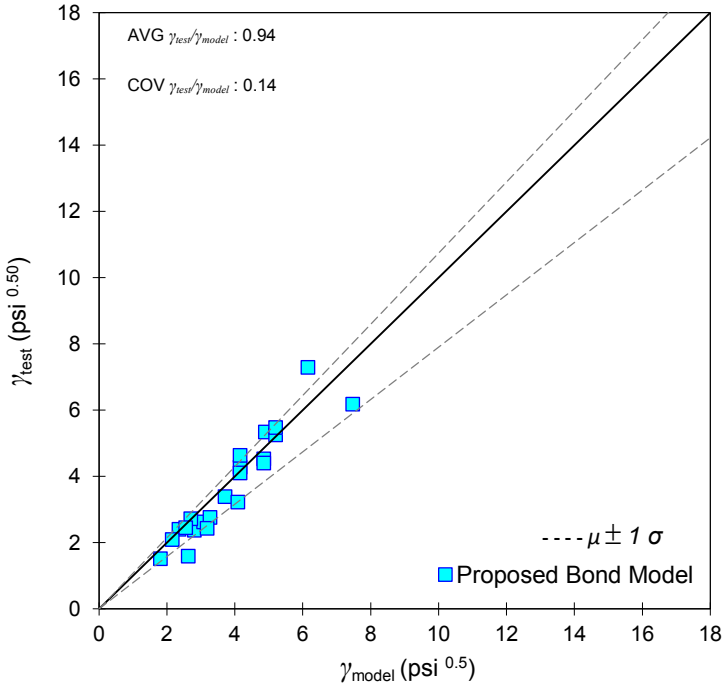

Figure 5.25 Experimental verification of proposed S-Failure bond strength model

5.6.8 Practical Criterion to Determine Joint Strength Limit State

After determining joint shear strength coefficients γ_j, γ_{bj}, γ_{cj} and γ_{sj} corresponding to the four failure modes J, BJ, CJ, and S, respectively, the least value should be chosen as a limiting joint shear strength for upward beam loading. For downward loading direction, the smallest of γ_j, γ_{bj}, γ_{cj} should be the governing joint shear strength.

5.6.9 Strength Reduction Factors (ϕ - Factor)

Figure 5.26 compares measured and design strengths, where design strength is calculated as the product of a strength reduction and nominal strength. Here the strength reduction factor is taken equal to 0.75. Nominal strength is either based on the proposed strut-and-tie model for J-Failure (Eq. 5.28) or proposed bond model for S-Failure (Eq. 5.38)

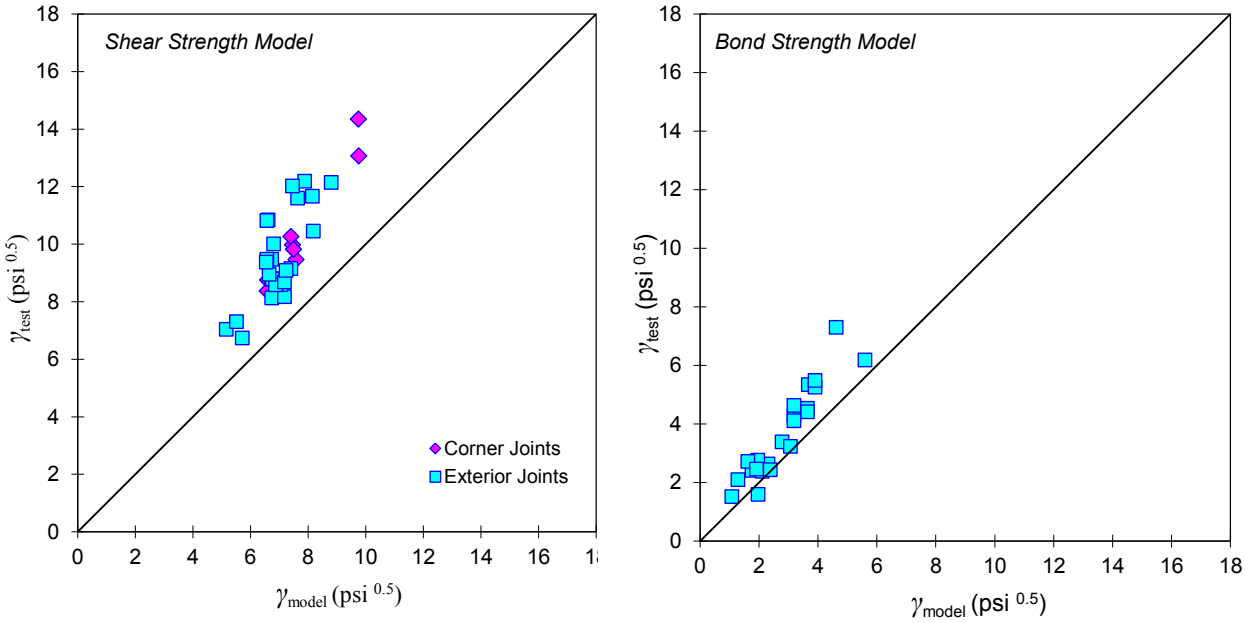

Figure 5.26 Proposed models strength prediction with a strength reduction factor of 0.75: (a) J-Failure strut-and-tie model (Eq. 5.28) (b) S-Failure bond strength model (Eq. 5.38)

5.6.10 Model Limitations

The models proposed in this chapter were based on limited range of test specimen parameters:

1. Joint aspect ratio ranging from 1 to 2, which is considered the most practical range in construction.
2. Concrete strength range of f_c' = 2500-6500 psi
3. No test data for unconfined exterior joints with two sided transverse spandrel beams was available to check the strut-and-tie model applicability to such cases. However, the use of this model in assessing shear strength of such joint should be conservative unless the transverse beams are seismically loaded, resulting in damage that reduces strength perpendicular to the spandrels.

Applicability outside the range of these parameters is uncertain.

CHAPTER 6

EXPERIMENTAL PROGRAM

6.1 INTRODUCTION

This chapter presents the details of the experimental program carried out at the *nees@berkeley* laboratories at the University of California, Berkeley to address the seismic performance of unconfined corner beam-column joints. The program comprised testing four full-scale corner beam-column joint subassemblies until total collapse. Test specimens were three dimensional corner bays of a prototype building; featuring the concrete slab and full story column height to represent the actual conditions of real buildings. The primary goal of the program was to gain an understanding of unconfined corner beam-column joint seismic performance and vulnerability to shear and axial failures. The four specimens were designed to simulate seismically substandard pre-1971 joint configurations, specifically the absence of joint transverse reinforcement. The specimens were tested under unidirectional and bi-directional quasi-static displacement controlled protocol. Axial column load was varied throughout the test to simulate the variation in a real corner column axial load due to overturning moment effect during ground shaking. Tests were continued until reaching the force and stroke capacity of the test setup, or until axial collapse load, whichever was earlier. Test specimens were extensively instrumented.

6.2 PROGRAM OBJECTIVES

The main objectives of the test program can be summarized as follows:

1. Understand the overall seismic performance of unconfined corner beam-column joints
2. Assess the joint shear strength under different loading schemes and joint configurations
3. Assess the effect of axial load on performance
4. Address the seismic vulnerability of shear-damaged joints to axial failure and evaluate the residual axial capacity after experiencing joint shear failure.
5. Serve as a basis for calibration and verification of joint shear strength and axial capacity models (Chapters 4, 5 and 8).

6.3 SHORTCOMINGS OF PREVIOUS TESTS

Due to the scarcity of experimental research on unconfined corner beam-column joints, there have been many aspects of joint behavior that are inadequately understood and that can be addressed by the current experimental program. These aspects include:

1. High axial load and its effects on joint shear strength and deformability.
2. Variable axial load during test to account for overturning moment effects.
3. Effect of joint aspect on vulnerability.
4. Slab contribution.
5. Realistic representation of boundary conditions in three dimensions.
6. Effect of loading history and realistic representation of bi-directional loading.
7. Axial collapse potential

6.4 TEST PARAMETERS

The main test parameters were selected based on study of previous joint tests and determination of issues related to strength and deformation capacity that were unresolved. These parameters were presented in Chapters 3 and 4. The four test parameters selected were beam reinforcement ratio, beam aspect ratio, axial load ratio, and loading history. Table 6.1 presents the test matrix and test parameter variation in different test specimens.

The test specimens are identified by three alphanumeric symbols. The first symbol is the letter *U* or *B*, referring to alternating unidirectional or simultaneous bidirectional displacement loading, respectively. The second symbol is either *J* or *BJ* reflecting the target failure mode; J refers to J-Failure (joint failing prior to significant beam longitudinal reinforcement yielding) and BJ refers to BJ-Failure (joint failing after significant yielding of beam longitudinal reinforcement). The third symbol is either 1 or 2, where 1 refers to joint aspect ratio 1.0 and 2 refers to joint aspect ratio 1.67.

Table 6.1 Test Parameters

Specimen ID	Test protocol	Joint aspect ratio α_j	Beam rein. ratio		Axial load ratio		Target failure mode
			ρ_t	ρ_b	Gravity	At shear failure	
U-J-1	Unidirectional	1	0.022	0.016	0.21	0.30	J
U-J-2	Unidirectional	1.67	0.01	0.007	0.21	0.45	J
B-J-1	Bidirectional	1	0.022	0.016	0.21	0.45	J
U-BJ-1	Unidirectional	1	0.0086	0.0069	0.21	0.45	BJ

6.4.1 Beam Reinforcement Ratio

Based on the detailed discussion presented in the previous chapters, the beam reinforcement ratio ρ was found to be decisive in determining whether joint failure would occur before (J-Failure) or after (BJ-Failure) beam yielding (assuming that other failure modes do not pre-empt these failure modes. Three of the test specimens (U-J-1, U-J-2, and B-J-1) have relatively high beam longitudinal reinforcement ratio to promote J-Failure mode, while the last specimen U-BJ-1 uses lower beam longitudinal reinforcement ratio with intent to promote BJ-Failure mode. The column-to-beam flexural strength ratio is chosen so that column yielding will not occur prior to joint failure. Flexural capacities of columns were confirmed to be adequate through inelastic sectional analysis of both columns and beams considering the range of axial and biaxial lateral loadings.

6.4.2 Joint aspect ratio

As discussed in Chapters 3, 4 and 5, the joint aspect ratio was proven to be one of the most significant parameters affecting joint performance. Two joint aspect ratios α_j were selected to reflect practical upper and lower bounds. The joint aspect ratio of specimens U-J-1, B-J-1, and U-BJ-1 is 1 while it is 1.67 for specimen U-J-2. Another more refined definition of joint aspect ratio is that defining the joint compression strut angle θ as shown in Chapter 4, that is the ratio of centerline distance between beam top and bottom bars and to its counterpart distance in column between the two outermost layers of column bars h''_b/h''_c. Using this definition, the joint aspect ratio for specimens U-J-1, B-J-1, and U-BJ-1 is 1 and that for specimen U-J-2 is 1.92. The latter definition can be used for shear strength assessment using the strut and tie model suggested in Chapter 5.

6.4.3 Axial Load Ratio

Mosier [104] reports results of a survey of the gravity axial load ratio of pre-1967 columns, finding it to range from 0.03 to 0.28 times the column axial capacity with an average value of 0.12. In a previous experimental phase of the current project [120], it was decided to choose a low value of 0.10 as a starting gravity load. However, since the main objective of the present study is to investigate the axial failure potential and the effect of high axial load on joint shear strength and deformability, it was decided to choose a gravity axial load ratio of 0.21 to represent the higher gravity load buildings comprising seven or more stories, which represent a considerable percentage of the inventory of gravity load designed buildings worldwide. It is believed that buildings having higher axial load ratios are more susceptible to axial collapse during earthquakes.

The overturning moment effect during earthquake ground shaking can generate additional axial loads on corner columns because bidirectional effects can be additive. Based on a preliminary dynamic analysis performed in the current study of a square footprint 8-story model building subjected to a suite of intense ground motions of rare seismic events (2% probability of

exceedence in 50 years for Los Angeles Metropolitan Area), it was decided to implement a 60% to 120% P_g overturning axial load in the design of axial load protocol.

6.4.4 Loading History

Many past tests have been unidirectional (that is, loading in the plane of frame). Due to testing complexities associated with three dimensional loading, very few tests have implemented multi-directional loading. For corner beam-column joints in actual buildings, simultaneous bidirectional seismic loads are very likely to govern the seismic demand on such joints. Accordingly, it was decided to dedicate one test to study the effect of simultaneous three dimensional loading, with the remaining three tests conducted by loading first in one direction, then in the other, and then repeating the process at higher amplitude.

6.5 SPECIMEN DESIGN AND CONSTRUCTION

6.5.1 Test Specimens Design Criteria

6.5.1.1 PROTOTYPE BUILDING

The full-scale corner beam-column subassembly is extracted, with some adjustments to accommodate laboratory space, from the seven-story Van-Nuys Holiday Inn building in Los Angeles City (Fig. 6.1). The corner beam-column subassembly represents the portion of corner bay lying between the inflection points. This building was designed using the LA City Building Code 1964, and suffered corner beam-column joint damage during past earthquake. No joint reinforcement was provided. Several researchers have performed dynamic analysis for the building to assess its vulnerability (e.g., [75] and [142]). The linear pushover analysis of the building performed on OpenSees finite element software as a 2D frame in each of the two orthogonal directions by Park, [120] was adopted to develop an expression for lateral load axial load relationship for specimen U-J-1. The axial load-lateral load relations for specimen U-J-2, U-BJ-1 and B-J-1 were based upon the linear dynamic analysis (Sec. 6.4.3) on 8 story fictitious building frame.

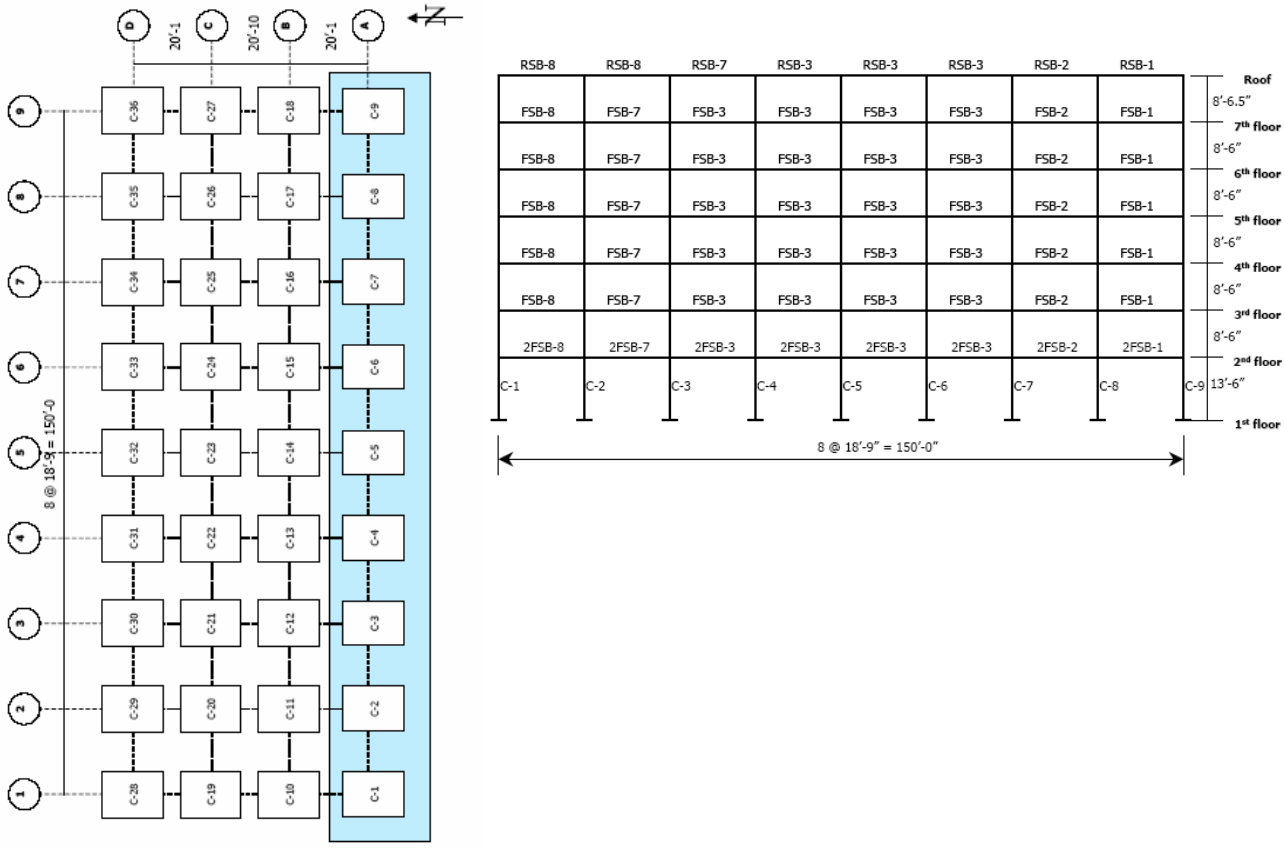

Figure 6.1 Van Nuys Hotel, the prototype building model, Kranwinkler [75]

6.5.1.2 LATERAL LOAD-AXIAL LOAD RELATIONSHIP

The axial load on a corner column during seismic event varies significantly based on the intensity of ground motion due to overturning moment effects from the two horizontal components of the ground motion in addition to the vertical component if any significant. If the peak ground acceleration is significantly large and/or the gravity load on corner column is quite small, the axial load from overturning moment could fluctuate significantly about the gravity load ranging from tension to high compression. Thus, it was crucial to simulate this overturning moment effect during the test. Details of axial load protocol used to achieve this goal are presented subsequently.

6.5.1.3 EFFECTIVE SLAB WIDTH

The effective slab width to account for slab reinforcement in tension has been investigated in many previous research studies. Design documents such as ACI 318 also suggest an effective slab width. It was decided to adopt the slab width suggested by Zerbe and Durrani [159], for exterior (corner) joint, namely:

$$B_{eff} = b_b + h_{tb} \quad (6.1)$$

where b_b is the width of the beam parallel to lateral load plane and h_{tb} is the transverse beam total depth.

6.5.1.4 FAILURE MODES AND DESIGN CRITERIA

As described earlier in Chapter 3, several joint failure modes may govern the failure of unconfined beam-column joints. Two of the characteristic failure modes were chosen to be the target failure modes of the test specimens:

1. J-Failure: Joint shear failure without beam or column yielding. As indicated in Table 6.2, this failure mode is expected in specimens U-J-1, U-J-2 and B-J-1
2. BJ-Failure: Joint shear failure after beam flexural yielding. The columns are made sufficiently strong that only mild or no yielding of columns is expected. This failure mode is expected in specimen U-BJ-1.

One very important objective of the test program is to monitor and record the post peak performance of the joint reflected by shear stress-strain relationship and joint shear stress-EDP relationships. This is particularly important in predicting the joint shear strength degradation profile.

6.5.2 Test Matrix and Specimen Design

The specimens were designed to isolate and expose target failure modes. To that end, column lap splices were avoided and the columns and beams were provided with closely spaced hoops. Figure 6.2 displays the overall geometry and concrete dimensions of test specimens. The specimen is a full-scale subassembly representing a corner bay of the prototype building, between the points of inflections assumed at mid-column height and mid-span of beams. Sectional analysis was performed using hand calculations and verified by different software packages including XTRACT and RESPONSE 2000.

Table 6.2 Test matrix and specimen design

Specimen ID	Beam Dim. *(in)*	Beam Reinforcement			Column Reinforcement		Loading	P/f'_cA_g		Target shear failure
		Top	Bottom	Stirrups	Long.	Hoops		Gravity	@ shear failure	
U-J-1	16 x 18	4#10	4#9	#3@3”	8#10	#3@3”	Unidirec.	0.21	0.30	J
U-J-2	16 x 30	4#9	4#8	#3@3”	8#10	#3@3”	Unidirec.	0.21	0.45	J
B-J-1	16 x 18	4#10	4#9	#3@3”	8#10	#3@3”	Bidirec.	0.21	0.45	J
U-BJ-1	16 x 18	4#6	4#6	#3@3”	8#10	#3@3”	Unidirec.	0.21	0.45	BJ

6.5.2.1 BEAM DESIGN

In specimens U-J-1, U-J-2 and B-J-1, a relatively high beam reinforcement ratio, but within the practical limits, was chosen to avoid yielding beam reinforcement before reaching the full shear capacity of the joint (J-Failure). In contrast, for specimen U-BJ-1 the beam reinforcement ratio was relatively low (1%) to promote beam yielding before joint shear failure (BJ-Failure).

The slab reinforcement within the effective flange width of b_b+h_{tb} was included estimating negative beam reinforcement ratio. Beam longitudinal reinforcement was chosen as 4#10 top and 4#9 bottom for specimens U-J-1 and B-J-1, and 4#9 top and 4#8 bottom for specimen U-J-2. By this selection of reinforcement, it was intended to keep the tensile stress level in the beam reinforcement the same for all specimens experiencing J-Failure mode such that the effect on concrete softening of the joint compression strut would be similar.

Beam longitudinal reinforcement terminates in the joint by a standard hook according to ACI 318-64 (which still holds in the current ACI 318-08 requirements). However, for the hooks in smaller joint aspect ratio specimens U-J-1, B-J-1, and U-BJ-1, the vertical distance available in the joint to hook the bar is smaller than the standard hook length requirement. Accordingly, it was decided to limit the hook length to the beam depth and terminate the hook right at the face of column (Fig. 6.3). The first reason of this decision is to simulate the actual construction practice in such cases. The second reason is to avoid additional confinement to the hook applied by the first hoop in the column, which may prevent the hook from bulging out during the test, which in turn could add unrealistic strut strength to the joint.

Beam stirrups were designed to resist the maximum shear stresses expected during the test (corresponding to the maximum of joint shear strength and beam flexural strength including strain-hardening and overstrength effects). Torsional stresses exerted on the beam stirrups due to slab presence were also accounted for in the stirrup design. Accordingly, it was decided to use #3@3 in. over the entire beam span. Additional transverse reinforcement was provided at the beam free end to accommodate actuator forces (Fig. 6.3).

6.5.2.2 COLUMN DESIGN

Column interaction diagrams were developed using XTRACT sectional analysis software. For all four specimens the column section is 18 x18 in. and column reinforcement is 8#10 deformed grade 60 (A706) (Fig. 6.3). The column was proportioned so that its flexural strength under all loading combinations during testing would be higher than demands imposed at beam flexural strength by at least a factor of 1.4. In the case of the bidirectionally loaded specimen B-J-1, the biaxial column flexural strength under different combinations of axial loads on 45^0 moment plane was considered the governing critical column flexural strength.

The column hoops were designed according to the current ACI 318-08 [1] seismic provisions to sustain the shear forces expected during tests, as well as to provide sufficient confinement to column section to achieve ductile performance. The expected tension forces

during test were transferred from test rig to column through embedded headed bars connecting columns to transition plates (Fig. 6.3).

6.5.2.3 SLAB DESIGN

The slab was designed according to pre-1970 standards (ACI 318-64). The slab reinforcement consisted of top and bottom meshes of #3@12 in. This results in a typical reinforcement ratio for pre-1970 construction. No diagonal reinforcement was provided at the corner of the slab as the current standards recommend.

6.5.2.4 BEAM-COLUMN JOINT DESIGN

The dimensions of the test specimens including the joint dimensions were selected to achieve the intended failure modes based on trends in past tests (Chapter 4) and models developed as part of this study (Chapter 5). Several iterations were required, as strengths of columns and joints were believed to be affected by beam reinforcement ratio, axial load ratio, and joint aspect ratio.

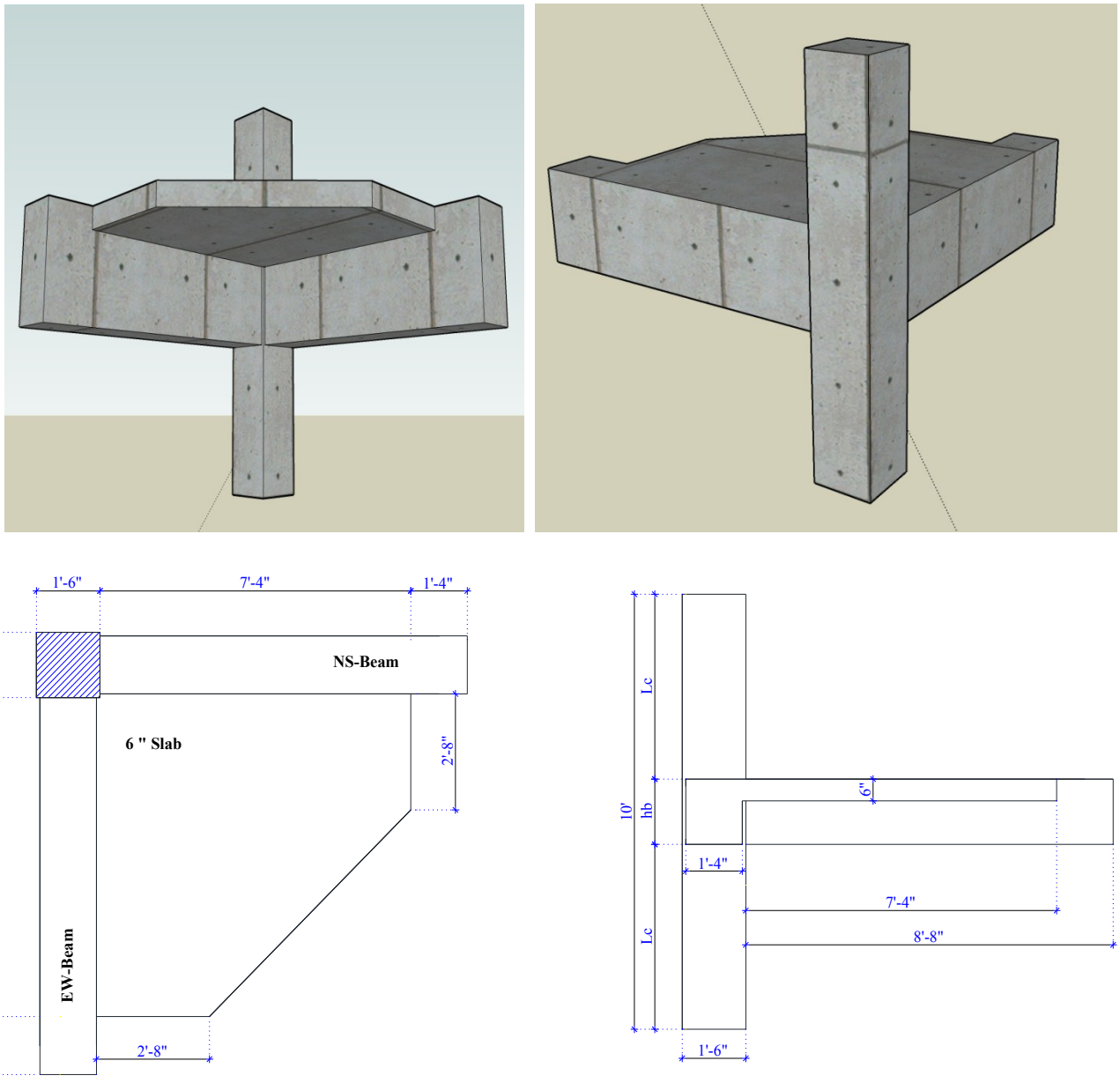

Figure 6.2 Schematic rendering and concrete dimensions of test specimen

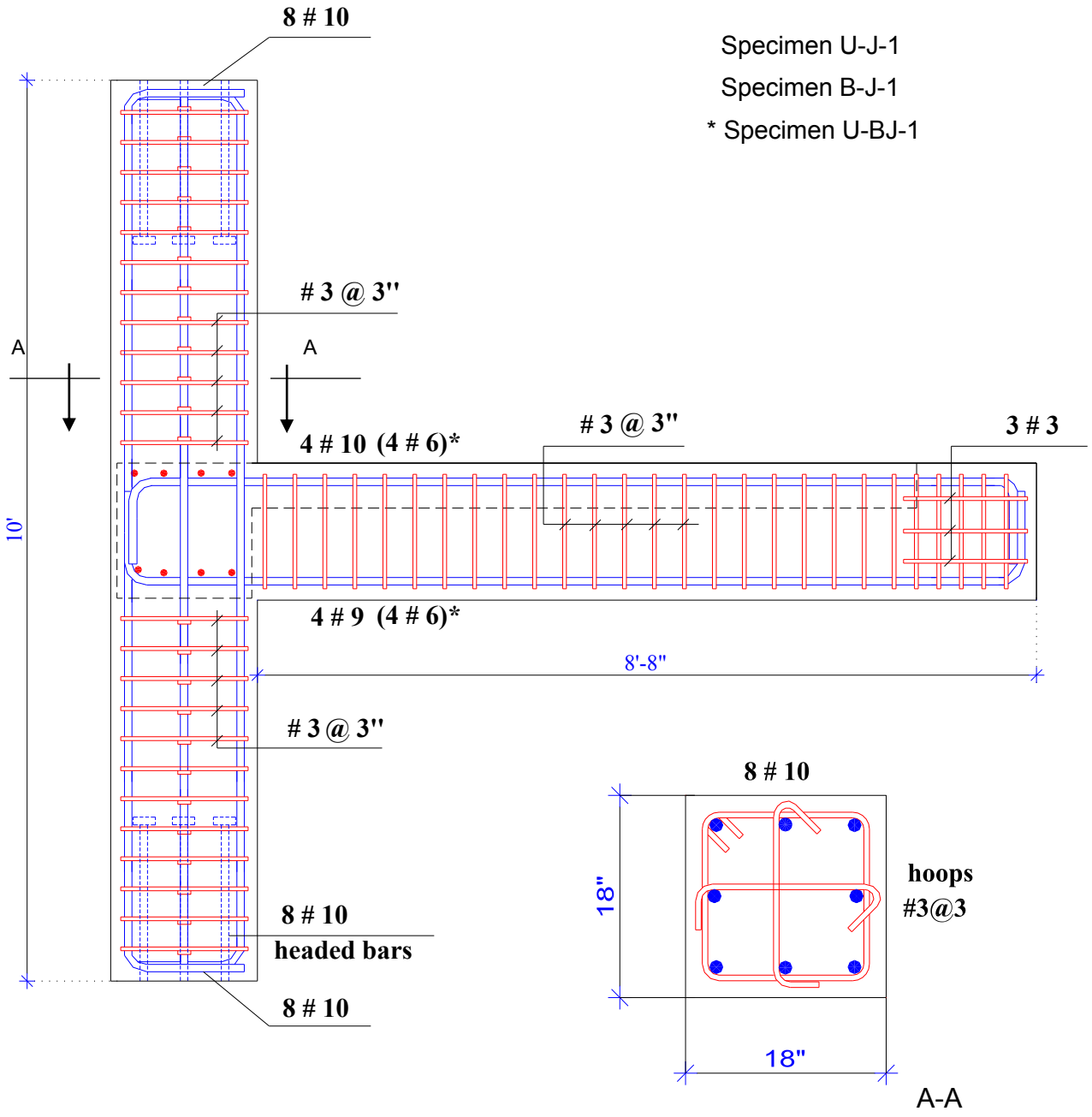

Figure 6.3.a Reinforcement details of test specimens

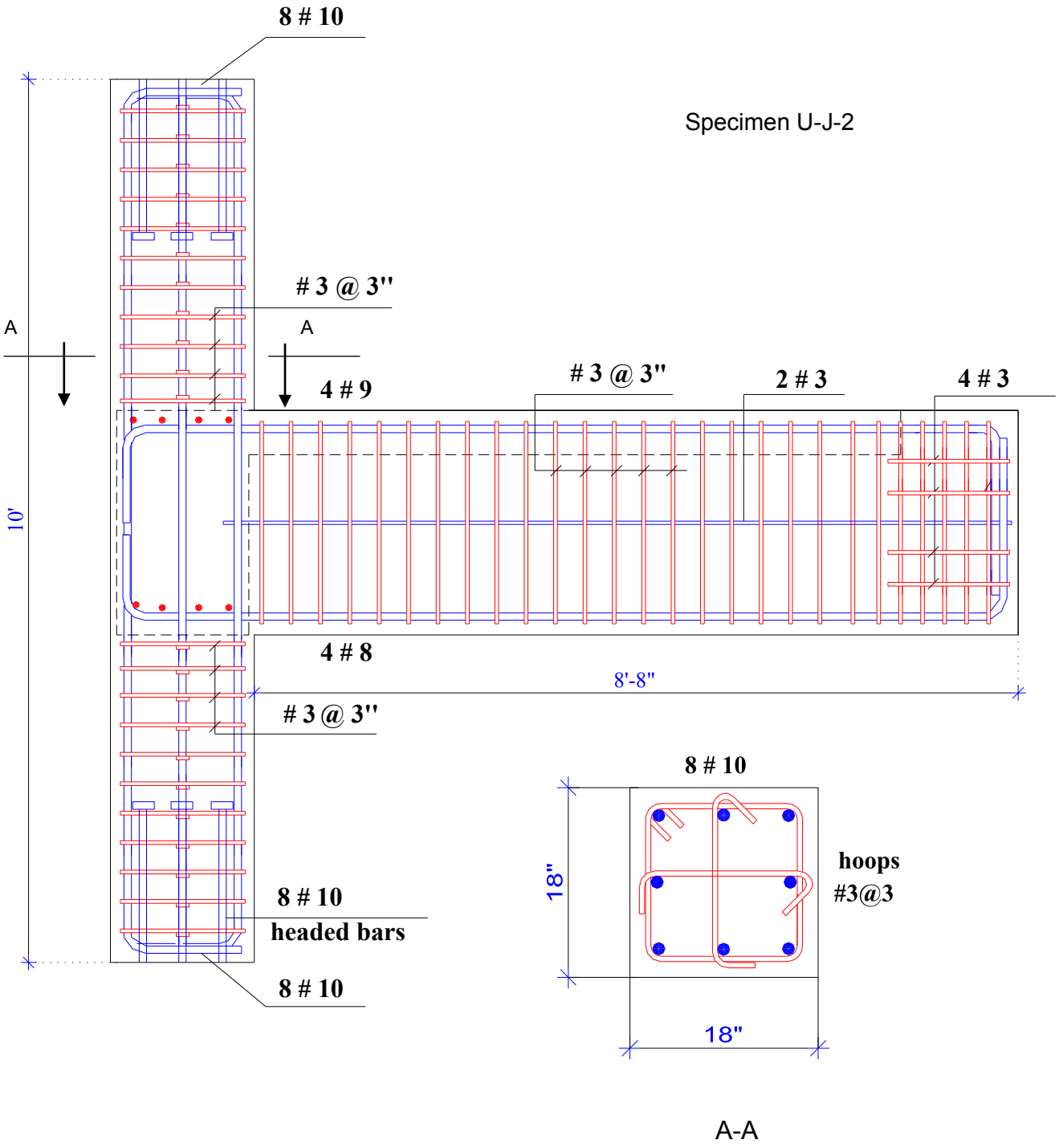

Figure 6.3.b Reinforcement details of specimen U-J-2

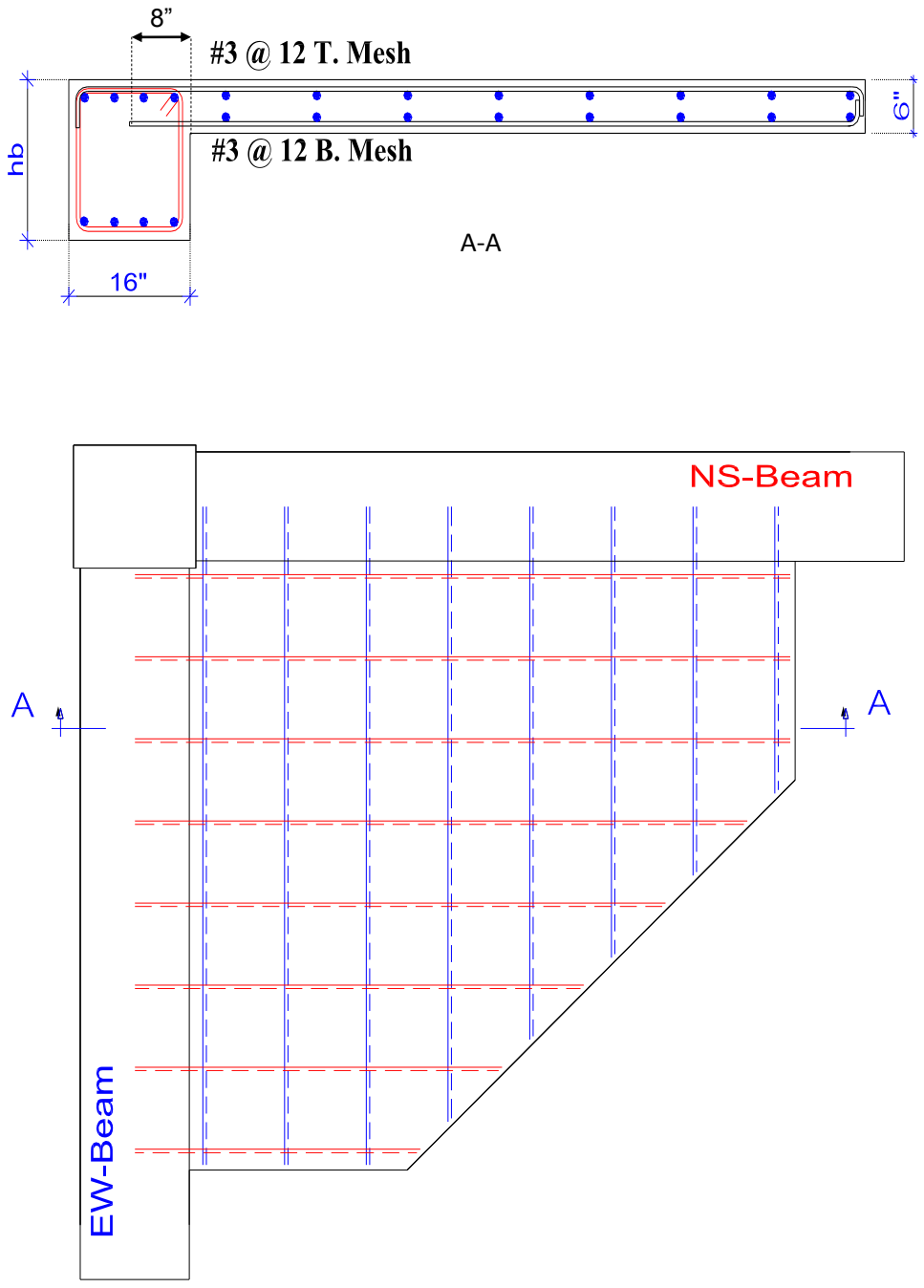

Figure 6.4 Slab reinforcement of test specimens

6.5.3 Specimen Construction

The construction site at *nees@berkeley* laboratories at *Richmond Field Station* was prepared by cleaning and leveling the ground, and building the wooden forms for the four specimens. Special care was given to leveling the formwork during construction to minimize the effects of eccentricities on the complex geometry of the three dimensional test specimens. The wooden forms were laterally braced after construction to avoid any tilting during concrete casting. The sides of the column forms were sufficiently stiffened and shored to prevent lateral bulging during casting. Templates containing hole locations to match the headed bar pattern were used on both ends of column formwork to ensure the accuracy of headed bar locations.

During construction of the formwork, steel reinforcement was undergoing strain gauging process at a separate venue. A meticulous labeling method was applied to the strain gauges installed onto the steel reinforcement that enables identification of strain gauge locations by quick inspection of the label. Throughout the construction process, functionality of strain gauges was checked to identify, fix, or replace any malfunctioning gauge.

The gauged steel reinforcement was transported and placed in the forms paying additional attention to the accuracy of installment to ensure that the strain gauge locations match the intended design. The process of placing steel reinforcement started with placing the lower column headed bars followed by installing the column longitudinal reinforcement and transverse hoops until the beam bottom level. The beam reinforcement was fully fabricated next, and the rest of column hoops and the slab reinforcement were installed last as indicated in Fig. 6.6. Top column headed bars were installed through a top wooden template that included a center opening to enable casting concrete from the top of the column. Headed bars arrangement are shown in Fig. 6.7

It is worthy to mention that installing the hooked beam longitudinal reinforcement within the joint was a quite challenging job since the two orthogonal beams had nearly intersecting reinforcement (Fig. 6.7). The sequence of placing the beam reinforcement in this juncture was as follows: the EW-beam longitudinal bottom reinforcement was placed first followed by the bottom NS-beam longitudinal reinforcement; the top EW-beam longitudinal reinforcement was then placed followed NS-beam top longitudinal reinforcement. This sequence of placing beam reinforcement had a significant effect on the effective depth of each beam as indicated in Fig. 6.5.

After finishing reinforcement installation, the strain gauge cables were extended, taped, placed inside protective plastic tubes, and routed inside the forms until reaching designated exit points in the form at locations of low stress levels.

Before casting concrete, final check on form dimensions, steel reinforcement spacing and alignment, concrete cover, and alignment of headed bars was performed. Inner surface of forms were slightly wetted before casting.

Concrete was supplied by *CEMEX* through a local contactor. The mix design required at least 5-6 inches of slump to facilitate casting in the congested areas of specimens, namely headed bar regions and joint hooked bar intersections. The casting process started with the lower column going up until casting the beams followed by the upper column and the slab deck (Fig 6.10). No special attention was given to mimic the condition of cold joint above and below beam level. Concrete was thoroughly compacted using electrical rod type vibrators that were applied internally within the fresh concrete body and externally on the column and joint wooden form surfaces as shown in Fig. 6.10. After casting, concrete was leveled by a screed.

Since the cast specimens were placed outdoors in a very windy season, special care was needed to avoid losing concrete surface moisture that could negatively affect the strength. Accordingly, the curing method chosen comprised keeping the cast specimens inside wooden forms for two weeks and watering the outer surfaces of the form using fresh water daily. The exposed concrete surfaces (slab and beam top surfaces) were cured by covering them with well anchored plastic sheets then applying a surface film of water beneath them (Fig. 6.11). The thin water film between concrete and plastic sheets was replenished as needed. Test specimens were cast in two different casting days; on the first day specimens U-J-1 and B-J-1 were cast, while the other two specimens U-J-2 and U-BJ-1 were cast on the second day. The finished specimens are shown in Fig. 6.13.

Eighteen standard concrete cylinders (6 inches in diameter and 12 inches in height) were sampled from the fresh concrete representing the properties of each cast specimen. Concrete cylinders were used in compression tests to monitor the progress of concrete strength at different ages until test date. At test date, three concrete cylinders were intended to be tested in compression to develop concrete stress-strain curve and give test date compressive strength. Three other cylinders were indented to undergo a splitting tension test. It is worthy to mention that concrete cylinders were cured under the same curing conditions of the test specimens they represent.

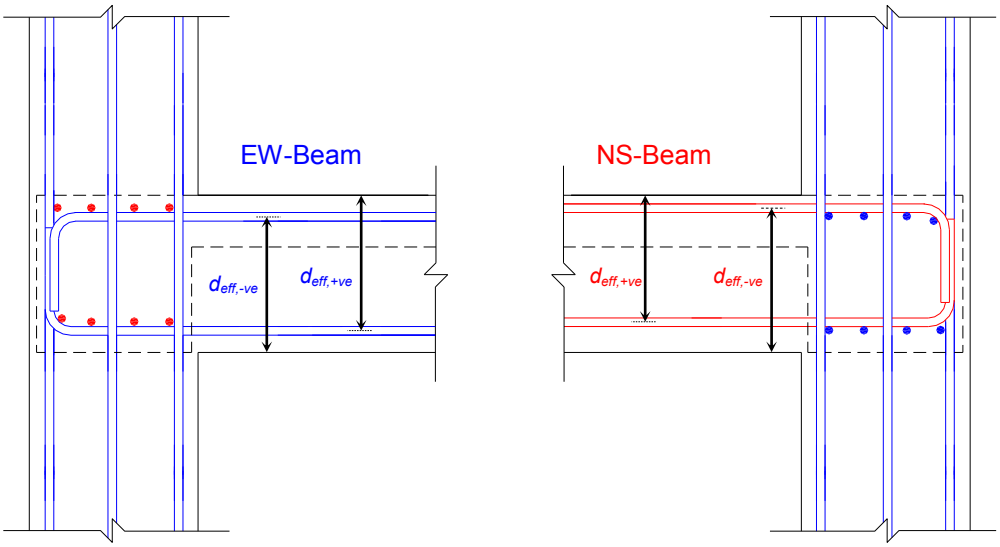

Figure 6.5 Effective depth of EW and NS beams of test specimens

Figure 6.6 Steel cage construction of specimen U-J-1

Figure 6.7 Congested beam reinforcement steel hooks inside the joint

Figure 6.8 Reinforcement cage of specimen U-J-2

Figure 6.9 Deck reinforcement and lower column headed bars of test specimens

Figure 6.10 Concrete casting and compaction of test specimens

Figure 6.11 Supervision of concrete casting and compaction

Figure 6.12 Cast specimens curing and finalized formwork and scaffolding

Figure 6.13 Finished test specimens after removing wood forms

6.5.4 Materials Properties

6.5.4.1 CONCRETE

The test specimens were constructed using normal weight conventional concrete supplied by a local contactor. The target compressive strength was 3500-4000 psi to simulate the prevailing strength in older construction. Table 6.3 displays the mix design used and the concrete strength for the test specimens at different ages. Standard 6x12 inches cylinders were used to determine concrete strength. Figures 6.14 represent the stress-strain relationship for concrete used in test specimens.

Table 6.3.a Concrete mix design

Cement (lb)	Water (gal)	Coarse aggregates (lb)	Fine aggregates (lb)	Super plasticizer (oz)	Fly ash (lb)
384	34	1750	1641	13.9	62

Table 6.3.b Concrete strength of test specimens

Specimen	Compressive Strength f'_c (psi)		Splitting Strength f_{ct} (psi)
	28 days	Test date	Test date
U-J-1	2940	4297/4537*	418
U-J-2	4058	4430	407
B-J-1	2940	4413	436
U-BJ-1	4058	4390	423

* Specimen U-J-1 was tested on two different test dates, the first day was for cyclic loading and the second was for the axial failure test as indicated in Chapter 7.

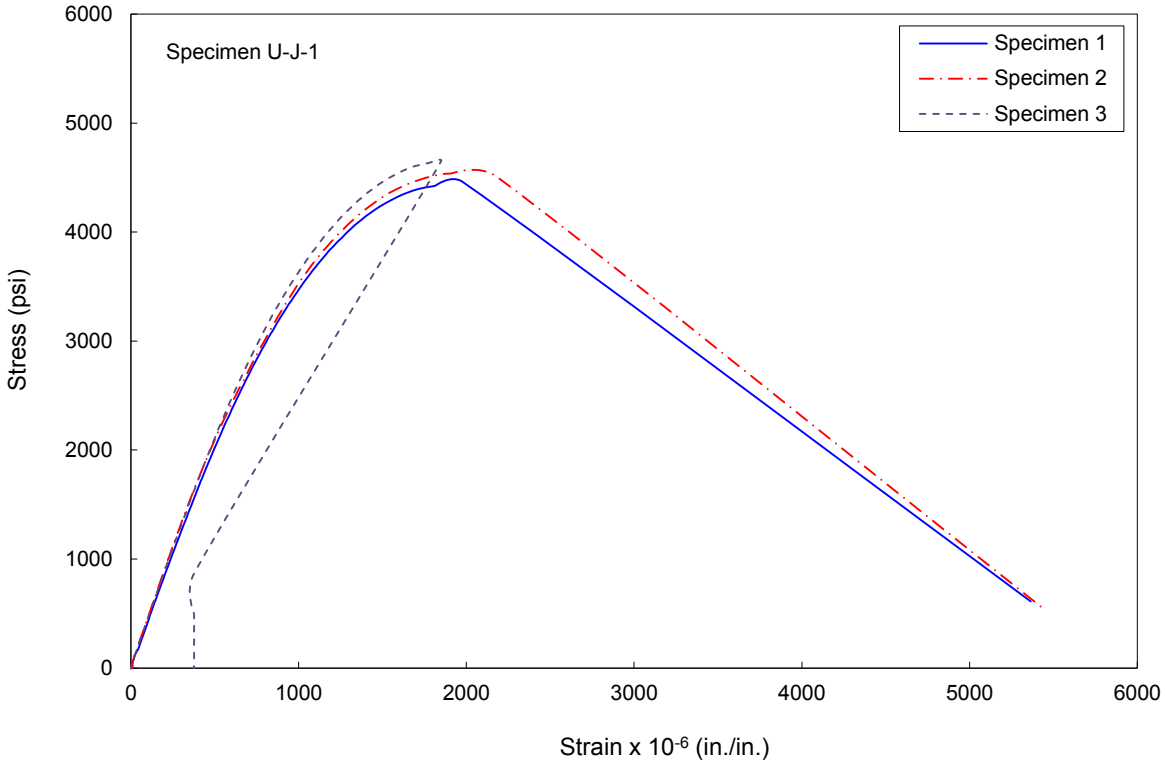

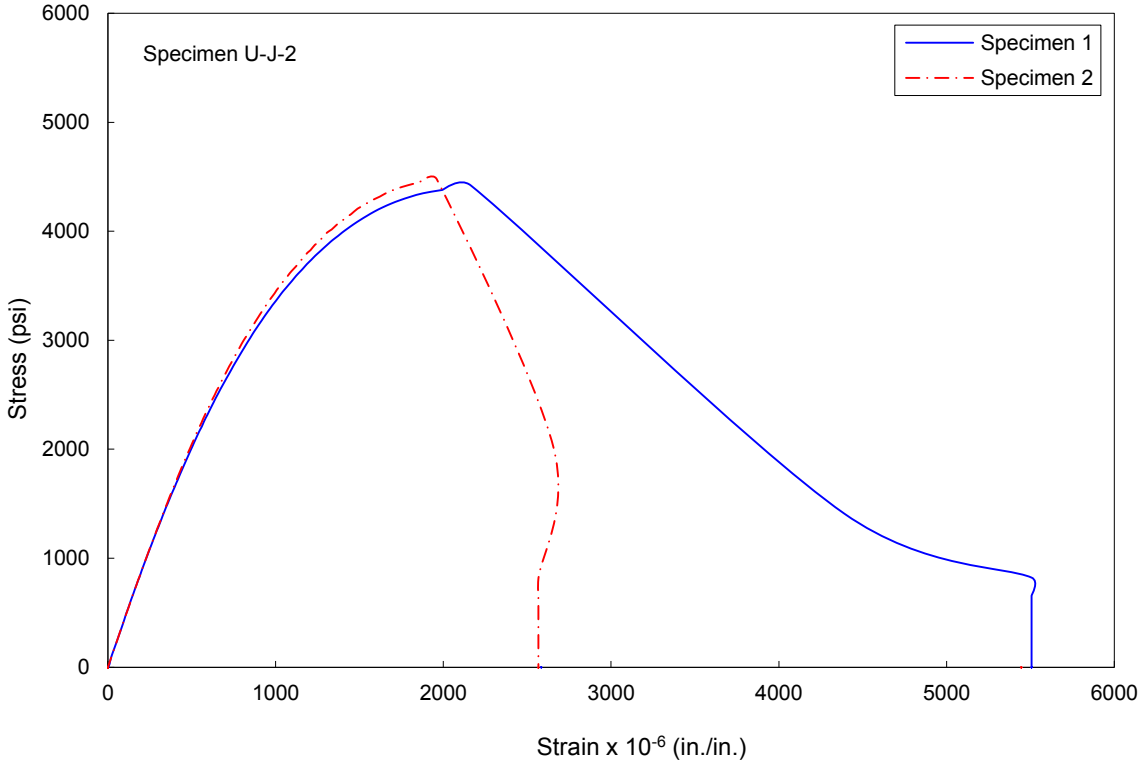

Figure 6.14.a Test date concrete compressive stress-strain relationship for specimens U-J-1 and U-J-2

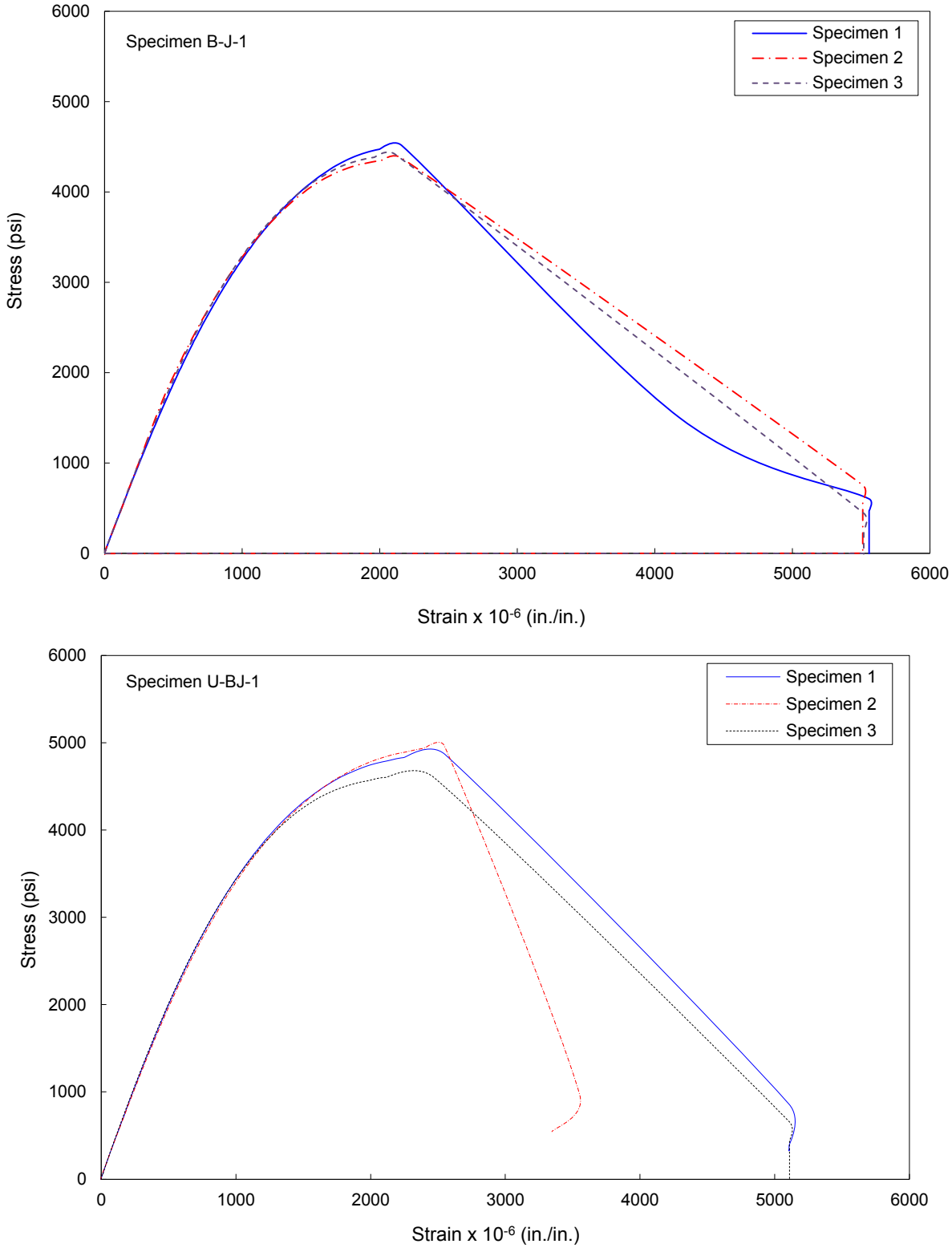

Figure 6.14.b Test date concrete compressive stress-strain relationship for specimens B-J-1 and U-BJ-1

6.5.4.2 REINFORCING STEEL

High strength deformed reinforcing steel A706 was used for beam and column longitudinal reinforcement. High strength deformed reinforcing steel A615 was used for slab longitudinal reinforcement and for beam and column transverse reinforcement. Table 6.4 and Figure 6.15 show the tensile test results for the reinforcing steel used.

Table 6.4 Steel reinforcement tensile test results

Specimen	Bar	Stress *(ksi)*		Strain (in./in.)	
		f_y	f_u	ε_u	ε_{fr}
U-J-1	#10	68.2	99.9	0.13	0.22
	#9	75.9	103	0.12	0.22
	#3	69.5	110	0.12	0.16
U-J-2	#10	77.6	109	0.11	0.23
	#9	73.0	107	0.12	0.22
	#8	63.2	92.8	0.13	0.23
	#3	69.5	110	0.12	0.16
B-J-1	#10	72.8	106	0.12	0.22
	#9	72.8	106	0.11	0.21
	#3	69.5	110	0.12	0.16
U-BJ-1	#10	77.6	109	0.11	0.23
	#6	74.3	103	0.12	NA
	#3	69.5	1010	0.12	0.16

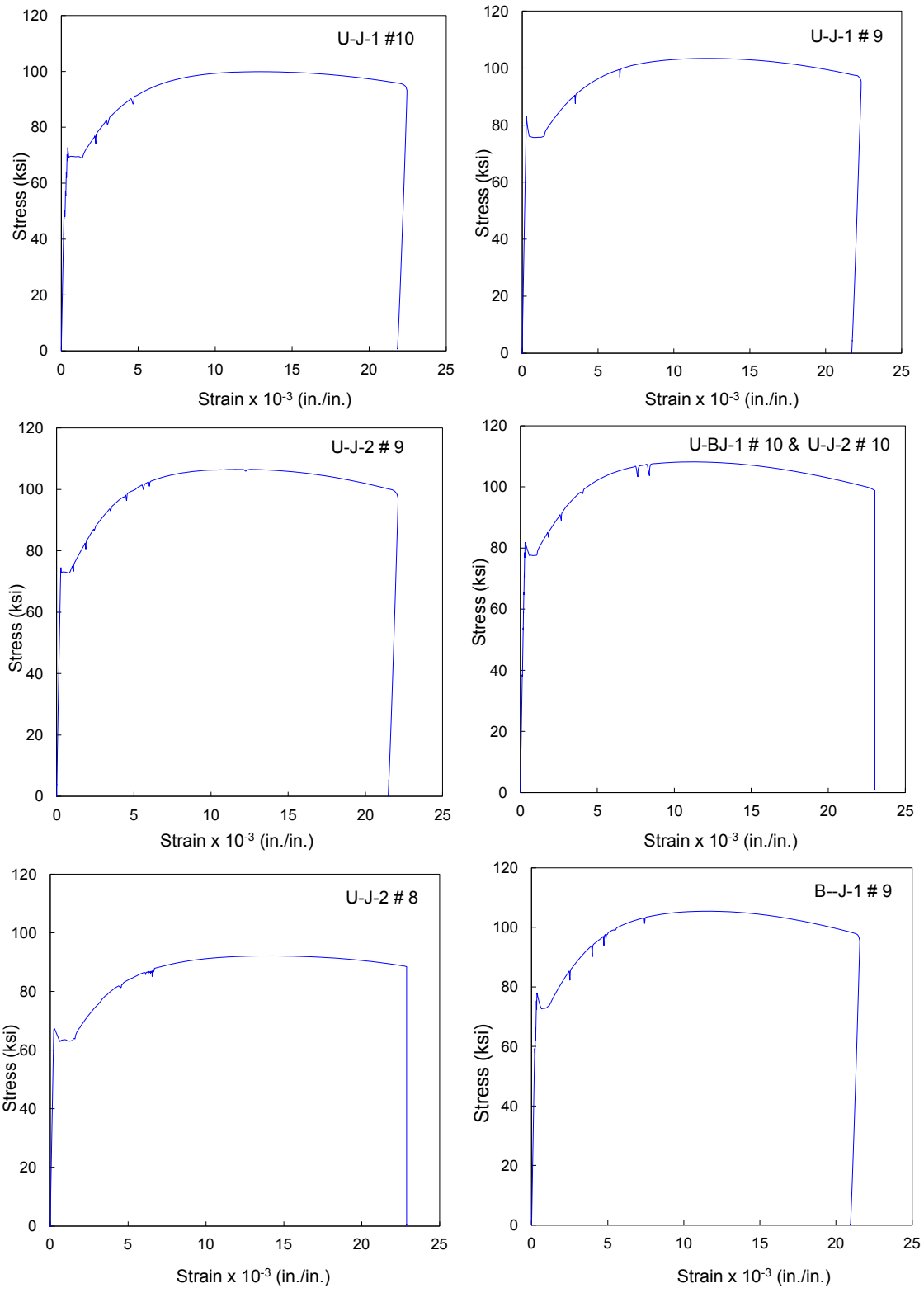

Figure 6.15 Steel coupon tensile test stress-strain relation

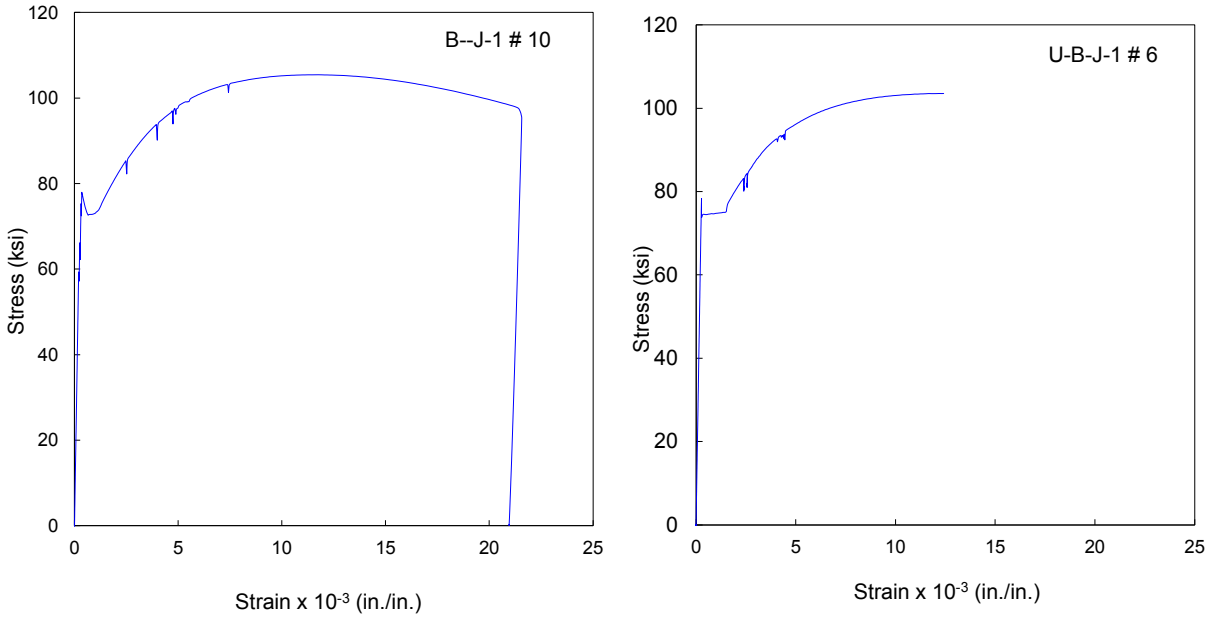

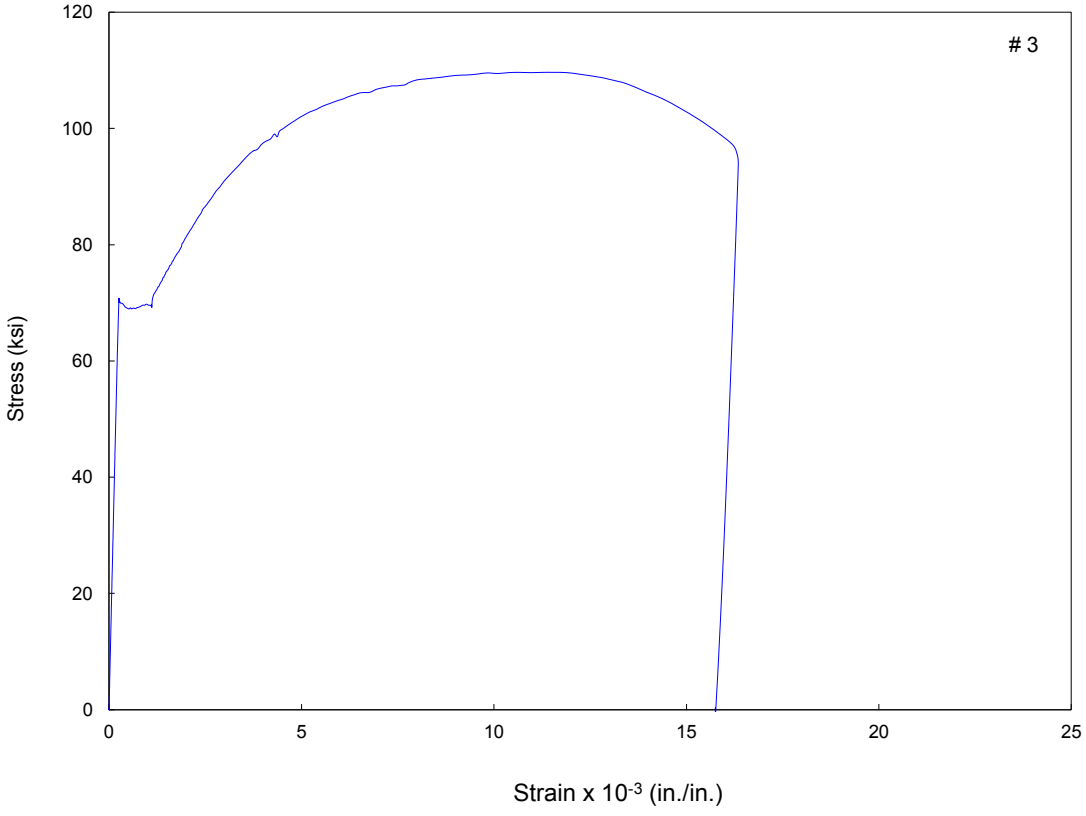

Figure 6.15 ***(Continued)*** Steel coupon tensile test stress-strain relation

6.5.5 Predicted Strength and Deformations of Test Specimens

6.5.5.1 BEAM AND COLUMN FLEXURAL STRENGTH

Based on the prescribed design criteria and target failure mechanism of specimens described above, elastic and inelastic analyses were performed to predict shear strength and deformations of test specimens. Table 6.8 shows the predicted strength parameters of different specimens at the key stages of loading, namely beam yielding, joint shear failure, column yielding, and ultimate beam and column strengths. Overstrength and strain-hardening effects have been taken into account in these results. Figures 6.16 and 6.17 exhibit moment-curvature diagrams of EW beam of test specimens based on inelastic sectional analysis using actual material properties. Unconfined concrete limiting crushing and spalling strains are 0.004 and 0.0055, respectively. Confined concrete limiting strain is 0.02. Mander's [92] confined concrete model was used in section analysis. Slab reinforcement within effective width was added to beam top reinforcement in the analysis. Steel strain hardening started at steel strain level of 0.005.

Figure 6.18 displays the column axial load-moment interaction diagram for the test specimens. The figure also shows the lower column forces at the predicted yield and ultimate strength of EW beam during downward loading direction, which implies axial compression on column. The lower column is considered more critical in the current test loading protocol. Figures 6.19 and 6.20 show the moment-curvature capacity diagrams of the lower column under the planned axial tension load during the upward loading direction. The axial load-moment interaction diagram is inappropriate to assess the column capacity of columns under tensile axial load. The test columns are tension controlled under the axial tension load imposed during the upward loading direction. Figures 6.19 and 6.20 also present the lower column forces due to beam yielding and beam ultimate strength. It is worth mentioning, as can be seen from Fig. 6.18 and Fig. 6.20, that the column flexural capacity about its longitudinal and transverse axes under simultaneous biaxial loading is significantly lower than that under unidirectional loading. However, column reinforcement was chosen to account for this effect such that the column strength exceeds demands during the test.

6.5.5.2 JOINT SHEAR STRENGTH

Using the modified ACI 318-08 strut-and-tie and the proposed empirical shear strength models developed in Chapter 5, along with previous exterior and corner joint test results, the joint shear strength of the test specimens was predicted and used to design the loading protocol. Table 6.5 shows the predicted values of the shear strength coefficient for the test specimens. The effective beam depth dictated by construction constraints, as depicted in Fig. 6.5, was used to calculate joint shear strength.

Table 6.5 Predicated joint shear strength for coefficients γ_j (psi$^{0.5}$) for EW beam downward loading

Specimen ID	At beam yield	At joint peak shear strength	At beam ultimate	Target failure mode
U-J-1	18.6	12.5	21.7	J
U-J-2	14.1	9.75	19.5	J
B-J-1	17.8	9.73	20.9	J
U-BJ-1	5.90	5.90	9.90	BJ

6.5.5.3 YIELD DISPLACEMENT

Many components contribute to beam displacement in beam-column joint subassembly. As described in Chapter 4, beam elastic and inelastic displacements, joint rotation, column elastic and inelastic displacements, and beam bar slip induced displacements are the main constituents of beam displacement. Adopting rigid joint analysis, the final yield displacement of the beam $\Delta_{y,rigid}$ was calculated as the sum of three components. The first component is the beam yield displacement Δ_{by} obtained through conventional beam sectional moment-curvature analysis assuming fully cracked section. The second component is the beam bar slip deflection $\Delta_{b,slip}$ and the third is the beam deflection from column elastic analysis contribution, $\Delta_{b,c}$. The final beam yield displacement can be then expressed as:

$$\Delta_{y,rigid} = \Delta_{by} + \Delta_{b,slip} + \Delta_{b,c} \tag{6.5}$$

$$\Delta_{by} = \frac{\phi_y L_b^2}{3} \tag{6.6}$$

$$\Delta_{b,slip} = L_b \theta_{slip} = L_b \frac{\phi_b f_y^2}{96\sqrt{f_c'} E_s d_b (1-k)} \tag{6.7}$$

$$\Delta_{b,c} = \frac{M_{by} H (L_b + 0.5 h_c)}{12 E_c I_c} \tag{6.8}$$

where ϕ_y is the yield curvature, M_{by} is beam yield moment, H is the height of column between centerlines of supports, L_b is the beam length from face of column to center of E_c is the elastic concrete modulus of elasticity, I_c is the gross inertia of column section, E_s is the elastic steel modulus of elasticity, θ_{slip} is the beam rotation due to bar slip, ϕ_b is the beam bar diameter, d_b is the effective beam depth, and k is defined by Eq. 5.15. Equation 6.7 implicitly implies a concrete bond capacity of $12\sqrt{f_c'}$. As discussed in previous chapters, the actual yield displacement is expected to exceed this calculated displacement because of addition contributions from the beam-column joint.

The contribution of the joint to test specimen displacements can be estimated based on past tests and recommendations (Park [120]). Table 6.6 depicts the assumed joint shear strains in flexible joint analysis. Joint shear strains at joint peak shear stress in the downward loading direction, implying high compression load, are assumed slightly lower than those in the upward loading direction under axial tension load. The joint shear strains of the case of the nonconforming joints with axial load ratio less than 0.10 according to ASCE 41 were used to speculate the joint shear strains under axial tension loading. ASCE 41 does not provide plastic shear strain recommendations for joints under high axial load ratio (> 0.40). Thus, previous experimental joint shear strains under lower axial loads [120] were used for the downward loading direction. The ASCE 41 recommendations for collapse prevention joint rotation were interpreted to simulate the beam ultimate capacity.

In addition, and based on Leon and Jirsa [84] and Engindeniz [41], simultaneous bidirectional loading might cause additional flexibility of the test specimens, hence, the joint shear strain are slightly increased for specimen B-J-1. The joint shear strain at peak joint shear strength for J-Failure joints was estimated based on linear interpolation between joint shear stress coefficient at joint peak strength and at beam yielding capacity.

Table 6.6 Speculated joint shear strains γ_s (rad.) for test specimens

	Loading direction	At joint peak	At beam yield	At beam ultimate
U-J-1	Downward	0.0025	0.004	0.007
	Upward	0.0035	0.005	0.01
U-J-2	Downward	0.003	0.005	0.0075
	Upward	0.004	0.005	0.01
B-J-1	Downward	0.0035	0.006	0.008
	Upward	0.005	0.007	0.01
U-BJ-1	Downward	0.0025	0.0025	0.005
	Upward	0.005	0.005	0.01

Based on the above discussion, the beam tip yield displacement including joint shear deformation contribution $\Delta_{b,j}$ is:

$$\Delta_{y,flex} = \Delta_{by} + \Delta_{b,slip} + \Delta_{b,c} + \Delta_{b,j} \tag{6.9}$$

$$\Delta_{b,j} = \gamma_s (L_b + 0.5h_c) \tag{6.10}$$

The beam tip displacement at ultimate can be expressed as:

$$\Delta_{u,flex} = \Delta_{bu} + \Delta_{b,c} + \Delta_{b,j} \tag{6.11}$$

$$\Delta_{bu} = \frac{\phi_y L_b^2}{3} + (\phi_u - \phi_y) l_p \left(L_b - \frac{l_p}{2} \right) \tag{6.12}$$

$$\Delta_{b,c} = \frac{M_{bu} H (L_b + 0.5 h_c)}{12 E_c I_c} \tag{6.13}$$

where ϕ_u is the ultimate beam curvature, M_{bu} is the beam ultimate moment, Δ_{bu} is the beam tip deformation due to beam action, and l_p is the plastic hinge length assumed as $0.5h_b$. It is worth mentioning that beam tip displacement due to beam bar slip is implicitly included in Eq. 6.12.

The beam tip displacement at joint shear capacity based on flexible joint analysis can be expressed as:

$$\Delta_{bj,flex} = \Delta_{b,js} + \Delta_{b,c} + \Delta_{b,j} \tag{6.14}$$

$$\Delta_{b,js} = \Delta_{by} \frac{M_{b,js}}{M_{by}} \qquad \text{for J-Failure joints} \tag{6.15}$$

$$\Delta_{b,js} = \Delta_{by} \qquad \text{for BJ-Failure joints} \tag{6.16}$$

$$\Delta_{b,c} = \frac{M_{b,js} H (L_b + 0.5 h_c)}{12 E_c I_c} \tag{6.17}$$

Where $M_{b,js}$ is the beam moment corresponding to joint shear capacity and $\Delta_{b,js}$ is the beam tip displacement at joint shear capacity due to beam elastic curvature, obtained by linear interpolation from beam yielding capacity. Based on the above analysis, Table 6.7 shows the predicted beam tip displacement based on rigid and flexible joint analyses at three different stages of loading, namely at beam yielding Δ_y , at joint shear capacity Δ_{bj}, and at beam ultimate capacity Δ_u.

Based on the theoretical prediction of beam shear forces according to beam sectional analysis and strut-and-tie and empirical joint shear strength models, along with displacement prediction performed above, theoretical force-deformation relations are depicted in Fig. 6.21 and Fig. 6.22. The theoretical curves of J-Failure mode joints, U-J-1, U-J-2 and B-J-1 are only graphical representation of predicted quantities, since the actual strength of test specimens is expected to degrade immediately after reaching joint shear strength. Predicting the softening curve of such specimens under the proposed substantial axial is uncertain due to the scarcity of previous tests with equivalently high axial load level. However, post-peak nonlinear analysis using scissors rotational spring model will be presented in Chapter 9.

Table 6.7 Predicted beam tip displacements, in inches, for EW beam of test specimens

Specimen ID	Loading direction	Rigid Joint Analysis			Flexible Joint Analysis		
		$\Delta_{y,rigid}$	$\Delta_{bj,rigid}$	$\Delta_{u,rigid}$	$\Delta_{y,flex}$	$\Delta_{bj,flex}$	$\Delta_{u,flex}$
U-J-1	Downward	-1.34	-0.93	-4.92	-1.76	-1.19	-5.65
	Upward	1.06	0.90	8.40	1.59	1.27	-8.49
U-J-2	Downward	-0.88	-0.64	-7.70	-1.41	-0.96	-5.76
	Upward	0.66	0.48	6.91	1.19	0.90	-8.99
B-J-1	Downward	-1.34	-0.74	-4.92	-1.97	-1.11	9.45
	Upward	1.18	0.81	8.48	1.91	1.33	7.96
U-BJ-1	Downward	-0.86	-0.86	-8.47	-1.13	-1.13	9.53
	Upward	0.81	0.81	7.91	1.33	1.33	8.96

Table 6.8.a Predicted strength of test specimens for EW-beam downward loading direction

	At Beam Yielding				At Joint Shear Strength				At Beam Ultimate Capacity			
Specimen	U-J-1	U-J-2	B-J-1	U-BJ-1	U-J-1	U-J-2	B-J-1	U-BJ-1	U-J-1	U-J-2	B-J-1	U-BJ-1
f'_c (ksi)	4.30	4.40	4.10	4.40	4.30	4.40	4.10	4.40	4.30	4.40	4.10	4.40
Failure Mode	J	J	J	BJ	J	J	J	BJ	J	J	J	BJ
V_b (kips)	53.0	82.0	52.0	21.0	37.0	59.0	29.0	21.0	62.0	113	61.0	30.0
V_c (kips)	38.0	59.0	38.0	15.0	27.0	43.0	21.0	15.0	45.0	82.0	44.0	22.0
M_b (kip.in)	5088	7829	5038	2018	3518	5709	2775	2018	5930	10820	5897	2896
T_b+T_s (kips)	360	303	350	136	249	221	193	136	420	419	410	195
f_s (ksi)	67.0	69.0	65.0	61.0	47.0	50.0	36.0	61.0	78.0	95.0	77.0	88.0
V_j (kips)	322	244	312	120	223	178	172	120	375	338	366	173
τ_{jh} (psi)	1052	798	1021	394	727	582	563	394	1226	1103	1195	565
γ_j (psi)	16.0	12.0	15.4	5.90	11.1	8.70	8.50	5.90	19.0	17.0	18.0	9.00
P_b (kips)	405	620	620	640	405	620	620	640	405	620	620	640
R_b (kips)	458	702	672	661	442	679	678	661	467	733	743	670
M_{cu} (kip.in)	2436	3395	2412	1032	1685	2476	1329	966	2840	4692	2824	1387
M_{cl} (kip.in)	2436	3395	2412	1032	1685	2476	1329	966	2840	4692	2824	1387
M_n/M_{cu}	2.45	1.90	1.36	6.23	3.55	2.60	2.47	6.66	2.10	1.37	1.16	4.64
M_n/M_{cl}	2.45	1.90	1.36	6.23	3.55	2.60	2.47	6.66	2.10	1.37	1.16	4.64
P_n/P_{bi}	4.04	2.15	2.01	3.23	4.60	2.77	2.78	3.23	4.60	2.77	2.78	3.23
R_n/R_{bi}	3.57	1.90	1.85	3.13	4.21	2.52	2.54	3.13	3.99	2.34	2.32	3.09
$\Sigma M_{cn}/\Sigma M_{bn}$	2.35	1.64	1.31	6.38	3.40	2.25	2.37	6.38	2.02	1.19	1.12	4.44

Table 6.8.b Predicted strength of test specimens for EW-beam upward loading direction

	At Beam Yielding				At Joint Shear Strength				At Beam Ultimate Capacity			
Specimen	U-J-1	U-J-2	B-J-1	U-BJ-1	U-J-1	U-J-2	B-J-1	U-BJ-1	U-J-1	U-J-2	B-J-1	U-BJ-1
Gravity Axial load	300	300	300	300	300	300	300	300	300	300	300	300
Failure Mode	J	J	J	BJ	J	J	J	BJ	J	J	J	BJ
V_b (kips)	41.0	60.0	41.0	19.0	35.0	44.0	28.0	19.0	55.0	83.0	55.0	25.0
V_c (kips)	30.0	44.0	29.0	14.0	25.0	32.0	20.0	14.0	40.0	60.0	40.0	18.0
M_b (kip.ft)	3945	5771	3893	1801	3334	4192	2665	1801	5276	7958	5275	2445
T_b+T_s (kips)	251	209	255	113	213	152	175	113	336	288	346	153
f_s (ksi)	63.0	66.0	64.0	64.0	53.0	48.0	44.0	64.0	85.0	92.0	87.0	86.0
V_{jh} (kips)	222	165	226	99.0	187	120	155	99.0	297	228	306	134
v_{jh} (psi)	725	540	738	323	612	392	505	323	969	745	1000	439
γ_j (psi)	11.1	8.10	11.1	4.90	9.30	5.90	7.60	4.90	15.0	11.0	15.0	7.00
P_{bi} (kips)	160	50.0	50.0	50.0	160	50.0	50.0	50.0	160	50.0	50.0	50.0
R_{bi} (kips)	201	110	91.0	69.0	195	94.0	78.0	69.0	215	133	105	75.0
M_{cu} (kip.in)	1889	2503	1864	862	1597	1818	1276	862	2527	3451	2526	1171
M_{cl} (kip.in)	1889	2503	1864	862	1597	1818	1276	862	2527	3451	2526	1171
M_n/M_{cu}	2.06	1.43	1.17	4.07	2.44	1.97	1.71	4.07	1.54	1.04	0.86	3.00
M_n/M_{cl}	2.06	1.43	1.17	4.07	2.44	1.97	1.71	4.07	1.54	1.04	0.86	3.00
$\Sigma M_{cn}/\Sigma M_{bn}$	1.97	1.24	1.12	3.90	2.34	1.70	1.64	3.90	1.48	0.90	0.83	2.87

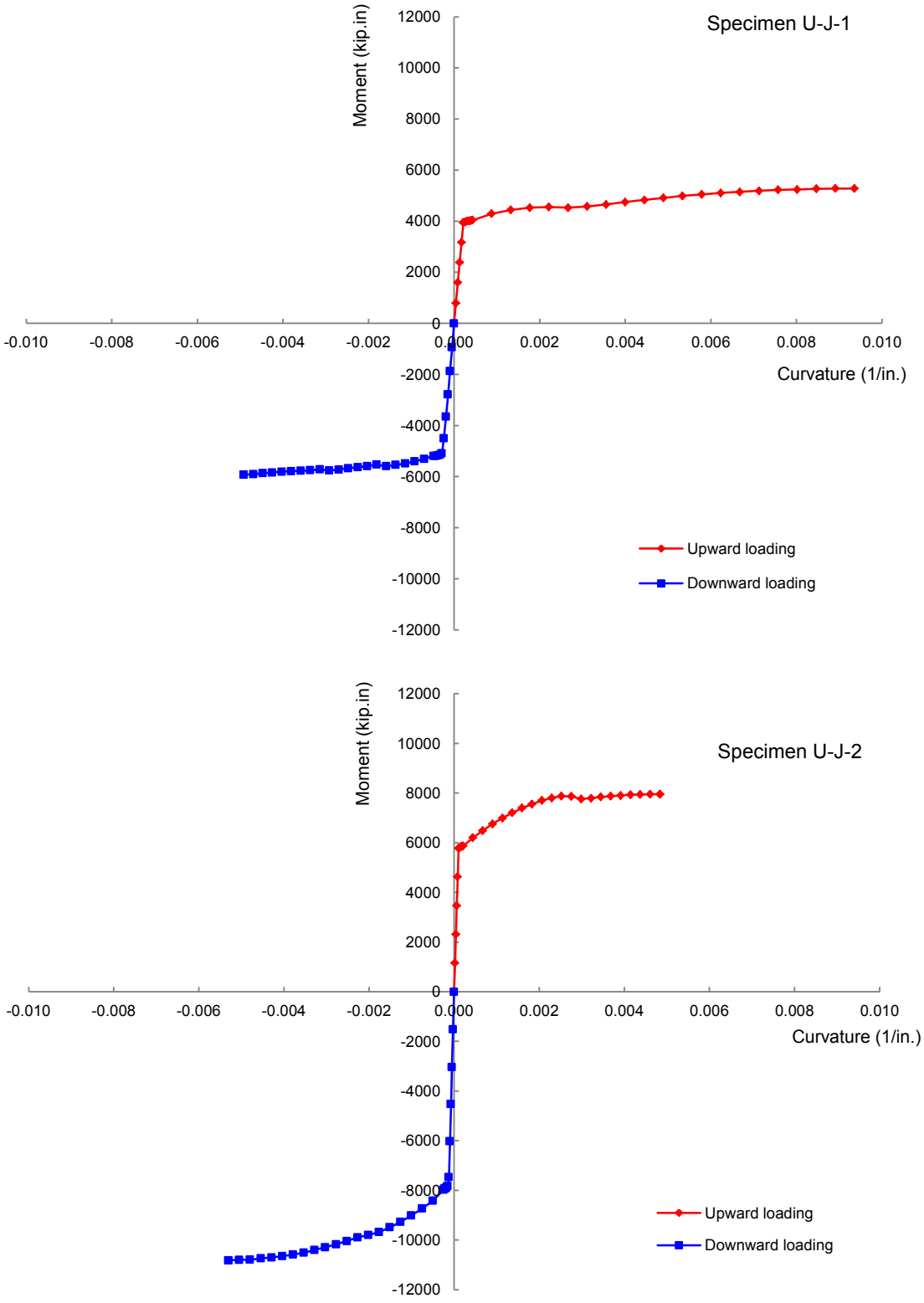

Figure 6.16 EW beam moment-curvature relation prediction for specimens U-J-1 and U-J-2

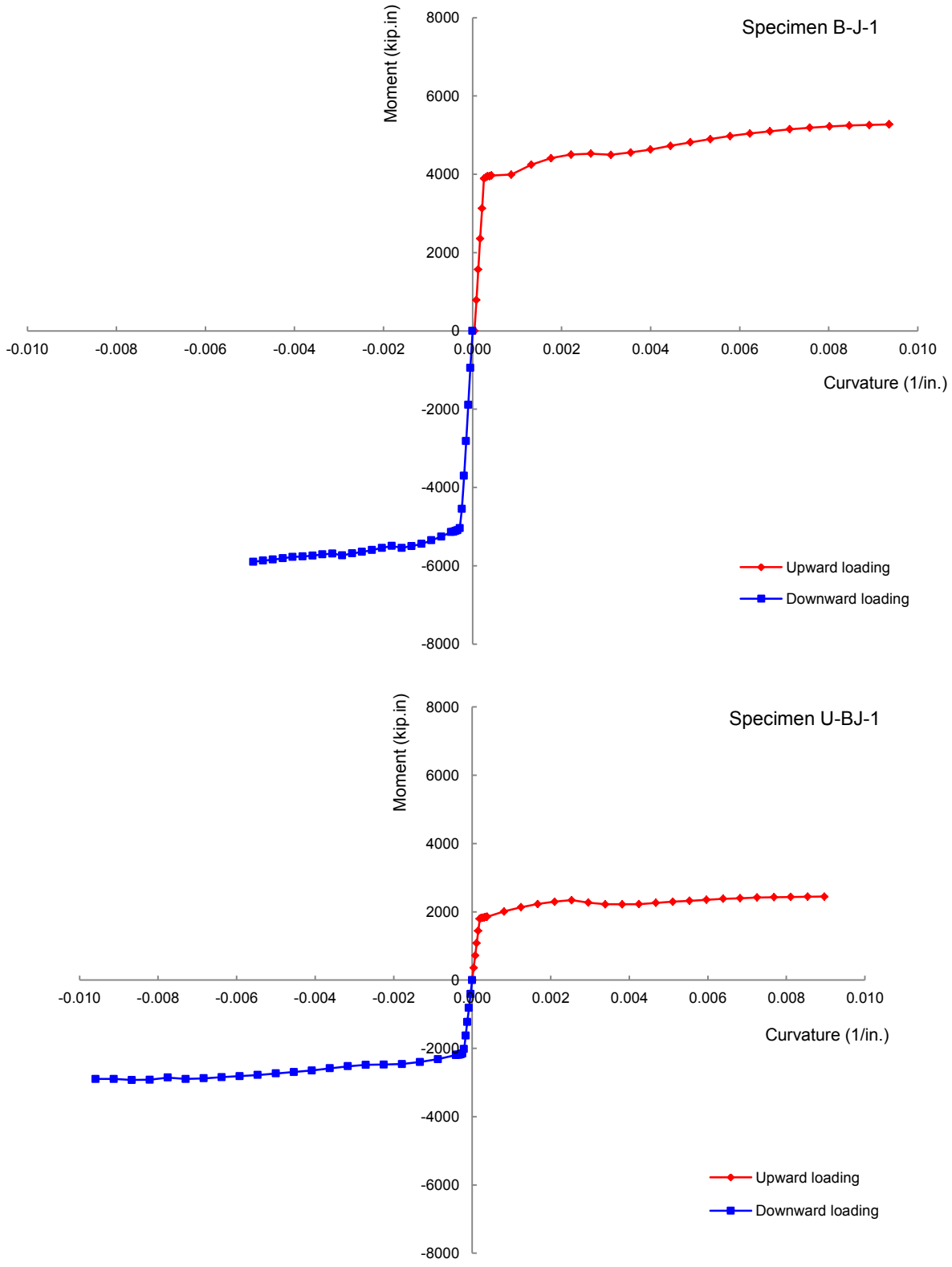

Figure 6.17 EW beam moment-curvature relation prediction for specimens B-J-1 and U-BJ-1

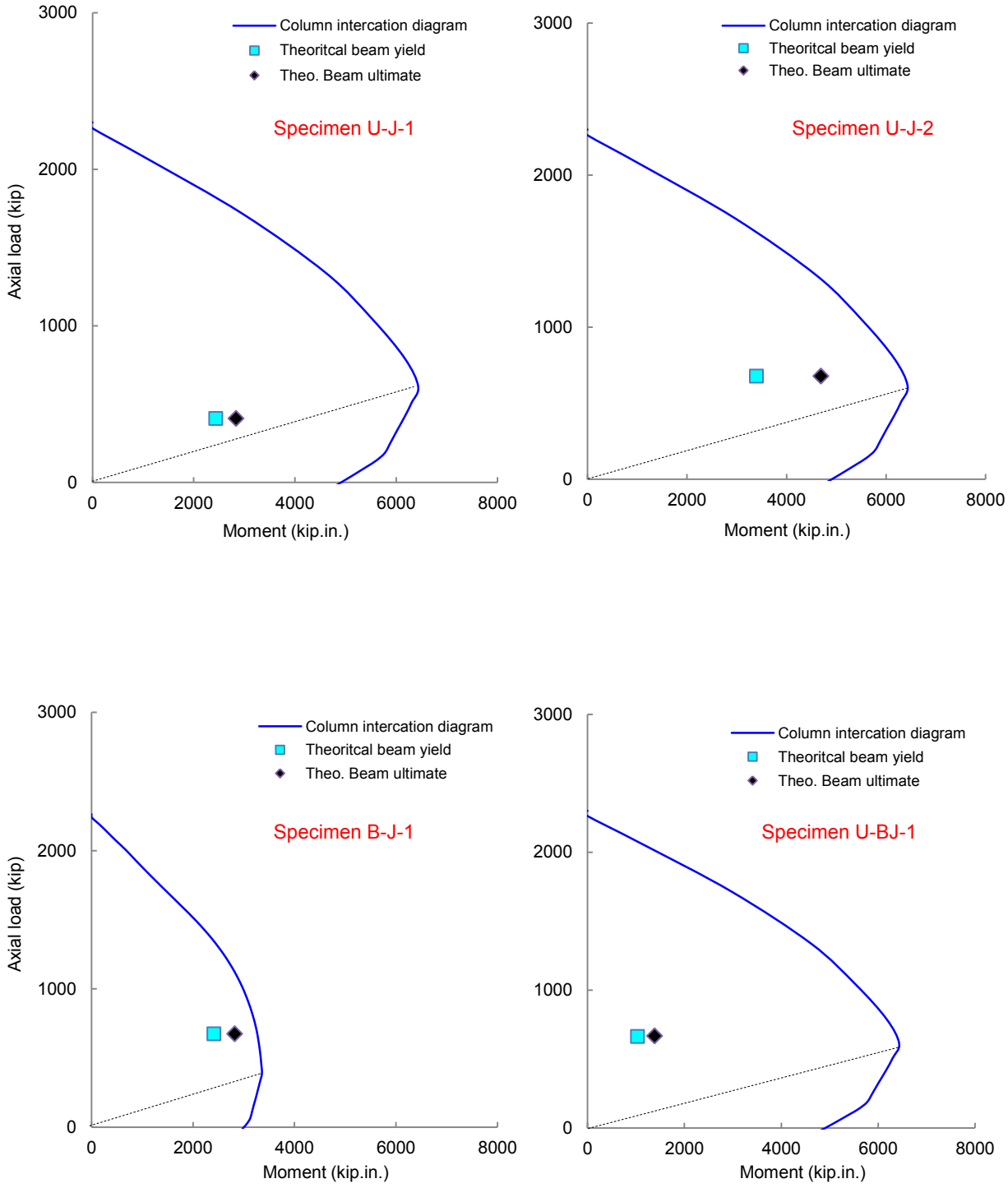

Figure 6.18 Column interaction diagram and predicted column compression forces at EW beam flexural strength for *downward* loading direction of test specimens

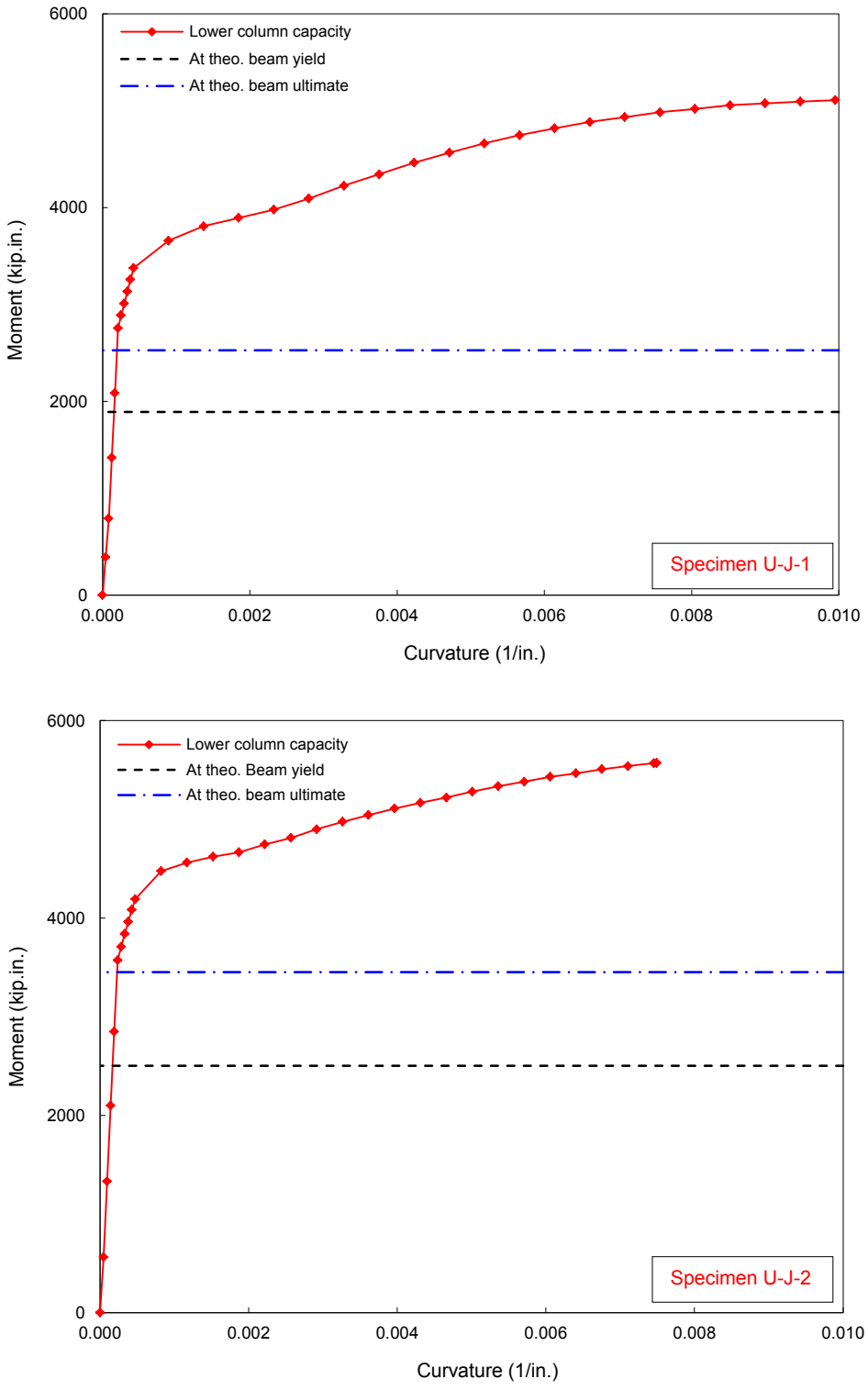

Figure 6.19 Column moment-curvature relation for loading in tension direction and predicted column forces at EW beam flexural strength for *upward* loading direction of test specimens, specimen U-J-1 and U-J-2

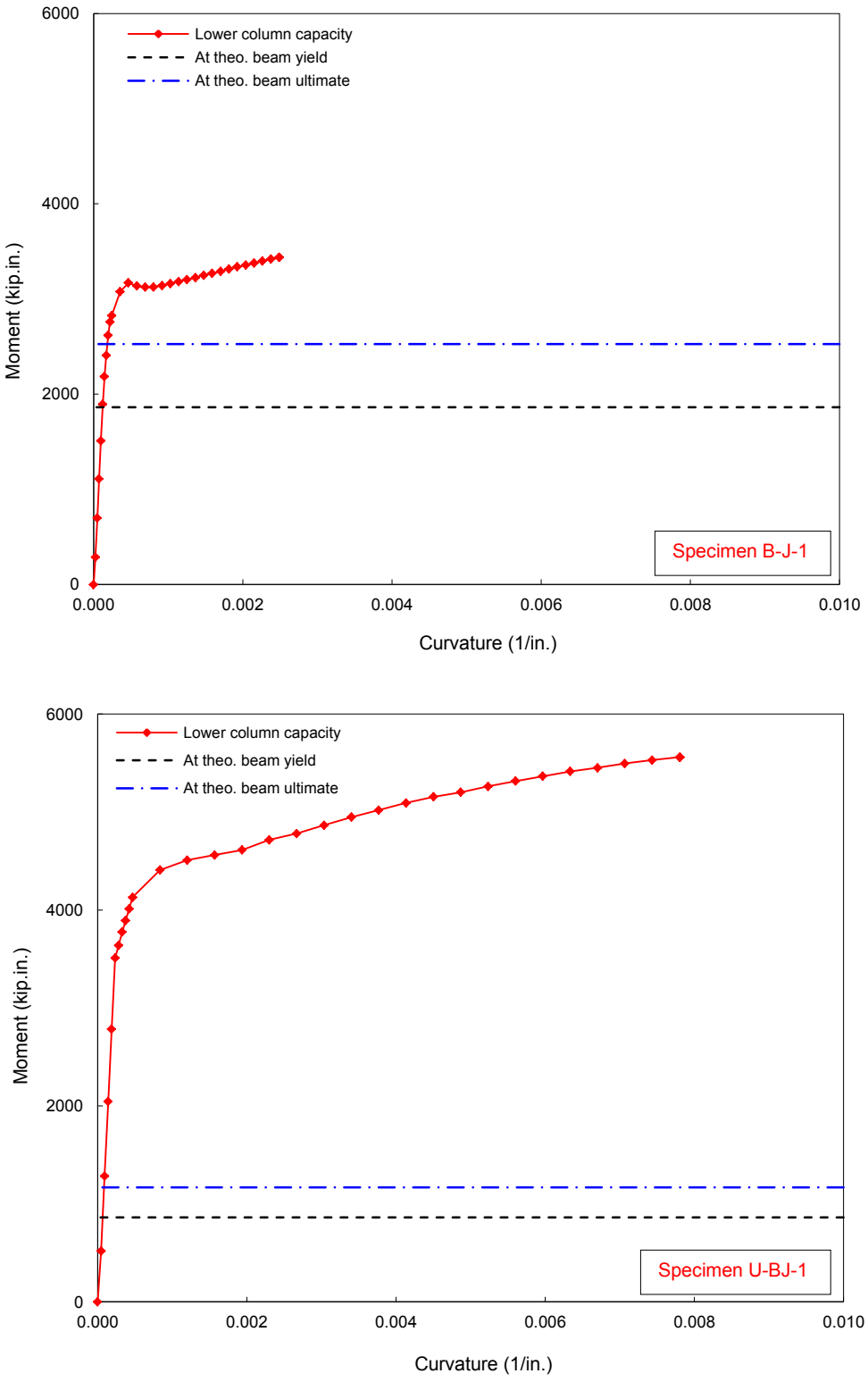

Figure 6.20 Column moment-curvature relation for loading in tension direction and predicted column forces at EW beam flexural strength for *upward* loading direction of test specimens, specimen B-J-1 and U-BJ-1

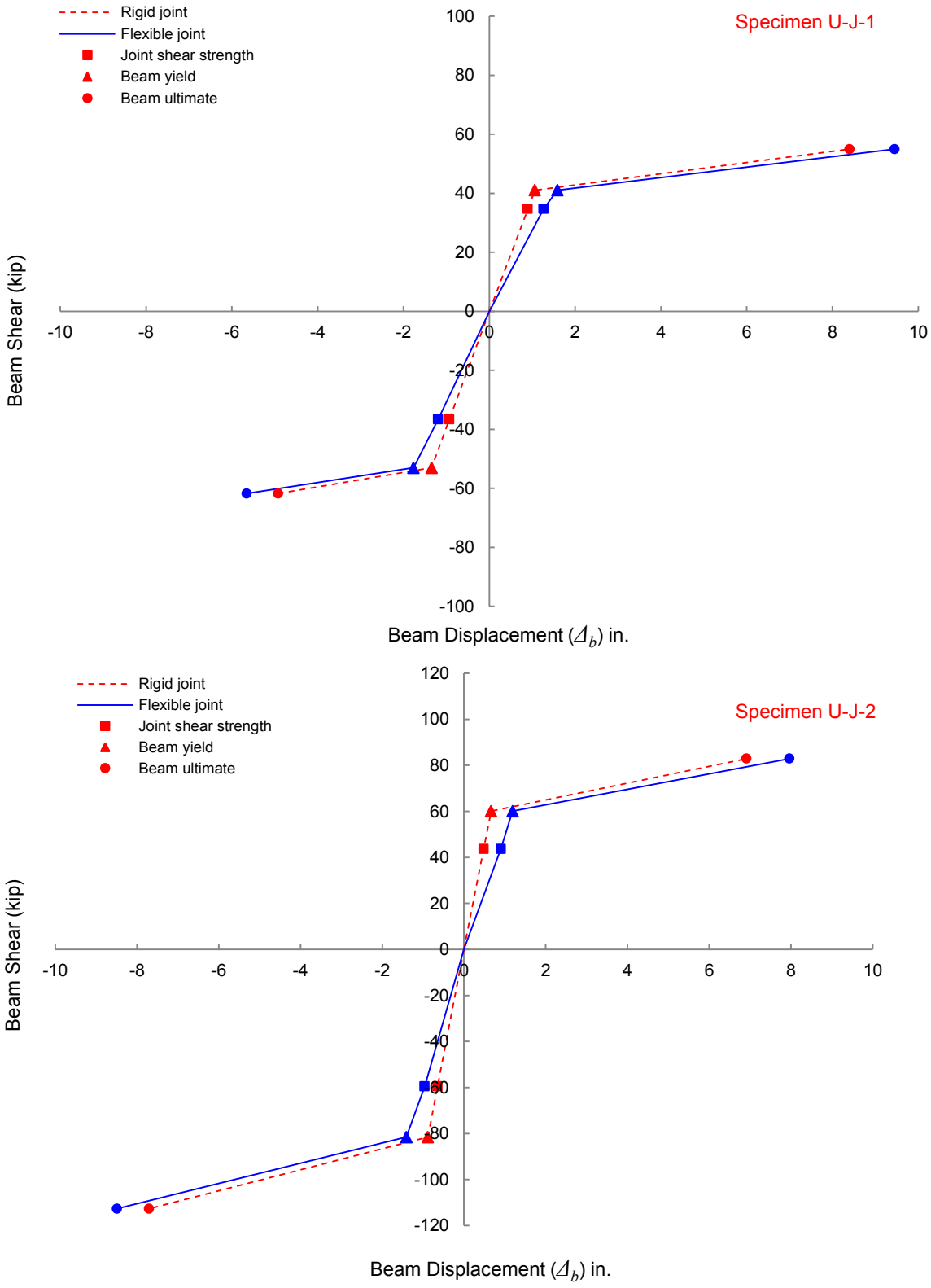

Figure 6.21 Force-displacement prediction for specimens U-J-1 and U-J-2

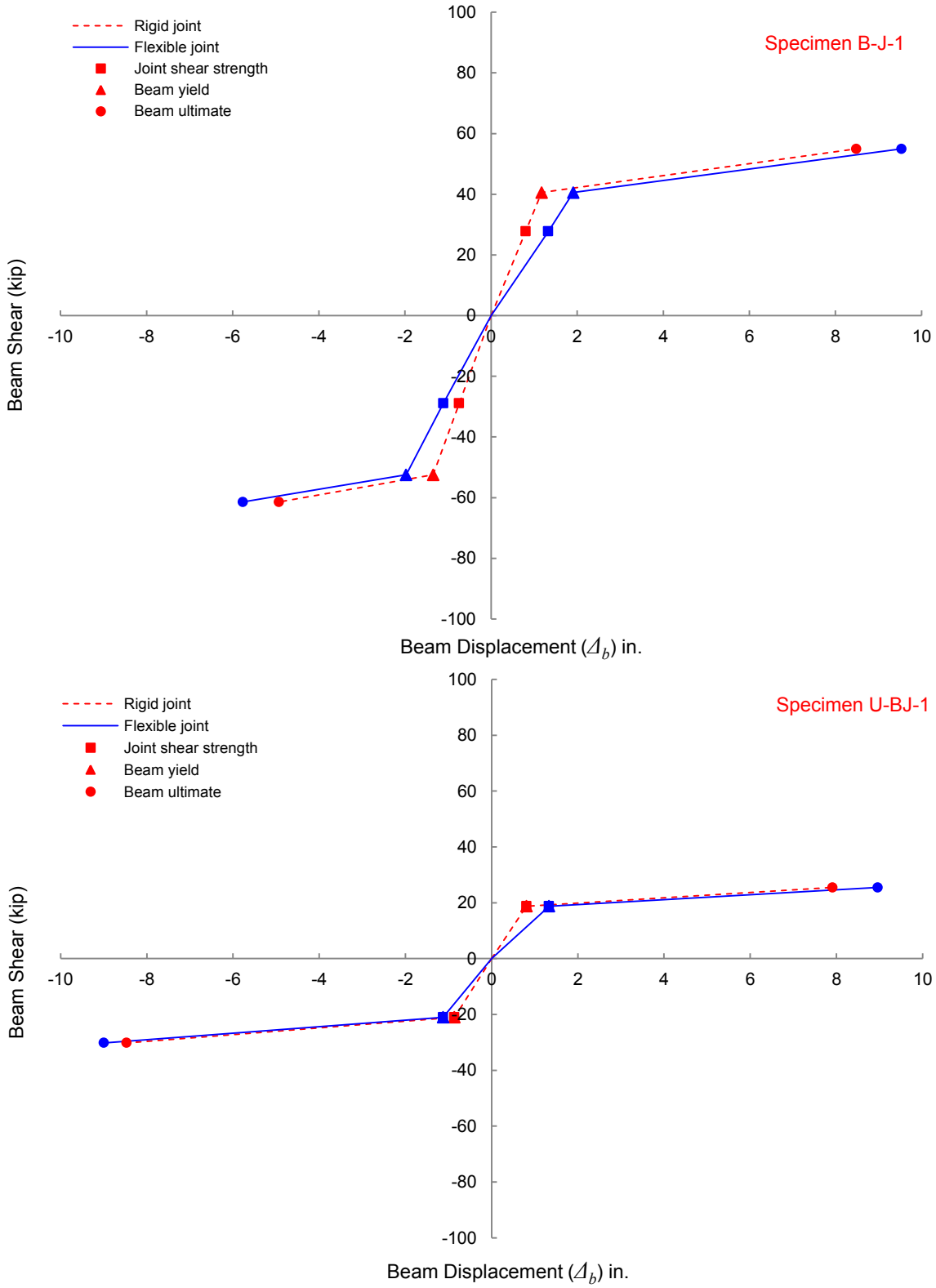

Figure 6.22 Force-displacement prediction for specimens B-J-1 and U-BJ-1

6.6 INSTRUMENTATION

6.6.1 Overview

The test specimens were instrumented to measure the global response, local deformations, and strains using a total of 200 data channels per test. The instrumentation scheme comprises internal devices, namely electrical strain gages to measure steel strains, external devices (Linear Displacement Potentiometers, LP) to measure the relative deformations of different points on the concrete surface, which can loosely refer to concrete strains, and finally external devices (LP) to measure global deformations of test specimens. Test setup was also instrumented to measure local strains at lateral restraint system and to measure global deformation of the different elements of the setup. Figure 6.25 exhibits a global view of the instrumentation attached to the specimen as it is installed to the test setup.

6.6.2 Internal Instrumentation: Steel Strains Gauges

Reinforcement bars were instrumented using 120Ω resistance electrical strain gauges at the locations indicated in Fig. 6.23. Each test specimen was instrumented using approximately 60 strain gages. Column bars were gauged at three locations; the column joint interface sections at the top of lower column and bottom of upper column where the most critical flexural sections are and at mid-joint height where the most critical buckling section is. Only edge bars in the beams were instrumented. The beam bar gauge locations were chosen to achieve a measure of the strain profile over the regions of interest, namely the joint region and the potential plastic hinge region of the beam. The joint region of the longitudinal beam bar included three gauges; the first is at the mid joint region to judge the yield penetration inside the joint, the second is at the end of the outermost straight segment of the bar immediately before the curved portion of the hook, and the third is at the hooked portion of the bar. Both EW and NS beams are gauged identically.

The slab reinforcement was gauged at the location of the expected most critical tensile strain to determine the slab contribution to shear stress demand of the joint by evaluating the number of bars engaged as tension reinforcement to be added to beam tension negative reinforcement. As indicated in Fig. 6.23, top layer of slab bars had four gauges installed on bars S1 through S4 in each direction, while bottom reinforcement layer was gauged only over the three bars S1 through S3.

Transverse reinforcement of the beams was lightly gauged (two gauges at the second stirrup from beam-joint interface) to monitor shear and torsion strains of the beams. The first two hoops of the column transverse reinforcement were instrumented to obtain the tendency of joint compression strut to utilize column transverse reinforcement because of the absence of joint hoops. The bi-directionally loaded specimen B-J-1 had additional column hoop gauges at the corners, as indicated in Fig. 6.23, to assess the tendency of a three dimensional joint compression strut to affect the column hoop strains. Special care was given to the process of strain gauge installation to ensure full protection of these vulnerable electric devices. The reinforcement bar was ground smooth over a 1.5 in. length. Next, the smooth bar surface was chemically treated and cleaned using alkali based solution and Alcohol. The prepared surface then was pre-warmed

using a lamp bulb to overcome the low laboratory temperature and reflect the ambient temperature strain measurements during actual test. The strain gauges were then mounted using clear film of special adhesive agent. After installing the gauges, several protective coating layers were applied to them. That included a polyurethane wax layer to keep moisture out, an adhesive flexible tape layer to articulate the gauge, a two component compound resin layer to ensure sufficient stiffness and protection after hardening, and finally a silicon caulk layer to absorb vibration, impact and friction during steel cage installation and concrete casting.

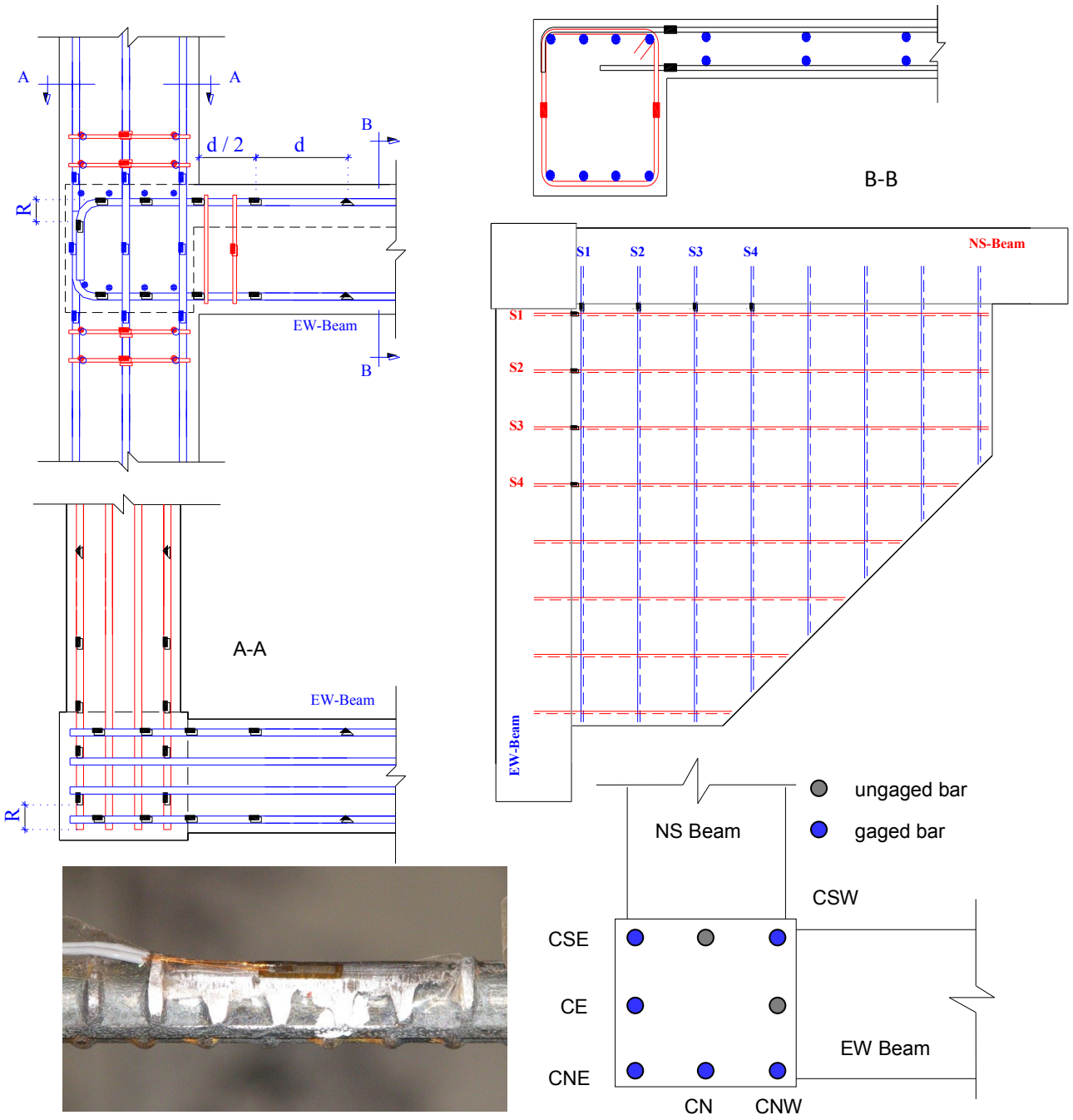

Figure 6.23 Strain gauge instrumentation

6.6.3 External Instrumentation

Linear Displacement Potentiometers (LP) were used to measure both global deformations and relative displacement between different points on the concrete surface of the specimen. The LP instrumentation scheme is depicted in Fig.6.24 and Fig. 6.25. The LPs were installed on ½ in. diameter stiff steel rods that were embedded in the subassembly before concrete casting. The steel rods penetrated the entire depth (or width) of the element they are embedded in. The distances between the steel rods were chosen prior to construction according to the layout in Fig. 6.24. However, before installing the LPs, the as-built distances were recorded to be used to estimate accurate curvature and strain calculations. The LPs were calibrated before conducting the tests to ensure accuracy of the measurements. The choice of pulley-type LPs enhanced the flexibility of installing large number of instruments is a relatively small region by adjusting the angle of rotation of the instrument around the pulley.

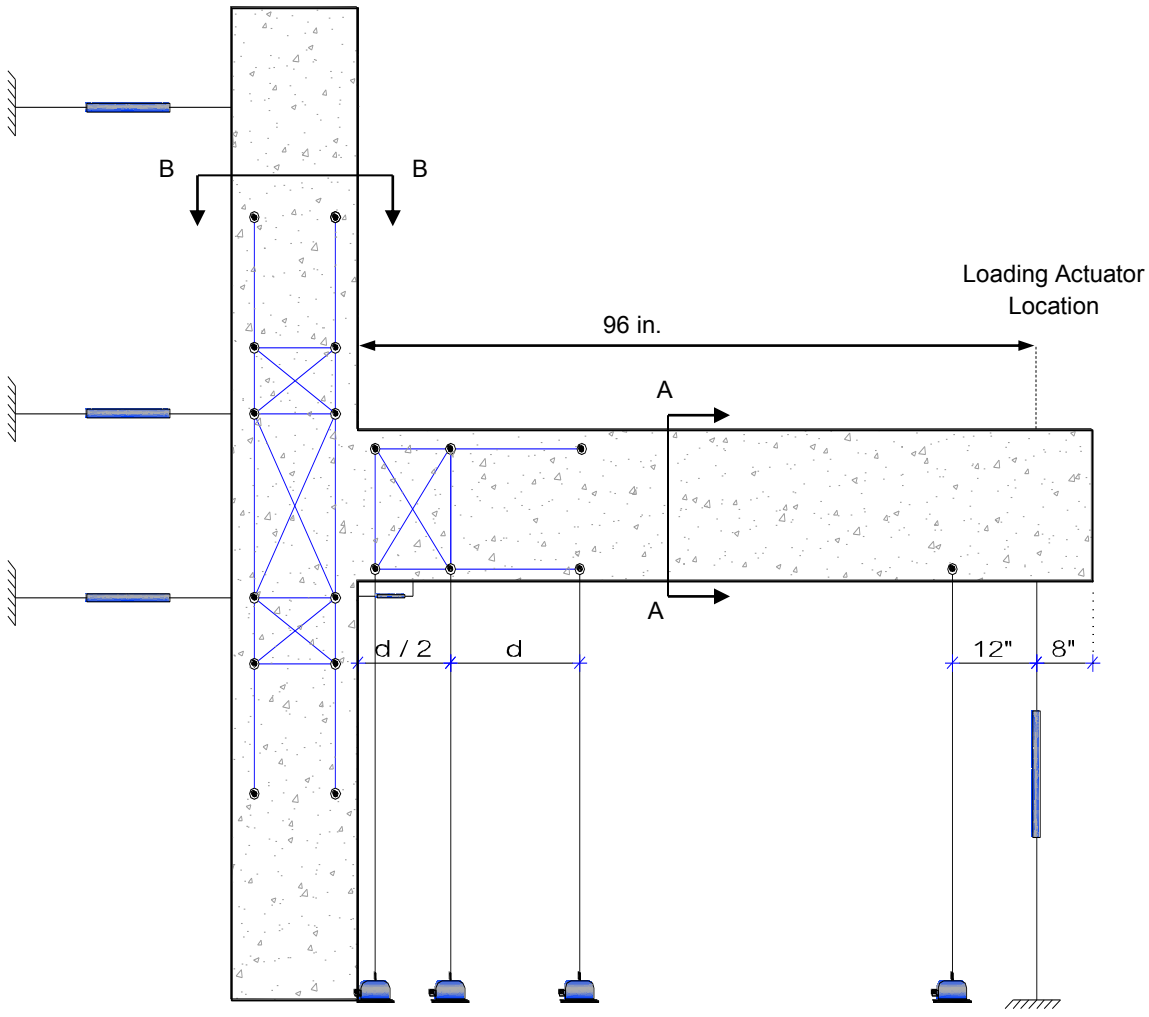

Figure 6.24 External instrumentation

The response quantities of interest were: joint shear strains, joint axial and transverse strains, column axial and shear deformations, beam longitudinal deformations, beam shear deformations, relative beam-column rotation, column and beam curvatures, joint lateral deformation in space, column and beam global deflections, column and beam torsional deformations, lateral restraint system strains, vertical translation, and longitudinal and transverse displacements of axial loading girder and lateral restraint system. The details are presented next.

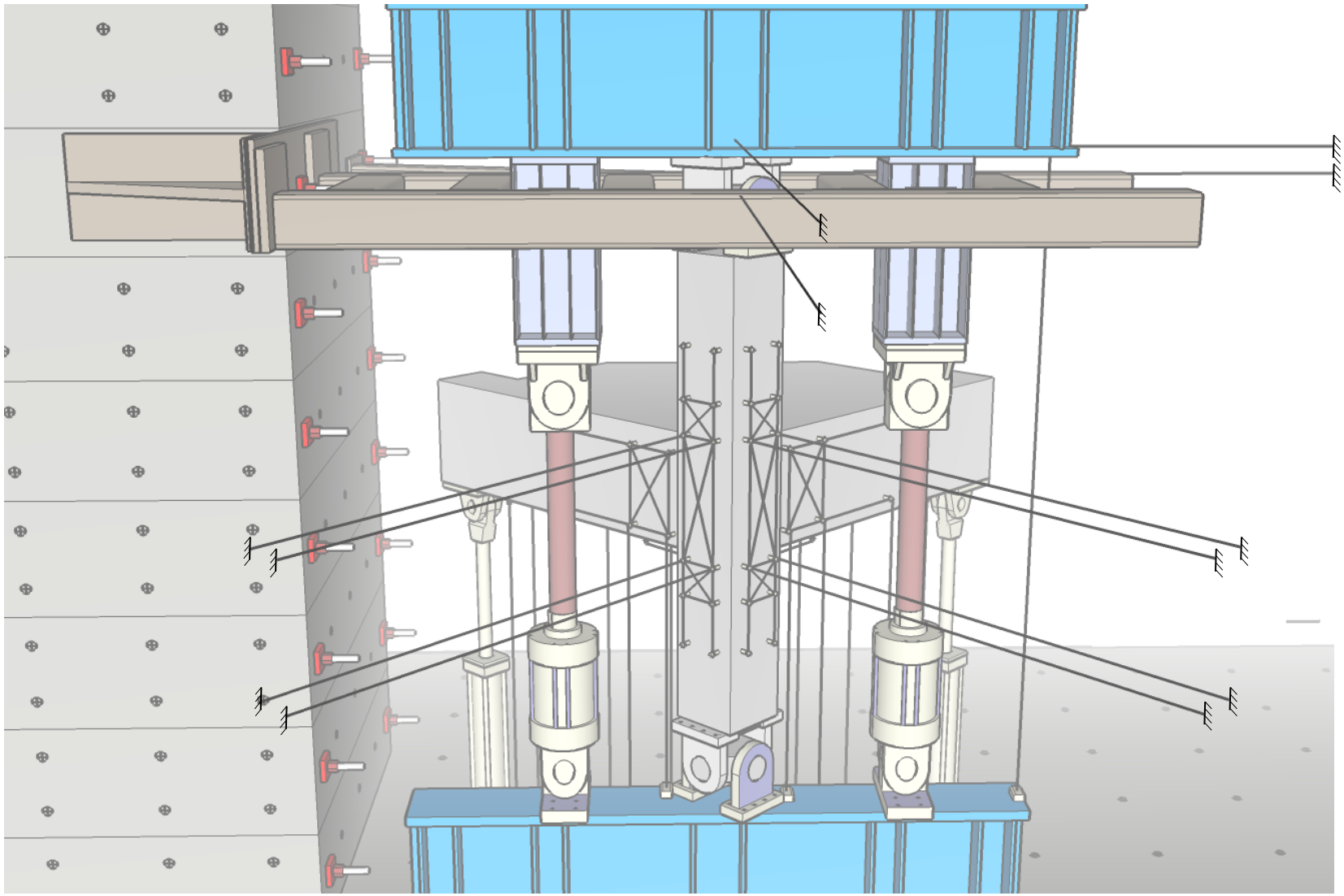

Figure 6.25 3D view of external instrumentation scheme

6.6.3.1 JOINT SHEAR STRAIN

Joint shear strains were monitored using six linear potentiometers (LP) for each external face of the joint (north face and east face) as depicted in Fig.5.1 using a plane-strain transformation of Equation 5.1. This procedure has been adopted from previous researchers such as Engindeniz [41], among others.

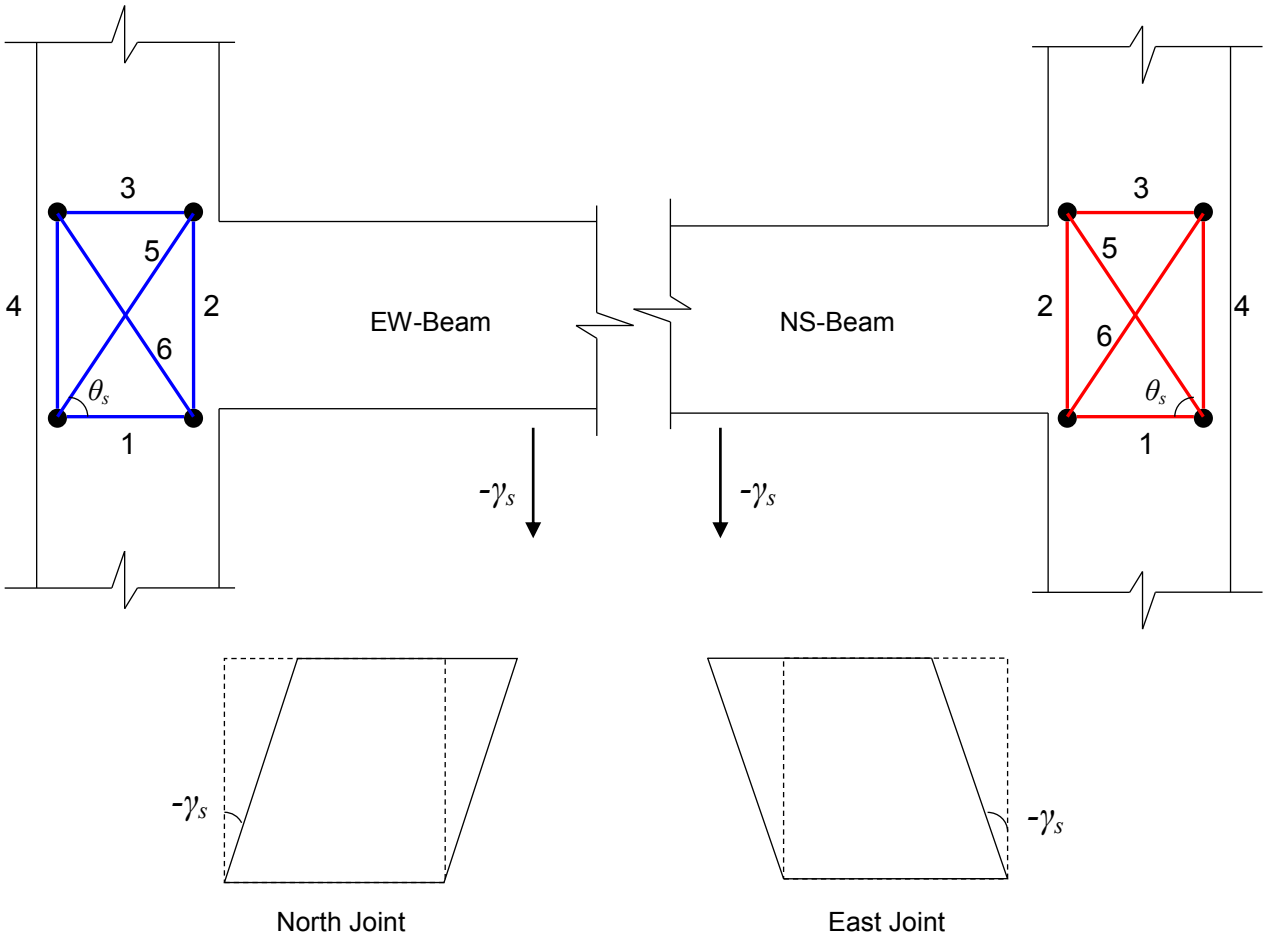

Figure 6.26 Shear strain measurement

$$\gamma_{s,i} = \frac{\varepsilon_{\theta.s} - \varepsilon_x \cos^2\theta_s - \varepsilon_z \sin^2\theta_s}{\sin\theta_s \cos\theta_s} \tag{6.18}$$

where, $\gamma_{s,i}$ is the joint shear strain obtained using a certain set of strain measurement, ε_x and ε_z are translational strains in the horizontal and vertical directions, respectively. $\varepsilon_{\theta s}$ is the strain in the diagonal direction with an angle of θ_s measured from the horizontal axis as indicated in Fig. 6.26

Sign convention for shear strain is consistent with beam displacement sign convention, i.e., negative joint shear strain corresponds to downward beam displacement. This is shown in Fig. 6.26.

For each joint face, the north and east faces, four estimates of the joint shear strain were obtained by forming triangular strain rosettes in the joint panel and by using plane strain transformation, as follows:

$$\gamma_{s,1} = \frac{\varepsilon_6 - \varepsilon_1 \cos^2 \theta_s - \varepsilon_4 \sin^2 \theta_s}{-\sin \theta_s \cos \theta_s} \tag{6.19}$$

$$\gamma_{s,2} = \frac{\varepsilon_5 - \varepsilon_1 \cos^2 \theta_s - \varepsilon_2 \sin^2 \theta_s}{\sin \theta_s \cos \theta_s} \tag{6.20}$$

$$\gamma_{s,3} = \frac{\varepsilon_5 - \varepsilon_3 \cos^2 \theta_s - \varepsilon_4 \sin^2 \theta_s}{\sin \theta_s \cos \theta_s} \tag{6.21}$$

$$\gamma_{s,4} = \frac{\varepsilon_6 - \varepsilon_3 \cos^2 \theta_s - \varepsilon_2 \sin^2 \theta_s}{-\sin \theta_s \cos \theta_s} \tag{6.22}$$

$$\varepsilon_i = \frac{\Delta L_i}{L_i} \tag{6.23}$$

where ΔL_i, L_i, and ε_i are the measured change in gage length, initial gage length (undeformed distance between instrumentation rods), and the resulting translational strain from the i^{th} LP, respectively. The final angular joint shear strain γ_s is expressed as the average of the four calculated values in Eq. 6.19 through Eq. 6.22.

6.6.3.2 JOINT GLOBAL ROTATION IN SPACE

The joint global rotation in space (θ_{jR}) was measured with respect to a fixed reference for both the north and east joint faces using four LPs horizontally attached to upper and lower columns right above and below joint interface at distance *a* (2 in.), respectively, as shown in Figure 6.24 The average measurement of both the exterior and interior LPs was used. Although it could be a minor adjustment, the LP readings were adjusted to account for the effect of deformations within the "*a"* distances above and below the joint. Hence, the final expression for θ_{jR} is:

$$\theta_{jR} = \frac{L_{i,top} - L_{i,bot} + 2\gamma_s a}{h_b + 2a} \tag{6.24}$$

where $L_{i,top}$ and $L_{i,bot}$ are the average of top LP reading and the average of bottom LP reading, respectively.

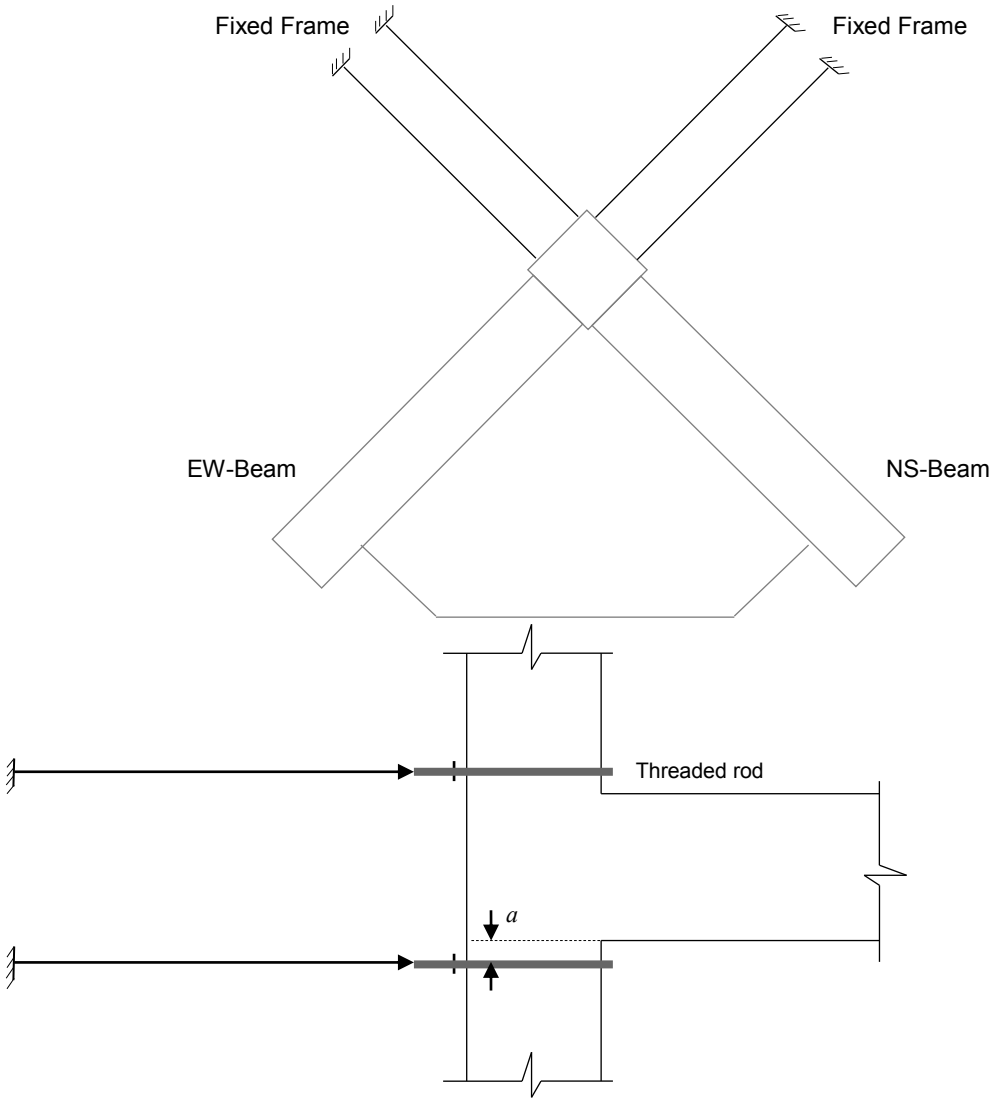

Figure 6.27 Joint global rotation instrumentation

6.6.3.3 BEAM RELATIVE ROTATION WITH RESPECT TO JOINT

Relative rotation of beams with respect to the joint/column (θ_{bcR}) was recorded using two LPs, one exterior and one interior, installed on the beam bottom surface at a distance equal to half the beam effective depth. These two LPs were horizontally connected to the lower column through a threaded rod located at a nominal 2 inch distance, denoted y, below column joint interface as seen in Fig. 6.28. L_{ext} and L_{int} are the measurements of the exterior and interior LPs, respectively. The average rotation obtained from the two LPs is considered the final beam relative rotation with respect to the joint, which can be expressed as:

$$\theta_{bcR} = \frac{(L_{ext} + L_{\text{int}})}{2y} \tag{6.25}$$

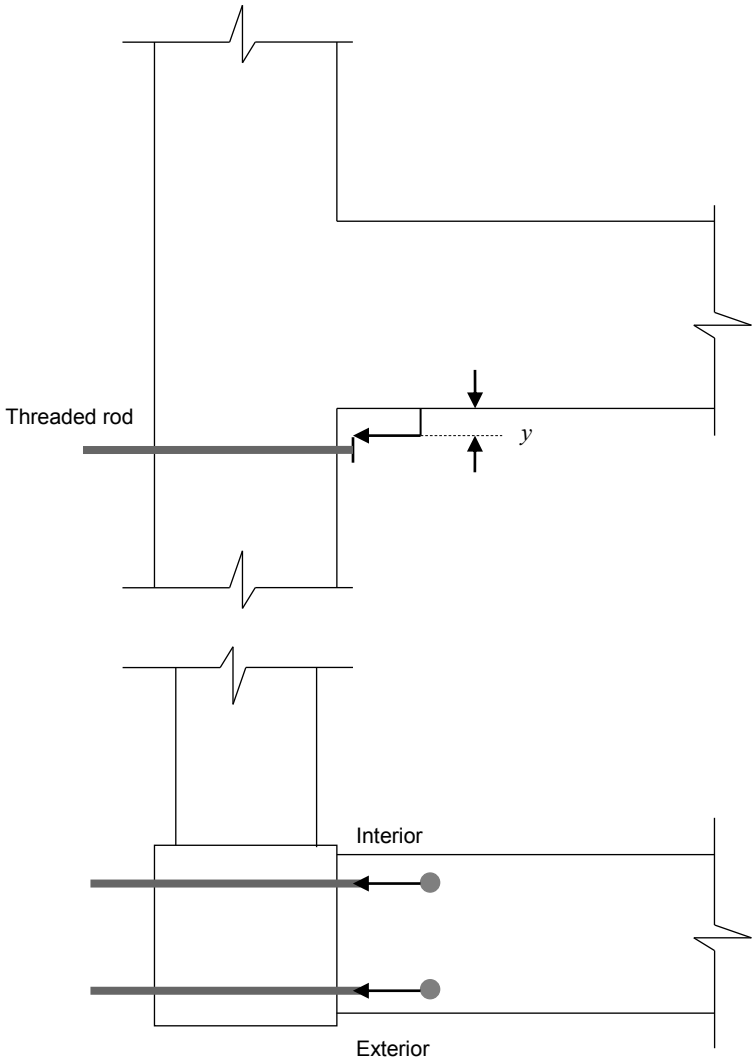

Figure 6.28 Beam-joint relative rotation instrumentation

6.6.3.4 BEAM TORSIONAL ROTATION

In a three dimensional beam-column joint test, torsional rotation due to twisting moment is inevitable. During the loading of a particular beam, the slab rigidity results in twisting moment on that beam and a transferred twisting moment to the orthogonal beam. To monitor these torsional rotations a set of LPs are installed along the beam span on both sides of the beam as shown in Figs. 6.25, 6.24 and 6.29. The twist angle ϕ_t, is measured by dividing the differential translation on both sides of the beam by the horizontal distance between the LPs as:

$$\phi_t = \frac{(L_{Ti,ext} - L_{Ti,\text{int}})}{x_t} \tag{6.26}$$

where $L_{Ti,\ ext}$ and $L_{Ti,\ int}$ are the exterior and interior readings of the LPs, respectively, and x_t is the horizontal distance between them.

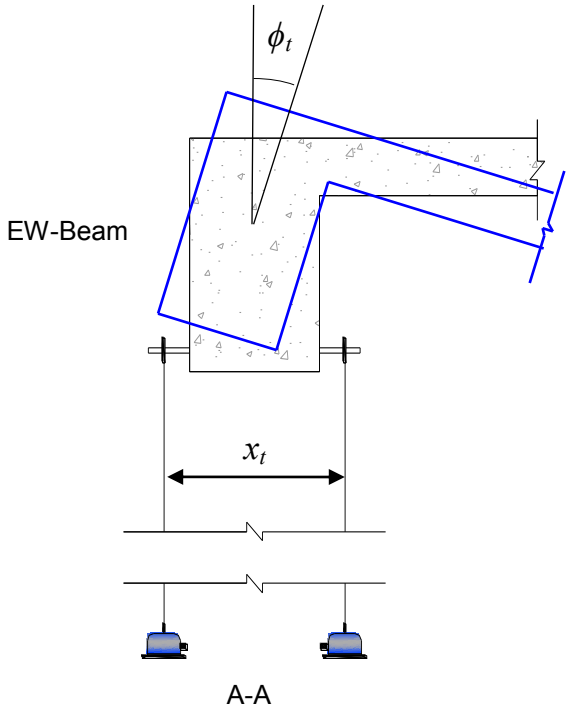

Figure 6.29 Beam torsional rotation measurements

6.7 DESIGN OF TEST SETUP

The test setup is designed to mimic the actual structure boundary conditions as closely as practicable and to satisfy loading protocol requirements. The required boundary conditions are to satisfy moment releases at top of upper column, bottom of lower column, and beam end sections. It is also intended to allow vertical translation of the column to accommodate the expected shortening or elongation during intense overturning axial load reversals. Finally, the horizontal translation of beams is permitted.

The test setup consists of several components; vertical axial loading system, lateral loading system, lateral restraint system, and connections and transitions elements. Figure 6.30 displays a schematic diagram for the test setup, while Fig. 6.34 and Fig. 6.35 show a test specimen installed in the actual laboratory setup.

The vertical axial loading system (Fig. 6.31) comprises two 360-kip capacity hydraulic actuators, giving a total test setup capacity of 720 kip in axial compression or 360 kip in tension. The two actuators are connected to two horizontal W36 loading girders, which are sufficiently stiffened to resist local deformations. The loading girders are connected to the specimen through 3D universal hinges (Fig. 6.30 through 6.33) and transition plates, manufactured particularly to mimic real pin ended boundary conditions. That means they are capable of transferring up to 720 kips axial compression and 360 kips axial tension while allowing rotations around two orthogonal horizontal axes and not allowing twisting rotation around the vertical axis.

The 3D hinges and their transition plates (Fig. 6.33) were analyzed for the expected load cases, checking for strength and deformation adequacy under multi-axial stress states using commercial finite element analysis software (SAP2000) along with hand calculations. The vertical loading system, including the specimen itself, is in stable equilibrium in the vertical plane. Out-of-plane stability requires a secondary lateral restraint system.

Confinement high tensile steel cylinders were used to encase the end portions of the upper and lower columns (Fig. 6.34) to provide additional confining resistance to expected high splitting forces at the column ends. The spacing between the steel cylinders and the concrete columns were filled with high strength hydro-stone to enable proper confinement passive pressure.

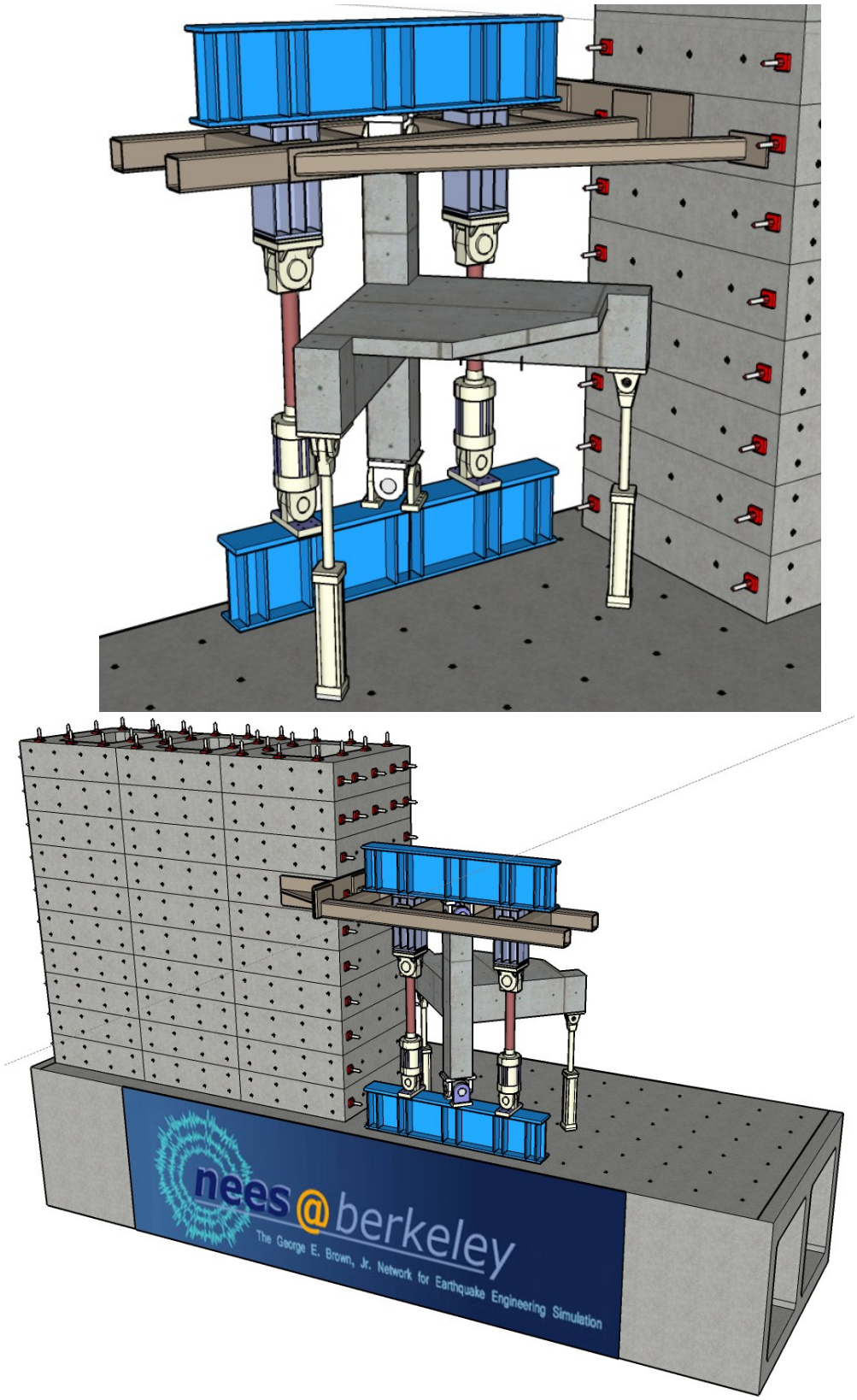

Figure 6.30 Schematic rendering of test setup

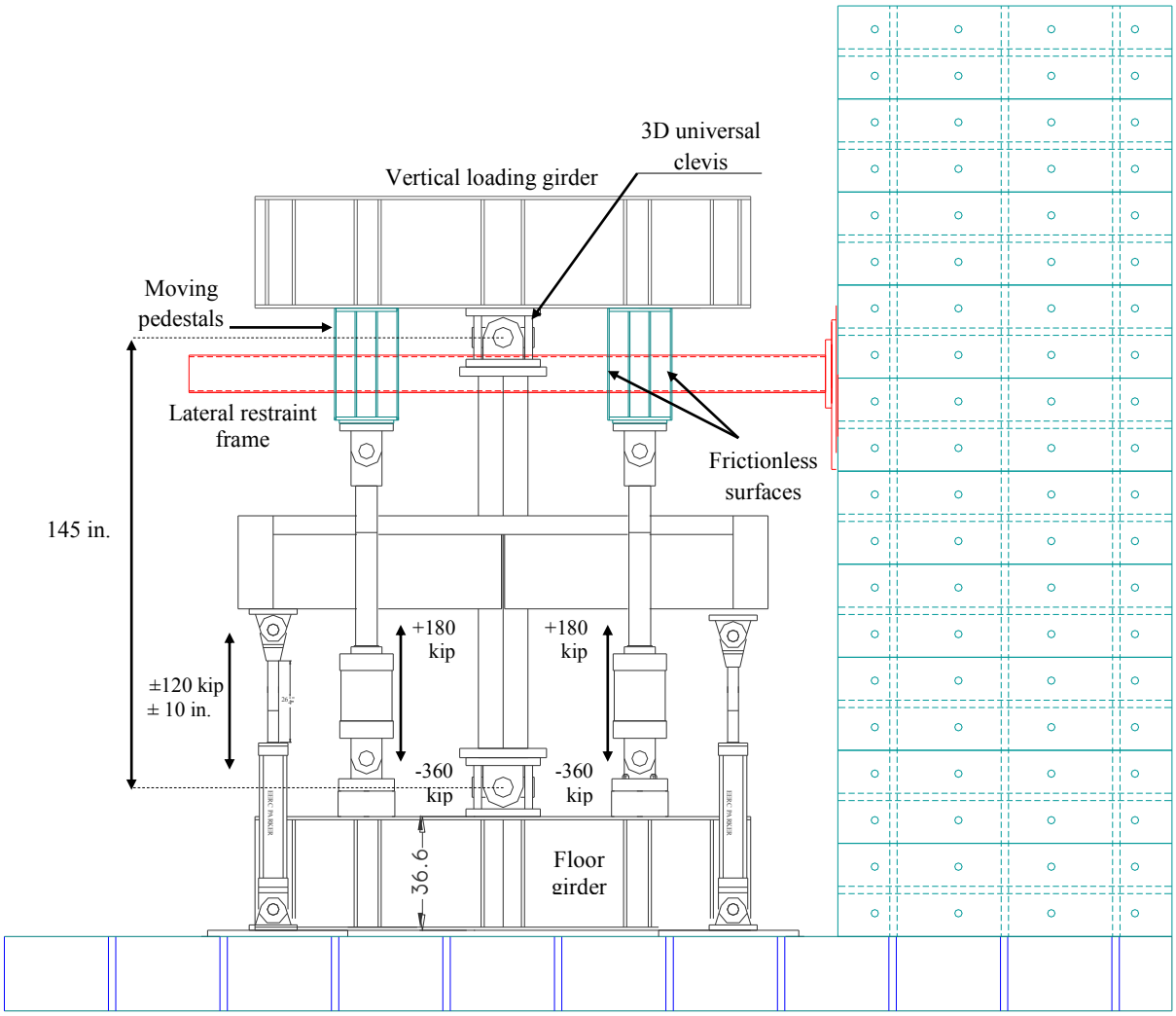

Figure 6.31 Test setup: vertical loading systems

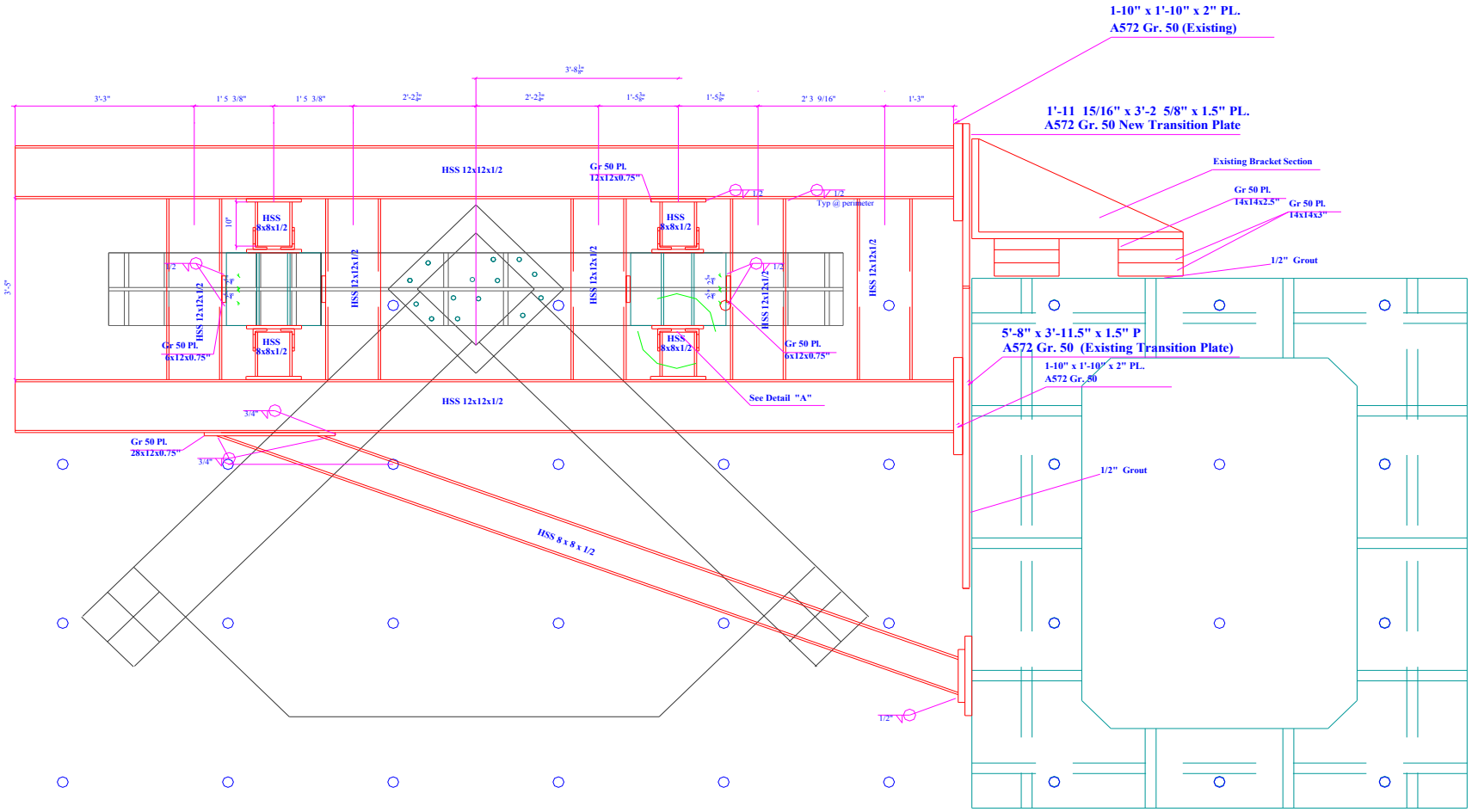

Figure 6.32 Test Setup: Lateral Restraint Frame

The lateral restraint system consists of the lateral frame depicted in Figures 6.30 and 6.32, which comprises two HSS 12x12x1/2" tube sections connected together with several HSS 12x12x1/2" connecters. A diagonal HSS 8x8x1/2" bracing member is provided to further stiffen the lateral frame as shown in Fig. 6.32. Arrangements were made to allow vertical displacement of the vertical loading system including the specimen, by permitting its "frictionless" motion through the vents of the lateral frame. The lateral restraint system was analyzed by commercial finite element analysis software (SAP 2000) to check its adequacy and to ensure that its deformations were within the acceptable limits.

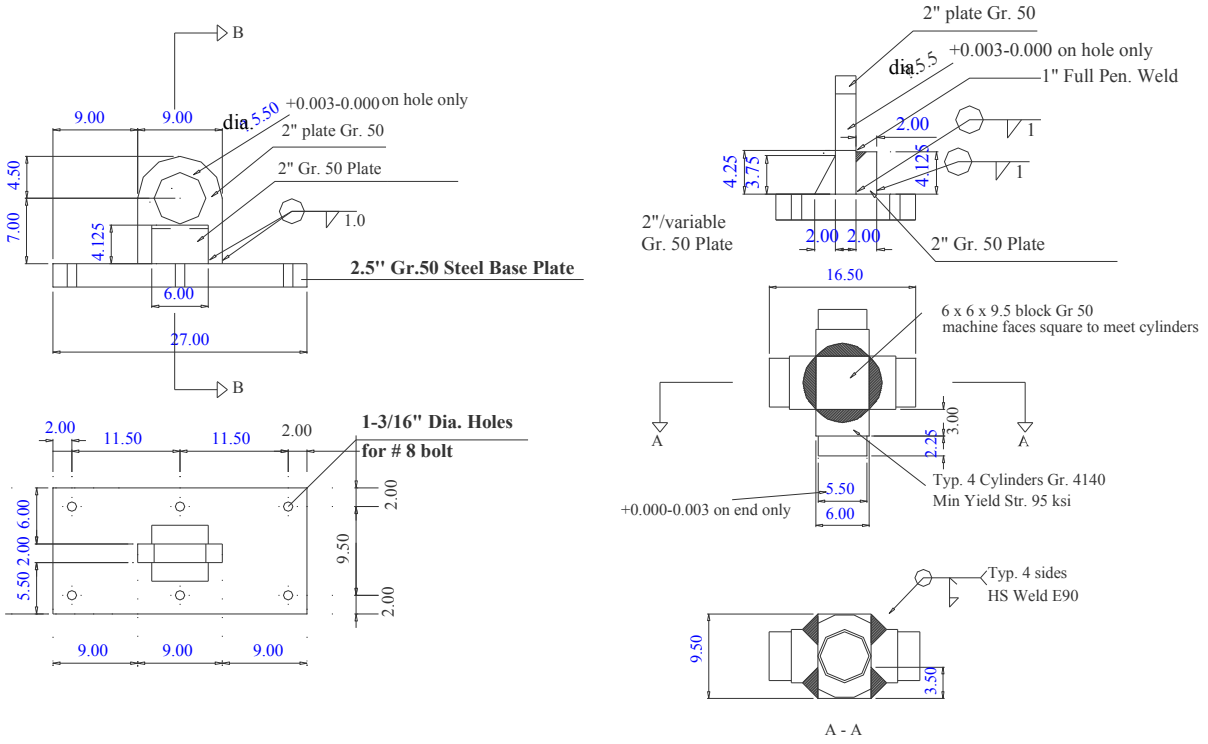

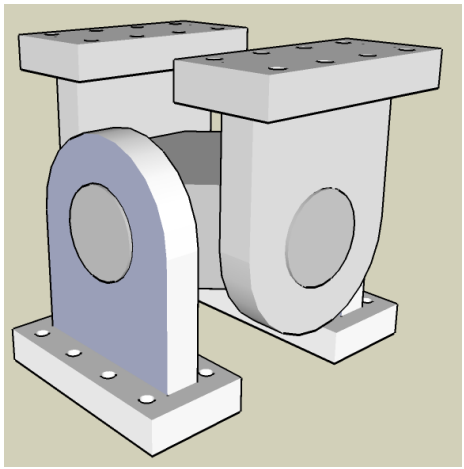

Figure 6.33.a 3D universal hinge

The lateral loading system consists of two vertical 120-kip capacity hydraulic actuators (Fig. 6.30 and 6.31), used to load the two orthogonal concrete beams of the specimen bi-directionally either simultaneously or in alternating fashion. From static equilibrium of the specimen, this loading arrangement produces beam shears that are equilibrated by column shears V_c that are considered the applied lateral load to the column. This laboratory arrangement of lateral loading is made to simplify loading setup and does not represent the P-Δ effect that occurs in real buildings. This shortcoming was accepted as the main interest was to test the joint, which can be done adequately without modeling the P-Δ effect.

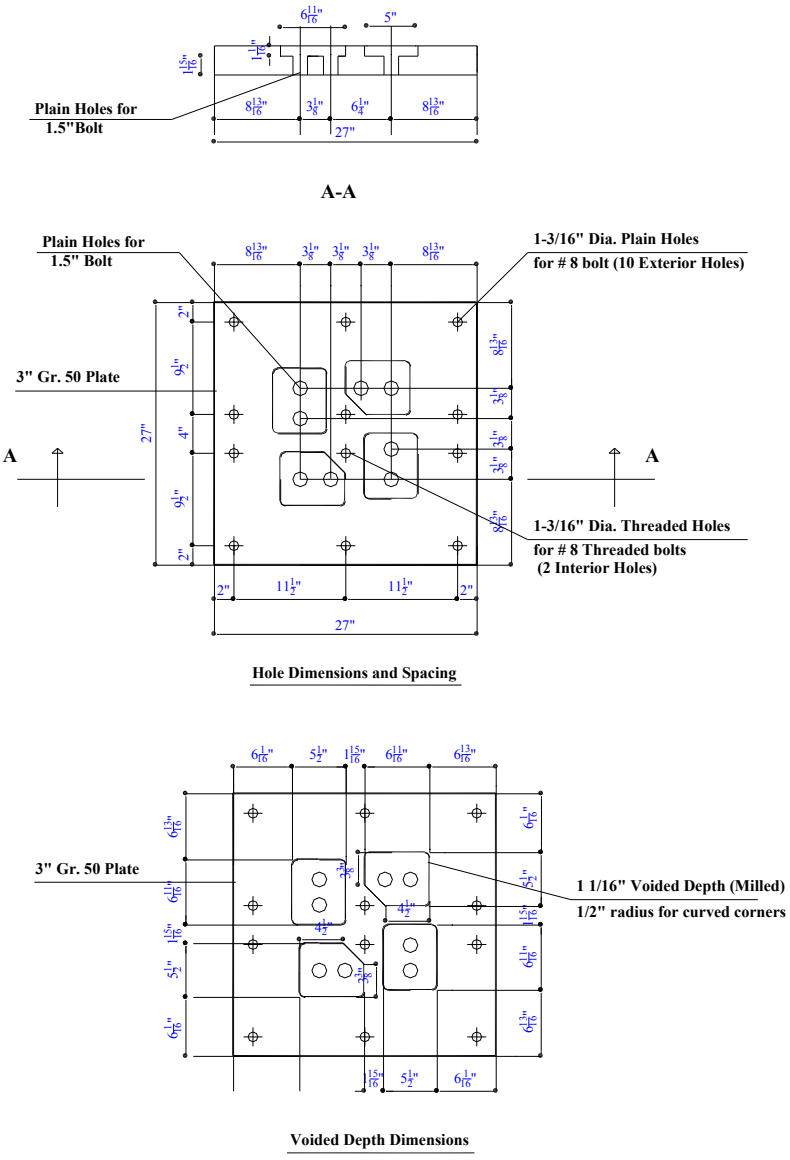

Figure 6.33.b Transition plate design between 3D universal hinge and concrete column

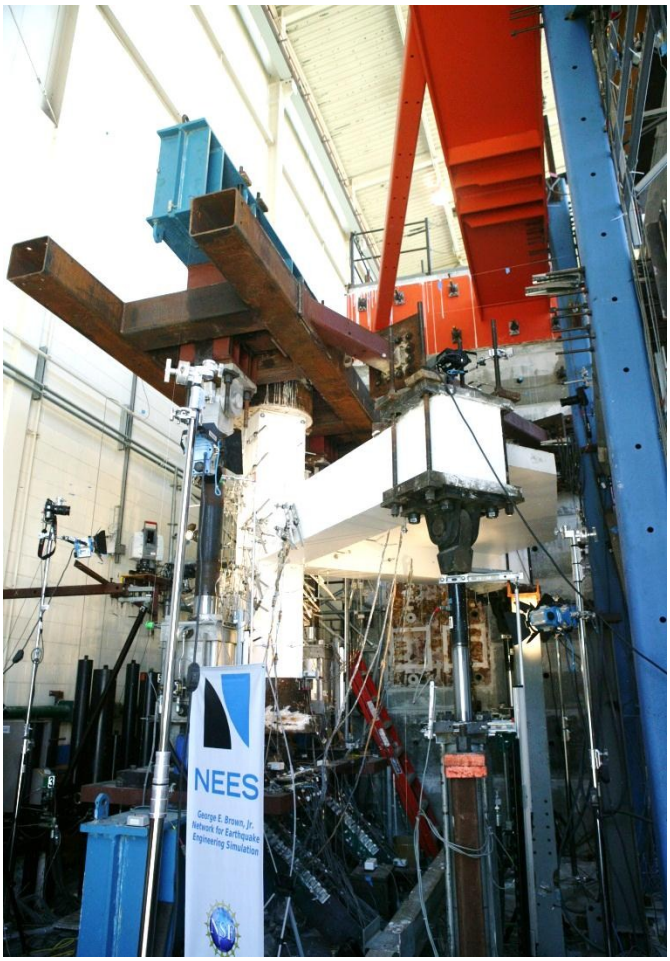

Figure 6.34 Specimens U-J-1 and U-J-2 in the test rig.

Figure 6.35 Specimens B-J-1and U-BJ-1 in the test rig.

6.8 TESTING PROTOCOL

6.8.1 Gravity Loading

To simulate service gravity loading of the prototype structure, the column is initially loaded monotonically with the designated gravity load ratio of about 21%, while both beams are simultaneously displaced with initial offset downward displacement of $\Delta_y/4$ to mimic floor gravity loading; where Δ_y is the beam downward theoretical first yield displacement. This corresponds to a service gravity floor load of 25% beam flexural strength. Downward (pull-down) beam displacements are considered negative throughout this manuscript.

6.8.2 Displacement History

Following simulated gravity loading, test specimens are subjected to a symmetric, quasi-static, cyclic, displacement pattern centered around the deformed gravity load position until collapse. Figure 6.36 and 6.37 display the adopted increasing amplitude displacement histories used for the unidirectional and bidirectional loading histories, respectively. The loading rate is 0.02 in./sec. The displacements are commanded to beam actuators unidirectionally in two orthogonal directions in alternating fashion as indicated in Fig. 6.36 for specimens U-J-1, U-J-2, and U-BJ-1 or simultaneously commanded to both beams in the bidirectionally loaded specimen B-J-1 as depicted in Fig. 6.36. A "small-amplitude" cycle is introduced at the beginning of each large amplitude group of cycles in the inelastic range beginning with group No.3. The small cycles are intended to provide data for analytical modeling of structures subjected to seismic loading.

Table 6.9 exhibits the chosen displacement amplitudes for the input displacement history as a function of the first yield displacement Δ_y. The displacement history for the unidirectional specimens consists of two cycles per displacement amplitude group for each beam for displacement amplitudes groups 1 to 7. At later stages of loading, with larger inelastic displacement demands after severe degradation of the joint, each displacement amplitude group consists only of one cycle.

The bidirectional displacement history is identical to the unidirectional one except that in the former both beams are loaded simultaneously. The relatively simple 45-degree loading path (Fig. 6.37) is intended to simplify results interpretation, and probably underestimates damage that occurs during more random patterns that occur during actual earthquakes.

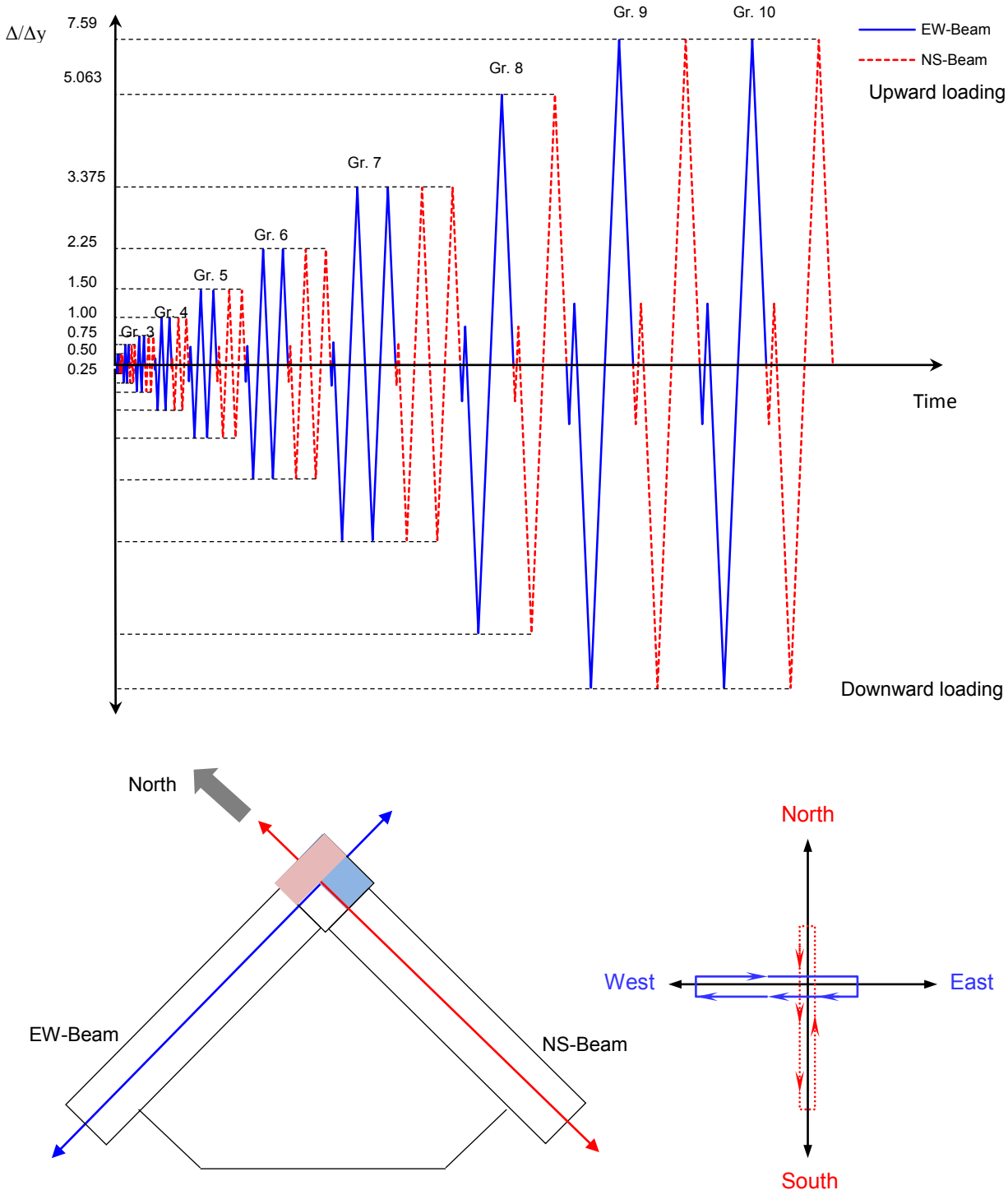

Figure 6.36 Unidirectional alternating loading history for specimens U-J-1, U-J-2 and U-BJ-1

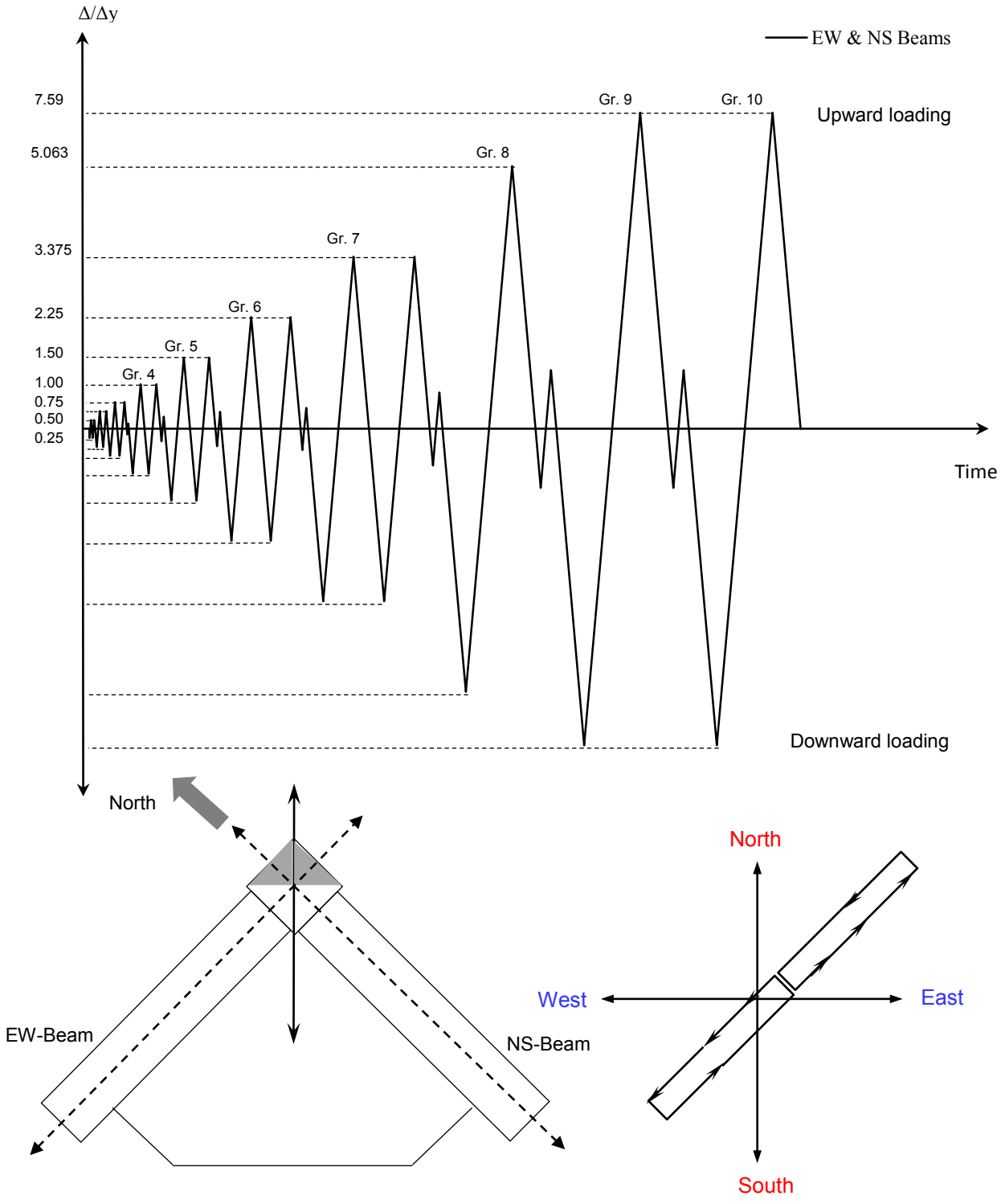

Figure 6.37 Bidirectional Loading History for specimen B-J-1

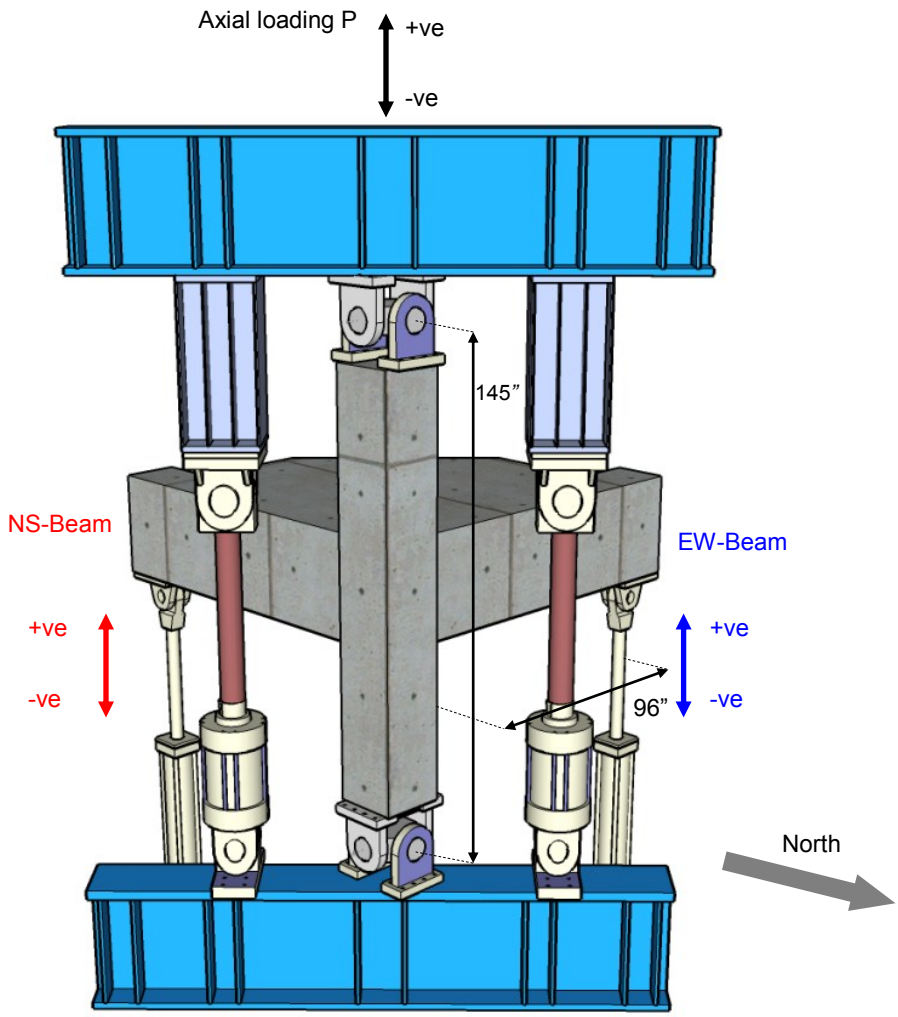

Figure 6.38 Loading sequence and sign convention

Table 6.9.a Displacement history amplitudes

Group	1	2	3	4	5	6	7	8	9	10
Δ/Δ_y	0.25	0.50	0.75	1.00	1.50	2.25	3.38	5.06	7.59	7.59

Table 6.9.b “Elastic” displacement cycles amplitudes

Group	*1*	*2*	*3*	*4*	*5*	*6*	*7*	*8*	*9*	*10*
Δ/Δ_y	*NA*	*NA*	*NA*	*0.15*	*0.35*	*0.55*	*0.80*	*1.00*	*1.65*	*1.65*

6.8.3 Axial Load Protocol

An objective of the axial loading protocol was to vary axial load to approximate the overturning effect of a building in which overturning produced relatively high axial loads. Assuming that most of the building would remain intact while localized failure occurred at lower-level joints, the axial load variation should continue at nearly the same level even after the tested joint sustained strength degradation (Fig. 6.39).

It was initially decided to simulate the overturning moment effect by varying the column axial load as function of the beam shear using a linear function. This function was obtained from linear 2D dynamic analyses of the Van Nuys Holiday Inn building under a suite of ground motions and static pushover analyses followed by regression analysis to yield a relationship between vertical axial loads, including overturning moment effect, and lateral loads as follows:

$$P_{uni} = P_g + \alpha V_b \tag{6.27}$$

$$P_{bi} = P_g + \alpha V_{b,EW} + \alpha V_{b,NS} \tag{6.28}$$

$$R_{uni} = P_g + (\alpha+1) V_b \tag{6.29}$$

$$R_{bi} = P_g + (\alpha+1) V_{b,EW} + (\alpha+1) V_{b,NS} \tag{6.30}$$

where V_b is the beam shear of the loaded beam (EW or NS), $V_{b,EW}$ is the beam shear in the EW-direction, $V_{b,NS}$ is the beam shear in the NS-direction. α is regression parameter which depends on the intensity of ground motion, number of floors, desired axial load level at expected joint shear strength, and the footprint dimensions of the analyzed structure.

Two relationships were derived; one is for ground floor and the other is for the first floor. As implied from the above equations (6.27 through 6.30), P_{uni} is the variable upper column axial load during unidirectional test in each direction, P_{bi} is the variable upper column axial load during bi-directional test, and R_{uni} and R_{bi} are the corresponding lower column variable axial load during unidirectional and bidirectional tests, respectively.

The axial load-lateral load relationships are derived first for uniaxial 2D loading, then the overturning moment part of the relation has been replicated to accommodate the bidirectional loading, an approximation which can be accurate enough in linear analysis.

It is noteworthy to mention that some deviations from exact prototype building dimensions have been made to accommodate available *nees@berkeley* laboratory space and test setup capacity. These deviations have been also reflected in axial load-lateral load relationship.

Upon starting the test and throughout the pre-peak joint shear strength regime, the parameter α was intended to be constant as obtained according to the aforementioned criteria. However, once joint shear strength is reached, the parameter α is supposed to be altered in each subsequent cycle to maintain the axial load corresponding to the joint shear strength peak throughout the

subsequent cycle peaks. Since the test is under quasi-static displacement control, the drawback of this procedure is the effect of the residual beam shear at zero displacement, which results in degradation of gravity column axial load throughout the nonlinear portion of the test.

Many correction criteria were suggested to overcome this drawback. First suggestion was to increase the initial column gravity load beyond the reasonable desired values to accommodate this drop during the inelastic cycles. One other measure used by Priestley and Hart [1] during a similar test to eliminate the effect of degrading beam shears was to increase the degrading axial load manually to the desired level at the end of each cycle. Obviously, the former measure alters the test results by implying unsymmetrical axial loading cycles about a variable datum (a degrading gravity load) and by amplifying joint axial stiffness prior to shear failure to a level different from desired. The randomness of the axial load history implied by the latter suggested correction is also evident, which in turn complicates drawing useful conclusions about the effect of high axial loads.

Based on the above discussion, it was decided to change the concept of axial load-lateral load (beam shear) dependence to a simplified displacement-based axial load protocol to avoid the drawback of relying on unknown degrading beam shear to vary the column axial load. The idea is to vary the column axial load with input displacement reversals until joint shear strength (or axial test setup capacity) is reached, which implies increasing axial load amplitudes based on Fig. 6.39. Afterwards, the axial-load protocol is to be altered before starting each subsequent cycle to maintain the threshold axial load level reached at joint shear strength peak throughout the subsequent displacement peaks.

This task is performed using the function:

$$P = P_g + \beta.\Delta_{EW} + \beta.\Delta_{NS} \tag{6.31}$$

where P is the upper column axial load, Δ_{EW} and Δ_{NS} are EW-beam and NS-beam displacements, respectively. The axial load parameter β has the following values:

$$\text{for} \quad \Delta_b \le \Delta_{bjn}: \quad \beta = \beta_o = \frac{P_{jn} - P_g}{\Delta_{bjn}} \tag{6.32.a}$$

$$\text{for} \quad \Delta_b \ge \Delta_{bjn}: \quad \beta = \beta_o \frac{\Delta_{bjn}}{\Delta_b} \tag{6.32.b}$$

where Δ_b is the applied beam displacement, Δ_{bjn} is the beam displacement corresponding to joint shear strength peak observed during test upon initiation of degradation of beam shear peaks, P_{jn} is the upper column axial load corresponding to joint shear strength peak obtained by observation during test. Figures 6.39 and 6.40 depict schematic representation of the axial load protocol. The overturning axial load history is intended to be symmetric about the gravity axial load; hence, the alteration of the axial load parameter β is only

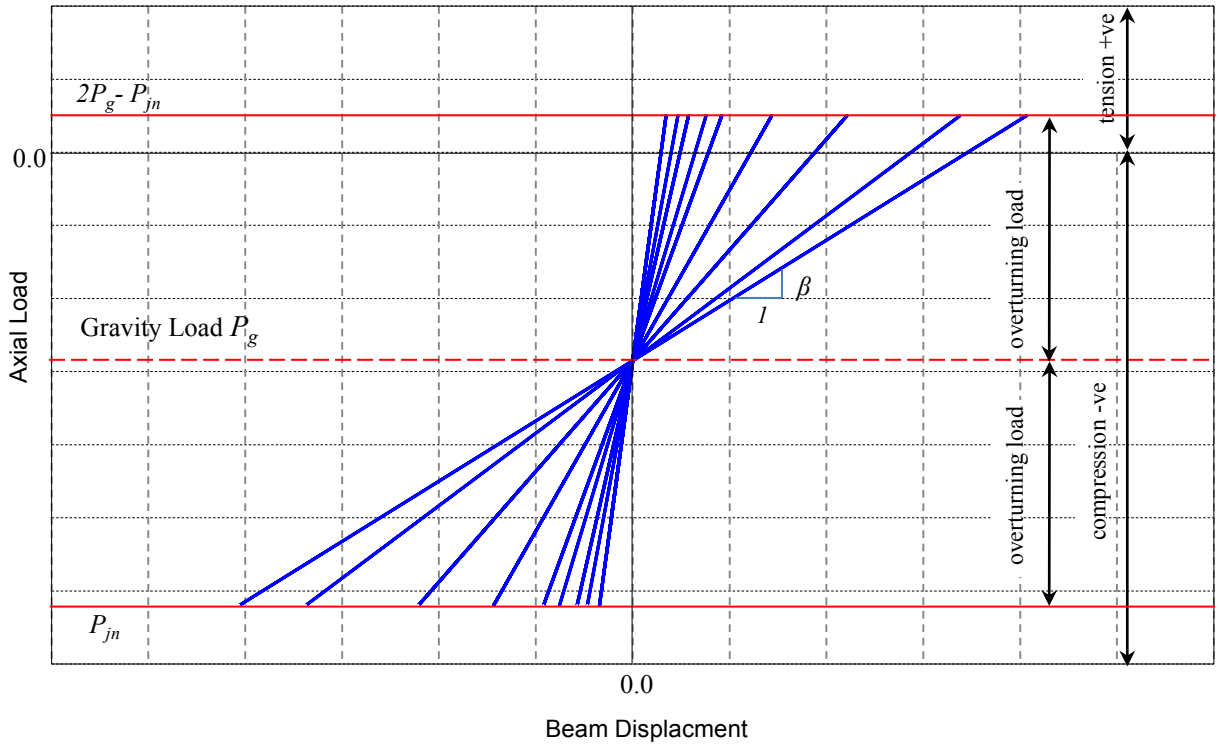

Figure 6.39 Displacement-based axial load protocol

performed once at the beginning of each post-peak displacement cycle to match the axial load peak corresponding to negative joint shear strength. In other words, to maintain the symmetry of axial load history it is not intended to alter the axial load protocol to maintain the axial load tension peak to match the positive joint shear strength peak.

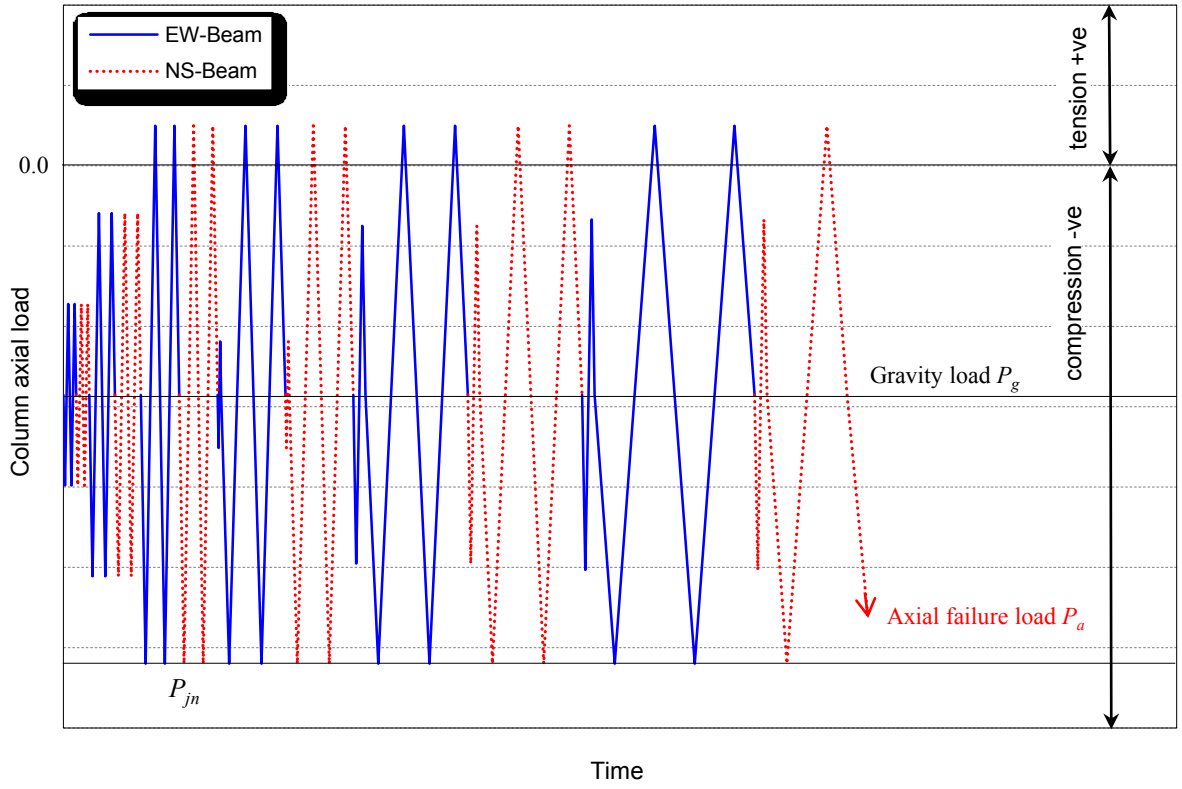

Figure 6.40 Displacement-based protocol axial load history

The approximation of axial load-lateral displacement by the linear function in Eq. 6.6 is considered an acceptable approximation for two reasons. First, the non-linearity imposed on this relationship by a yielding beam or a degrading joint has an insignificant effect since it was intended to model the most critical axial loading case as mentioned in a previous section, which is joint degradation only at the first floor of a multi-story building, while the rest of beams and joints are still linear. Accordingly, the nonlinear degrading first floor joint or beam contribution to the overall axial load is quite small. Second, even if many floor beams and joints were performing inelastically, the degrading slope of the axial load-lateral displacement response can be well represented by a linear function with a degrading slope as depicted in Fig. 6.41.

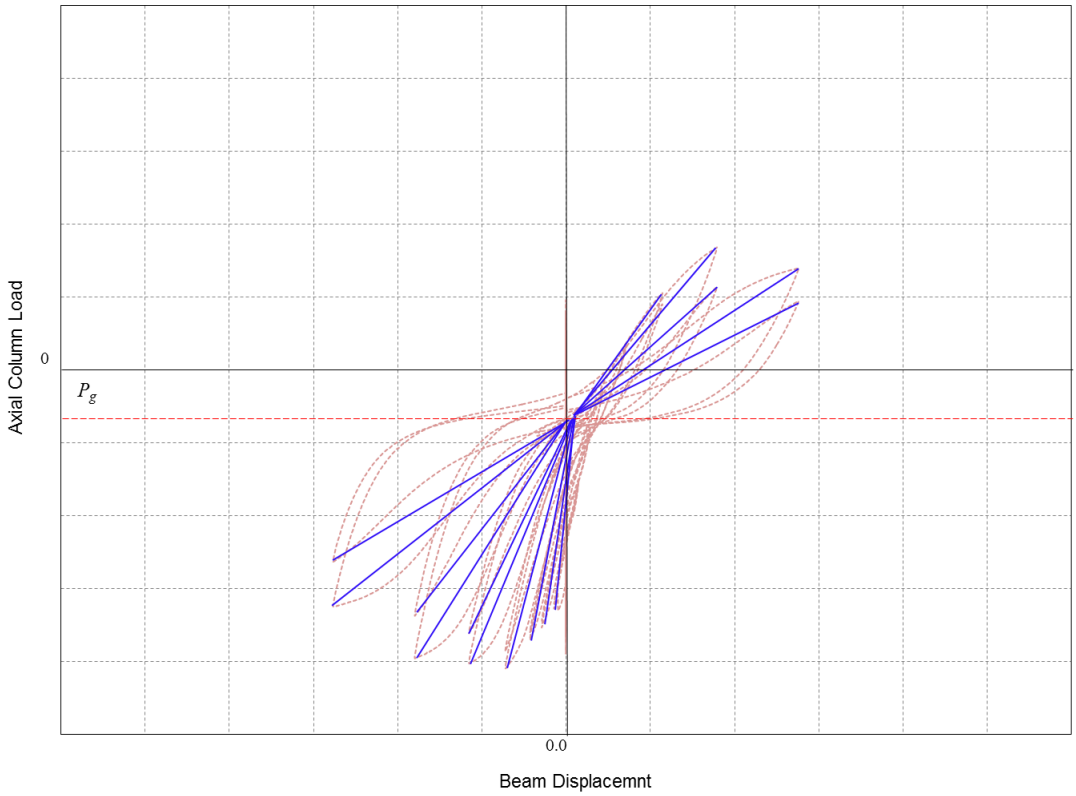

Figure 6.41 Effective stiffness of actual axial load-beam displacement relation

6.9 DATA ACQUISITION

The total number of data acquisition channels used was about 200 channels. This includes 65 strain gage channels, 120 displacement transducer channels, and 15 test control channels and automatic trigger channels for cameras and laser scanner. Data were acquired at a rate of 20 scans per second using Flex-Test software developed by MTS.

6.10 PHOTOGRAPHY AND LASER SCANNING

The typical procedure of pausing quasi-static cyclic tests to monitor and mark crack development was not practical during the current testing program. In these full-scale specimens, the location of the joint was at an elevation for which access required ladders or hydraulic man-lifts. In addition, the substantial axial load used in the test protocol imposed high risk that dictated ruling out the crack marking process during loading. Instead, it was decided to use heavy photography in lieu of crack marking to monitor the degradation of test specimens.

Eight Canon high speed shutter digital still cameras were placed around the specimen and setup at locations of interest including north joint, east joint, external beam and column surfaces,

slab top and bottom surfaces and two cameras for global monitoring of specimen failure. Two video cameras were also used to capture real-time axial collapse.

All still cameras were synchronized with beam displacements through a specifically written program that triggers the cameras every 0.10 inch of beam displacement to guarantee capturing crack development at a reasonable increment. This increment resulted in about 15000 pictures per test that were used later to generate seven condensed video clips covering the entire specimen surfaces. These video clips, along with the pictures and hysteretic loops, were used later to analyze and monitor crack development and progression.

A synchronized video clip (Fig. 6.42) that includes the five views of the test specimen along with the EW and NS beam hysteresis loops and axial load history was generated using a sophisticated Matlab code specially designed to suite the current test configurations.

A laser scanning technique was used to monitor joint deformations and cracking through *Leica* Laser Scanner, Fig. 6.43. The laser scanner rotated around its vertical axis capturing joint deformation every 0.20 inches of beam displacement. The joint global rotation obtained by laser scanning was compared to that obtained using conventional LPs. The laser scanning technique proved to be very accurate and efficient in recording global deformations of concrete specimens, [141]. However, on the local level, joint cracking and distortion affected the accuracy of laser scanning measurements.

Three dimensional panoramic-fish eye navigable pictures (Fig. 6.44) were created after testing to enable the author and future researchers to thoroughly investigate the collapse details of test specimens.

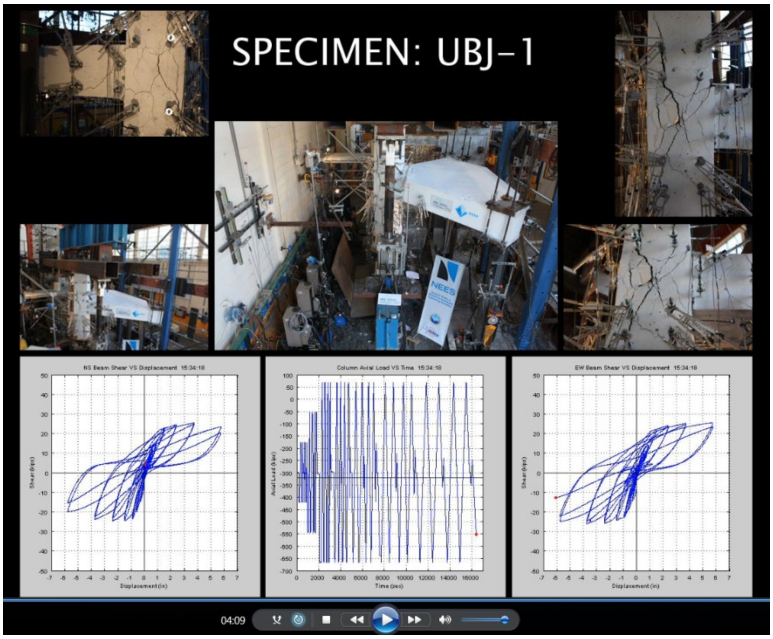

Figure 6.42 Synchronized video clip for specimen monitoring

Figure 6.43 3D laser scanning machine

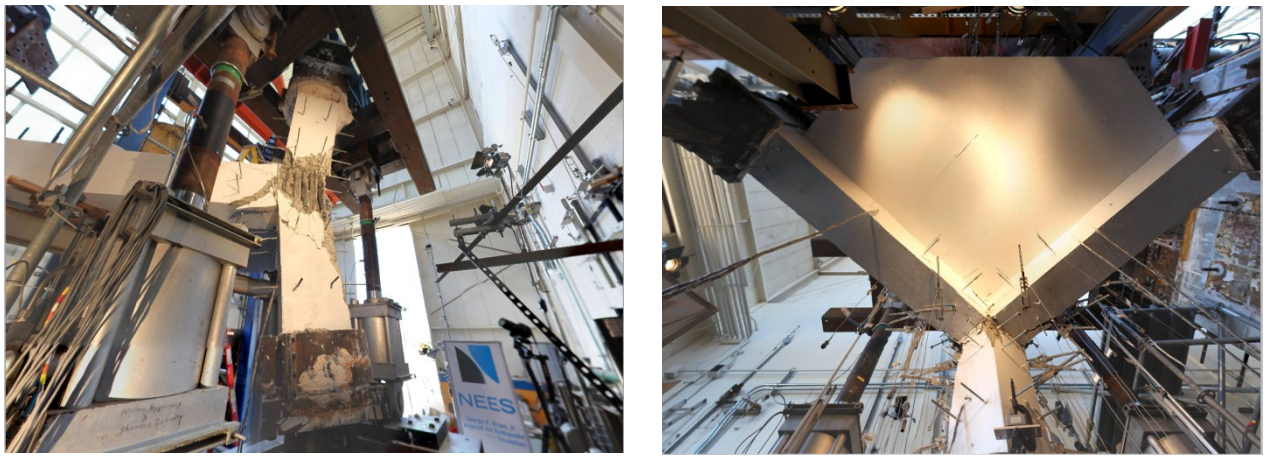

Figure 6.44 Fish-eye generated navigable 3D images for collapse inspection

CHAPTER 7

EXPERIMENTAL RESULTS AND DISCUSSION

7.1 INTRODUCTION

This chapter presents the test results of the experimental investigation described in Chapter 6. The chapter is divided into two major sections. The first section presents and discusses the general performance of test specimens, while the second section discusses the effect of test parameters on the response of unconfined corner joints in the light of current and previous test results.

7.2 SEISMIC PERFORMANCE MEASURES

The seismic performance of the test specimens will be presented and discussed through key performance measures that characterize the response of each specimen. The performance measures include modes of failure, joint cracking patterns and progression, force-drift relationships, joint shear stress-strain relationships, axial load history, beam shear history, joint deformation contribution to overall drift, displacement ductility capacity, joint shear strength, axial load residual capacity, cumulative energy dissipation, reinforcement strains, and torsional deformation. Using these performance measures, the effects of test parameters and geometric and design configurations on unconfined corner beam-column joints can be assessed. These effects include the effect of high axial compression loading, tensile loading, simultaneous bidirectional loading, joint aspect ratio, beam reinforcement ratio, presence of column intermediate reinforcement concrete slab presence, and finally the effect of geometry of corner joints.

7.3 GENERAL SEISMIC BEHAVIOR OF TEST SPECIMENS

7.3.1 Specimen U-J-1

Table 7.1 presents the characteristic response parameters of specimen U-J-1. It is worth mentioning that any axial load ratio presented in this chapter is based on upper column axial load and effective joint area A_j. Figures 7.1 and 7.2 display the force-drift ratio relations for the EW beam and the NS beam, respectively, while Fig. 7.3 presents the development of joint cracking and distress throughout the test. The mode of shear failure of specimen U-J-1 was J-failure for both EW-beam and NS-beam in both downward and upward loading directions.

Diagonal cracking of the north joint face was first observed during downward loading at negative drift peak of -1.37% (peak 4b) and during upward loading at positive drift peak of 1.37% (peak 4b).

The maximum shear force in the downward loading direction was reached at negative drift peak of 2.19% (peak 5a) for EW-beam loading and at 1.37% drift (peak 4a) for NS-beam loading. The corresponding maximum negative joint shear strength coefficient γ_j was 14.3 for the north joint face and 12.6 for the east joint face. The maximum applied upper column axial compression load ratio of 0.31 was reached at negative drift peak 5a of 2.19%, the same peak the north beam-column joint reached its shear capacity.

The maximum beam shear force in the positive direction was reached at positive drift peaks of 3.42% (peak 6a) and 2.19% (peak 5a) for EW and NS beam loading, respectively. The corresponding joint shear strength coefficient γ_j was 10.9 and 9.6 for north joint face and east joint face, respectively. The EW beam bottom reinforcement experienced yielding at positive drift peak 5a (2.19%). The maximum applied upper column axial tension load ratio of 0.13 was reached at positive drift peak 6a for the EW beam upward loading.

It can be observed that the NS-beam loading resulted in lower east joint face shear strength at lower drift ratios compared to the EW-beam loading and north joint face strength. This result is primarily because of the design of the uniaxial loading protocol which alternated loading the EW and NS beams starting with the EW-beam. This contributed to develop torsional cracks due to concrete slab effect in the NS beam due to EW-beam loading cycles, along with joint shear cracks, which led to the lower strength at earlier drift of NS beam loading. Accordingly, it was decided to use test results of EW beam loading verify and develop analytical models in the present study.

Figure 7.1 and 7.2 show that ASCE 41 provisions are very conservative. However, both joint shear strength models proposed in Chapter 5 were able to accurately predict the joint shear strength of the current specimen. Details of this prediction were presented in Chapter 5.

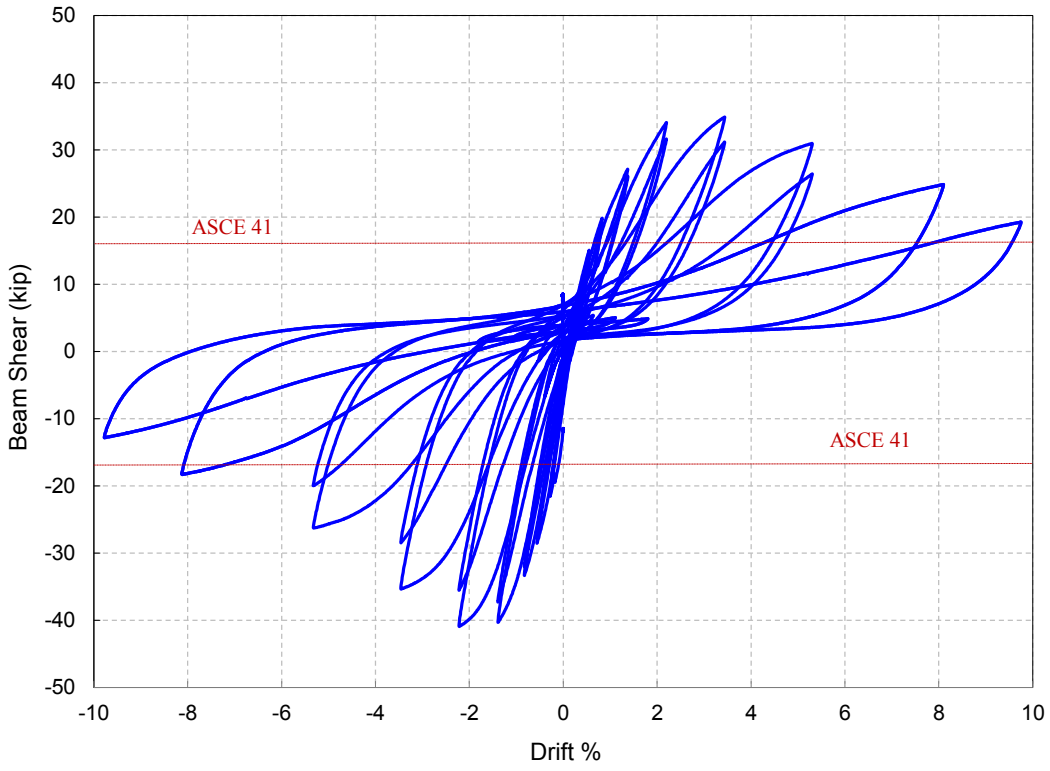

Figure 7.1 Relation between applied force and drift for EW beam of specimen U-J-1

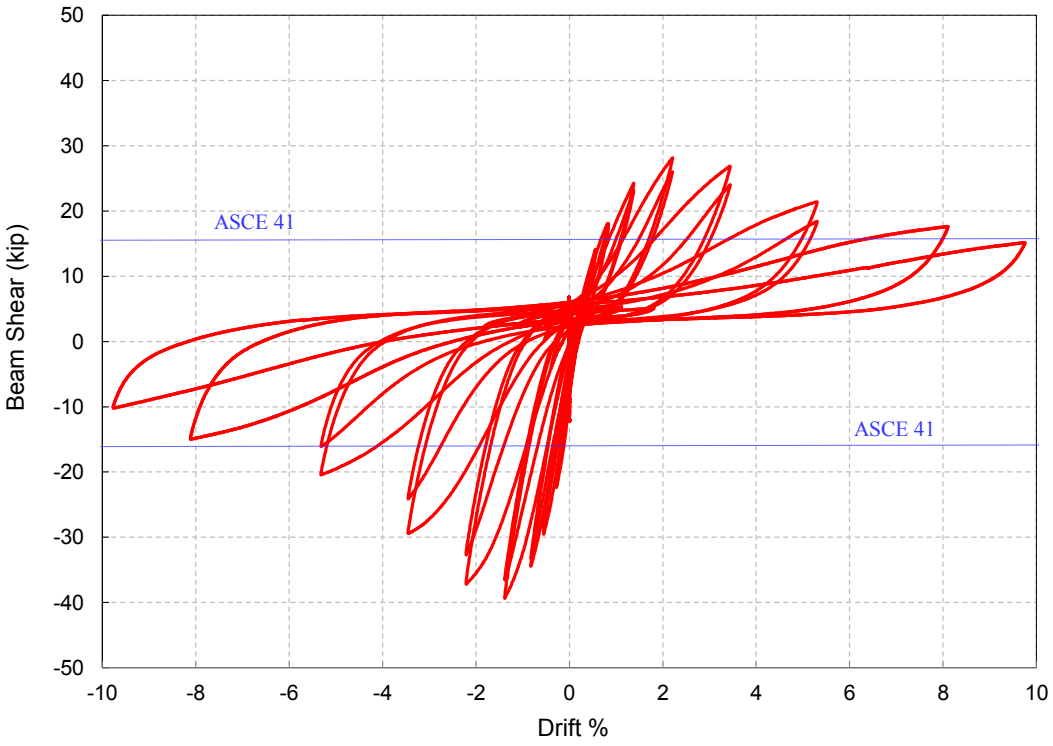

Figure 7.2 Relation between applied force and drift for NS beam of specimen U-J-1

Peak 4a (-1.37% drift)

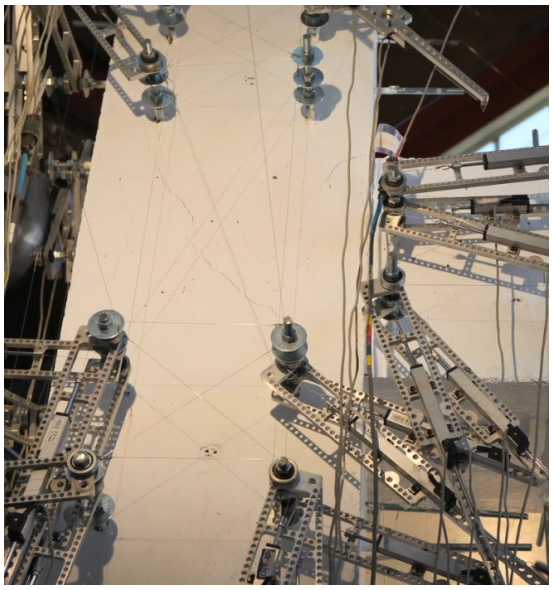

Peak 5a (-2.19% drift)

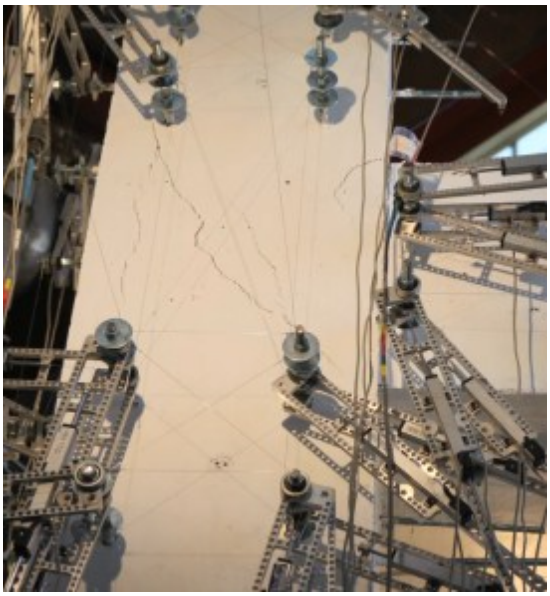

Peak 5a (2.19% drift)

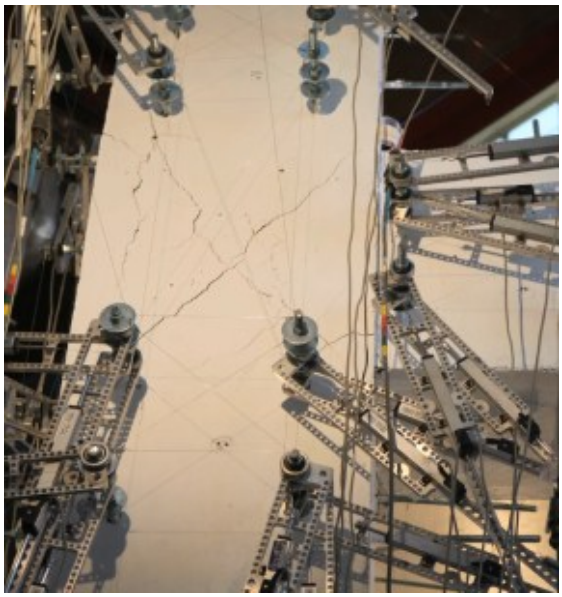

Figure 7.3 Development of north joint face cracking and distress of specimen U-J-1

Peak 6a (-3.42% drift)

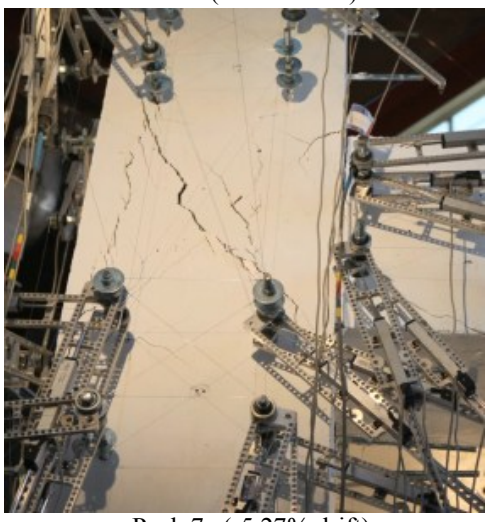

Peak 6a (3.42% drift)

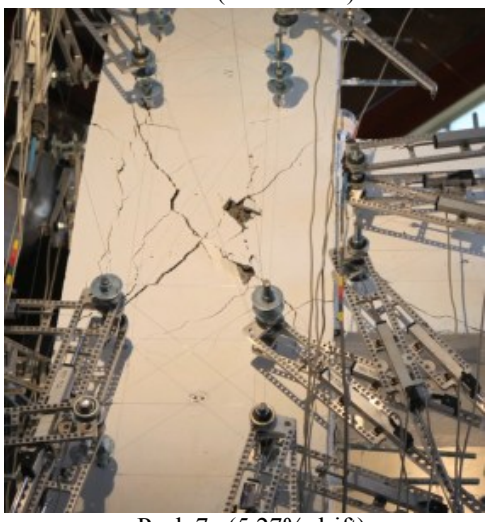

Peak 7a (-5.27% drift)

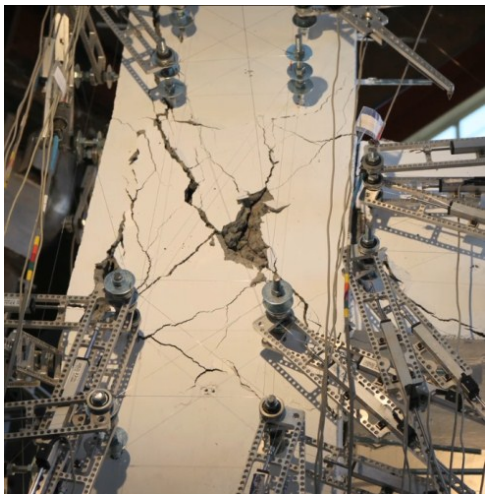

Peak 7a (5.27% drift)

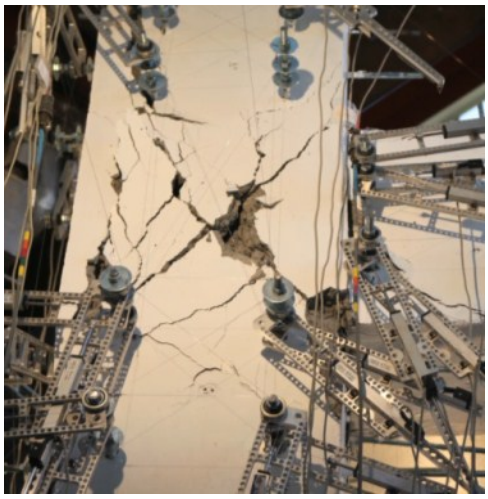

Peak 8a (-8.04% drift)

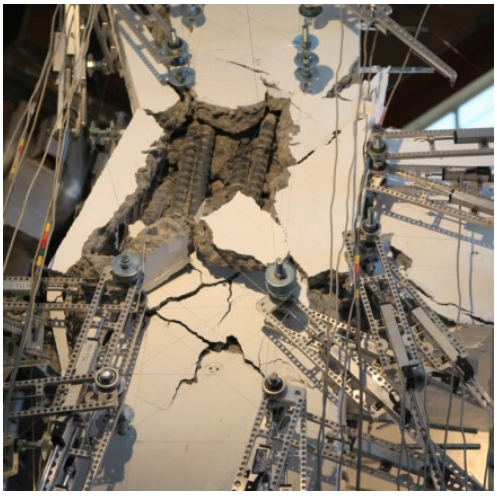

Peak 8a (8.04% drift)

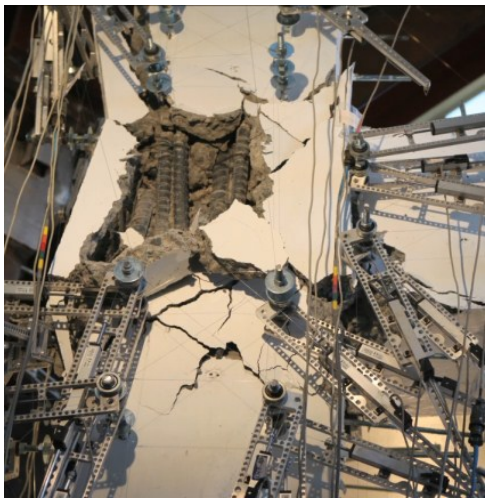

Figure 7.3 ***(Continued)*** Development of north joint face cracking and distress specimen U-J-1

Peak 9a (-9.68% drift)

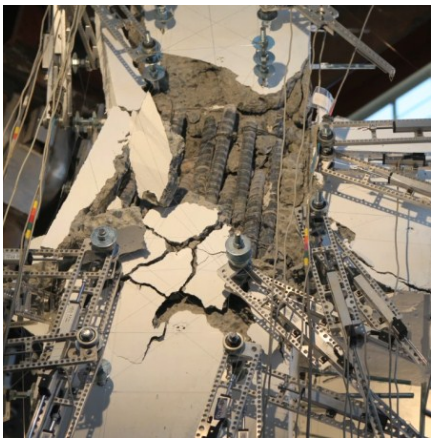

Peak 9a (9.68% drift)

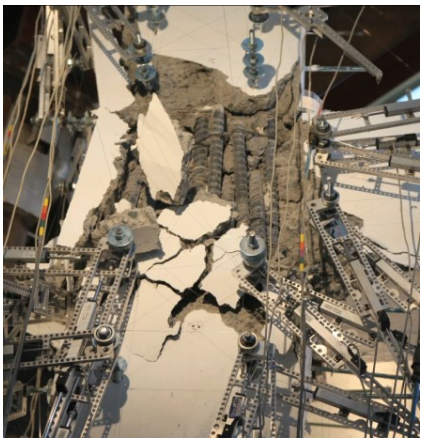

Figure 7.3 ***(Continued)*** Development of north joint face cracking and distress of specimen U-J-1

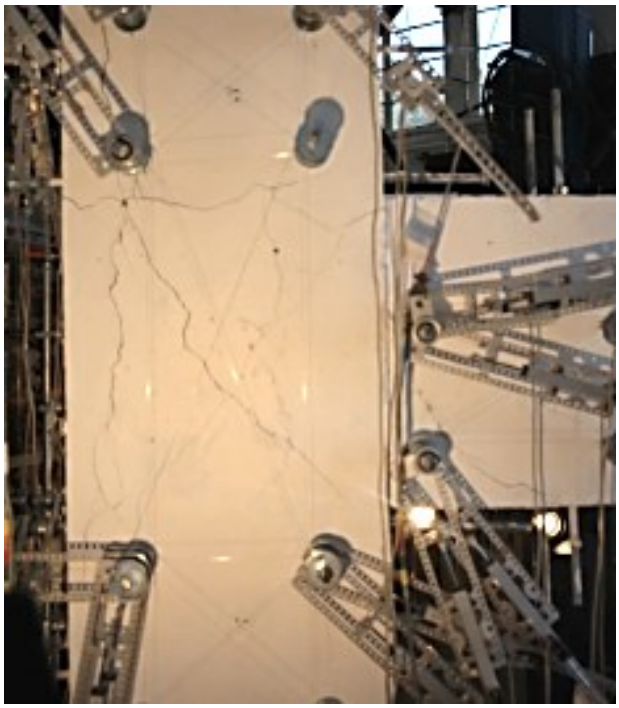

Figure 7.4 Characteristic joint panel cracks

Figure 7.3 shows joint crack propagation throughout the test. Several inclined cracks were observed in both north and east joint face faces after reaching negative peak shear strength. The main and the widest diagonal crack is the one corresponding to the main diagonal strut supported by beam reinforcement hook. The inclination of that crack matches the theoretical diagonal strut inclination of 45°-50°. The second inclined crack observed was the steeper one corresponding to the secondary strut action developed by bond forces along top beam reinforcement discussed in Chapter 2. Some other minor discontinuous inclined cracks were observed during later stages of loading. Similar crack pattern was observed during upward loading drift peaks. The X-shape of the main diagonal cracks can be noticed along with several other smaller distributed cracks. The main diagonal cracks extend outside the joint towards the outermost side of the column for a distance equal to joint height. A vertical crack was also initiated towards the outer edge of the joint at downward drift of 2.19%, which is the result of cover splitting action because of the high axial load the specimen was experiencing in the negative loading cycle. Cracks on the north and east joint face sides were connected diagonally through the joint and connected to the vertical cover splitting crack forming a large triangular concrete wedge that tended to separate from the outside corner of the column. This separation was prevented by the first column hoop above and below the joint. Prying action of the beam reinforcement end hook was not remarkable during the test. Horizontal column-joint interface flexural cracking due to tensile action on the column was observed starting at positive drift peak of 2.19%. Joint cover concrete spalling started at 3.42% drift ratio.

Figures 7.9 and 7.10 show upper column axial load and beam shear histories for the specimen. It can be observed from Fig. 7.10 that the residual beam shear forces tend to zero instead of the initial gravity preloading negative shear forces by the time the joint shear capacity is reached. Afterwards, these residual forces are essentially reversed to positive forces indicating strength degradation and gross nonlinearity in the joint performance. Since the axial loading protocol for specimen U-J-1 was based on beam shear force input, the peak axial load was reached at peak joint shear strength. Subsequently, the degradation in loaded beam shear forces and the positive residual shear forces of the unloaded beam of the unidirectional beam loading protocol resulted in the reduction of the axial load level achieved at negative drift peaks subsequent to joint shear capacity loading peak. The positive residual beam shear forces at zero displacement resulted also in the degradation of the initial gravity loading since they were fed into the axial loading protocol. Accordingly, the specimen was apple to survive lateral loading up to ± 9.68% drift ratio. The applied upper column axial load ratio at -9.68% EW drift was 0.13.

To drive the specimen to axial collapse, it was decided to switch the axial load protocol to the displacement based one described in Chapter 6 to avoid the effect of degrading beam shear forces. The test was continued using the new protocol until the axial collapse was reached at EW beam negative drift loading at -9.68%. The upper column axial load ratio at joint axial failure was 0.20. It is worth mentioning that the joint core was severely damaged through shear stresses due to excessive drift loading prior to axial failure. That was reflected by the ratio of joint shear strength coefficient at -9.68% drift to that at joint shear capacity, which was about 20%.

Figure 7.6 shows snapshots of the north joint face immediately before and during axial failure, as well as a global view of the specimens after axial collapse. The axial failure was sudden and was characterized by swaying column bar deformation mode and finally substantial dynamic instability of the subassembly represented by large side-sway of the column and slab. The test setup permitted 5 inches of side-sway of the slab and more than 2 inches of axial shortening of the column/joint before triggering a self-restraining displacement control system to secure the specimen. Detailed discussion about the mechanics of axial failure is presented in Chapter 8.

Immediately before axial failure

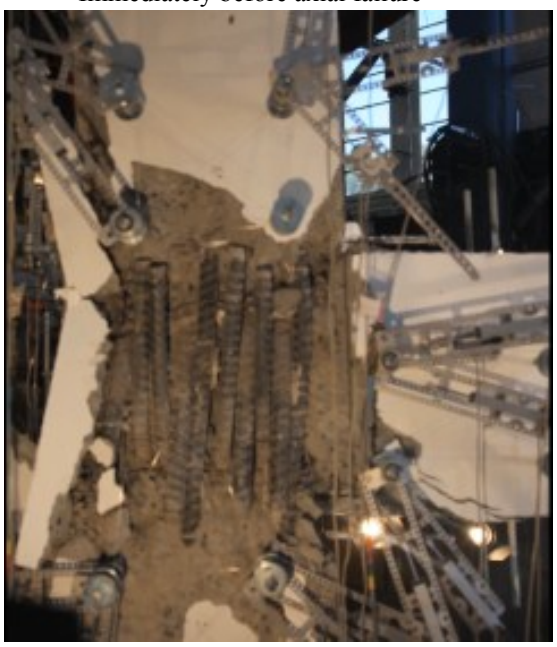

During axial failure

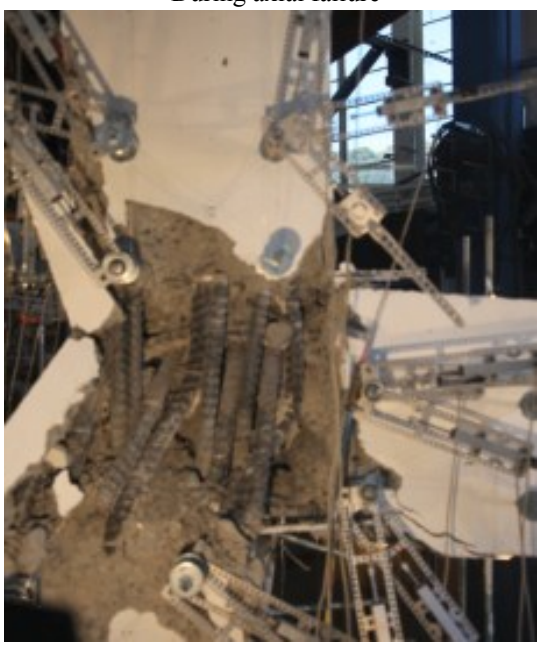

Global views of the collapsed specimen

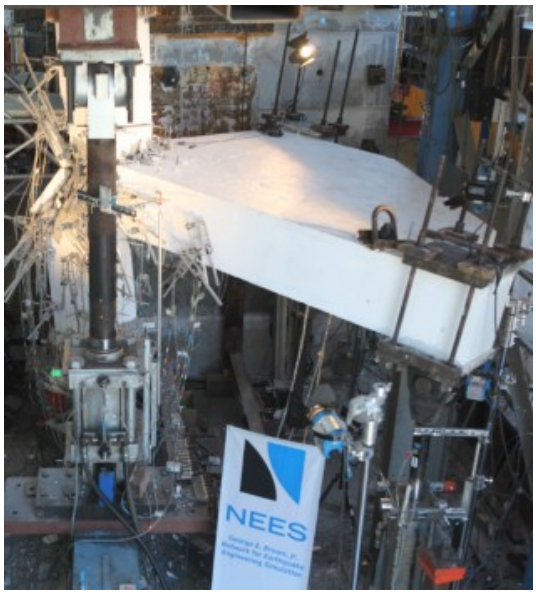

Figure 7.6 Axial failure of specimen U-J-1

Figures 7.1 and 7.2 display the force-drift relations of EW and NS beams of specimen U-J-1. The hysteretic characteristics are similar for both beams except that NS beam exhibited more pronounced pinching behavior since it was loaded already after EW beam in the alternating load protocol which amplified the effect of torsional cracking on the NS beam. The pinching behavior is characteristic in unconfined beam-column joint. It is attributed to the opening of shear cracks and bond-slip cracks that may not be closed completely in the reversed load cycle due to concrete aggregate bearing against crack surface. The pinching phenomenon is very pronounced at high drift due to severe joint distress as can be seen in Figs. 7.1 and 7.2.

Figure 7.7 and Fig. 7.8 depict the beam shear force-drift and joint shear strength-drift envelope curves for the specimen, respectively. It can be observed that the initial stiffness for EW and NS beam loading is similar until prior to reaching joint shear capacity. The joint shear strength and post peak strength envelope for the NS beam loading were lower than those of EW beam loading. In addition, an observation that can be considered characteristic in these types of tests is that the EW beam shear reached about 97% of its peak strength at peak 4a and was able to attain its peak strength at peak 5a, which is reflected by the nearly flat horizontal segment in the backbone curve. However, NS beam attained its peak strength at peak 4a and started degrading immediately afterwards, such that the horizontal segment of the backbone curve is absent. This might be attributed to the fact that the NS beam was loaded after the EW beam in the alternating loading protocol described in Chapter 6. It is worth mentioning that is was decided to put more reliance on EW beam strength and deformation characteristics in establishing and verifying analytical models in the current study.

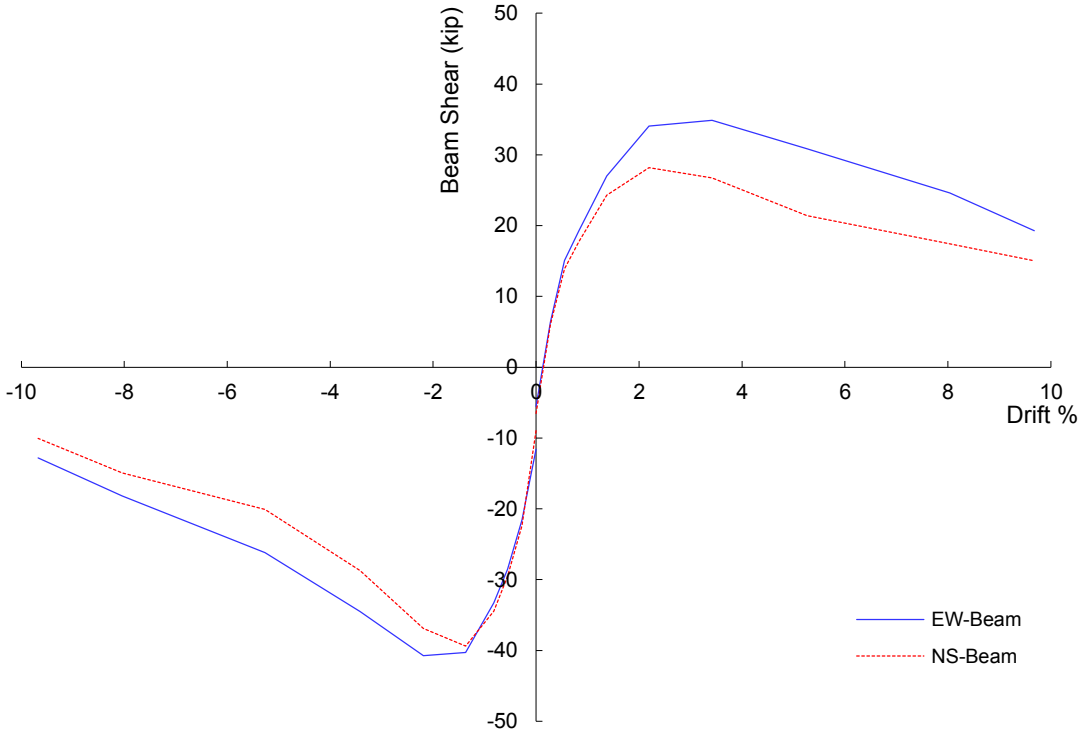

Figure 7.7 Backbone curves of specimen U-J-1 beam shear forces

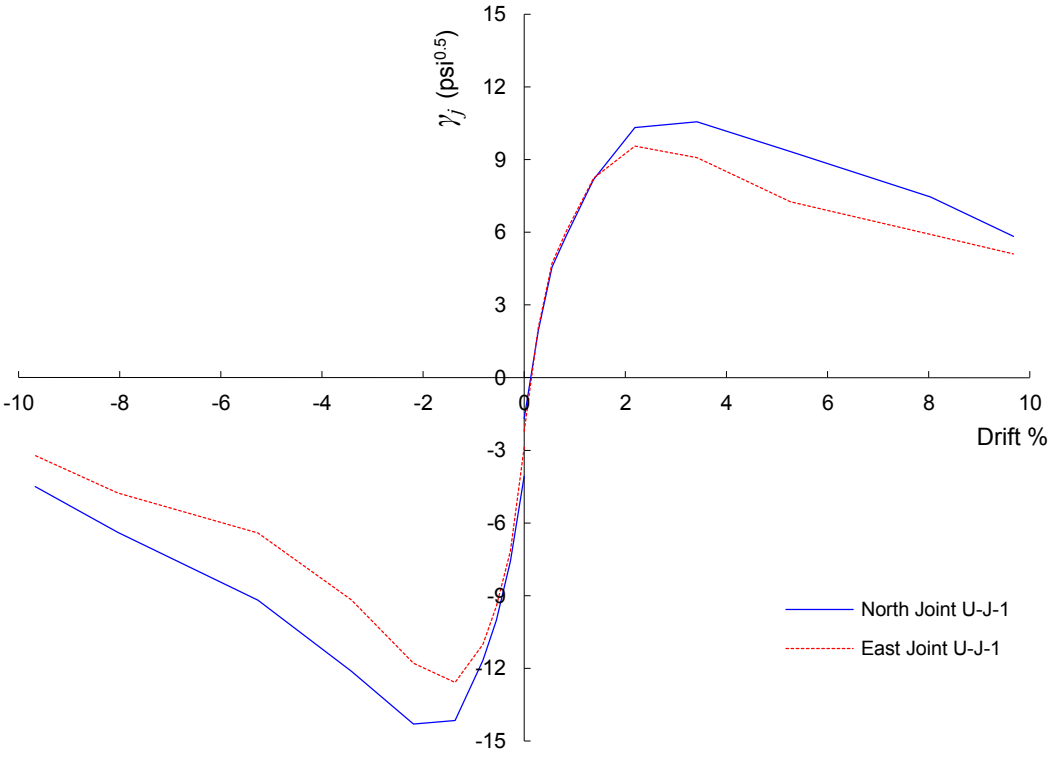

Figure 7.8 Backbone curves of specimen U-J-1 joint shear stresses

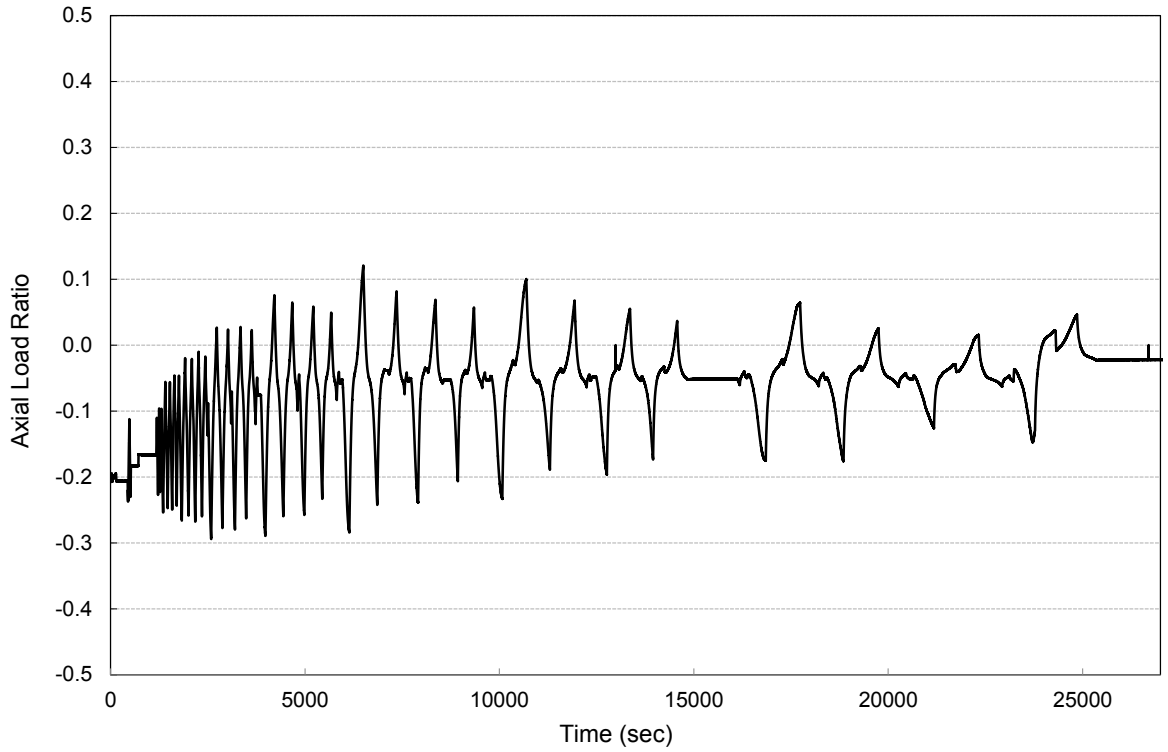

Figure 7.9 Upper column axial load History of specimen U-J-1

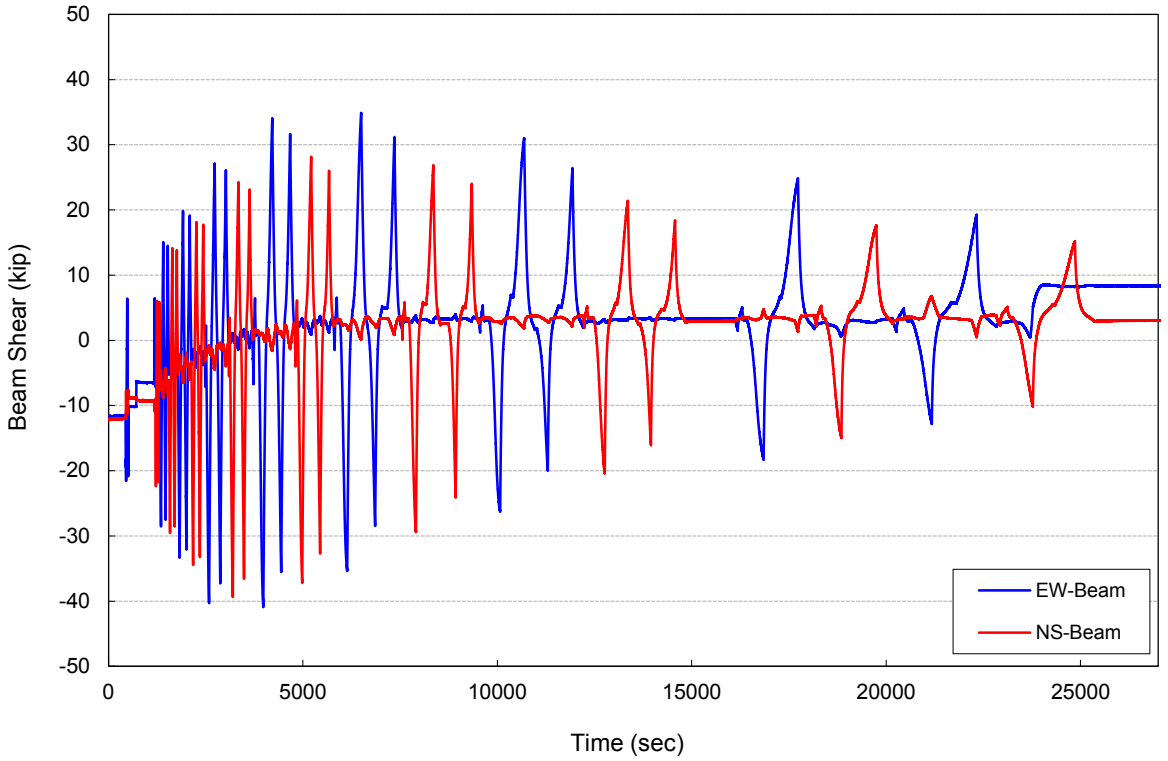

Figure 7.10 Beam shear History of specimen U-J-1

Figures 7.12 and 7.13 display the normalized joint shear stress-strain hysteretic behavior of north and east joint faces. It is worth mentioning that the strain measurements are approximate as averaged from diagonal, transverse and longitudinal displacement transducers as explained in Chapter 6. The north joint face downward loading shear capacity corresponded to a shear strain of -0.0066 radians, while the shear strain recorded at peak positive joint shear strength was 0.0132 radians. The east joint face downward loading shear capacity corresponded to a shear strain of -0.0039 radians, while the shear strain recorded at peak positive joint shear stress was 0.0048 radians. The envelope curves for the joint shear stress-strain hysteresis are presented in Fig. 7.11 for potential use to develop backbone curves for joint modeling in concrete building frame simulation.

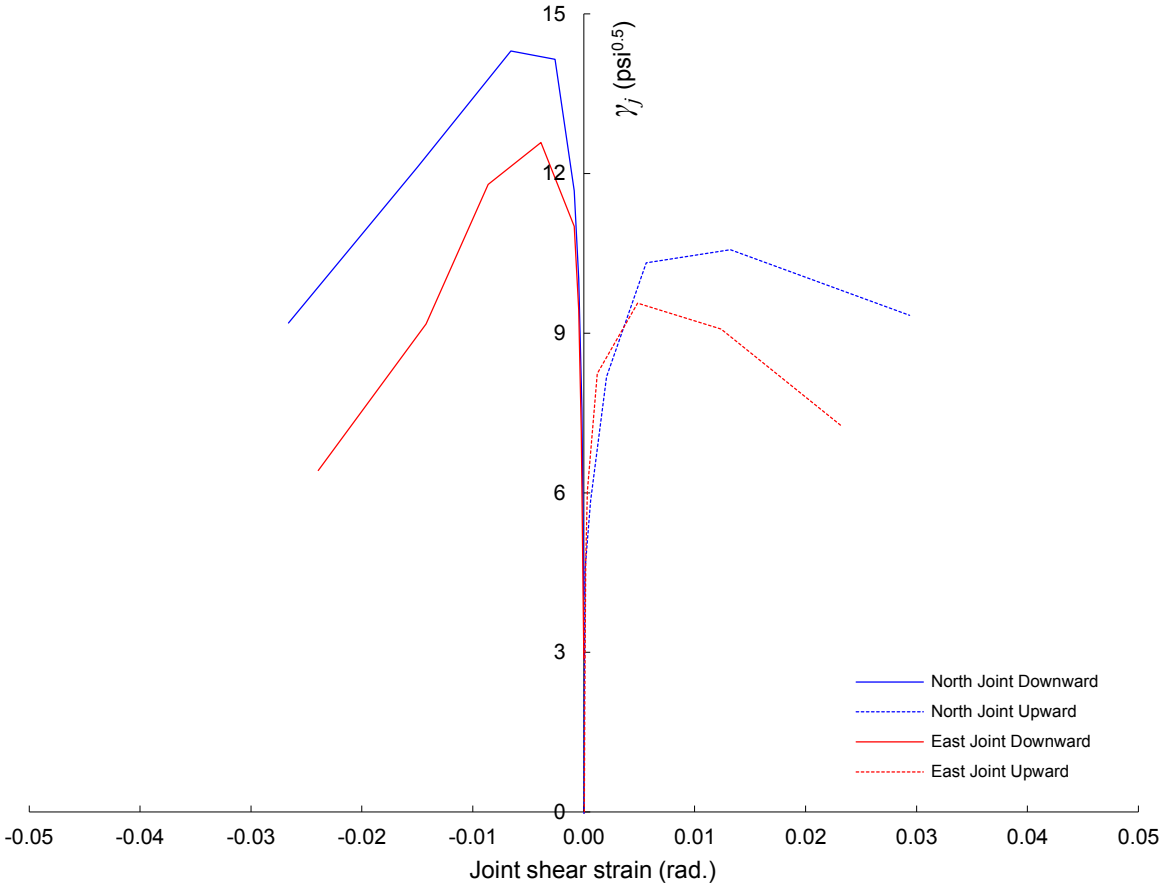

Figure 7.11 Joint shear stress-strain envelopes for specimen U-J-1

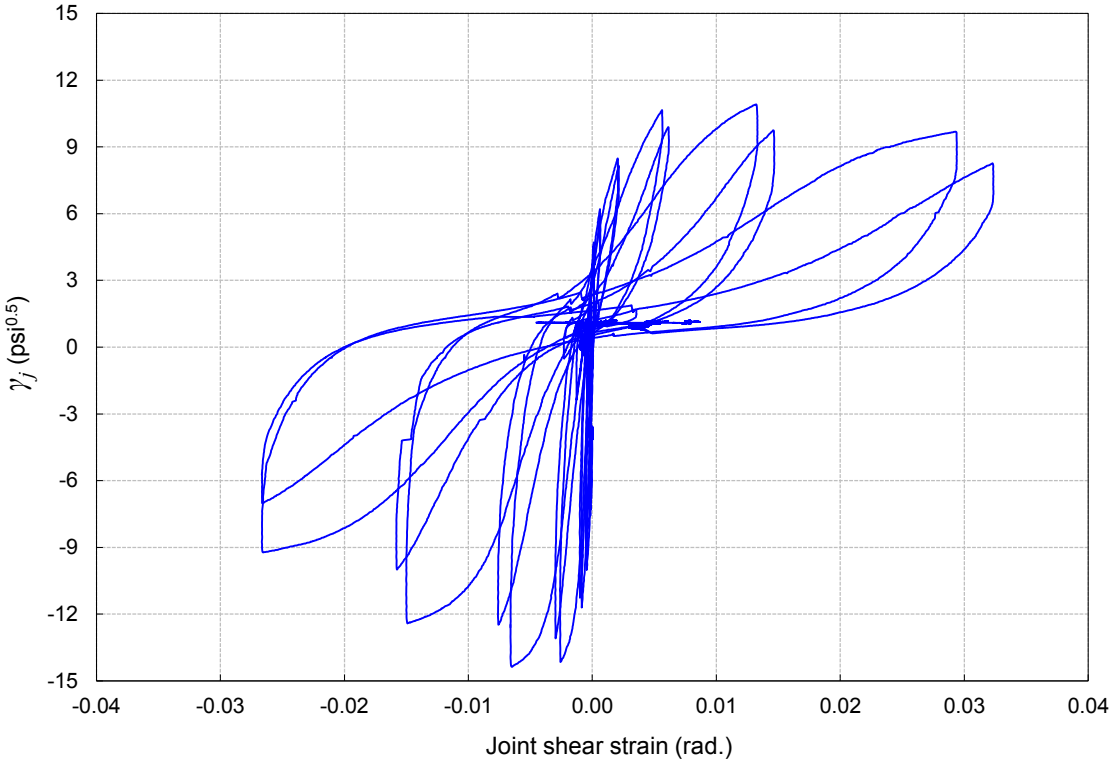

Figure 7.12 North joint face shear stress-strain relation for specimen U-J-1

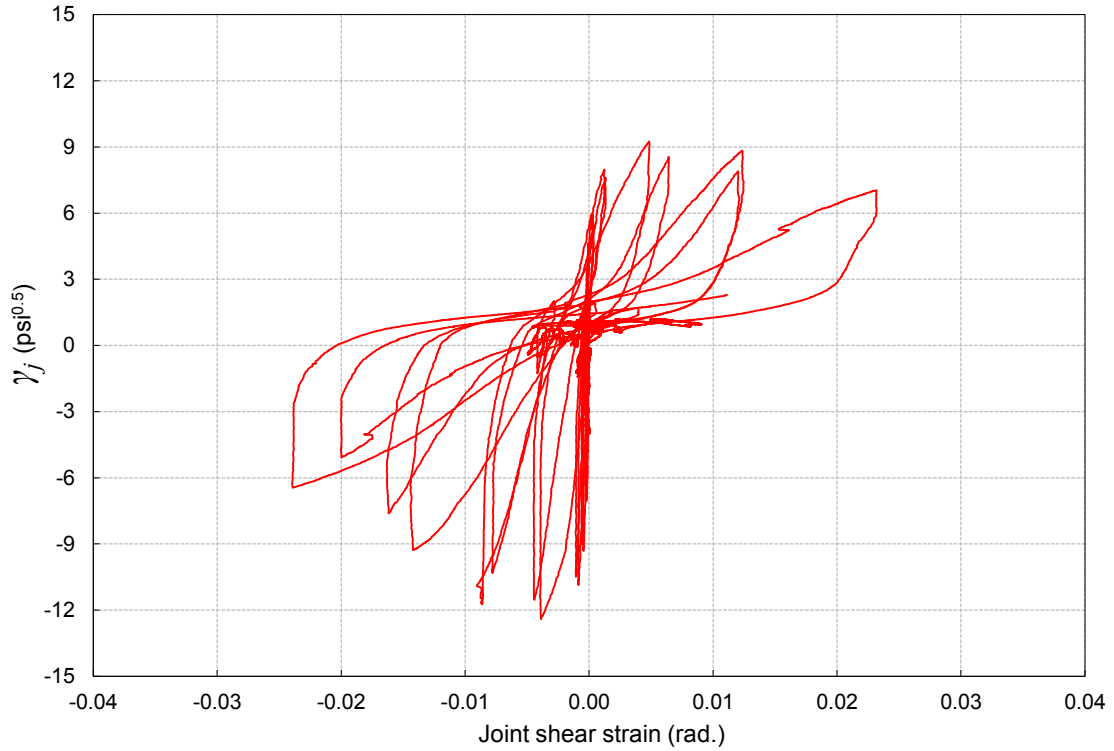

Figure 7.13 East joint face shear stress-strain relation for specimen U-J-1

Figure 7.14 displays the peak-to-peak effective stiffness degradation plots for both EW and NS beam loading. It can be noticed that the effective stiffness of both loading beams is very similar except after reaching joint shear capacity, after which the NS beam has less effective stiffness. Effective stiffness degradation is identical for both directions throughout. The stiffness degradation between the first and second peak of each displacement step is much less pronounced than that between the different levels of displacement amplitudes until reaching very high drift ratios at which the difference between the said stiffnesses is not significant.

Figure 7.15 displays cumulative energy dissipation of specimen U-J-1 during EW and NS beams loading. It is clear that energy dissipation of both beams is identical until nearly peak 6a (±3.42% drift), which is approximately the peak corresponding to joint shear capacity. Afterwards, that is, in the post-peak regime, the energy dissipation of EW-beam (north joint face) is more significant than that of NS-beam (east joint face), especially in the later stages of loading. Given the equal displacement input, this reflects less post-peak strength and stiffness degradation and wider post-peak hysteretic loops during EW beam loading. This is evident from Figs. 7.1, 7.2, 7.11, 7.12 and 7.13. The reason for this is because EW beam was loaded first which exhausted NS beam due to torsional cracking and east joint face due to shear cracking before they were loaded in their own plane. The rate of energy dissipation increased exponentially in the post-peak region which reflects the highly pinched behavior of the unconfined beam-column joint.

Figure 7.16 shows the contribution of joint shear strain to the overall drift of the joint subassembly represented by the ratio of the beam tip displacement induced by joint shear deformation to the total beam displacement. The contribution of the north joint face to the EW-beam drift was 15% and 30% for the negative and positive peak joint shear strength, respectively. The east joint face shear deformation contribution to the total drift of NS-beam at joint shear capacity peaks was about 9% and 27% for negative and positive loading cycles, respectively. At drift peak of ±5.27%, joint shear strain contribution was more than 40% for both loading direction. Measurements obtained beyond this peak were not reliable due to the effect of spalling concrete cover. These values confirm the need to model the joint as a flexible element in analytical simulation of RC frames, especially for unconfined beam-column joints in older buildings.

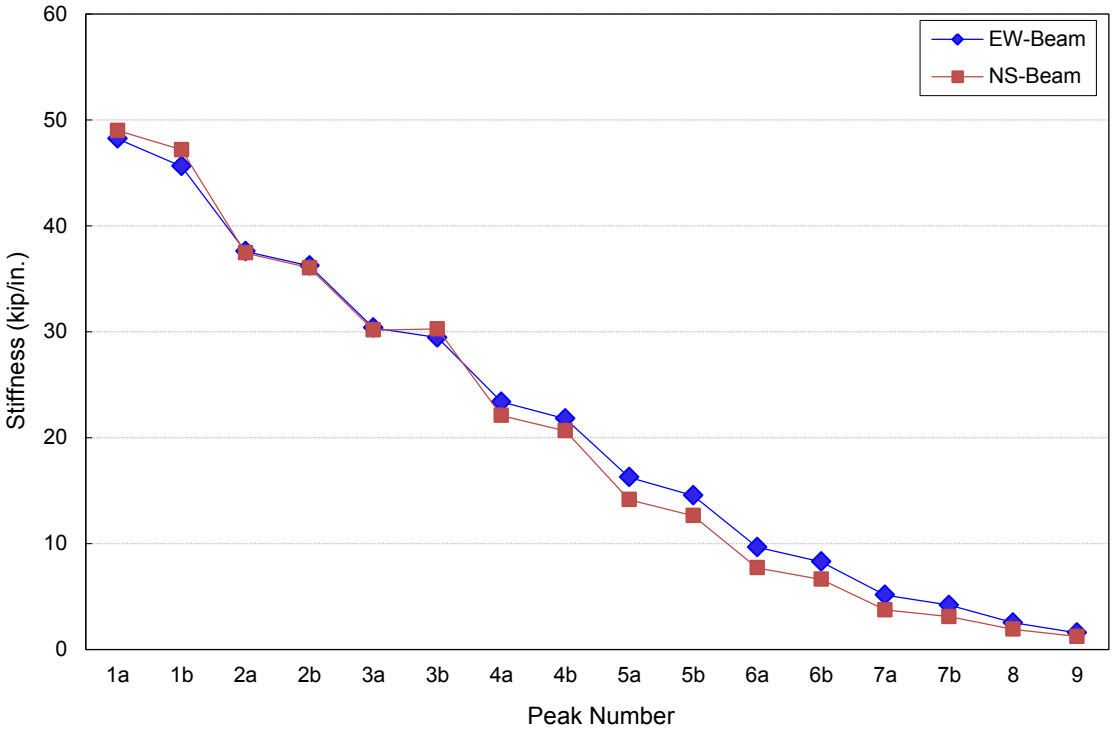

Figure 7.14 Peak-to-peak stiffness for specimen U-J-1

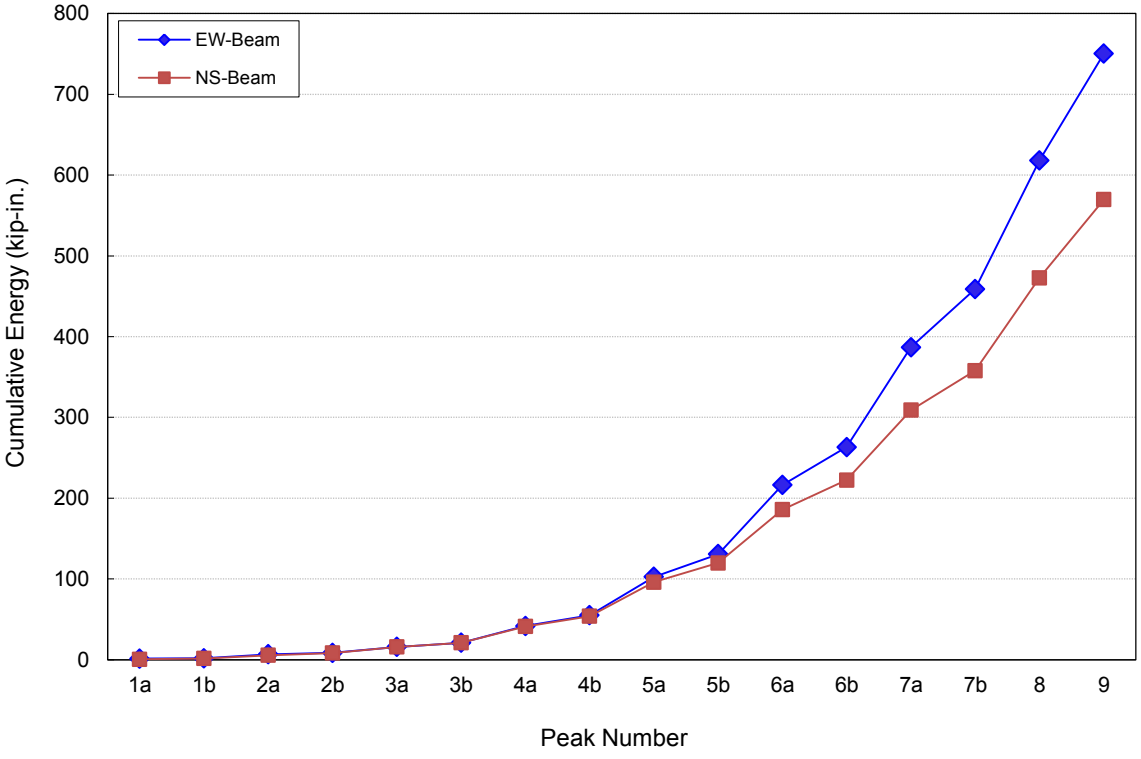

Figure 7.15 Peak-to-peak cumulative energy dissipation for specimen U-J-1

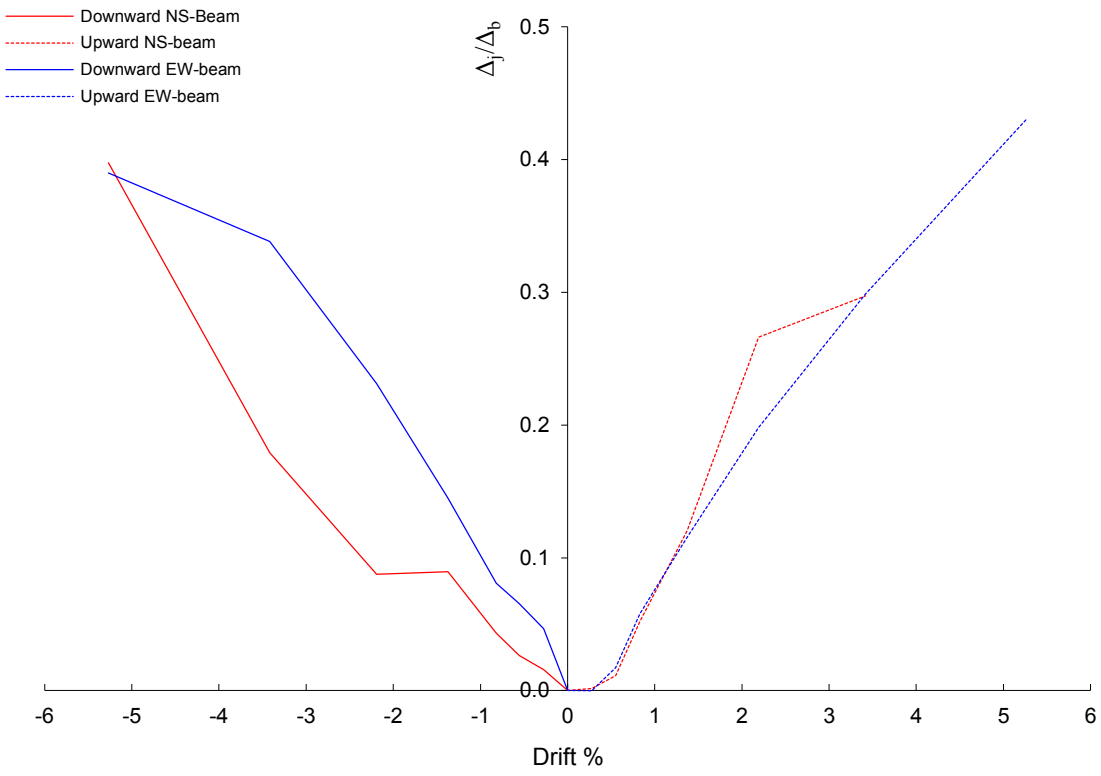

Figure 7.16 Joint shear strain contribution to total drift ratio for specimen U-J-1

Figure 7.17 and Fig. 7.18 exhibit the strain distribution of slab top reinforcement at first cycles of negative drift peaks of EW and NS beam loading. Strain profile is normalized by yield strain ε_y. The first and second slab reinforcement bars adjacent to the EW-beam yielded prior to the negative joint shear strength peak 5a (-2.19% drift) although beam reinforcement did not yield at this peak. The slab reinforcement parallel to NS beam did not yield throughout the test. Bottom slab reinforcement bars did not yield due to their location near neutral axis and their poor anchorage.

Figures 7.19 and 7.20 display the strain profile of the exterior and interior beam reinforcement bars under the first negative drift loading peaks of EW beam. The beam reinforcement did not experience yield before joint shear strength peak during EW and NS beam negative drift loading. Figures 7.21 and 7.22 show the strain profile of the exterior and interior beam reinforcement for the first positive drift loading peaks of NS beam. EW beam interior reinforcement bar just reached yield prior to reaching north joint face shear capacity during positive drift loading. However, the rest of bottom beam bars did not yield. In an average since, this failure mode can be also considered J-Failure. NS beam reinforcement did not yield until after reaching east joint face shear capacity. Strain profile might suggest that at later stages of EW positive loading, yielding penetrated into the joint core. The beam reinforcement longitudinal strain was reversed from tensile strain at beam-joint interface into compressive strain adjacent to the starting point of hook bent which might suggest either bond failure or full development of tensile force at earlier point. Outermost corner reinforcing bar CNE of the upper column did not yield in tension during the downward EW beam loading. After peak shear

strength, this column bar yielded in compression. During the NS beam downward loading, the CNE column bar did not yield throughout the test. The lower column corner bar CNW yielded in tension after reaching joint shear strength in the EW beam downward loading direction. Similarly, the CNE lower column and CNW upper column bars did not yield in tension before reaching joint shear strength during upward loading of EW beam and NS beam. However, they yielded afterwards. Appendix A presents the strain distribution of all column bars recorded during different stage of loading.

Figures 7.23 and 7.24 show strain profile along the height of the intermediate column reinforcement bars CN and CE during first drift loading peaks, respectively. It can be observed that longitudinal strains at the joint mid-height never reached yield. An increase in joint mid-height intermediate column bar strains over their counterpart at column joint interface was observed with increasing axial compression loads. This is attributed to the buckling effect of the unrestrained column bars in the middle of the joint. At high drifts associated with high axial tensile load, the strains of the intermediate column bars at mid-joint height are similar to those at column joint interface indicating that these bars apparently did not act as vertical joint reinforcement. This suggests that the contribution of such column reinforcement bars to joint shear strength may be negligible. This observation is contrary to that made by Wong [155].

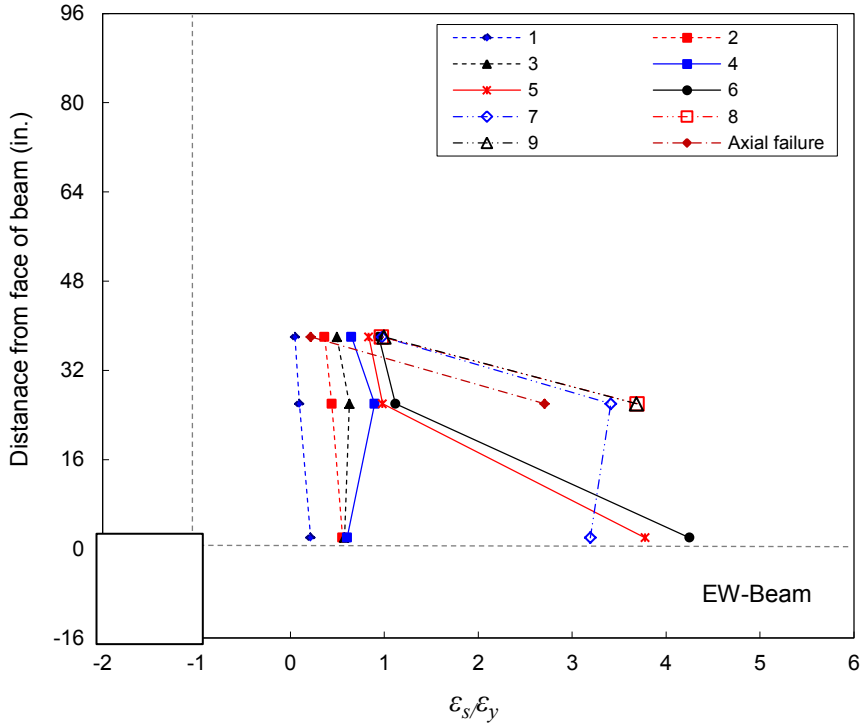

Figure 7.17 Slab top reinforcement strain distribution for U-J-1 first negative drift peaks for EW-Beam loading

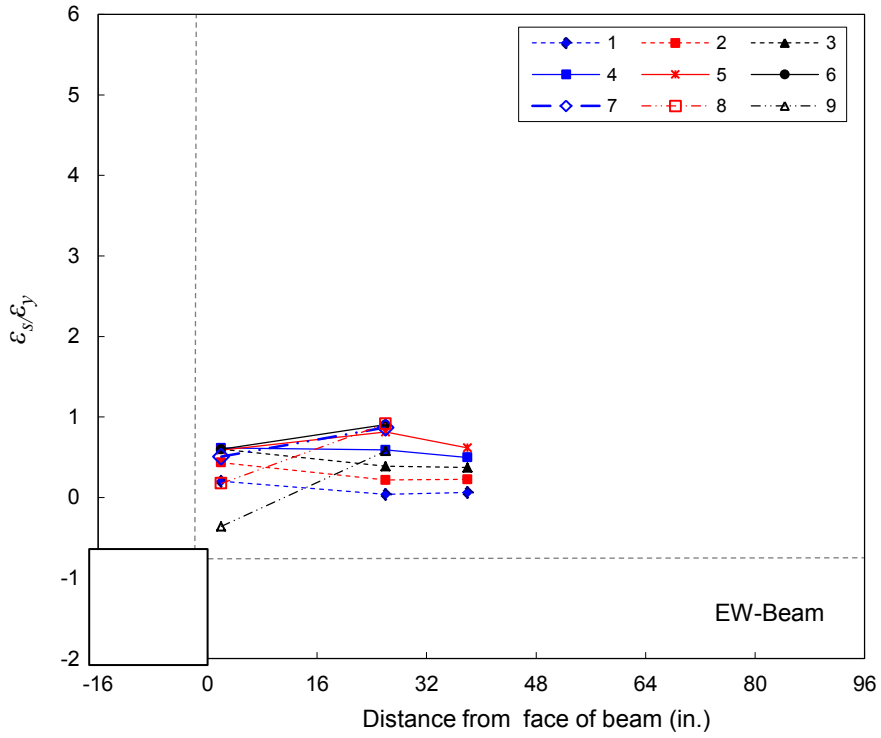

Figure 7.18 Slab top reinforcement strain distribution for U-J-1 first negative drift peaks for NS-beam loading

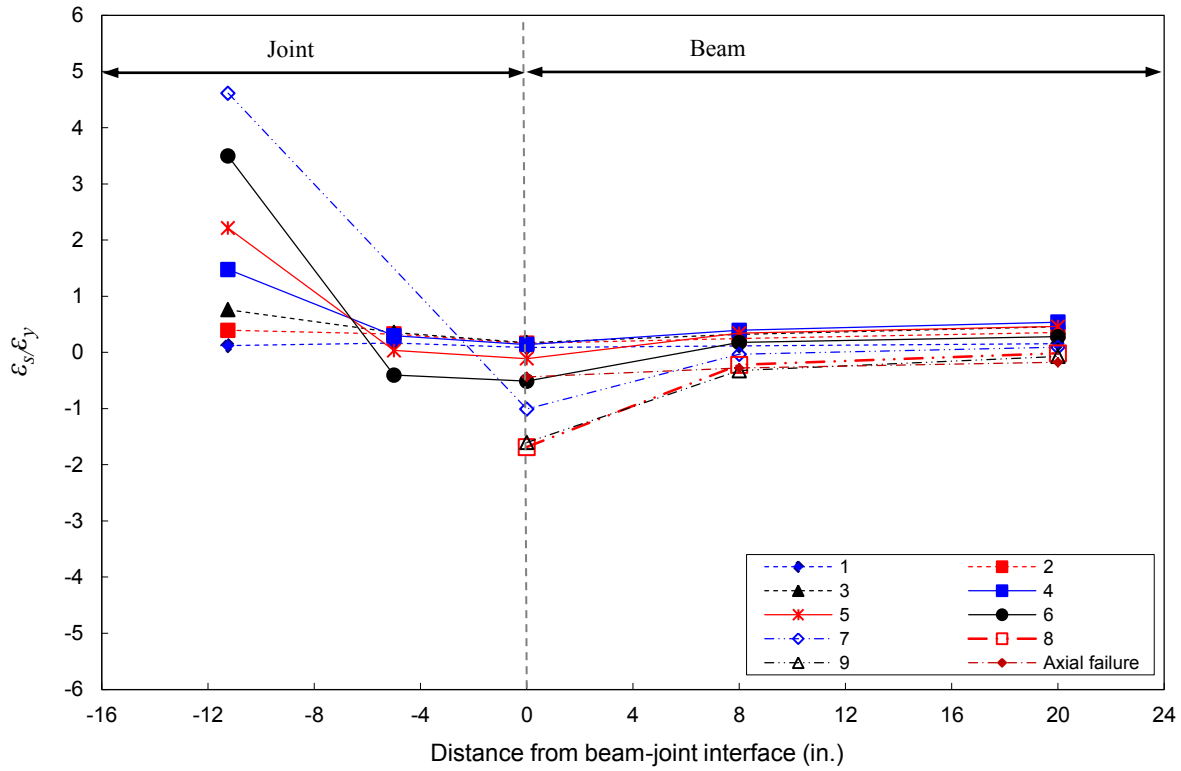

Figure 7.19 EW-beam top exterior longitudinal reinforcement strain for U-J-1 first negative drift peaks

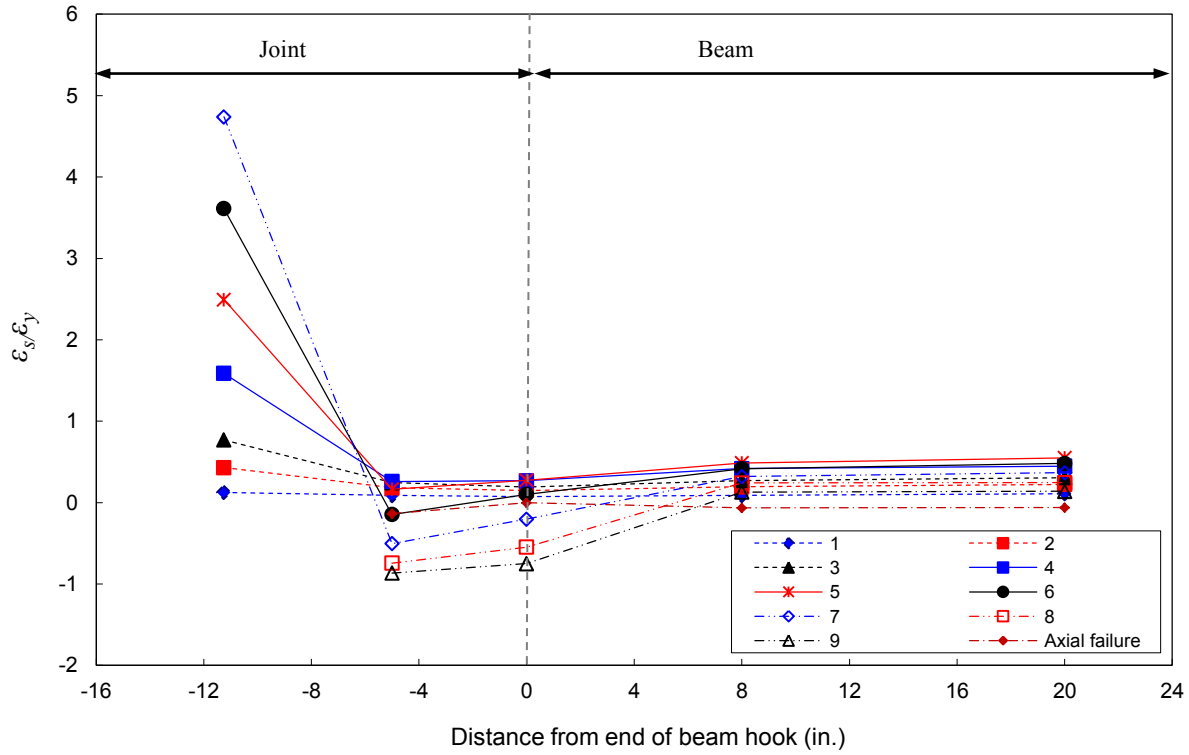

Figure 7.20 EW-beam top interior longitudinal reinforcement strain for U-J-1 first negative drift peaks

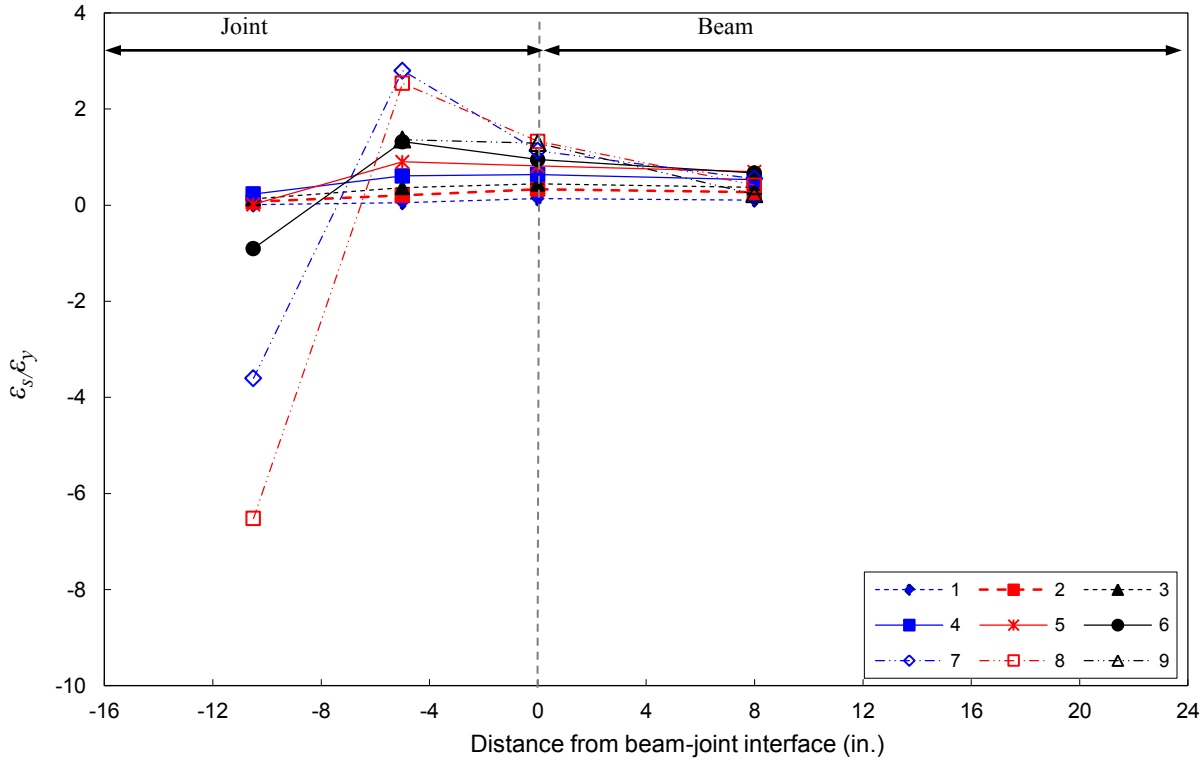

Figure 7.21 EW-beam bottom exterior longitudinal reinforcement strain for U-J-1 first positive drift peaks

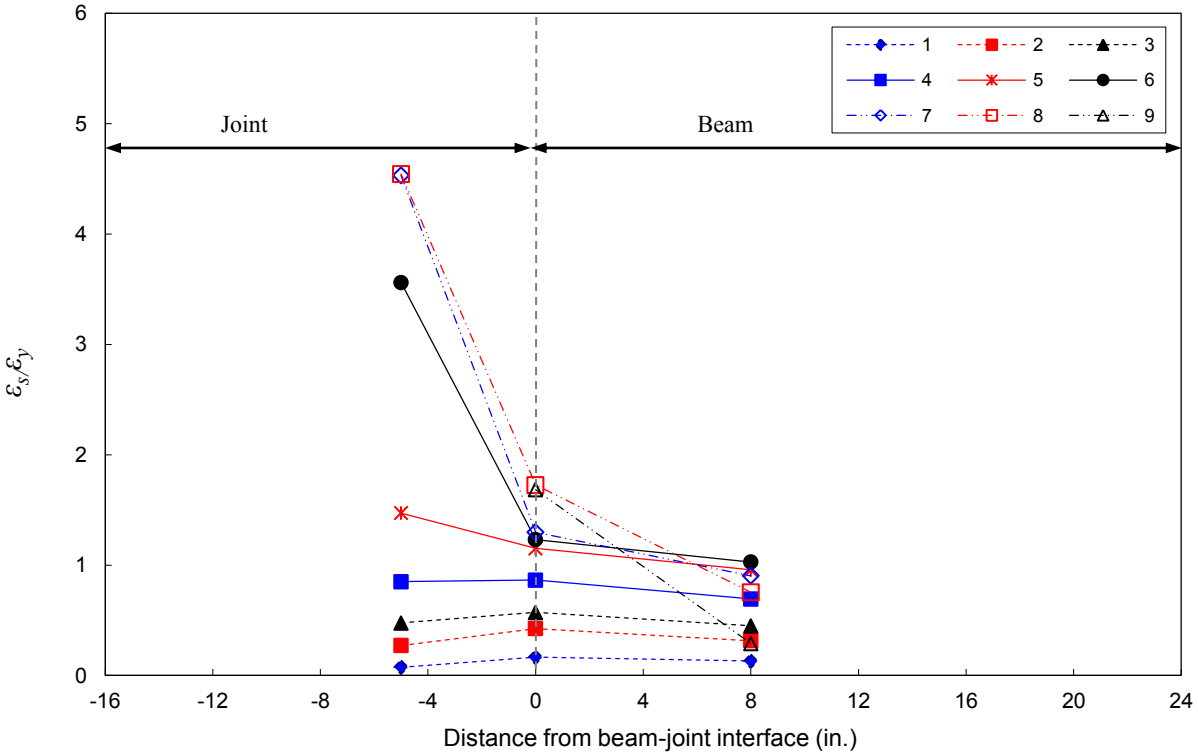

Figure 7.22 EW-beam bottom interior longitudinal reinforcement strain for U-J-1 first positive drift peaks

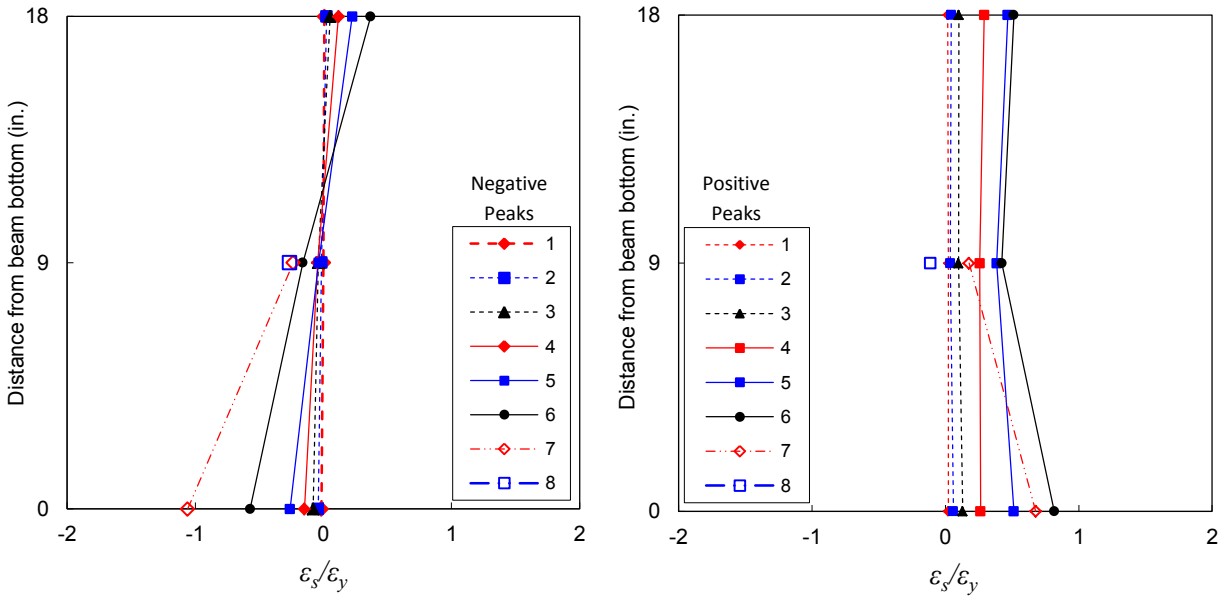

Figure 7.23 Strain development for column intermediate reinforcement CN of U-J-1 EW-beam drift peaks

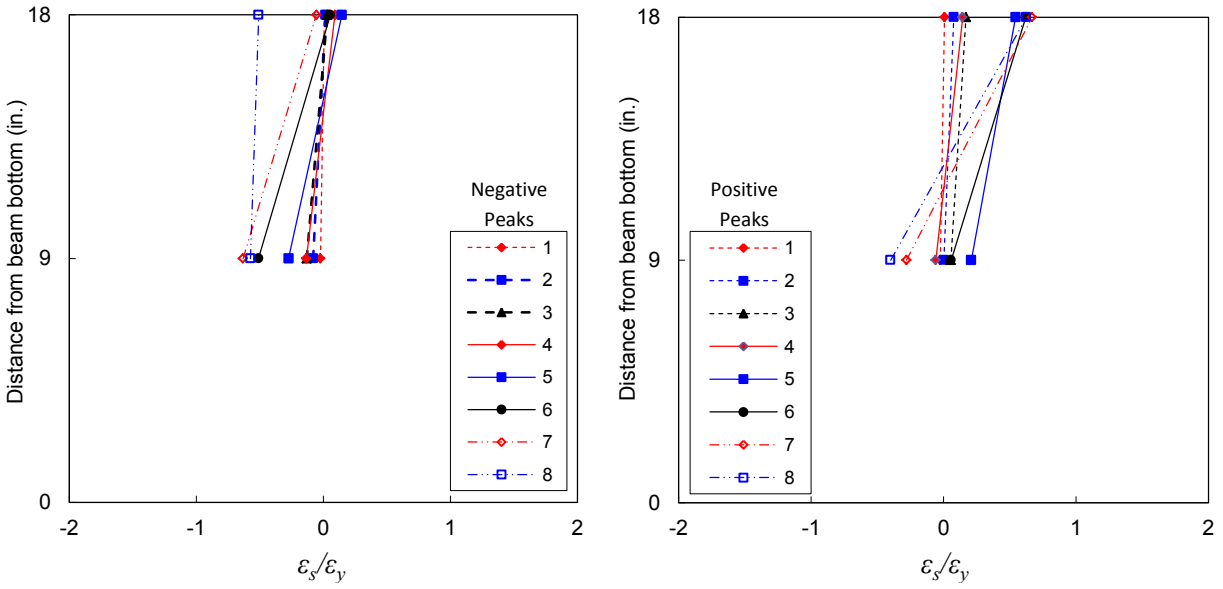

Figure 7.24 Strain development for column intermediate reinforcement CE of U-J-1 NS-beam drift peaks

Table 7.1.a Summary of performance parameters of specimen U-J-1, EW direction, downward loading

Load Peak	*Drift* (%)	$V_{b\text{-}EW}$ (kip)	$V_{c\text{-}EW}$ (kip)	$V_{j\text{-}N}$ (kip)	γ_j ($psi^{0.5}$)	γ_s (rad.)	$P_{u,col}$ (kip)	$P_{L,col}$ (kip)	Axial load ratio	K_P (kip/in.)	E_i (kip-in.)	$E_{cum.}$ (kip-in.)
0	0.00	-11.6	-8.38	-80.7	-4.06	0.0000	-287	-310	-0.22	-	-	-
1a	-0.28	-21.6	-15.6	-151	-7.57	-0.0002	-328	-357	-0.25	48.2	1.35	1.35
1b	-0.28	-20.7	-14.9	-144	-7.25	-0.0002	-319	-348	-0.24	45.6	0.43	1.79
2a	-0.55	-28.6	-20.7	-199	-10.0	-0.0005	-354	-386	-0.27	37.6	4.95	6.74
2b	-0.55	-27.6	-19.9	-192	-9.66	-0.0005	-344	-376	-0.26	36.2	1.77	8.52
3a	-0.82	-33.3	-24.1	-23.0	-11.7	-0.0009	-370	-406	-0.28	30.4	7.29	15.8
3b	-0.82	-31.8	-23.0	-222	-11.2	-0.0010	-358	-392	-0.27	29.5	5.09	20.9
4a	-1.37	-40.3	-29.2	-281	-14.2	-0.0026	-410	-451	-0.31	23.4	20.9	41.8
4b	-1.37	-36.7	-26.5	-256	-12.9	-0.0030	-382	-419	-0.29	21.8	13.1	54.9
5a	-2.19	-40.7	-29.5	-284	-14.3	-0.0066	-402	-442	-0.31	16.3	47.7	103
5b	-2.19	-35.4	-25.6	-247	-12.4	-0.0075	-360	-394	-0.27	14.5	28.0	131
6a	-3.42	-34.5	-25.0	-241	-12.1	-0.0150	-389	-425	-0.30	9.67	85.6	216
6b	-3.42	-28.5	-20.6	-199	-10.0	-0.0158	-337	-364	-0.26	8.29	46.9	263
7a	-5.27	-26.2	-19.0	-183	-9.19	-0.0266	-325	-348	-0.25	5.15	124	387
7b	-5.27	-20.0	-14.5	-139	-7.01	-0.0266	-263	-280	-0.20	4.19	72.0	459
8a	-8.04	-18.2	-13.2	-127	-6.38	-0.0130	-243	-257	-0.18	2.54	159	618
9a	-9.68	-12.8	-9.27	-89.3	-4.49	NA	-175	-181	-0.13	1.58	132	750

Table 7.1.b Summary of performance parameters of specimen U-J-1, NS direction, downward loading

Load Peak	*Drift* (%)	$V_{b\text{-}NS}$ (kip)	$V_{c\text{-}NS}$ (kip)	$V_{j\text{-}E}$ (kip)	γ_j ($psi^{0.5}$)	γ_s (rad.)	$P_{u,col}$ (kip)	$P_{L,col}$ (kip)	Axial load ratio	K_P (kip/in.)	E_i (kip-in.)	$E_{cum.}$ (kip-in.)
0	0.00	-8.98	-6.5	-57.1	-2.87	-0.0002	-233	-249	-0.18	-	-	-
1a	-0.28	-22.4	-16.2	-142	-7.15	-0.0002	-316	-344	-0.24	49.0	0.57	0.57
1b	-0.28	-21.8	-15.8	-138	-6.95	-0.0002	-310	-337	-0.24	47.2	0.92	1.49
2a	-0.55	-29.5	-21.4	-188	-9.44	-0.0004	-347	-380	-0.26	37.5	3.99	5.47
2b	-0.55	-28.6	-20.7	-181	-9.12	-0.0006	-339	-370	-0.26	36.0	2.70	8.18
3a	-0.82	-34.4	-24.9	-219	-11.0	-0.0009	-373	-409	-0.28	30.2	7.66	15.8
3b	-0.82	-33.2	-24.1	-211	-10.6	-0.0011	-362	-396	-0.28	30.3	5.18	21.0
4a	-1.37	-39.4	-28.5	-250	-12.6	-0.0039	-390	-428	-0.30	22.1	20.1	41.1
4b	-1.37	-36.3	-26.3	-231	-11.6	-0.0045	-365	-400	-0.28	20.7	12.7	53.8
5a	-2.19	-36.9	-26.7	-235	-11.8	-0.0086	-357	-391	-0.27	14.2	42.2	96.0
5b	-2.19	-32.3	-23.4	-205	-10.3	-0.0078	-322	-351	-0.24	12.7	23.8	120
6a	-3.42	-28.7	-20.8	-182	-9.18	-0.0142	-328	-353	-0.25	7.70	65.9	186
6b	-3.42	-23.6	-17.1	-150	-7.53	-0.0162	-283	-303	-0.22	6.63	36.8	222
7a	-5.27	-20.1	-14.5	-128	-6.42	-0.0239	-271	-288	-0.21	3.75	86.5	309
7b	-5.27	-16.1	-11.7	-102	-5.14	-0.0200	-241	-254	-0.18	3.12	48.9	358
8a	-8.04	-14.9	-10.8	-95.0	-4.77	-	-245	-259	-0.19	1.92	115	473
9a	-9.68	-10.1	-7.29	-64.0	-3.22	-	-177	-182	-0.13	1.24	96.9	570

Table 7.1.c Summary of performance parameters of specimen U-J-1, EW direction, upward loading

Load Peak	*Drift* (%)	$V_{b\text{-}EW}$ (kip)	$V_{c\text{-}EW}$ (kip)	$V_{j\text{-}N}$ (kip)	γ_j ($psi^{0.5}$)	γ_s (rad.)	$P_{u,col}$ (kip)	$P_{L,col}$ (kip)	Axial load ratio	K_P (kip/in.)	E_i (kip-in.)	$E_{cum.}$ (kip-in.)
1a	0.28	6.40	4.63	39.2	2.00	-0.0001	-156	-161	-0.12	48.2	1.35	1.35
1b	0.28	5.83	4.22	35.7	1.82	-0.0001	-157	-162	-0.12	45.6	0.43	1.79
2a	0.55	15.1	10.9	92.4	4.71	0.0001	-77.7	-71.4	-0.06	37.6	4.95	6.74
2b	0.55	14.5	10.5	89.0	4.54	0.0001	-78.2	-72.0	-0.06	36.2	1.77	8.52
3a	0.83	19.3	14.0	118	6.03	0.0006	-31.7	-18.9	-0.02	30.4	7.29	15.8
3b	0.83	19.1	13.9	117	5.98	0.0006	-29.2	-16.0	-0.02	29.5	5.09	20.9
4a	1.37	27.0	19. 6	166	8.44	0.0020	35.7	58.2	0.03	23.4	20.9	41.8
4b	1.37	26.1	18.9	160	8.16	0.0021	32.9	55.0	0.03	21.8	13.1	54.9
5a	2.19	34.1	24.7	209	10.7	0.0056	105	138	0.08	16.3	47.7	103
5b	2.19	31.5	22.8	193	9.85	0.0062	89.8	120	0.07	14.5	28.0	131
6a	3.42	34.9	25.3	214	10.9	0.0132	168	203	0.13	9.67	85.6	216
6b	3.42	31.1	22.5	190	9.71	0.0146	113	145	0.09	8.29	46.9	263
7a	5.27	30.8	22.3	189	9.64	0.0294	139	171	0.11	5.15	124	387
7b	5.27	26.4	19.1	162	8.26	0.0323	94.3	123	0.07	4.19	72.0	459
8a	8.04	24.6	17.8	151	7.70	0.0405	87.5	113	0.07	2.54	159.	618
9a	9.68	19.3	14.0	118	6.00	0.15	21.4	41.2	0.02	1.58	132	750

Table 7.1.d Summary of performance parameters of specimen U-J-1, NS direction, upward loading

Loading Peak	*Drift* (%)	$V_{b\text{-}NS}$ (kip)	$V_{c\text{-}NS}$ (kip)	$V_{j\text{-}E}$ (kip)	γ_j ($psi^{0.5}$)	γ_s (rad.)	$P_{u,col}$ (kip)	$P_{L,col}$ (kip)	Axial load ratio	K_P (kip/in.)	E_i (kip-in.)	$E_{cum.}$ (kip-in.)
1a	0.28	6.05	4.38	41.6	2.05	-0.0001	-134	-135	-0.10	49.0	0.57	0.57
1b	0.28	5.61	4.06	38.6	1.91	-0.0001	-135	-137	-0.10	47.2	0.92	1.49
2a	0.55	13.9	10.1	95.6	4.72	-0.0001	-65.2	-57.1	-0.05	37.5	3.99	5.47
2b	0.55	13.3	9.60	91.2	4.50	-0.0001	-68.1	-60.4	-0.05	36.0	2.70	8.18
3a	0.83	17.8	12.9	122	6.03	0.0003	-14.0	-0.14	-0.01	30.2	7.66	15.8
3b	0.83	19.1	13.9	132	6.50	0.0003	-29.2	-16.0	-0.02	30.3	5.18	21.0
4a	1.37	24.3	17.6	167	8.24	0.0012	38.3	61.2	0.03	22.1	20.1	41.1
4b	1.37	23.1	16.8	159	7.86	0.0013	31.7	53.7	0.02	20.7	12.7	53.8
5a	2.19	28.2	20.4	194	9.56	0.0048	81.3	110	0.06	14.2	42.2	96.0
5b	2.19	25.9	18.8	178	8.79	0.0065	68.0	95.1	0.05	12.7	23.8	120
6a	3.42	26.7	19.4	184	9.08	0.0124	95.0	124	0.07	7.72	65.9	186
6b	3.42	24	17.4	165	8.16	0.0120	79.0	106	0.06	6.63	36.8	222
7a	5.27	21.4	15.5	147	7.27	0.0232	77.0	101	0.06	3.75	86.5	309
7b	5.27	18.4	13.3	126	6.24	-	51.1	73.0	0.04	3.12	48.9	358
8a	8.04	17.4	12.6	120	5.92	-	34.0	54.2	0.03	1.92	115	473
9a	9.68	15.1	10.9	103	5.11	-	64.0	87.2	0.05	1.24	96.9	570

7.3.2 Specimen U-J-2

Table 7.2 presents the characteristic response parameters of specimen U-J-2. Figures 7.28 and 7.29 display the force-drift ratio relations of specimen U-J-2 for EW beam and NS beam, respectively. The force-drift response of EW and NS beams are very similar except for a slight variation in the maximum beam shear probably resulting from loading EW beam before NS beam in the unidirectional loading protocol as mentioned earlier. Pinching in the post-peak regime is evident.

The first north joint face diagonal crack occurred at EW beam drift peak of ±0.82% (peak 3a). The first east joint face diagonal crack developed at NS beam negative drift peak of -0.82% (peak 3a) and positive drift peak of 1.37% (peak 4a). The mode of shear failure of specimen U-J-2 was J-failure for both EW-beam and NS-beam downward and upward loading. Figure 7.25 exhibits north joint face crack development and propagation during the test.

The axial failure of the joint took place during the second cycle of negative EW-beam displacement group 6b at -3.06% drift. This corresponds to an upper column axial load level of 0.43 and joint shear strength coefficient of 4.30. Prior to axial failure, joint diagonal and vertical cracks significantly widened, and a very significant bulging of joint concrete cover was observed, possibly caused by buckling of column longitudinal reinforcement within the joint. Unlike specimen U-J-1 with lower axial load, no joint concrete cover spalling occurred, hence the axial failure was relatively sudden. Inspection following the axial failure indicated that the joint core was not as much damaged as that of specimen U-J-1. The axial failure was characterized by global spalling of joint concrete cover, severe buckling of column unconfined reinforcement within the joint, significant crushing of joint concrete core, breaking of the concrete wedge supported by column ties and longitudinal bars, and finally substantial dynamic instability of the subassembly represented by large side-sway of the column and slab.

The maximum shear force in the downward loading direction was reached at negative drift peak of -1.30% (peak 4a) for EW-beam loading and at -0.82% drift (peak 3a) for NS-beam loading. Major diagonal cracking was observed in the joint and at these drift peaks. The corresponding maximum negative joint shear strength coefficient γ_j was 9.98 for the north joint face and 8.97 for the east joint face, respectively. The maximum applied upper column axial compression load ratio of 0.46 was reached at negative drift peak 4a, the same peak the beam-column joint reached its shear capacity. The maximum beam shear force in the positive direction was reached at positive drift peak of 2.19% (peak 5a) for both EW and NS beam loading. The corresponding joint shear strength coefficient γ_j was 7.01 and 6.60 for north joint face and east joint face, respectively. The maximum applied upper column axial tension load ratio of 0.03 was reached at positive drift peak 5a. Similar to specimen U-J-1, NS-beam loading resulted in lower east joint face shear strength at lower drift ratios compared to the EW-beam loading and north joint face strength. The ratio of joint shear strength coefficient at axial failure to that at joint shear capacity was 0.43.

Both joint shear strength models proposed in Chapter 5 were able to accurately predict joint shear strength of the current specimen, (Table 5.1). ASCE 41 provisions significantly underestimated joint shear strength.

Several long inclined cracks were observed in both north and east joint face faces after reaching negative peak shear strength. At later stages of loading, distributed shorter and narrower cracks developed. The main and the widest diagonal crack is the one corresponding to the main diagonal strut supported by beam reinforcement hook. The inclination of that crack matched the theoretical diagonal strut angle. The second inclined crack observed corresponding to the secondary strut action developed by bond forces along beam reinforcement was less apparent in the current specimen. A similar crack pattern was observed during positive loading drift peaks. The X-shape of the main diagonal cracks is less apparent in the current specimen due to the presence of pure J-failure mode and the higher axial load that affected the principal stress inclination. The main diagonal cracks extended outside the joint towards the outermost side of the column for about the same joint height. A vertical crack developed towards the outer edge of the joint at negative drift peak 4a (-1.30%), which is the result of cover splitting action because of the high axial load the specimen was experiencing in the negative loading cycle. Horizontal upper column-joint interface flexural cracking due to tensile action on column was observed starting at positive drift peak of 1.37%. EW beam torsional cracks due to NS beam loading appeared at ±1.37% drift on NS beam.

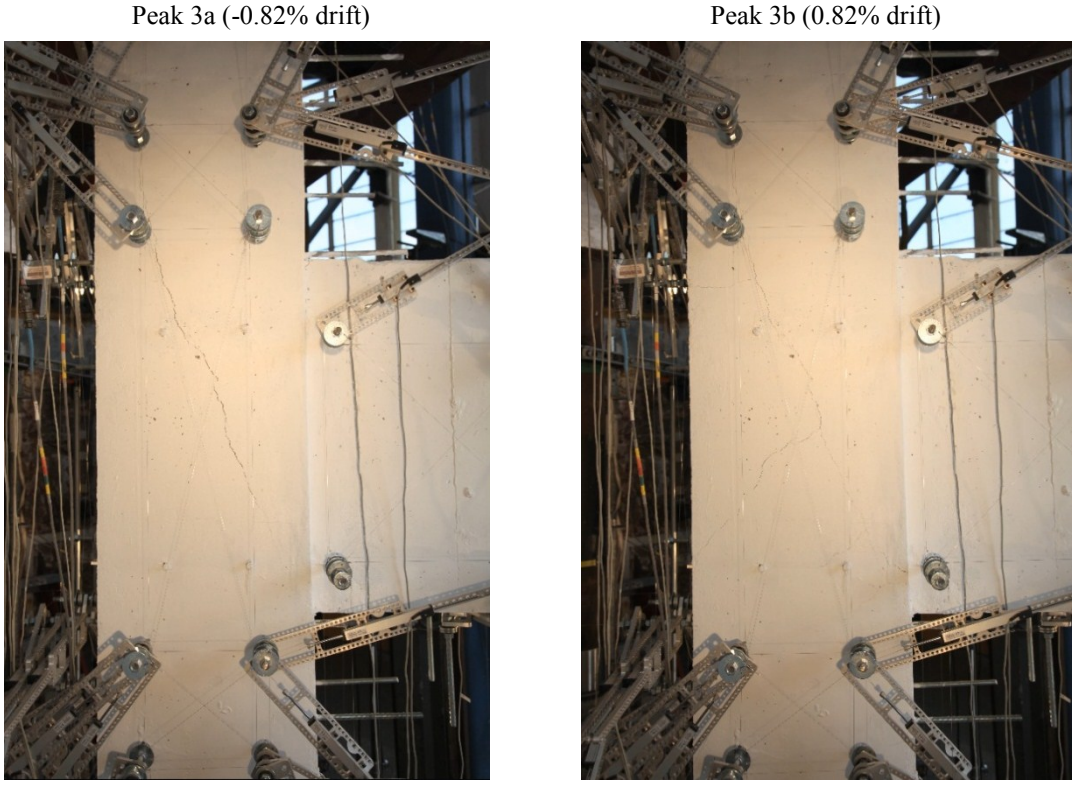

Figure 7.25 North joint face crack development and progression during EW beam loading of specimen U-J-2

Peak 4a (-1.30% drift)

Peak 4a (1.37% drift)

Peak 5a (-2.19% drift)

Peak 5a (2.19% drift)

Figure 7.25 ***(Continued)*** North joint face crack development and progression during EW beam loading of specimen U-J-2

Peak 6a (-3.42% drift)

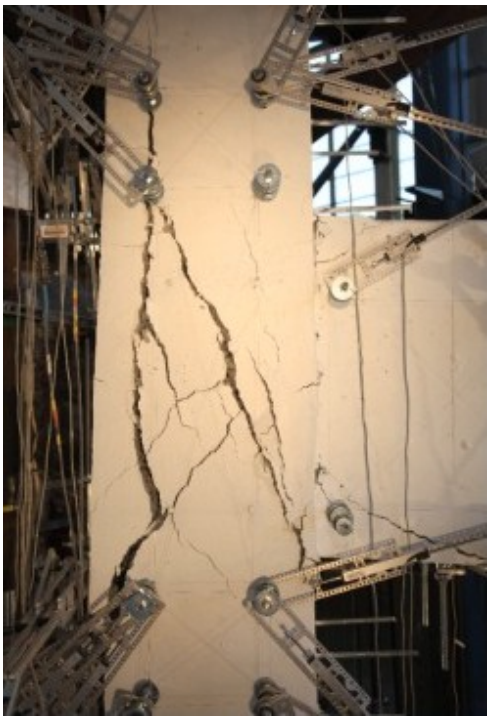

Peak 6a (3.42% drift)

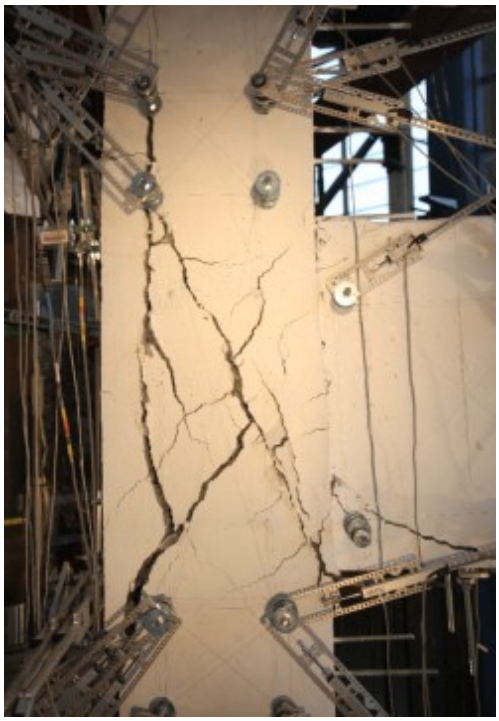

Instantly before axial failure (-3.06% drift)

At axial failure

Figure 7.25 ***(Continued)*** North joint face crack development and progression during EW beam loading of specimen U-J-2

(a)

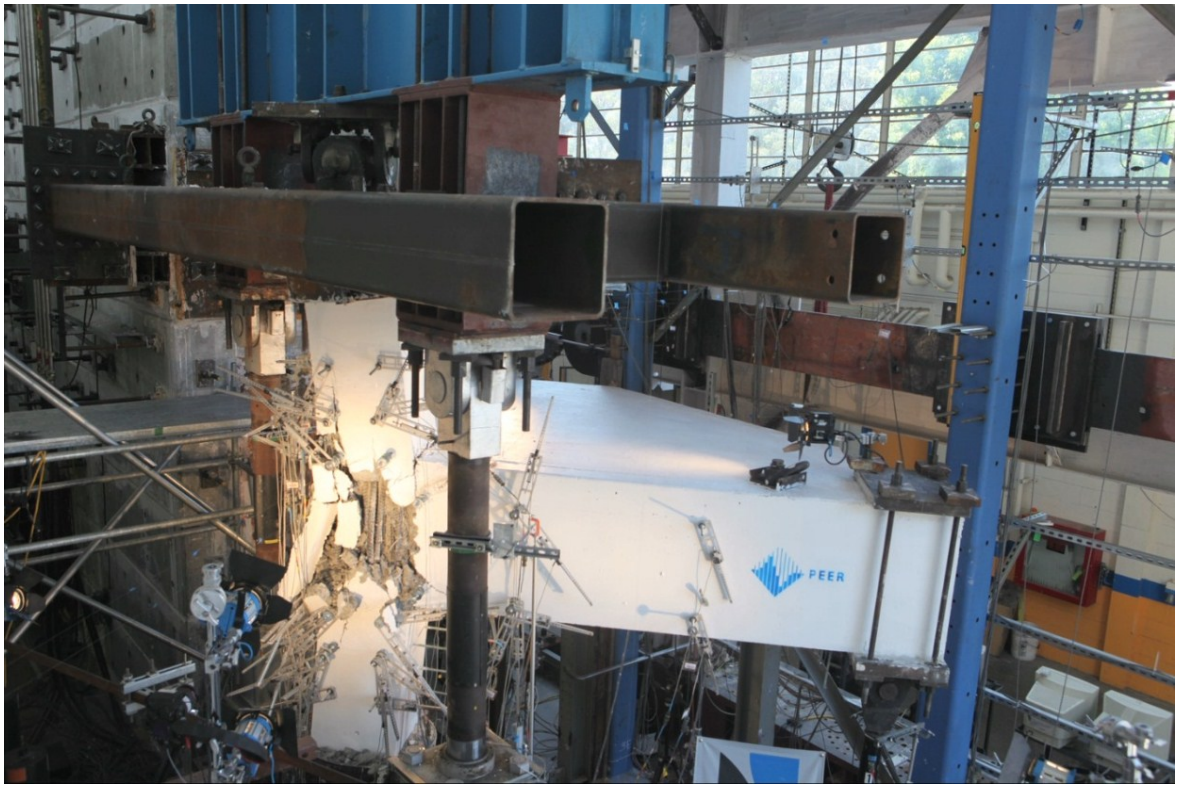

(b)

Figure 7.26 Axial failure of specimen U-J-2: (a) Bar buckling and core damage after axial failure, (b) Global view of specimen after axial failure

Figure 7.30 and 7.31 depict the beam shear force-drift and joint shear strength-drift envelope curves for the specimen, respectively. It can be observed that the initial stiffness for EW and NS beam loading is near identical until prior to reaching joint shear capacity. Similar to specimen U-J-1, the joint shear strength and post-peak strength envelope for the NS beam loading were lower than those of EW beam loading.

Figures 7.32 and 7.33 show upper column axial load and beam shear histories for the specimen. The axial load protocol used for specimen U-J-2 was displacement based as described in Chapter 6. It was designed so that the peak axial compression load is reached at or before reaching joint shear capacity. Since the axial load was independent of beam shear force, it was possible, through a control parameter, to prevent axial load degradation in the post peak regime and to keep the initial gravity load at the intended level. Since the axial load ratio was kept at the intended higher level of 0.46, the specimen could not survive the entire displacement protocol until 9.68% drift. The loading protocol parameter β_i used to maintain the peak axial load was manually adjusted before each loading cycle. Before the beginning of negative loading cycle 4a, the test controller accidently paused the test at a displacement slightly higher than zero before adjusting the loading parameter β_i; hence it was decided to manually increase the axial load using very small increments of the loading parameter until reaching the desired peak level. That is the reason of the zigzag seen in cycle 4a in beam shear and axial load history.

Figures 7.34 displays the normalized joint shear stress-strain hysteretic behavior of north joint face. The north joint face negative shear capacity corresponded to a shear strain of -0.0045 radians, while the shear strain recorded at peak positive joint shear strength was 0.011 radians. The east joint face negative shear capacity corresponded to a shear strain of -0.0011 radians, while the shear strain recorded at peak positive joint shear stress was 0.0043 radians. The envelope curves for the joint shear stress-strain hysteresis are presented in Fig. 7.35.

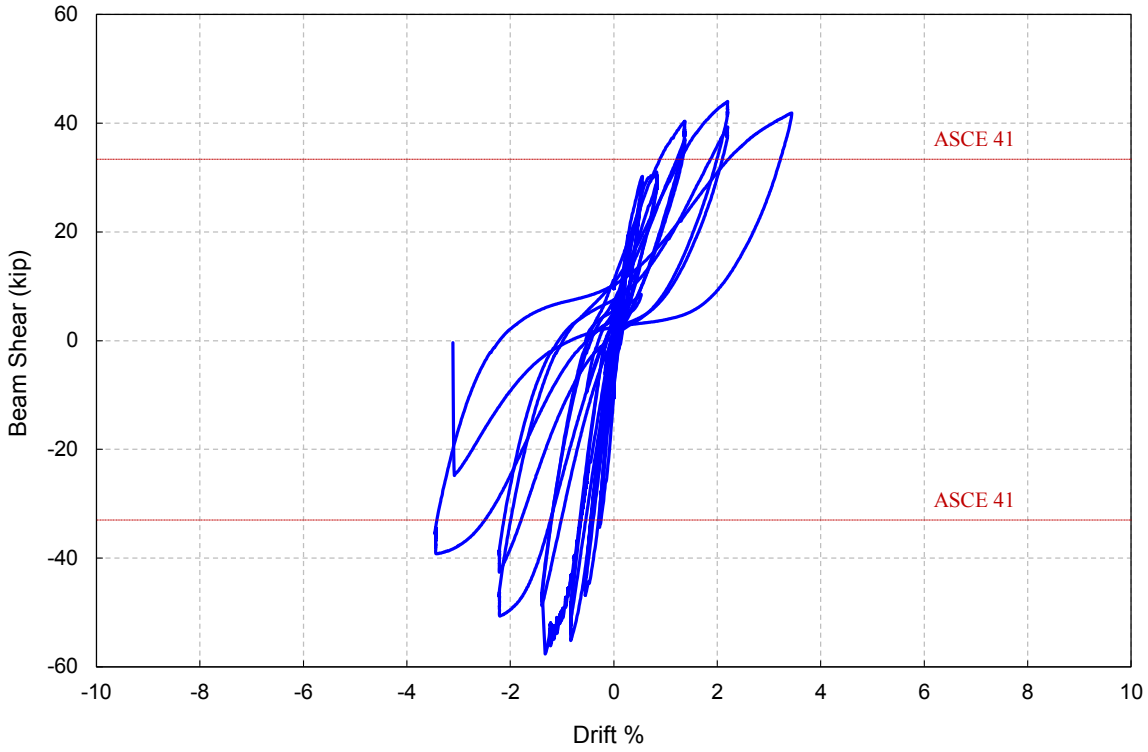

Figure 7.28 Relation between applied force and drift for EW-beam of specimen U-J-2

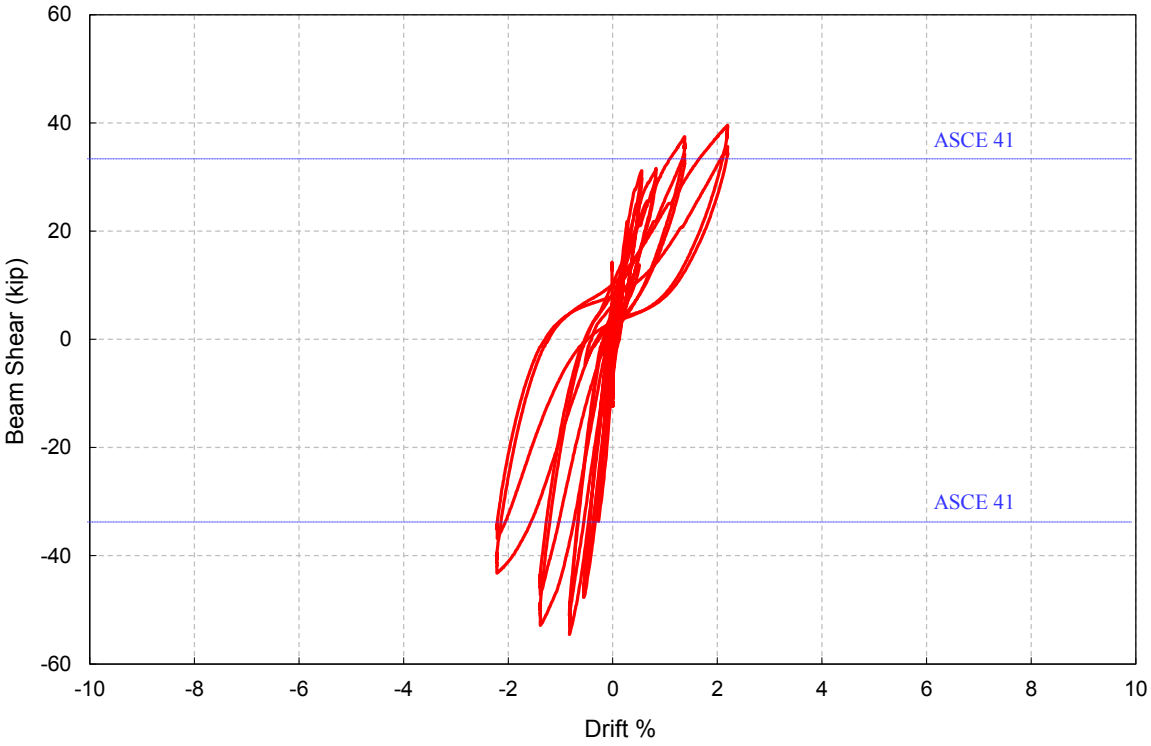

Figure 7.29 Relation between applied force and drift for EW-beam of specimen U-J-2

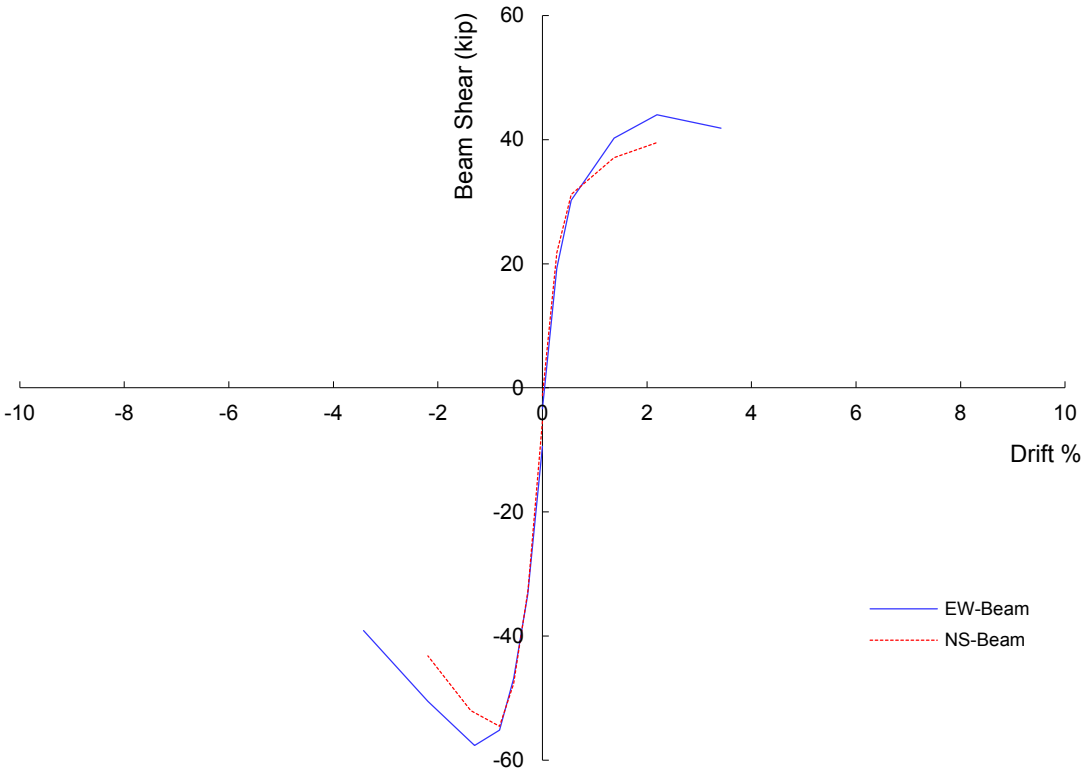

Figure 7.30 Backbone curves of specimen U-J-2

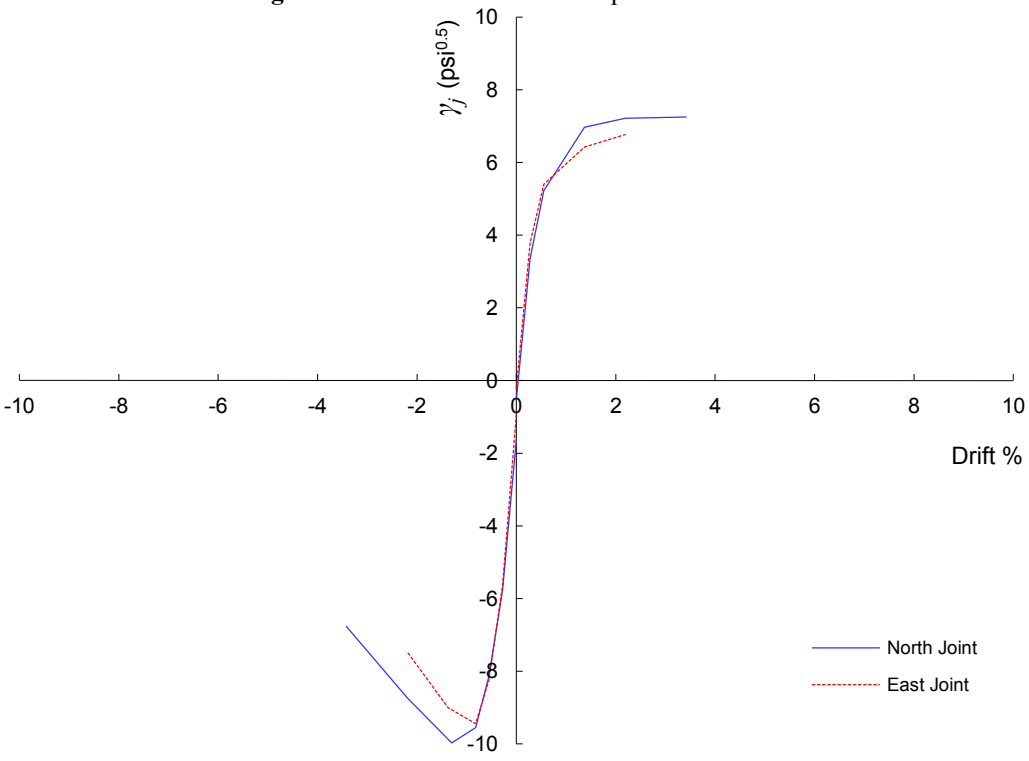

Figure 7.31 Backbone curves of specimen U-J-2

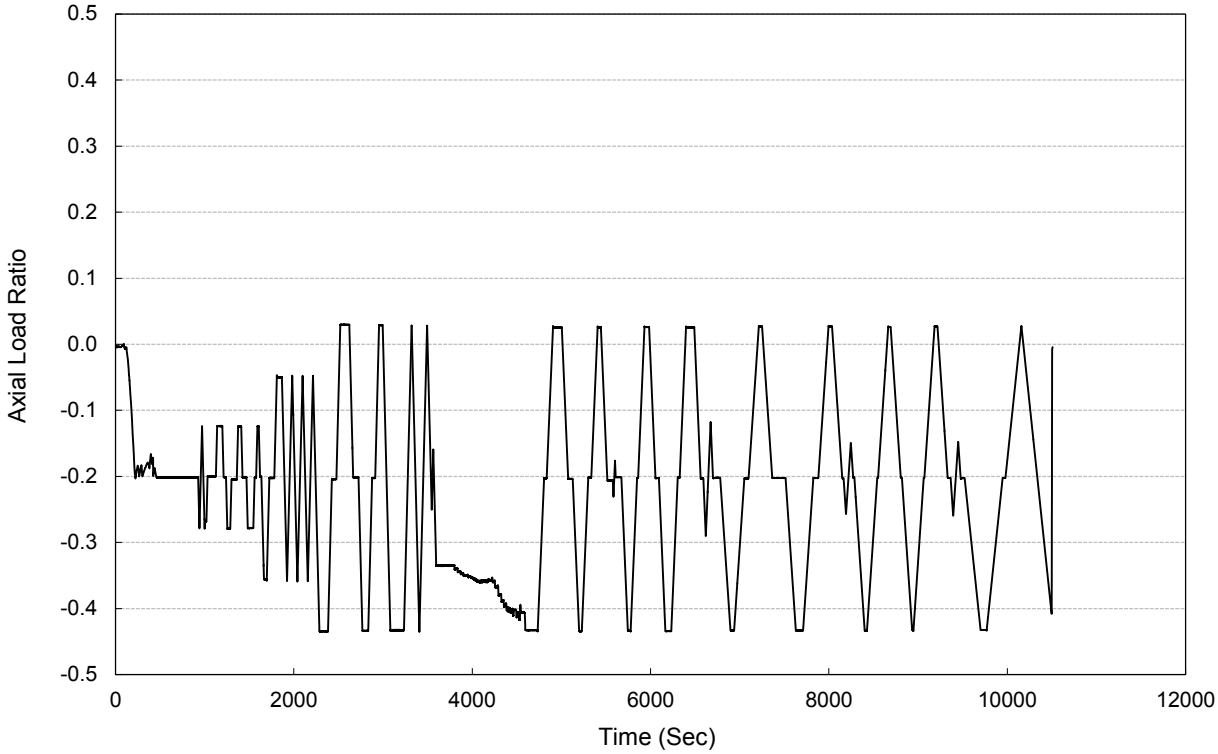

Figure 7.32 Upper column axial load History of specimen U-J-2

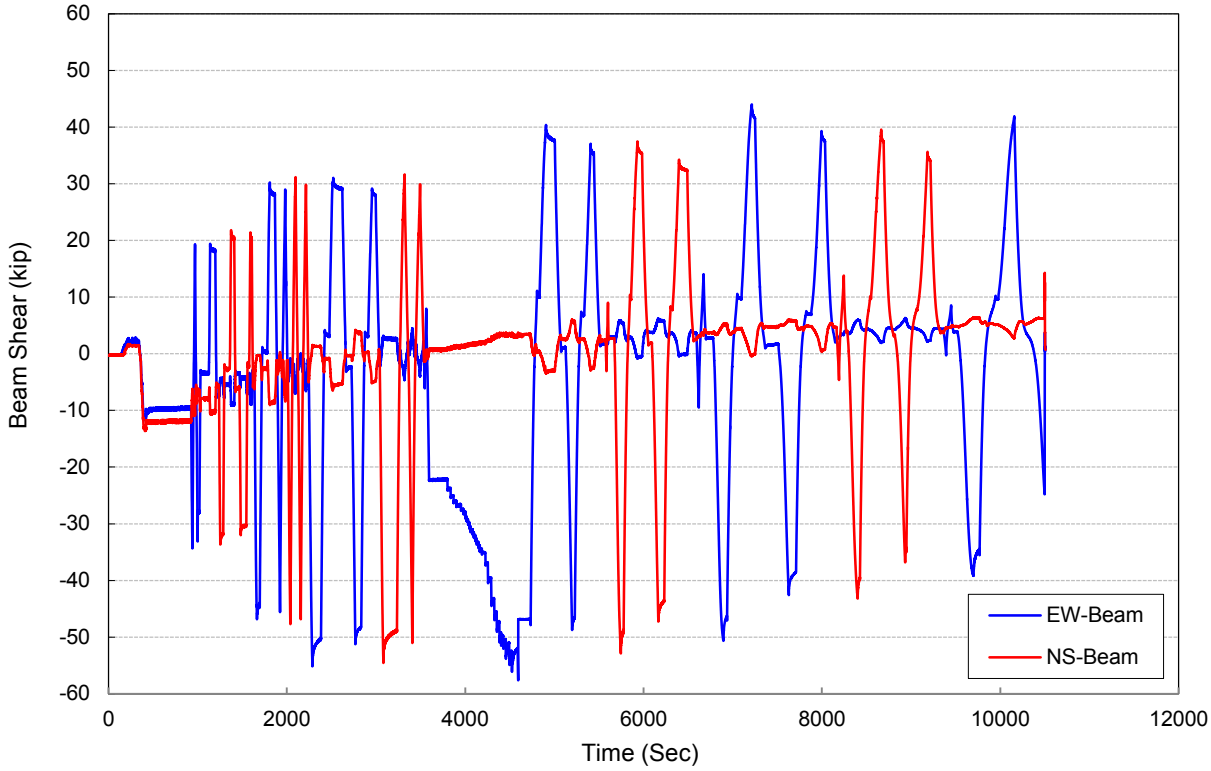

Figure 7.33 Beam shear History of specimen U-J-2

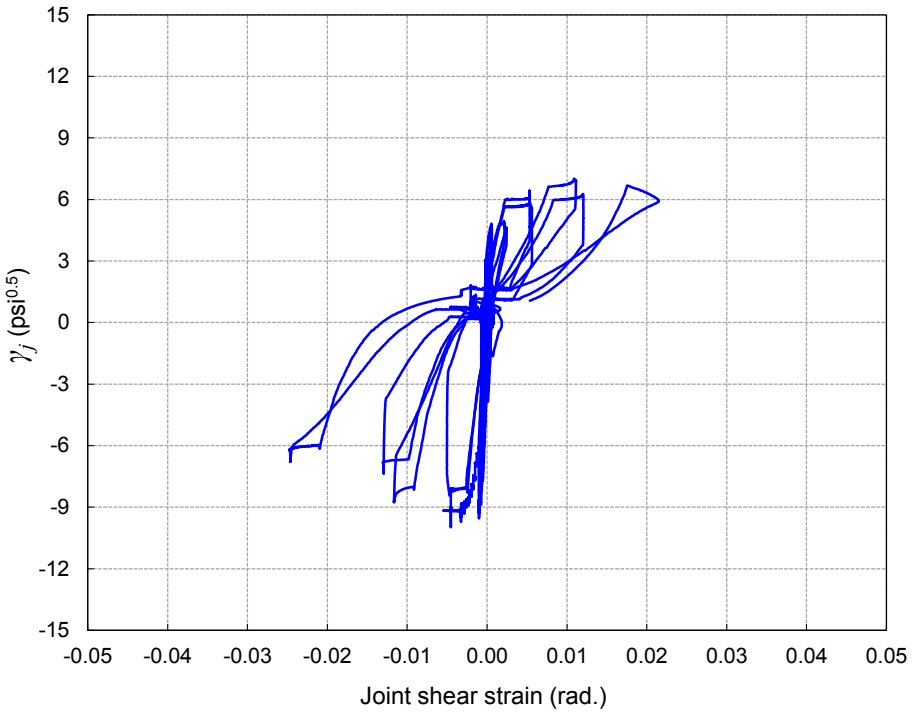

Figure 7.34 North joint face shear stress-strain relation for specimen U-J-2

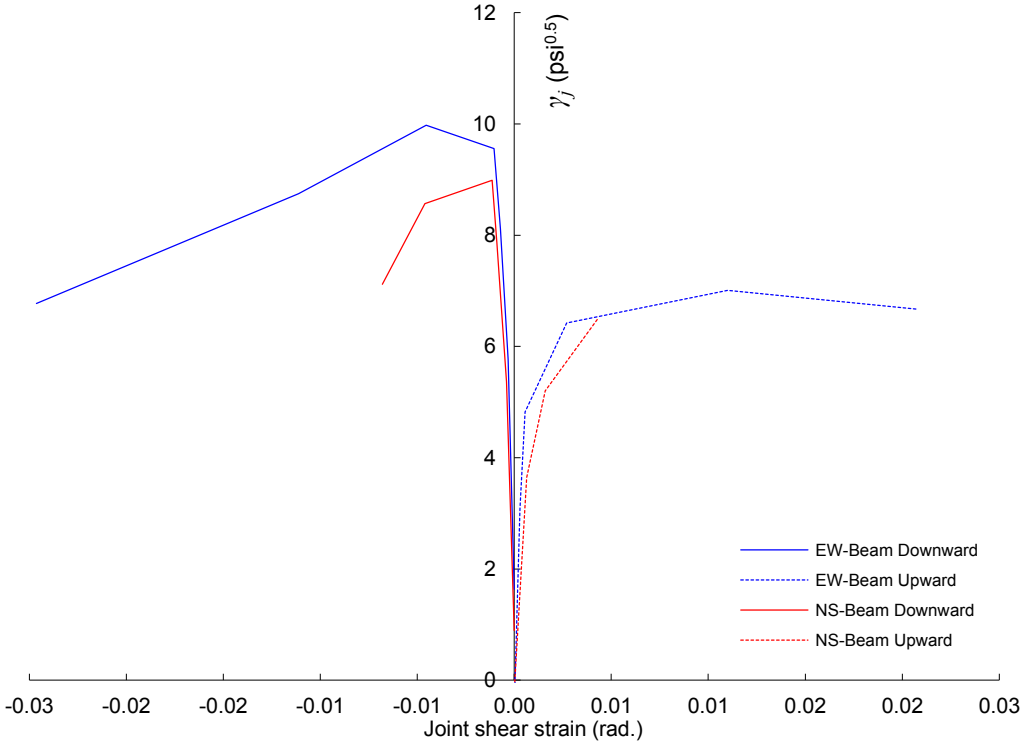

Figure 7.35 Joint shear stress-strain envelopes for specimen U-J-2

Figure 7.36 shows the contribution of joint shear strain to the overall drift of the joint subassembly represented by the ratio of the beam tip displacement induced by joint shear deformation to the total beam displacement. The contribution of the north joint face to the EW-beam drift was 23% and 26% for the negative and positive peak joint shear strength, respectively. The east joint face shear deformation contribution to the total drift of NS-beam at joint shear capacity peaks was about 9% and 27% for negative and positive loading cycles, respectively. At drift peak of ±3.42%, joint shear strain contribution was more than 48% for EW beam positive loading and 34% for negative loading direction. Measurements obtained beyond this peak were not reliable due to the effect of falling concrete particles.

Figure 7.37 displays the peak-to-peak effective stiffness degradation plots for both EW and NS beam loading. It can be noticed that the effective stiffness and stiffness degradation are similar for both loading directions. The peak-to-peak effective stiffness degradation is much less significant within the same drift level than that between different drift levels.

Figure 7.38 shows the cumulative energy dissipation of during EW beam and NS beam loading of specimen U-J-2. Energy dissipation of both beams is almost identical except for post-peak shear strength where energy dissipation of EW beam is slightly higher than that of NS.

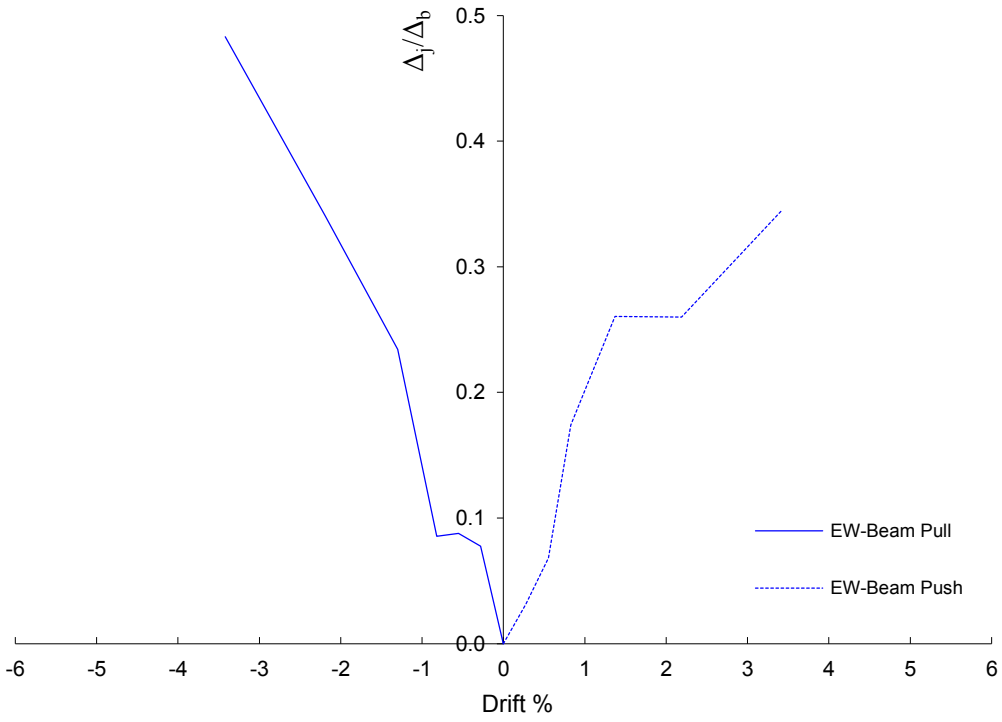

Figure 7.36 North joint face deformation contribution to total drift ratio of EW-beam for specimen U-J-2

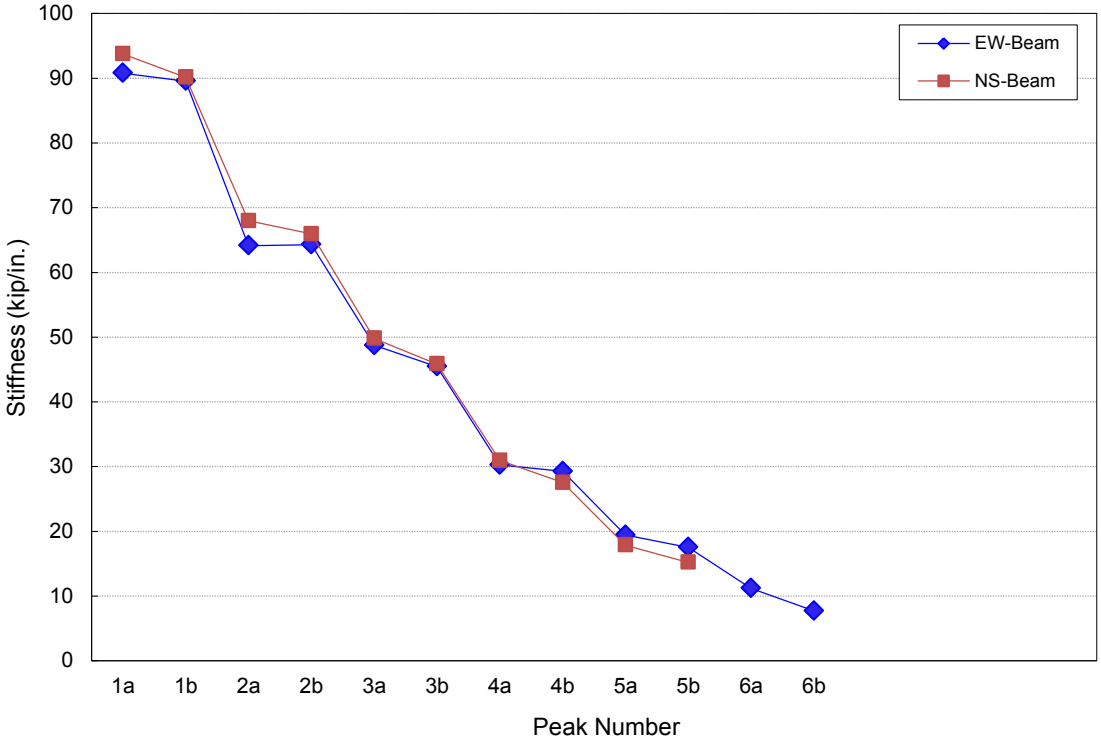

Figure 7.37 Peak-to-peak stiffness for specimen U-J-2

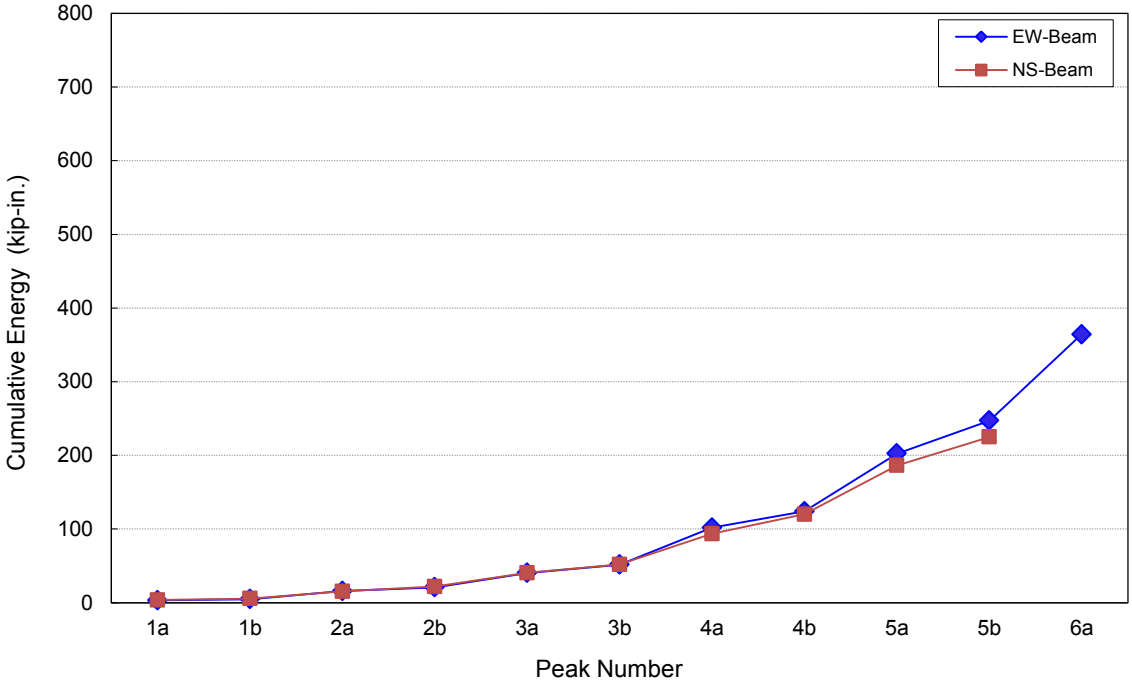

Figure 7.38 Peak-to-peak cumulative energy dissipation for specimen U-J-2

Figure 7.39 and Fig. 7.40 exhibit the strain distribution of slab top reinforcement at first cycles of negative drift peaks of EW and NS beam loading. The first slab reinforcement bar adjacent to the EW-beam yielded at the negative joint shear strength peak 4a (-1.30% drift) although beam reinforcement did not yield at this peak. The next slab bar, however, was very close to yield at this drift peak. The slab reinforcement parallel to NS beam did not yield throughout the test. This observation is similar to that in specimen U-J-1. Bottom slab reinforcement did not yield throughout test.

Figures 7.41 and 7.42 display the strain profile of the exterior and interior beam reinforcement bars under the first negative drift loading peaks of EW beam. The beam reinforcement did not experience yield prior to joint shear strength peak during EW and NS beam negative drift loading. Figures 7.43 and 7.44 depict the strain profile of beam reinforcement for the first positive drift loading peaks of EW beam. The only yielding that occurred prior to reaching joint shear strength was for the exterior beam bottom reinforcement bar during upward loading, whose strain was 1.10 times the yield strain at joint shear strength peak. However, the interior beam reinforcement bar strain was only 60% of yield strain at that peak. On the basis that only slight yielding occurred, the joint failure is considered to be J-failure. NS beam bottom reinforcement did not yield during positive drift loading throughout the test. EW beam top reinforcement did not yield during negative drift loading throughout the test. At negative drift peak 4a of NS beam loading, NS beam reinforcement underwent yielding that penetrated into the joint core. Unlike specimen U-J-1, it is worth mentioning that beam reinforcement longitudinal strains were not reversed from tensile strain along joint core into compressive strain adjacent to end hook.

None of the column reinforcement bars reached yield at the upper or lower column-joint interface before joint shear strength peak during downward or upward loading directions of beam EW and NS beams. Moreover, most column bars did not even yield afterwards. Only column bars CE, CSE, CNW, and CNE experienced slight yielding at positive drift peak 6a prior to axial failure. After reaching joint shear strength, some column bars experienced yield in compression at mid-joint height due to buckling. Appendix A includes all column bar strain profiles.

Figures 7.45 and 7.46 show strain profile along the height of the intermediate column reinforcement bars CN and CE during first drift loading peaks, respectively. It can be observed that longitudinal strains at the joint mid-height are insignificant until reaching joint shear capacity. Afterwards compression strain increased at mid-joint height due to bar buckling. However, column intermediate bars did not reach yield at mid-column height until drift peak 5a, but yielded afterward due to bar buckling. This suggests that the contribution of such column reinforcement bars to joint shear strength was negligible.

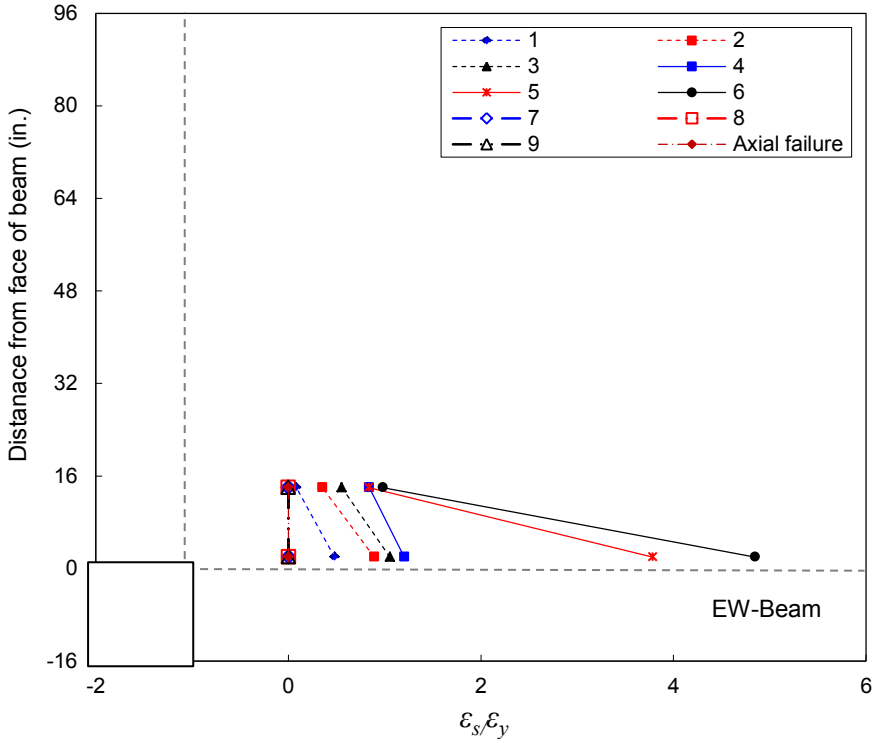

Figure 7.39 Slab top reinforcement strain distribution for U-J-2 negative first drift peaks for EW-Beam loading

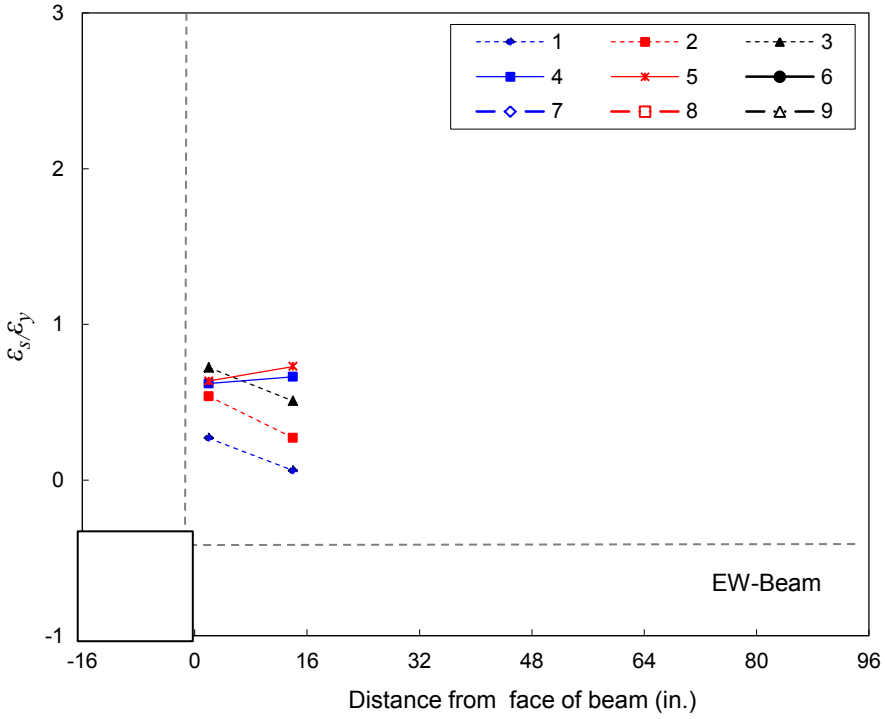

Figure 7.40 Slab top reinforcement strain distribution for U-J-2 negative first drift peaks for NS-Beam loading

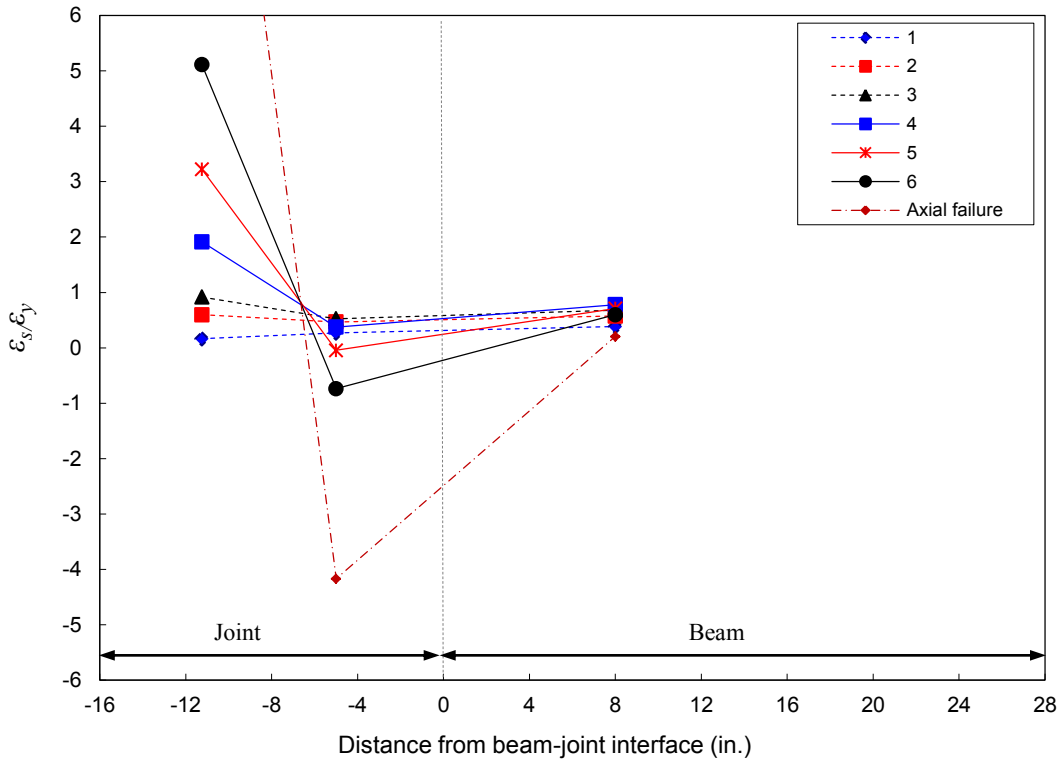

Figure 7.41 EW-beam top exterior longitudinal reinforcement strain for U-J-2 first negative drift peaks

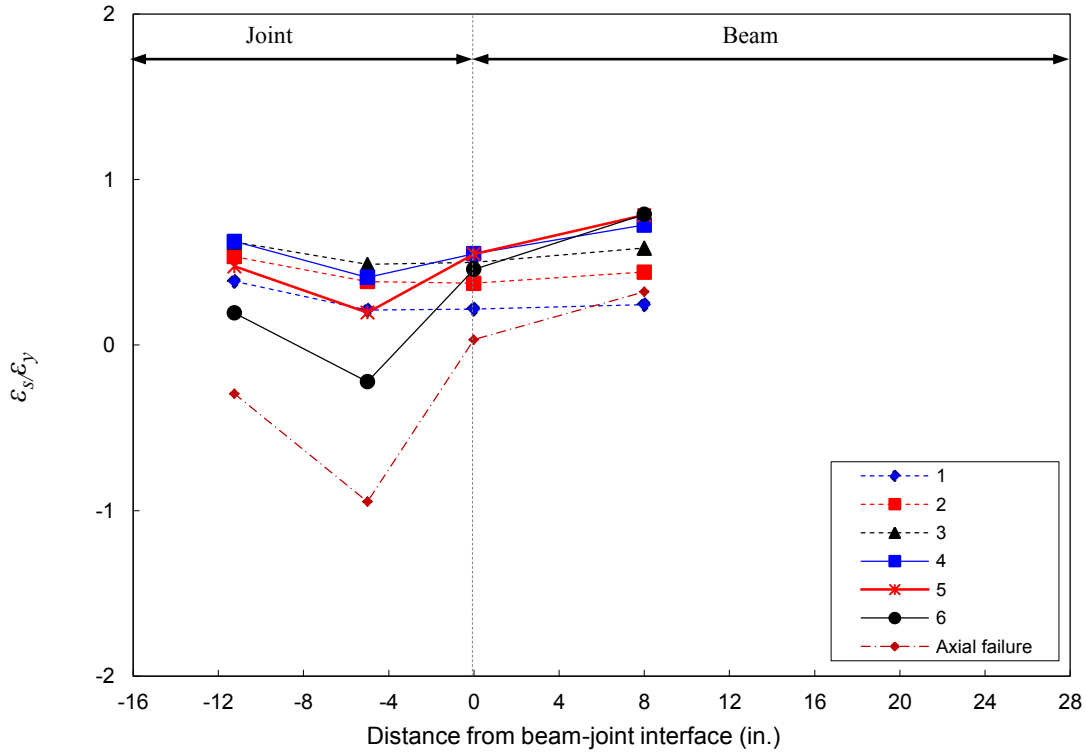

Figure 7.42 EW-beam top interior longitudinal reinforcement strain for U-J-2 first negative drift peaks

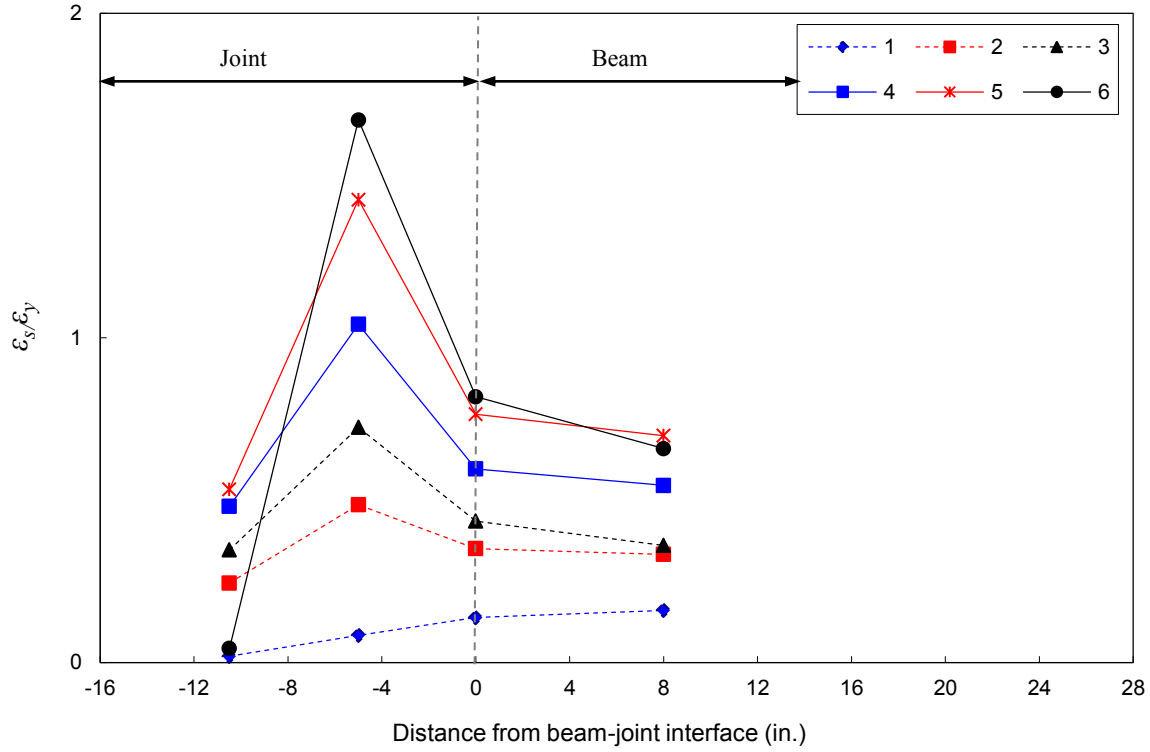

Figure 7.43 EW-beam bottom exterior longitudinal reinforcement strain for U-J-2 first positive drift peaks

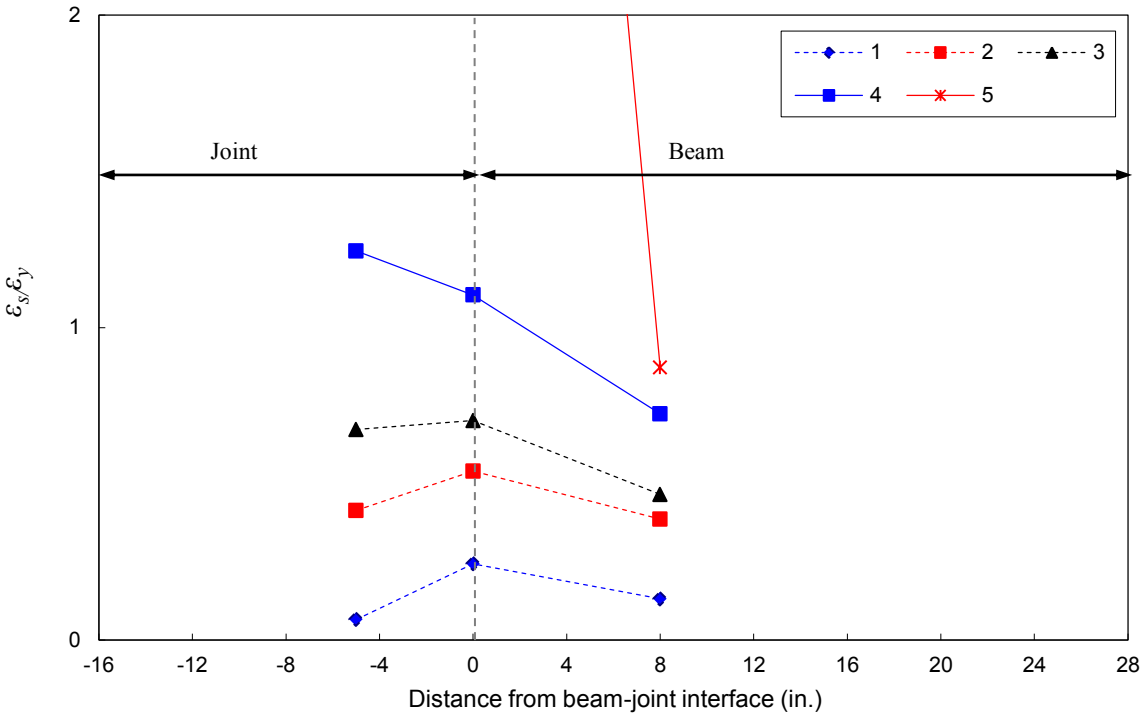

Figure 7.44 EW-beam bottom interior longitudinal reinforcement strain for U-J-2 first positive drift peaks

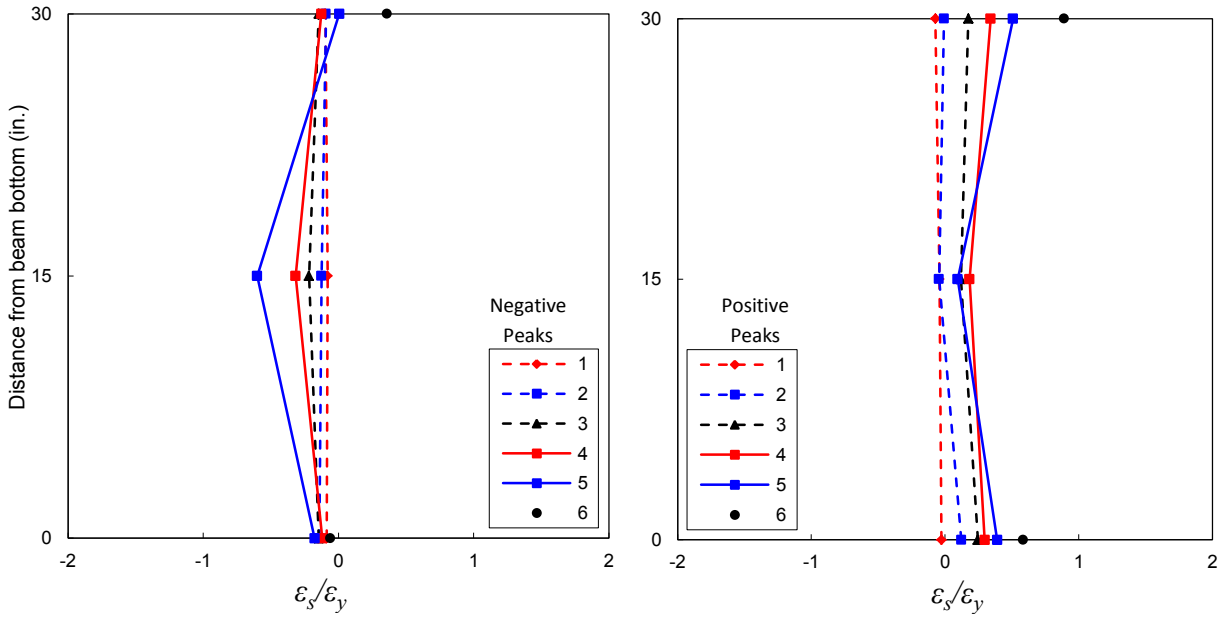

Figure 7.45 Strain development for column intermediate reinforcement CN of U-J-2 EW-beam drift peaks

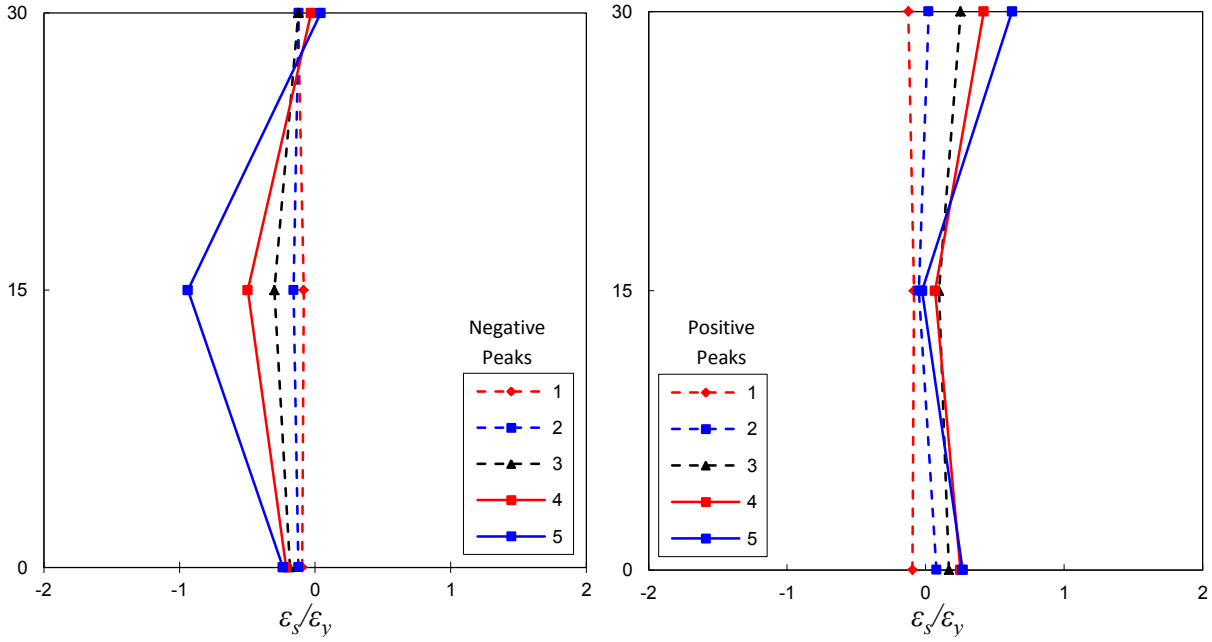

Figure 7.46 Strain development for column intermediate reinforcement CE of U-J-2 NS-beam drift peaks

Table 7.2.a Summary of performance parameters of specimen U-J-2, EW direction, downward loading

Load Peak	*Drift* (%)	$V_{b\text{-}EW}$ (kip)	$V_{c\text{-}EW}$ (kip)	$V_{j\text{-}N}$ (kip)	γ_j (psi$^{0.5}$)	γ_s (rad.)	$P_{u,col}$ (kip)	$P_{L,col}$ (kip)	Axial load ratio	K_P (kip/in.)	E_i (kip-in.)	$E_{cum.}$ (kip-in.)
0	0	-9.43	-6.8	-32.3	-1.63	-0.0001	-288	-310	-0.21	-	-	-
1a	-0.28	-33.3	-24.1	-114	-5.77	-0.0003	-400	-440	-0.30	90.8	3.27	3.27
1b	-0.28	-33.1	-24.0	-114	-5.74	-0.0003	-401	-440	-0.30	89.6	1.45	4.73
2a	-0.55	-46.9	-32.0	-151	-8.11	-0.0007	-510	-555	-0.38	64.1	11.0	15.7
2b	-0.55	-45.6	-33.0	-156	-7.89	-0.0007	-514	-560	-0.38	64.3	5.11	20.8
3a	-0.82	-55.2	-39.2	-185	-9.56	-0.0010	-624	-676	-0.46	48.8	19.5	40.3
3b	-0.82	-50.4	-36.5	-173	-8.72	-0.0008	-622	-669	-0.46	45.5	11.3	51.6
4a	-1.37	-57.6	-33.9	-161	-9.98	-0.0045	-621	-664	-0.46	30.3	50.1	102
4b	-1.37	-47.2	-34.2	-162	-8.18	-0.0040	-623	-665	-0.46	29.3	22.1	124
5a	-2.19	-50.5	-34.6	-164	-8.74	-0.0111	-621	-664	-0.46	19.4	79.0	202
5b	-2.19	-41.4	-29.9	-142	-7.16	-0.013	-622	-657	-0.46	17.5	44.6	247
6a	-3.42	-39.1	-28.0	-132	-6.77	-0.025	-621	-653	-0.46	11.2	117	364
Axl. Fail	-3.06	-24.8	-18.0	-85.0	-4.30	-	-587	-604	-0.43	7.70	-	-

Table 7.2.b Summary of performance parameters of specimen U-J-2, NS direction, downward loading

Load Peak	*Drift* (%)	$V_{b\text{-}NS}$ (kip)	$V_{c\text{-}NS}$ (kip)	$V_{j\text{-}E}$ (kip)	γ_j (psi$^{0.5}$)	γ_s (rad.)	$P_{u,col}$ (kip)	$P_{L,col}$ (kip)	Axial load ratio	K_P (kip/in.)	E_i (kip-in.)	$E_{cum.}$ (kip-in.)
0	0.00	-5.40	-3.90	-17.6	-0.89	0.0000	-288	-301	-0.21	-	-	-
1a	-0.28	-32.6	-23.6	-106	-5.35	-0.0009	-401	-438	-0.30	93.7	3.57	3.57
1b	-0.28	-31.3	-22.6	-102	-5.14	-0.0009	-399	-435	-0.29	90.0	2.00	5.57
2a	-0.55	-47.7	-34.5	-155	-7.84	-0.0010	-516	-564	-0.38	68.0	9.80	15.4
2b	-0.55	-46.9	-33.9	-152	-7.70	-0.0011	-515	-562	-0.38	66.0	6.58	22.0
3a	-0.82	-54.6	-39.5	-177	-8.97	-0.0011	-623	-675	-0.46	49.8	18.5	40.5
3b	-0.82	-51.0	-37.0	-166	-8.39	-0.0014	-625	-676	-0.46	45.9	11.4	51.9
4a	-1.37	-52.0	-37.7	-169	-8.55	-0.0045	-623	-670	-0.46	31.1	41.5	93.5
4b	-1.37	-45.0	-32.6	-146	-7.40	-0.0059	-623	-662	-0.46	27.5	26.5	120
5a	-2.19	-43.2	-31.3	-140	-7.10	-0.0068	-622	-660	-0.46	17.9	66.4	186
5b	-2.19	-35.7	-25.9	-116	-5.87	-0.0059	-621	-651	-0.46	15.2	38.5	225

Table 7.2.c Summary of performance parameters of specimen U-J-2, EW direction, upward loading

Load Peak	*Drift* (%)	$V_{b\text{-}EW}$ (kip)	$V_{c\text{-}EW}$ (kip)	$V_{j\text{-}N}$ (kip)	γ_j (psi$^{0.5}$)	γ_s (rad.)	$P_{u,col}$ (kip)	$P_{L,col}$ (kip)	Axial load ratio	K_P (kip/in.)	E_i (kip-in.)	$E_{cum.}$ (kip-in.)
1a	0.28	19.3	14.0	62.8	3.08	-0.0001	-178	-169	-0.13	90.8	3.27	3.27
1b	0.28	18.8	13.6	61.1	3.00	-0.0001	-177	-169	-0.13	89.6	1.45	4.73
2a	0.55	30.2	21.9	98.2	4.82	0.0006	-67.0	-45.8	-0.05	64.1	11.0	15.7
2b	0.55	29.0	21.0	94.1	4.62	0.0006	-68.0	-47.3	-0.05	64.3	5.11	20.8
3a	0.83	30.2	21.9	98.1	4.82	0.0022	42.8	67.2	0.03	48.8	19.5	40.3
3b	0.83	28.3	20.5	91.9	4.51	0.0024	41.5	64.8	0.03	45.5	11.3	51.6
4a	1.37	40.3	29.2	131	6.42	0.0053	40.0	76.8	0.03	30.3	50.1	102
4b	1.37	37.1	26.8	120	5.91	0.0053	39.1	73.2	0.03	29.3	22.1	124
5a	2.19	41.7	30.2	135	6.65	0.0085	39.2	80.9	0.03	19.4	78.6	202
5b	2.19	39.3	28.4	128	6.26	0.0120	40.3	80.0	0.03	17.5	44.6	247
6a	3.42	41.9	30.3	136	6.67	0.0176	39.3	83.8	0.03	11.2	117	364

Table 7.2.d Summary of performance parameters of specimen U-J-2, NS direction, upward loading

Load Peak	*Drift* (%)	$V_{b\text{-}NS}$ (kip)	$V_{c\text{-}NS}$ (kip)	$V_{jh\text{-}E}$ (kip)	γ_j (psi$^{0.5}$)	γ_s (rad.)	$P_{u,col}$ (kip)	$P_{L,col}$ (kip)	Axial load ratio	K_P (kip/in.)	E_i (kip-in.)	$E_{cum.}$ (kip-in.)
1a	0.28	21.8	15.8	74.1	3.64	-0.0006	-178	-165	-0.13	93.7	3.57	3.57
1b	0.28	21.0	15.2	71.4	3.50	-0.0007	-179	-167	-0.13	90.1	2.00	5.57
2a	0.55	31.2	22.6	106	5.20	0.0001	-68.4	-44.3	-0.05	68.0	9.81	15.4
2b	0.55	29.6	21.5	101	4.94	0.0001	-68.2	-44.9	-0.05	65.9	6.58	22.0
3a	0.83	31.6	22.9	107	5.27	0.0026	40.2	67.2	0.03	49.8	18.6	40.5
3b	0.83	28.3	20.5	96.1	4.72	0.0025	41.5	64.8	0.03	45.9	11.4	51.9
4a	1.37	37.1	26.9	126	6.19	0.0043	39.3	75.6	0.03	31.0	41.6	93.5
4b	1.37	34.3	24.8	116	5.71	0.0037	39.1	72.9	0.03	27.5	26.5	120
5a	2.19	39.1	28.3	133	6.52	0.0019	39.3	80.3	0.03	17.8	66.4	186
5b	2.19	34.3	24.8	116	5.71	0.0010	38.7	75.3	0.03	15.2	38.5	225

7.3.3 Specimen B-J-1

Table 7.3 presents the characteristic response parameters of specimen B-J-1. Figures 7.51 and 7.52 display the force-drift ratio hysteretic performance of specimen B-J-1 for EW beam and NS beam, respectively. Figure 7.47 presents the development of joint cracking and distress throughout the test. The first north joint face downward diagonal crack occurred at negative drift peak of -0.82% (peak 3a). The first north joint face upward diagonal crack occurred at positive drift peak of 1.37% (peak 4a).

The beam reinforcement outside the joint region did not yield throughout the test. Thus, the joint failure mode was J-Failure in both loading directions EW and NS and both loading cycles upward and downward, consistent with the design intent. Both joint shear strength models proposed in Chapter 5 were able to predict the joint shear strength of the current joint. Details of this prediction were presented in Chapter 5.

Several diagonal cracks were observed in both north and east joint face after reaching negative peak shear strength. Two of these cracks are considered major cracks reflecting beam reinforcement bond forces strut and beam reinforcement hook strut discussed in Chapter 2. However, the main diagonal strut crack was not as apparent as its counterpart in unidirectionally loaded specimens. This might be attributed to the idealization that in biaxially loaded joint the main strut is a three dimensional strut spanning between the two outermost apexes of the joint (Leon and Jirsa [84]). This can be confirmed by observing the damage at the column apexes post joint shear failure, Fig 7.49. Furthermore, the inclination of diagonal cracks in the downward loading direction was affected by the higher axial loads. The cracks tended to be steeper towards the vertical. The typical X-shape diagonal crack pattern is not evident, which is consistent with J-Failure mode

A nearly vertical crack was appeared towards the outer edge of the joint at negative drift peak 4a (-1.37%), which is believed to be a result of splitting action of the substantial axial load the specimen was experiencing. Cracks on the north and east joint face sides were connected diagonally through the joint, forming a large triangular concrete wedge that tended to separate from the outside corner of the column. However, this wedge was less remarkable than that in specimens loaded in unidirectional fashion. This separation was prevented by the first column hoop outside the joint. Prying action of the beam reinforcement end hook was not observed during the test.

The maximum shear force in the negative direction was reached at negative drift peak of -1.37% (peak 4a). Hairline joint diagonal cracking and minor flexural cracking were observed at the beam top at this drift peak. The corresponding maximum negative joint shear strength coefficient γ_j was 11.7 for north joint face and 10.8 for east joint face. The maximum applied upper column axial load ratio of 0.45 was reached at drift peak 4a of -1.37%, the same peak the beam-column joint reached its shear capacity. The maximum beam shear force in the positive direction was reached at positive drift peak of 2.19% (peak 5a). This force corresponds to joint shear strength coefficient γ_j of 10.1 and 9.83 for north joint face and east joint face, respectively. Major diagonal joint shear cracking and horizontal column-joint interface flexural cracking due

to tensile action on column were observed at this peak. The force-drift response of EW and NS beams are almost identical except for a slight variation in the maximum beam shear in the positive loading direction. This was expected since both beams were loaded simultaneously. The force-drift envelopes of both beams are identical. However, the joint shear stress coefficient-drift envelopes are slightly different for both beams due to the variation of the beam effective depths.

The axial failure of the joint took place during the second cycle of negative displacement group 6b at a drift ratio of 3.36%. This corresponds to an upper column axial load level of 0.45 and joint shear strength coefficient of 5.75 which is about 49% that at peak joint shear strength. Prior to axial failure, joint diagonal and vertical cracks significantly widened, minor joint concrete cover spalling occurred and very slight bulging of the joint concrete cover was observed, probably caused by buckling of column reinforcement within the joint. Comparing to specimens with lower axial load, however, these could not serve as confirmed precursors of axial failure, thus the axial failure was completely sudden. Immediately before the dramatic axial failure, cracking and "banging" sound was heard. Axial failure was represented by global spalling of joint concrete cover, buckling of column unconfined reinforcement within the joint, crushing of joint concrete core, breaking of the concrete wedge supported by column ties and longitudinal bars, and finally substantial dynamic instability of the subassembly represented by large side-sway of the column and slab. Figures 7.47 and 7.48 exhibit the axial failure of the specimen.

Peak 4a (-1.37% drift)

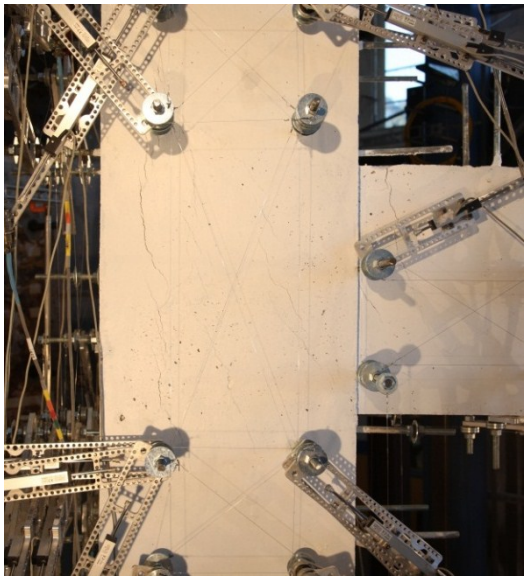

Peak 4a (1.37% drift)

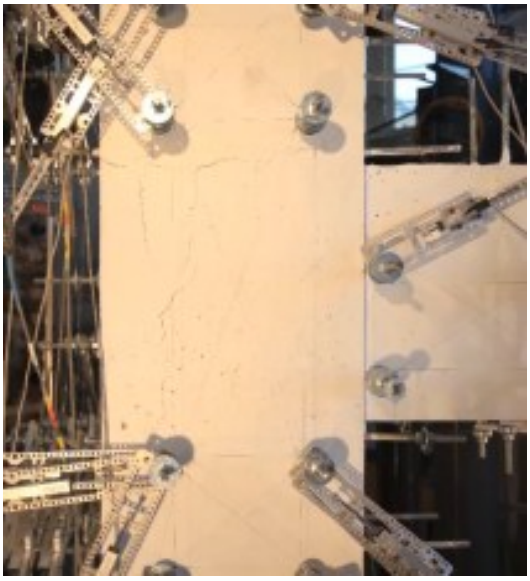

Peak 5a (-2.19% drift)

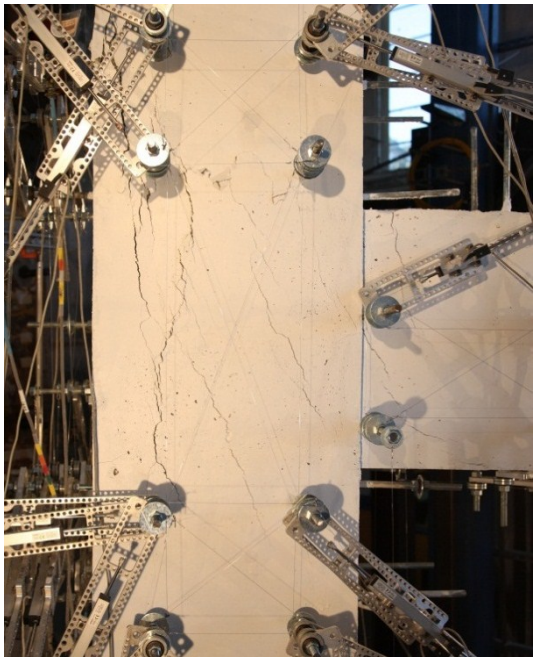

Peak 5a (2.19% drift)

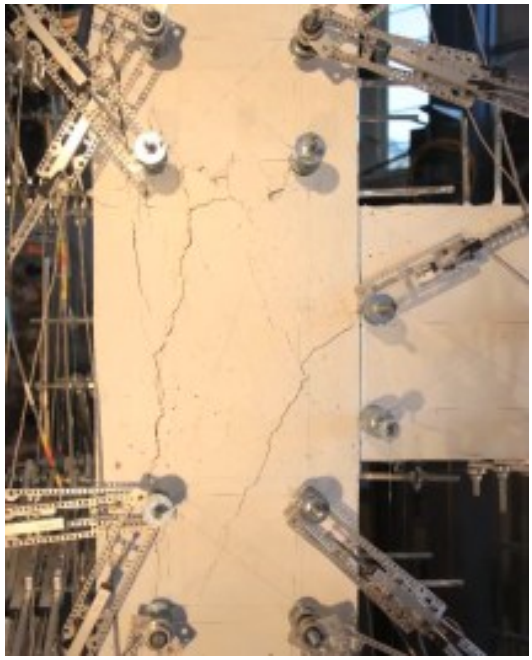

Figure 7.47 Crack development and distress of Specimen B-J-1 north joint face

Peak 6a (-3.42% drift)

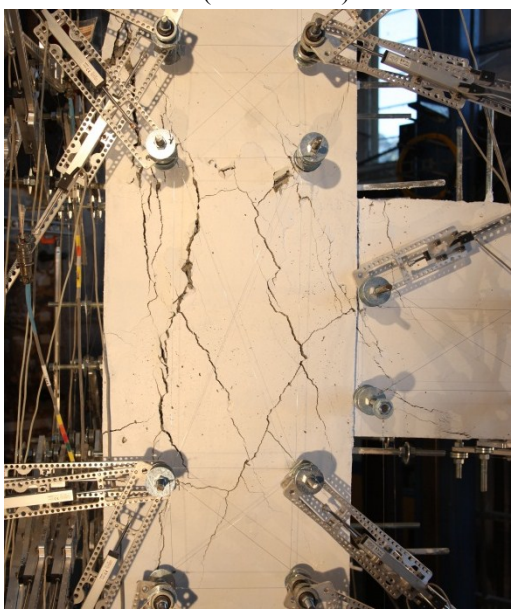

Instantly before axial failure

Peak 6a (3.42% drift)

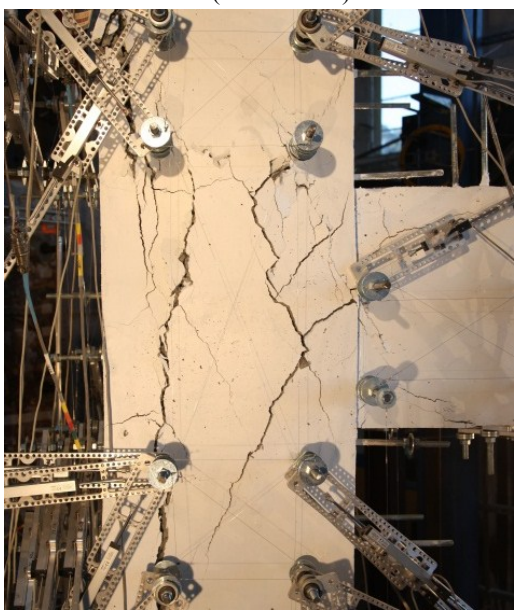

During axial failure

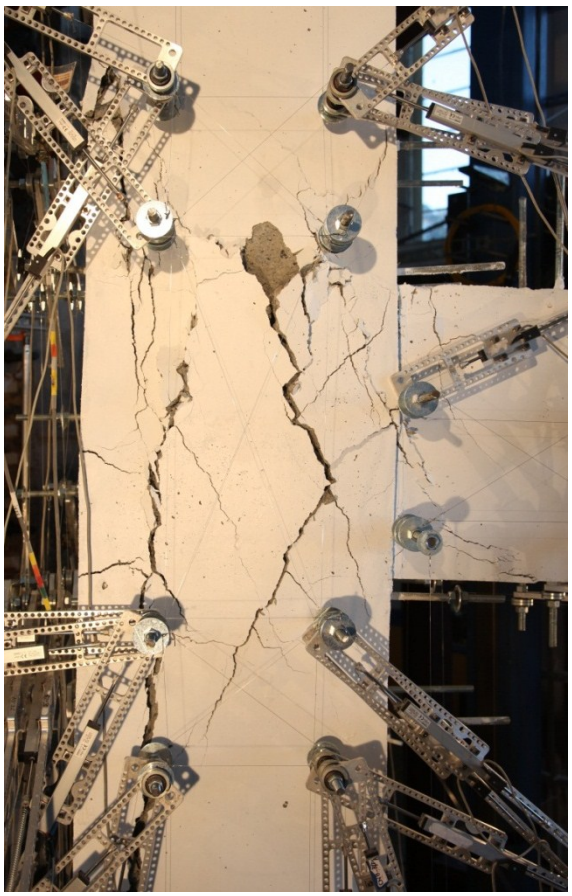

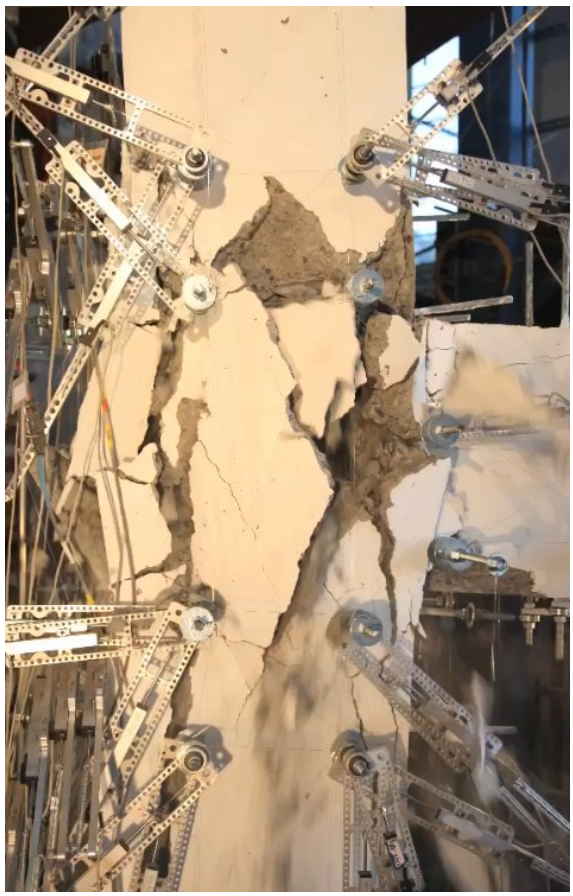

Figure 7.47 ***(Continued)*** Crack development and distress of Specimen B-J-1 north joint face

Figure 7.48 Global views of Specimen B-J-1 axial collapse

Figure 7.49 Evidence of 3D shear diagonal strut through the joint of specimen B-J-1

Figures 7.51 and 7.52 display the force-drift ratio hysteretic performance of specimen B-J-1 for EW beam and NS beam, respectively. The post-peak pinching behavior of the joint is evident. However, the post-peak hysteretic loops are distinctively different from those of unidirectional specimen; they appear to be wider and more pinched. This could be attributed to two reasons. The first reason is the more flexible nature of the biaxially loaded specimen since the column compression zone bounded by the inclined neutral axis is smaller than that in uniaxially loaded specimen, which reflects lower column stiffness. The second reason is the amplified effect of joint distress and internal cracking because of the simultaneous loading which reduces the joint stiffness and increases pinching.

Figures 7.53 and 7.54 depict the beam shear force-drift and joint shear strength-drift envelope curves for the specimen, respectively. It can be observed that the envelope curves for EW and NS beams are nearly identical particularly for initial stiffness. Figures 7.55 and 7.56 show upper column axial load and beam shear histories for the specimen. The horizontal segments of the plots refer to pausing periods for monitoring cracks and changing loading protocol parameters. It can be observed from Fig. 7.56 that the residual beam shear forces tend to become zero instead of the initial gravity preloading negative shear forces by the time the joint shear capacity is reached. Afterwards, these residual forces are essentially reversed to tensile forces indicating strength degradation and gross nonlinearity in the joint performance.

Figures 7.57 and 7.58 exhibit the normalized joint shear stress-strain hysteretic behavior of north and east joint faces. The peak negative north joint face shear stress corresponded to a shear strain of -0.0036 radians, while the shear strain recorded at peak positive joint shear stress was 0.007 radians. The north joint face shear strain at the onset of axial collapse was -0.02 radians. The east joint face shear strain measurements were less reliable possibly because of movement of the instrument during the test.

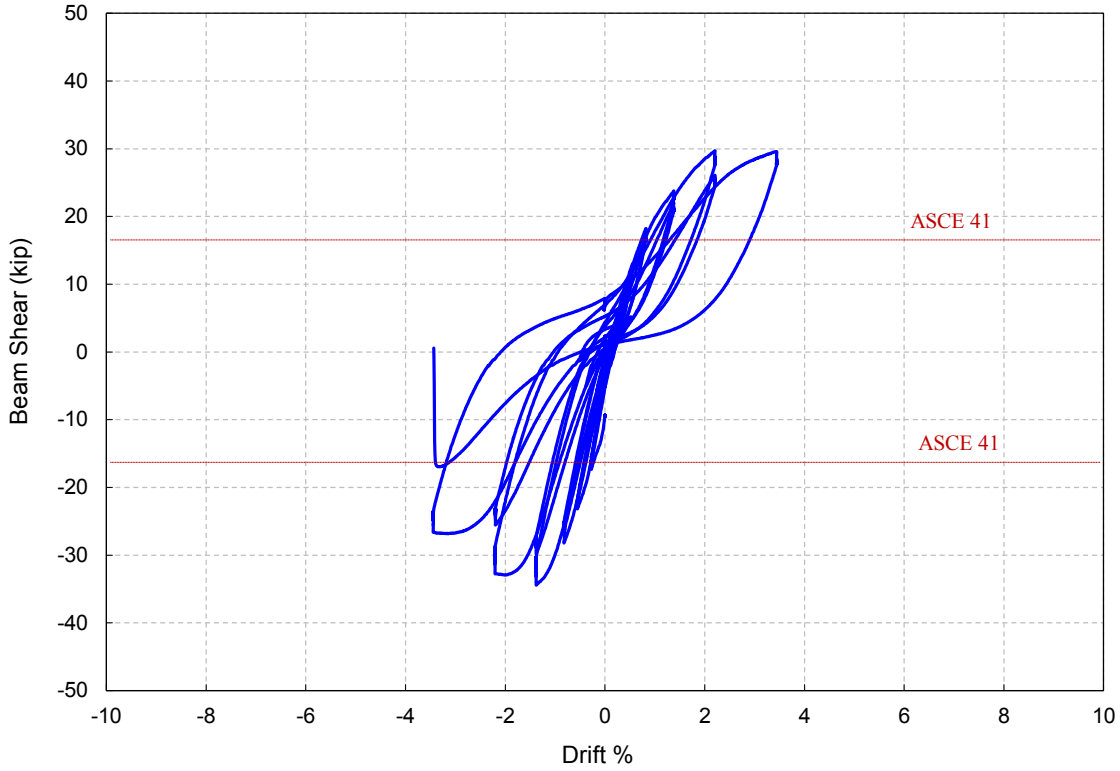

Figure 7.51 Relation between force and drift for EW-beam of specimen B-J-1

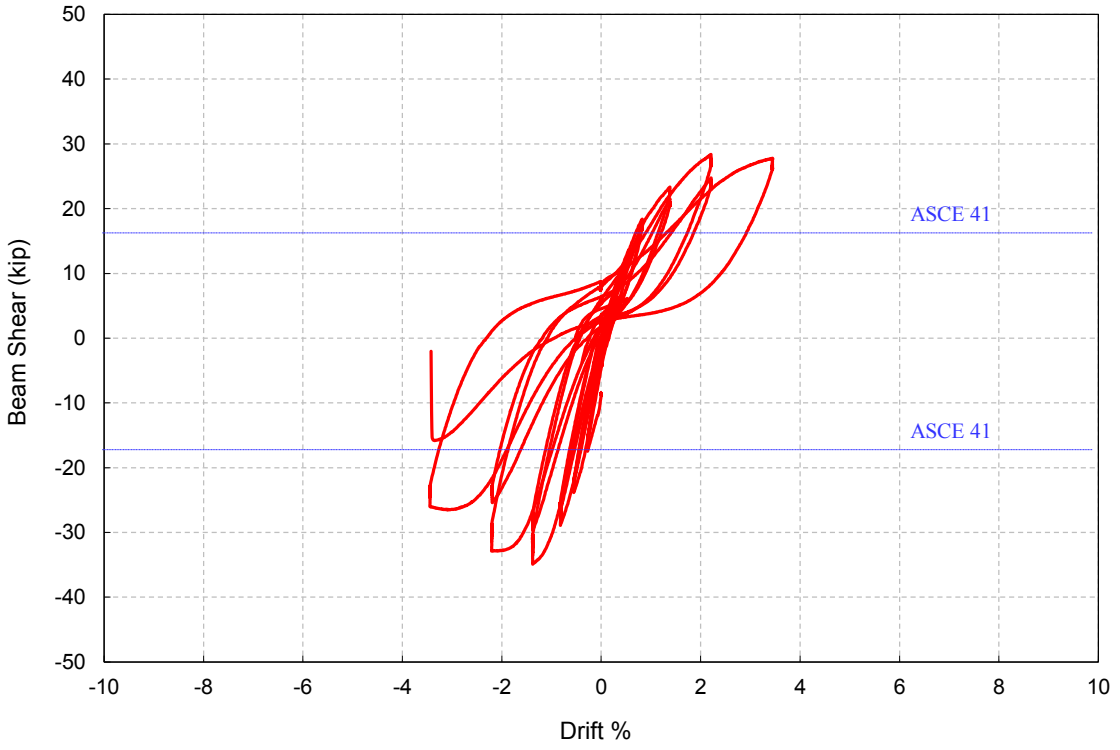

Figure 7.52 Relation between force and drift for NS-beam of specimen B-J-1

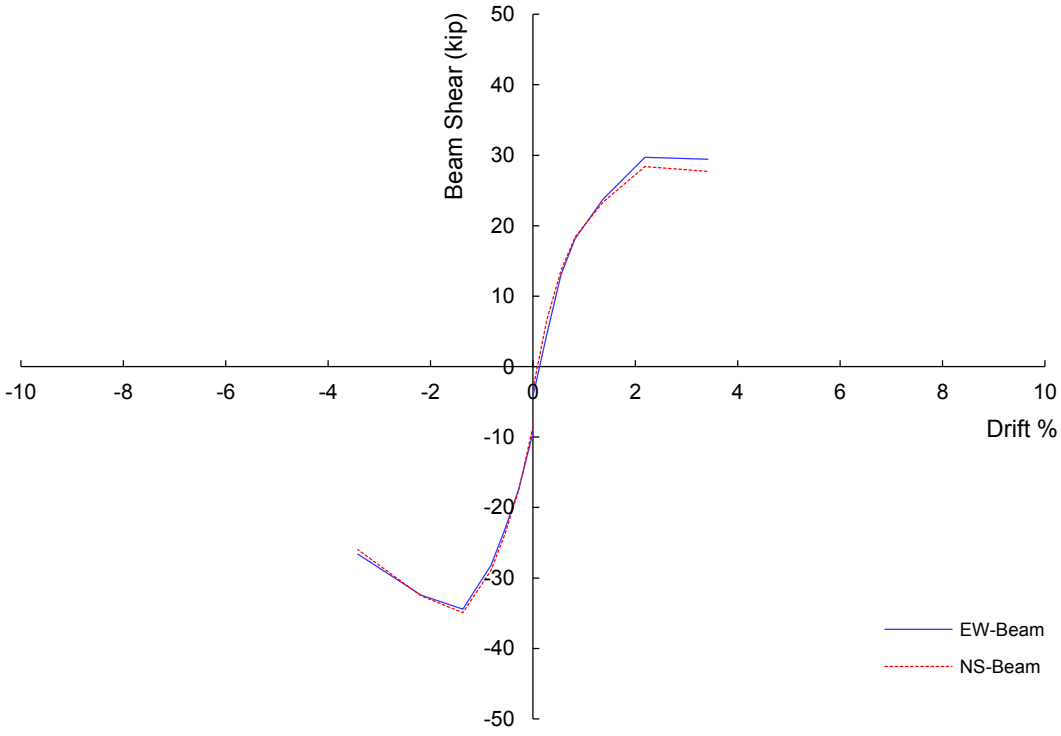

Figure 7.53 Backbone curves of specimen B-J-1

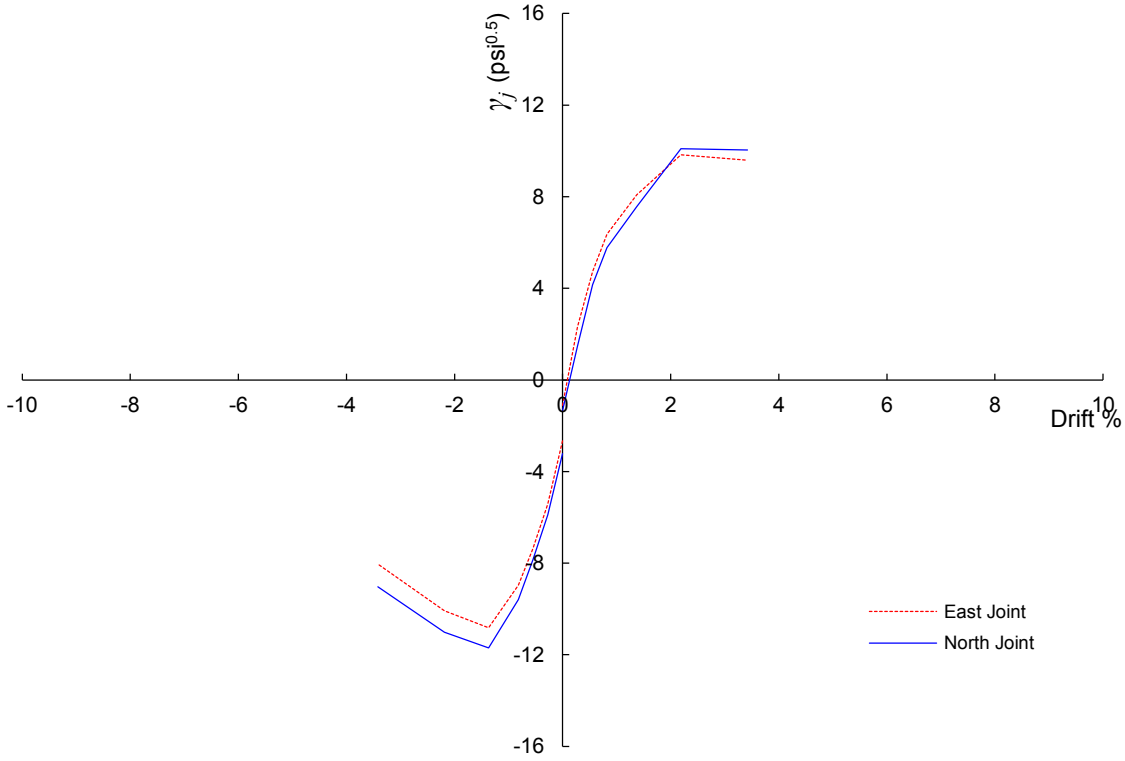

Figure 7.54 Backbone curves of specimen B-J-1

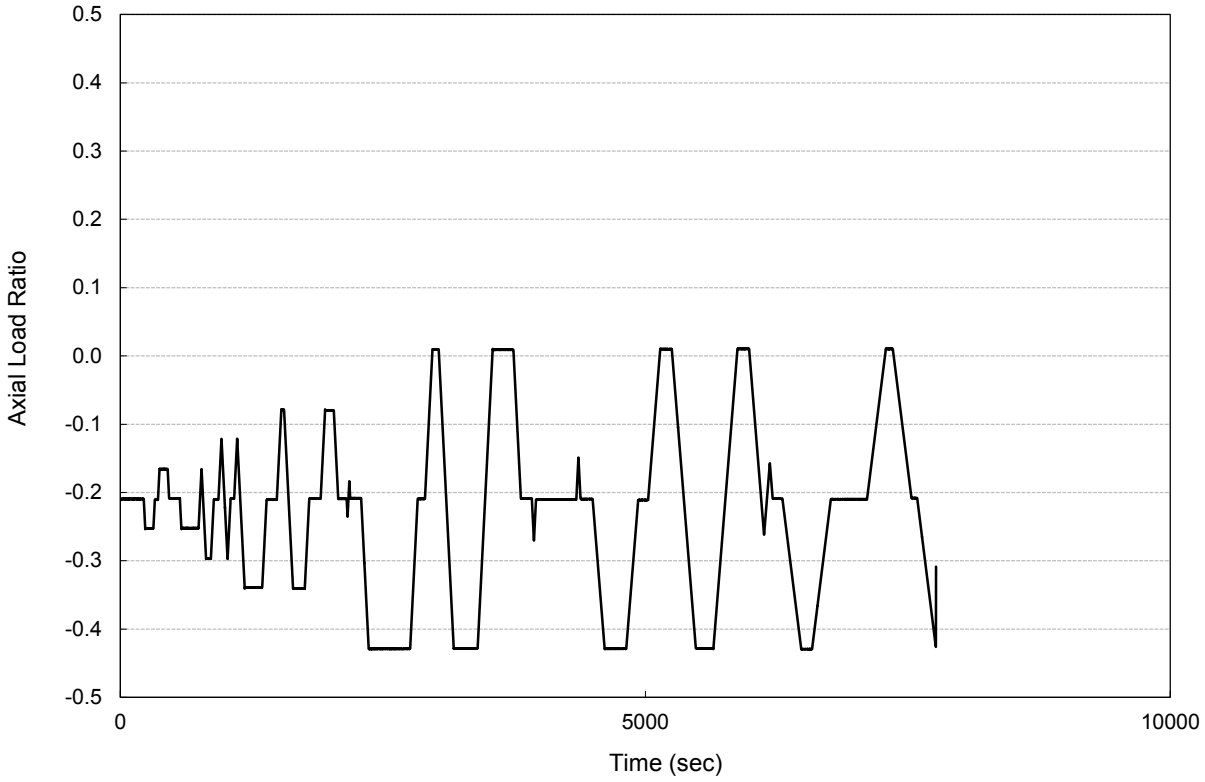

Figure 7.55 Upper column axial load History of specimen B-J-1

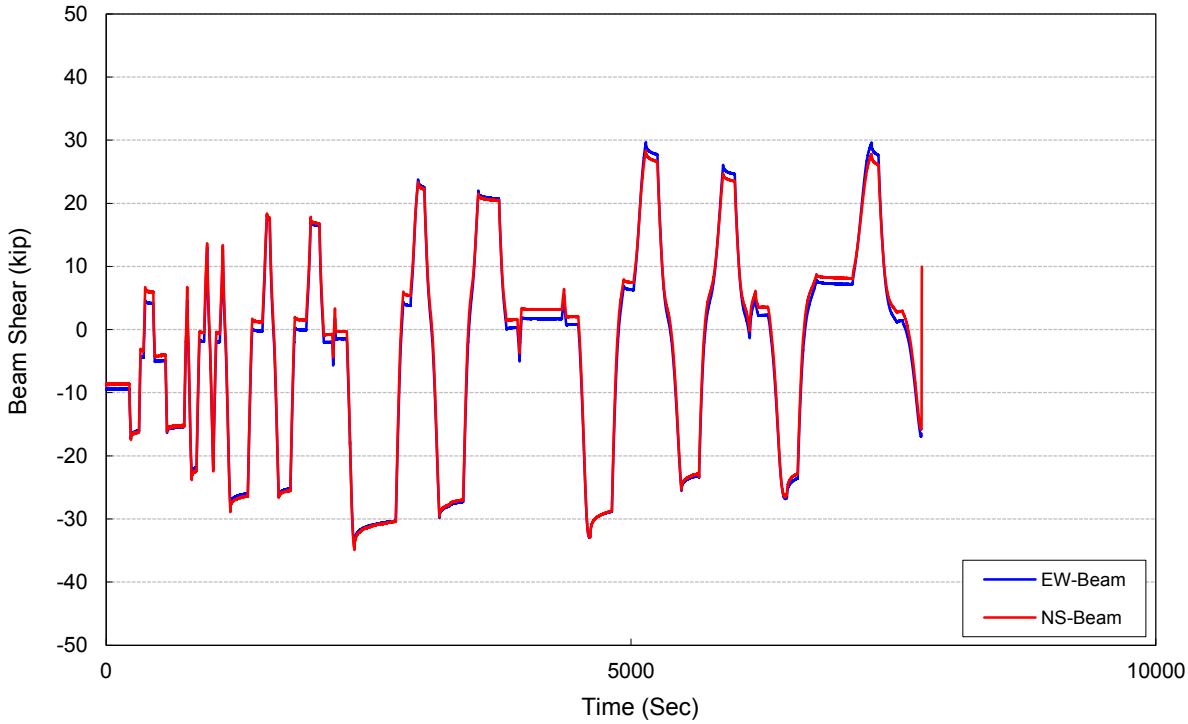

Figure 7.56 Beam shear History of specimen B-J-1

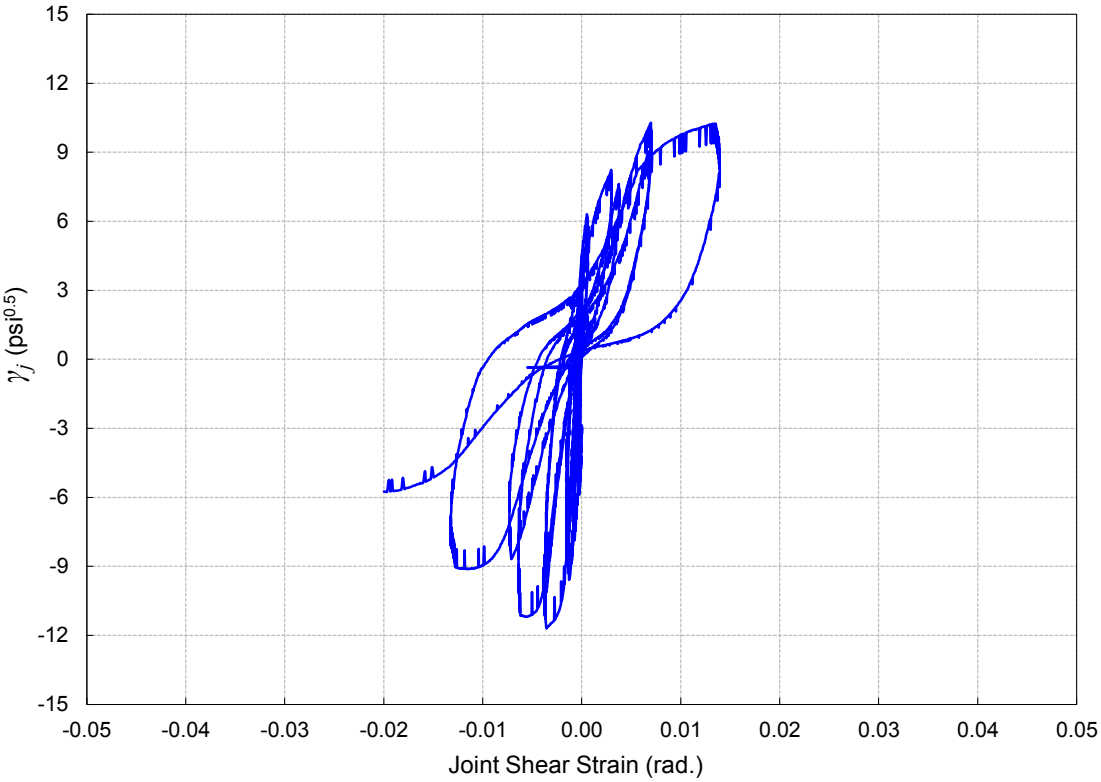

Figure 7.57 North joint face shear stress-strain relation for specimen B-J-1

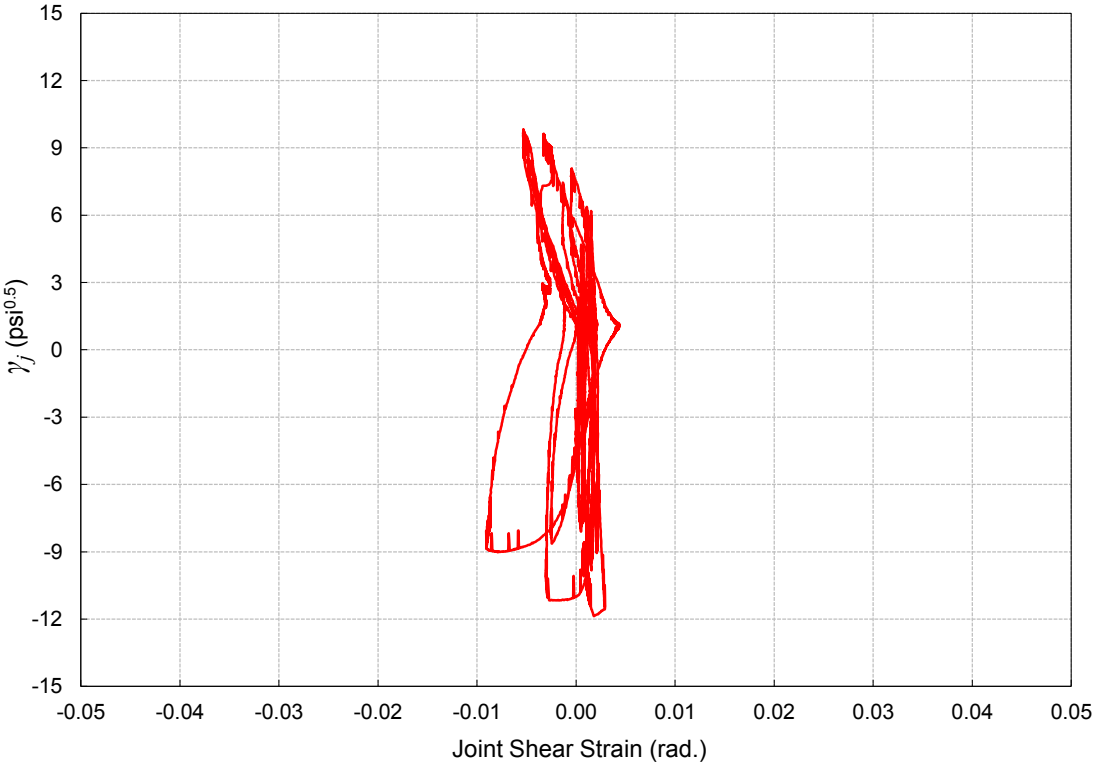

Figure 7.58 East joint face shear stress-strain relation for specimen B-J-1

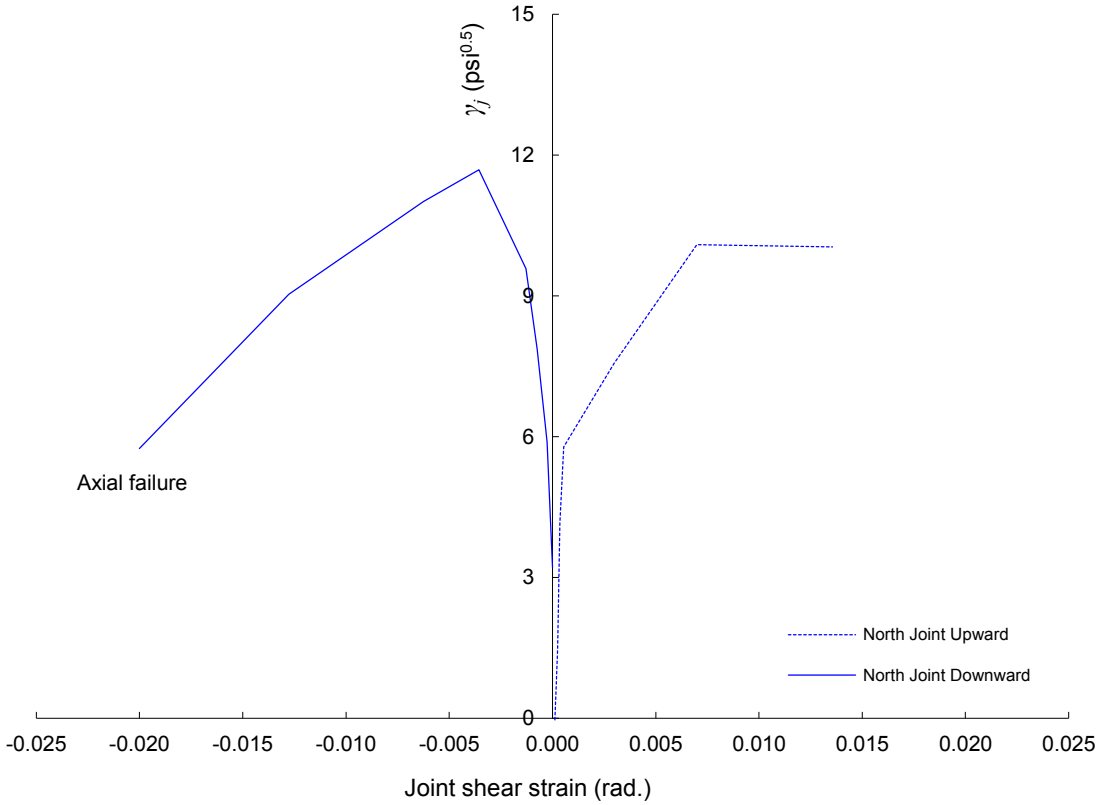

Figure 7.59 North joint face shear stress-strain envelope for specimen B-J-1

Figure 7.60 shows the contribution of joint shear deformation to the overall drift of the joint subassembly represented by the ratio of the beam tip displacement induced by joint shear deformation to the total beam displacement. The contribution of the north joint face to the EW beam drift reached 20% and 25% for the negative and positive peak joint shear strength, respectively. The north joint face shear deformation contribution to the total drift prior to axial collapse was about 30% for both negative and positive loading cycles.

Figure 7.61 displays the peak-to-peak effective stiffness degradation plots for both EW and NS beam loading. It can be observed that the effective stiffness of both loading beams is identical except for the first few loading steps at which stiffness may have differed because of the differences in cracking strength in the positive loading direction. However, effective stiffness degradation is identical for both sides throughout. Effective stiffness at peak joint shear strength and all the subsequent peaks is identical for both beams.

Figure 7.62 exhibits the cumulative energy dissipation during B-J-1 specimen loading. Unlike alternating uniaxially loaded specimens, it is clear that the energy dissipated through EW and NS beams is identical. This confirms the reason for lower energy dissipation of NS beams compared to EW beams in specimens U-J-1 and U-J-2. For specimen B-J-1, the energy dissipated during post-peak cycles was significantly higher than that of the elastic cycles.

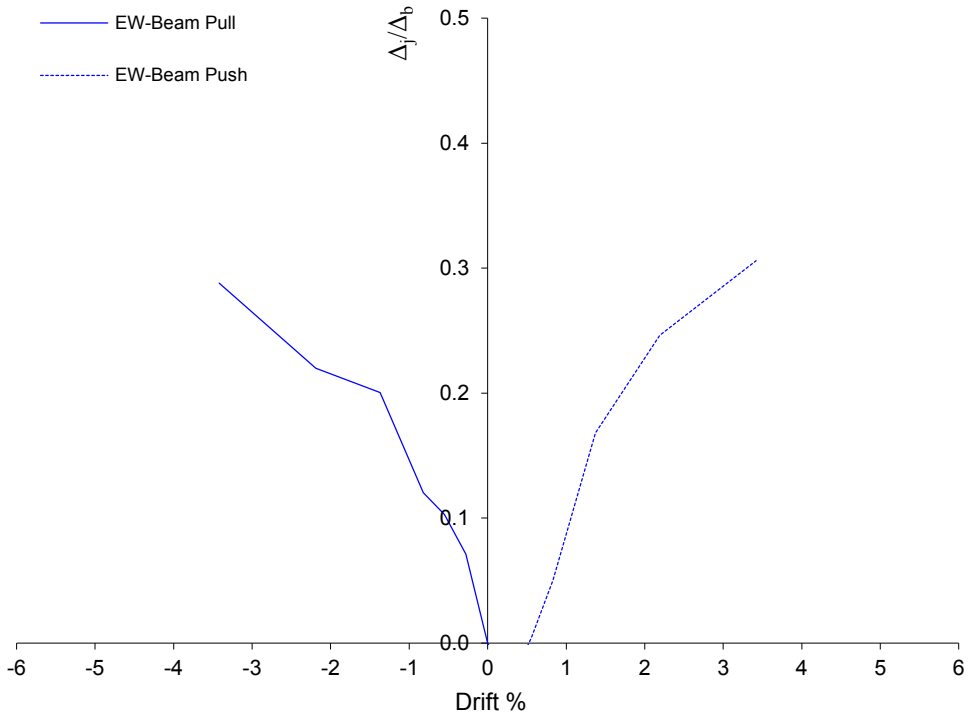

Figure 7.60 North joint face deformation contribution to total drift ratio of EW-beam for specimen B-J-1

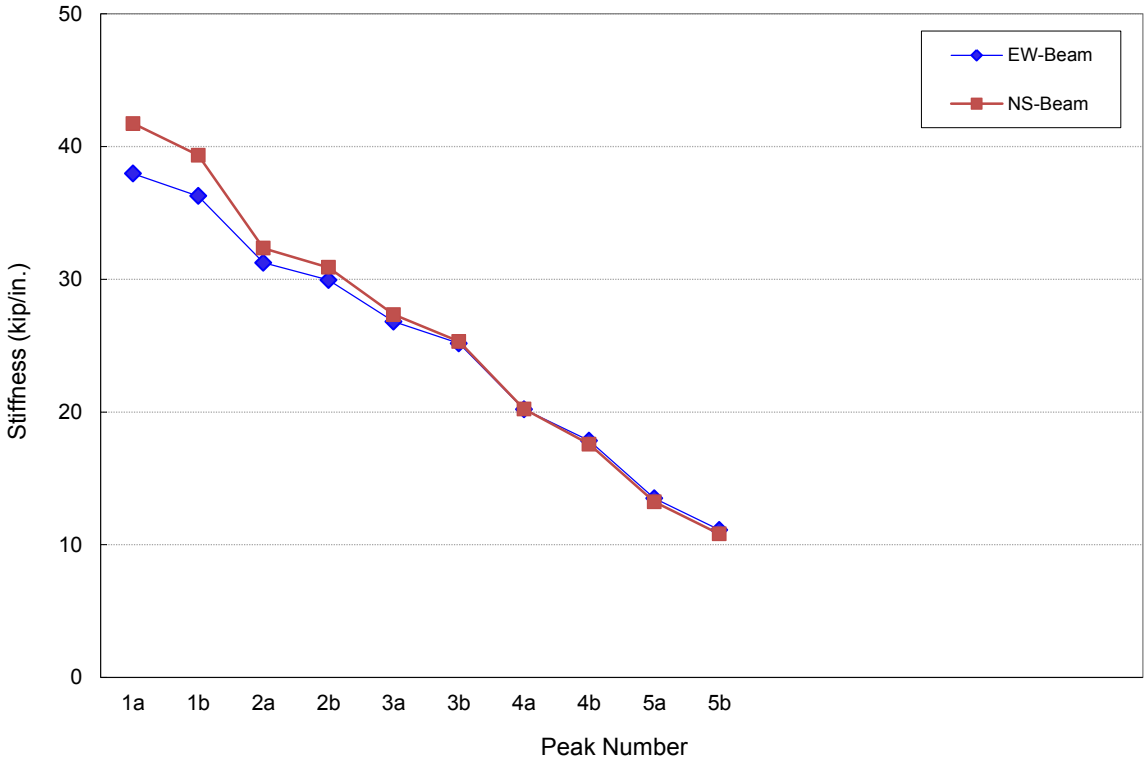

Figure 7.61 Peak-to-peak stiffness for specimen B-J-1

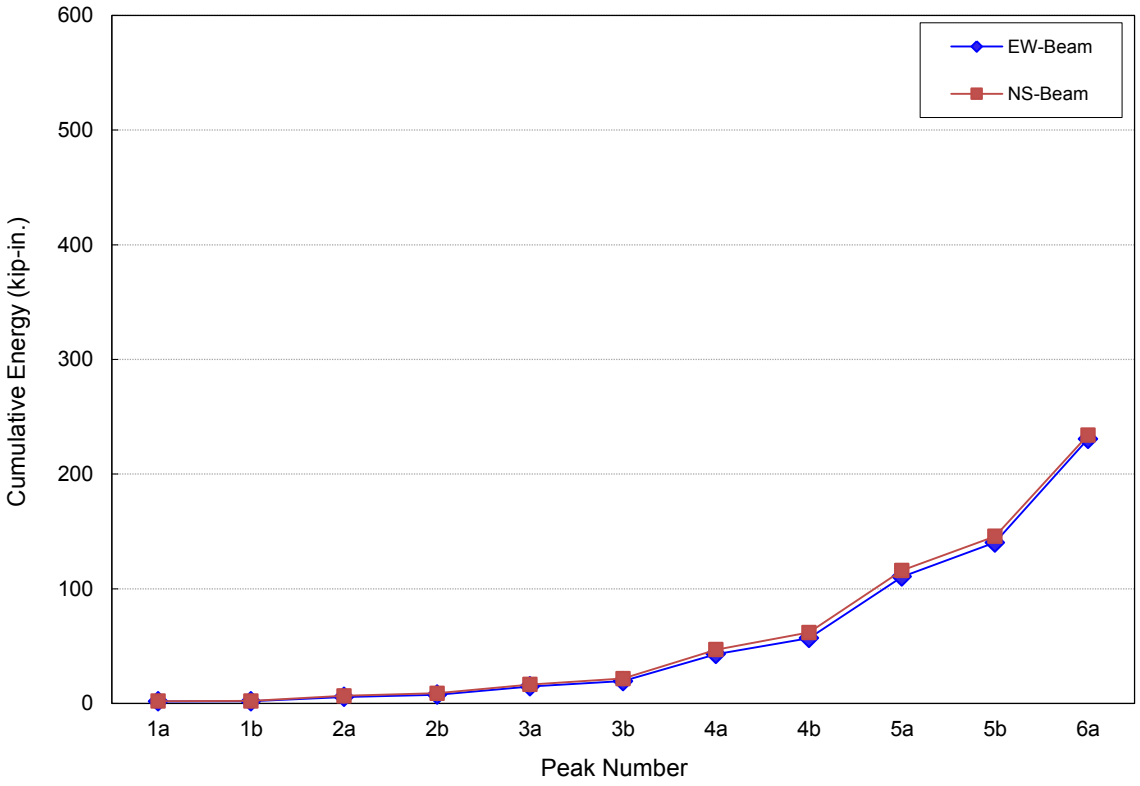

Figure 7.62 Peak-to-peak cumulative energy dissipation for specimen B-J-1

Figure 7.63 and Fig. 7.64 exhibit the strain distribution of slab top reinforcement at first cycles of negative drift peaks of EW and NS beam loading. Strain profile is normalized by yield strain ε_y. It is clear that the first slab reinforcement bar adjacent to the EW beam and NS beam yielded at the negative joint shear strength peak 4a (-1.37% drift) although beam reinforcement did not yield at this peak. The second slab reinforcement bar parallel to EW beam and NS beam did not reach yield at the negative joint shear strength peak. However, it was very close to yield at this peak. This indicates that the slab contribution was somewhat reduced for bidirectional loading as compared to unidirectional loading.

Figures 7.65 and 7.66 display the strain profile of the exterior and interior beam reinforcement bars under the first negative drift loading peaks of EW beam. The EW beam reinforcement did not experience yield throughout the test. Strains of the exterior bars are higher than those of the interior bars. NS top beam exterior reinforcement experienced yielding at negative peak 5a (2.19% drift) after reaching joint shear capacity.

Figures 7.67 and 7.68 display the strain profile of the exterior and interior beam reinforcement for the first positive drift loading peaks of NS beam. Beam reinforcement along beam span did not yield throughout the test, including the joint-beam interface location. However, yielding of this reinforcement took place within the joint core after reaching the joint shear capacity due to excessive cracking in the joint.

No column reinforcement bars yielded at column-joint interface before reaching joint shear capacity in both upward and downward loading directions. However, as strain profiles presented in Appendix A depict, yielding of some column bars, especially during upward cycle, took place. This confirms the possibility of slight yielding of most stressed column bars even in the case of strong column-weak beam design following ACI 318-08 provisions in the case of bidirectional loading. Yielding of some column bars at mid-joint height during downward loading after joint shear capacity was reached because of bar buckling. Figures 7.69 and 7.70 show the strain profile along the height of the intermediate column reinforcement bars CN and CE during first drift loading peaks, respectively. It can be observed that longitudinal strains at the joint mid-height are insignificant until reaching joint shear capacity at negative drift peak 4a, after which the strains were eventually reached yield because of bar buckling. This suggests that the intermediate column bars do not contribute significantly to joint strength in the biaxial loading case, similar to the uniaxial case. The excessive strains observed after reaching peak joint strength are attributed to buckling effect due to the high axial loads combined with loss of bond between concrete and column bars. In the positive drift cycles, the contribution of the central column bars to joint shear strength was also negligible. The yielding of bar CN shown in Figure 7.8 at mid-joint height at the positive drift peak following joint shear capacity (peak 6a) is attributed to tensile force penetration from the column reinforcement outside the joint because of the simultaneous loading of the two beams rather than presence of vertical column reinforcement truss mechanism.

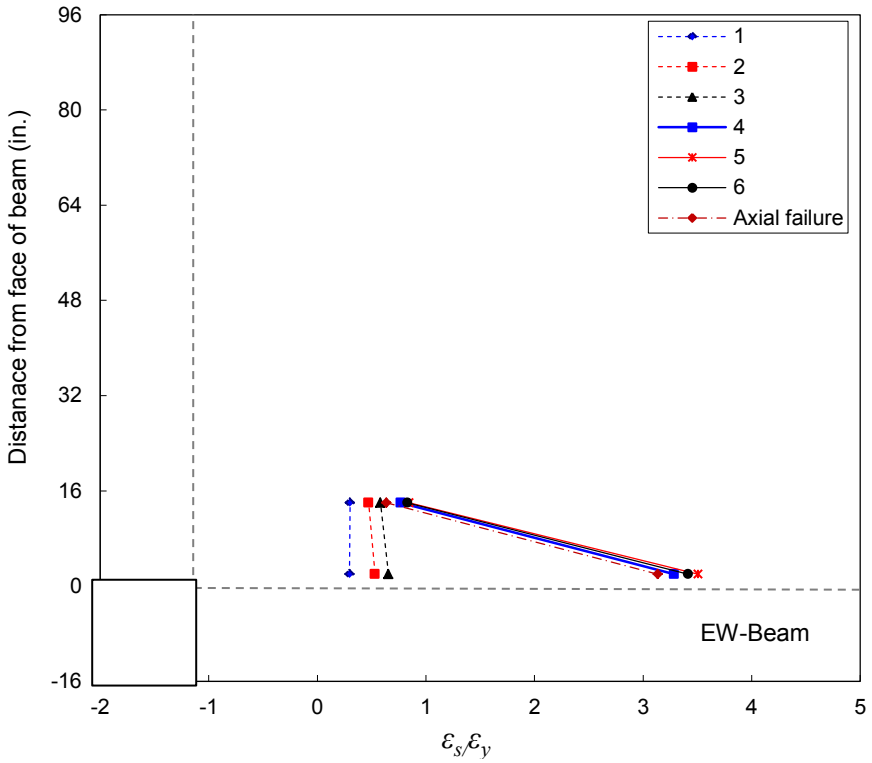

Figure 7.63 Bottom slab reinforcement strain distribution for B-J-1 during first negative drift peaks

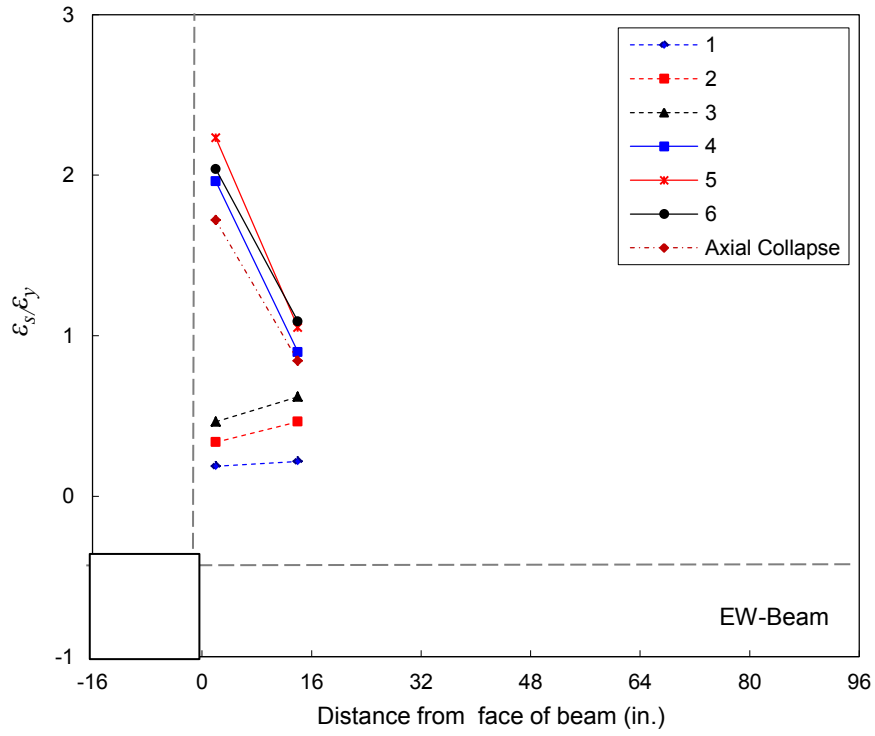

Figure 7.64 Top slab reinforcement strain distribution for B-J-1 during first negative NS drift peaks

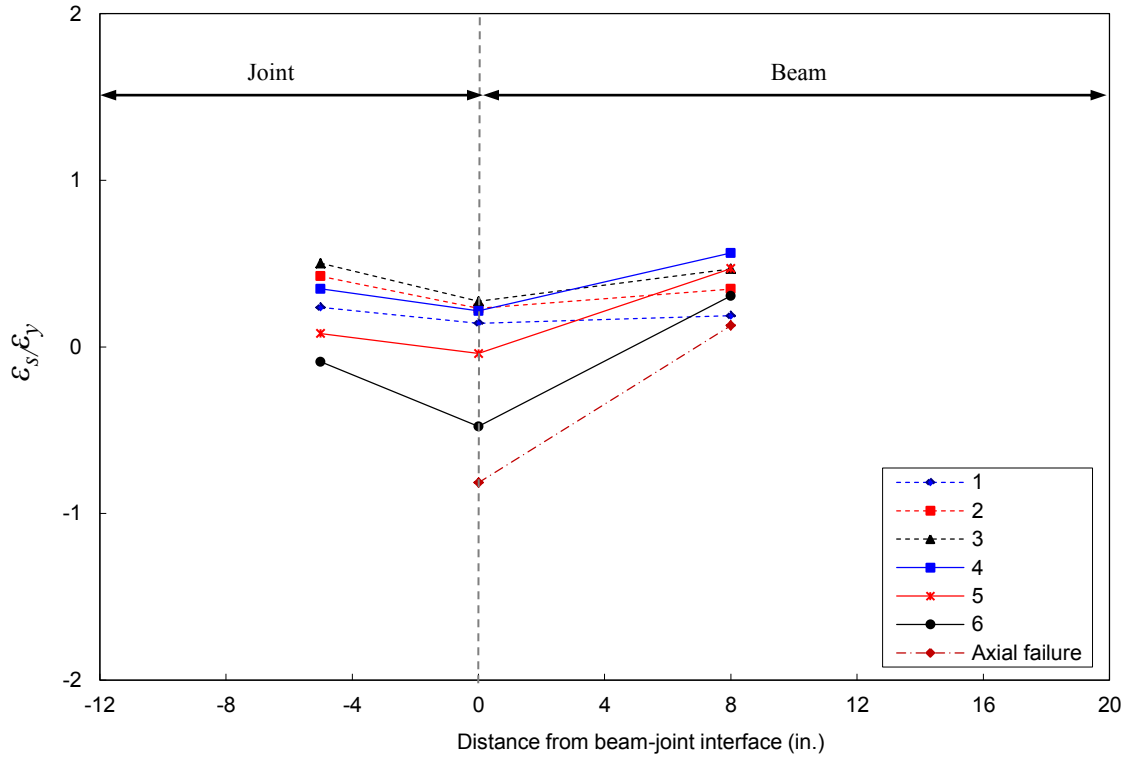

Figure 7.65 EW-beam top exterior longitudinal reinforcement strain for B-J-1 negative first drift peaks

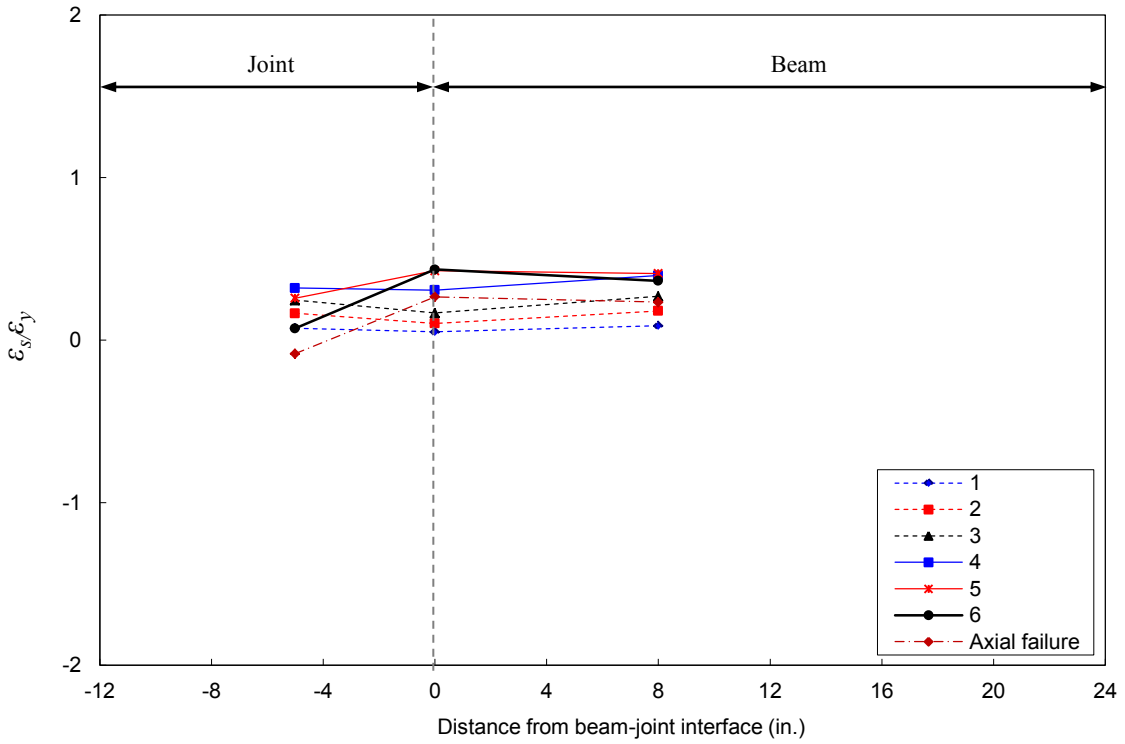

Figure 7.66 EW-beam top interior longitudinal reinforcement strain for B-J-1 negative first drift peaks

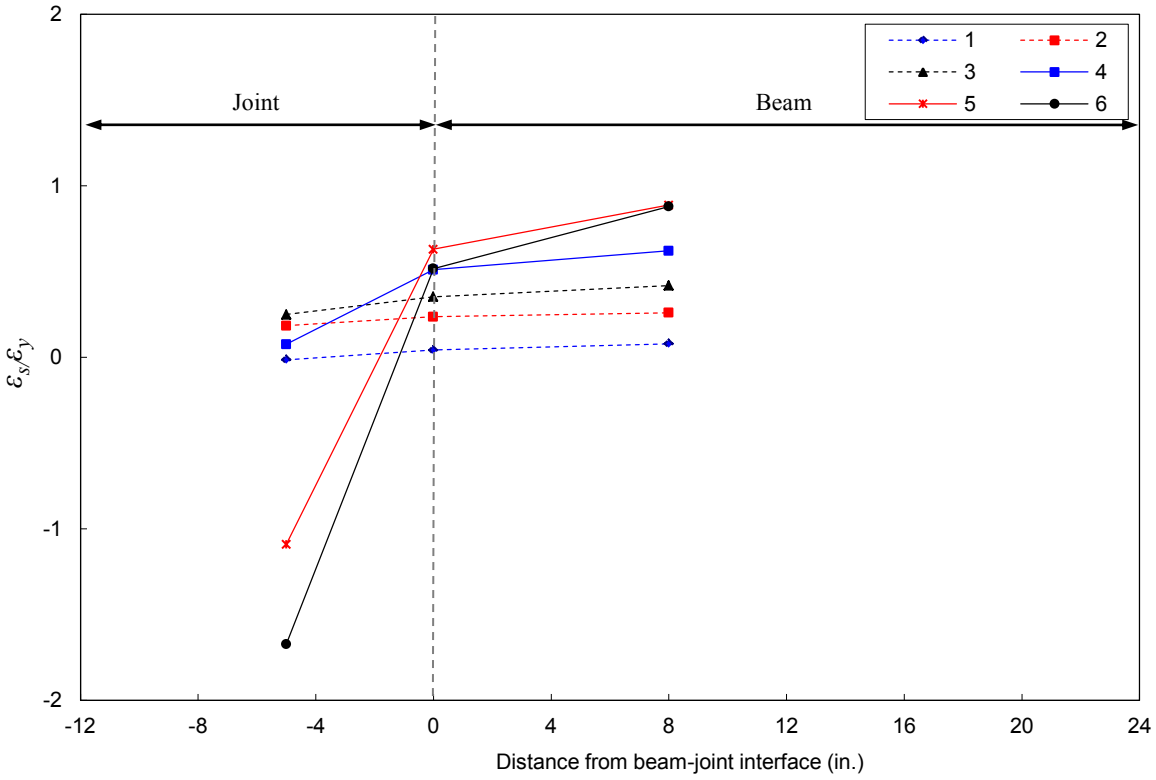

Figure 7.67 NS-beam bottom exterior longitudinal reinforcement strain for B-J-1 positive first drift peaks

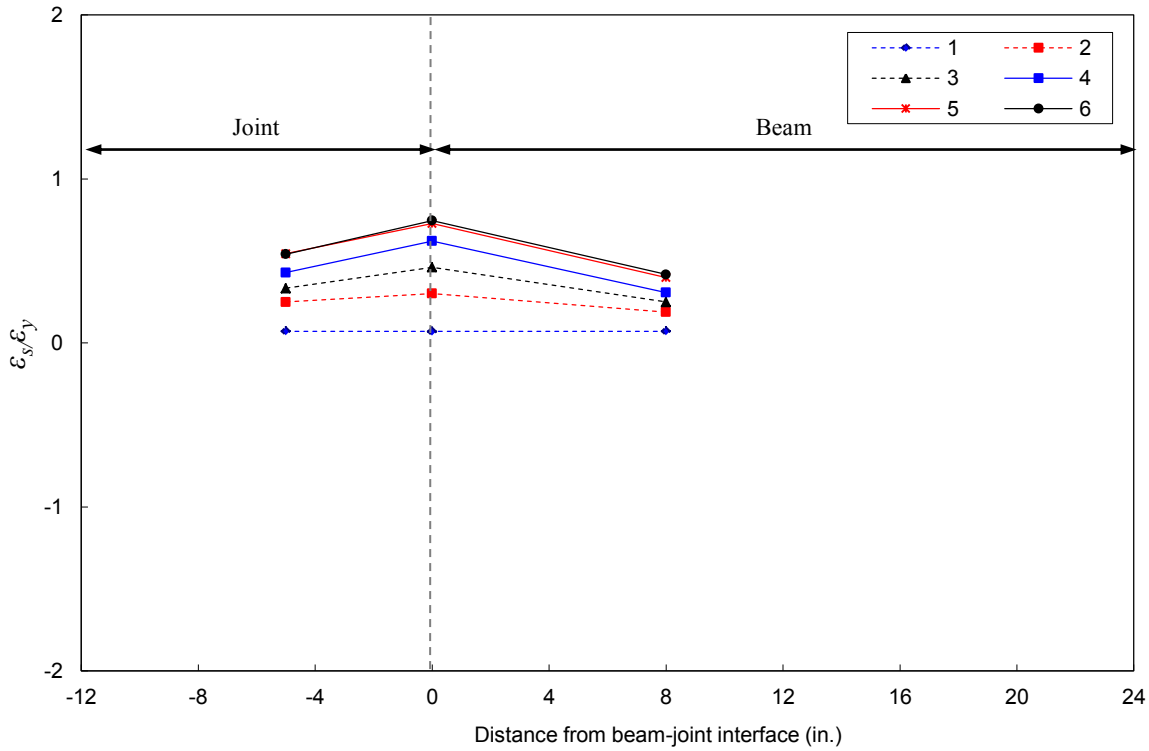

Figure 7.68 NS-beam bottom interior longitudinal reinforcement strain for B-J-1 positive first drift peaks

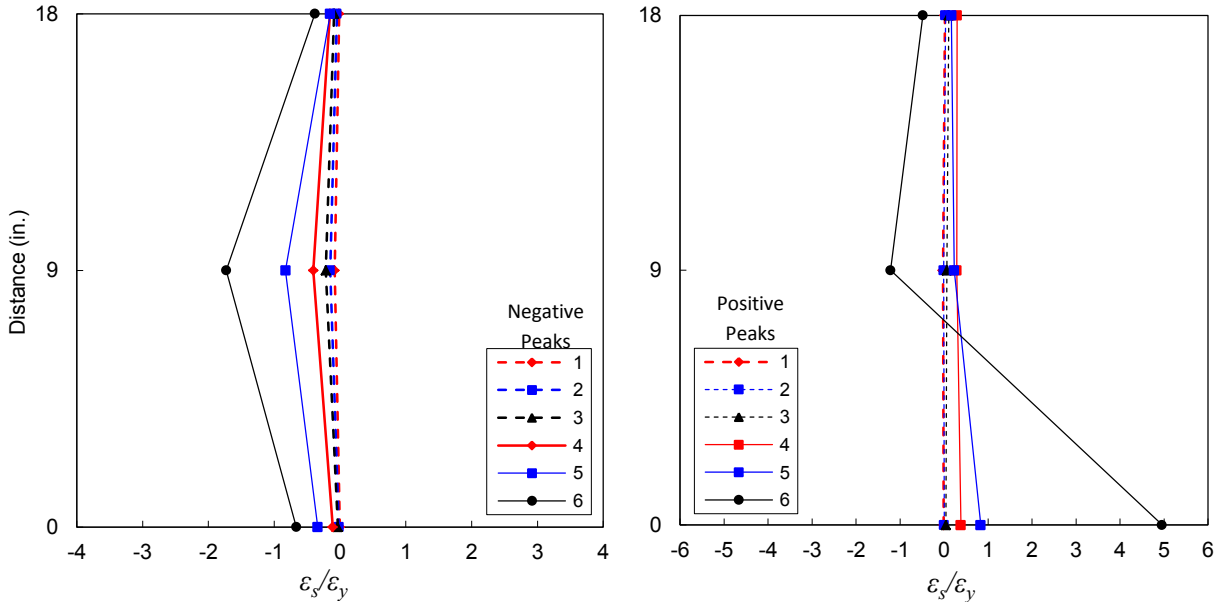

Figure 7.69 Strain development for column intermediate reinforcement CN of B-J-1 first drift peaks

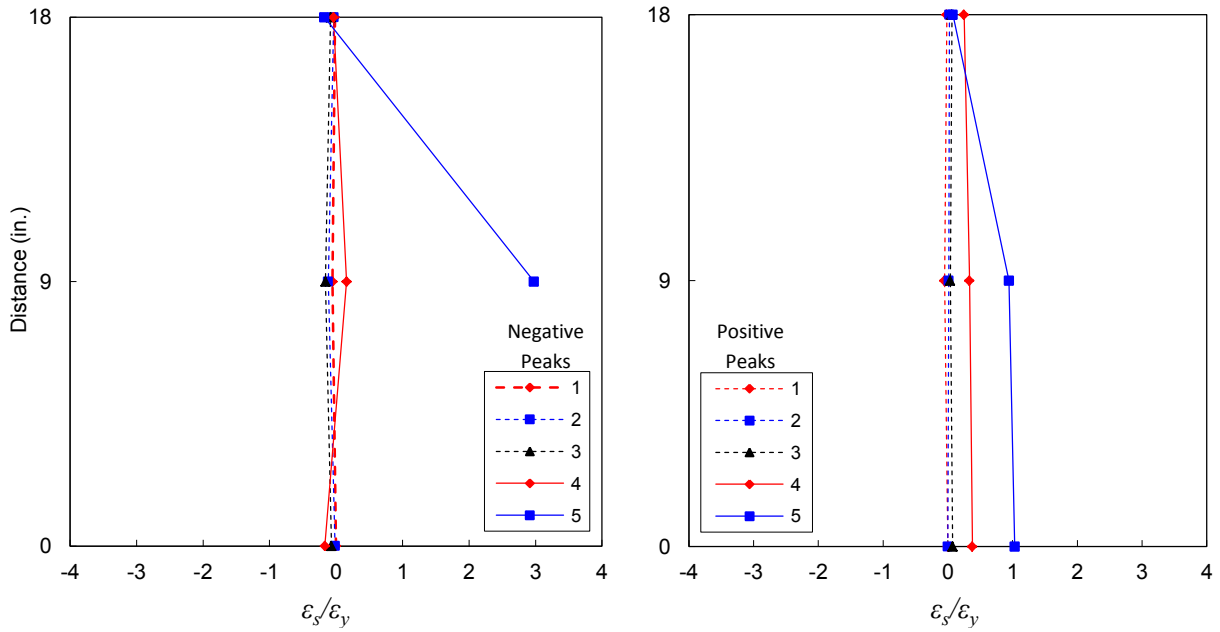

Figure 7.70 Strain development for column intermediate reinforcement CE of B-J-1 first drift peaks

Table 7.3.a Summary of performance parameters of specimen B-J-1, EW direction, downward loading

Load Peak	*Drift* (%)	$V_{b\text{-}EW}$ (kip)	$V_{c\text{-}EW}$ (kip)	$V_{j\text{-}N}$ (kip)	γ_j (psi$^{0.5}$)	γ_s (rad.)	$P_{u,col}$ (kip)	$P_{L,col}$ (kip)	Axial load ratio	K_P (kip/in.)	E_i (kip-in.)	$E_{cum.}$ (kip-in.)
0	0.00	-9.45	-6.84	-60.1	-3.20	0.0000	-303	-321	-0.22	-	-	-
1a	-0.28	-17.3	-12.6	-110	-5.89	-0.0003	-363	-398	-0.27	38.0	1.69	1.69
1b	-0.28	-16.4	-11.9	-104	-5.56	-0.0003	-363	-395	-0.27	36.3	0.15	1.84
2a	-0.55	-23.2	-16.8	-147	-7.87	-0.0007	-425	-472	-0.31	31.2	3.88	5.72
2b	-0.55	-22.0	-16.0	-140	-7.49	-0.0008	-425	-470	-0.31	29.9	1.90	7.62
3a	-0.82	-28.2	-20.4	-179	-9.58	-0.0013	-487	-545	-0.36	26.8	7.21	14.8
3b	-0.82	-26.1	-18.9	-166	-8.86	-0.0015	-487	-540	-0.36	25.2	4.58	19.4
4a	-1.37	-34.4	-24.9	-219	-11.7	-0.0036	-614	-683	-0.45	20.2	23.6	43.1
4b	-1.37	-29.4	-21.3	-187	-9.98	-0.0036	-613	-671	-0.45	17.8	14	57.0
5a	-2.19	-32.4	-23.5	-206	-11.0	-0.0062	-614	-679	-0.45	13.5	53.5	111
5b	-2.19	-25.6	-18.5	-162	-8.68	-0.0071	-612	-663	-0.45	11.1	29.7	140
6a	-3.42	-26.6	-19.3	-169	-9.03	-0.0128	-615	-667	-0.46	7.80	90.5	231
Axl. Fail	-3.36	-16.5	-11.9	-105	-5.60	-0.0202	-609	-641	-0.45	-	-	-

Table 7.3.b Summary of performance parameters of specimen B-J-1, NS direction, downward loading

Load Peak	*Drift* (%)	$V_{b\text{-}NS}$ (kip)	$V_{c\text{-}NS}$ (kip)	$V_{j\text{-}E}$ (kip)	γ_j (psi$^{0.5}$)	γ_s (rad.)	$P_{u,col}$ (kip)	$P_{L,col}$ (kip)	Axial load ratio	K_P (kip/in.)	E_i (kip-in.)	$E_{cum.}$ (kip-in.)
0	0.00	-8.57	-6.20	-54.2	-2.65	NA	-303	-321	-0.22	-	-	-
1a	-0.28	-17.5	-12.7	-111	-5.41	NA	-363	-398	-0.27	41.7	2.03	2.03
1b	-0.28	-16.1	-11.6	-102	-4.98	NA	-363	-395	-0.27	39.3	0.20	2.23
2a	-0.55	-23.8	-17.3	-151	-7.38	NA	-425	-472	-0.31	32.3	4.35	6.58
2b	-0.55	-22.5	-16.3	-142	-6.96	NA	-425	-470	-0.31	30.9	2.26	8.84
3a	-0.82	-28.9	-20.9	-183	-8.96	NA	-487	-545	-0.36	27.3	7.74	16.6
3b	-0.82	-26.3	-19.1	-167	-8.16	NA	-487	-540	-0.36	25.3	5.16	21.7
4a	-1.37	-34.9	-25.3	-221	-10.8	NA	-614	-683	-0.45	20.2	25.2	46.9
4b	-1.37	-29.1	-21.1	-184	-9.02	NA	-613	-671	-0.45	17.6	15	61.9
5a	-2.19	-32.5	-23.5	-206	-10.1	NA	-614	-679	-0.45	13.2	54.1	116
5b	-2.19	-25.4	-18.4	-161	-7.86	NA	-612	-663	-0.45	10.8	29.7	145
6a	-3.42	-26.0	-18.8	-164	-8.04	NA	-615	-667	-0.46	7.47	88.3	234
Axl. Fail	-3.36	-15.5	-11.2	-98.2	-4.81	NA	-609	-641	-0.45	-	-	-

Table 7.3.c Summary of performance parameters of specimen B-J-1, EW direction, upward loading

Load Peak	*Drift* (%)	$V_{b\text{-}EW}$ (kip)	$V_{c\text{-}EW}$ (kip)	$V_{j\text{-}N}$ (kip)	γ_j (psi$^{0.5}$)	γ_s (rad.)	$P_{u,col}$ (kip)	$P_{L,col}$ (kip)	Axial load ratio	K_P (kip/in.)	E_i (kip-in.)	$E_{cum.}$ (kip-in.)
1a	0.28	4.68	3.39	28.4	1.49	-0.0001	-236	-225	-0.17	38	1.69	1.69
1b	0.28	4.66	3.38	28.4	1.48	-0.0001	-237	-225	-0.18	36.3	0.15	1.84
2a	0.55	13.1	9.46	79.5	4.16	0.0000	-174	-147	-0.13	31.2	3.88	5.72
2b	0.55	12.7	9.19	77.2	4.04	0.0000	-173	-147	-0.13	29.9	1.90	7.62
3a	0.83	18.2	13.2	110	5.78	0.0005	-112	-75.2	-0.08	26.8	7.21	14.8
3b	0.83	17.5	12.6	106	5.56	0.0006	-112	-76.6	-0.08	25.2	4.58	19.4
4a	1.37	23.8	17.2	145	7.57	0.0030	14.0	61.2	0.01	20.2	23.6	43.1
4b	1.37	22.0	15.9	134	7.01	0.0038	14.8	58.3	0.01	17.8	14.0	57.0
5a	2.19	29.7	21.5	181	9.45	0.0070	15.0	73.0	0.01	13.5	53.5	110
5b	2.19	25.6	18.5	156	8.14	0.0068	14.6	64.5	0.01	11.1	29.7	140
6a	3.42	29.4	21.3	179	9.36	0.0136	15.1	72.2	0.01	7.80	90.5	231

Table 7.3.d Summary of performance parameters of specimen B-J-1, NS direction, upward loading

Load Peak	*Drift* (%)	$V_{b\text{-}NS}$ (kip)	$V_{c\text{-}NS}$ (kip)	$V_{j\text{-}E}$ (kip)	γ_j (psi$^{0.5}$)	γ_s (rad.)	$P_{u,col}$ (kip)	$P_{L,col}$ (kip)	Axial load ratio	K_P (kip/in.)	E_i (kip-in.)	$E_{cum.}$ (kip-in.)
1a	0.28	6.73	4.87	44.4	2.33	NA	-236	-225	-0.17	41.7	2.03	2.03
1b	0.28	6.74	4.88	44.4	2.34	NA	-237	-225	-0.18	39.3	0.20	2.23
2a	0.55	13.7	9.90	90.1	4.74	NA	-174	-147	-0.13	32.3	4.35	6.58
2b	0.55	13.4	9.69	88.2	4.64	NA	-173	-147	-0.13	30.9	2.26	8.84
3a	0.83	18.4	13.3	121	6.37	NA	-112	-75.2	-0.08	27.3	7.74	16.6
3b	0.83	17.5	12.6	115	6.05	NA	-112	-76.6	-0.08	25.3	5.16	21.7
4a	1.37	23.3	16.9	154	8.09	NA	14.0	61.2	0.01	20.2	25.2	46.9
4b	1.37	21.5	15.6	142	7.45	NA	14.8	58.3	0.01	17.6	15.0	61.9
5a	2.19	28.4	20.5	187	9.83	NA	15.0	73.0	0.01	13.2	54.1	116
5b	2.19	24.3	17.6	160	8.43	NA	14.6	64.5	0.01	10.8	29.7	146
6a	3.42	27.7	20.1	182	9.59	NA	15.1	72.2	0.01	7.50	88.3	234

7.3.4 Specimen U-BJ-1

Table 7.4 presents the characteristic response parameters of specimen U-BJ-1. Figures 7.75 and 7.76 display the force-drift ratio hysteretic loops of specimen U-BJ-1 for EW beam and NS beam, respectively. Both EW beam and NS beam fully yielded before joint started to degrade. Thus, the mode of failure of specimen U-BJ-1 was BJ-failure for both EW-beam and NS-beam downward and upward loading; satisfying the theoretical design. Both beams' flexural capacity matches the theoretical prediction in Chapter 6.It is clear that the hysteretic performance is significantly different from that of J-Failure specimens. Inflated loops characterizing yielding elements with long hardening plateau are evident. During later stages of loading, pinching due to shear degradation of joint is evident.

Figure 7.71 shows crack development and progression of north joint face and EW beam of specimen U-BJ-1. First EW beam flexural crack in the downward loading direction occurred during cycle 4a at 1.43% drift. A Second major EW beam flexural crack developed at -2.29% drift ratio. The first and second flexural cracks kept widening and several other beam flexural cracks formed in the subsequent negative cycles. The first and second observed EW beam upward loading major flexural cracks were at peak 5a (2.29% drift) and peak 6a (3.57% drift), respectively. A joint-beam interface flexural crack also developed at peak 5a indicating bond-slip deformation. The joint-beam interface crack kept widening afterwards indicating bond-slip nonlinear behavior. Unlike the other three specimens, beam reinforcement hook prying action was evidently clear.

The first north joint face diagonal crack occurred at EW beam downward drift peak of -5.5% (peak 7a). The inclination of this main diagonal crack was very steep closer to the vertical. This crack inclination is steeper than the theoretical prediction by strut-and-tie model due to the effect of the substantial axial load that affected principal stresses. A vertical north joint face cover splitting crack developed at the second drift peak of -5.5%. The first north joint face diagonal crack in the upward loading direction was at drift peak of 2.29% (peak 5a). The inclination of the main diagonal crack in the north joint face due to upward beam loading perfectly matches the theoretical inclination of diagonal strut. A north joint face second diagonal crack developed at upward loading peak 6b. These two parallel diagonal cracks in the upward loading direction (Fig. 7.71) along with the close to vertical diagonal crack in the downward loading direction form a distinct crack pattern different from the regular X-shape pattern in BJ-Failure specimens with low to moderate axial loads.

The first east joint face diagonal crack developed at NS beam negative drift peak of -5.5% (peak 7a) and positive drift peak of 2.29% (peak 5a). Two east joint face distinct diagonal cracks developed during the first downward loading cycle of -5.5%. The first resembles the main diagonal strut while the second represents the secondary strut generated by bond bearing of beam bars, Fig. 7.71. It is worth mentioning that the east and north joint face crack patterns were notably different.

Similar to previous specimens, horizontal column-joint interface cracks developed at the column tension side. Beam and slab torsional cracks similar to those observed in previous

specimens were also present. A vertical cover splitting crack developed at very late stage of loading prior to axial failure.

The axial failure of the joint took place during the first cycle of EW-beam downward loading displacement group 8a at -7.71% drift. This corresponds to an upper column axial load level of 0.47 and joint shear strength coefficient of 4.19. The ratio of joint shear strength coefficient at axial failure to that at joint shear capacity was 51%. Prior to axial failure, joint diagonal and vertical cracks significantly widened. Bulging of concrete cover indicating buckling of column bars was not as significant as specimen U-J-2 with higher aspect ratio. Hence, axial failure was very dramatic. Figure 7.72 shows snap shots of axial failure.

EW beam yielded at -0.92% drift ratio during downward drift cycle 4a. This corresponds to EW beam shear of -22.2 kips. The EW beam yielded at 1.02% drift ratio during upward drift cycle 4a at 20.2 kip beam shear. Based on flexible joint assumption, this drift is 15% lower than the theoretical yield drift in the downward loading direction and 19% lower than the theoretical yield drift in the upward loading direction. Based on the rigid joint assumption, the experimental yield drift in the downward and upward loading direction is 2% and 17% higher than their theoretical counterpart. It seems that rigid joint assumption is more suitable for yield calculations for downward loading direction while flexible joint assumption is more appropriate for upward loading direction. The sole reason of this is the high rigidity of the joint in the downward loading direction associated with substantial axial load in combination with very flexible beam behavior due to small reinforcement ratio. The joint shear strength coefficient corresponding to EW beam first yield in the downward loading direction was 7.06. The shear stress coefficient at yield value of upward loading direction was 5.92. The theoretical prediction for joint shear strength coefficient at EW beam yield for downward loading direction was 5.9 while that for downward loading and 4.9 for upward loading. The NS beam reached yield during the fourth displacement cycle 4a at -0.90% drift (-21 kips) in downward loading and 1% (21.1 kip) in upward loading. The corresponding joint shear stress coefficients are 6.32 and 6.35, respectively. The experimental joint shear stress coefficients corresponding to beam yield are lowers than the pure J-Failure stress coefficients predicted by strut-and-tie models proposed in Chapter 5. The long strain hardening plateau noticed in the response confirms the flexural dominated response.

The maximum shear force in the downward loading direction was reached at drift peak of -2.29% (peak 5a) for both EW-beam loading and NS-beam loading. The corresponding maximum negative joint shear strength coefficient γ_j was 8.20 for the north joint face and 7.37 for the east joint face, respectively. The average strain hardening force ratio for specimen U-BJ-1 was 20% which is consistent with steel tensile test results. The maximum applied upper column axial compression load ratio of 0.45 was reached at negative drift peak 3a (-0.86% drift).

The maximum beam shear force in the positive direction was reached at positive drift peak of 5.5% (peak 7a) for EW and drift peak of 3.57% (peak 6a) for NS beam loading. The corresponding joint shear strength coefficient γ_j was 7.51 and 7.6 for north joint face and east joint face, respectively. The maximum applied upper column axial tension load ratio of 0.05 the compression capacity was reached at positive drift peak 3a (0.86% drift).

Peak 5a (-2.29% Drift)

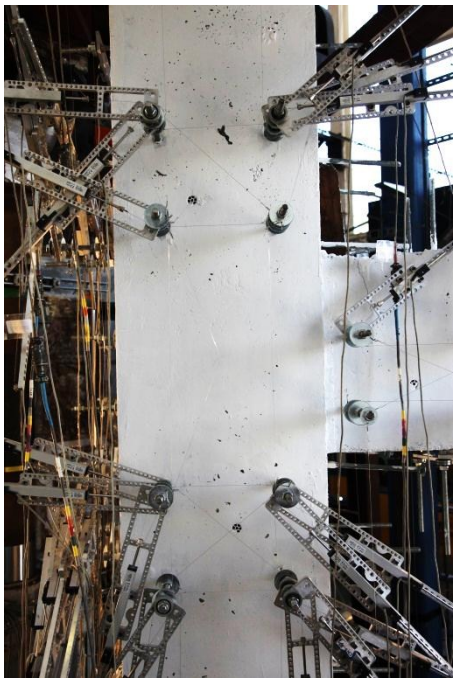

Peak 5a (2.29% Drift)

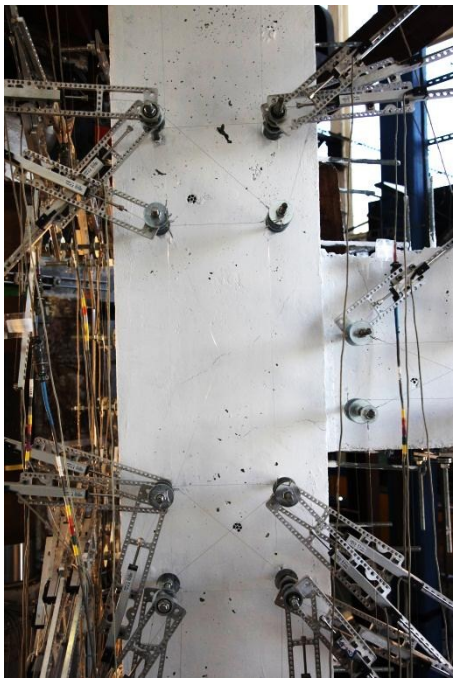

Peak 6a (-3.57% Drift)

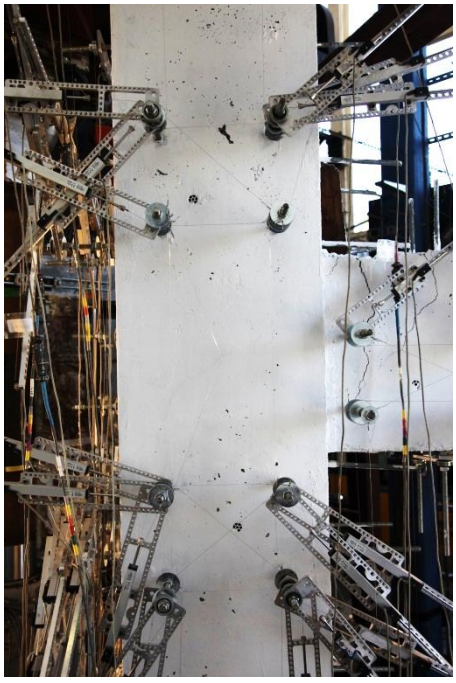

Peak 6a (3.57% Drift)

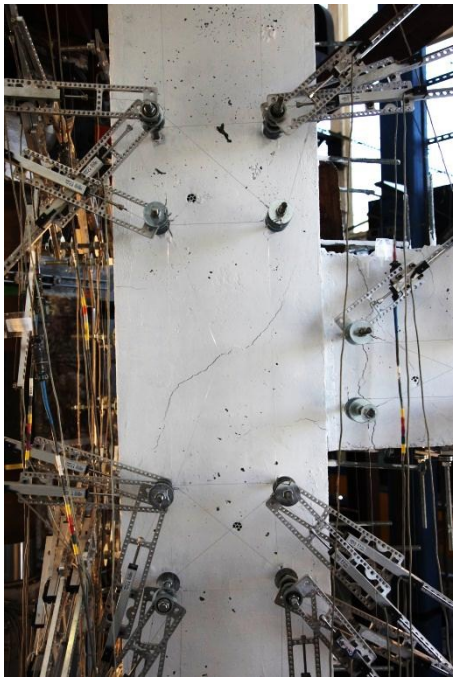

Figure 7.71 North joint face crack development and joint distress at first drift peaks in specimen U-BJ-1

Peak 7a (-5.5% Drift)

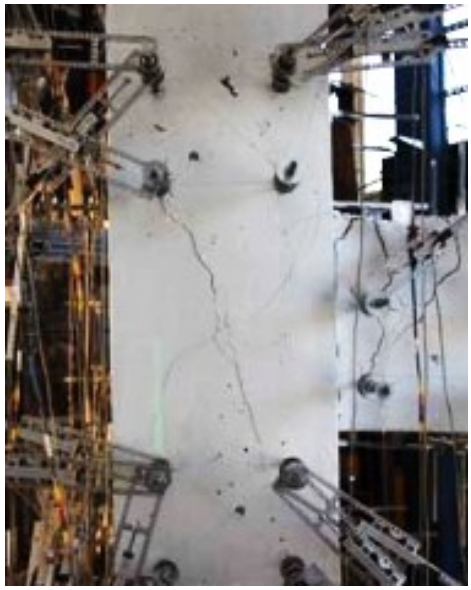

Peak 7a (5.5% Drift)

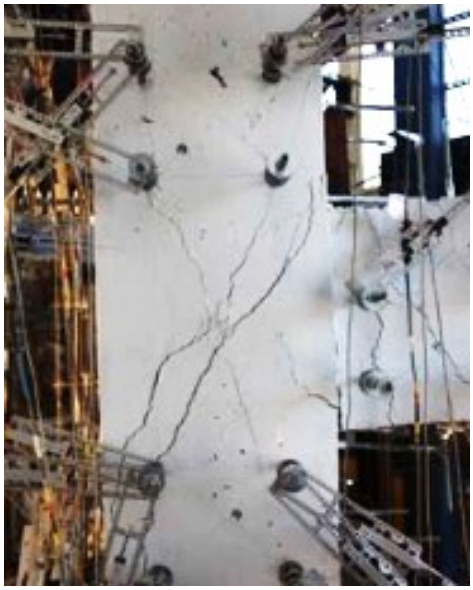

Instantly before axial failure (-7.71% drift)

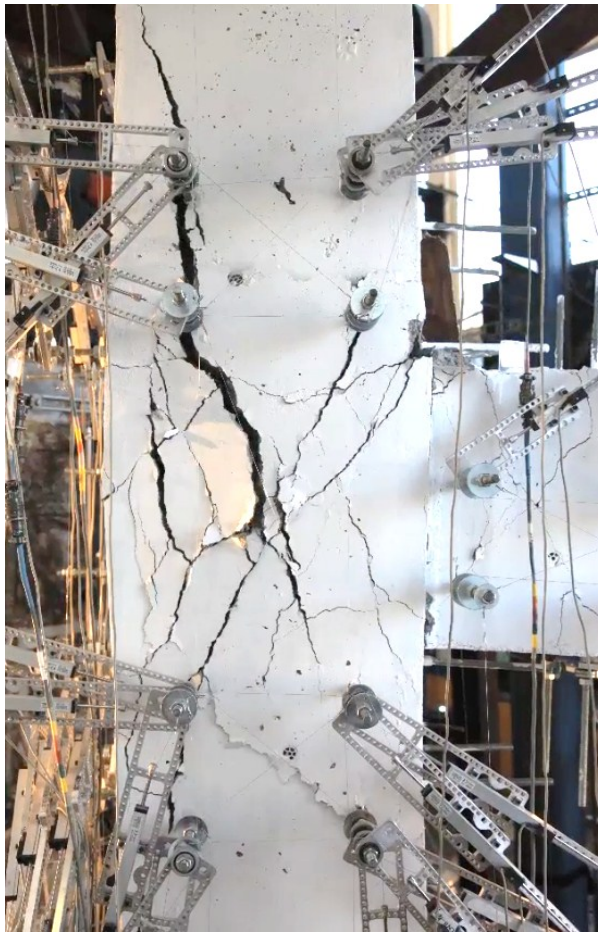

During axial failure

Figure 7.71 (*Continued*) North joint face crack development and joint distress at first peaks in specimen U-BJ-1

Figure 7.72 Global views of specimen U-BJ-1 after axial failure

Peak 5a (-2.29% drift)

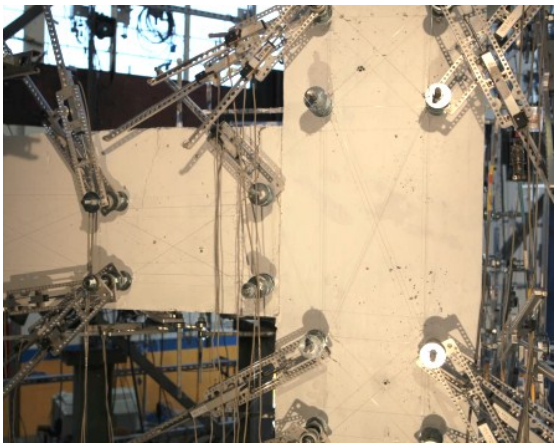

Peak 5a (2.29% drift)

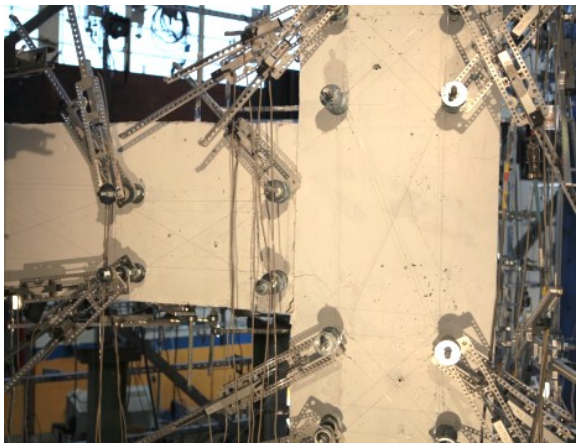

Peak 6a (-3.57% drift)

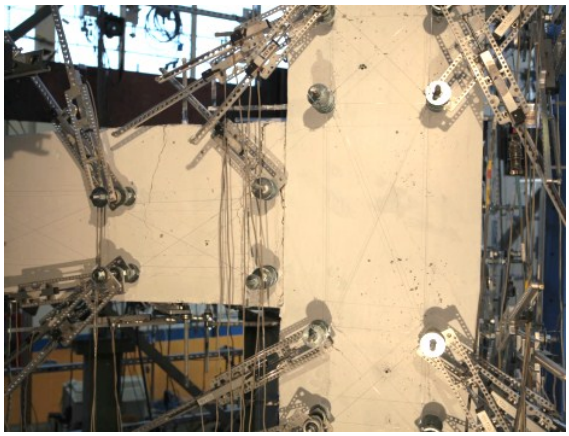

Peak 6a (3.57% drift)

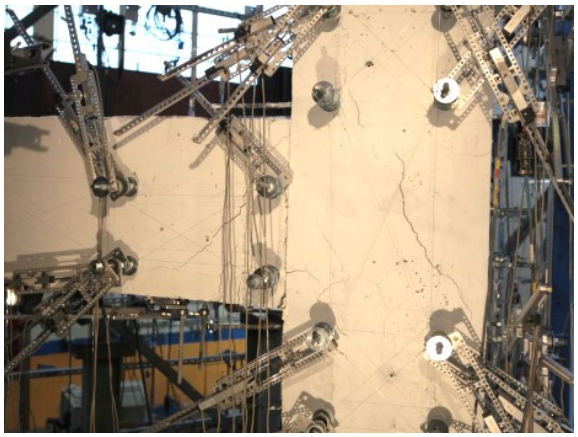

Peak 7a (-5.5% drift)

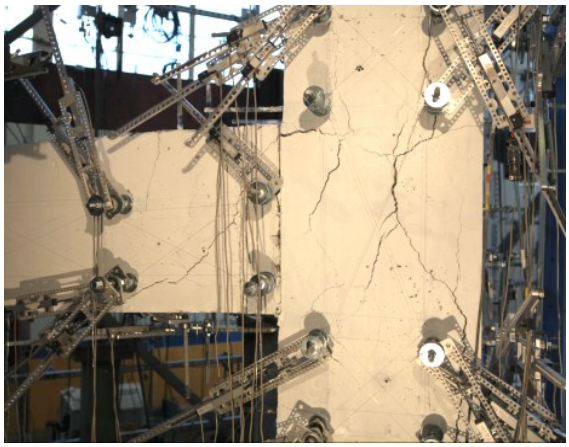

Peak 7a (5.5% drift)

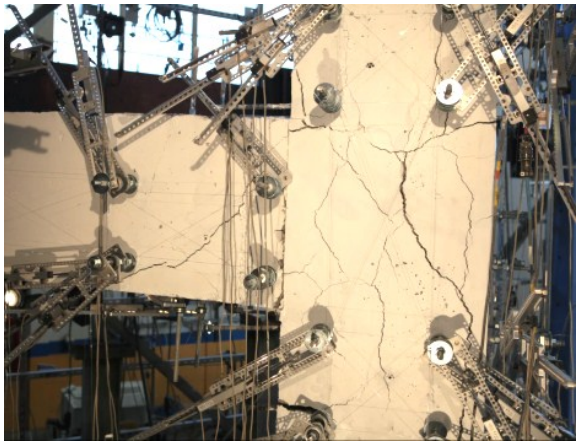

Figure 7.73 East joint face crack development and progression during NS beam loading of specimen U-BJ-1

Instantly before axial failure

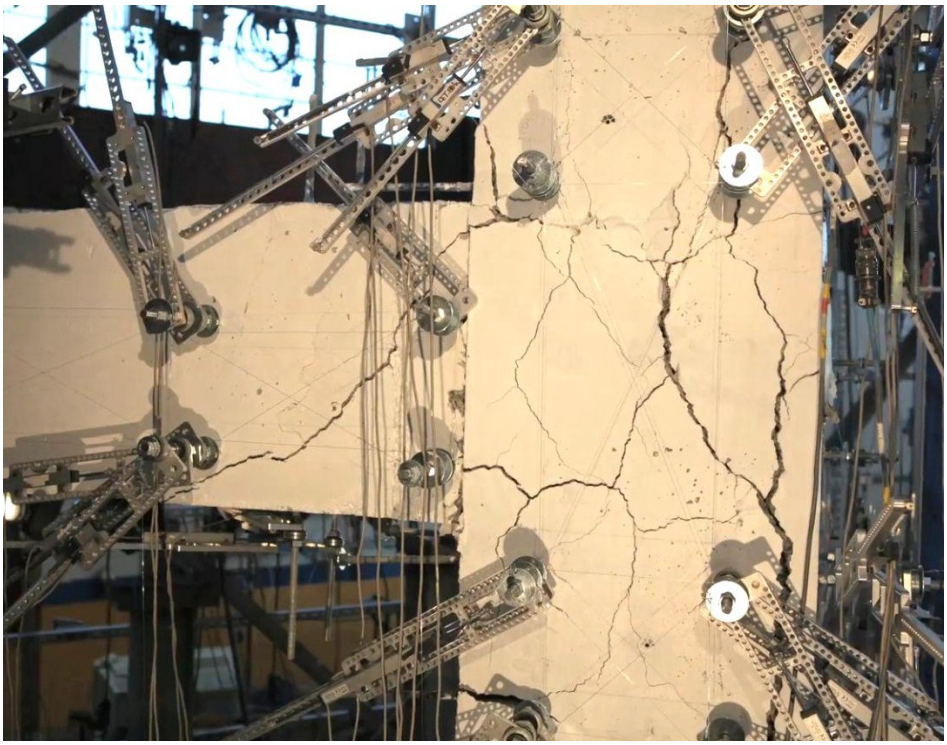

During axial failure

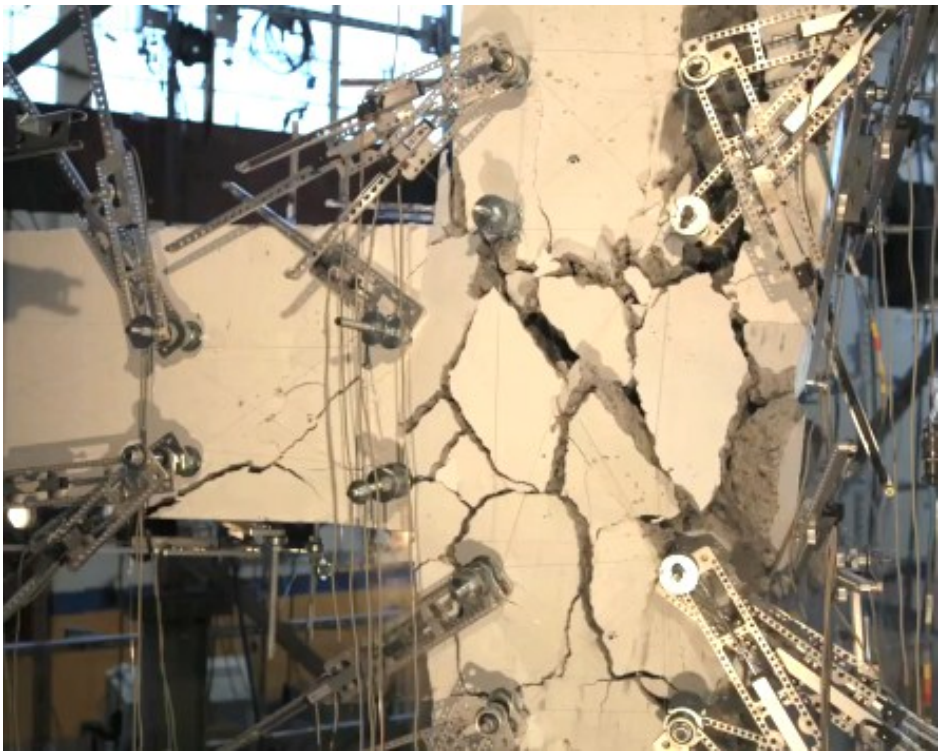

Figure 7.74 East joint face axial failure during EW beam loading of specimen U-BJ-1

Figures 7.75 and Fig. 7.76 display the beam shear-drift ratio relation of EW and NS beams, respectively. During the strain hardening of beam reinforcement, and up to drift ratio of ±3.57%, the hysteresis loops of EW and NS beams were similar. This is expected since the behavior up to that point is based on flexural yielding of the beam with little distress in the joint. Afterwards, when joint started to crack and degrade, pinching of the loops is more pronounced in the NS beam indicating more shear distress of east joint face compared to north joint face which may be attributable due to the torsional cracking effect and pre-loading of EW beam before NS beam.

Figures 7.77 and 7.78 depicts the beam shear force-drift and joint shear strength-drift envelope curves for specimen U-BJ-1. It can be observed that the initial stiffness for EW and NS beam loading is identical until beam yielding. The hardening profile of NS beam is shorter than that of EW beam for both downward and upward loading directions. In other words, the north joint face distress and degradation was less pronounced than those of east joint face. This is expected due to the aforementioned reason. Thus, the joint post-peak strength envelope for the NS beam loading was lower than that of EW beam loading.

Figures 7.79 and 7.80 show upper column axial load and beam shear histories for the specimen. The axial load protocol used for specimen U-BJ-1 was the displacement based one described in Chapter 6. It was designed so that the peak axial compression load is reached simultaneously with beam yielding. Afterwards, the peak cycle axial load was maintained at the designated maximum value in compression and tension.

Figure 7.81 displays the normalized joint shear stress-strain hysteretic behavior of north joint face. The north joint face downward loading shear capacity corresponded to a shear strain of -0.00009 radians, while the shear strain recorded at peak upward loading joint shear strength was 0.016 radians. The east joint face downward loading shear capacity corresponded to a shear strain of -0.00012 radians, while that recorded at peak upward loading joint shear capacity was 0.0079 radians. The envelope curves for the joint shear stress-strain hysteresis are presented in Fig. 7.82 for potential use to develop backbone curves for joint modeling in non-ductile building concrete frame simulation.

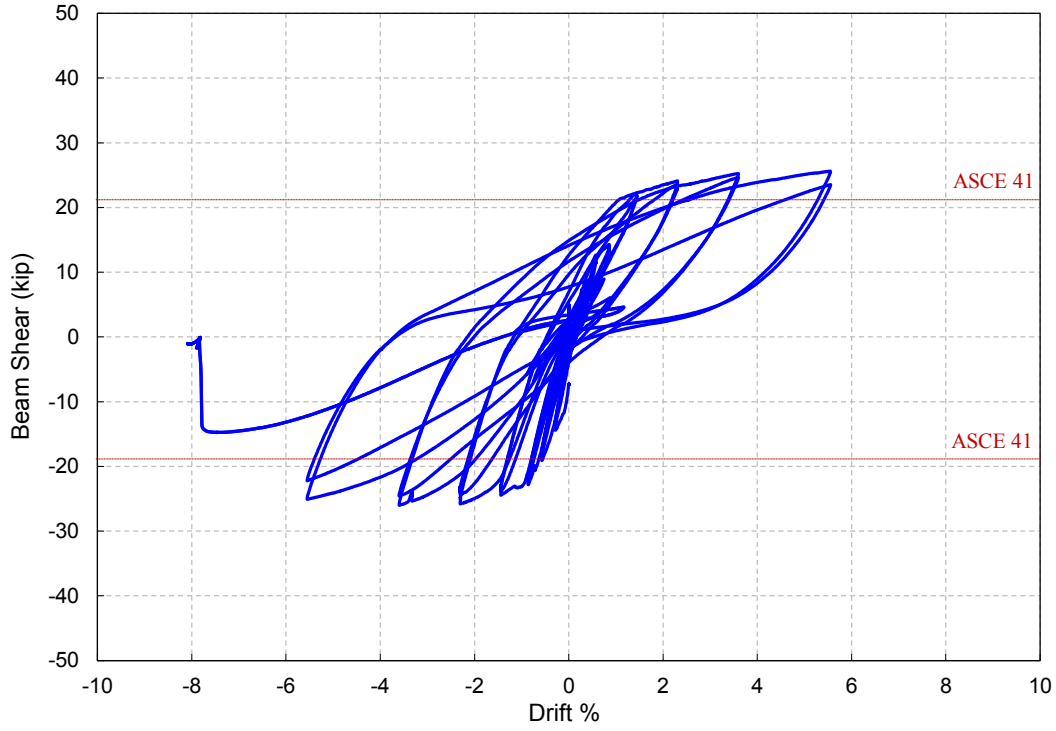

Figure 7.75 Relation between force and drift for EW-beam of specimen U-BJ-1

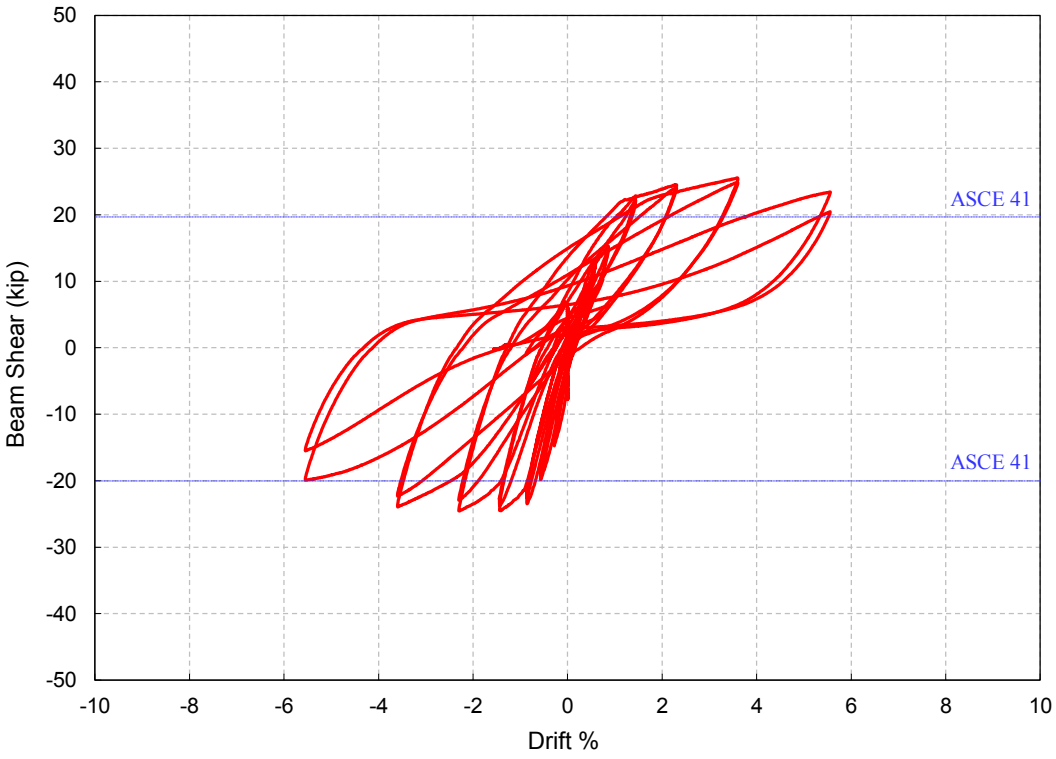

Figure 7.76 Relation between force and drift for NS-beam of specimen U-BJ-1

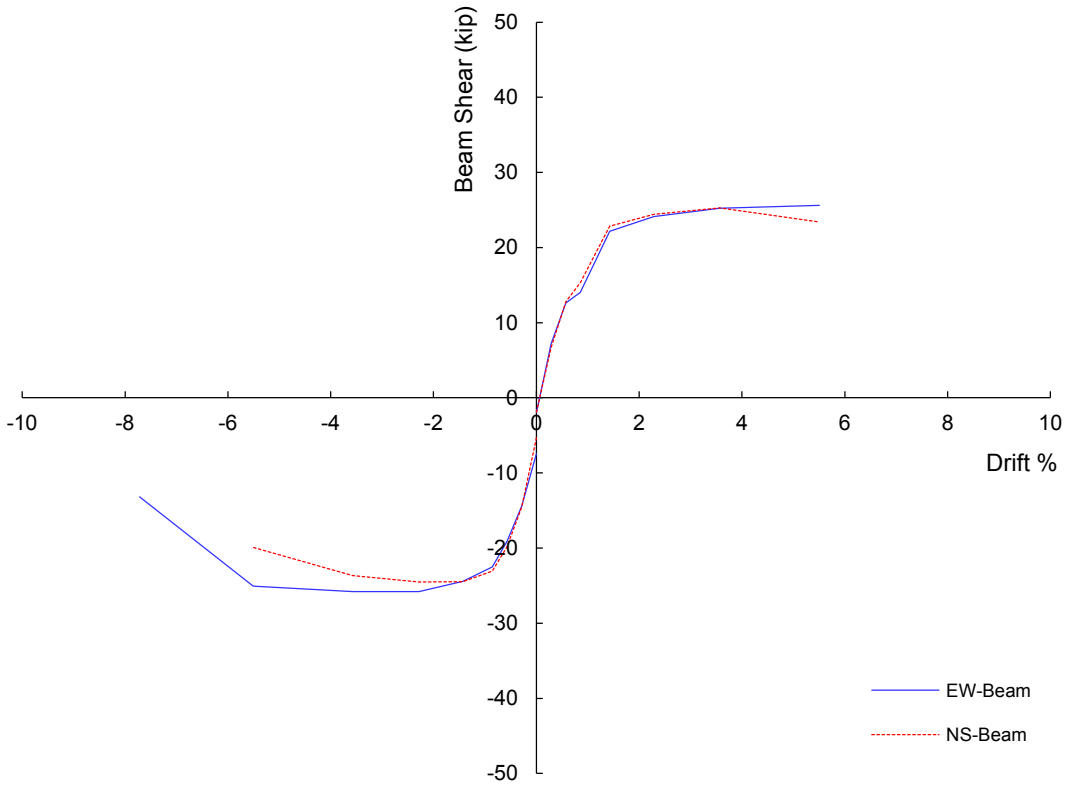

Figure 7.77 Backbone curves of specimen U-BJ-1

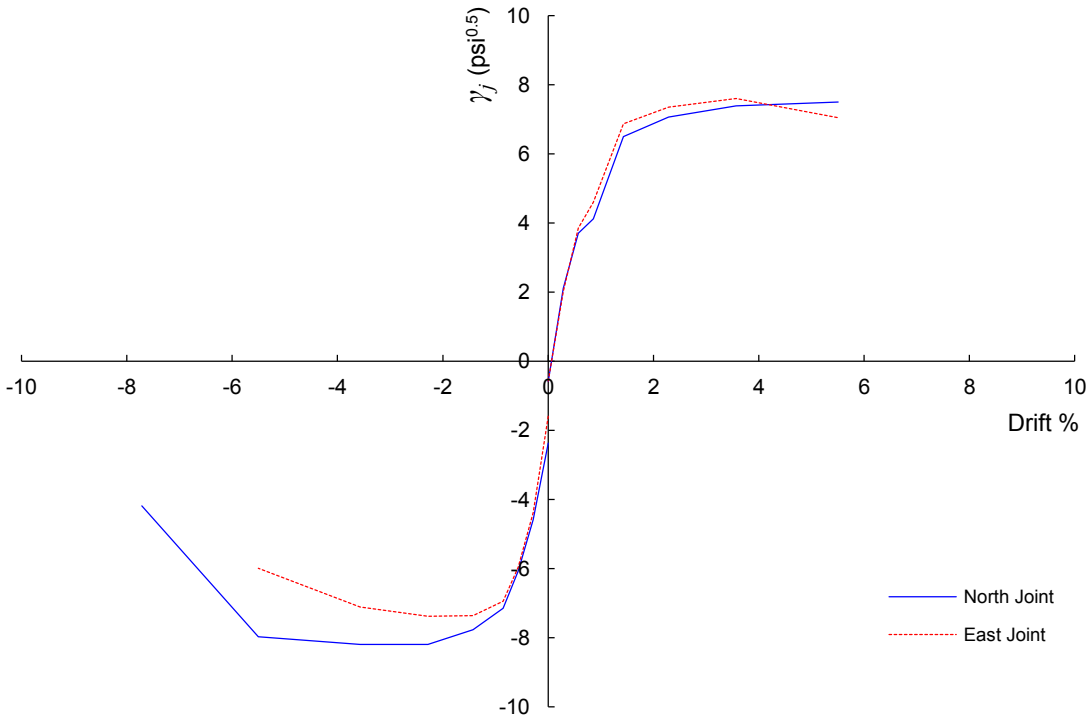

Figure 7.78 Backbone curves of specimen U-BJ-1

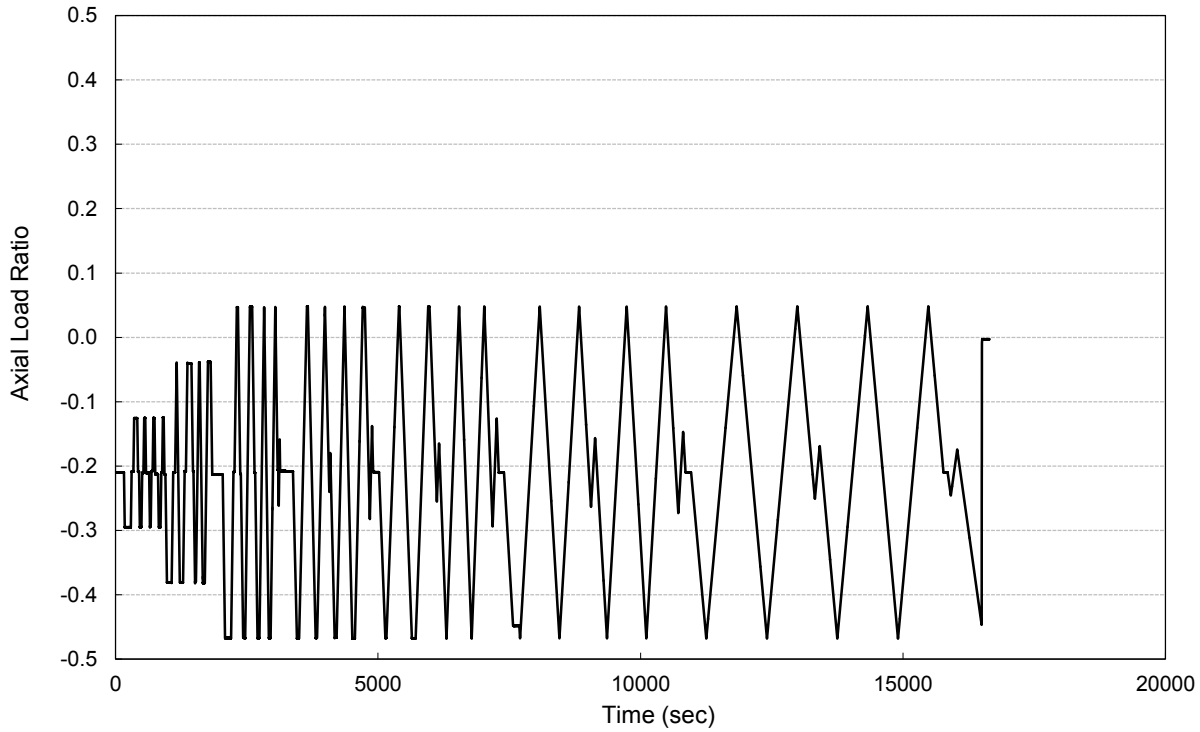

Figure 7.79 Upper column axial load History of specimen U-BJ-1

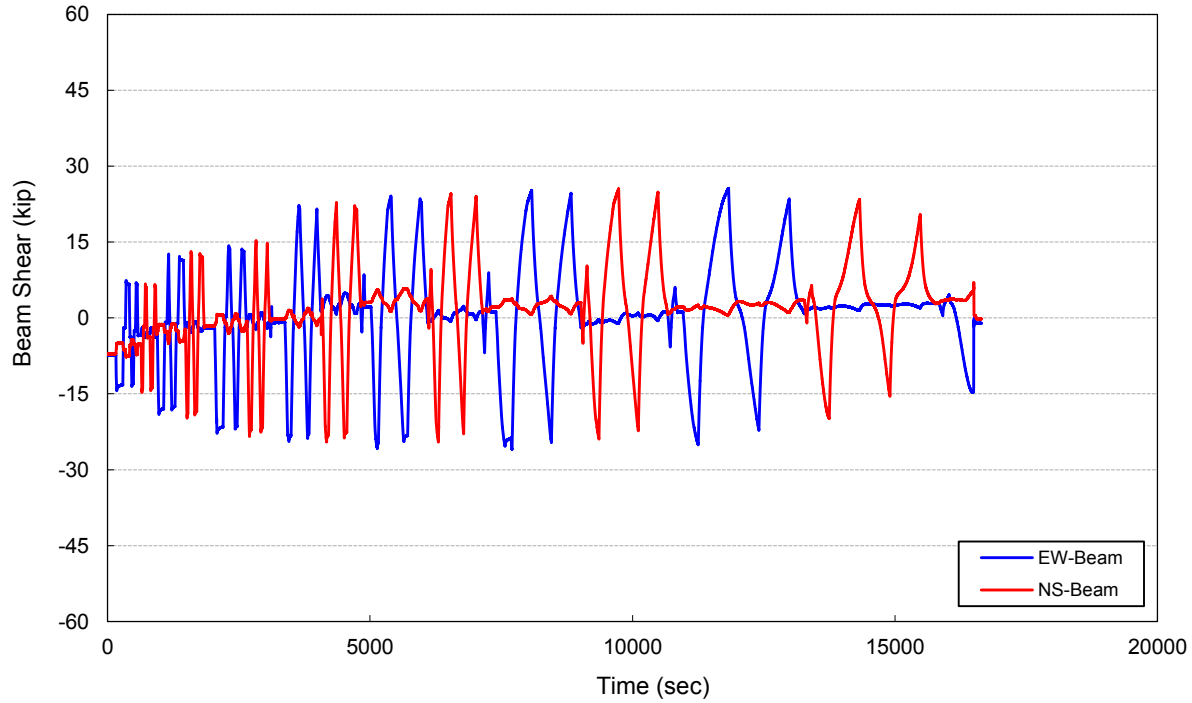

Figure 7.80 Beam shear History of specimen U-BJ-1

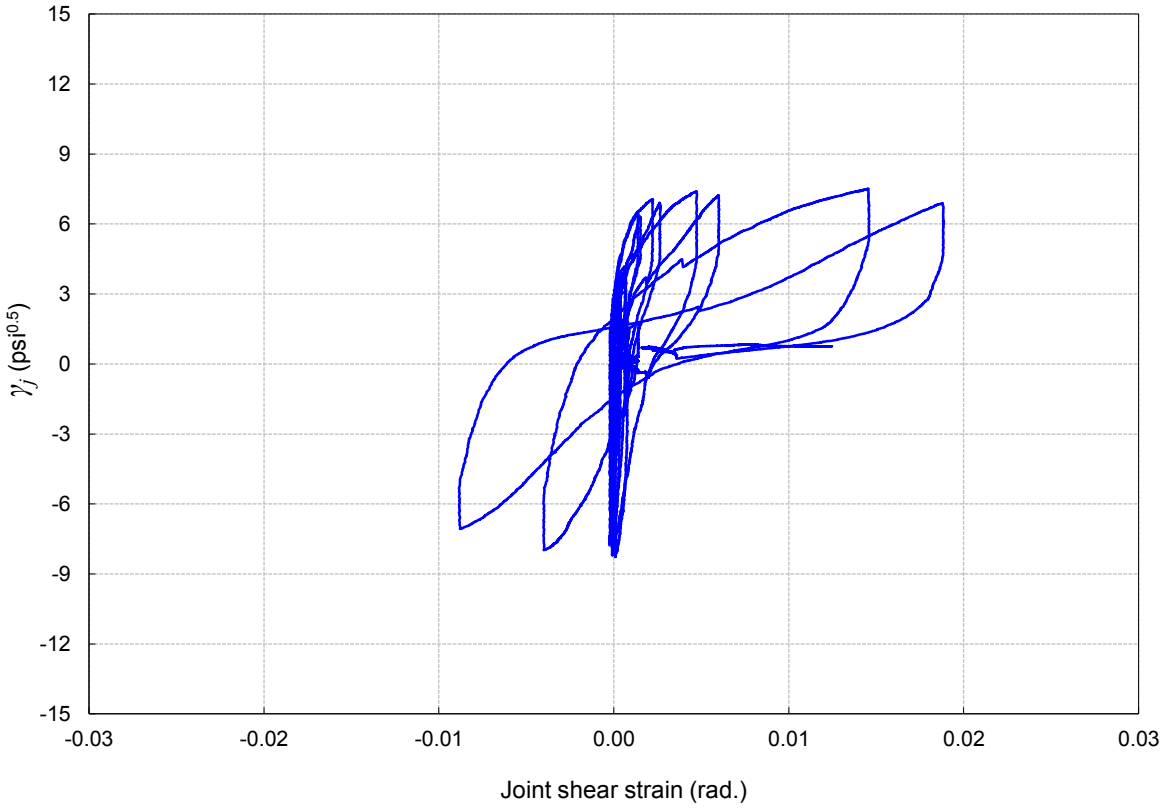

Figure 7.81 North joint face shear stress-strain relation for specimen U-BJ-1

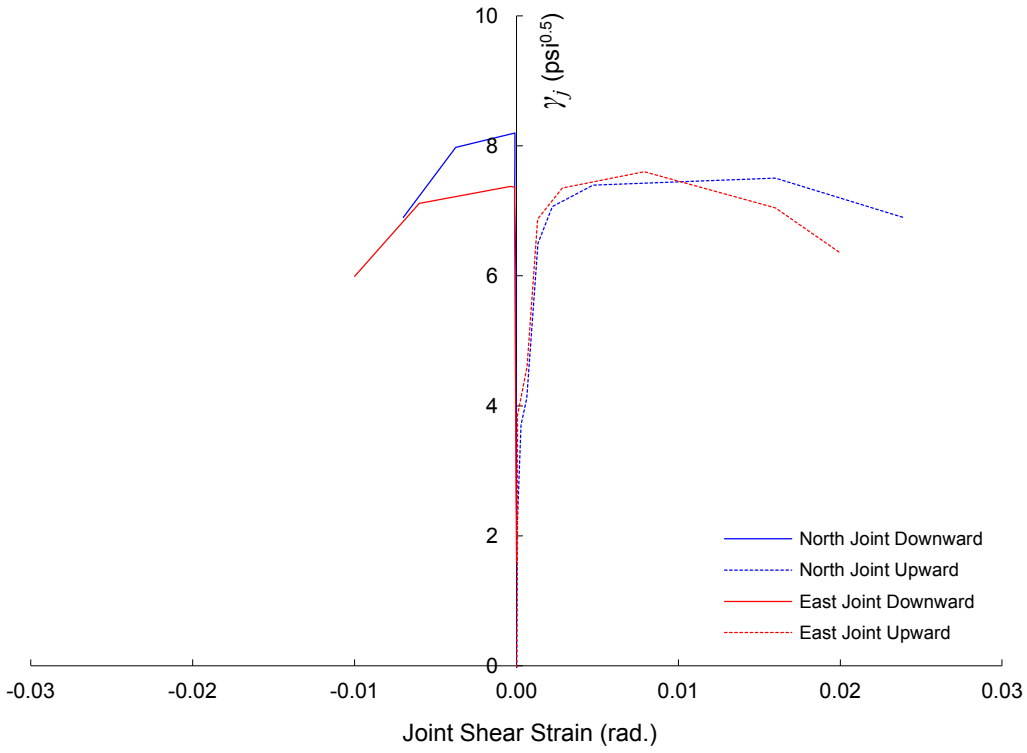

Figure 7.82 Shear stress-strain backbone curves for specimen U-BJ-1

Figure 7.83 shows the contribution of joint shear strain to the overall drift of the joint subassembly represented by the ratio of the beam tip displacement induced by joint shear deformation to the total beam displacement. Consistent with the observations of shear strains in Fig. 7.82, the joint shear deformation contribution to the total drift in the downward loading direction is insignificant especially up to peak beam shear. The reason is that beam flexural deformations due to yielding are many times those due to joint shear deformations under very high axial load. This behavior seems to be characteristic for BJ-Failure beams under high axial load. However, the joint shear deformation contribution in the EW beam upward loading direction is more significant. It reached 22% at 5.5% drift ratio. This is due to the tensile axial force applied to the joint during the upward loading which permits the joint flexibility to contribute to total story drift.

Figure 7.84 displays the peak-to-peak effective stiffness degradation plots for both EW and NS beam loading. It can be noticed that the effective stiffness and stiffness degradation are similar for both loading directions. Unlike the previous specimens, the peak-to-peak effective stiffness degradation within the same drift ratio is noticeably smaller than that between different drift peaks. This result is consistent with the fact that the behavior is essentially governed by beam yielding rather than joint shear. Within the same drift ratio, repeated cycle have less degradation effect on the steel-controlled beam ductile response compared to the brittle concrete-controlled joint behavior.

Figure 7.85 depicts the cumulative energy dissipation during EW and NS beam loading of specimen U-BJ-1. Starting at displacement peak 5b, significant energy dissipation of both beams was observed due to the high strain hardening and elongated plastic profile in the compression cycle due to the high axial load applied. Similar to other uniaxially loaded specimens, the energy dissipated through EW beam loading was higher than that dissipated through NS beam loading due to loading the former beam before the latter one.

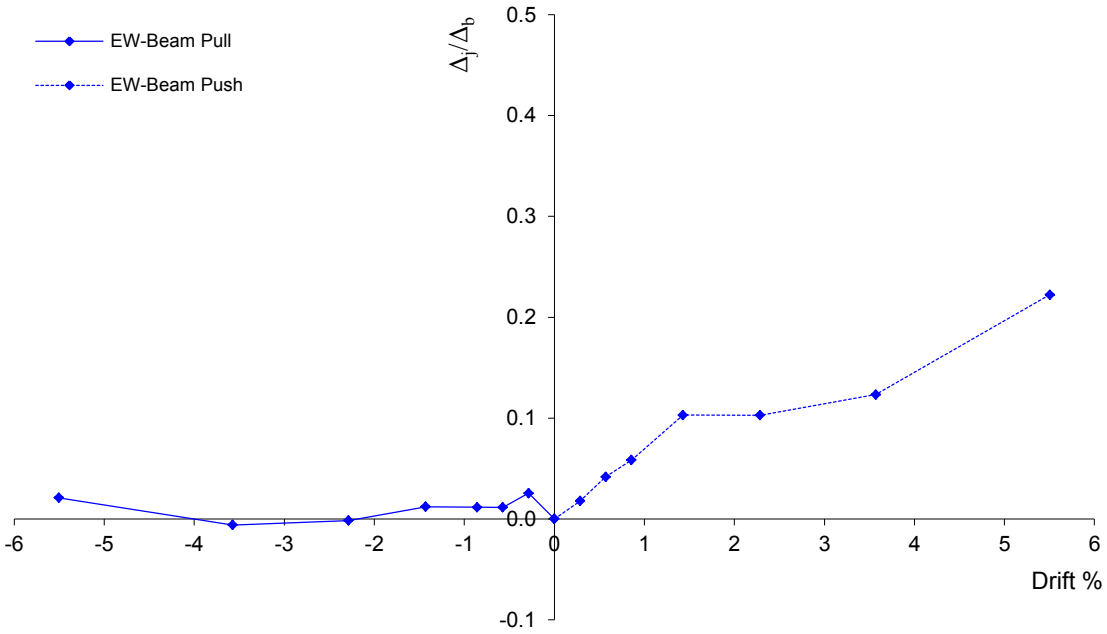

Figure 7.83 Joint deformation contribution to total interstory drift ratio specimen U-BJ-1

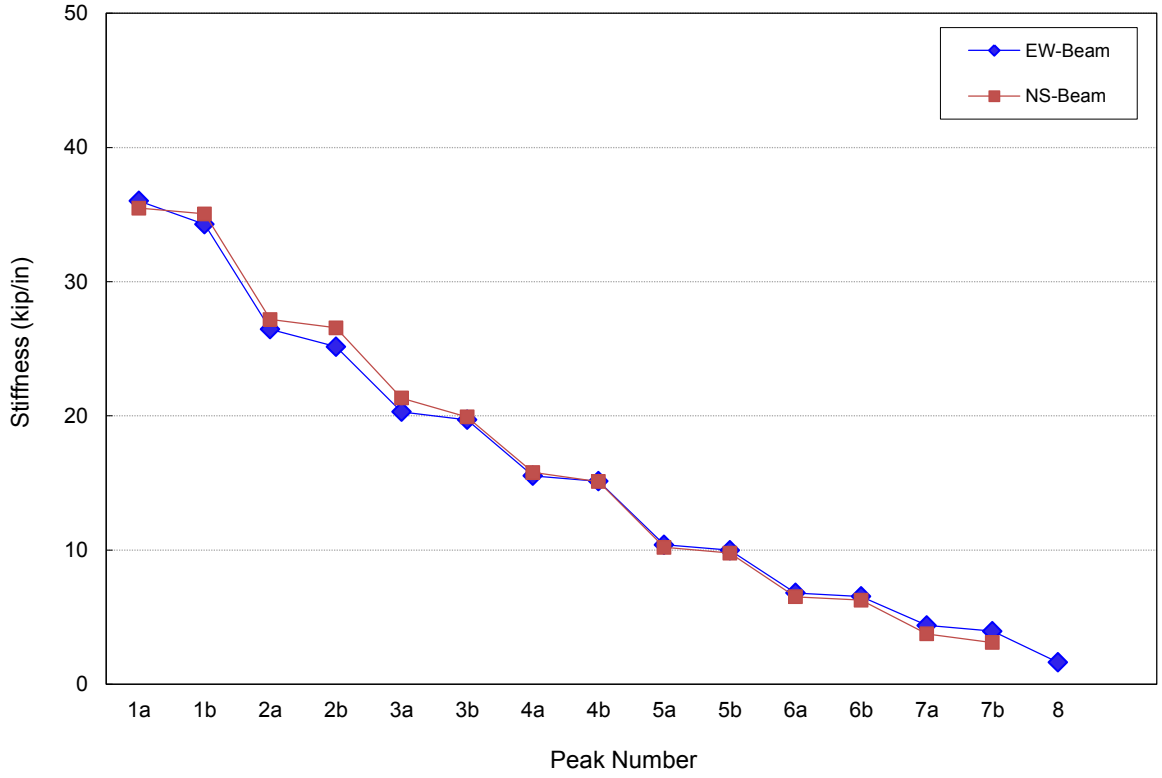

Figure 7.84 Peak-to-peak stiffness for specimen U-BJ-1

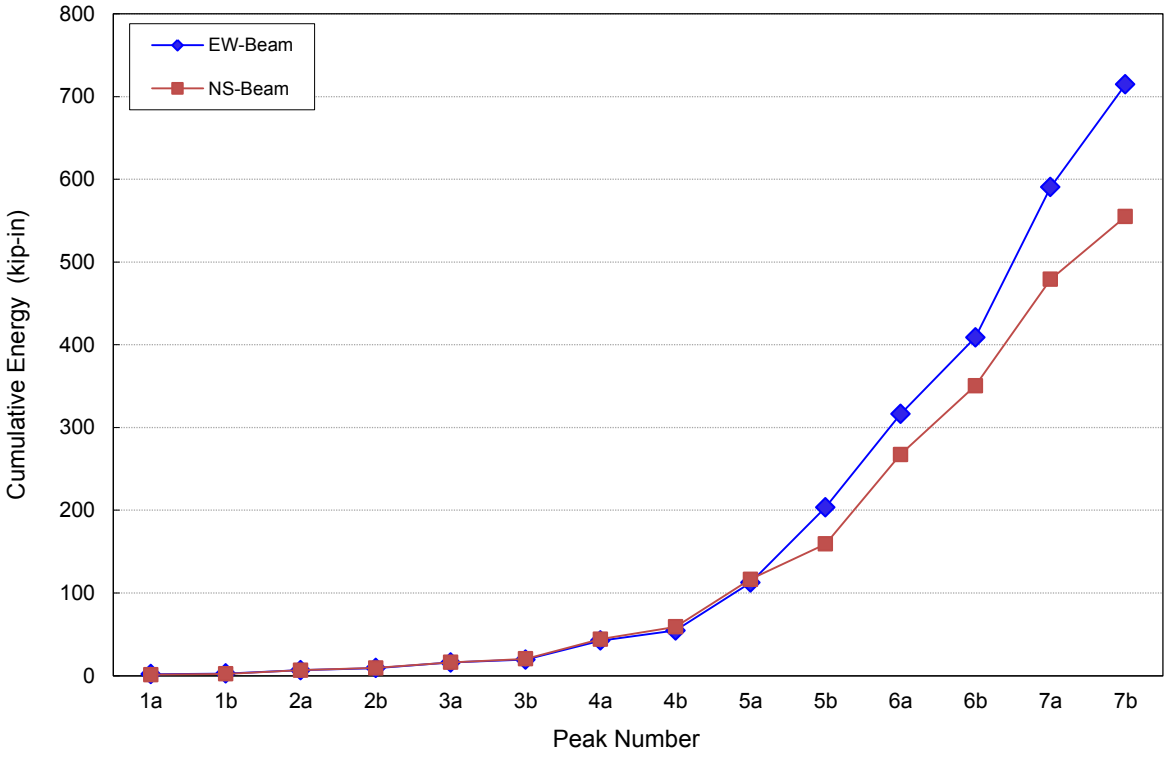

Figure 7.85 Peak-to-peak cumulative energy dissipation for specimen U-BJ-1

Figure 7.86 and Fig. 7.87 exhibit the strain distribution of slab top reinforcement at first cycles of negative drift peaks of EW and NS beam loading. The first slab reinforcement bar adjacent to the EW-beam yielded as early as downward drift peak 2a (-0.57% drift). The first slab reinforcement bar parallel to NS beam yielded at downward drift peak 3b (-0.86% drift). The strain gauge mounted to the second slab bar parallel to the EW beam malfunctioned and hence strains were not measured. The third slab bar parallel to EW beam yielded at peak 6a (-3.57% drift) towards the end of the strain hardening process of beam reinforcement. By linear interpolation between the first and third bar strains, it appears that the second bar reached yield strain. The second slab bar parallel to NS direction did not yield throughout the test. Bottom slab reinforcement did not yield throughout the test.

Figures 7.88 and 7.89 display the strain profile of the exterior and interior beam reinforcement bars under the first negative drift loading peaks of EW beam. The exterior bar strains are evidently higher than those of interior bars. The yielding drift peaks were presented in an earlier section. The yield penetration of EW beam top bars into north joint face during downward loading started at drift peak 6a (-3.57%) while the yield penetration of EW bottom bars during upward loading started at drift peak 4a (1.43%). The apparent delay in yield penetration during the downward loading cycle is attributed to the clamping action of the high column axial load that delayed bond deterioration and yield propagation.

Considering the strains of the most stresses column bars, the outermost corner column reinforcement bar CNE did not yield at the upper or lower column-joint interface in the negative EW and NS beam cyclic loading, throughout the test, respectively. However, this bar experienced slight yielding at upward EW beam drift peak 7a (5.5%). Column bars CNW and CSW at the column-joint interface also did not yield throughout the test during downward loading of both beams, however, slight yielding was observed at upper column-joint interface at the late stages of EW beam upward loading. The mid-joint height column bar strain of bars CNE and CNW approached or exceeded yield strain during last downward loading cycles of EW and NS beams due to bar buckling prior to axial failure.

Figure 7.92 and Fig. 7.93 show the strain profile along the height of the intermediate column reinforcement bars CN and CE during first drift loading peaks, respectively. It can be observed that longitudinal strains at the joint mid-height during downward loading cycles are insignificant until late stages of loading, at which the strains started to slightly increase due to bar buckling. This suggests that the contribution of such column reinforcement bars to joint shear strength is negligible. In the positive drift cycles, the contribution of the central column bars to joint shear strength was also negligible with no mid-joint height yield throughout the test.

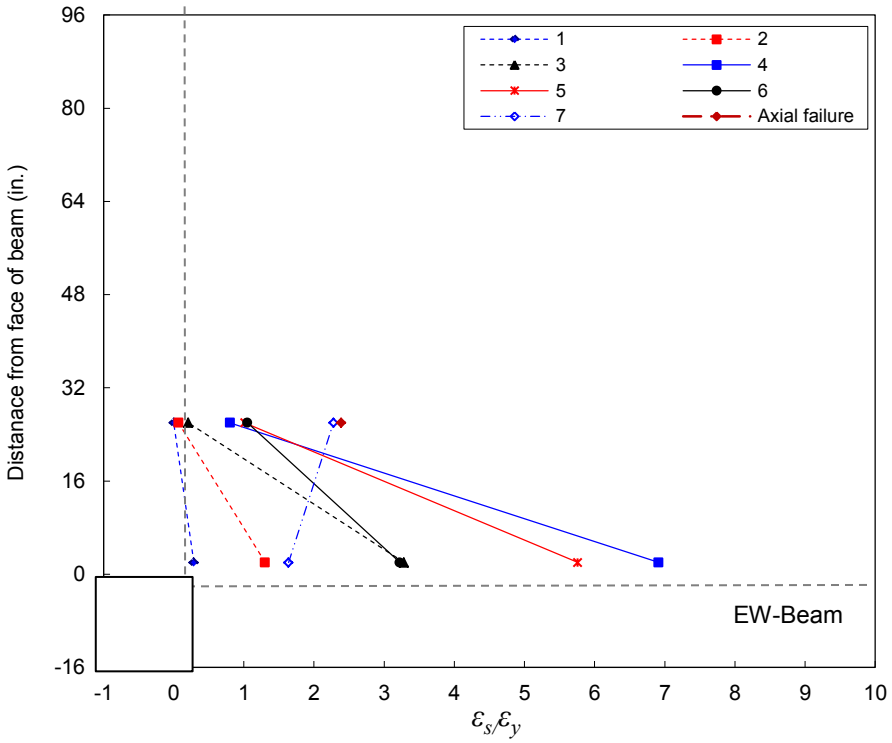

Figure 7.86 Slab top reinforcement strain distribution for U-BJ-1 negative first drift peaks for EW-Beam loading

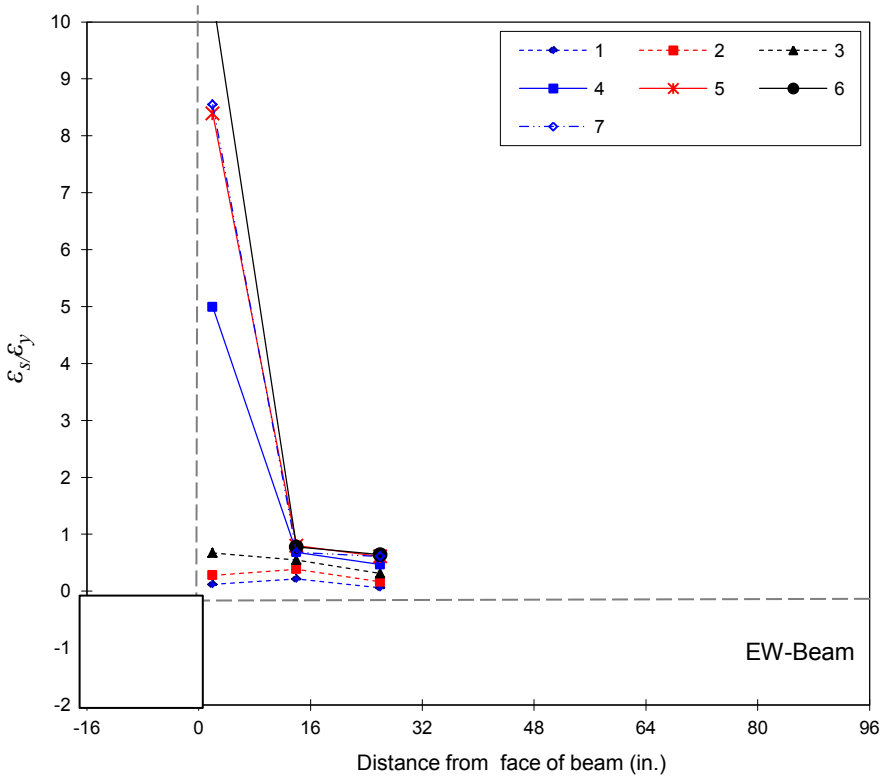

Figure 7.87 Slab top reinforcement strain distribution for U-BJ-1 negative first drift peaks for NS-Beam loading

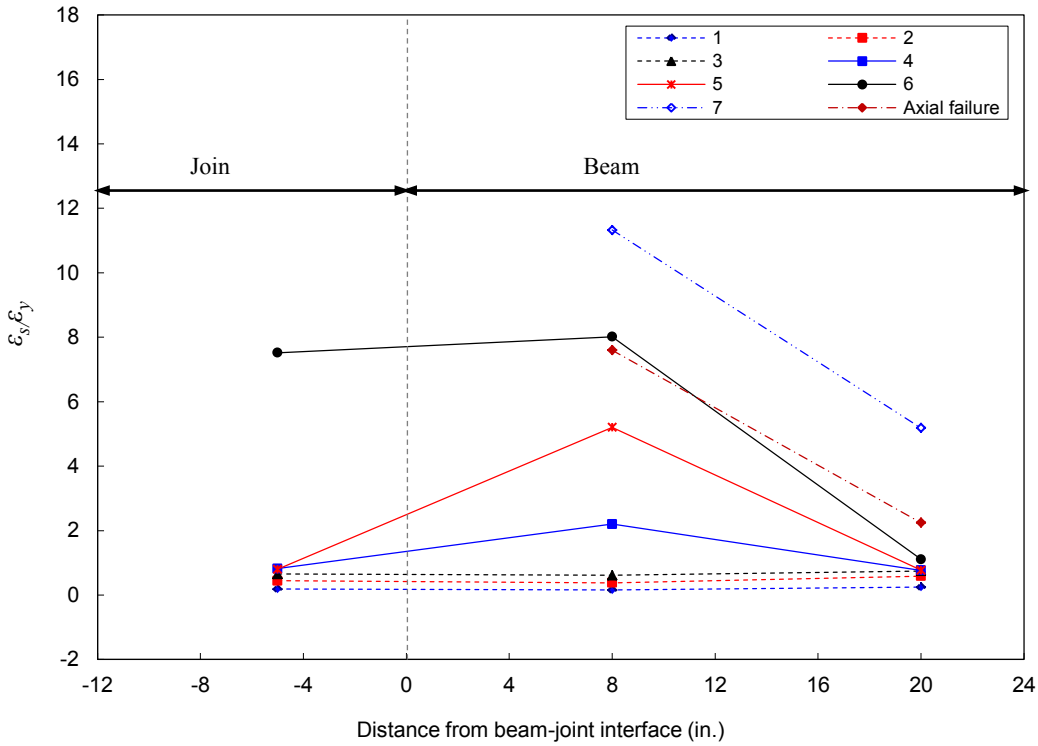

Figure 7.88 EW-beam top exterior longitudinal reinforcement strain for U-BJ-1 first negative drift peaks

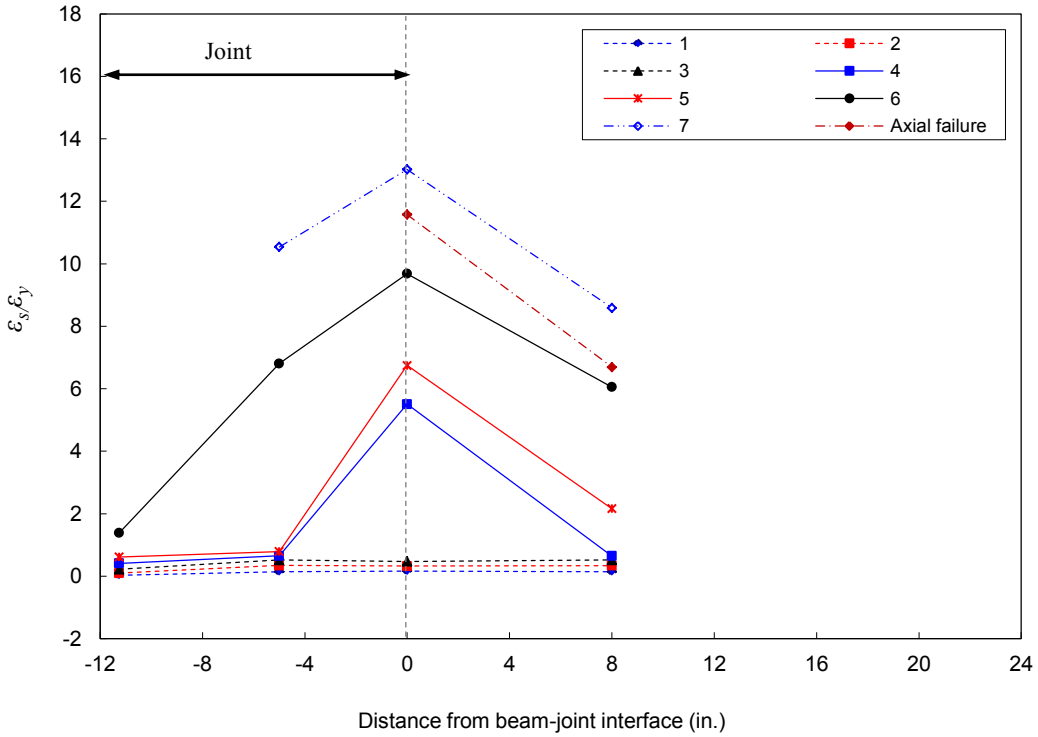

Figure 7.89 EW-beam top interior longitudinal reinforcement strain for U-BJ-1 first negative drift peaks

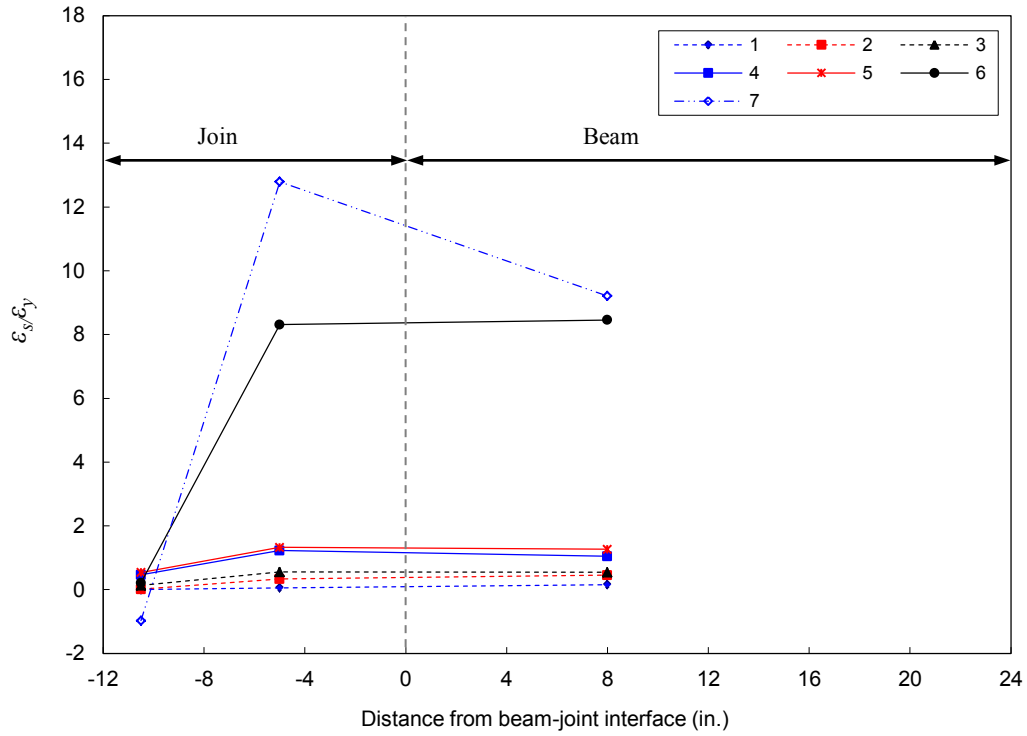

Figure 7.90 EW-beam bottom exterior longitudinal reinforcement strain for U-BJ-1 first positive drift peaks

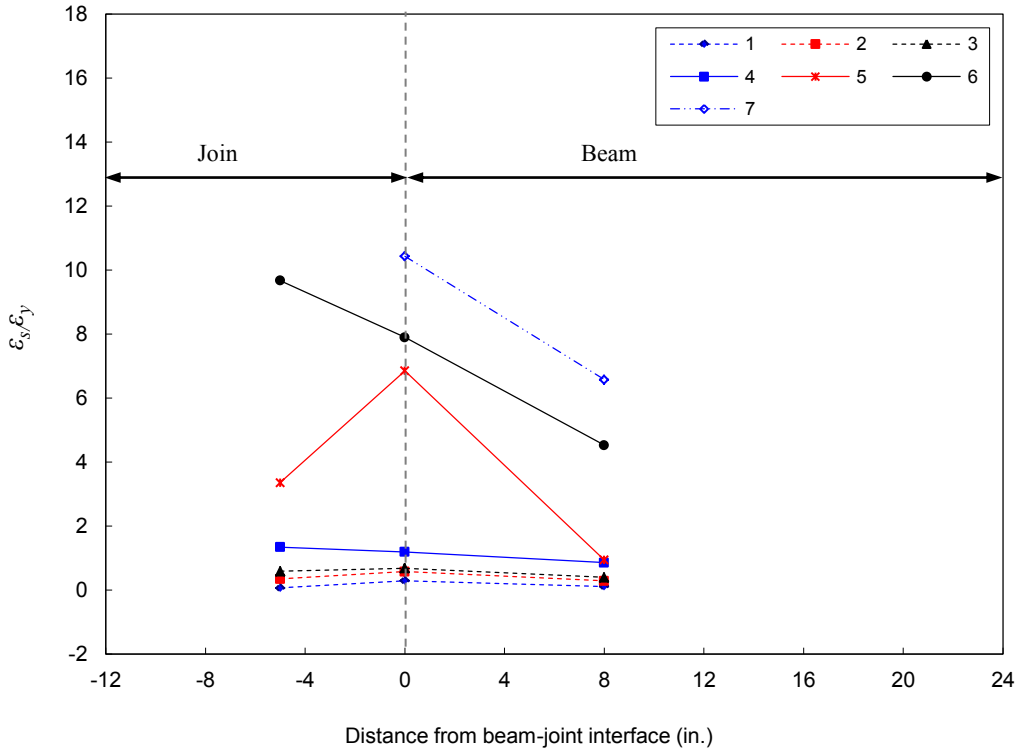

Figure 7.91 EW-beam bottom interior longitudinal reinforcement strain for U-BJ-1 first positive drift peaks

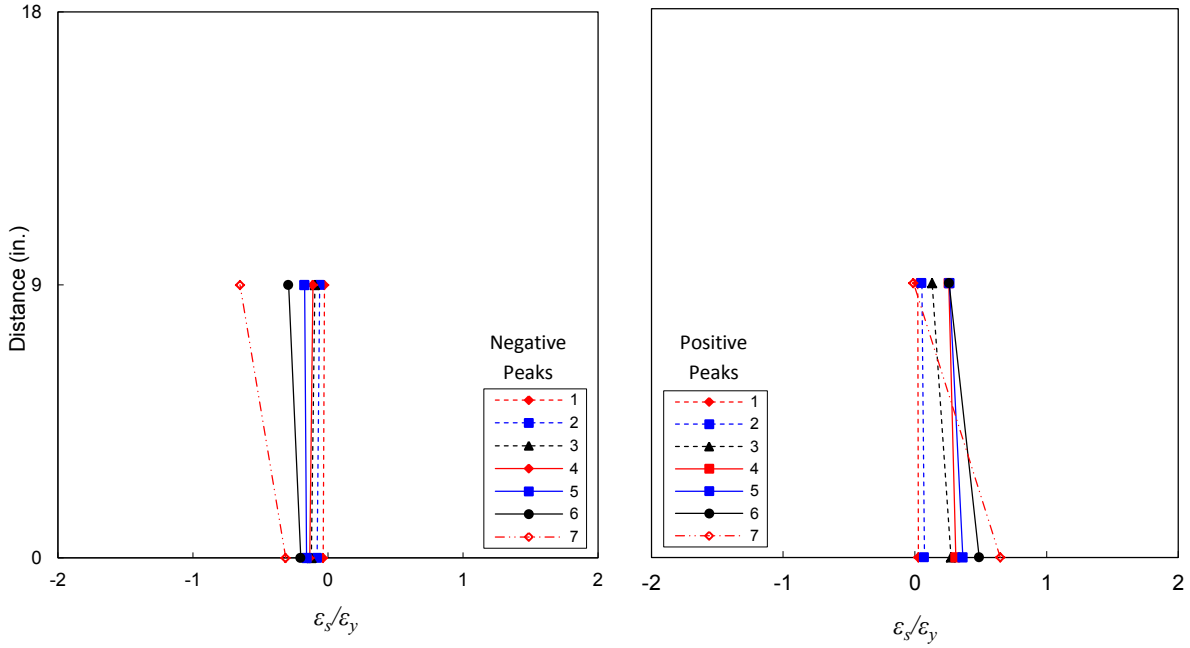

Figure 7.92 Strain development for column intermediate reinforcement CN of U-BJ-1 EW-beam first drift peaks

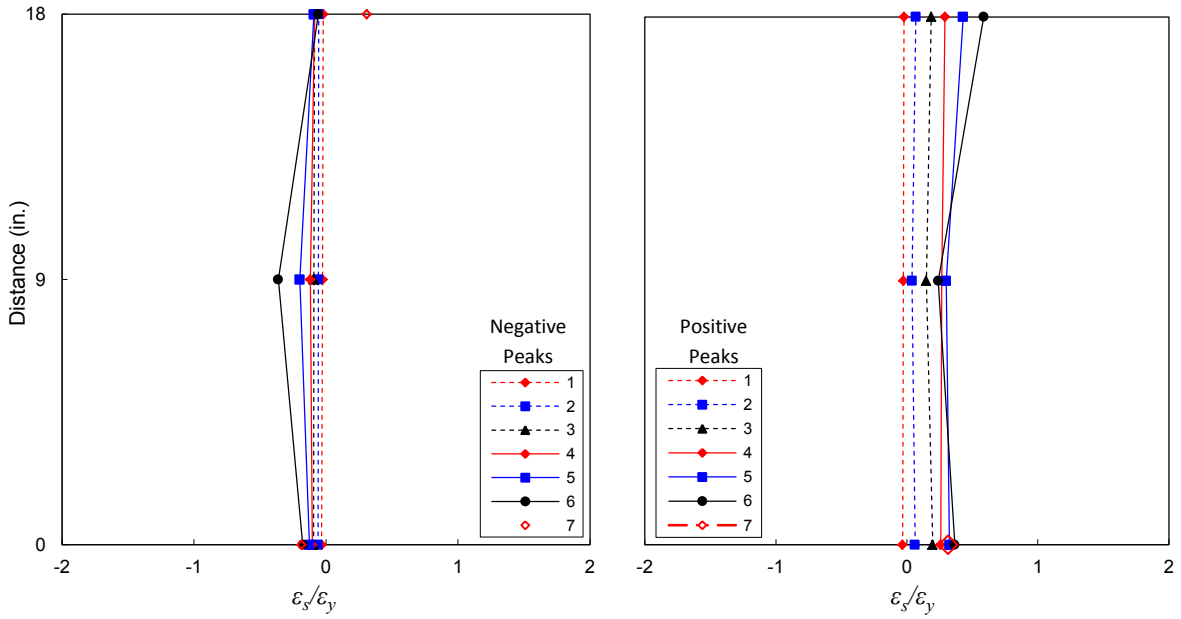

Figure 7.93 Strain development for column intermediate reinforcement CE of U-BJ-1 NS-beam first drift peaks

Table 7.4.a Summary of performance parameters of specimen U-BJ-1, EW direction, downward loading

Load Peak	*Drift* (%)	$V_{b\text{-}EW}$ (kip)	$V_{c\text{-}EW}$ (kip)	$V_{j\text{-}N}$ (kip)	γ_j ($psi^{0.5}$)	γ_s (rad.)	$P_{u,col}$ (kip)	$P_{L,col}$ (kip)	Axial load ratio	K_P (kip/in.)	E_i (kip-in.)	$E_{cum.}$ (kip-in.)
0	0.00	-7.45	-5.4	-47.6	-2.37	0.0000	-299	-313	-0.22	-	-	-
1a	-0.29	-14.4	-10.4	-92.0	-4.58	-0.0001	-421	-440	-0.31	36.0	1.89	1.89
1b	-0.29	-13.6	-9.8	-86.6	-4.31	-0.0001	-421	-438	-0.31	34.3	0.72	2.61
2a	-0.57	-19.1	-13.8	-122	-6.07	-0.0001	-542	-562	-0.40	26.5	4.18	6.80
2b	-0.57	-18.2	-13.2	-116	-5.79	-0.0001	-542	-560	-0.40	25.2	2.43	9.22
3a	-0.86	-22.5	-16.3	-144	-7.15	-0.0001	-665	-687	-0.50	20.3	6.80	16.0
3b	-0.86	-21.9	-15.9	-140	-6.97	-0.0002	-665	-685	-0.50	19.7	3.50	19.5
4a	-1.43	-24.4	-17.7	-156	-7.77	-0.0002	-666	-689	-0.50	15.5	22.9	42.4
4b	-1.43	-23.9	-17.3	-152	-7.58	0.0000	-665	-687	-0.50	15.1	12.2	54.6
5a	-2.29	-25.8	-18.7	-165	-8.20	0.0000	-666	-686	-0.50	10.4	57.8	112
5b	-2.29	-24.3	-17.6	-155	-7.74	0.0002	-666	-684	-0.50	9.98	91.2	204
6a	-3.57	-25.8	-18.7	-165	-8.20	0.0003	-665	-687	-0.50	6.80	113	316
6b	-3.57	-24.4	-17.7	-156	-7.75	0.0003	-665	-685	-0.50	6.54	93	409
7a	-5.50	-25.1	-18.2	-160	-7.97	-0.0015	-666	-688	-0.50	4.39	182	591
7b	-5.50	-22.2	-16.1	-142	-7.06	-0.0027	-666	-685	-0.50	3.96	124	715
Axl. Fail	-7.71	-13.2	-9.5	-84	-4.19	-	-632	-640	-0.47	-	-	-

Table 7.4.b Summary of performance parameters of specimen U-BJ-1, NS direction, downward loading

Load Peak	*Drift* (%)	$V_{b\text{-}NS}$ (kip)	$V_{c\text{-}NS}$ (kip)	$V_{j\text{-}E}$ (kip)	γ_j ($psi^{0.5}$)	γ_s (rad.)	$P_{u,col}$ (kip)	$P_{L,col}$ (kip)	Axial load ratio	K_P (kip/in.)	E_i (kip-in.)	$E_{cum.}$ (kip-in.)
0	0.00	-5.30	-3.84	-32.1	-1.60	0.0000	-300	-309	-0.22	-	-	-
1a	-0.29	-14.6	-10.5	-88.1	-4.38	0.0000	-421	-437	-0.31	35.5	1.40	1.40
1b	-0.29	-14.4	-10.4	-87.1	-4.33	0.0000	-420	-436	-0.31	35.1	0.90	2.29
2a	-0.57	-19.8	-14.4	-120	-5.96	-0.0002	-544	-564	-0.40	27.2	4.50	6.80
2b	-0.57	-19.1	-13.9	-116	-5.76	-0.0001	-543	-563	-0.40	26.6	2.58	9.37
3a	-0.86	-23.	-16.7	-140	-6.94	-0.0003	-666	-688	-0.50	21.3	6.83	16.2
3b	-0.86	-22.3	-16.2	-135	-6.71	-0.0003	-665	-686	-0.50	19.9	4.25	20.5
4a	-1.43	-24.5	-17.7	-148	-7.37	-0.0003	-665	-685	-0.50	15.8	23.8	44.3
4b	-1.43	-23.1	-16.7	-140	-6.95	-0.0003	-666	-684	-0.50	15.1	14.8	59.0
5a	-2.29	-24.5	-17.8	-148	-7.38	-0.0001	-666	-689	-0.50	10.2	57.6	117
5b	-2.29	-22.9	-16.6	-139	-6.90	-0.0002	-666	-687	-0.50	9.77	42.7	159
6a	-3.57	-23.7	-17.1	-143	-7.12	-0.0013	-665	-689	-0.50	6.52	108	267
6b	-3.57	-22.3	-16.2	-135	-6.72	-0.0032	-665	-686	-0.50	6.26	83.3	351
7a	-5.50	-19.9	-14.4	-120	-5.99	-	-666	-684	-0.50	3.75	129	479
7b	-5.50	-15.5	-11.2	-93.7	-4.66	-	-666	-679	-0.50	3.11	75.7	555

Table 7.4.c Summary of performance parameters of specimen U-BJ-1, EW direction, upward loading

Load Peak	*Drift* (%)	$V_{b\text{-}EW}$ (kip)	$V_{c\text{-}EW}$ (kip)	$V_{j\text{-}N}$ (kip)	γ_j (psi$^{0.5}$)	γ_s (rad.)	$P_{u,col}$ (kip)	$P_{L,col}$ (kip)	Axial load ratio	K_P (kip/in.)	E_i (kip-in.)	$E_{cum.}$ (kip-in.)
1a	0.29	7.20	5.21	43.6	2.11	0.0001	-178	-179	-0.13	36.0	1.89	1.89
1b	0.29	7.00	5.07	42.4	2.05	0.0001	-178	-179	-0.13	34.3	0.72	2.61
2a	0.57	12.6	9.15	76.4	3.70	0.0003	-55.7	-48.0	-0.04	26.5	4.18	6.80
2b	0.57	12	8.65	72.3	3.50	0.0003	-56.1	-48.9	-0.04	25.2	2.43	9.22
3a	0.86	14.1	10.2	85.0	4.12	0.0007	66.4	77.5	0.05	20.3	6.80	16.0
3b	0.86	13.6	9.81	82.0	3.97	0.0007	67.2	78.1	0.05	19.7	3.50	19.5
4a	1.43	22.2	16.1	134	6.50	0.0019	68.6	89.0	0.05	15.5	22.9	42.4
4b	1.43	21.5	15.6	130	6.31	0.0021	67.5	87.5	0.05	15.1	12.2	54.6
5a	2.29	24.1	17.5	146	7.07	0.0031	68.4	93.8	0.05	10.4	57.8	112
5b	2.29	23.6	17.1	143	6.91	0.0035	67.7	92.7	0.05	9.98	91.2	204
6a	3.57	25.2	18.3	153	7.39	0.0058	68.0	93.9	0.05	6.80	113	316
6b	3.57	24.6	17.8	149	7.22	0.0068	68.0	93.5	0.05	6.54	92.6	409
7a	5.50	25.6	18.5	155	7.51	0.0160	68.6	94.8	0.05	4.39	182	591
7b	5.50	23.5	17.0	142	6.90	0.0239	68.7	93.24	0.05	3.96	124	715

Table 7.4.d Summary of performance parameters of specimen U-BJ-1, NS direction, upward loading

Load Peak	*Drift* (%)	$V_{b\text{-}NS}$ (kip)	$V_{c\text{-}NS}$ (kip)	$V_{j\text{-}E}$ (kip)	γ_j (psi$^{0.5}$)	γ_s (rad.)	$P_{u,col}$ (kip)	$P_{L,col}$ (kip)	Axial load ratio	K_P (kip/in.)	E_i (kip-in.)	$E_{cum.}$ (kip-in.)
1a	0.29	6.72	4.87	42.9	2.02	-0.0002	-177	-175	-0.13	35.5	1.40	1.40
1b	0.29	6.63	4.80	42.3	1.99	-0.0002	-176	-174	-0.13	35.1	0.90	2.29
2a	0.57	12.8	9.27	81.7	3.85	-0.0001	-56.0	-46	-0.04	27.2	4.50	6.80
2b	0.57	12.7	9.23	81.4	3.83	-0.0001	-54.2	-44.1	-0.04	26.6	2.58	9.37
3a	0.86	15.3	11.1	97.7	4.60	0.0004	66.7	79.7	0.05	21.3	6.83	16.2
3b	0.86	13.6	9.81	86.5	4.08	0.0004	67.2	78.1	0.05	19.9	4.25	20.5
4a	1.43	22.9	16.5	146	6.87	0.0010	68.4	91.9	0.05	15.8	23.8	44.3
4b	1.43	22.2	16.1	142	6.68	0.0011	67.6	90.6	0.05	15.1	14.8	59.0
5a	2.29	24.4	17.7	156	7.35	0.0024	68.4	92.2	0.05	10.2	57.6	117
5b	2.29	24.0	17.4	153	7.22	0.0031	68.4	92.0	0.05	9.77	42.7	159
6a	3.57	25.3	18.3	161	7.60	0.0079	68.0	92.3	0.05	6.52	108	267
6b	3.57	24.7	17.9	157	7.42	0.0113	68.3	92.4	0.05	6.26	83.3	351
7a	5.50	23.41	17.0	150	7.04	0.0182	68.8	93.7	0.05	3.75	128.5	479
7b	5.50	20.5	14.8	131	6.16	-	68.6	91.0	0.05	3.11	75.7	555

Table 7.5 Characteristic response measures for tested corner beam-column joints

Specimen ID	Beam	Direction	Geometry		Shear Failure			Axial Failure			
			d_{eff} (in.)	No. of slab bars yielded*	Drift %	γ_j (psi$^{0.5}$)	$\frac{P}{f_c' A_j}$	Drift %	Max. reached drift %	$\frac{P}{f_c' A_j}$	γ_j (psi$^{0.5}$)
U-J-1	EW	Downward	14.1	2 top	-2.19	14.3	-0.31	-9.68	-9.68	-0.20	2.87
		Upward	15.7	-	3.42	10.9	0.09	-	9.68	-	-
	NS	Downward	15.4	-	-1.37	12.6	-0.30	-	-9.68	-	-
		Upward	14.6	-	2.19	9.6	0.05	-	9.68	-	-
U-J-2	EW	Downward	25.8	1 top	-1.30	9.98	-0.46	-3.06	-3.42	-0.43	4.30
		Upward	27.6	-	2.19	7.01	0.03	-	3.42	-	-
	NS	Downward	26.9	-	-0.82	8.97	-0.46	-	-2.19	-	-
		Upward	26.6	-	2.19	6.59	0.03	-	2.19	-	-
B-J-1	EW	Downward	14.8	1 top	-1.37	11.7	-0.45	-3.36	-3.42	-0.45	5.60
		Upward	15.3	-	2.19	10.1	0.01	-	3.42	-	-
	NS	Downward	15.6	1 top	-1.37	10.8	-0.45	-3.36	-3.42	-0.45	4.81
		Upward	14.1	-	2.19	9.83	0.01	-	3.42	-	-
U-BJ-1	EW	Downward	14.9	2 top	-2.29	8.20	-0.50	-7.71	-7.71	-0.47	4.19
		Upward	16.0	-	5.50	7.51	0.05	-	5.50	-	-
	NS	Downward	15.6	1 top	-2.29	7.38	-0.50	-	-5.50	-	-
		Upward	15.6	-	3.57	7.60	0.05	-	5.50	-	-
Phase I SP1[120]	EW	Downward	15	4 top	-2.34	8.47	-0.12	-	-	-	-
		Upward	15.8	-	3.57	8.59	0.07	-	-	-	-
	NS	Downward	15.8	2 top	-2.34	7.57	-0.12	-	-	-	-
		Upward	15	-	2.34	8.35	0.07	-	-	-	-
Phase I SP4[120]	EW	Downward	26.6	-	-1.75	8.63	-0.17	-	-	-	-
		Upward	27.7	-	1.75	7.66	0.00	-	-	-	-
	NS	Downward	27.6	-	-1.10	7.39	-0.15	-	-	-	-
		Upward	26.8	-	1.75	6.86	-0.01	-	-	-	-

* Slab reinforcement bar yielding does not necessarily imply slab effective width

Table 7.6 Displacement ductility factors for tested corner beam-column joints

Specimen ID	Beam	Direction	Displacement Ductility Factors	
			$\mu_{\Delta\text{-}b}$	$\mu_{\Delta\text{-}f}$
U-J-1	EW	Downward	4.89	4.42
		Upward	3.42	2.83
	NS	Downward	3.33	7.07
		Upward	2.87	4.42
U-J-2	EW	Downward	3.30	2.63
		Upward	3.89	1.56
	NS	Downward	3.85	2.67
		Upward	3.65	1.00
B-J-1	EW	Downward	3.00	2.5
		Upward	1.90	1.56
	NS	Downward	2.90	2.5
		Upward	2.28	1.56
U-BJ-1	EW	Downward	6.45	3.37
		Upward	3.06	1.00
	NS	Downward	8.18	2.4
		Upward	3.70	1.54
Phase I_SP1[120]	EW	Downward	3.57	NA
		Upward	2.81	NA
	NS	Downward	3.85	NA
		Upward	2.65	NA
Phase I_SP4[120]	EW	Downward	4.00	NA
		Upward	3.34	NA
	NS	Downward	5.00	NA
		Upward	3.43	NA

7.4 EFFECT OF TEST PARAMETERS ON PERFORMANCE MEASURES

7.4.1 Effect of Axial Load Level

To investigate the effect of axial load level on performance of unconfined corner beam-column joints, this discussion is organized to contrast specimens that experienced J-Failure and BJ-failure under the effect of different axial load levels. The corner joints tested in the current study were tested to assess seismic joint shear, drift, and axial load capacities under moderate to high axial load levels representing intense ground shaking of 10 story-building or higher. A relevant set of tests by Park [120] (denoted as Phase I throughout this manuscript) was concerned with investigating joint shear strength and drift capacity of low axial load level specimens representing low-rise non-ductile buildings, mainly experiencing BJ-Failure. The design concept and geometry of Phase I specimens is similar to those of the current specimens. Details of Phase I specimen reinforcement and material properties are presented in the abovementioned reference, while Tables 7.5 and 7.6 presents a comparison between axial load level and design parameters of specimens of the current study and those of Phase I. It is worth mentioning that it was not intended in Phase I series of tests to drive test specimens to axial failure. In addition, the axial load protocol of Phase I was beam shear force-based similar to that of specimen U-J-1 in the current study. Thus, the axial load degraded significantly in the post peak regime of Phase I specimens. The comparison between the current test specimen and the corresponding ones in Phase I with lower starting gravity and overturning axial loads helps reveal the effect of axial load level on joint performance.

7.4.1.1 JOINT SHEAR STRENGTH

J-Failure Mode

Figures 7.94 through 7.99 compares load-drift relations and envelope curves of specimen U-J-2 and Phase I specimen SP4, which is similar in geometry and reinforcement. Both specimens experienced J-Failure in both negative loading (downward) and positive loading (upward) directions. The starting gravity load ratio of specimen U-J-2 was 0.21 while that of Phase I SP4 was 0.11. The overturning seismic axial load was 57% and 119% of the starting gravity load for the two specimens, respectively. The axial load ratio at peak negative joint shear strength of specimen U-J-2 was 0.46 while that of Phase I SP4 was 0.17. Due to the force-based axial load protocol used in Phase I, the gravity load ratio at peak joint shear strength deteriorated to 0.07 while it was maintained using the drift-based axial load protocol of the current study at 0.21. The EW-beam peak shear force of specimen U-J-2 is 17.8% higher than that of Phase I SP4. However, when normalized by concrete strength, the north joint face shear strength coefficient of U-J-1 is 15.6% higher than that of SP4. Similarly, NS-beam peak shear force and east joint face shear strength coefficient of specimen U-J-1 are higher than those of SP4 by 24.7% and 21.7%, respectively. In an average sense, the joint shear strength enhancement due to higher axial load was about 18.7%. This enhancement should be viewed as specific to joints with 1.67 aspect ratio. It is anticipated that axial load enhancement of joint shear strength in joints with lower aspect ratio is slightly higher, with an upper limit of enhancement of 25% for joints with 1:1 aspect ratio under 0.60 axial load ratio as indicated in the empirical shear strength model developed in

Chapter 5. The prediction of shear strength enhancement factor of that model is slightly more conservative than the average test strength enhancement of 18.7%.

The post-peak joint shear strength degradation, represented by softening slope of backbone curve, of negative EW beam loading of specimen U-J-2 is 23.8% higher than that of specimen SP4. The corresponding strength degradation in NS beam loading was 37%. In general the post-peak strength degradation due to high axial load was significantly higher than that in the case of low axial load for J-Failure specimens.

The joint shear strength trend in the positive (upward) loading direction of both EW and NS loading (under tension or small compression axial load) was different from that of peak negative loading. The peak axial tension load ratio at the positive drift loading joint shear strength was 3% and 0 in specimens U-J-2 and SP4, respectively. The joint shear strength in the positive loading direction of EW beam and NS beam of specimen SP4 was higher than that of U-J-2 by 9% and 4%, respectively. Both specimens experienced J-Failure mode in the positive loading direction. This slight reduction in joint shear strength when introducing small tension can be explained as follows. The tensile stresses developed by axial tensile load increase nominal principal tension stresses in the joint and lead to additional transverse cracking of joint concrete and widening of existing joint cracks between the uncracked segments that still hold full bond with column longitudinal reinforcement within the joint. Inclined shear cracks are also widened because of column tensile force. This results in an additional concrete softening effect of the joint diagonal concrete strut, the main shear transfer mechanism. This result is consistent, if linear interpolation of shear strength is considered, with Higazy et al. [59], who cyclically tested interior joint under the effect of 5% compression and 5% tensile axial load ratios and concluded an average reduction of 12% in lightly reinforced joint shear strength in the latter case.

The post-peak joint shear strength degradation, represented by softening slope of backbone curve, of positive EW beam loading of specimen U-J-2 is 5.75% lower than that of specimen SP4. This may be attributed to the higher tension axial load ratio of the former (3%) compared to the zero axial load at the shear strength peak of the latter.

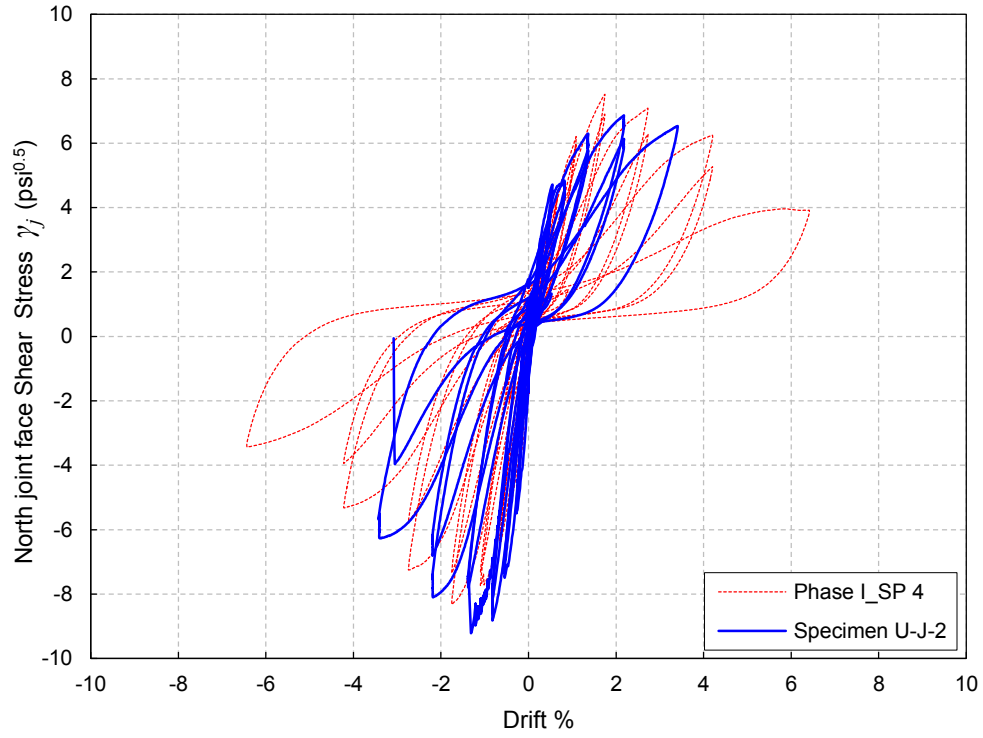

Figure 7.94 Effect of axial load level on load drift response of EW-beam for J-Failure specimens

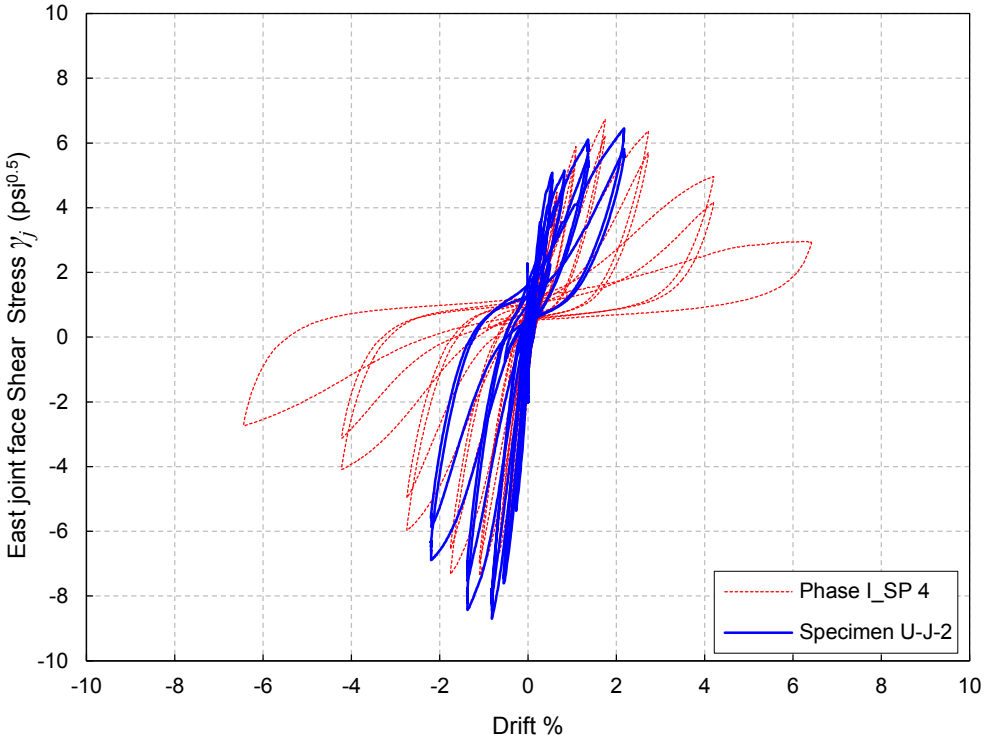

Figure 7.95 Effect of axial load level on load-drift response of NS-beam for J-Failure specimens

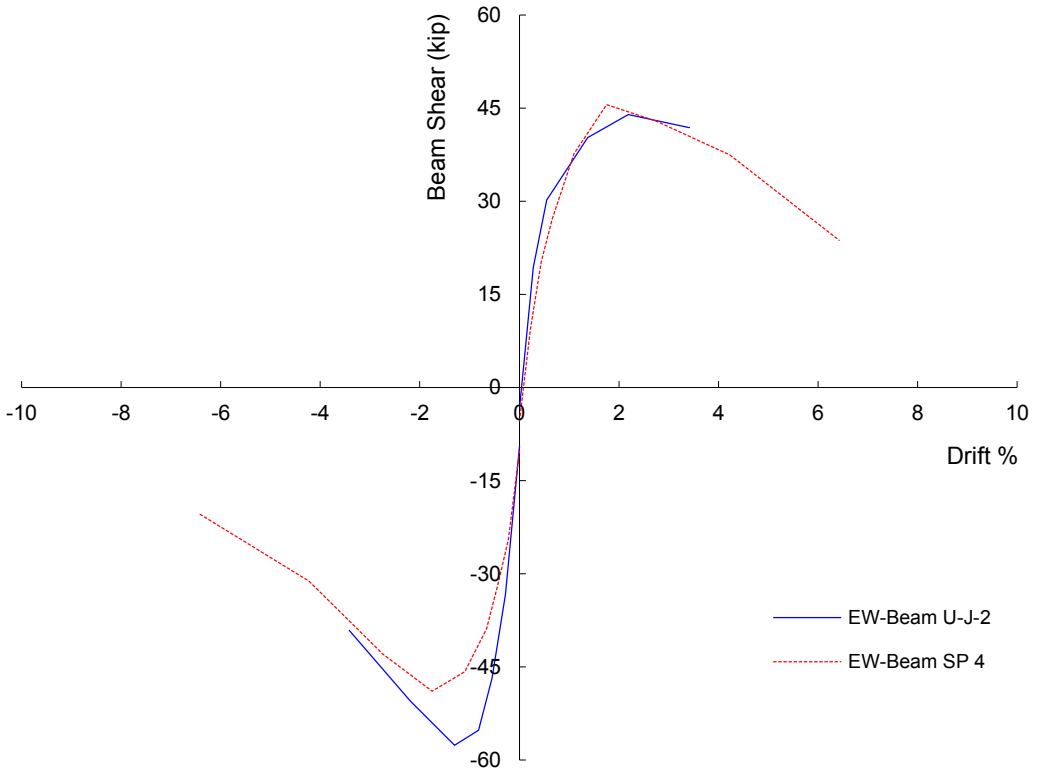

Figure 7.96 Effect of axial load level on backbone curves for J-Failure specimens (EW-Beam/North joint face)

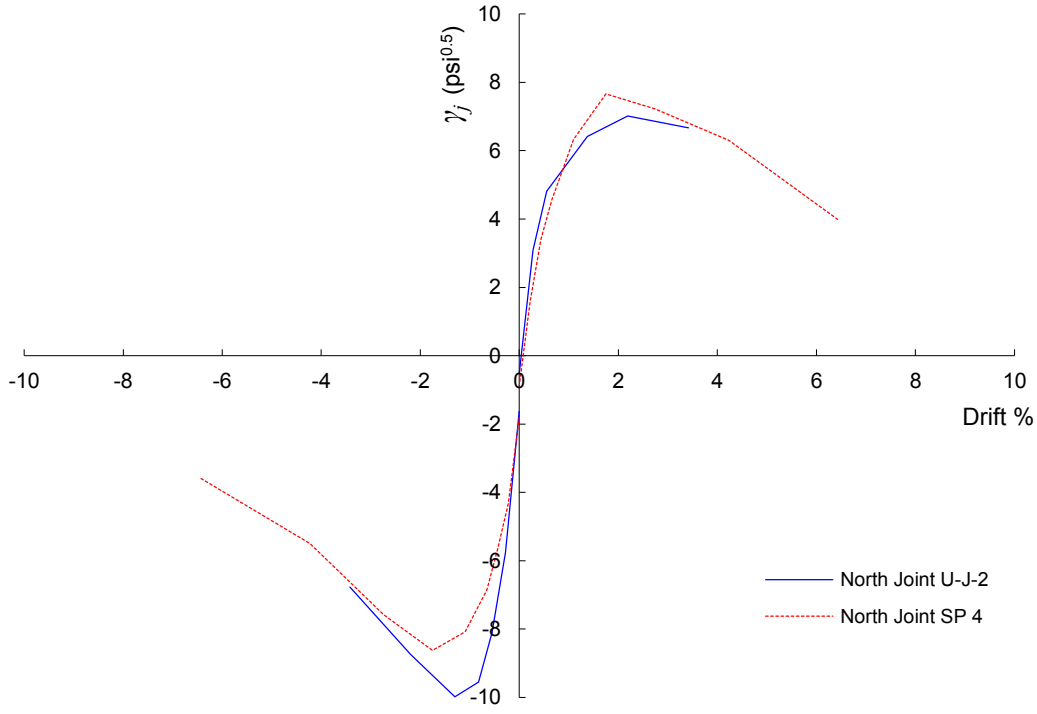

Figure 7.97 Effect of axial load level on backbone curves for J-Failure specimens (EW-Beam/North joint face)

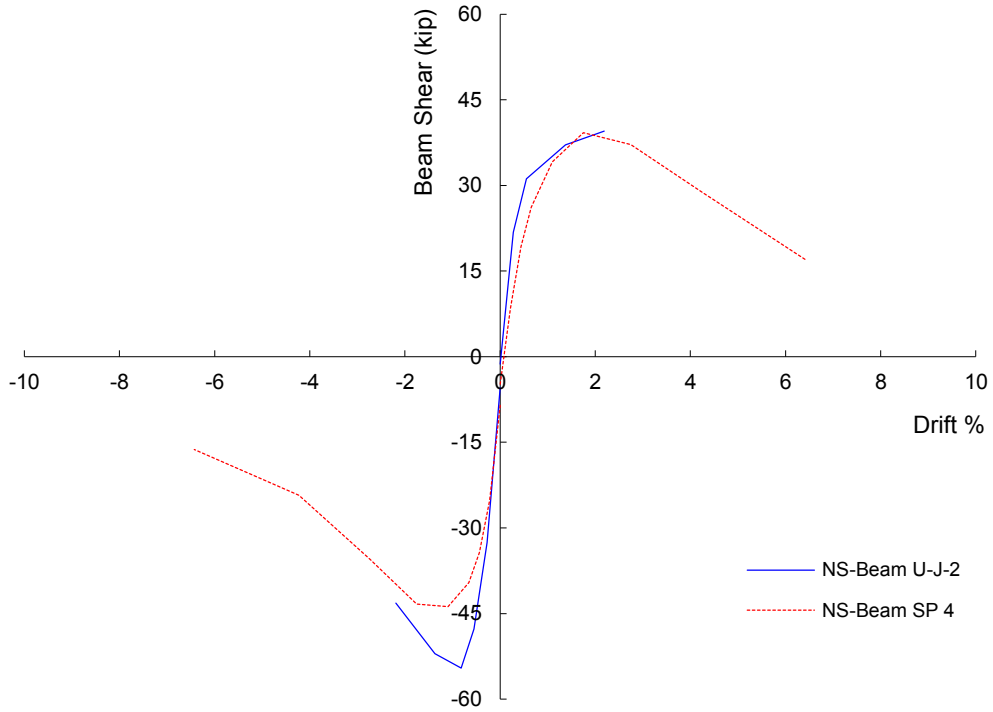

Figure 7.98 Effect of axial load level on backbone curves for J-Failure specimens (NS-Beam/East joint face)

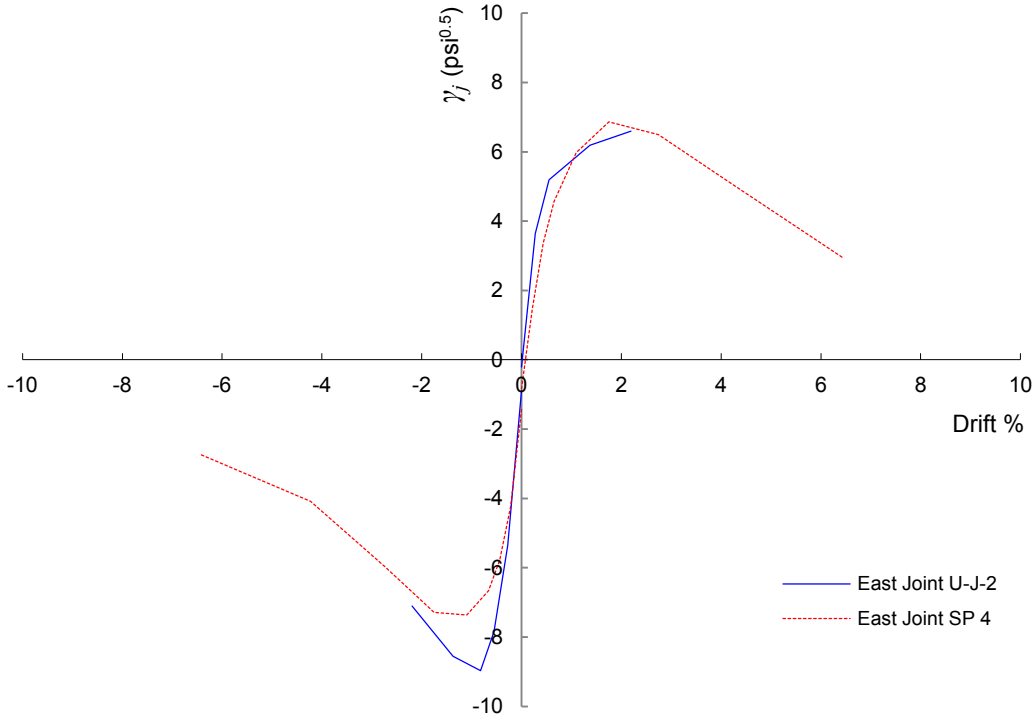

Figure 7.99 Effect of axial load level on backbone curves for J-Failure specimens (NS-Beam/East joint face)

BJ-Failure Mode

Figures 7.103 through 7.108 show comparisons between the hysteresis loops and envelope curves of specimen U-BJ-1 and Phase I specimen SP1, which is similar in geometry and reinforcement. Both specimens experienced BJ-Failure in both downward and upward loading directions. The starting gravity load ratio of specimen U-BJ-1 was 0.22 while that of Phase I SP1 was 0.08. The overturning seismic axial load was 51% and 127% of the starting gravity load for the two specimens, respectively. Gravity axial load ratio at negative peak shear strength of specimen U-BJ-1 was maintained at starting level of 0.22 while its counterpart of Phase I-SP1 vanished to zero because of the force based protocol used. The axial load ratio at peak negative joint shear strength of specimen U-BJ-1 was 0.50 while that of Phase I SP1 was 0.12. The north and east joint face shear strength coefficients for peak negative EW beam and NS beam loading in specimen U-BJ-1 are almost identical to those of Phase I-SP1. This implies that the substantially higher axial load level in specimen U-BJ-1 (4 times that of SP1) has no effect on enhancing shear capacity of unconfined corner or exterior joints experiencing BJ-Failure mode. As discussed in Chapter 4 and Chapter 5, joint shear strength in the case of yielding beam (BJ-Failure) is decided based on the flexural capacity of the beam. This is due to significant yield penetration into the joint core that softens joint concrete strut and dictates the joint shear strength not to exceed shear stress demand by the strain hardening flexural capacity of the beam. This phenomenon is well documented through many previous tests ([120], [83], and [6] among others).

It may be reasonable to hypothesize that higher axial load in the case of BJ-Failure may help "close the shear diagonal cracks", and hence "increase" joint shear strength. During the test of specimen U-BJ-1 the development of joint shear cracking was "delayed" due to the higher axial load compared to specimen SP1. This was the result of the "clamping action" of the high axial load. During the yielding and strain hardening processes of beams in specimen U-BJ-1, the joint showed very little evidence of shear cracking, distress, and deformation compared to SP1. Meanwhile the beams experienced significant cracking and deformation reaching the full strain hardening capacity, which is considered the main inelastic mechanism at that instance to determine the shear capacity of the subassembly. During later stages of loading, after significant strain hardening, yielding substantially penetrated the joint which started to experience notable shear cracking and distress and bond deterioration with beam reinforcement. Beam reinforcement steel strains of specimen U-BJ-1 during peak negative drift loading support this theory. Figure 7.88 shows that significant yielding of beam bars took place at the EW beam-joint interface before drift peak 4a, however, it did not significantly penetrate the joint until drift peak 6a, after which joint cracking and disintegration started to appear. This behavior was completely absent in specimen SP1 whose joint experienced substantial shear cracking soon after reaching the beam flexural capacity. In conclusion, the higher axial compression load delayed joint cracking and shear stress deterioration by clamping action of beam bars in the joint which delayed yield penetration and bond strength degradation. The axial load, however, *did not help* increase shear strength since the full beam flexural strain hardening capacity was reached before significant joint shear distress and this determined the maximum shear stress demand from beams to joints after which the inelastic regime tended to be force stabilized and deformation

driven until full yield penetration that led to shear and bond strength deterioration within the joint.

The post-peak north joint face shear strength of specimen SP1 significantly deteriorated from peak negative shear strength by 23.4% at peak 7a featuring significant softening slope, while the corresponding deterioration in specimen U-BJ-1 was 2.8%. In the east joint face, post-peak strength deterioration at negative peak 7a was 44.6% and 18.6% for specimens U-BJ-1 and SP1, respectively. These values reflect the major beneficial effect for the higher axial load in maintaining the peak shear strength in the post-peak regime and allowing longer profile of strain hardening by the clamping action to the joint. This allows full utilization of plastic mechanism by reaching the very large plastic rotation in the beam with negligible degradation in joint shear strength. The favorable effect of this ductile behavior on energy dissipation during intense ground shaking without losing shear capacity is evident. This result contradicts the observations of some researchers [116] and [150] who suggested that the higher axial load is detrimental to the post peak strength and stiffness degradation. However, this result is in line with other studies that showed more gradual strength degradation [54]. The key point here is that axial load can improve the joint post-peak behavior if the failure mechanism is a BJ-Failure.

Considering upward drift loading, the peak joint shear strength coefficients of north and east joint faces during EW beam and NS beam of specimen U-BJ-1 are lower than their counterparts in Phase I SP1 by 6.5% and 8.5%, respectively. It is worth mentioning that the joint shear stress corresponding to beam yielding in both specimens is almost identical. In addition, the yield displacements of both specimens are also identical. The beam shear associated with strain hardening of specimen U-BJ-1 EW and NS beams are higher than yield values by 13.7% and 11%, respectively, while those of SP1 are 27.8% and 17%, respectively. The axial tensile load ratios at peak joint shear strength in specimen SP 1 was 4.2% that of compression while that of specimen U-BJ-1 was 3.5%. The difference in joint shear stress coefficient in upward loading direction between both specimens might be due to difference in material strain hardening ratios, although this was not checked in this study.

The post yielding force-positive drift plateau of specimen U-BJ-1 reveals no strength degradation during EW beam loading. Instead, a strain hardening profile is dominant. On the contrary, a softening strength degradation of 10% slope was noticed in SP1. As for NS beam positive drift loading, 17.9% lower post peak strength degradation was observed in specimen U-BJ-1 compared to specimen SP1. This may be attributed to the lower joint distress and cracking in specimen U-BJ-1 due to the higher axial load in compression cycle that delayed joint degradation and reflected positively even in the upward loading cycle.

As mentioned in Chapter 4, different researchers have offered different opinions on effect of axial load on joint shear strength. The results of the current investigation confirm the favorable effect of high axial load on unconfined corner joint shear strength in joints experiencing J-Failure mode. However, it was shown that for specimens experiencing BJ-Failure, peak joint shear strength is independent of axial load effect since it is primarily determined by the flexural and strain hardening strength of the yielding beam. However, high axial compression helps delay the strength degradation and maintain plastic capacity until axial failure in BJ-Failure specimens.

Thus, how the axial load affects behavior depends on the failure mode of the beam-column joint assembly.

7.4.1.2 INTERSTORY DRIFT RATIO AND DISPLACEMENT DUCTILITY

J-Failure Mode

Table 7.6 presents the displacement ductility factors for the test specimens calculated using method B described in Chapter 4 It also depicts the ratio between the maximum drift achieved before axial failure and that corresponding to peak joint shear strength, denoted *failure displacement ductility factor* $\mu_{\Delta\text{-}f}$, as a measure of post-peak maximum deformation capacity of test specimens before axial collapse of the subassembly.

Considering specimens U-J-2 and Phase I SP4 that experienced J-Failure, it can be observed from Fig. 7.97 and Table 7.5 that the north joint face of the former attained its peak shear strength at 25.7% lower negative drift than that of the latter. Similarly, the corresponding value for negative drift loading of the east joint face was 25.5%. This is associated with the higher joint pre-peak stiffness in specimen U-J-2 with higher axial load. This indicates the negative effect of higher axial compression load ratio on the drift capacity at peak joint strength of unconfined corner beam-column joints with J-Failure mode. Due to axial collapse of specimen U-J-2, the maximum negative drifts reached were 46.8% and 65.9% lower than those of specimen SP4 for EW and NS beam loading, respectively. These ratios reflect the substantial negative effect of high axial loading on the overall drift capacity of J-Failure unconfined corner beam-column joints.

The displacement ductility $\mu_{\Delta\text{-}b}$ of specimen U-J-2 in the EW downward loading direction was 18% lower than that of specimen SP4. It was decided to consider the EW beam loading only to compare displacement ductility factors to avoid the bias of NS beam initial response resulted from torsional cracking developed when EW is loaded first. The failure displacement ductility factors $\mu_{\Delta\text{-}f}$ of specimen U-J-2 during EW beam loading and NS beam loading were 43.8% and 50% lower than those of specimen SP4, respectively; noting that the SP4 test was terminated without reaching axial failure, which may suggest even higher reduction in relative displacement ductility had SP4 test been continued until axial failure. These values indicate that the higher axial compression was detrimental to displacement ductility and seriously harmful to the post-peak deformation capacity of J-Failure unconfined corner beam-column joints.

The EW beam "yield" drifts according to the definition adopted in Chapter 4 for specimens U-J-2 and SP4 for the upward loading direction are 0.44% and 0.63%, respectively. The peak shear strength drift capacity of EW beam upward loading of specimen U-J-2 was 25% higher than that of SP4. The displacement ductility $\mu_{\Delta\text{-}b}$ of specimen U-J-2 and SP4 in the EW upward loading direction was 3.98 and 3.34, respectively. This implies higher ductility and drift capacity in specimen U-J-2 compared to specimen SP4. Recall that the upper axial load history of specimen SP4 was all compression loads, with zero axial compression at the upward peak joint shear strength, while specimen U-J-2 axial loading history comprised 3% axial tension ratio at the peak joint shear strength. The slightly less ductile response of specimen SP4 in the upward

loading direction can be attributed to the all-compression axial load history compared to tensile-compression history of specimen U-J-2.

BJ-Failure Mode

For specimens U-BJ-1 and Phase I SP1 that experienced BJ-Failure, it can be noticed from Table 7.5 and Figs. 7.106 and 7.108 that both north and east joint faces reached their peak shear strength at the same drift ratio. This indicates the higher axial compression load has no effect on peak shear strength drift capacity of unconfined corner beam-column joints with BJ-Failure mode. This is expected since the performance is not controlled by the joint but rather by the beam flexural capacity until strain hardening capacity. At axial collapse of specimen U-BJ-1, the maximum negative drift reached was 44.4% higher than that in specimen SP1 for EW beam loading. However, this ratio does is not representative of the actual axial failure drift since specimen SP1 test was terminated before axial failure.

The displacement ductility $\mu_{\Delta\text{-}b}$ of U-BJ-1 was about twice that of SP1. This indicates that higher axial compression has substantial effect on improving ductility capacity of unconfined joints undergoing BJ-Failure mode due to the lower joint degradation condition.

The failure displacement ductility factors $\mu_{\Delta\text{-}f}$ of specimen U-BJ-1 during EW beam loading was 50% higher than test termination displacement ductility of specimen SP1; noting that the SP1 test was terminated without reaching axial failure. However, had SP1 test been continued until axial collapse, it is anticipated that specimen SP1 failure displacement ductility would have been higher than that of U-BJ-1; hence no conclusive post-peak ductility observation can be deduced.

7.4.1.3 STIFFNESS AND STIFFNESS DEGRADATION

J-Failure Mode

The initial stiffness of specimen U-J-2 in the EW and NS negative loading directions is identical to that of specimen SP4. Afterwards, the stiffness of the latter specimen started to decline relative to that of the former. This indicates that the higher axial load is helpful to increase pre-peak stiffness. However, this behavior is reversed in the post-peak stiffness. The higher axial load tends to increase post-peak stiffness degradation. The initial stiffness of specimen U-J-2 in the EW and NS positive loading directions is also higher than that of SP4. Given that the axial load in the first few positive loading cycles was still compression, the higher axial load of specimen U-J-2 led to its higher stiffness in both positive loading directions.

The peak-to-peak effective stiffness degradation curves for both specimens are shown in Fig. 7.100. It can be observed that the first cycle effective stiffness of specimen U-J-2 is about 25% higher than that of SP4. For the first few cycles, the effective stiffness of specimen U-J-2 is higher than that of specimen SP4 for both EW and NS beam loading. However, this effective stiffness enhancement due to higher axial load decreases as the loading cycles proceeded towards

reaching peak shear strength after which the effective stiffness of specimen U-J-2 started to decline below that of specimen SP4. The rate of effective stiffness degradation post-peak shear strength is similar for both specimens, however.

BJ-Failure Mode

As for the case of BJ-Failure mode, Fig. 7.109 indicates that the initial stiffness of EW and NS beams in the negative loading direction is identical for both specimens U-BJ-1 and SP1. Prior reaching joint shear capacity/beam flexural capacity, the stiffness degradation of the latter is more pronounced than that of the former. However, it can be clearly observed that the higher axial load significantly reduced stiffness degradation after reaching peak joint shear strength and plastic strain hardening capacity. The reduction of stiffness degradation at the same drift peak was about 50% for NS beam and 90% for EW beam. This post-peak behavior is the opposite of that of J-Failure mode in which higher axial load accelerated stiffness degradation. This is attributed to that the plastic mechanism was concentrated at the yielding beam not in the joint, which allowed additional deformation capacity before yield penetration disintegrated the joint core. The higher axial load clamping force in the joint was more efficient in bond strength enhancement in the case of smaller beam bar diameter in the BJ-Failure mode specimens.

The initial stiffness of EW and NS beams in the positive loading direction for both BJ-Failure specimens was almost identical. However, the same observation of accelerated post-peak stiffness degradation in specimen SP1 applies. This can be explained by the much higher axial tension force in SP1 that contributed to higher joint principal stresses caused by the axial tension strains in column longitudinal bars that led to more severe joint distress.

As observed from Fig. 7.100, the effective peak-to-peak stiffness of specimen U-BJ-1 is higher than that of SP1 prior to reaching joint shear capacity after which the effective stiffnesses of both specimens are almost equal indicating marginal effect of axial load. The rate of effective stiffness degradation post-peak shear strength is similar for both specimens.

7.4.1.4 JOINT DEFORMATIONS

The joint deformation reflected by joint shear strain can be useful in many aspects. It can be used as threshold limits to determine strength at different terminals such as joint cracking limit, joint shear strength, and joint axial strength. Joint shear strains can be also implemented in analytical strut-and-tie and panel zone principal strains models for joint shear strength. In addition, they can be used to calibrate and model the inelastic performance parameters of joints in analytical simulation components models. The joint deformation represented by joint shear strain γ_s or joint rotation can be indicative of joint flexibility under different geometric and loading configurations as a main contributor to the overall lateral drifts of reinforcement concrete frames, especially in the nonlinear range of older-type construction frames.

J-Failure Mode

Figure 7.101 displays the hysteresis curves of specimen U-J-2 and SP4 for joint shear stress-joint rotation. Generally, the joint shear strain in specimen SP4 is more significant than that in specimen U-J-2. This is attributed to the higher axial load in the latter that enhanced joint rigidity and helped delay significant cracking.

Figure 7.102 shows the crack pattern at north joint face shear strength downward loading peak for specimens U-J-2 and SP4. It can observed that SP4 with lower axial load suffers more pronounced joint cracking compared to specimen U-J-2 that exhibited a single diagonal crack at peak joint shear strength. This could be indicative of two aspects. The first is the better bond capacity associated with higher axial load that delayed secondary joint strut cracking associated with bond forces of beam reinforcement within the joint. The second aspect is the higher flexibility of the joint under low axial loads compared to that under high axial load. It might be reasonable to think that the higher axial load helped "close" or delay "opening" of non-major joint cracks. It is worth mentioning that the vertical cover splitting crack observed in specimen U-J-2 was absent in specimen SP4 which is consistent with lower axial load in the latter. The cover spalling of the latter was totally shear deformation initiated.

BJ-Failure Mode

Figure 7.110 depicts a contrast between joint shear stress-strain response for specimen U-BJ-1 and SP1 of Phase I; both experienced BJ-Failure. The effect of higher axial load in U-BJ-1 can be observed through its much narrower loops and smaller shear strains in the first few drift groups under axial compression in the downward negative direction compared to SP1 (notice that test termination drift in both specimens is different). This implies that the joint flexibility is much lower with higher axial compression load. This is attributed to the "clamping action" of higher axial load that delayed yield penetration into the joint core, especially with the small diameter beam bars used, and maintained bond stress between beam bars and joint core concrete until higher drifts and delayed joint disintegration. This is confirmed by comparing crack pattern (Fig. 7.111), beam steel strains (Fig. 7.112) of both specimens at the same post peak drift level. It can be observed that specimen U-BJ-1 joint is almost intact during the 6a peak negative cycle, while SP1 joint was suffering major diagonal cracking. The EW beam top reinforcement yielding during downward loading penetrated the north joint face in specimen SP1 as early as -1.77% drift (peak 4a). However, in specimen U-BJ-1, this yield penetration started at the second drift peak (5b) of -2.29% drift. In both specimens there was significant beam yielding and plastic deformations. However, in specimen U-BJ-1 the contribution of joint shear deformation to the overall drift was very limited in the negative loading direction (Fig. 7.83). On the contrary in SP1, this contribution was more significant and comparable to that of beam flexural yielding. It is also noticed that beam flexural crack width and intensity of beam plastic action were more apparent in specimen U-BJ-1 compared to SP1. For modeling purposes, the plastic mechanism of joint U-BJ-1 can be visualized an elastic-plastic rotational spring at the beam-joint interface with a rigid-plastic joint rotational spring representing joint deformation, while the plastic mechanism of SP1 can be visualized as two elastic-plastic rotational springs representing beam and joint.

Another aspect of the higher axial load is the diagonal strut inclination angle. This angle closely matches the theoretical value in SP1 whose X-shaped crack patterns match the typical crack pattern of BJ-Failure with low axial loads. The main "diagonal" crack in the downward loading cycle in U-BJ-1 does not match the theoretical strut angle for 1:1 joint aspect ratio. This diagonal crack started from the center of the joint as a nearly vertical crack. This can be explained by the high axial compression load that generated a substantial column compression zones above and below the joint that sandwiched the joint as a compression element until significant yielding penetrated the joint and disintegrated it so that the shear behavior dominated afterwards. Hence the closer-to-vertical crack can be viewed as splitting crack caused by compression mechanism dominating over the joint shear mechanism in the early post-peak stages. Principal strain trajectories also can be used to interpret the observed crack angle.

The joint deformation behavior in the upward loading direction is completely different. The first shear stress-strain hysteresis loops of specimen U-BJ-1 are slightly narrower with smaller shear strains than those of SP1 due to the higher axial compression of the former before reaching joint shear strength. However, this behavior changed to similar loops and shear strains afterwards, when both specimens were under axial tension at the positive drift peaks. Both specimens U-BJ-1 and SP1 reached similar shear strain levels at the same positive drift peaks at later stages of loading. The upward cycle joint diagonal cracks of both specimens are identical featuring an inclination angle that matches the theoretical value due to the absence of high compression.

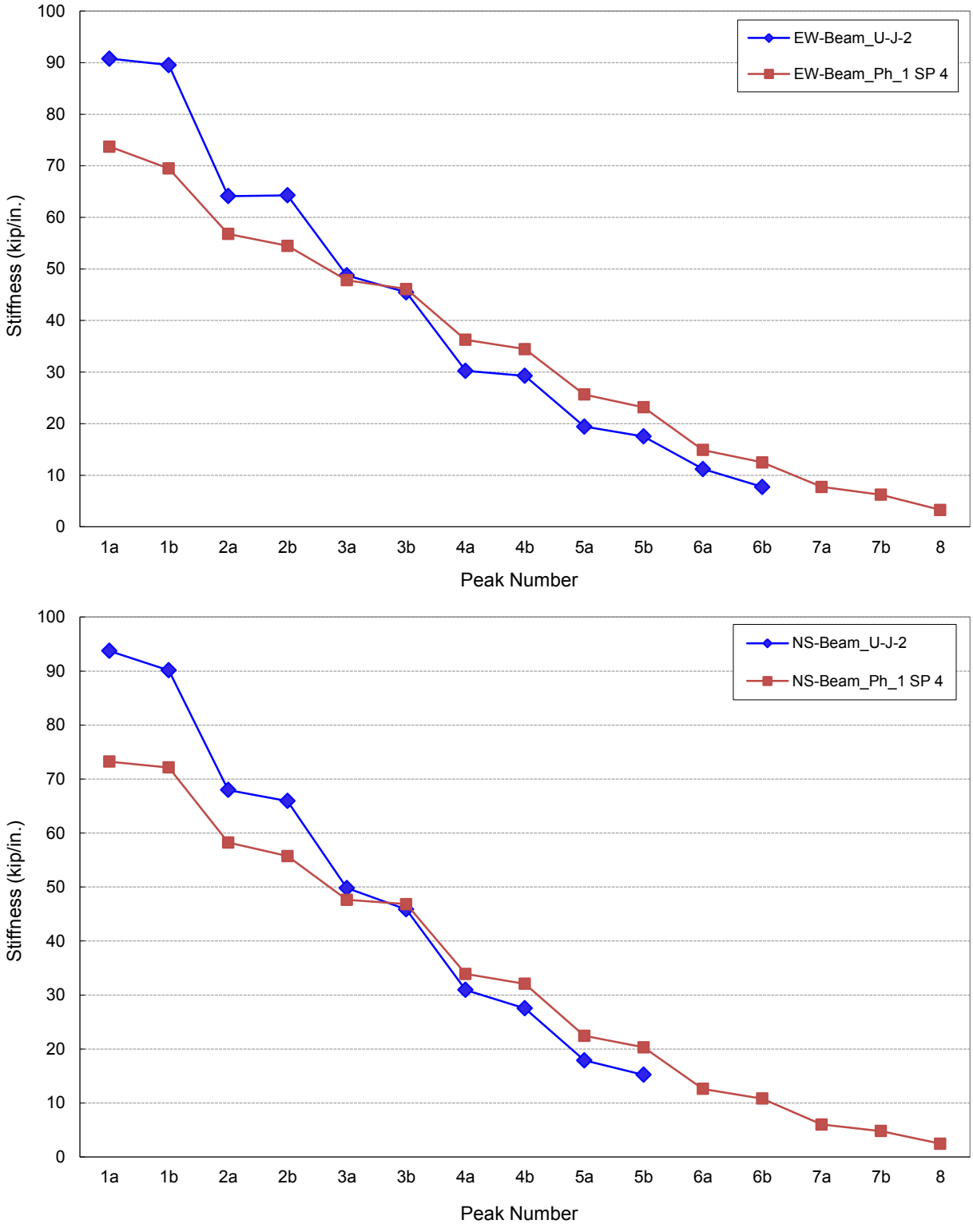

Figure 7.100 Effect of axial load level on peak-to-peak stiffness degradation for J-Failure specimens

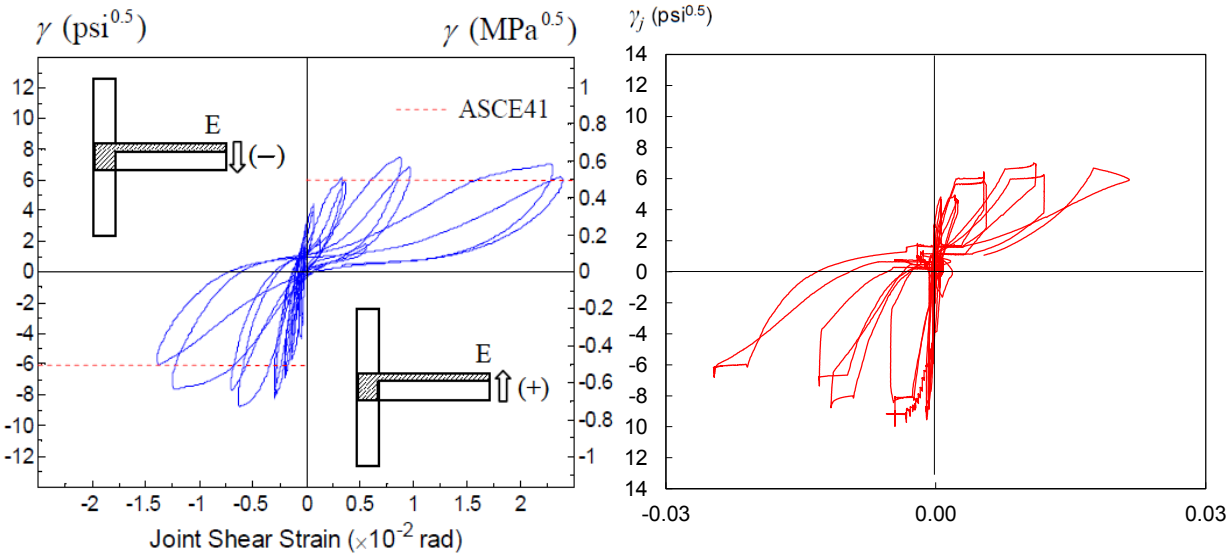

Figure 7.101 The effect of high axial load on joint shear stress-joint rotation backbone for J-Failure specimens (a) Specimen SP4, [120] (b) Specimen U-J-2

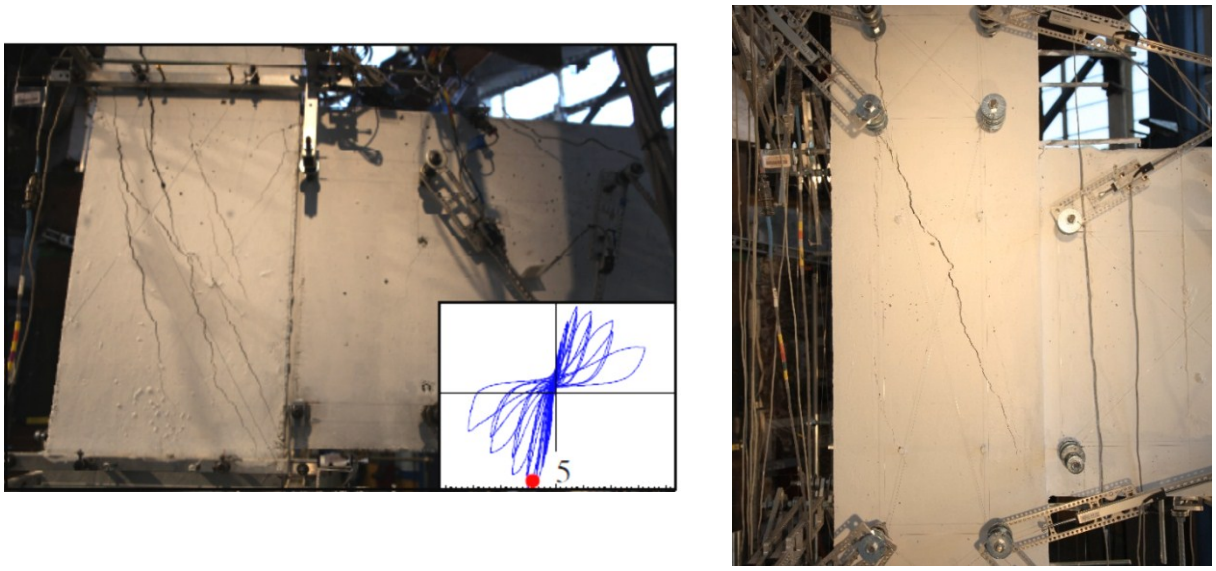

Figure 7.102 Crack pattern of north joint face at peak joint shear strength of downward drift loading for: (a) Specimen SP4 Peak 5 (-1.75% drift), [120] (b) Specimen U-J-2 Peak 4 (-1.30% drift)

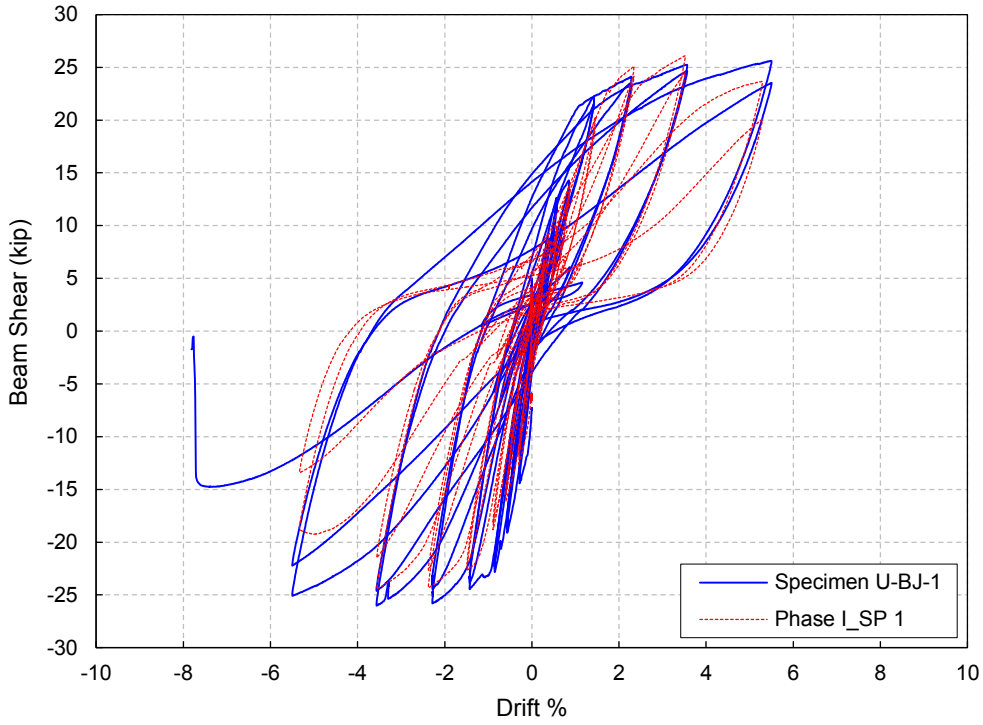

Figure 7.103 Effect of axial load level on load-drift response of EW-beam for BJ-Failure specimens

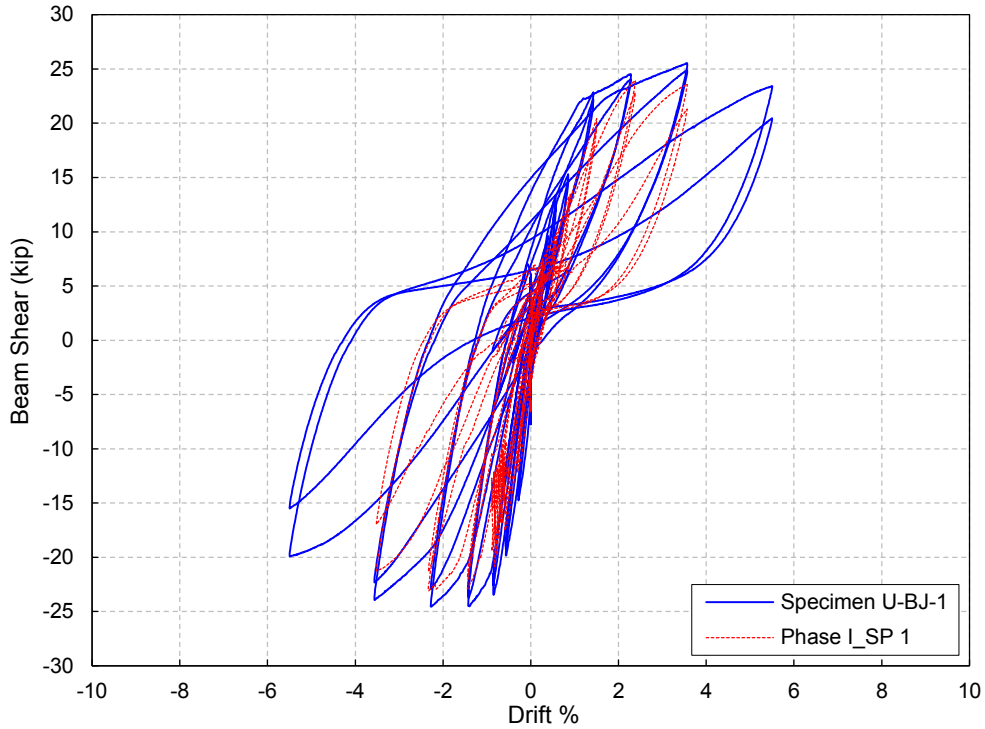

Figure 7.104 Effect of axial load level on load-drift response of NS-beam for BJ-Failure specimens

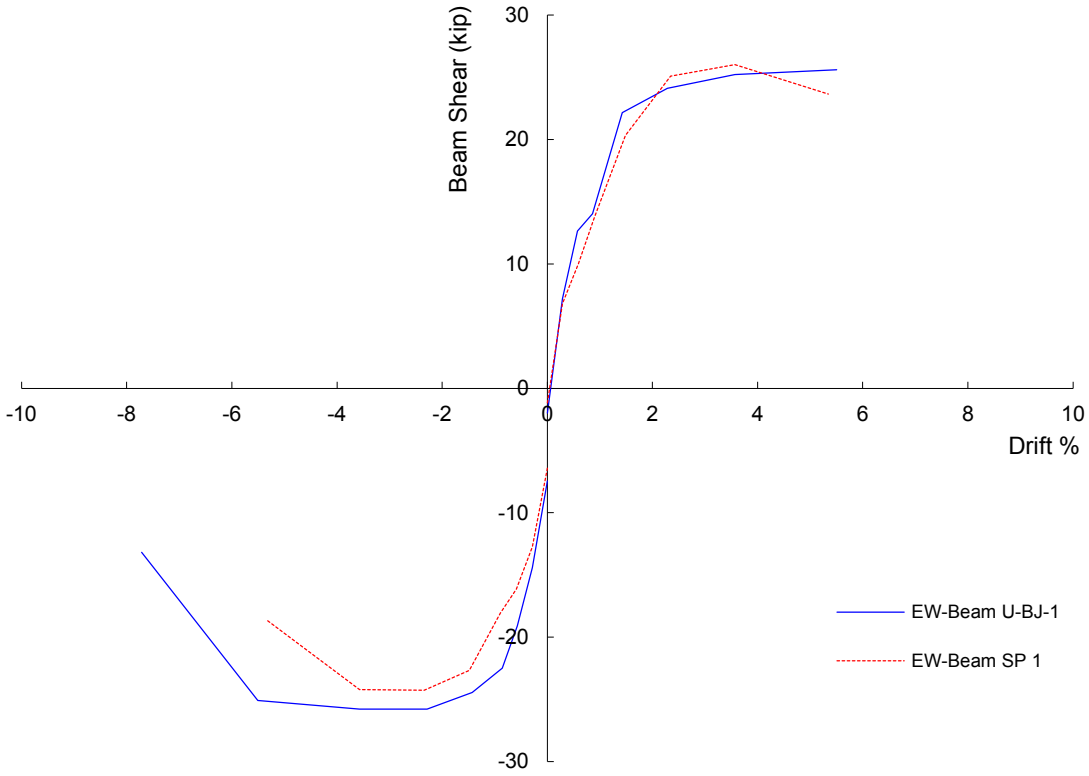

Figure 7.105 Effect of axial load level on backbone curves for BJ-Failure specimens (EW-Beam/North joint face)

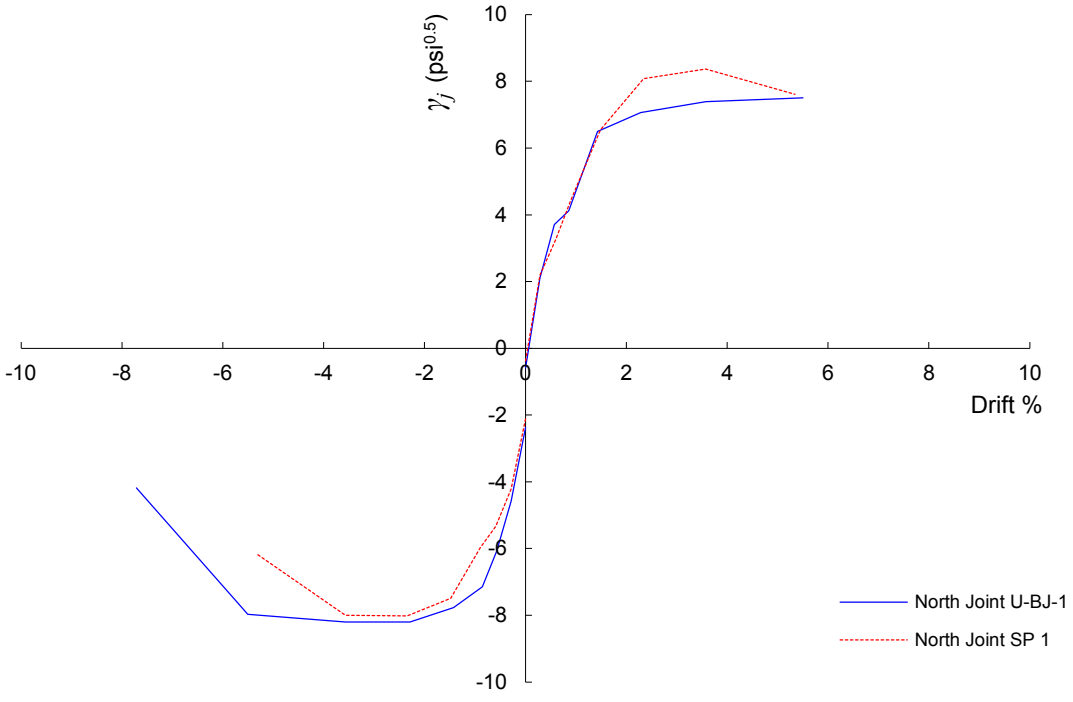

Figure 7.106 Effect of axial load level on backbone curves for BJ-Failure specimens (EW-Beam/North joint face)

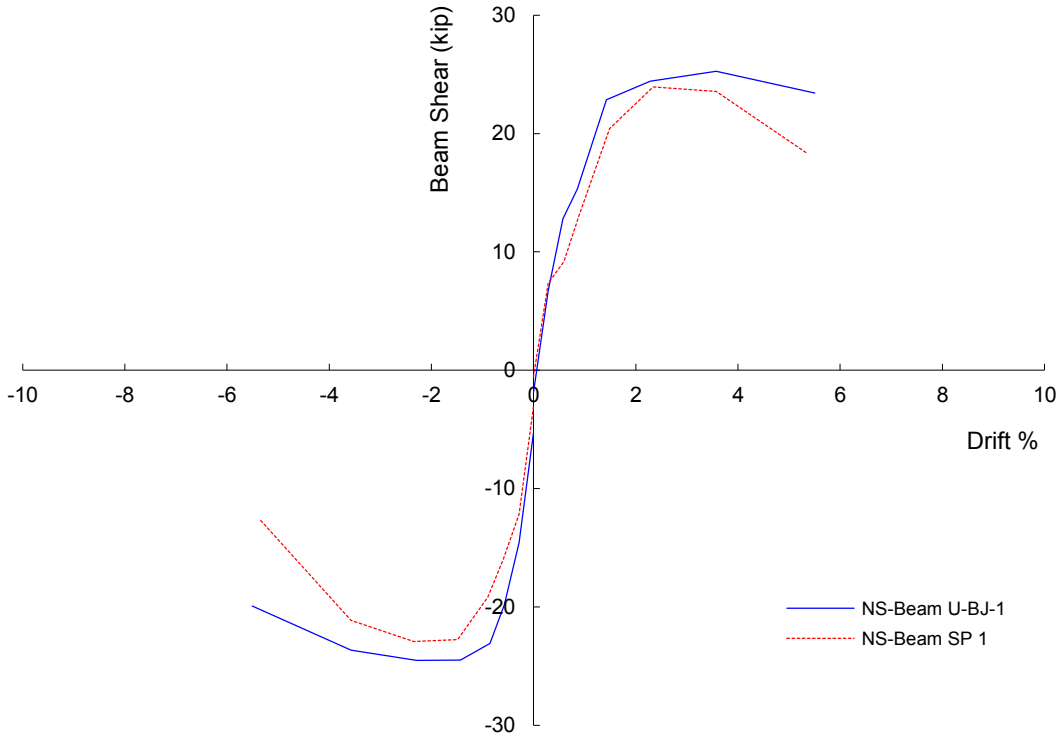

Figure 7.107 Effect of axial load level on backbone curves for BJ-Failure specimens (NS-Beam/East joint face)

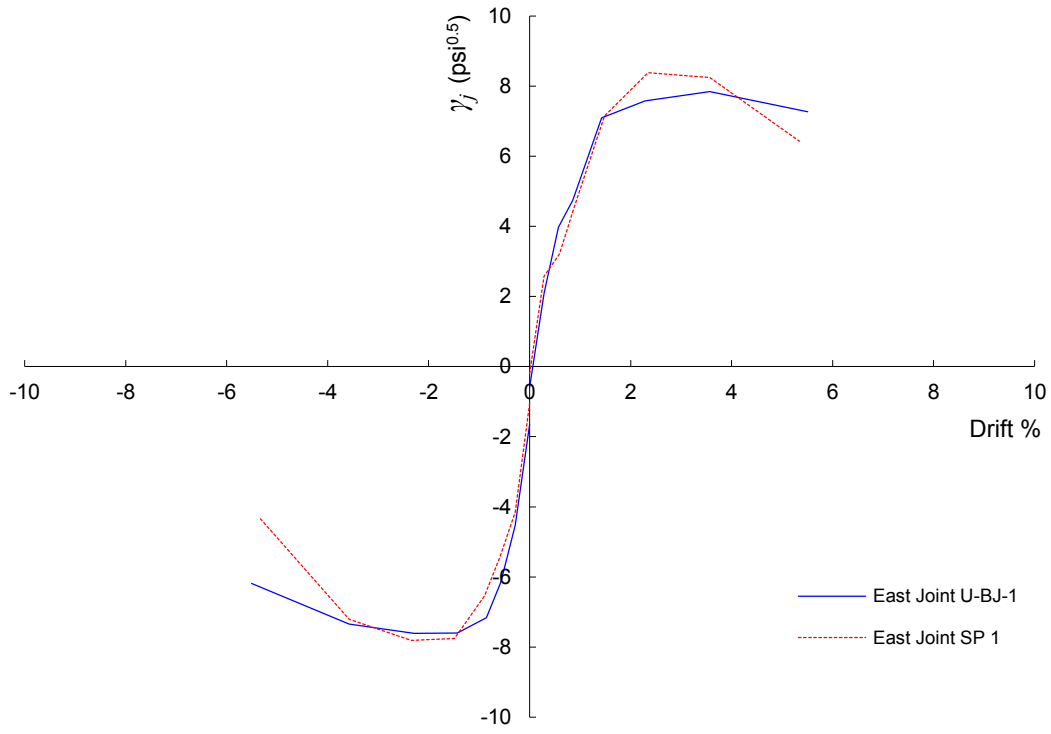

Figure 7.108 Effect of axial load level on backbone curves for BJ-Failure specimens (NS-Beam/East joint face)

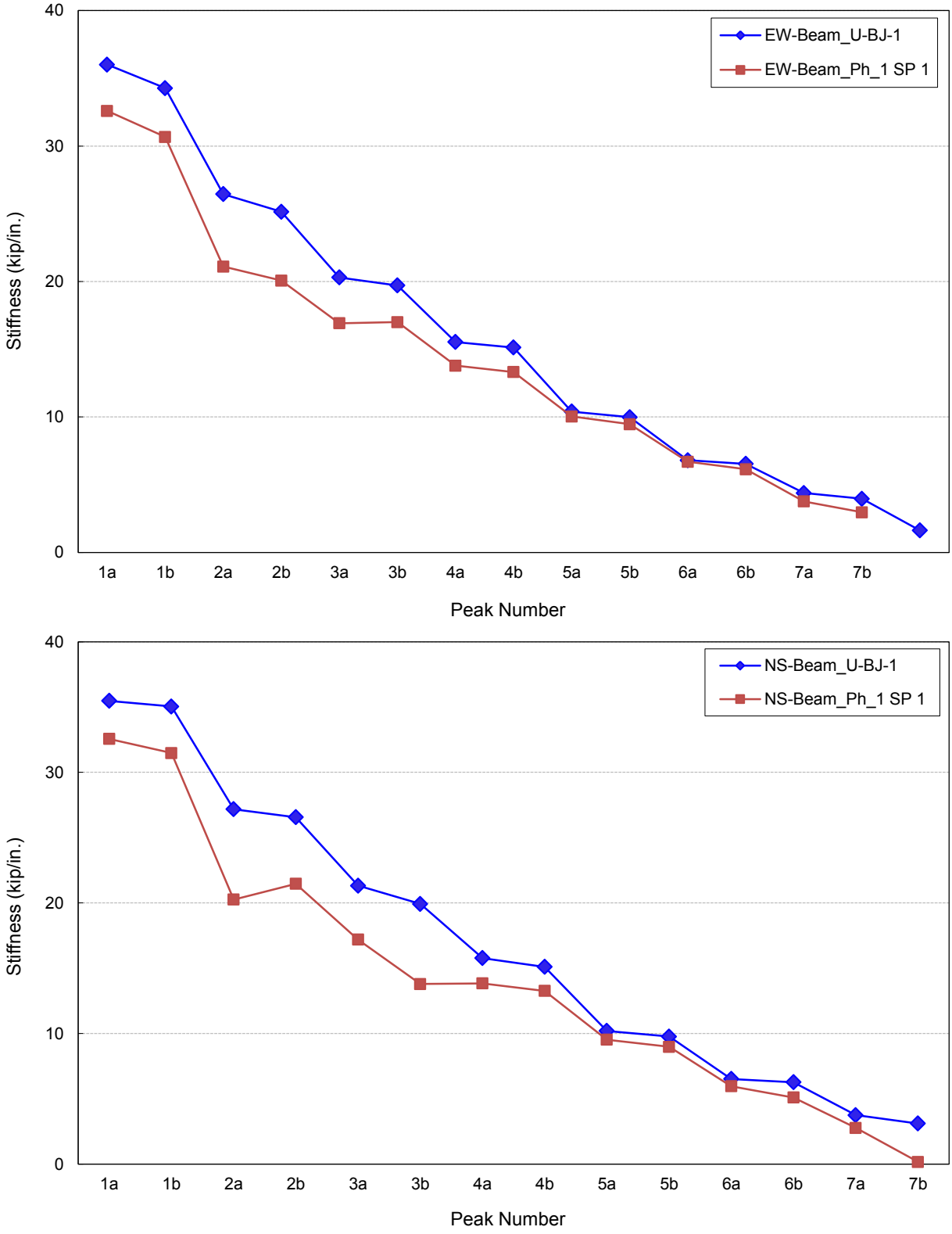

Figure 7.109 Effect of axial load level on peak-to-peak stiffness degradation for BJ-Failure specimens

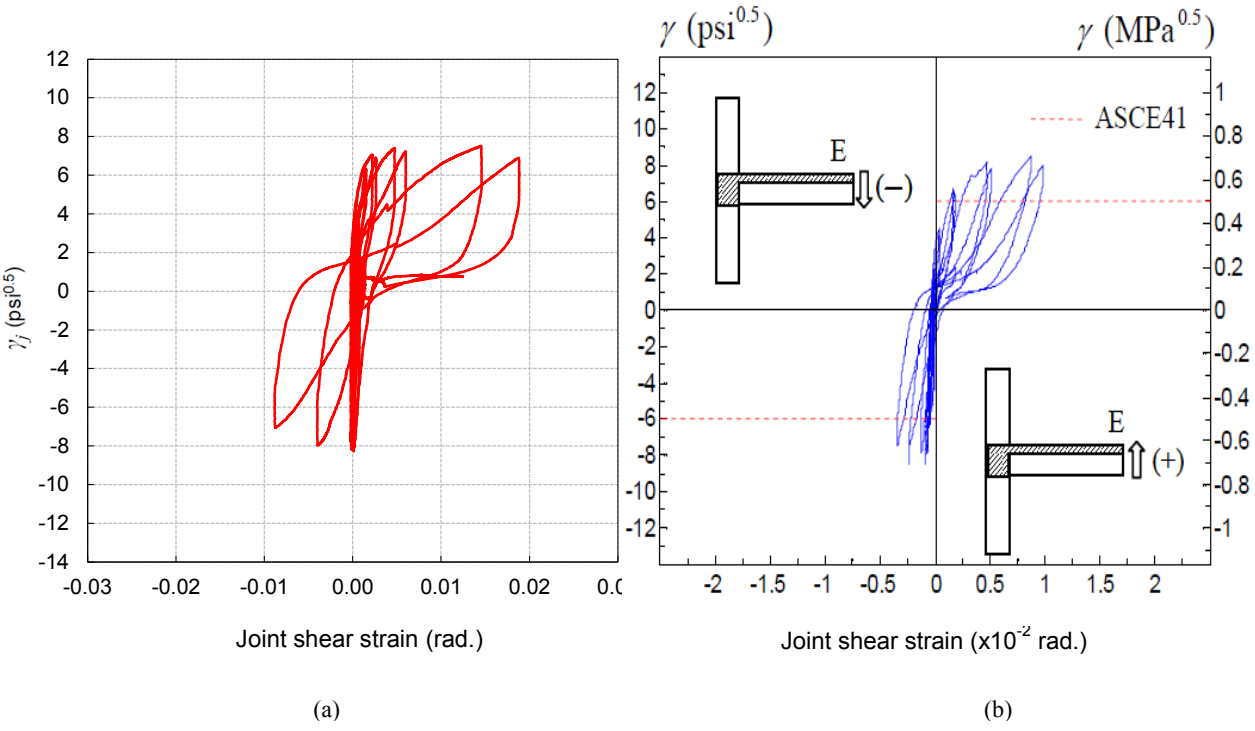

Figure 7.110 Effect of axial load on joint shear stress-joint rotation hysteresis for BJ-Failure specimens (a) Specimen U-BJ-1, (b) Specimen SP1, [1]

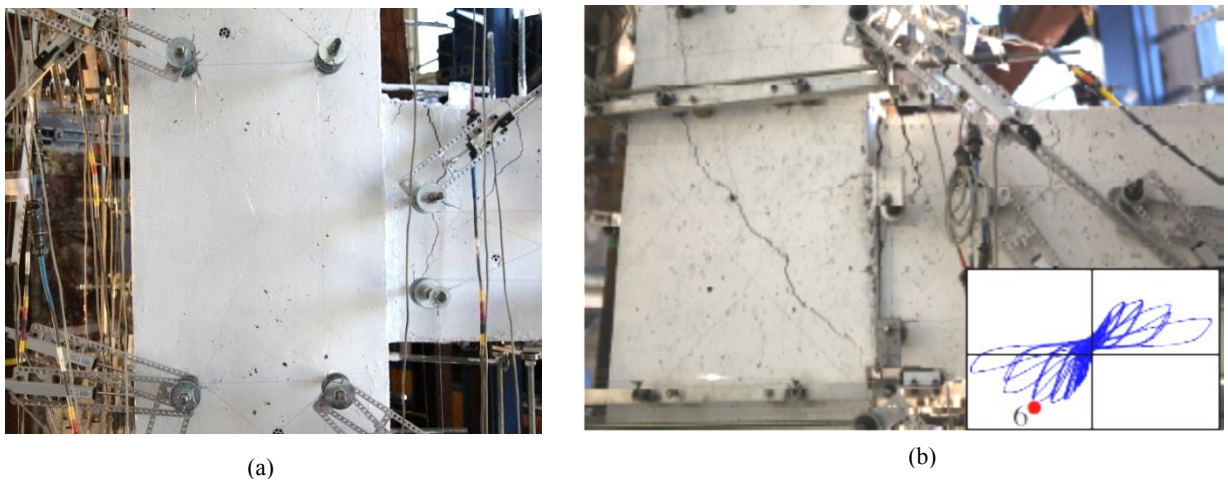

Figure 7.111 Crack pattern of EW beam and north joint face at peak 6a (-3.6%) downward drift loading for: (a) Specimen U-BJ-1, (b) Specimen SP1, [120]

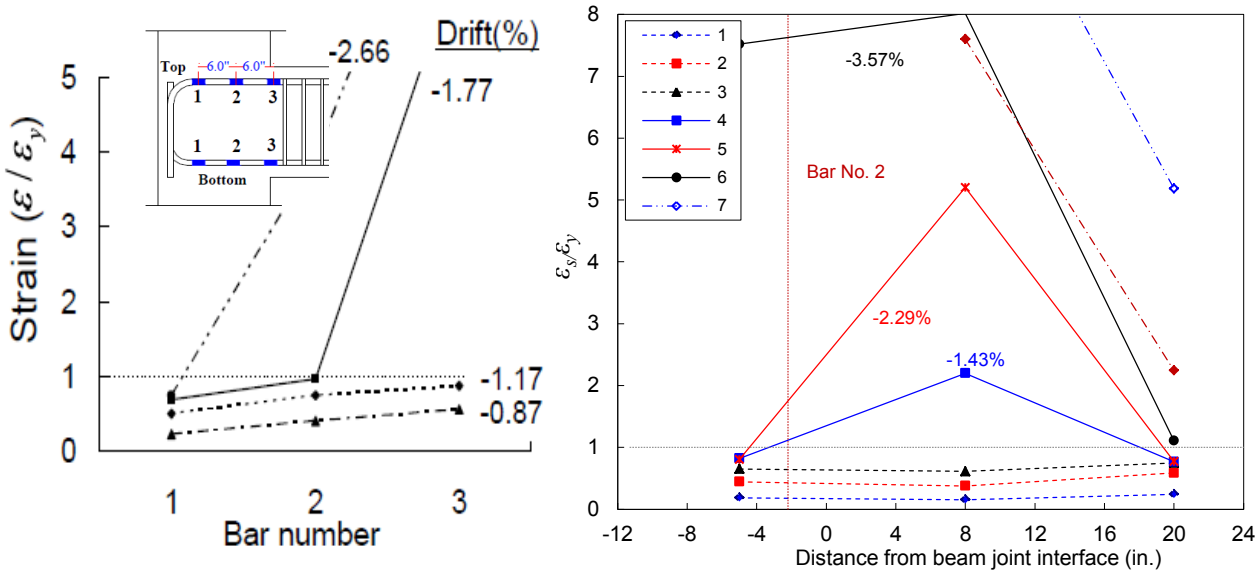

Figure 7.112 EW Beam steel strain distribution:
(a) Specimen SP1, [120], (b) Specimen U-BJ-1

7.4.2 Effect of Joint Aspect Ratio

To investigate the effect of joint aspect ratio on the performance of unconfined corner beam-column joints, two specimens that experienced J-Failure are compared. The first is from the current study (specimen U-J-1) and the other is of Phase I (Park [120]) (specimen SP4). Axial load protocol of both specimens was beam shear force based. The Details of Phase I SP4 are presented in the abovementioned reference.

7.4.2.1 JOINT SHEAR STRENGTH

Figures 7.5 and 7.6 show comparisons between the load-drift response of specimen U-J-1 and that of Phase I specimen SP4. Both specimens experienced J-Failure in the negative loading (downward) direction. The starting gravity load ratio of specimen U-J-1 was 0.22 while that of Phase I SP4 was 0.11. The overturning seismic axial load was 52% and 48% of the starting gravity load for the two specimens, respectively. The axial load ratio at peak negative joint shear strength of specimen U-J-1 was 0.31 while that of Phase I SP4 was 0.17. Due to the force based axial load protocol used in both specimens, the gravity load ratio at peak joint shear strength deteriorated to 0.12 and 0.07 for specimens U-J-1 and SP4, respectively. Although gravity axial load ratio and overall axial load ratio at peak joint shear strength are different in both specimens, the variation is not substantial so that it could introduce significant strength differences. The enhancement of joint shear strength due to axial load within the range of 0 to 0.20 is low as proven in Chapter 4. To further account for the variation of axial load in the two specimens, the peak response of specimen U-J-1 was reduced by the factor of 7%. This factor was determined using the empirical shear strength model axial load enhancement factor k developed in Chapter 5.

The north joint face normalized shear strength of specimen U-J-1 in the downward loading direction is 65.8% higher than that of Phase I-SP4. Similarly, east joint face shear strength coefficient of specimen U-J-1 in the downward loading direction is higher than that of SP4 by 59%. This strength increase in smaller aspect ratio specimen is consistent with diagonal strut theory for shear strength transfer mechanism. Using the strut-and-tie model presented in Chapter 5, the average theoretical strength increase in lower aspect ratio specimen over that of higher aspect ratio is 36% compared to experimental enhancement of 53.5%. This bias is due the conservative limit set for the effect of axial load enhancement in the strut-and-tie model by limiting the depth of column compression zone to $0.4h_c$. The prediction of joint shear strength using the empirical shear strength model developed in Chapter 5 reveals 40% strength increase in lower joint aspect ratio specimen. This also reflects the empirical model's slight conservatism and suggests its suitability for quick estimation of exterior and corner joint shear strength.

It can be observed from Fig. 7.116 that post-peak strength degradation of downward drift loading of both EW and NS beams of specimen U-J-1 is almost identical to that of SP4 for the same drift peaks. This implies the negligible effect of joint aspect ratio on the post peak strength degradation of J-Failure unconfined corner beam-column joints.

Considering the upward drift loading direction, the peak joint shear strength coefficients of north and east joint face of specimen U-J-1 are 42.2% and 40% higher than those of specimen

SP4, respectively. Contrasting the average strength increase (53.5%) for higher aspect ratio joint under the same axial compression load with that under axial tension (41.1%) indicates better enhancement in the case of axial compression. However, that should be viewed in the light of the level of axial tension on both specimens. The axial tension load ratio at the positive peak shear strength of specimen U-J-1 was 0.13 while that of specimen SP4 was zero. As discussed before, Higazy et al. [59] showed that joints under axial tension showed about 15% less strength than those under small axial compression load. The variation between strength enhancements due to lower aspect ratio in the negative and positive loading directions is consistent with that result.

The post-peak strength degradation slope in specimen U-J-1 upward drift EW and NS beam loading is 38.6% and 33% lower than the corresponding SP4 degradation. This implies that joint shear strength degradation is accelerated for higher aspect ratio specimen in the absence of axial compression load.

7.4.2.2 INTERSTORY DRIFT RATIO AND DISPLACEMENT DUCTILITY

It can be observed from Figs. 7.116 and 7.118 and Table 7.5 that the north and east joint faces of specimen U-J-1 and SP4 attained their peak shear strength at the same downward drift peaks (5a), and (4a), respectively. However, the drift value at these peaks was different since it is based on yield displacement that is smaller in specimen SP4. EW beam downward peak 5a corresponds to -2.19% in specimen U-J-1 drift while it corresponds to -1.75% in SP4. Similarly in east joint face, downward peak 4a corresponds to -1.37% in specimen U-J-1 and -1.1% in specimen SP4.

This indicates that drift capacity at peak shear strength is reduced by about 20% for higher joint aspect ratio. This might be attributed to the lower shear strain capacity at joint shear strength peak of the higher aspect ratio specimen. However, the displacement ductility $\mu_{\Delta\text{-}b}$ of specimen U-J-1 in the EW negative loading direction was 6.1% lower than that of specimen SP4. Although NS beam was initially cracked by torsional stresses developed when EW is loaded first, its displacement ductility factors were close to those of EW beam loading.

Similar drift capacity observations can be deduced for upward loading direction. An average drift capacity reduction of 35% was observed with higher aspect ratio. Again, the displacement ductility factors were little influenced.

The above observations reveal that drift capacity at joint shear strength for unconfined corner joints experiencing J-Failure is reduced with higher aspect ratio; however, the effect of joint aspect ratio on displacement ductility is minimal.

7.4.2.3 STIFFNESS AND STIFFNESS DEGRADATION

Figures 7.115 through 7.119 can be used to assess the relation between joint aspect ratio and stiffness. As expected, the deeper beam in specimen SP4 showed higher initial stiffness than that of specimen U-J-1 in both negative and positive loading directions. The post-peak stiffness degradation rate is much higher for SP4, suggesting faster joint deterioration with higher aspect ratio. However, and upon normalizing the joint shear stress and accounting for the slight

difference in axial load ratio, it can be seen that the shallower joint in specimen U-J-1 has higher overall loading stiffness than SP4 in both negative and positive loading directions. This intuitive result was expected since it reflects the smaller flexibility of shallow joint due to a shallower joint strut angle that gives better resistance to lateral loading. Considering normalized joint shear stress-drift relationship, the "joint stiffness" degradation prior to reaching joint shear strength is higher for higher aspect ratio joint for both negative and positive loading directions. However, the post-peak "joint stiffness" degradation is very similar for both joint aspect ratios.

The peak-to-peak effective stiffness degradation curves for both specimens are shown in Fig. 7.119. The figure was developed based on beam shear forces not joint shear stresses. Thus, the beam effective stiffness of SP4 is generally higher than that of U-J-1 due to the higher beam depth. It is generally observed that higher joint aspect ratio specimen is characterized by more rapid effective beam stiffness degradation than that of smaller joint aspect ratio. In particular, this is more pronounced in the post-peak shear strength regime.

7.4.2.4 JOINT SHEAR DEFORMATIONS

Figures 7.120 and 7.121 show joint shear stress-strain response and cracking of specimen U-J-1 and specimen SP4 of Phase I, [120]. At peak shear strength of north joint face of specimen U-J-1, -2.19% drift, less shear cracking and narrower cracks were observed compared to shear cracking of north joint face of specimen SP4 at its peak shear strength at -1.75% drift. Since axial loads at peak shear strength of both specimens were close, the difference in shear cracking is primarily attributed to the different joint aspect ratio, which implied higher flexibility and more shear cracking for the high aspect ratio specimen. This observation is also reflected in the joint shear stress-rotation load-drift response at the corresponding drifts depicted in Fig. 7.120. Thus, it can be concluded that the increasing joint aspect ratio increase joint shear cracking at the same drift level due to higher joint flexibility.

It is worth mentioning that Park [120] concluded that generally total joint rotation is inversely proportional to aspect ratio based on the comparison of responses of specimens SP4 and SP2. The reason this conclusion was arrived at is that he included in the joint deformation the beam bar slip induced rotation which was less significant in specimen SP4 with higher aspect ratio. This was a result of the less tensile force demand on beam bar in higher aspect ratio specimen due to large lever arm and also as a result of shear failure mode which was J-Failure in specimen SP4 while beams yielded before reaching joint shear capacity in specimen SP2. This imposed higher slip rotation in the specimen SP2 which led to aforementioned conclusion.

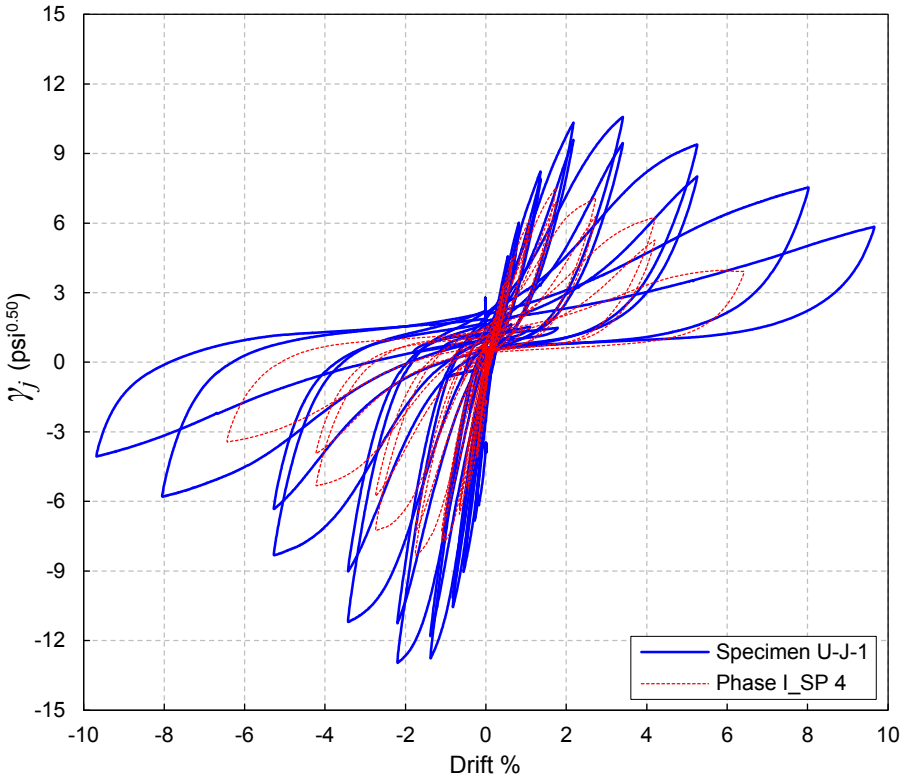

Figure 7.113 Effect of joint aspect ratio on load-drift response of north joint face for J-Failure specimens

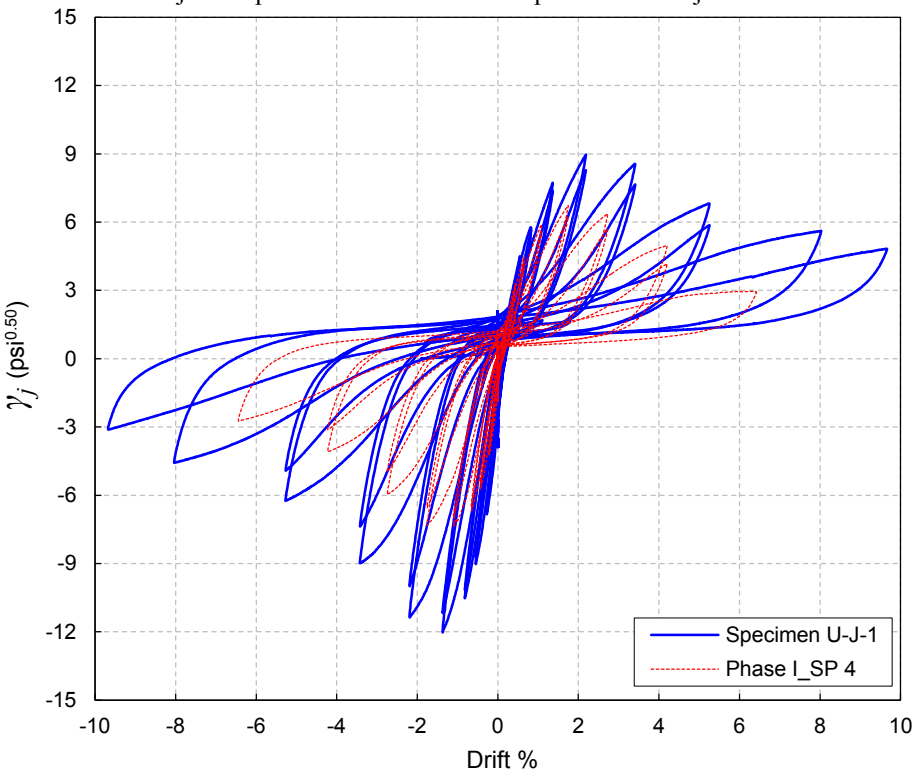

Figure 7.114 Effect of joint aspect ratio on load-drift response of east joint face for J-Failure specimens

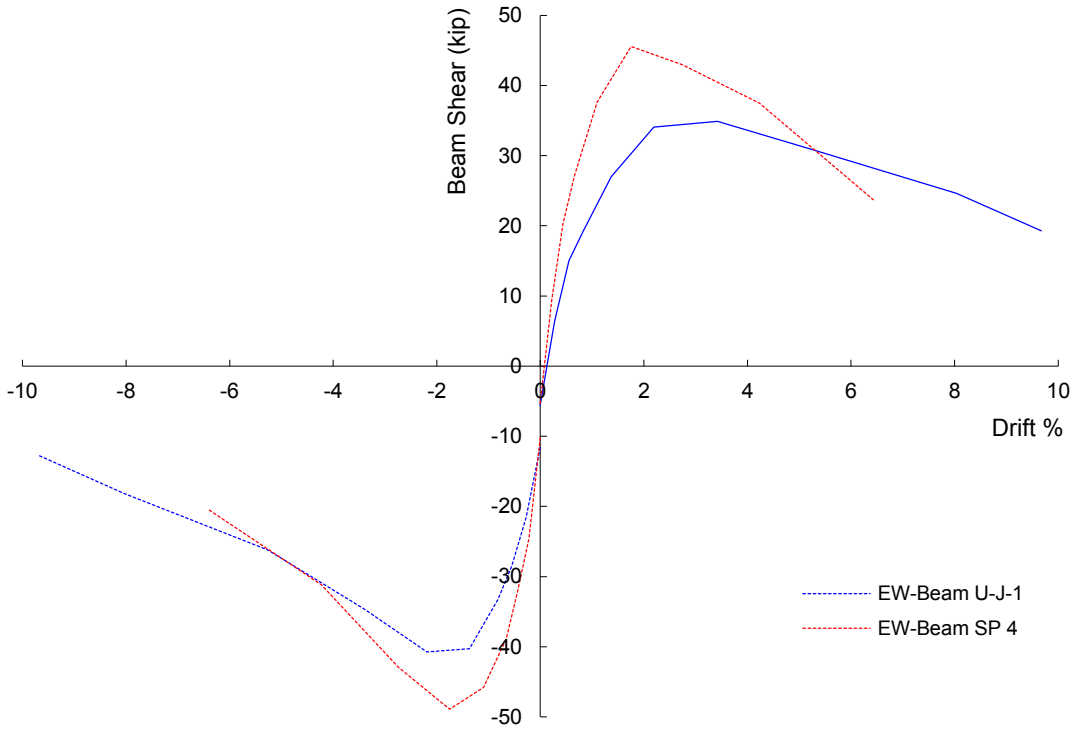

Figure 7.115 Effect of joint aspect ratio on backbone curves for J-Failure specimens (EW-Beam/North joint face)

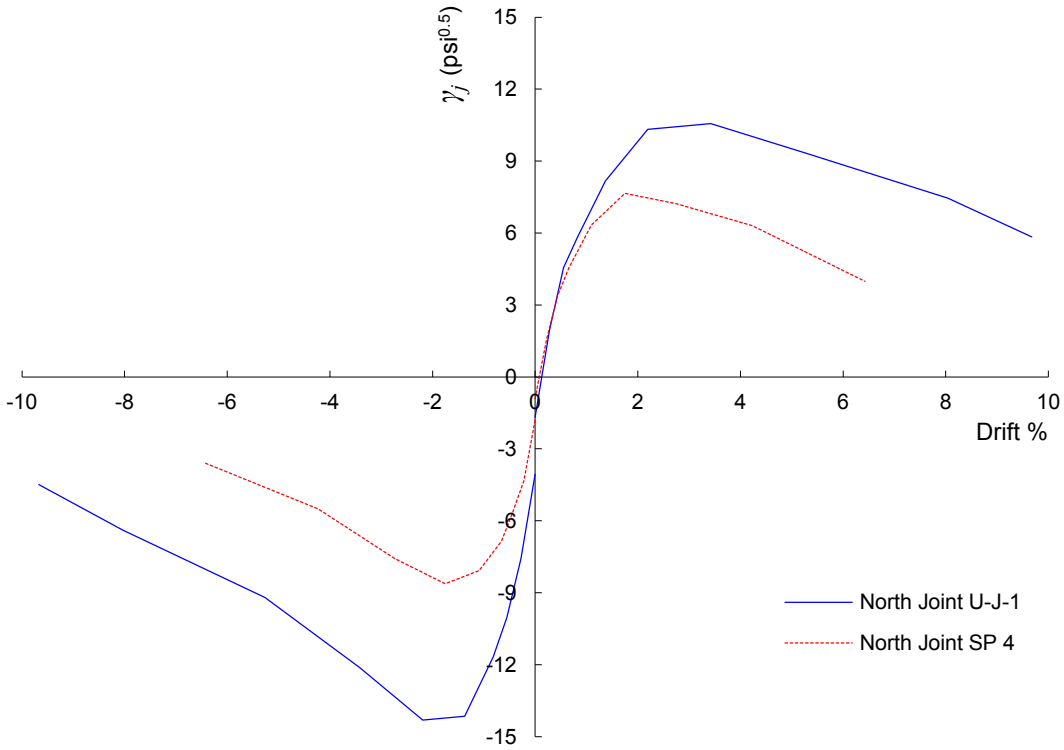

Figure 7.116 Effect of joint aspect ratio on backbone curves for J-Failure specimens (EW-Beam/North joint face)

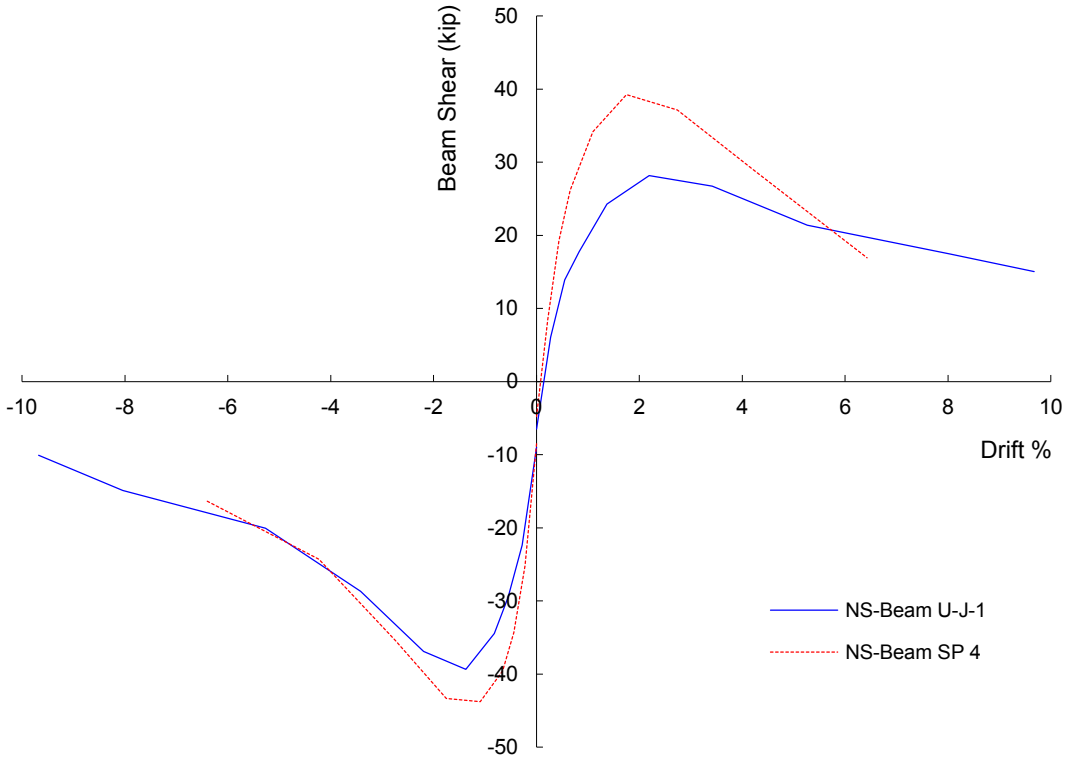

Figure 7.117 Effect of joint aspect ratio on backbone curves for J-Failure specimens (NS-Beam/East joint face)

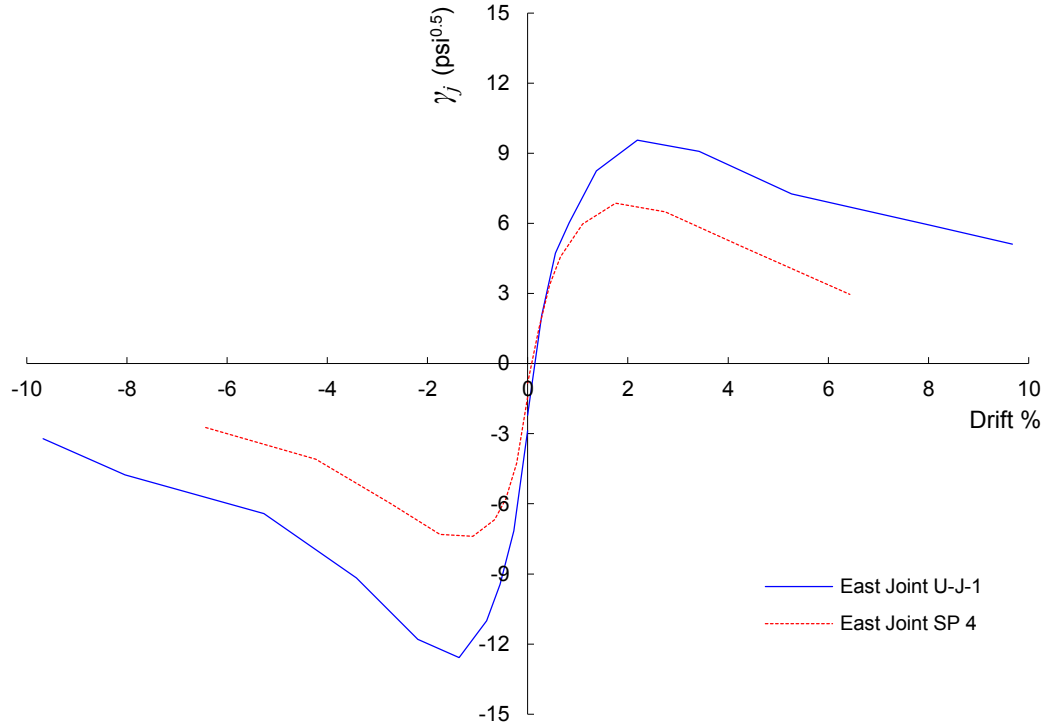

Figure 7.118 Effect of joint aspect ratio on backbone curves for J-Failure specimens (NS-Beam/East joint face)

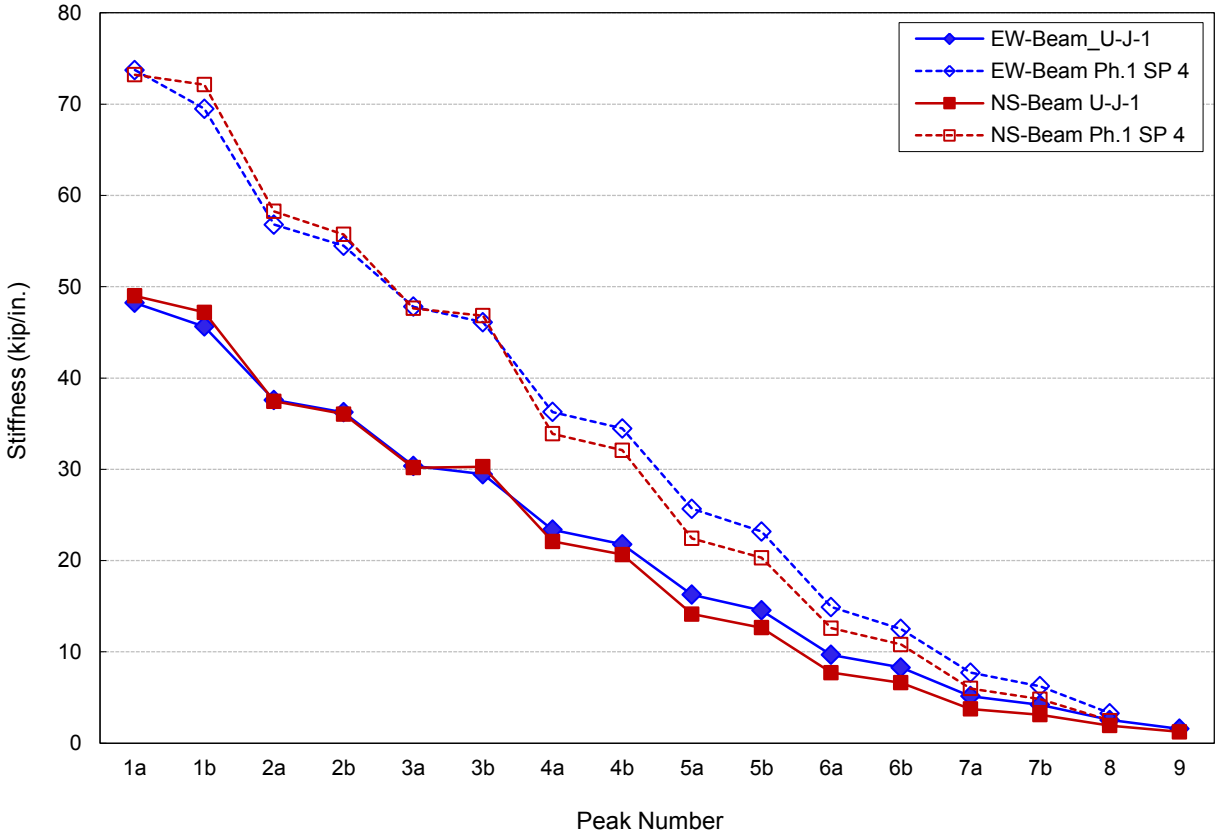

Figure 7.119 Effect of joint aspect ratio on peak-to-peak stiffness degradation for J-Failure specimens

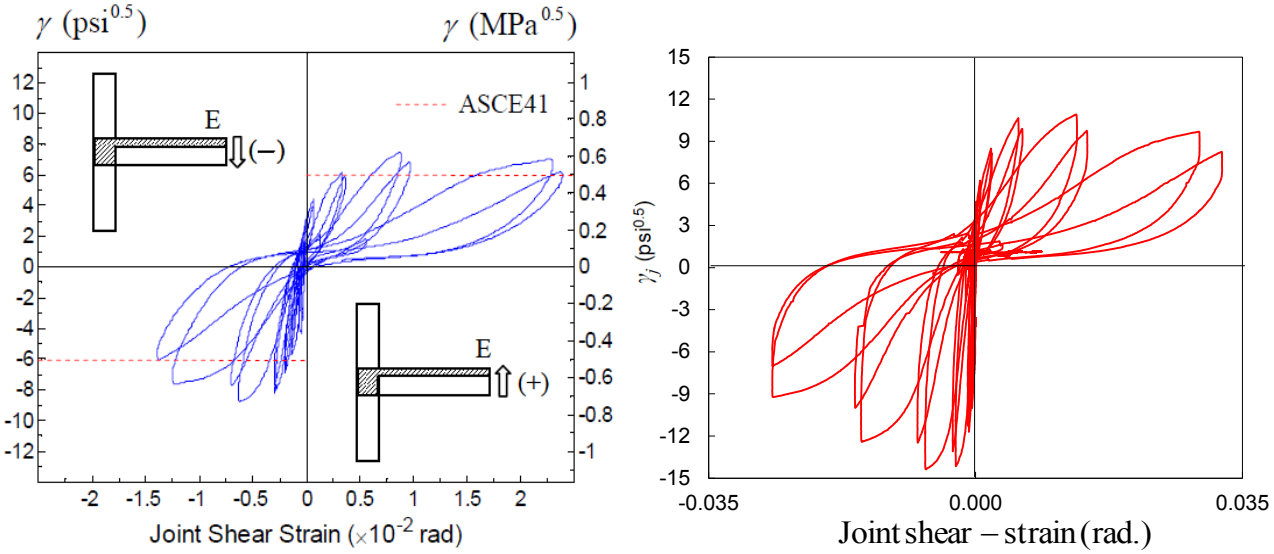

Figure 7.120 The effect of joint aspect ratio on north joint face shear stress-joint rotation relations for J-Failure specimens; (a) Specimen SP4, [120] (b) Specimen U-J-1

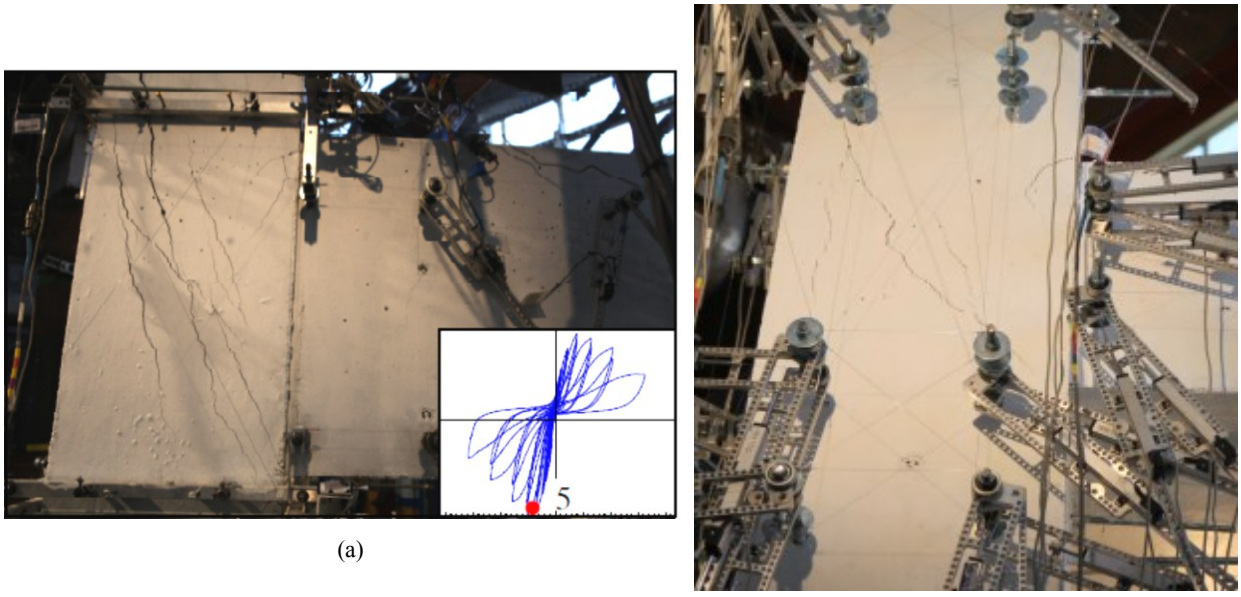

(a) (b)

Figure 7.121 Crack pattern of north joint face at peak joint shear strength of downward drift loading for: (a) Specimen SP4 (peak 5a, -1.75% drift), [1] (b) Specimen U-J-1 (peak 5a, -2.19% drift)

7.4.3 Effect of Loading History

The effect of loading history on the performance of unconfined corner beam-column joints is investigated through comparing the performance of specimens U-J-1 and B-J-1. Both specimens experienced J-Failure mode. Specimen U-J-1 was uniaxially loaded in alternating fashion as described in Chapter 6 while specimen B-J-1 underwent simultaneous biaxial loading for both beams. However, the axial loading protocol is different in the two specimens. Specimen U-J-1 was loaded using a force-based axial load protocol that did not maintain the peak axial load reached at joint shear strength throughout the test, while specimen B-J-1 was loaded using a displacement-based axial load protocol that maintained the axial load level reached at peak joint strength during the post peak regime.

7.4.3.1 JOINT SHEAR STRENGTH

Figures 7.5 through 7.6 show the hysteresis loops and envelope curves for specimens U-J-1 and B-J-1. Both specimens experienced J-Failure in the negative loading (downward) direction. The starting gravity load ratio of both specimens was 0.22. The overturning seismic axial load was 48% and 105% of the starting gravity load for the two specimens, respectively. The axial load ratio at peak negative joint shear strength of specimen U-J-1 was 0.31 while that of B-J-1 was 0.45. To account for the variation of axial load in the two specimens, the response of specimen B-J-1 was reduced by the factor of 7.5% for EW beam downward loading and 10% for NS beam downward loading. This factor was determined using experimental observation from the effect of axial load on shear strength presented in Section 7.4.1 and the empirical shear strength model axial load enhancement factor k developed in Chapter 5. In the upward loading direction, both specimens experienced J-Failure mode for both EW and NS beams. The maximum axial tension load ratio of 0.01 was reached at positive joint shear strength peak in specimen B-J-1, while the corresponding ratio in specimen U-J-1 was 0.08. Using linear extrapolation for the effect of axial tension on joint stresses between zero tension and 5% tension as determined by Higazy et al. [59], the response of B-J-1 specimen in the upward loading direction was amplified by 10%. Previous studies [77], [84] and [2] suggested circular shear strength interaction to account for the effect of biaxial loading on shear strength of joints with transverse reinforcement. A graphical representation of the circular interaction assumption is shown in Fig. 7.127. To investigate the validity of this assumption for unconfined joints, the response of EW beam and NS beam of specimen B-J-1 to the diagonal biaxial loading scheme presented in Chapter 6 was modified to account for this loading and enable comparison to the uniaxially loaded specimen U-J-1 response. Since the biaxial loading is diagonal to the axes of square column section, this implies using circular interaction that enables vectorial summation of orthogonal components of biaxial joint shear strength to give the corresponding uniaxial one. Accordingly, the response of B-J-1 EW and NS beams was increased by a factor of $\sqrt{2}$.

The modified response to account for the difference in axial load level and the circular shear interaction is denoted “B-J-1-Modified” in the plots presented in this section. Plots not denoted by “Modified” are for the actual test results of specimen B-J-1.

The north joint face shear strength coefficient of specimen B-J-1-Modified in the downward EW beam drift loading was 7% higher than that of specimen U-J-1, while the corresponding value in east joint face was 10%. This implies that the circular interaction of strength is an appropriate measure for unconfined joint biaxial shear strength, since it is slightly on the conservative side. It can be also observed that the circular shear strength interaction is highly accurate in the linear range; a result that is consistent with intuition. The accuracy of this circular interaction decreases towards the conservative side for the peak joint shear strength. Figure 7.122 depicts the normalized joint shear stress contours of north and east joint faces of specimen B-J-1. The contours reveal almost linear relationship between joint shear stress in both orthogonal directions indicating equal participation of each direction to the resultant joint shear strength developed by circular interaction.

Post-peak strength degradation of both north and east joint faces during the downward drift loading in specimen B-J-1-Modified is almost identical to that of specimen U-J-1. This confirms the suitability of circular shear strength interaction even for the post-peak strength degradation.

Considering the upward drift loading direction, the north joint face shear strength coefficient of specimen B-J-1-Modified is higher than that of specimen U-J-1 by 18.8%, while the corresponding value for east joint face is 28.5%. These higher values in the positive drift loading direction must be viewed in the light of the speculation of the effect higher peak tension axial load ratio (0.13) in specimen U-J-1 compared to that in specimen B-J-1-Modified (0.01). It is expected that the higher positive shear strength of the biaxially loaded specimens is partially attributed to its lower tension axial load and partially due to the conservatism of circular shear strength interaction.

The above results and the illustration and the ACI-352-02 [2] provisions depicted in blue line in Fig. 7.127 suggest that the circular interaction of orthogonal components of shear stresses can be considered an appropriate approximation to the effect of bidirectional loading on unconfined corner beam-column joints since it is slightly on the conservative side.

7.4.3.2 INTERSTORY DRIFT AND DISPLACEMENT DUCTILITY

It can be noticed from Fig. 7.125 and Table 7.5 that the north and east joint faces of specimens U-J-1 and B-J-1 generally attained their peak shear strength nearly at the same drift positive and negative peaks. This indicates that drift capacity at peak shear strength is little influenced by the biaxial loading. Moreover, the displacement ductility $\mu_{\Delta\text{-}b}$ of specimen U-J-1 is slightly higher than that of B-J-1 for NS beam loading (Table 7.6). However, the ductility for the EW beam loading for specimen B-J-1 is much smaller than that of specimen U-J-1. One should notice that the loading of both beams in specimen B-J-1 was simultaneous, which contributed to exhaust deformation capacity of both joint faces equally starting from early loading stages. However, in specimen U-J-1, NS beam and east joint face deformation capacity was exhausted more than EW beam and north joint face. Accordingly, it might be appropriate to compare ductility of NS beam loading rather than EW beam loading of specimens U-J-1 and B-J-1, which reflects minimal effect of bidirectional loading on ductility. The ductility factor of specimen B-J-1-Modified is close to that of specimen U-J-1. Another factor that might have contributed to the lower ductility in specimen B-J-1 is the vectorial resolving of uniaxial strength that led to lower initial stiffness

of B-J-1 and hence lower ductility factor. Another factor that contributed to the lower stiffness of specimen B-J-1 is the higher flexibility of the column due to the inclined neutral axis that resulted in a smaller compression zone. This is particularly apparent in the post-peak more inflated hysteresis loops of specimen B-J-1 compared to those of U-J-1.

The above discussion reveals that bidirectional loading has little effect on the drift capacity at peak shear strength. It also slightly affects the displacement ductility capacity.

Similar observations to those of downward loading direction can be applied to the upward loading direction as Tables 7.5 and 7.6 suggests.

7.4.3.3 STIFFNESS AND STIFFNESS DEGRADATION

Figures 7.125 and 7.126 can be used to assess the effect of simultaneous biaxial loading on stiffness of subassemblies. The initial stiffness of specimen B-J-1 is slightly lower than that of specimen U-J-1 in the negative loading direction of EW and NS beams. As loading proceeded towards reaching joint shear strength, the stiffness degradation under simultaneous biaxial loading was more pronounced than that under alternating uniaxial loading. The more flexible nature of the biaxially loaded specimen is evident. Factors contributed to this are the more flexible column under biaxial loading and the biaxial joint shear strength circular interaction, which reduces shear capacity under the same drift level for each individual orthogonal direction. Upon modifying the response of specimen B-J-1 to account for biaxial loading by circular shear strength interaction, it can be observed that the loading stiffness in the linear range until near reaching joint shear strength is slightly higher than that of the unidirectional specimen. The post-peak stiffness of specimens U-J-1 and B-J-1-Modified are close, with the exception of first post-peak loading cycles of EW beam, suggesting good agreement with circular shear strength interaction assumption.

The stiffness comparison in the positive drift peak EW beam loading direction suggests that circular biaxial shear interaction is more conservative than that in the negative loading direction. However, given the higher tension force in specimen U-J-1, the circular shear interaction may be as accurate as the negative loading case for the linear range. Similar observation applies for NS beam loading. However, during the NS beam positive loading, the B-J-1 and U-J-1 stiffnesses are almost identical. This can be explained that the slab torsional cracking effect on NS beam due to preloading EW beam, that reduced the stiffness and strength of former, is less significant in the case of simultaneous biaxial loading, which appeared as extra conservatism of circular shear strength interaction for NS beam positive loading direction.

The peak-to-peak effective stiffness comparison is depicted in Fig. 7.132. Specimen B-J-1 showed lower initial effective stiffness than that of U-J-1. However, the degradation rate of the former was less than that of the latter.

7.4.3.4 JOINT DEFORMATIONS

Figure 7.129 depicts joint shear strain envelopes of specimens B-J-1 and U-J-1. In the pre-cracking linear range, the joint shear strains of specimen B-J-1 were similar to those of specimen U-J-1. However, after joint cracking, the bidirectionally loaded specimen exhibits higher joint shear strains and lower shear stiffness than those of unidirectionally loaded specimens. Confirming this observation, Figure 7.131 shows slightly more intense cracking in specimen B-J-1 at the same drift level compared to specimen U-J-1. This may be attributed to the effect of bidirectional loading that strains the joint simultaneously in both directions, which reduces joint resistance to cracking in each individual direction and reduces possible confining effect of the orthogonal beam. Moreover, the smaller column compression zone under biaxial loading contributes to smaller strut depth that leads to higher strut principal compression stresses and in turn higher perpendicular principal tensile strains. However, after reaching peak joint shear strength, the joint shear strains of B-J-1 were marginally smaller than those of U-J-1 due to the effect of post-peak axial load deterioration in specimen U-J-1 that led to more joint flexibility. In general, the shear strains of both specimens were close indicating slight effect of loading history on joint deformation characteristics. The same behavior can be also seen in Fig. 7.130 depicting the joint deformation contribution to overall drift of the subassembly.

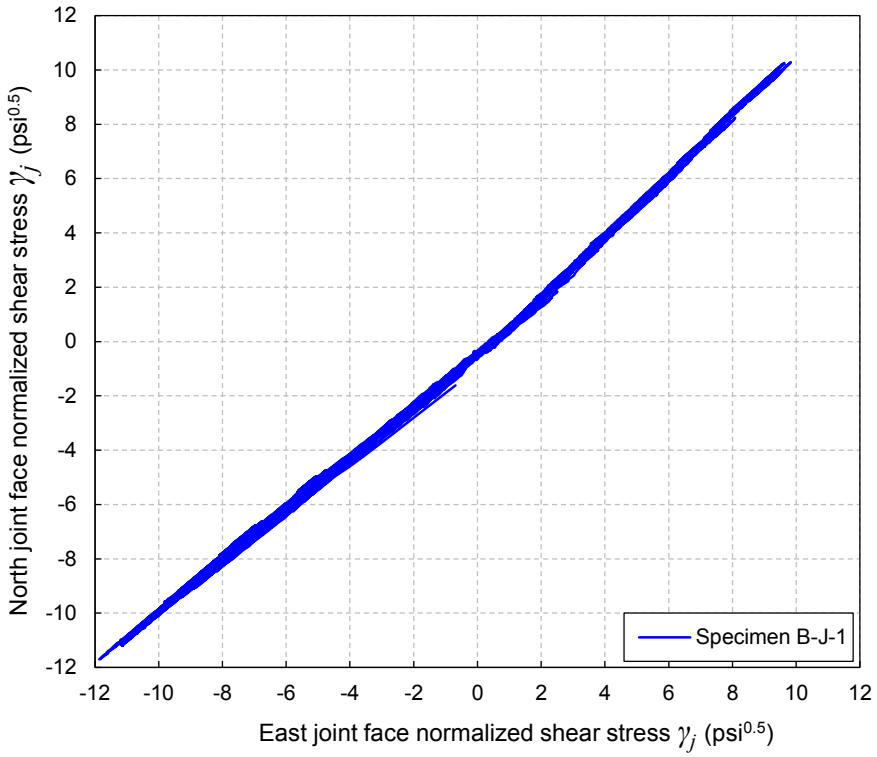

Figure 7.122 Experimental joint shear stresses in specimen B-J-1

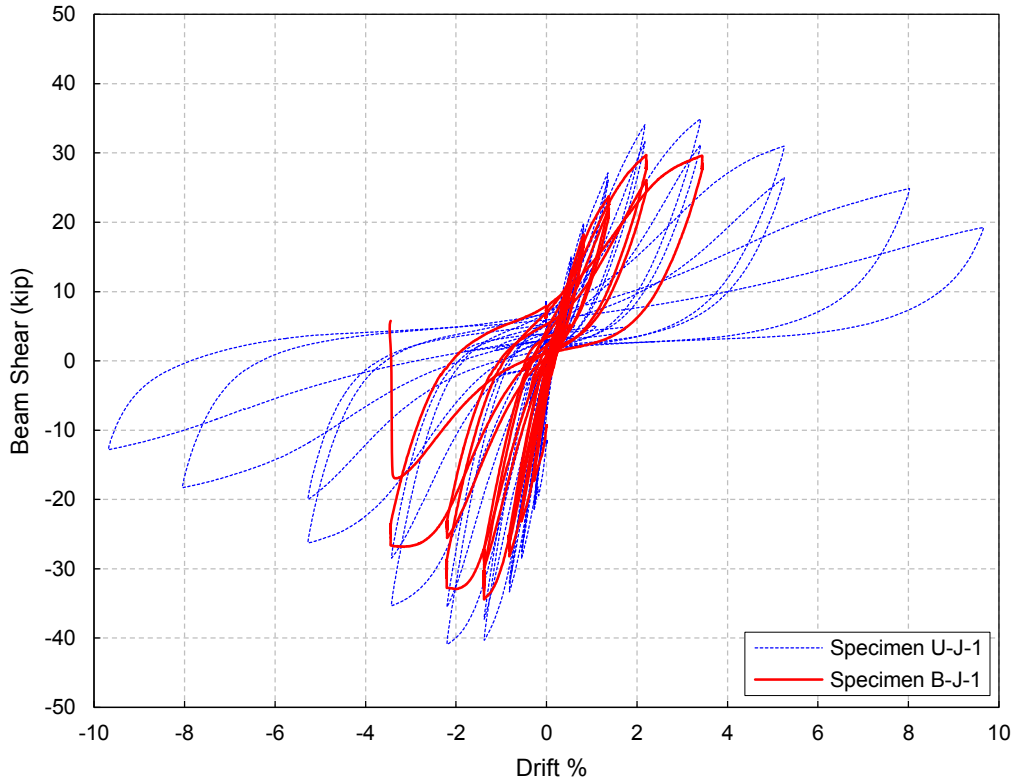

Figure 7.123 Effect of loading history on load-drift response of EW-beam for J-Failure specimens

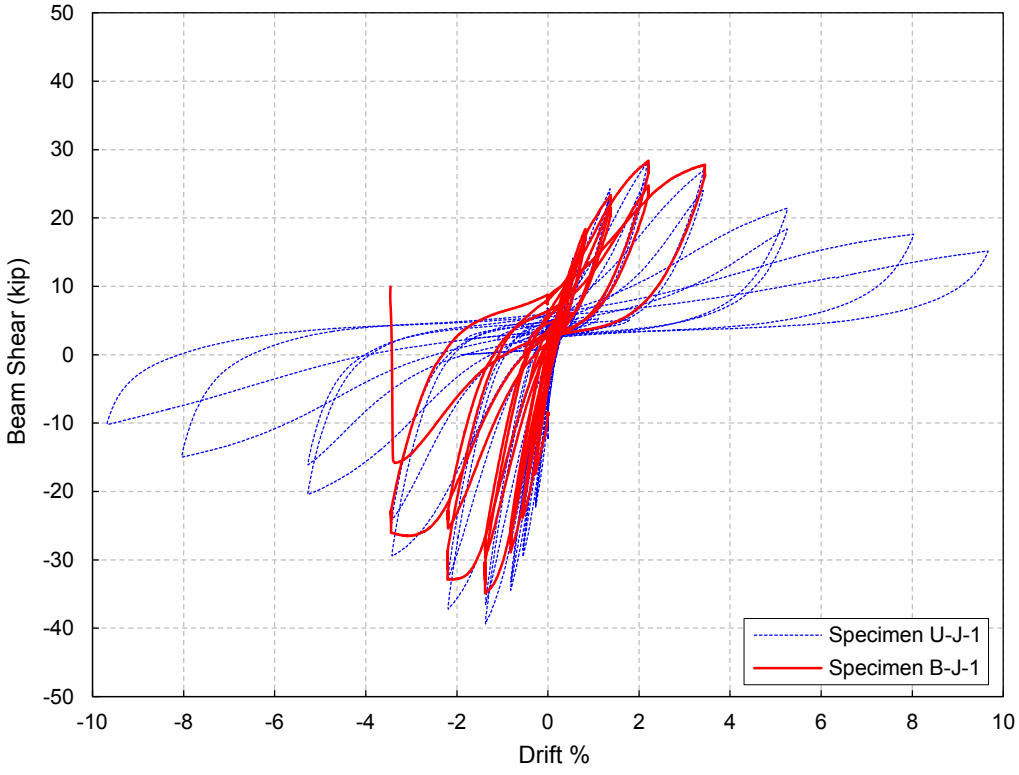

Figure 7.124 Effect of loading history on load-drift response of NS-beam for J-Failure specimens

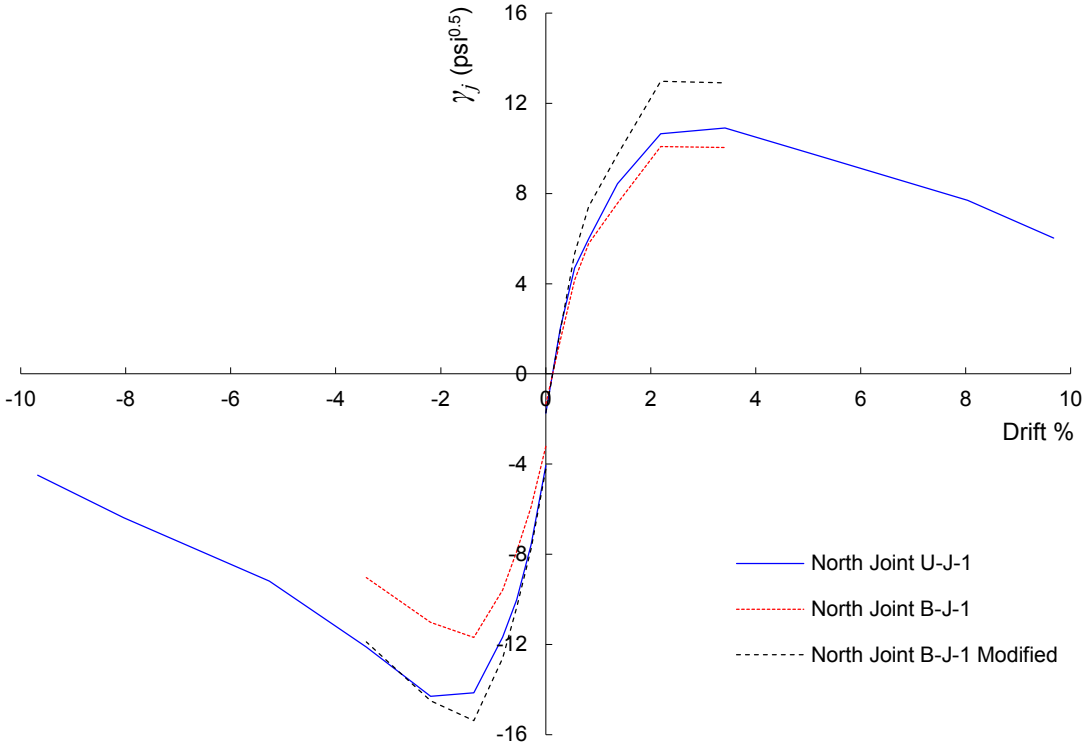

Figure 7.125 Effect of loading history on backbone curves for J-Failure specimens

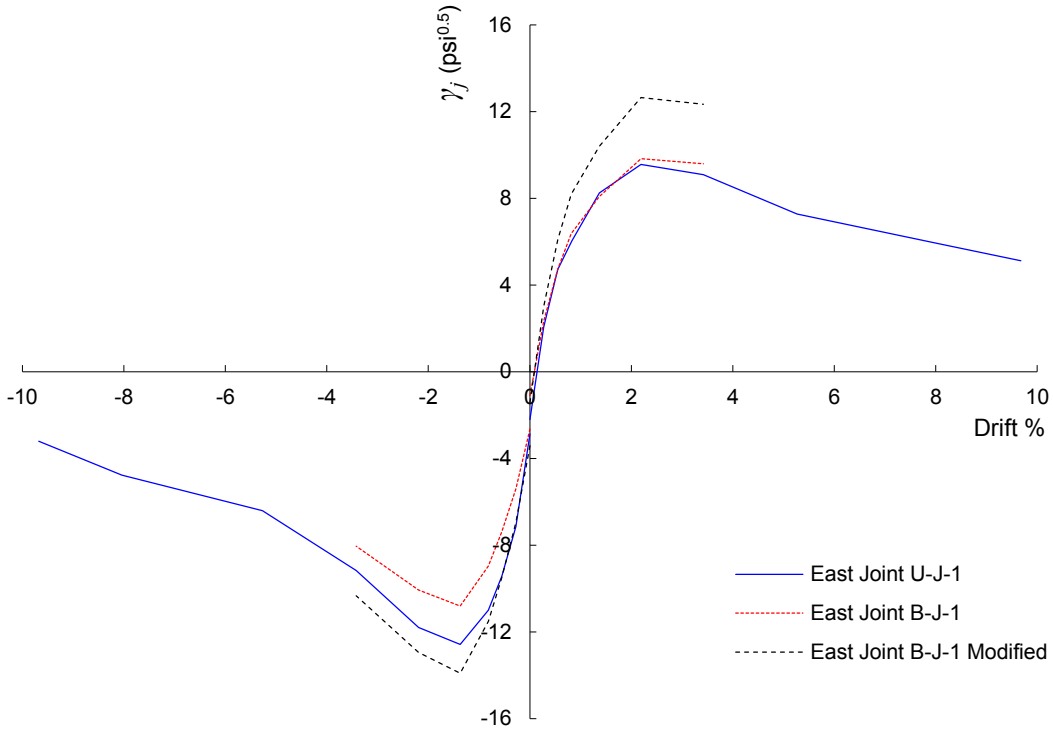

Figure 7.126 Effect of loading history on backbone curves for J-Failure specimens

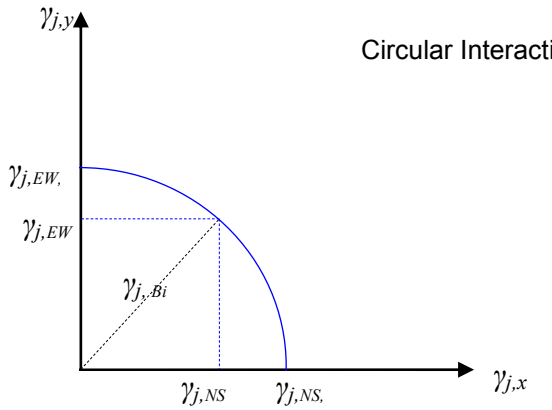

Figure 7.127 Biaxial loading shear strength interaction for unconfined

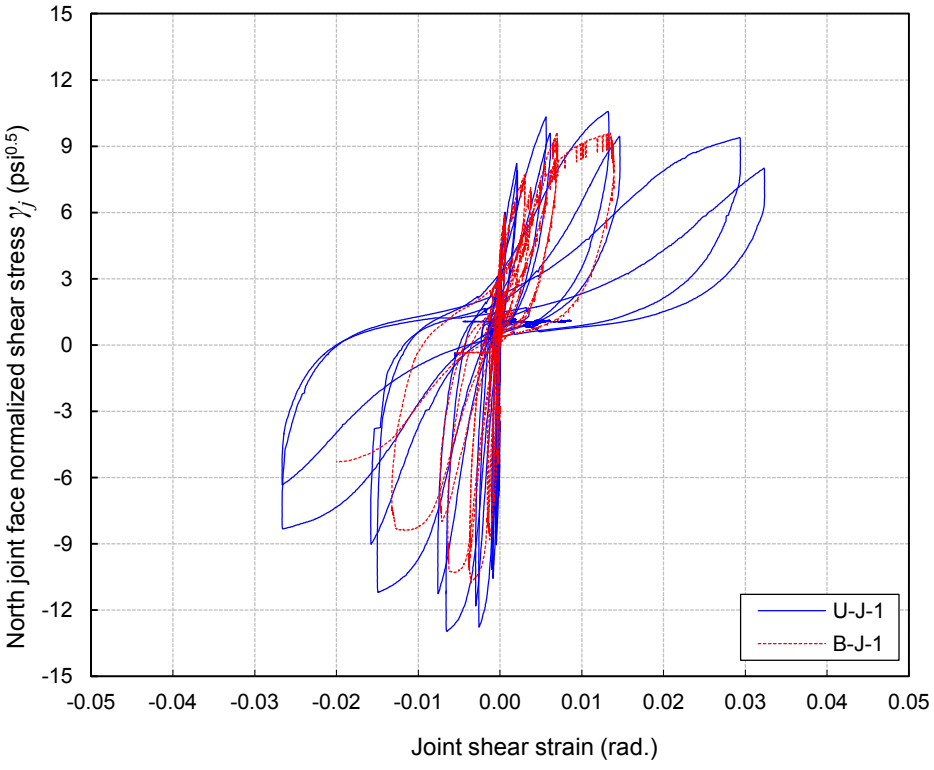

Figure 7.128 Effect of loading history on joint shear stress-strain relations for J-Failure specimens

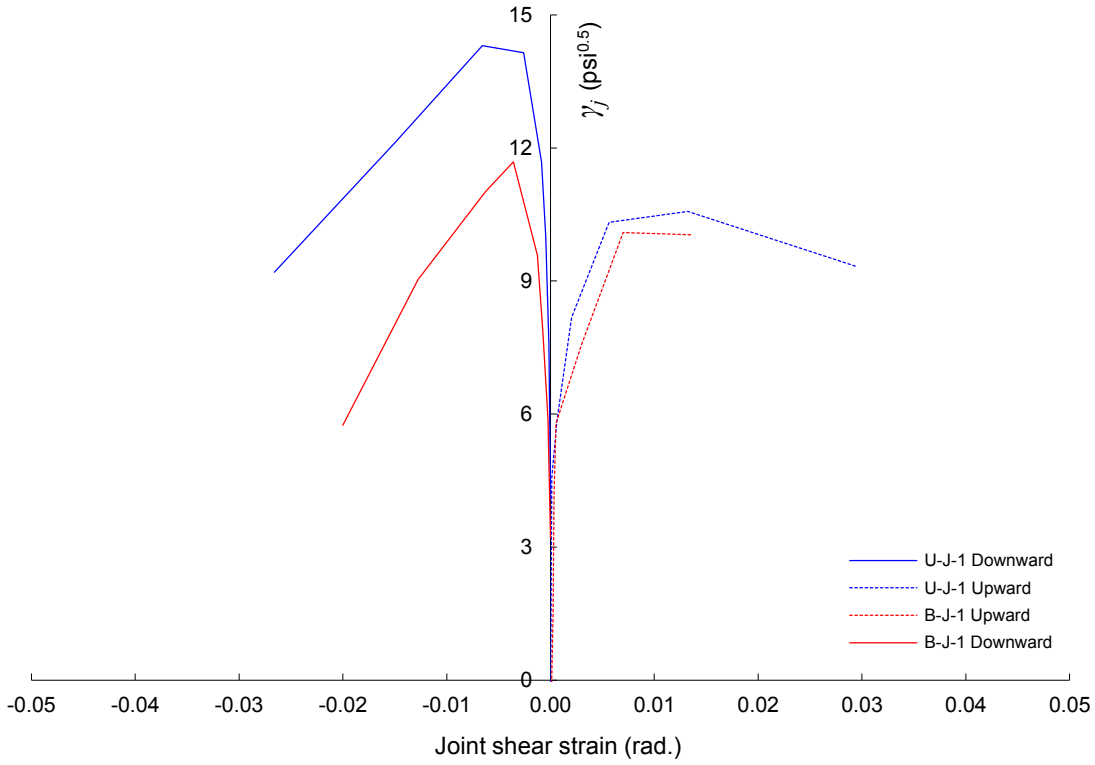

Figure 7.129 Effect of loading history on north joint face shear stress-strain envelope for J-Failure specimens

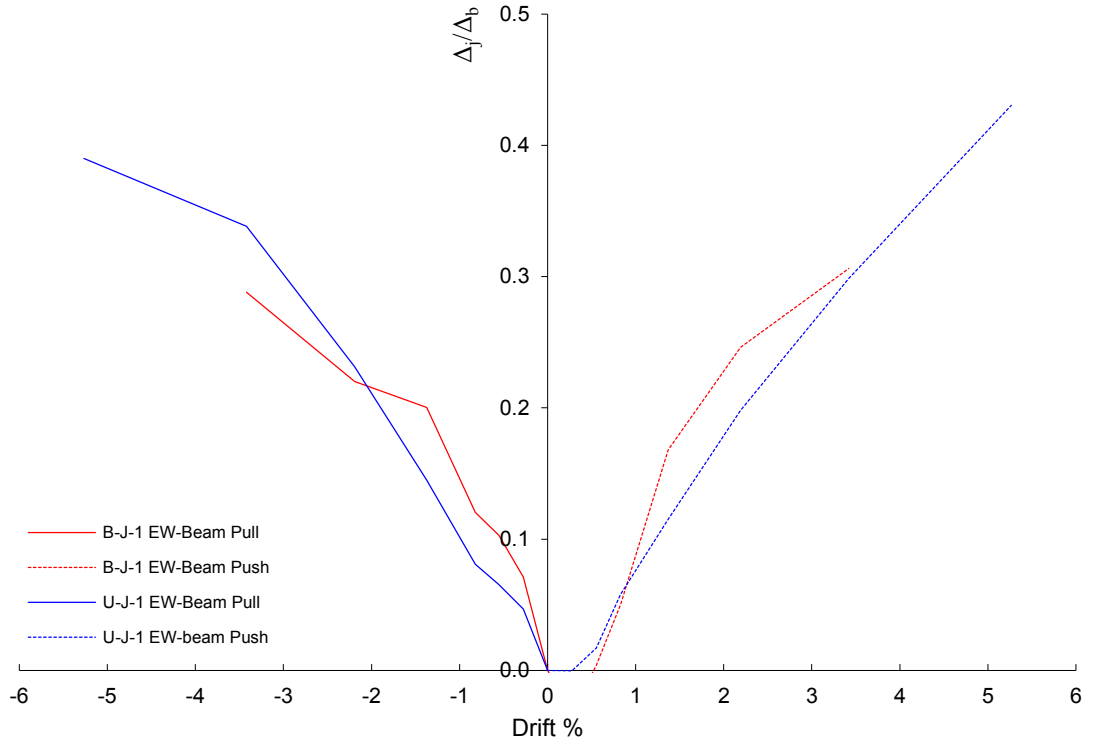

Figure 7.130 Effect of loading history on joint shear deformation contribution for J-Failure specimens

U-J-1 (-2.19%) Drift

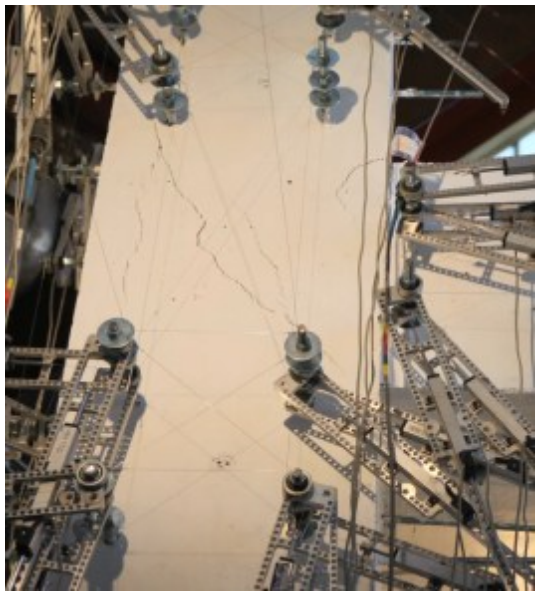

U-J-1 (2.19%) Drift

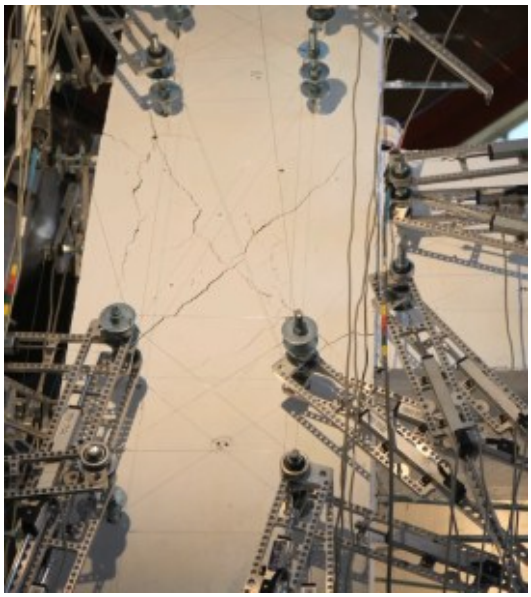

B-J-1 (-2.19%) Drift

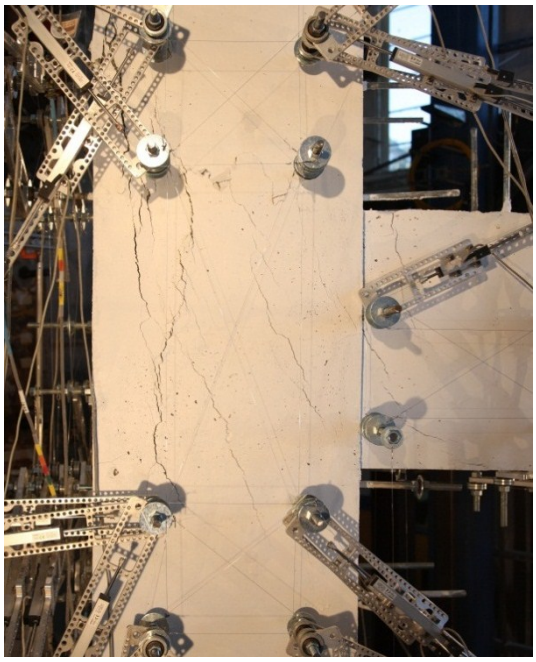

B-J-1 (2.19%) Drift

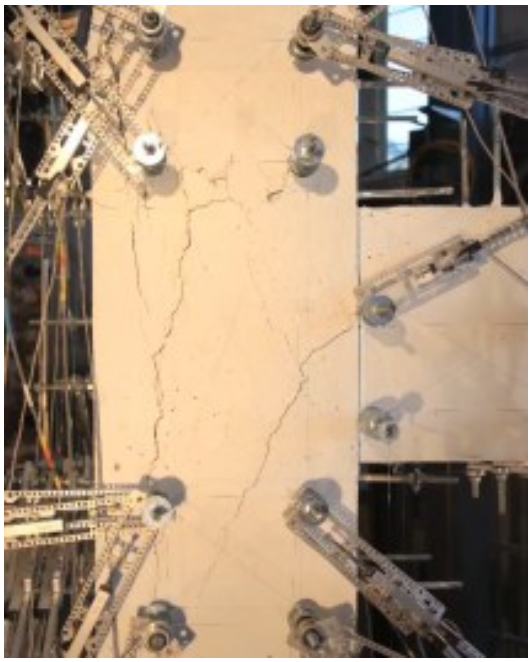

Figure 7.131 Effect of loading history on north joint face cracking for J-Failure specimens

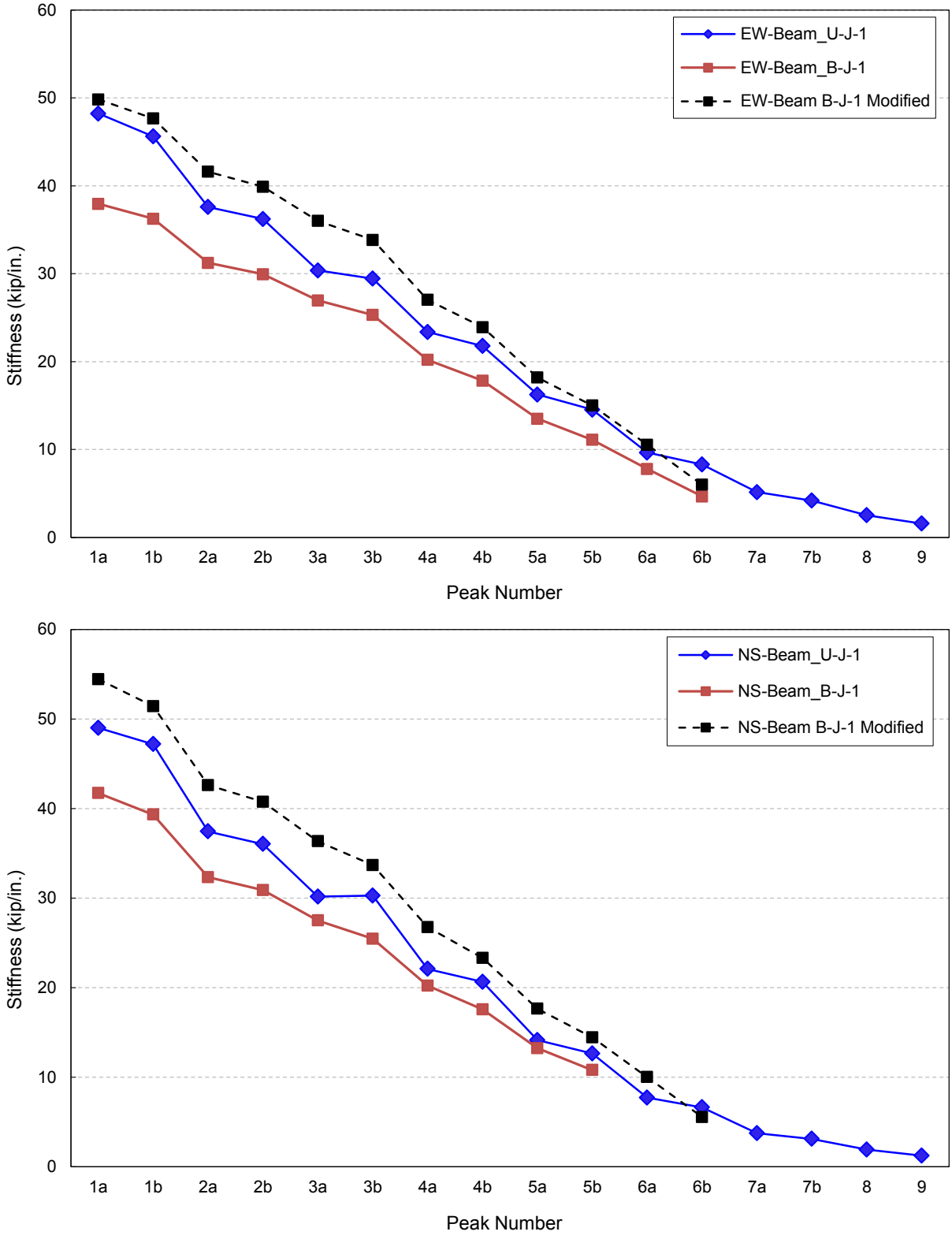

Figure 7.132 Effect of joint aspect ratio on peak-to-peak stiffness degradation for J-Failure specimens

7.4.4 Effect of Beam Reinforcement Ratio

The effect of beam reinforcement ratio on the performance and mode of failure of unconfined corner beam-column joints is investigated through comparing the performance of specimen U-J-1 with that of specimen U-BJ-1. Specimen U-J-1 experienced J-Failure mode while specimen U-BJ-1 experienced BJ-Failure mode.

7.4.4.1 JOINT SHEAR STRENGTH

Figures 7.133 through 7.134 show the hysteresis loops and envelope curves for specimens U-J-1 and U-BJ-1. The axial load ratio at peak negative joint shear strength of specimen U-J-1 was 0.31 while that of U-BJ-1 was 0.50. The maximum axial tension load ratio of 0.05 was reached at positive joint shear strength in specimen U-BJ-1, while the corresponding ratio in specimen U-J-1 was 0.08.

The joint shear strength coefficient of north joint face during EW beam downward loading was 14.3 and 8.20 (including strain hardening effect) for specimens U-J-1 and U-BJ-1, respectively. The joint shear stress coefficient corresponding to first theoretical beam yield (not accounting for strain hardening) in both specimens was 16 and 5.9, respectively. The actual yield of beam reinforcement in specimen U-BJ-1 was at joint shear strength coefficient of 7.06. The maximum joint shear strength coefficient reached in specimen U-BJ-1 was 16% higher than that at actual beam yield. This enhancement is due to strain hardening effect as discussed earlier. There is no evidence that the high axial load in specimen U-BJ-1 resulted in shear strength enhancement as presented in Section 7.4.1. The beam flexural capacity was not triggered in specimen U-J-1 since the joint failed in shear before reaching the joint shear stress corresponding to beam flexural capacity. Similar results can be drawn for east joint face shear strength during the NS beam downward loading.

The joint shear strength coefficient of north joint face during EW beam upward loading was 10.9 and 7.51 (including strain hardening effect) for specimens U-J-1 and U-BJ-1, respectively. The joint shear stress coefficient corresponding to first theoretical beam yield (not accounting for strain hardening) in both specimens was 11.1 and 4.9, respectively. The actual yield of beam reinforcement in specimen U-BJ-1 was at joint shear stress coefficient of 6.32. The maximum joint shear strength coefficient reached in specimen U-BJ-1 was 18% higher than that at actual beam yield, which is primarily attributed to strain hardening effect. The joint shear strength of north joint face during upward loading EW beam of specimen U-J-1 was reached at the onset of beam first yield. Similar observations can be stated for east joint face during NS beam upward loading in both specimens, except that the NS beam first yield occurred after reaching joint shear strength.

The above discussion confirms that the joint shear capacity cannot exceed beam flexural strain hardening capacity. In other words, joint shear strength is essentially equal to beam flexural strain hardening capacity up to the threshold limit of J-Failure direct shear strength of the joint obtained using the strut-and-tie model suggested in Chapter 5.

The post-peak profile of yielding beam specimens U-BJ-1 is distinctively different from that of J-Failure specimen U-J-1. The long strain hardening flat plateau of yielding beam specimen is characteristic. As discussed earlier, this flat plateau is more evident with high axial loads. This profile contrasts with the degrading post-peak profile in J-Failure specimens, whose degradation can be a function of many parameters including the high axial load effect. Recalling the conceptual representation of the difference between J-Failure and BJ-Failure depicted in Fig. 2.1 and confirmed by the experimental results in Figs. 7.135 and 7.136, the effect of beam reinforcement can be visualized.

7.4.4.2 INTERSTORY DRIFT AND DISPLACEMENT DUCTILITY

It can be noticed from Fig. 7.135 and Table 7.5 that the north joint face of specimens U-J-1 and U-BJ-1 attained peak shear strength (including strain hardening effect) nearly at the same negative drift level. However, the north joint face of specimen U-BJ-1 attained peak shear strength at 61% higher drift than that of specimen U-J-1 in the upward loading direction. For the east joint face, peak joint shear strength of specimen U-BJ-1 was reached at a 67% and 63% higher drifts than those of specimen U-J-1 for the downward loading and upward loading, respectively. As can be seen in Fig. 7.135, significant degradation started immediately after reaching joint shear strength in specimen U-J-1 as opposed to no degradation or very slight degradation in specimen U-BJ-1. These observations emphasize the more ductile nature of BJ-Failure mode compared to J-Failure mode.

The displacement ductility factor $\mu_{\Delta\text{-}b}$ of specimen U-BJ-1 was 6.45 and 8.18 for EW and NS beam downward loading, respectively. This ductility factor for upward loading was 3.06 and 3.7 for EW and NS beam loading, respectively. The average $\mu_{\Delta\text{-}b}$ of specimen SP1 for Phase I was 3.71 for downward loading direction. It is believed that the much higher displacement ductility factor in the downward loading of specimen U-BJ-1 compared to SP1 is due to the substantially higher axial load in the former. The average displacement ductility factor $\mu_{\Delta\text{-}b}$ of specimen U-J-1 was 4.1. Thus, it is reasonable to note that the difference in beam reinforcement ratio between specimen U-J-1 and SP1 did not result in a notable change in ductility factor since the axial loads were low to moderate. In addition, the difference of beam reinforcement ratio in specimen U-J-1 and U-BJ-1, along with higher axial load in the latter specimen, resulted in approximately twice as much ductility as of the former.

The displacement ductility factor $\mu_{\Delta\text{-}b}$ of specimen U-BJ-1 is marginally higher than that of specimen U-J-1 for both EW and NS beam loading.

7.4.4.3 STIFFNESS AND LOAD-DRIFT RESPONSE

Figures 7.135 and 7.136 can be used to assess the effect of beam reinforcement ratio on the stiffness of subassemblies. The initial stiffness of specimen U-J-1 is significantly higher than that of specimen U-BJ-1 for both EW and NS beams. This is expected due to the more flexible beam in the latter specimen. The effective peak-to-peak stiffness degradation between different drift ratios is more significant in specimen U-J-1 was J-Failure mode. The peak-to-peak stiffness degradation (Fig. 7.139) within the same drift ratio in both specimens are similar until reaching joint shear capacity of specimen U-J-1, after which this stiffness degrades much faster than that

of specimen U-BJ-1 due to the significant joint cracking and pinching in U-J-1 as opposed to a ductile response with most nonlinearity is concentrated in flexural yielding in specimen U-BJ-1. At later stages of loading, after 5% drift, the effective stiffness of U-J-1 approaches that of specimen U-BJ-1 and then they degrade in a very similar fashion until axial failure. This similarity in the later stages is due to the full yield penetration of the joint in specimen U-BJ-1 at that stage that triggered the shear failure and joint shear distress and severe degradation which was similar to the J-Failure joint degradation in specimen U-J-1.

The characteristic difference between hysteresis loops of specimen U-J-1 and U-BJ-1 in Fig. 7.133 and Fig. 7.134 is evident. The hysteresis loops of specimen U-BJ-1 in the vicinity of peak shear strength are wider and flatter due to the beam flexural hardening, compared to sharper and narrower loops of specimen U-J-1 that experienced J-Failure. However, in the post-peak cycles of specimen U-J-1, the pinching effect started to appear due to joint distress and crack widening, which made these loops similar to those at later stages of loading of specimen U-BJ-1 when the joint distress effect became obvious. Another important observation is that the unloading response of specimen U-J-1 in the from the peak negative drifts is highly pinched at later stages of loading compared to that of specimen U-BJ-1 which is consistent with the more severe damage observed during the test in the joint of the former specimen.

7.4.4.4 JOINT SHEAR DEFORMATIONS

The joint shear stress-strain backbone curves shown in Fig. 7.138 indicate similarity between the two specimens in the upward loading direction, which reflects the early cracking and degradation of the joint under tensile loading. However, the backbone curves are distinctly different under axial compression. It can be observed that in specimen U-BJ-1 the stress-strain relation reflects very high shear rigidity before reaching peak shear strength. This represents the fact that the behavior is primarily controlled by beam yielding not by joint distress, accompanied by high axial loads on the joint which delayed the yield penetration that triggers joint distress and degradation. This behavior is absent in specimen U-J-1 where the main degradation mechanism is joint cracking and distress. The shear strain at which significant degradation started in specimen U-J-1 downward loading was about twice that of specimen U-BJ-1. This reflects the fact that specimen U-J-1 failed in J-Failure mode and hence there was no yield penetration inside the joint to accelerate joint degradation.

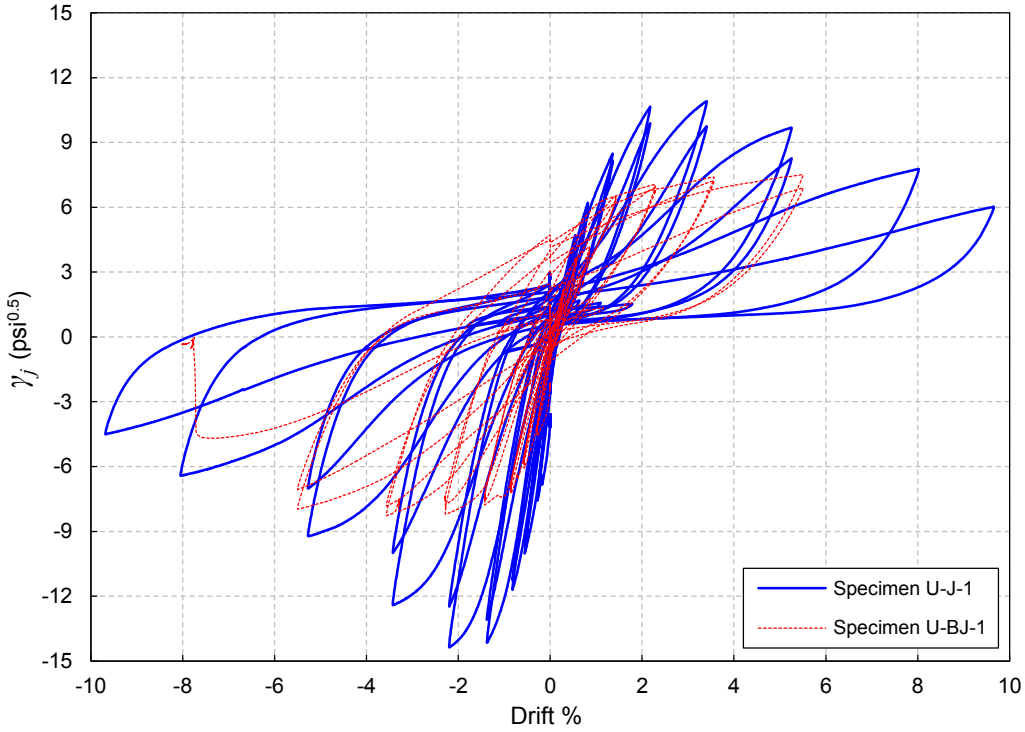

Figure 7.133 Effect of beam reinforcement ratio on load-drift response of EW-beam

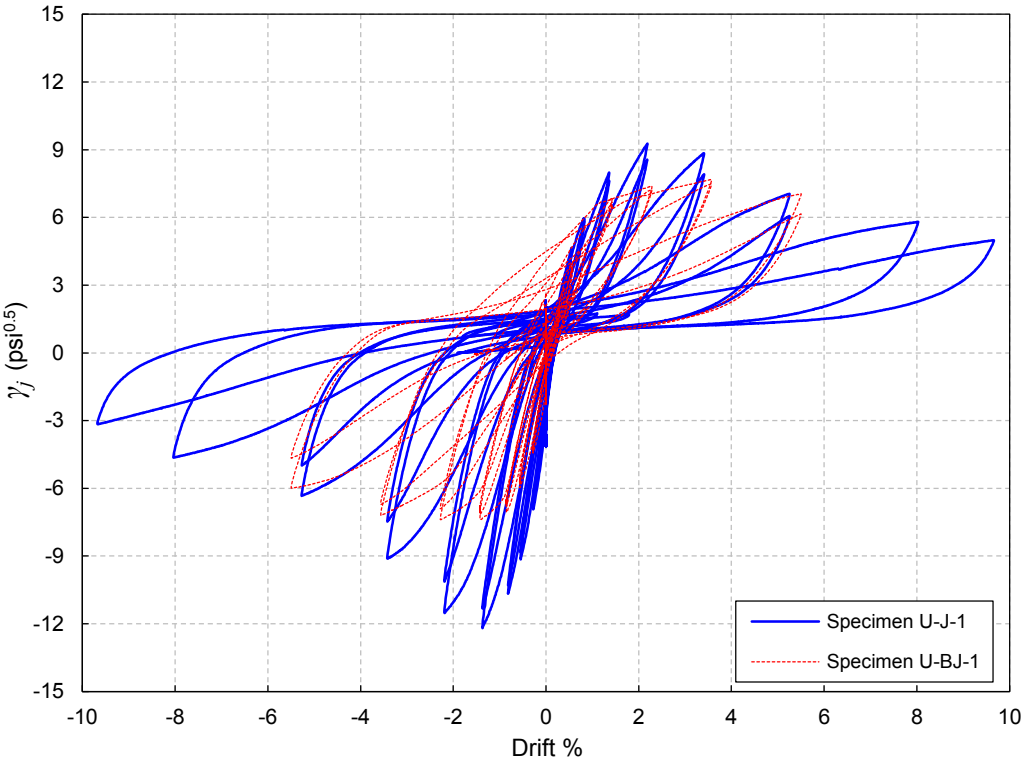

Figure 7.134 Effect of beam reinforcement ratio on load-drift response of NS-beam

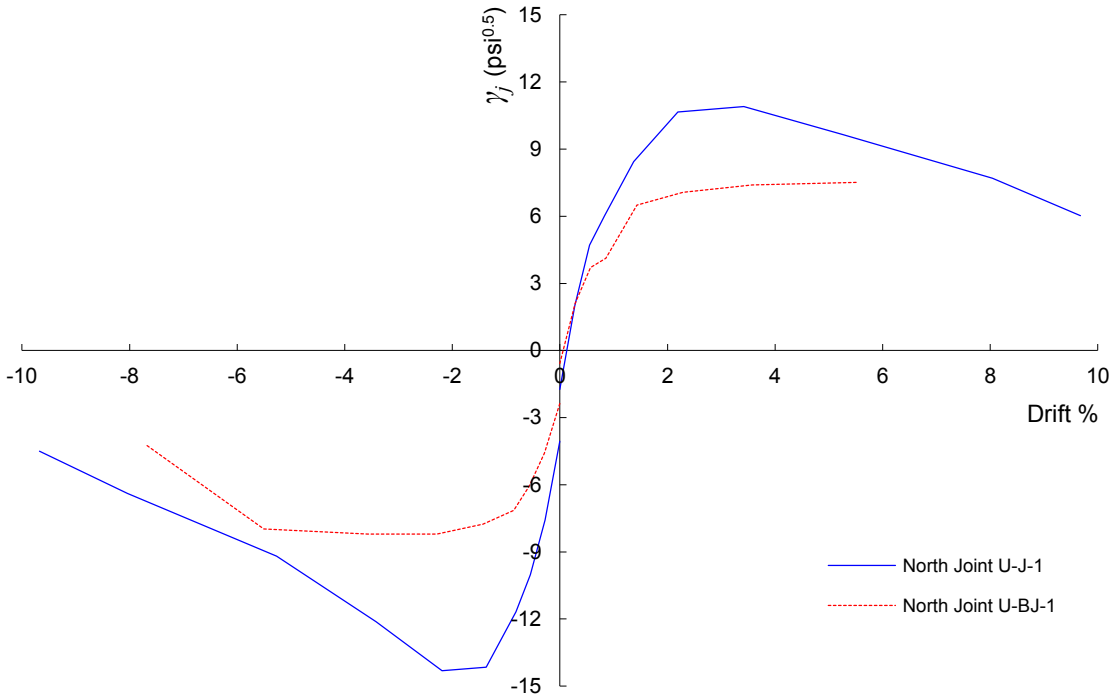

Figure 7.135 Effect of failure mode on backbone curves

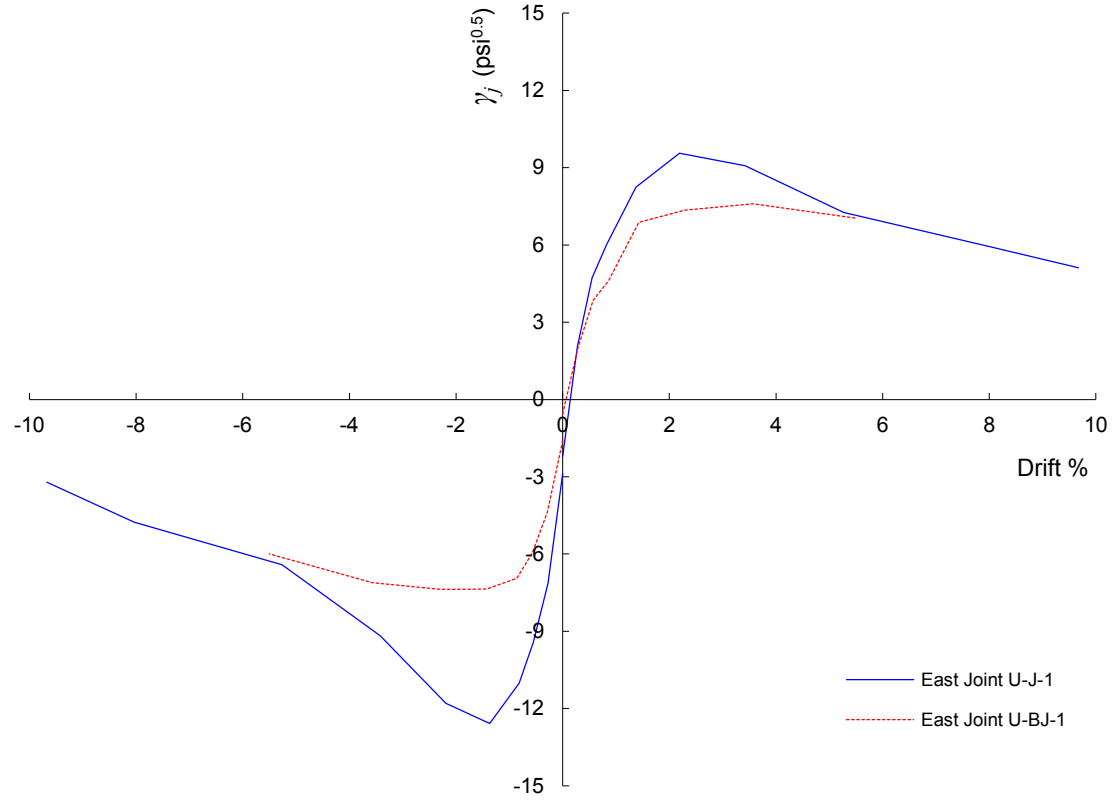

Figure 7.136 Effect of failure mode on backbone curves

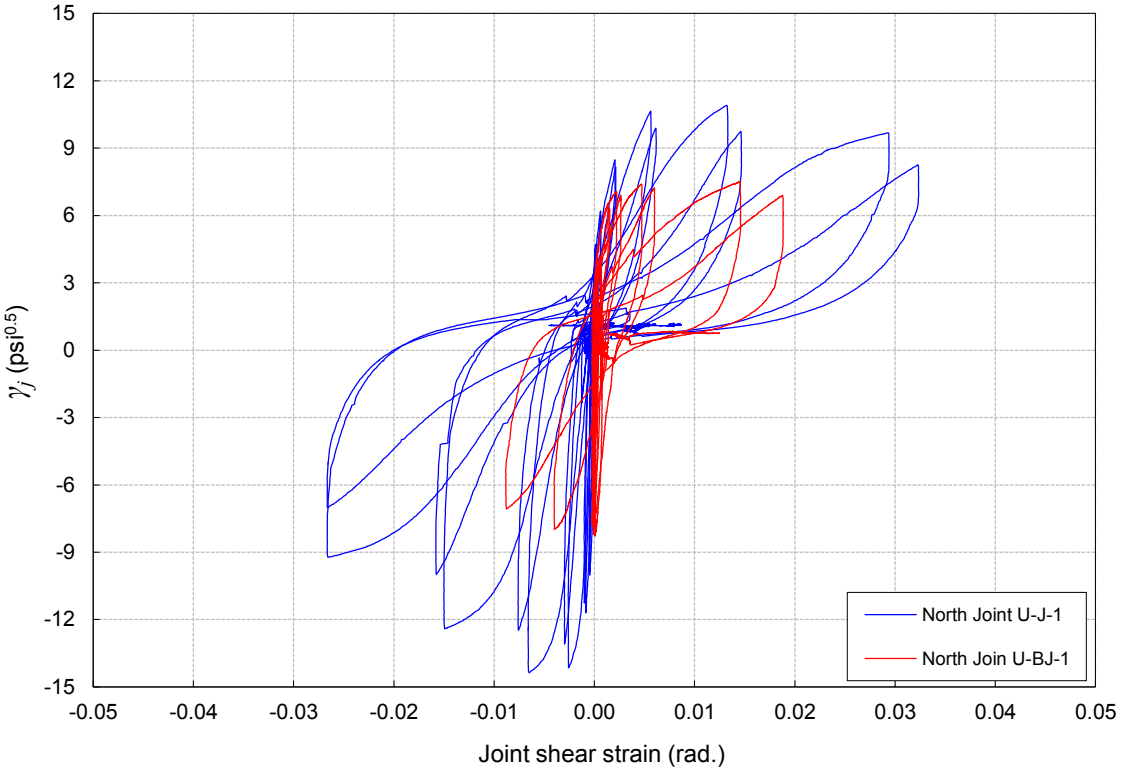

Figure 7.137 Effect of beam reinforcement ratio on joint shear stress-strain hysteresis

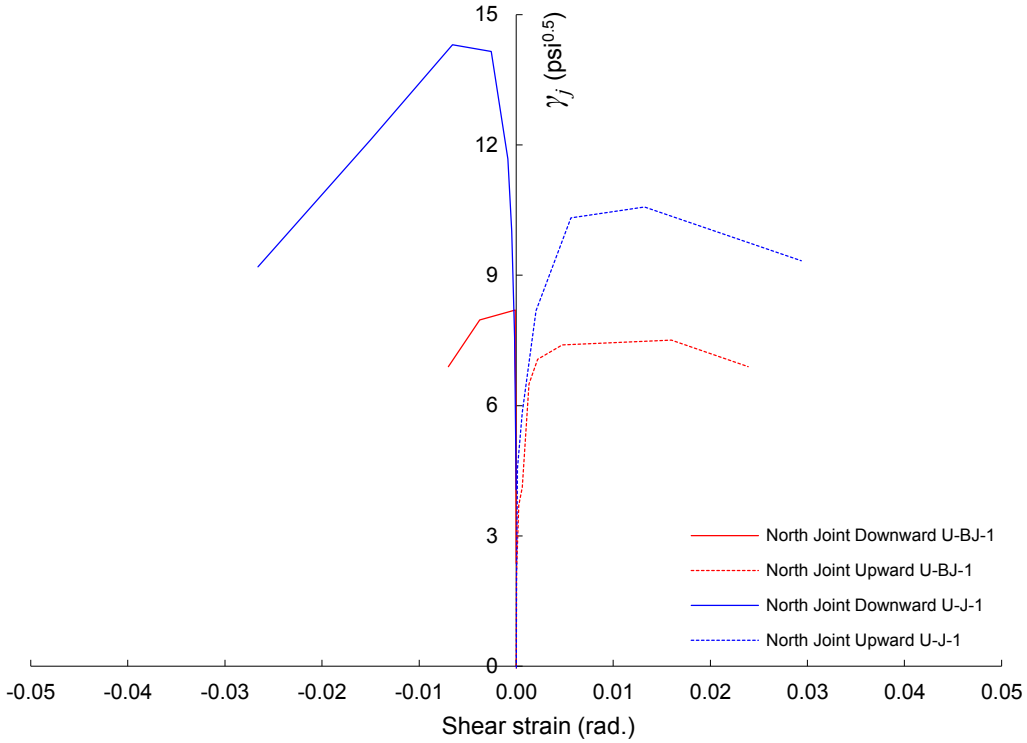

Figure 7.138 Effect of beam reinforcement ratio on joint shear stress-strain envelopes

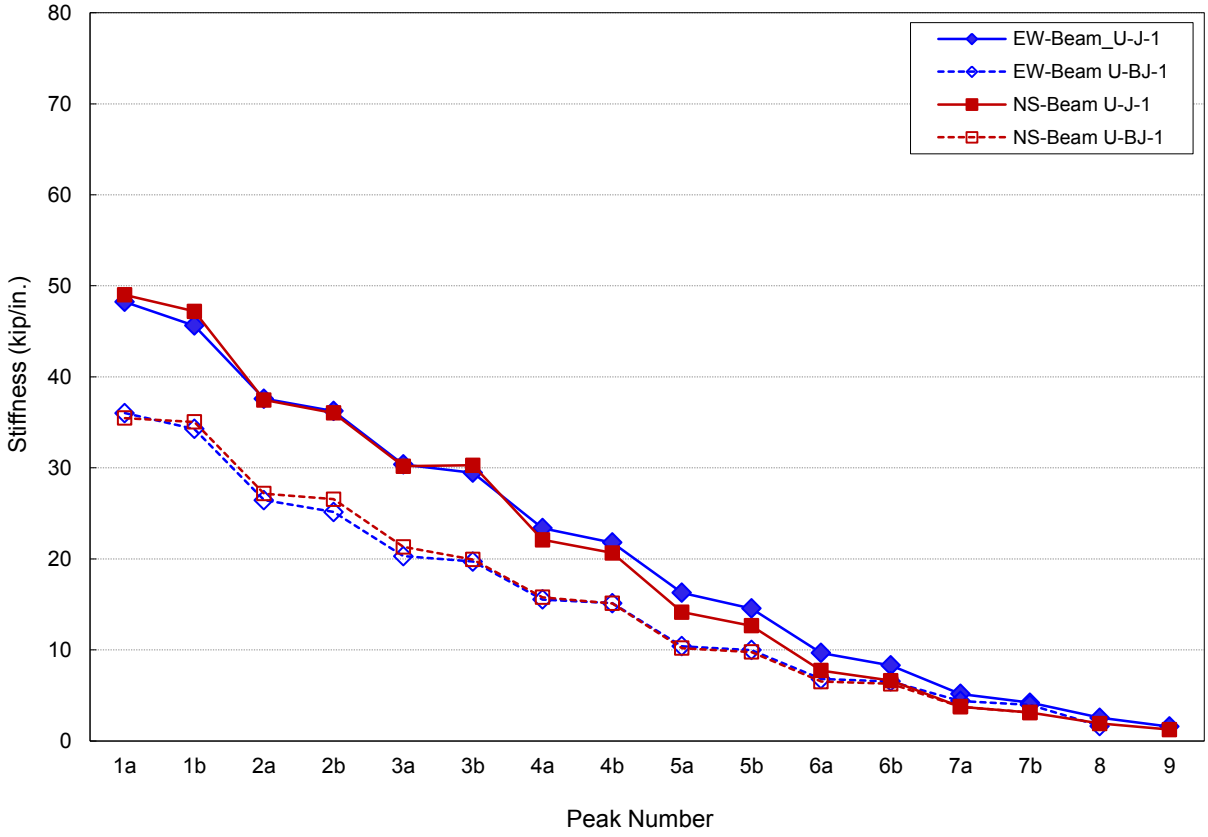

Figure 7.139 Effect of failure mode on peak-to-peak stiffness degradation

7.4.5 Effect of Concrete Slab

The effect of the presence of concrete slab on the behavior of test specimens can be discussed through investigating two aspects. The first aspect is the slab reinforcement contribution in tension to the joint shear stress demand during the downward loading cycle, which can be expressed in terms of effective slab width. This can be investigated by inspecting beam and slab steel strains and strain distribution at the drift peak corresponding to joint shear strength. The second aspect is the torsional cracking and twisting deformation exerted due to the restraining effect of the slab.

7.4.5.1 EFFECTIVE SLAB WIDTH

The slab reinforcement strain distribution was presented in Section 7.4.3. Table 7.5 shows the number of slab bars that yielded prior to reaching joint shear strength for different test specimens. It is worth mentioning that in even J-Failure specimen, U-J-1, U-J-2 and B-J-1, first one or two top slab bars adjacent to the loaded beam reached yielding strain immediately prior to reaching joint shear capacity although beams did not reach yield strain at that point. This might be attributed to the location of top slab bars which is further away from beam neutral axis towards extreme tension fiber since their concrete cover was ¾ inches compared to 1.875 inches of cover for beam reinforcement.

Ideally, to estimate slab effective width that possibly contributed to the joint shear stress demand at joint shear capacity, that requires the total force across the slab entire width be calculated and then the width that would produce the same total force if acting at strain equal to the strain of the beam longitudinal reinforcement is determined. However, using this approach requires strain instrumentation for all slab reinforcement which was not available in this study.

Accordingly, it was decided to use alternative calculation based on the available slab steel strains only. As mentioned in Chapter 6, the four top slab steel bars and the first three bottom steel bars were gauged. This alternative calculation method is based on comparing the peak tension force observed during the test $T_{b,test}$, based on peak shear force, with beam tension force $T_{b,calc}$ calculated using measured beam reinforcement strains at peak joint shear strength combined with slab tension force $T_{s,calc}$ for the available instrumented bars based on strain results .Due to the twisting effect, it was decided to consider only EW beam loading to estimate effective slab width. Table 7.7 shows the calculated and measured tension forces for test specimens. Although bottom slab reinforcement was suspected to have a small contribution to shear stress demand due to its poor anchorage, its tensile forces are also included in the calculations. Since only three bottom bars were instrumented, a linear strain extrapolation to determine the forth bottom bar strain was assumed.

It can observed from Table 7.7 that the contribution of the first four slab top and bottom bars for specimens U-J-2 and B-J-1 can be considered appropriate to represent the slab contribution to joint shear stress demand. This implies an effective width of b_b+2h_{bt}. However, the tension force comparison for specimen U-J-1 indicates that the slab contribution is beyond the first four bars adjacent to the beam. However, no definitive conclusion can be made about the effective slab

width in the case due to lack of strain data. If the linear extrapolation assumption holds, an effective slab width of $b_b+2.75h_{bt}$ may be suggested for specimen U-J-1.

For the BJ-Failure specimen U-BJ-1, slab top reinforcement yielded at the same drift peak the beam yielding. As Table 7.7 shows, the tension force equilibrium was achieved with the contribution of only the first two top and bottom slab bars, which implies an effective slab width of b_b+h_{bt} . The reason the slab contribution is less significant in the case of BJ-Failure compared to J-Failure specimens is the high beam reinforcement strains in the former case due to beam yielding.

The above discussion indicates that the assumed effective width in Chapter 6, b_b+h_{bt} , is appropriate only for BJ-Failure and a larger width of b_b+2h_{bt} can be considered a minimum value for J-Failure.

Table 7.7.a Slab contribution to joint shear stress demand (bottom slab bar considered)

Specimen	$T_{b,test}$ (kip)	$T_{b,calc}$ (kip)	Number of slab bars considered		$T_{s,calc}$ (kip)	$T_{calc,total}$ (kip)	$T_{b,test}/T_{calc,total}$	Min. B_{eff} (in.)
			Top	Bottom				
U-J-1	316	67	4	4	157	224	1.41	50
U-J-2	243	145	4	4	110	255	0.95	38
B-J-1	255	89.6	4	4	164	254	1.00	38
U-BJ-1	185	145	2	2	47.6	192	0.96	20

Table 7.7.b Slab contribution to joint shear stress demand (bottom slab bar excluded)

Specimen	$T_{b,test}$ (kip)	$T_{b,calc}$ (kip)	Number of slab bars considered		$T_{s,calc}$ (kip)	$T_{calc,total}$ (kip)	$T_{b,test}/T_{calc,total}$	Min. B_{eff} (in.)
			Top	Bottom				
U-J-1	316	67	4	0	127.0	194.0	1.63	50
U-J-2	243	145	4	0	60.7	206.0	1.18	38
B-J-1	255	89.6	4	0	85.2	175.0	1.45	38
U-BJ-1	185	145	2	0	35.3	180.0	1.03	20

7.4.5.2 TWISTING EFFECT

The alternating uniaxial loading protocol used to test specimens U-J-1, U-J-2 and U-BJ-1 comprised loading one beam while holding the other beam in the undeformed position. In the presence of concrete slab that is monolithically cast with beams and connected to them with hooked reinforcement, the held-at-rest beam and its tributary width of the slab restrain the motion of the loaded beam through beam torsional rigidity and slab flexural rigidity. Since the loaded beam is displacement controlled, this in turn will result in longitudinal cracking in the slab parallel to the unloaded beam, especially at the beam-slab interface, to accommodate the increasing displacement. It will also result in helical torsional cracking in the unloaded beam resulted from twisting moment due to the absence of slab continuity on both sides of the unloaded beam. This type of torsion is a compatibility torsion that is similar to the case in flat plate edge beam. This effect is also present to a lesser extent in the bidirectionally loaded specimen due the slab rigidity and the rigidity exerted by the column and beam intersection at the interior column apex.

Figure 7.140 displays the torsional cracking of NS beam of specimen U-BJ-1 during the EW beam downward loading. The blue lines refer to NS beam torsional cracking and slab cracking during the EW beam downward loading, while the red lines refer to EW beam torsional cracking during NS beam downward loading. The beam region in the vicinity of the column is particularly cracked in torsion since it represents the support vicinity. The torsional curved crack at the top beam surface forms a nearly quarter circle whose diameter is about the same beam width. Figure 7.144 shows the twist angle profile along the NS beam during EW beam loading, while Fig. 7.145 shows the twist angle profile along the EW beam during NS beam loading. A nearly horizontal crack, shown in dashed blue line in Fig. 7.140, developed at the east joint face when the EW beam was loaded. This crack was hypothesized by Park [120] to be a torsional crack exerted from twisting of NS beam during EW beam loading. However, since the upper column outer surface is in flexural tension at the same instance, this crack might be also a result for this tensile force that might have cracked a weakened joint section due to excessive joint shear stress.

Besides torsional cracking of the unloaded beam during loading the other beam, the loaded beam itself experience twisting deformation due to the restraining effect the slab and the unloaded beam provide. Figure 7.143 shows the torsional angle at the EW beam tip displacement at large EW beam downward drift. The crack pattern of top and bottom surfaces of slab and beams of specimen U-BJ-1 is shown in Fig. 7.141. The beam flexural cracks are evident.

Figure 7.140 Torsional cracking in specimen U-BJ-1

Figure 7.141 Crack pattern of slab in specimen U-BJ-1

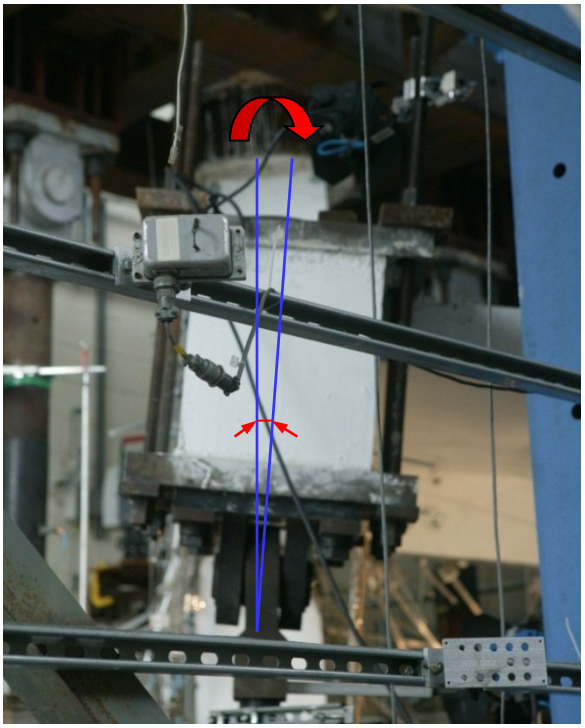

Figure 7.142 Twisting angle of EW beam during its downward loading

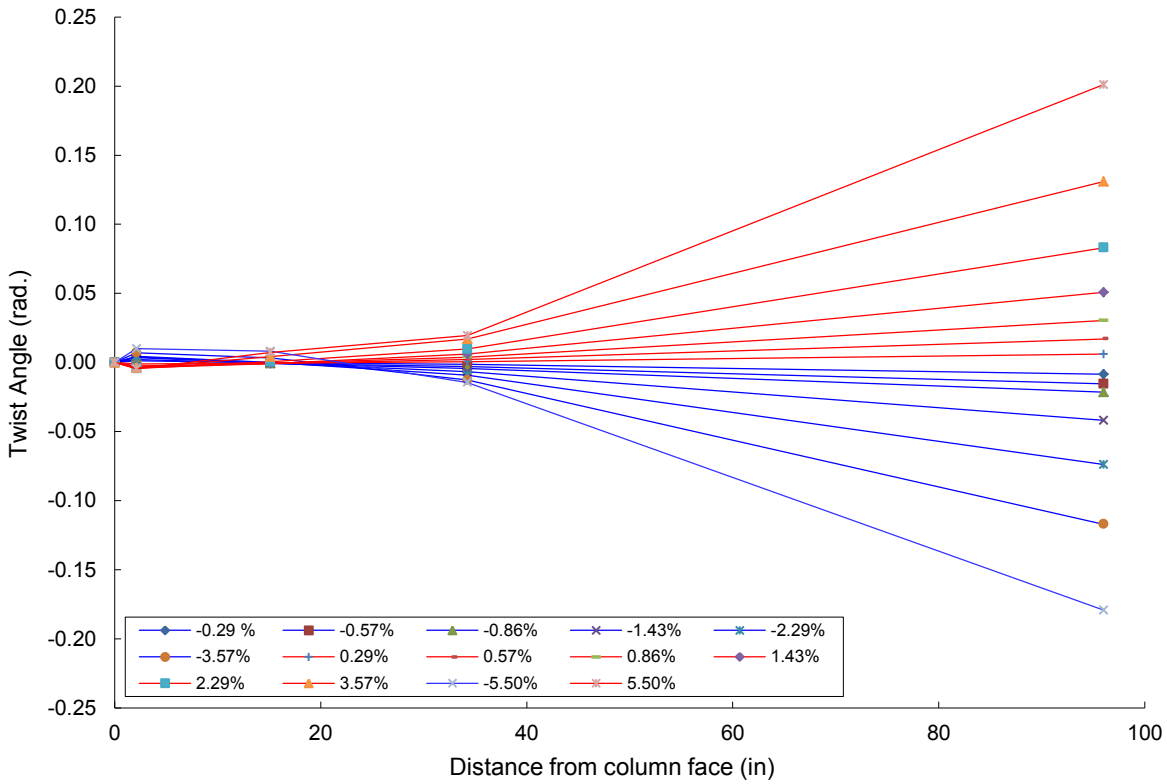

Figure 7.143 Twisting angle profile along EW beam during its loading in specimen U-BJ-1

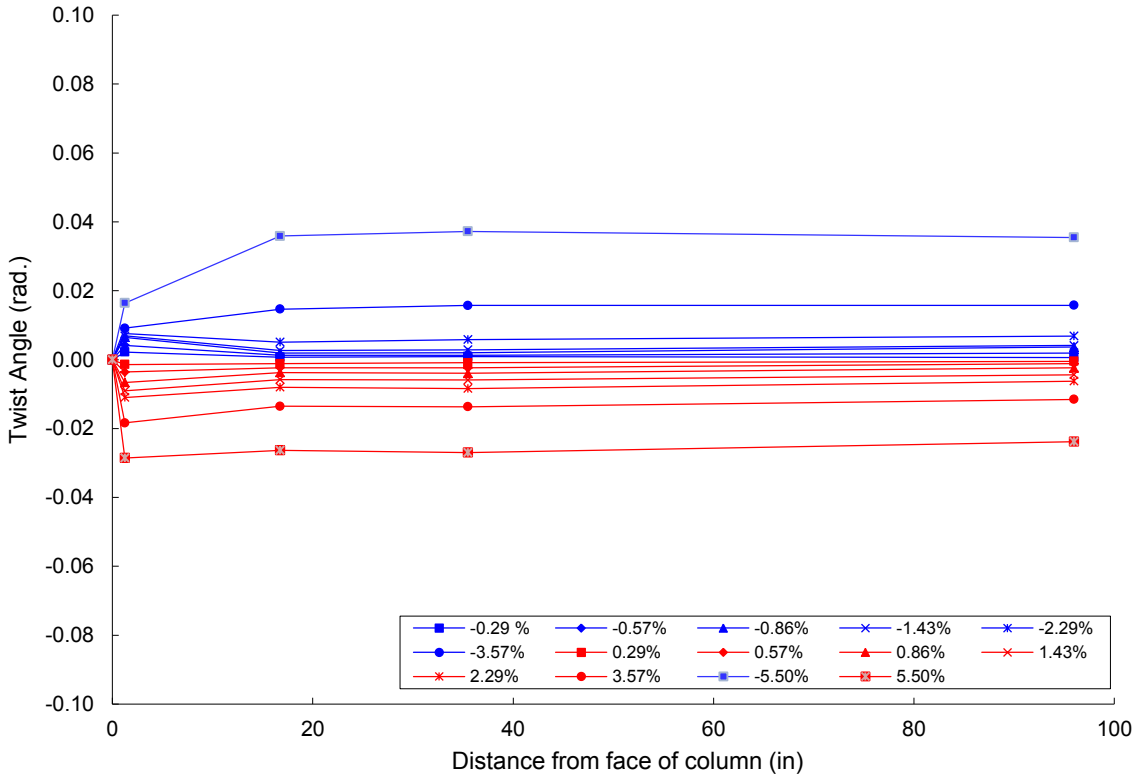

Figure 7.144 Twist deformation of NS beam during EW beam loading in specimen U-BJ-1

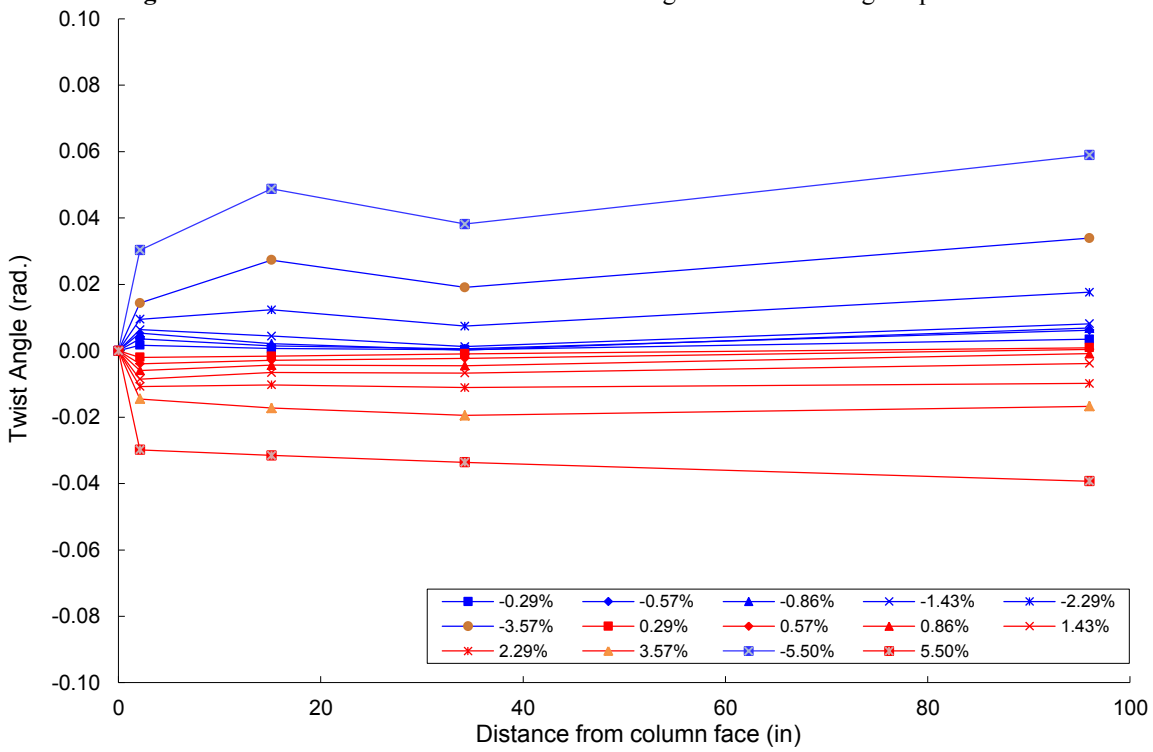

Figure 7.145 Twist deformation of EW beam during NS beam loading in specimen U-BJ-1

Figure 7.146 displays the torsional cracking of the EW beam during NS beam downward and upward loading in specimen U-J-2. In general, torsional cracking and twisting deformations were less intense in specimen U-J-2 than in specimen U-BJ-1 due to the higher torsional resistance of the deeper beams in the former specimen. It was generally observed in most specimens that the torsional deformations of NS beam due to its own loading were less than those of EW beam due to its own loading. This could be attributed to the fact that NS beam is loaded after the EW beam, which may have resulted in NS beam torsional deformations measured from a deformed position of partially opened cracks due to EW beam loading. It other words, twisting moment relief to NS beam results due its initial cracking. It is difficult to quantify this effect accurately. Top and bottom slab crack patterns observed in specimen U-J-2 were similar to those of specimen U-BJ-1.

(a) **(b)**

Figure 7.146 Torsional cracking of EW beam during NS beam
(a) Downward loading (b) Upward loading in specimen U-J-2

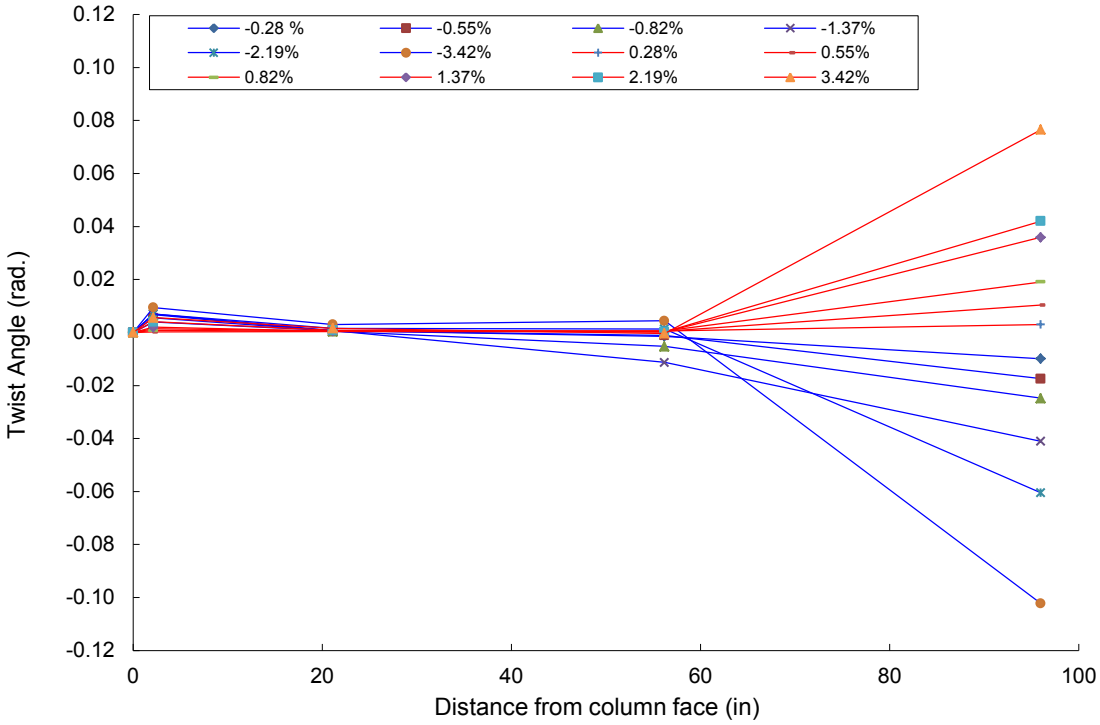

Figure 7.147 Twisting angle profile along EW beam during its loading in specimen U-J-2

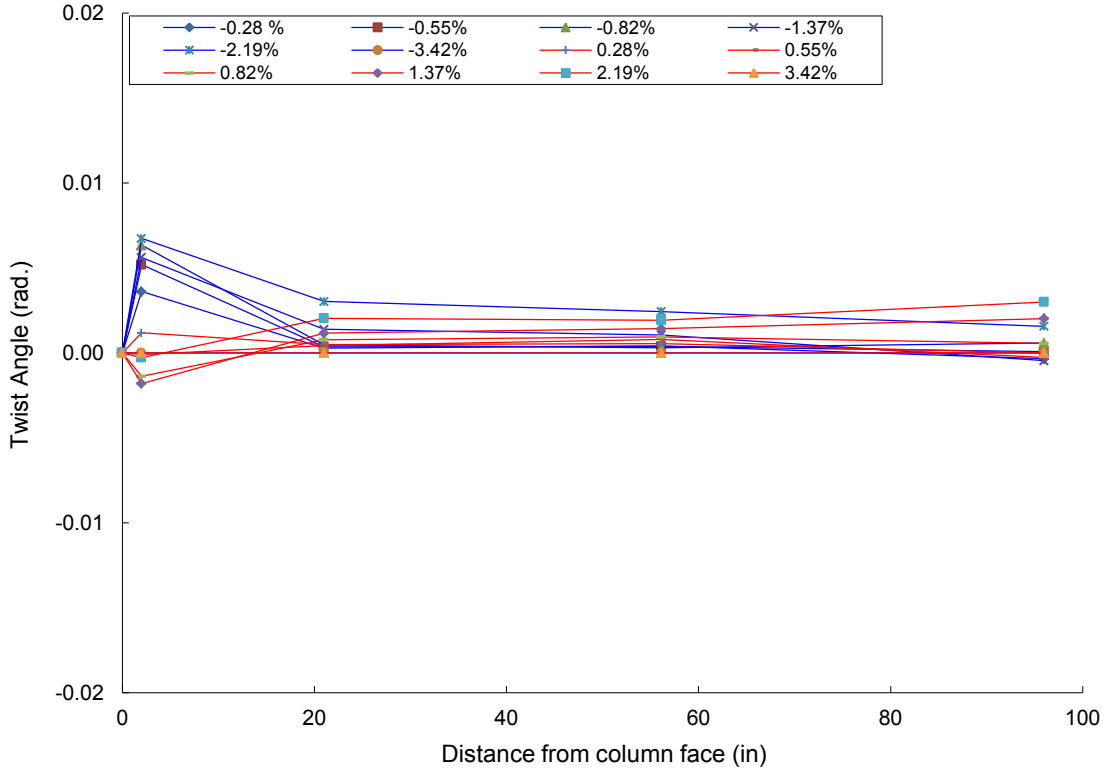

Figure 7.148 Twisting angle profile along NS beam during its loading in specimen U-J-2

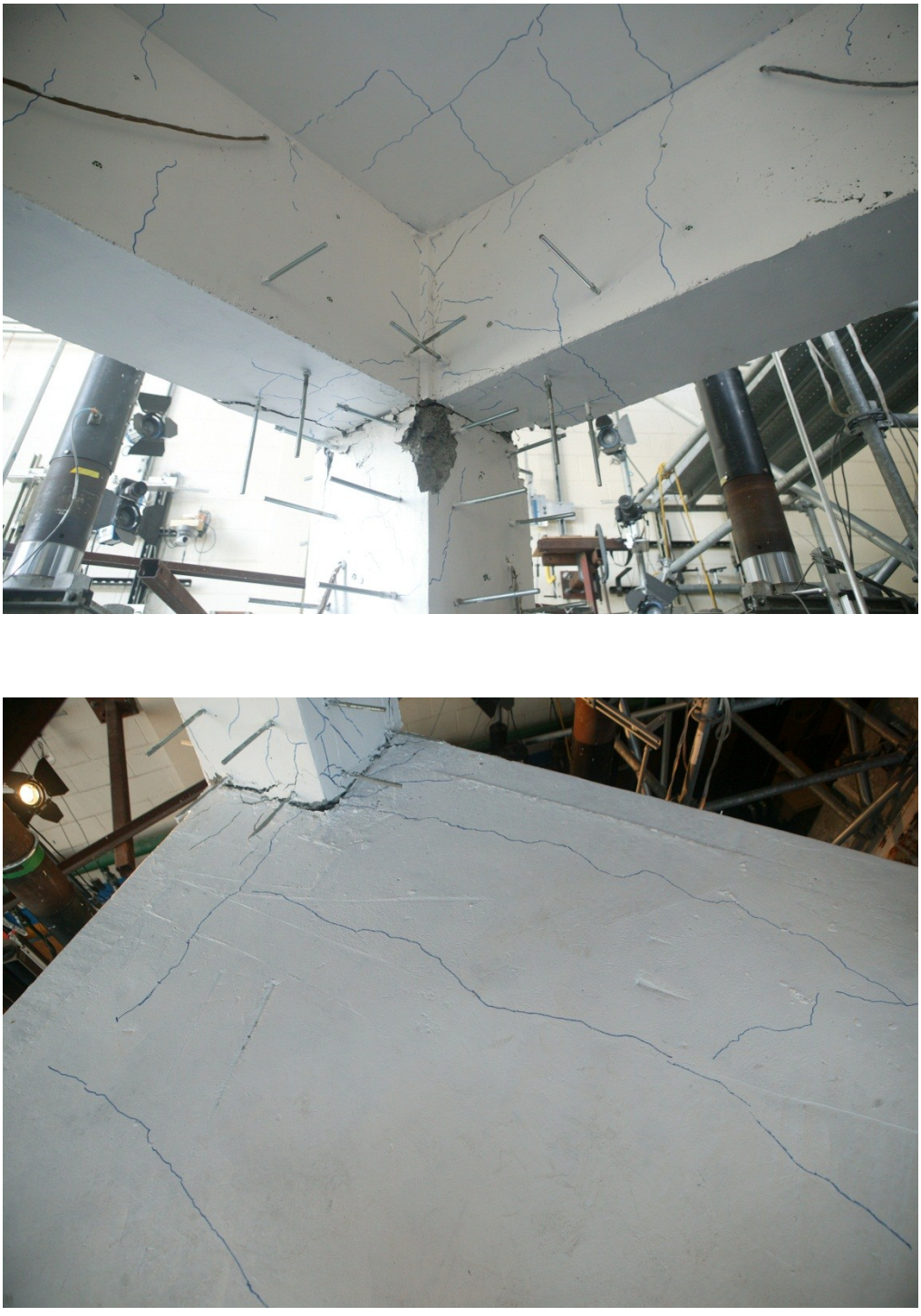

Figure 7.149 Crack pattern of slab in specimen U-J-2

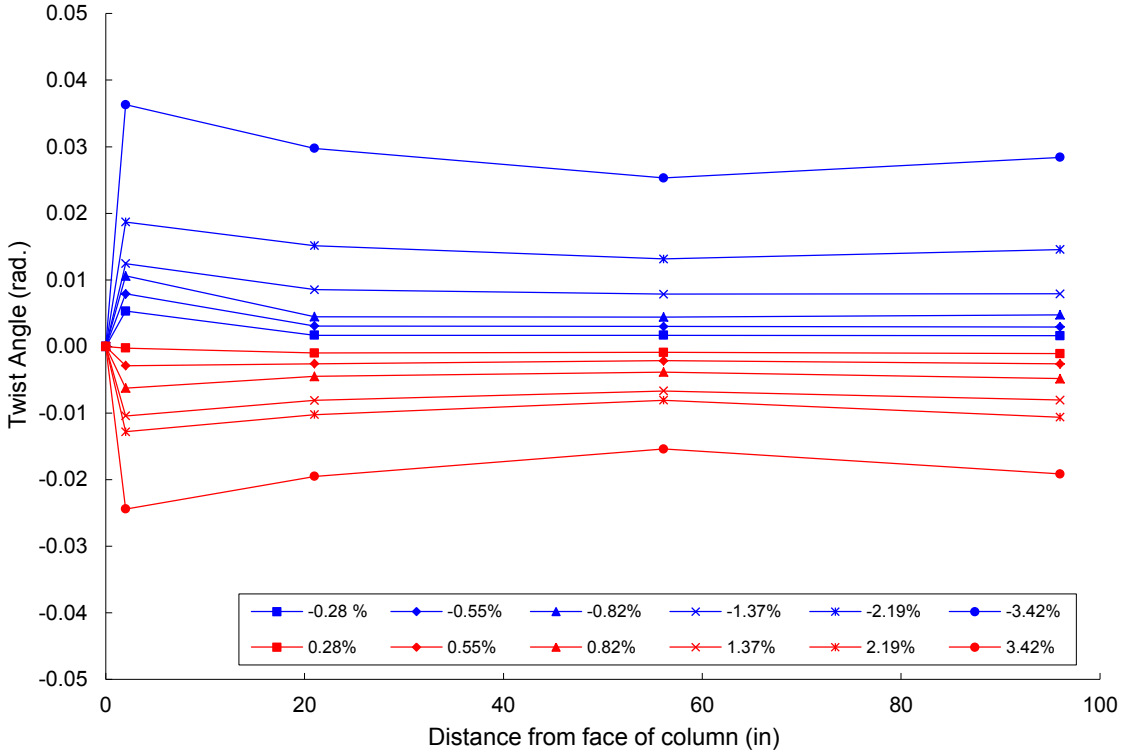

Figure 7.150 Twist deformation of NS beam during EW beam loading of specimen U-J-2

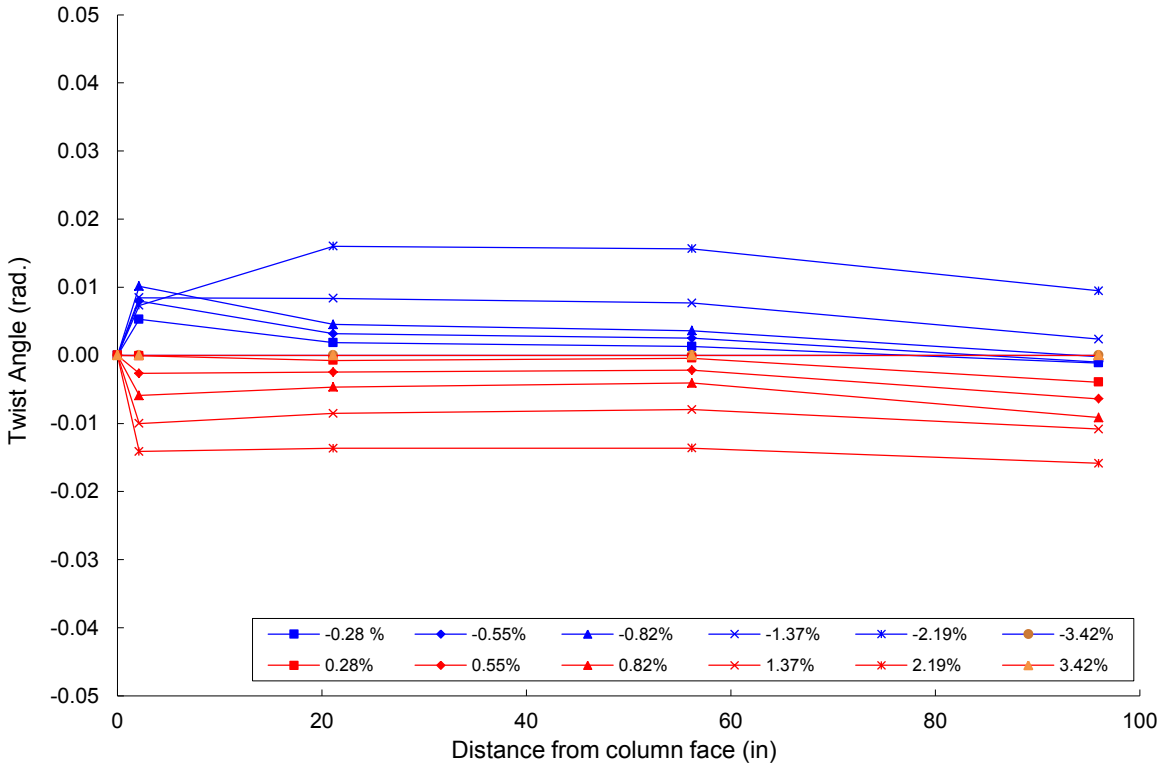

Figure 7.151 Twist deformation of EW beam during NS beam loading of specimen U-J-2

Figure 7.152 shows the torsional cracking of EW beam in specimen U-J-1 during NS beam downward loading. Beam crack pattern is similar to that in formerly presented specimens. The characteristic difference in cracking of specimen U-J-1 from other specimens that did not undergo very large drift is the slab crack pattern shown in Fig. 7.153. It can be observed that slab cracking due to twisting restraining effect is similar to other specimens, however, some other diagonal cracks stemming from the column internal apex adjacent to slab can be observed. These are shear cracks that developed due to very high drift in specimen U-J-1. Since concrete slab was lightly reinforced to mimic older construction, the diagonal shear cracking reinforcement at slab corners was not provided. This evident slab shear cracking confirms the appropriateness of providing corner shear reinforcement in concrete slabs to overcome diagonal tension stress concentration at the corner.

Figure 7.156 displays the cracking patterns of EW beam and NS beam during simultaneous bidirectional loading of specimen B-J-1. Although the loading is simultaneous, it is evident that some slab restraint was still present. Bottom slab crack pattern also confirms this. However, the torsional deformations and cracking were evidently less intense than those of the other three specimens, yet the torsional deformations were still significant. Figures 7.154 and 7.155 present the twisting angle profiles along EW and NS beams in specimen B-J-1. A recommended calculation method for twisting moment and additional joint shear stress due to torsion and 3D effects is presented in Engindeniz [41].

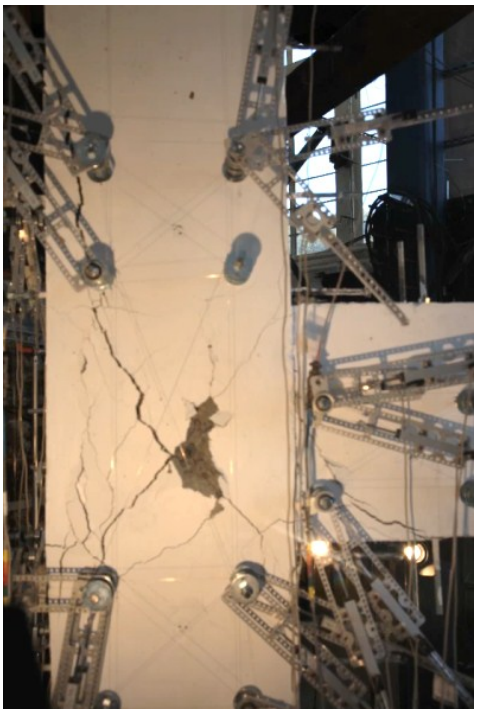

Figure 7.152 Torsional cracking of EW beam during NS beam downward loading in specimen U-J-1

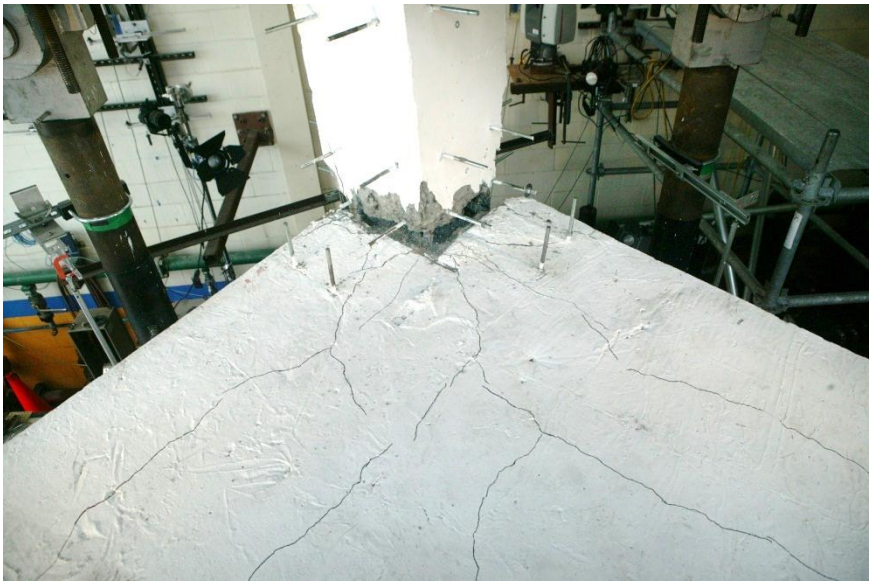

Figure 7.153 Crack pattern of slab in specimen U-J-1

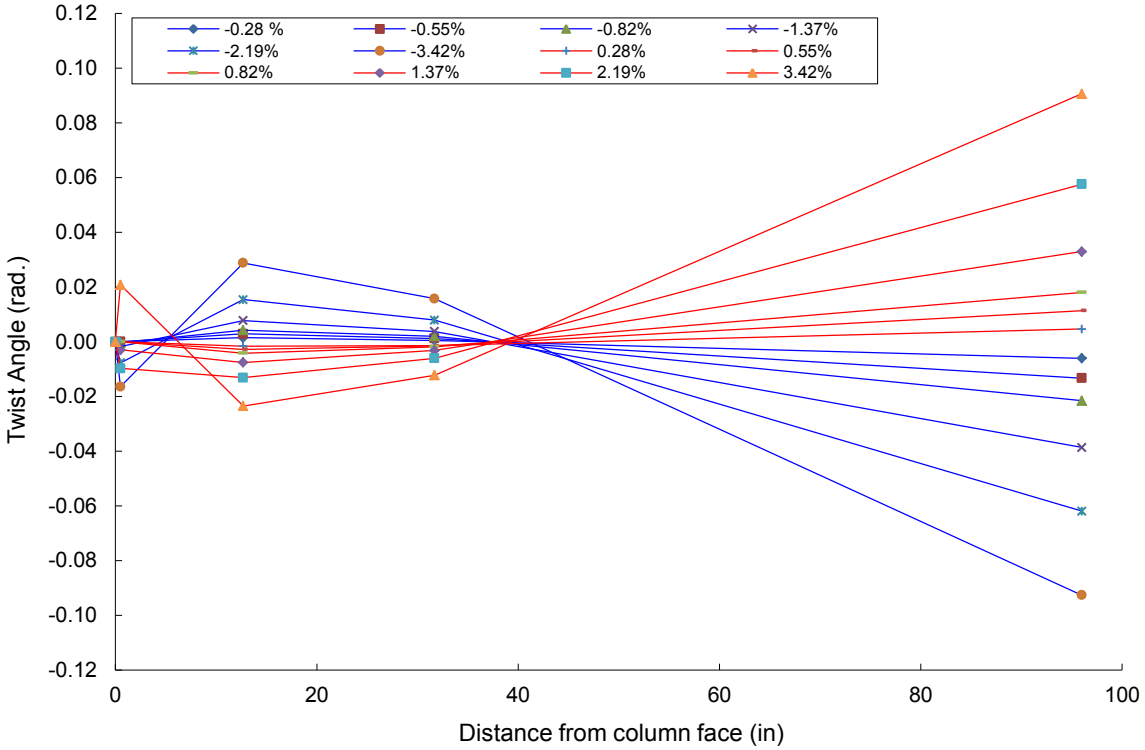

Figure 7.154 Twist deformation of EW beam for specimen B-J-1

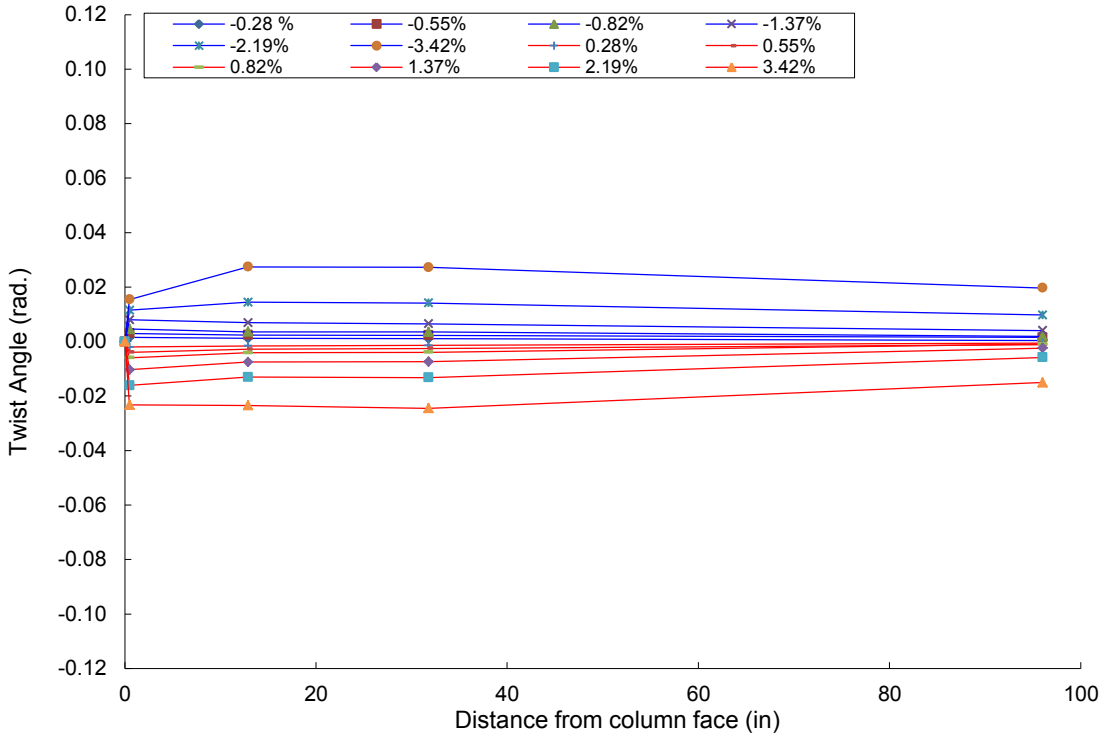

Figure 7.155 Twist deformation of NS beam for specimen B-J-1

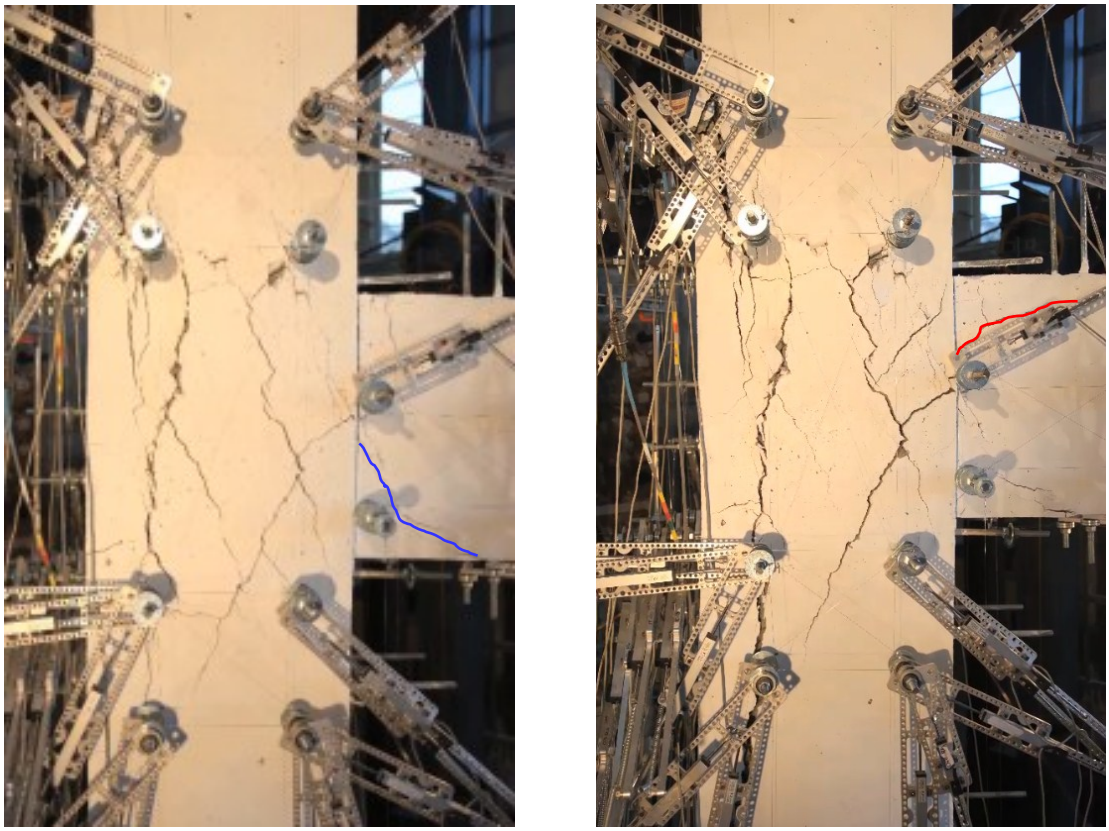

Figure 7.156 Torsional cracking of EW and NS beam
(a) Downward loading (b) Upward loading in specimen B-J-1

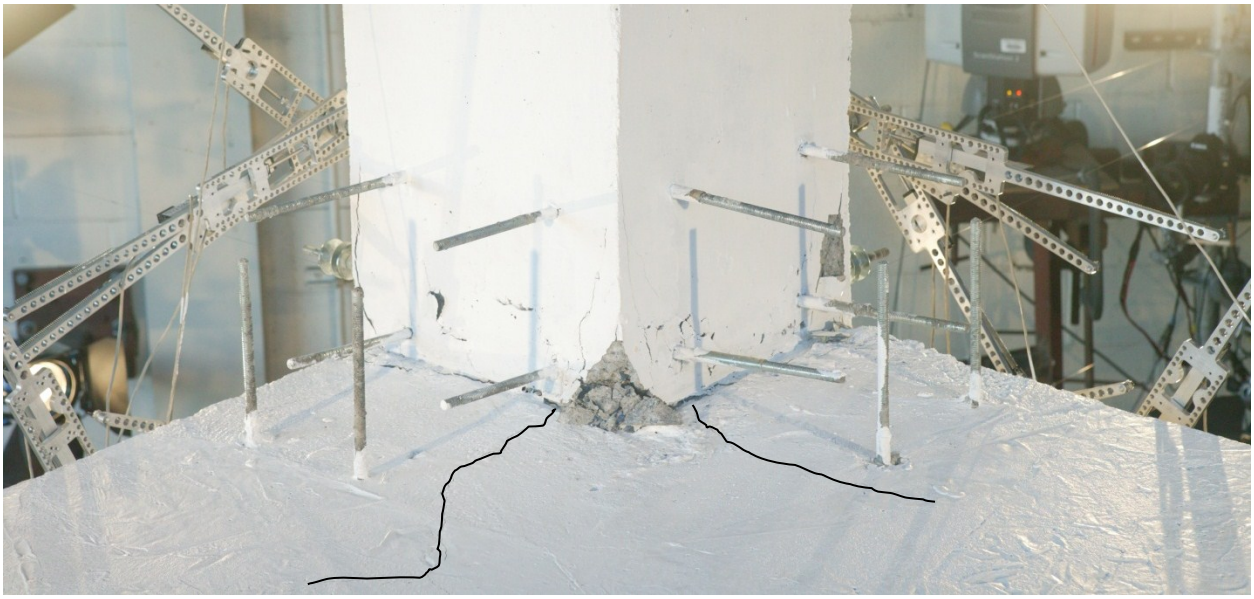

Figure 7.157 Crack pattern of slab in specimen B-J-1

7.4.6 Effect of Intermediate Column Reinforcement

Although the contribution of column intermediate reinforcement bars to joint shear strength was not an explicit test parameter in the current investigation, useful conclusions can be drawn based on the current experimental results.

Experimental observations of the current study confirmed the negligible effect of column intermediate reinforcement, in the case of using only one row of bars, in enhancing joint shear strength. This conclusion was based on steel strain results of this reinforcement within the joint core. The column intermediate reinforcement longitudinal strains at the joint mid-height are insignificant until reaching joint shear capacity in both negative and positive loading directions. The fact that column intermediate reinforcement at mid-joint height never yielded throughout the test of specimen U-J-1 with moderate axial load level initially suggests minor contribution of this reinforcement to joint shear strength. In specimen U-J-2 with higher axial load ratio, this reinforcement did not yield also throughout the test except for the CE bar during the negative NS beam loading after already reaching peak joint shear strength. However, an increase in strain level of that reinforcement within the joint core is observed during the negative and positive drift loading, particularly after reaching joint shear capacity. The excessive strains observed after reaching peak joint strength in the downward loading direction are attributed to bar buckling effect due to the high axial loads combined with loss of bond between concrete and column bars. In the positive drift cycles, the contribution of the central column bars to joint shear strength was also negligible. The slight increase of mid-joint height column bar strains in the positive loading direction is attributed to tensile strain penetration because of the axial tension force on column and the column flexural tension strains progressing from column-joint interface.

Similarly in specimen U-BJ-1, intermediate column bar strains within the joint core never experienced yielding before reaching full plastic capacity of beam and slightly increased because of bar buckling and axial tension force afterwards.

Higher mid-joint column intermediate reinforcement strains were observed in specimen B-J-1 after reaching peak joint shear strength due to the nature of simultaneous biaxial loading. The biaxial loading implies lower column flexural capacity by creating an inclined column neutral axis and hence developing higher strains at the location of central column bars at column-joint interface, that later penetrated into joint core. This strain increase does not necessarily imply additional contribution of column intermediate bars to joint shear strength since it took place after reaching peak strength.

This suggests that the contribution of such column reinforcement bars to joint shear strength is negligible as possible vertical truss mechanism. It is interesting to note that Wong [155] cites experimental evidence contrary to this observation.

7.4.7 Effect of Joint Geometry

The strut-and-tie shear strength model, empirical shear strength model and shear strength degradation model presented in Chapter 5 were able to predict shear strength of specimens U-J-2 and SP4 with reasonable accuracy (see Chapter 5). Although these models were developed and calibrated based on isolated exterior joints, they also proved to be accurate for the corner joints reported here. Comparing test results of the current study with previous exterior joint shear strength results available in the literature indicates that the corner joint shear strength is not substantively different from shear strength of exterior isolated joint or corner simulated joint with pre-cracked transverse stub. This observation is in line with Kurose [78]. From a geometry viewpoint, the exterior surfaces of corner joints are not confined by any adjacent concrete beams; hence, corner joints are likely to behave similar to isolated exterior joint on these surfaces. In addition, even at the two joint surfaces adjacent to beams, beam-joint interface cracking (Fig. 7.3) due to gravity and lateral loading of orthogonal direction in bidirectional loading (which is more realistic in actual ground motions) hinders concrete confinement of the orthogonal beam to joint surface. Experimental observations in the current test program reveal that wide joint beam interface cracks are evident under cyclic load reversals.

CHAPTER 8

AXIAL CAPACITY OF UNCONFINED BEAM-COLUMN JOINTS

8.1 INTRODUCTION

This chapter deals with the problem of axial capacity and axial failure of unconfined exterior and corner joints. It presents a background about the state of knowledge and the importance of axial capacity estimation for unconfined joints. The chapter explores the observed axial failure modes during past earthquakes and laboratory tests, along with observed trends of drift ratio-axial load ratio relations. It also presents an axial capacity models for unconfined joints.

8.2 BACKGROUND

Very few unconfined joint tests are available with confirmed axial failure. Unfortunately during laboratory joint tests, a common practice has been to terminate the test after dropping to 80% of lateral load resistance without testing the axial capacity of the joint. However, many post-earthquake reconnaissance studies report building damage or collapse that might be attributed to exterior and corner beam-column joint failures. No interior joint axial failures have been identified.

An important aspect of the assessment of an existing building is to assess drift capacity after onset of shear failure until onset of axial failure. Shear failure of joints and columns in non-ductile buildings can occur at relatively low drifts. Whether the axial failure of a shear damaged joint will precede the axial failure of shear damaged column leading to a progressive collapse is not certain. The axial capacity of shear damaged columns and joints should be input as limit states in building simulation models to realistically represent the ignition of progressive collapse. From an economic viewpoint, if a joint can reliably support gravity load after its lateral strength degradation begins, it may be possible to achieve considerable savings by considering this particular joint as a secondary component.

8.3 MODES AND MECHANISMS OF JOINT AXIAL FAILURE

Different approaches were used to decide the point of joint axial failure during previous joint tests. Since most tests were performed under constant axial load, a common sign of joint axial failure was a significant drop in axial load even without full disintegration of the joint. This approach could be sometimes misleading since the axial load may decrease for several reasons including axial stiffness degradation because of cracking, or hydraulic pressure drop for a mechanical reason. A better indicative sign of axial failure is the axial shortening below a threshold limit. As indicated in Chapter 7, axial failure in most of the joints tested in the experimental phase of the current study seemed indicated for an axial joint strain of about 0.005 to 0.006.

The third approach of confirming axial failure is the total collapse of the specimen by dynamic instability due to reaching joint axial capacity. As described in previous chapters, this approach was used to test the axial capacity of unconfined corner beam-column joints of the current study.

Different modes of joint axial failure were observed during previous tests and following past earthquakes. Fig 8.1 shows joint damage interpreted as axial failure during past earthquakes and joint tests. For the past earthquake axial failures, whether the joint axial failure occurred first, triggering partial or total collapse, or the joint axial failure was a consequence of other column axial failure is unknown.

Figures 8.2 and 8.3 display the axial failure modes of specimens U-J-1, U-J-2, U-BJ-1 and B-J-1 of the current investigation. In specimen U-J-1, the starting gravity load ratio was 0.21. The axial load ratio at peak joint shear strength was 0.31 while that at axial failure was 0.20. The drift ratio capacity at axial failure was relatively high (9.68%). The joint core was severely damaged prior to reaching axial failure. During axial failure, a sliding failure on a diagonal shear failure plane occurred. As can be seen in Fig. 8.2 the failure mode of the column longitudinal reinforcement is a “side- sway” mode rather than an axial buckling mode.

Figure 8.2.c shows the failure mode of specimen U-J-2 whose axial load ratio at peak joint shear strength was 0.44 while that at axial failure was 0.41. The drift capacity at axial failure was 3.06%, with a maximum drift ratio 3.42% before axial failure. A buckling failure mode of column reinforcing bars is obvious. A sliding failure on the diagonal shear failure surface was observed following removal of damaged concrete debris, although it was less apparent than that in specimen U-J-1. Similar axial failure modes to that of specimen U-J-2 were observed in specimens B-J-1 and U-BJ-1.

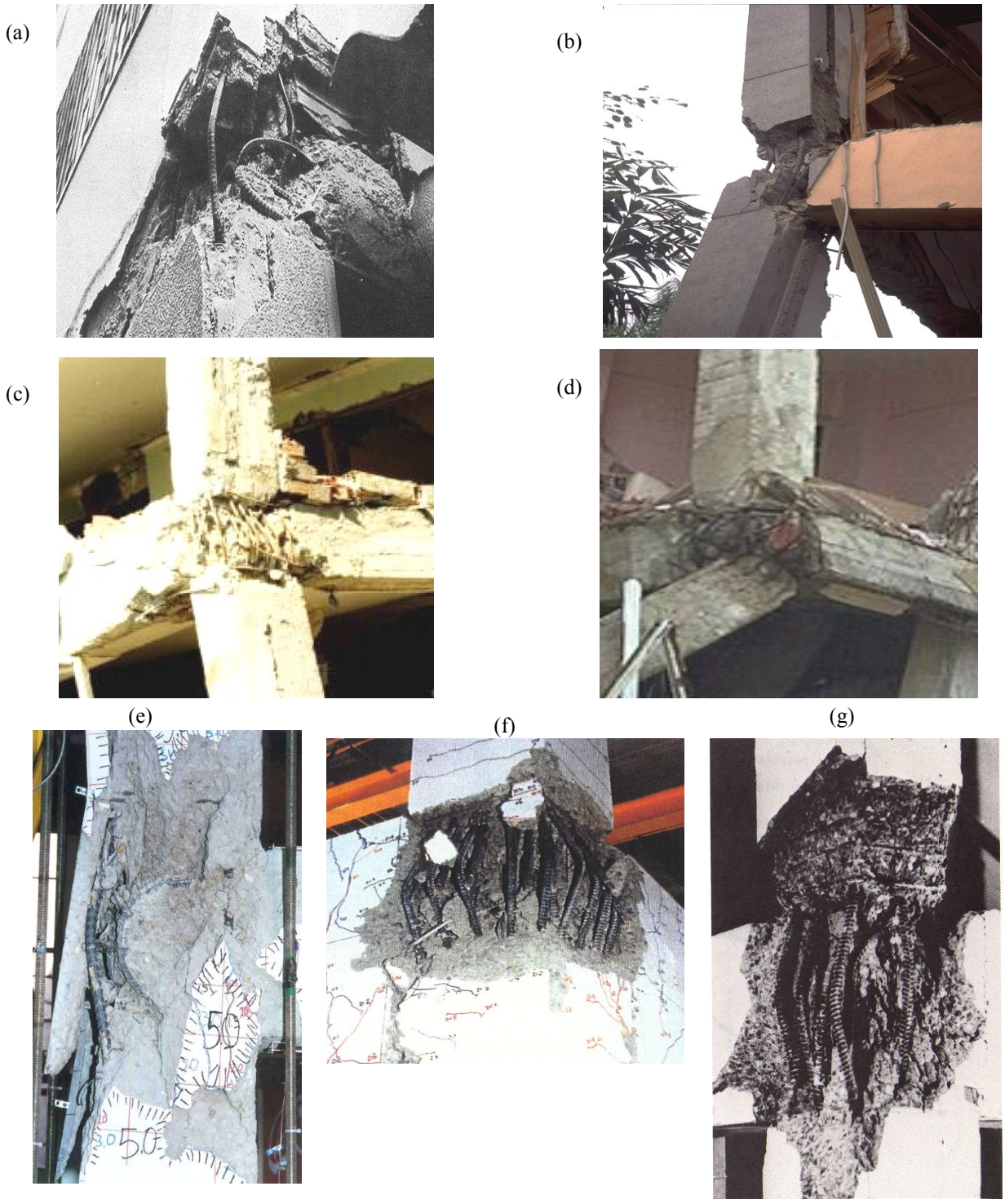

Figure 8.1 Joint axial failure during past earthquakes and laboratory tests: Caracas, Venezuela earthquake, Pagni [110], (b) Taiwan Chi-Chi 1999 earthquake, NISEE [106], (c) Izmit, Turkey earthquake of 1999, Engindeniz [41], (d) Izmit, Turkey earthquake of 1999, NISEE [106], (e) Exterior joint test, Pantelides et al. [116], (f) Corner joint test, Priestley and Hart [129], (g) Corner simulated joint test, Uzumeri [150]

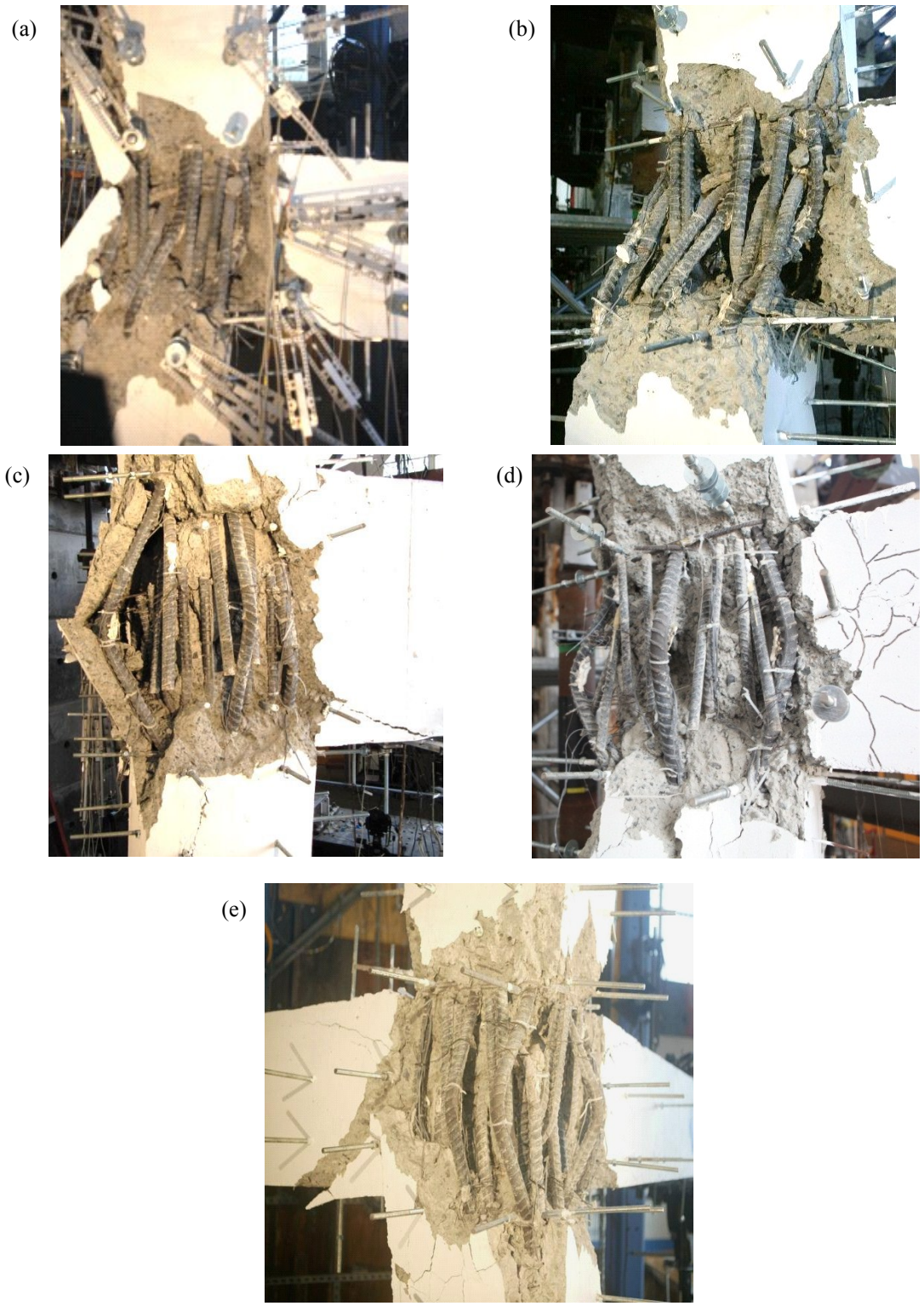

Figure 8.2 (a), (b) Column bar side-sway axial failure mode in specimen U-J-1, (c) Bar buckling axial failure mode in specimen U-J-2, (d) specimen U-BJ-1, and (e) specimen B-J-1

The different failure modes observed for the different test specimens are believed to be due to the different levels of axial loads in the tests. The sliding axial failure on the previously damaged shear failure plane in the joint suggests that the classical shear friction theory can be used to explain the failure mechanism. Elwood and Moehle [39] presented a derivation for an axial capacity model for columns damaged in shear based on the interaction between shear-friction surface and axial capacity of column longitudinal reinforcement. The details of this model will be presented in a subsequent section.

Figure 8.3 Global failures of specimens, B-J-1, U-J-1, U-BJ-1, and U-J-2

As described by Elwood and Moehle [39], axial failure of a shear-damaged column can occur by sliding along an inclined crack plane, with resistance provided by transverse reinforcement clamping the crack and longitudinal reinforcement supporting axial force directly. Axial failure of a joint can be viewed similarly. After developing joint shear failure, the axial load will be supported by shear friction on the diagonal shear failure plane and the axial capacity of column reinforcing bars. Whether these two mechanisms work concurrently is dependent on the location of column bar within the joint. The share of each column bar of the axial load at the joint region might not be equal. However, for simplification purpose, it will be generally assumed that all column bars will share equally a small portion of axial load in the shear damaged joint.

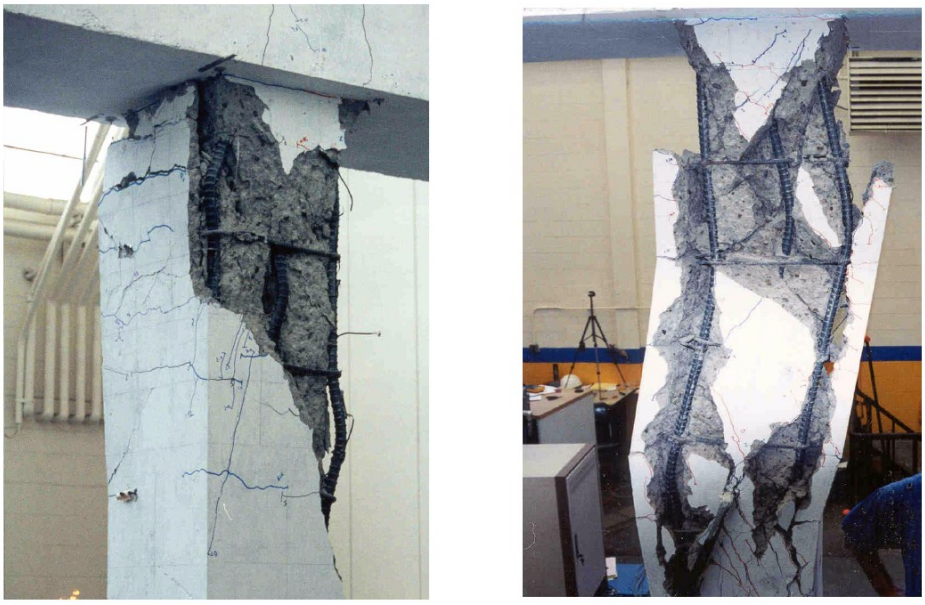

(a) (b)

Figure 8.4 Deformed shape for longitudinal bars at loss of axial load capacity for column with (a) high axial load and (b) with low axial load, Sezen [137]

In deriving an axial capacity model, it will be assumed that shear friction along an inclined plane resists a majority of the axial load and that its capacity will be reached prior to reaching axial capacity of column bars. As sliding occurs on the shear failure plane, the full axial load is then transferred to the column bars, driving them to axial capacity. Since the axial failure always occurred during the downward beam loading direction, the most axially stressed column bars were the outermost column bars. These bars reach their axial capacity and either buckle or sway and lose their bearing capacity and transfer their load to the rest of column bars. Thus, the failure progresses as the rest of the column bars get overstressed and lose their bearing capacity leading to dynamic instability and total collapse of specimen.

Based on the abovementioned mechanism, the joint axial capacity should be decided by the shear friction capacity on the shear failure plane. In specimen U-J-2, with high axial load and deeper beam, the failure axial load per column bar is *higher* than the elastic and plastic bar

buckling capacity and *lower* than the pure bar plastic capacity as shown in Fig. 8.6. The elastic bar buckling capacity can be expressed as:

$$P_{s,eb} = \frac{\pi^2 E_s I_{bar}}{(0.8s)^2} \tag{8.1}$$

where E_s is the elastic modulus of elasticity. The unsupported bar length can be assumed as $0.8s$ where s is the distance between the first column hoops above and below the joint. The choice of $0.8s$ intends to represent bar boundary conditions between ideal pinned-pinned and fixed-fixed conditions. I_{bar} is the moment of inertia the reinforcing bar.

The plastic bar buckling capacity depends on the tangent modulus of elasticity which can be estimated by $0.07\ E_s$ [39]. Thus, the plastic bar buckling capacity is:

$$P_{s,pb} = 0.11 \frac{\pi^2 E_s I_{bar}}{s^2} \tag{8.2}$$

The pure plastic capacity of a reinforcing bar is:

$$P_{s,pp} = A_{sc} f_{yc} \tag{8.3}$$

However, this pure plastic capacity is governing only when the effect of eccentricity in the deformed bar configuration (Fig. 8.5) is limited. In columns subjected to lateral loading, it is likely that the bar eccentricity due to displacement will be large, hence the deformed plastic bar capacity (Eq. 8.4) will be governing. The lateral deformation of column bars within the joint is restrained by diaphragm rigidity at the column-joint interface. Accordingly, it is not likely for the deformed bar plastic capacity (Eq. 8.4) to govern unless severe diaphragm disintegration and substantial joint shear strains take place prior to joint axial failure.

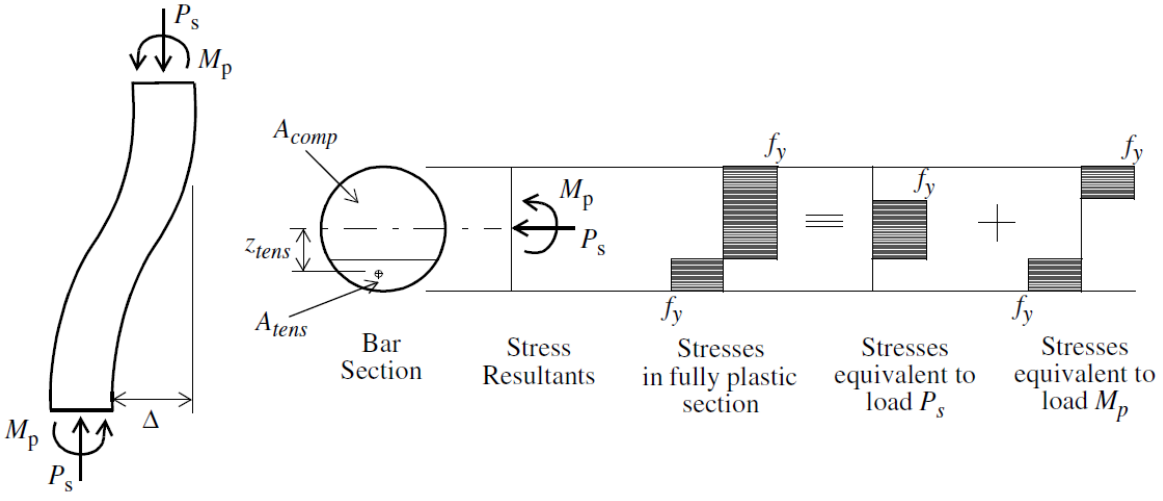

Figure 8.5 Plastic strength of longitudinal reinforcement in deformed configuration, Elwood and Moehle [39]

Based on this analysis, the governing axial failure mode in specimen U-J-2 was bar buckling mode immediately following the shear friction failure on the damaged shear plane leading to axial failure. Signs of bar buckling represented by bulging of concrete cover were evident immediately before the axial failure. Furthermore, consistent with the assumptions of this failure mode, strains at mid-joint height of the outermost column bars CNE, CN, and CE exceeded yield strain prior to reaching axial failure (see Appendix A).

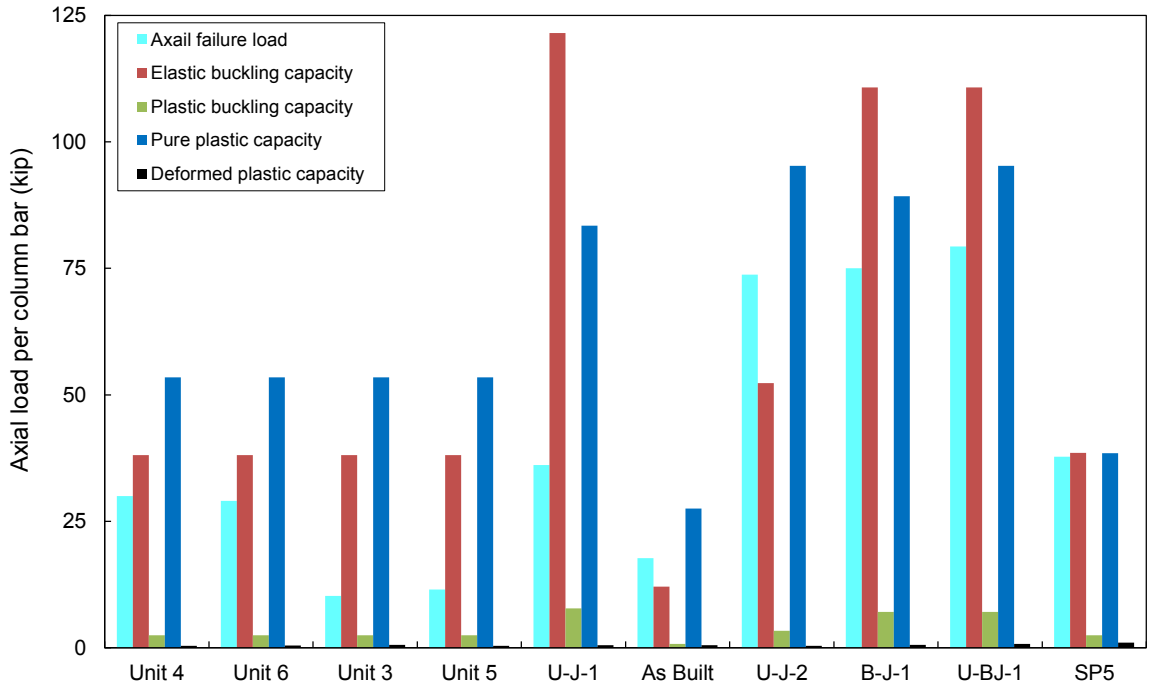

Figure 8.6 Bar axial capacity comparison for unconfined joints with axial failure

Assuming equal axial load share to each column bar, the axial failure load per column bar in specimens B-J-1 and U-BJ-1, Figure 8.6 shows that the governing axial capacity of column bars is the lesser of plastic bar buckling capacity $P_{s,pb}$ and deformed bar plastic capacity $P_{s,pd}$ considering the effect of lateral displacement of the element containing that bar (Elwood and Moehle [39]).

The applied axial load in specimen B-J-1 and U-BJ-1 was very high. Thus, joint flexibility was limited in these specimens. This makes $P_{s,pd}$ based on Eq. 8.4 not critical. Accordingly, the governing bar capacity in this case might be reasonably assumed equal to the plastic bar buckling capacity $P_{s,pb}$. Based on this hypothesis, bar buckling failure occurred following the transfer of axial forces to column bars after shear friction failure on the damaged shear plane.

In specimen U-J-1, with moderate axial load, the failure axial load per column bar was less than the pure bar plastic capacity and the elastic buckling capacity as shown in Fig. 8.6. In this case, the governing bar axial capacity is the deformed plastic capacity [39]. Deformed bar plastic capacity is critical in joint U-J-1 since it was able to survive 9.68% drift (because of the lower

axial load) and hence the joint flexibility and deformations were significant enough to deploy the local bar deformation P-Δ effect.

The deformed plastic capacity of the outermost column reinforcing bars in joints can be approximated through an expression developed by Elwood and Moehle [39] for columns, with replacing drift ration in Elwood's expression by joint shear strain as follows:

$$P_{s,pd} = \frac{\phi_b / s}{0.75.\pi.\gamma_s + \phi_b / s} \tag{8.4}$$

where γ_s is joint shear strain and ϕ_b is column bar diameter. The effect of bar sway was further amplified because of the severe crushing of beams prior to axial failure at this very large drift that led to decreased confinement to the joint and column bars which amplified their deformation and tendency to sway. Signs of bar sway at the upper column –joint interface were noticed before axial failure. Column steel strains at mid-joint height did not reach yield strain prior to axial failure as indicated in Appendix A. Thus, a side-sway bar plastic failure mechanism was triggered following force transfer from shear friction failure on the shear failure plane.

8.4 OBSERVED AXIAL CAPACITY OF UNCONFINED BEAM-COLUMN JOINTS

As mentioned earlier, few previous joint tests were continued until reaching axial failure. For exterior unconfined joint tests, four such test specimens were reported by Pantelides et al. [116]. In this group of tests called Unit 3, Unit 4, Unit 5, and Unit 6, axial failure was identified by a drop in the constant axial load applied to the column. Priestley and Hart [129] report axial failure of an unconfined corner joint. Axial failure of this corner joint, denoted "As built", was identified by crushing of joint core along with buckling of column bars in the joint and eventually loss of axial carrying capacity. In addition, one corner simulated joint, SP5, with a pre-cracked transverse stub experienced axial failure in tests performed by Uzumeri [150]. All four unconfined corner joints tested in the current investigation (denoted NEES Joints) experienced axial failure as described in a previous section. Table 8.1 shows the design and loading details of specimens as well as the important response quantities.

Figure 8.7 plots the relationship between axial failure load and the maximum drift reached prior to axial failure for the ten joints mentioned above. In addition, a database of 37 previous exterior and corner joint tests in which axial failure was not reached also is included. The axial load ratio and drift ratio for this database reflect the test termination values. This database includes the four joints of phase I of the current NEES investigation [120]. Tables 3.1 and 5.1 show the design parameters of each of those specimens. They include the joints tested by Wong [155], Park [120], Hwang et al. [65], Karayannis et al. [68], Clyde et al. [26], Uzumeri [150], Tsonos [145], Hanson and Conner [53] and [54] and Antonopoulos and Triantafillou [10]. The size of axial failure joints database is relatively small compared to that of non-axial failure joints. However, several useful observations can be made from this plot:

1. It appears that exterior and corner joints may be susceptible to axial failure under very large drifts or under high axial loads.

2. A general trend of a decreased axial failure drift capacity is associated with higher axial loads except for joint U-BJ-1, which will be discussed later.

3. Excluding joint U-BJ-1, an inverse proportionality between axial failure load and drift ratio can be observed.

4. The proportionality between axial failure load and drift ratio for the NEES J-Failure joints is offset from that between previous joint tests with axial failure. Some differences exist between NEES J-Failure joints and other tests. The NEES tests include a slab whereas others did not, and relatively fewer cycles were included than were included for some of the other tests.

5. Based on previous joint tests that did not experience axial failure, an axial failure safe zone can be drawn as shown in Fig. 8.7. Inclined line A defines a fairly clear demarcation between tests with and without axial failure. Line B is more tenuous, as it extends to high axial load levels for which few tests are available. The inclined line A can be algebraically expressed as $\left(\frac{\Delta}{L}\right) \leq \frac{1}{9} - \frac{P}{2.72 f_c^{'} A_g}$

6. One test shown in Fig. 8.7 is the first unconfined joint test reported by Hanson and Conner (Specimen V) [53]. In this test, an unrealistically constant high axial load ratio of 0.95 was used. In spite of the substantial axial load, the specimen was able to survive 5.2% drift without axial failure. The somewhat peculiar combination of high axial load and high drift ratio could not be explained.

7. Specimen U-BJ-1 also stands apart from the trend of the other data. The reason for this is that the drift ratio is not the best marker of joint deformation capacity in this specimen, since most of the drift was contributed by significant beam yielding, with joint failure delayed until very late stages of loading. Specimen 7 tested by Hanson and Conner [1] showed similar behavior. Specimen 7 was loaded under 0.50 constant axial load ratio and experienced a BJ-shear failure mode, with a substantial yielding and deformation of the beam, similar to specimen U-BJ-1. Under this high axial load, the specimen was able to survive a 5.1% drift ratio without axial failure. This result is also off the trend shown in Fig. 8.7 and suggests a much more relaxed axial failure drift capacity for specimens failing in shear by BJ failure mode under very high axial load. It is worth mentioning that the distinction of BJ failure mode in specimens with low axial load was not made in Fig. 8.7 since they follow similar trend to J-failure mode in terms of joint shear deterioration and deformation as explained in Chapter 7. In other words, it is likely that joints with BJ-Failure mode under high axial load ratio (more than 0.30) will survive drift ratios much larger than their J-Failure counterparts.

8. It is surprising that joint SP5, with 0.51 axial load ratio, experienced a BJ-Failure mode at 1.6% drift and axial failure at 3.5% drift only, unlike specimens U-BJ-1 and Specimen 7 [54] mentioned above. This might be attributed to the arbitrary loading history used by Uzumeri [150] that decided number of cycles and displacement amplitudes during the test based on the observed behavior.

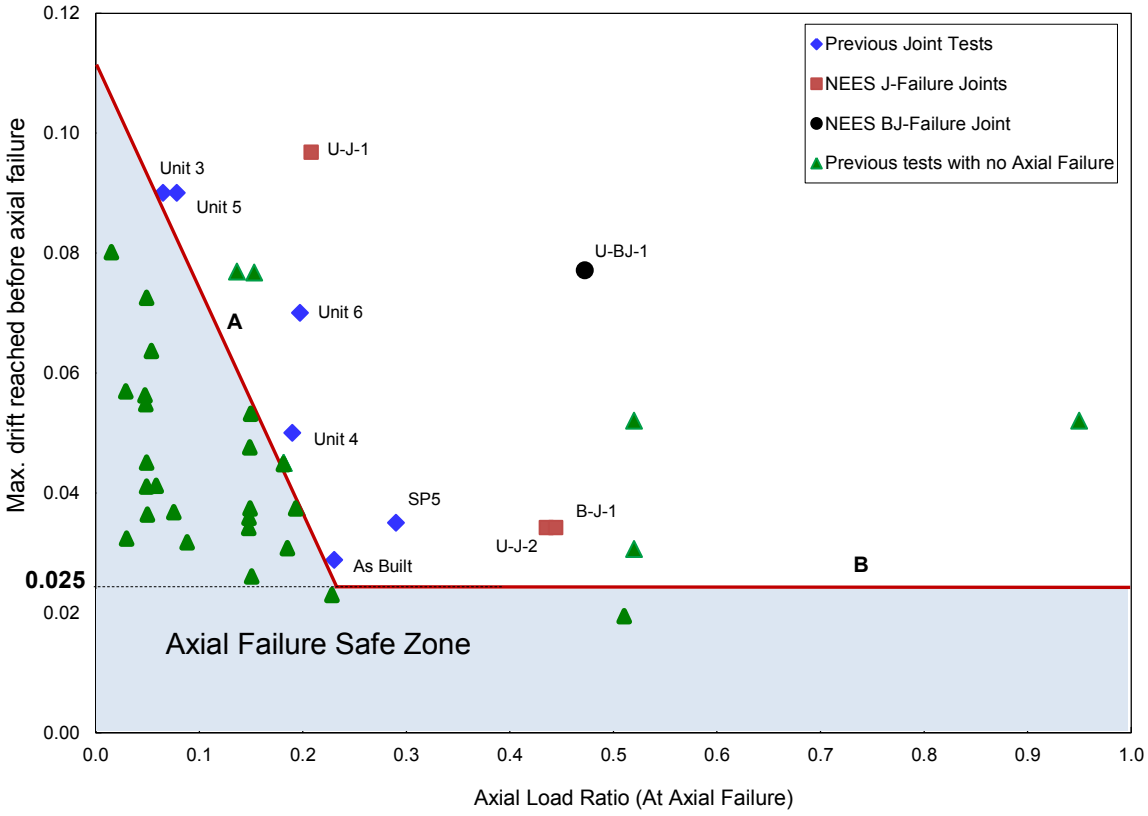

Figure 8.7 Axial load-drift ratio relationship at axial failure (or test termination) point for exterior and corner joints

Table 8.1 Database of unconfined beam-column joints with axial failure

Investigator	Specimen ID	Joint Type	Materials			Dimensions and Reinforcement						Shear failure mode	At Shear Failure			At Axial Failure*#			Loading cycles	Loading Type
			f_c' (ksi)	f_{yc} (ksi)	f_{yb} (ksi)	b_b (in.)	h_b (in.)	b_c (in.)	h_c (in.)	A_{sb} (in.^{2})	A_{sc} (in.^{2})		P/f'_cA_j	γ_j (psi$^{0.5}$)	(Δ/L)	P/f'_cA_j	γ_j (psi$^{0.5}$)	(Δ/L)		
Pantelides et al.[116]	Unit 3	Ext	4.93	68	66.5	16	16	16	16	3.79	6.28	BJ*	0.14	10.5	0.016	0.065	1.60	0.09	3	U
	Unit 4	Ext	4.93	68	66.5	16	16	16	16	3.79	6.28	BJ*	0.28	11.7	0.016	0.19	5.80	0.05	3	U
	Unit 5	Ext	4.6	68	66.5	16	16	16	16	3.79	6.28	BJ*	0.15	11.7	0.029	0.078	2.40	0.09	3	U
	Unit 6	Ext	4.6	68	66.5	16	16	16	16	3.79	6.28	BJ*	0.31	11.7	0.017	0.20	4.20	0.07	3	U
Priestley & Hart[129] [1]	As built	Corner#	4.8	62	62.2	16	20	16	16	1.32	7.07	BJ	0.29	11.0	0.007	0.23	3.85	0.029	2-2	UA-B
NEES Joints	U-J-1-EW	Corner	4.54	68	75.9	16	18	18	18	3.79	9.82	J	0.31	14.3	0.022	0.20	2.87	0.097	2	UA
	U-J-2-EW	Corner	4.43	77.6	63.2	16	30	18	18	3.14	9.82	J	0.46	9.98	0.013	0.42	4.30	0.034	2	UA
	B-J-1-EW	Corner	4.41	72.7	72.8	16	18	18	18	3.79	9.82	J	0.45	16.0**	0.014	0.43	7.50	0.034	2	B
	U-BJ-1-E	Corner	4.39	77.6	74.3	16	18	18	18	1.77	9.82	BJ	0.48	8.20	0.023	0.46	4.20	0.077	2	UA
Uzumeri[150]	SP5	Corner simulated	4.63	48.7	50.4	15	20	15	15	1.99	6.28	BJ*	0.51	8.67	0.016	0.29	5.08	0.033	Arbitrary	U

Notation: *: minor yielding before joint failure, A_{sb}: bottom beam reinforcement, (Δ/L): test drift ratio, #: corner specimen has no slab, *#: axial load ratio at the actual axial failure, drift is the maximum value reached before axial failure, residual shear strength at actual axial failure. **:The strength of biaxially loaded specimen B-J-1 is modified according to circular interaction suggested in Chapter 7
U: uniaxial loading, *UA*: uniaxial alternating, *B*: biaxial loading, *UA-B*: uniaxial alternating followed by simultaneous biaxial loading

Figures 8.8 and 8.9 compare drifts at shear failure and drifts at axial failure for joints sustaining axial failures. The vertical axial plots the axial load at axial failure. Joints with higher axial load tended to sustain axial failure sooner after shear failure than did joints with lower axial loads, although the trend is not strong and there are exceptional cases. Specimen U-BJ-1 is one of the exceptions, for the reason explained earlier. A minimum μ_f of 2 seems a lower bound for drift ratio at axial failure to that at shear failure.

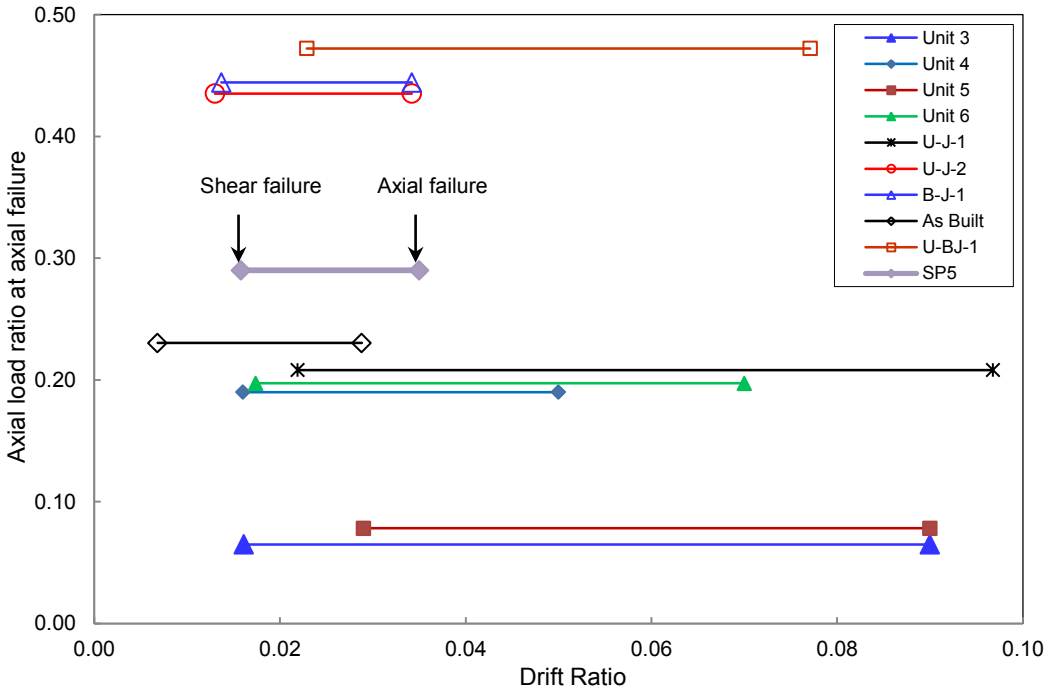

Figure 8.8 Relation between axial load at axial failure and drift ratio

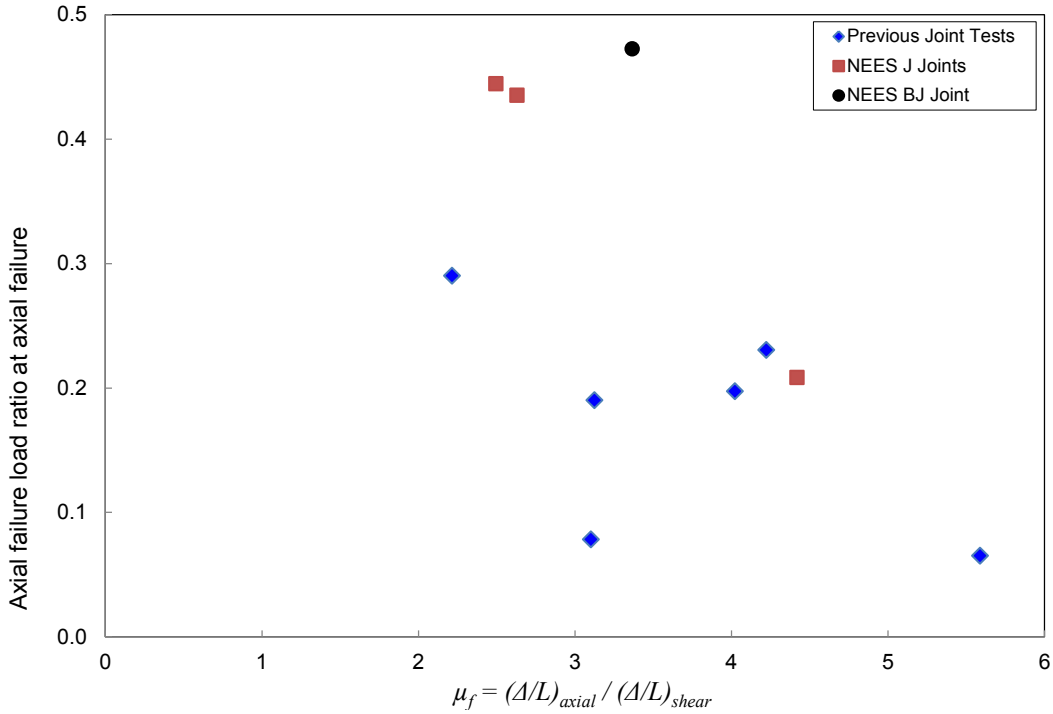

Figure 8.9 Relation between axial load at axial failure and drift at shear failure and at axial failure.

Figure 8.10 displays the relationship of axial failure load ratio and "joint shear strain at axial failure." There is no clear trend. It is worth mentioning that measured joint shear strain is an average across a joint that is highly fractured at the point of axial failure, such that the measurement of strain itself may be flawed. Consistent with previous observations, the shear strain of specimen U-BJ-1 at axial failure is relatively low compared with all the other specimens because of the clamping action of high axial load that hindered yield penetration from beam.

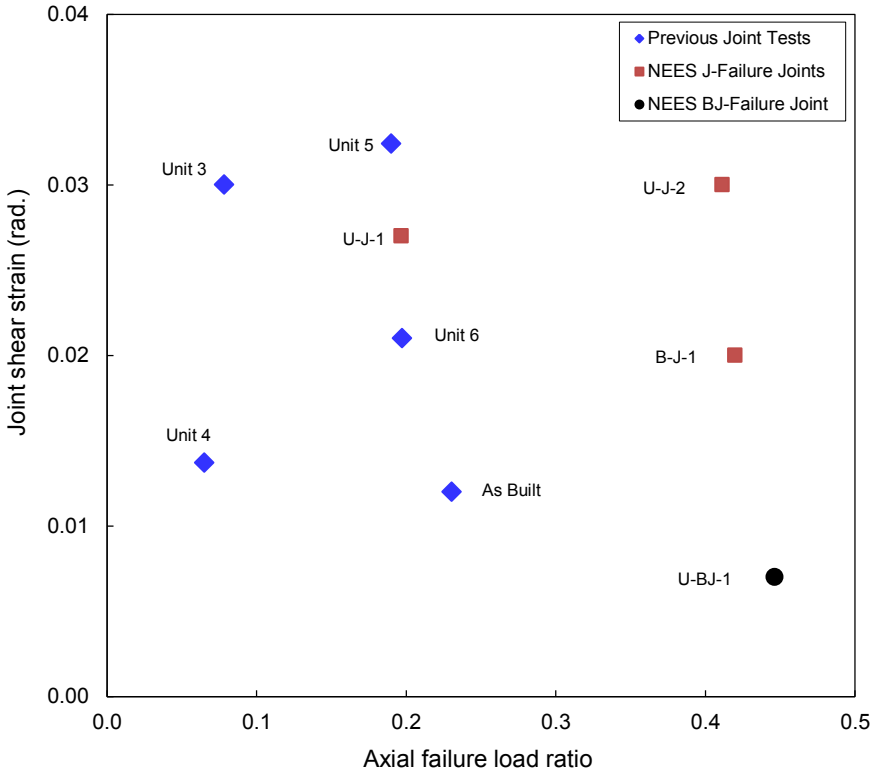

Figure 8.10 Relations between joint shear strain and axial failure load

Figure 8.11 shows the relationship between maximum drift ratio reached before axial failure and the ratio of residual joint shear capacity at axial failure to that at shear failure. As might be expected, specimens deformed to greater deformations have sustained greater strength degradation. Figure 8.12 plots the relation between axial load at failure and shear strength degradation ratio for the NEES joint tests and for previous joint tests.

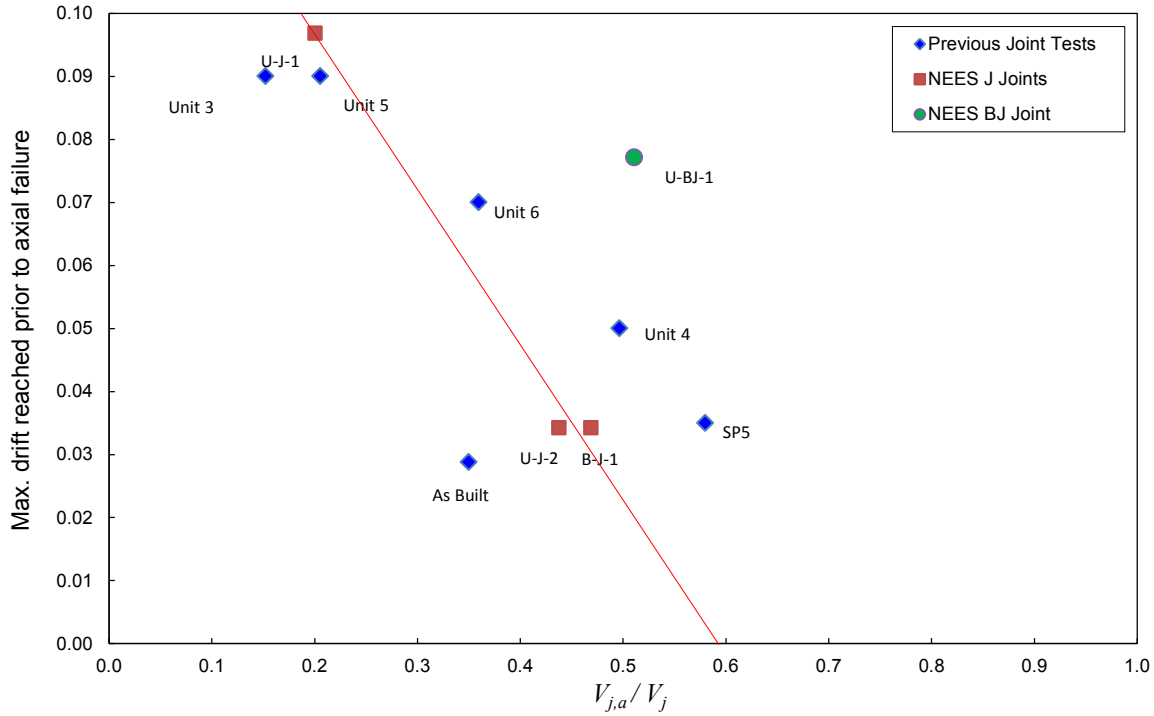

Figure 8.11 Relation between residual joint shear capacity (at axial failure) and maximum drift capacity reached prior to axial failure

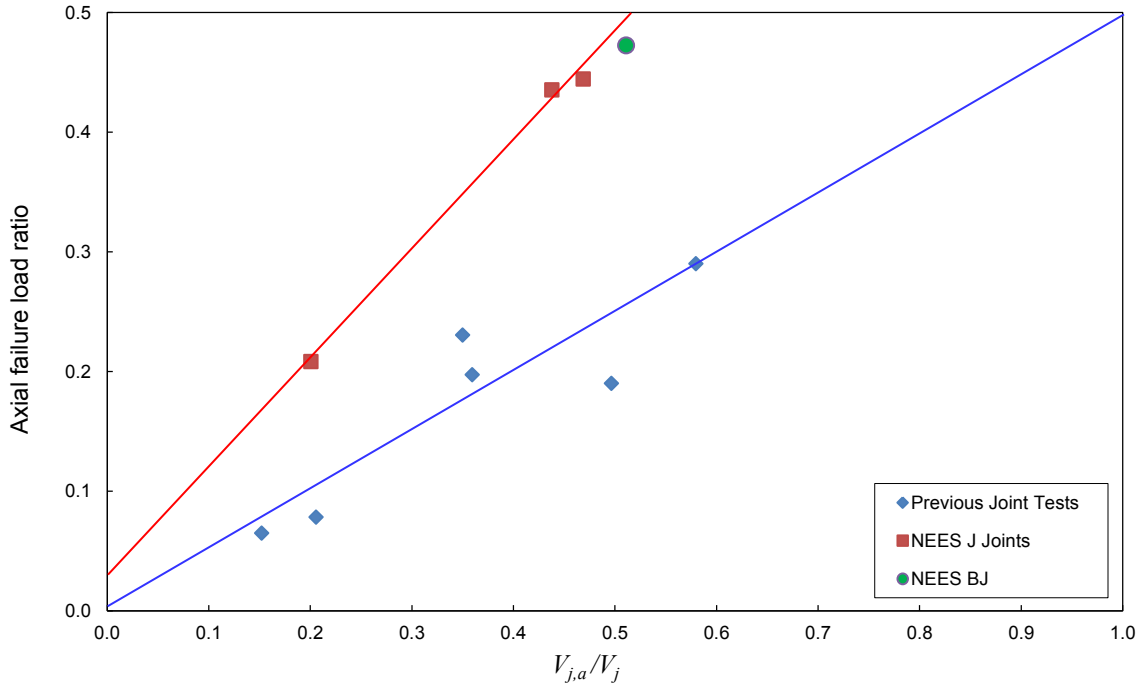

Figure 8.12 Relation between residual joint shear capacity and axial failure load ratio

8.5 AXIAL CAPACITY MODEL FOR COLUMNS

Elwood and Moehle [39] developed an axial capacity model for shear critical columns based on the shear-friction concept (Fig. 8.13) and observations from laboratory tests on columns with light transverse reinforcement ratio. The model aimed at developing an axial load-drift ratio expression at axial failure. Two concepts were investigated; the first is the total capacity model where the sum of shear-friction mechanism axial capacity and column bar capacity are summed to give the total axial column capacity. The second is the maximum capacity model where the maximum of the axial capacity of shear-friction mechanism and that of column bar capacity is used to determine the column axial capacity. Elwood showed that the shear friction mechanism is the main axial load resistance mechanism after shear failure for the available column tests. Accordingly, he developed an expression for drift capacity at axial failure of columns as:

$$\left(\frac{\Delta}{L}\right)_{axial} = \frac{4}{100}\frac{1+(\tan\theta)^2}{\tan\theta + P\left(\dfrac{s}{A_{st} f_{yt} d_c \tan\theta}\right)} \tag{8.5}$$

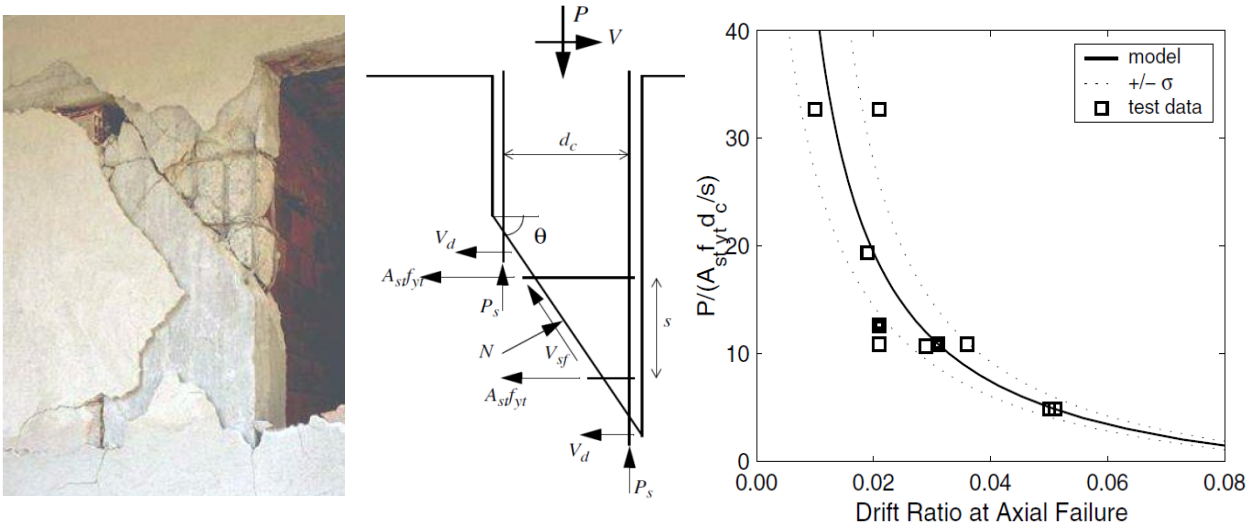

Figure 8.13 (a) Damaged column from 1999 Kocaeli earthquake,
(b) Free body diagram of column at shear failure, (c) Model correlation to test results, Elwood and Moehle [39]

The model shows good correlation with test results. However, it was based on relatively small number of tests. Some model deficiencies were reported by Elwood and Moehle [39].

8.6 PROPOSED AXIAL CAPACITY MODELS FOR UNCONFINED JOINTS

Based on Elwood and Moehle [39] axial capacity model for columns, an analogous model for application to unconfined joints is proposed. The model is based on observation of axial failure modes. The model assumes that the primary failure mechanism is along a shear friction surface, with column longitudinal reinforcement acting in axial load providing a secondary mechanism triggered after shear-friction failure on the shear failure plane. This section presents two axial capacity models for unconfined beam-column joints. These models are intended to be used with joints experiencing J-shear failure mode with any axial load level and BJ-failure mode with axial load ratio below 0.3. As discussed in a previous section, the axial failure of a BJ shear failure controlled joint under high axial load is not likely until very large drifts.

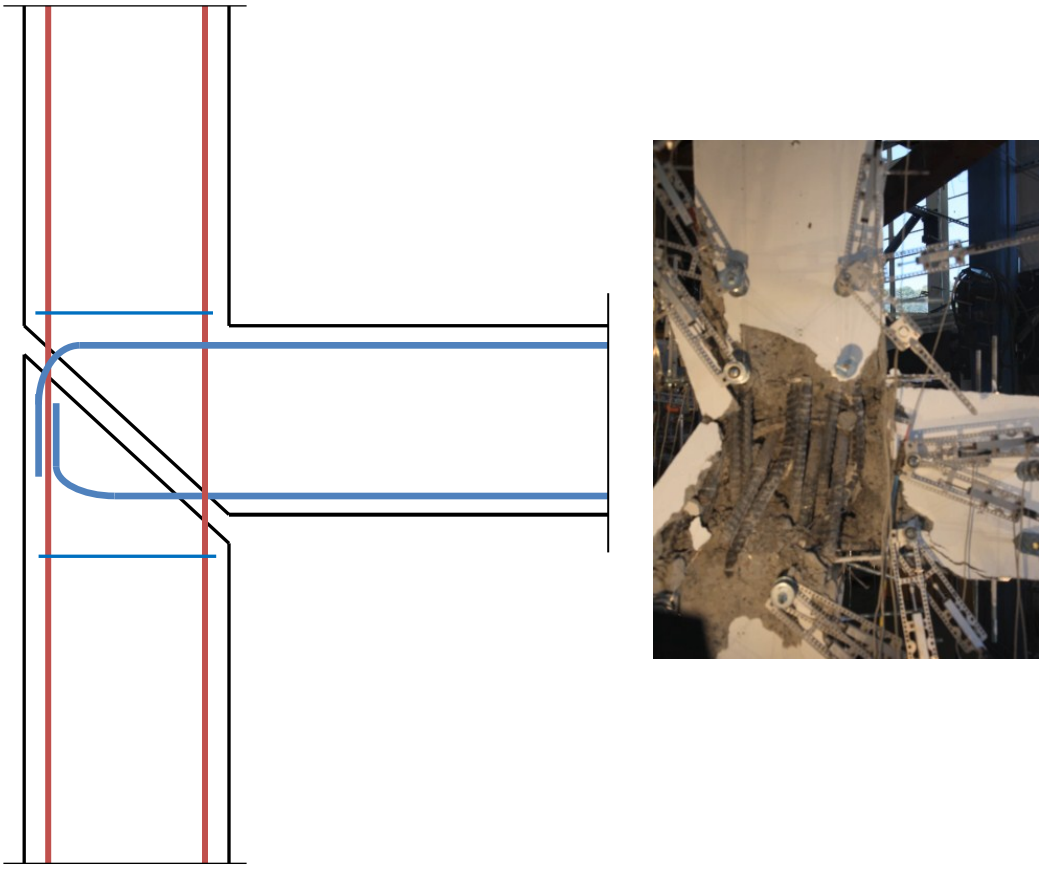

Figure 8.14 Development of shear-friction model for joint axial capacity based on experimental observation, (a) Proposed sliding mechanism, (b) Observed damage after axial failure, specimen U-J-1

8.6.1 Analytical Shear-Friction Capacity Model

8.6.1.1 ASSUMPTIONS AND EQUILIBRIUM EQUATIONS

After joint shear failure along the major diagonal crack corresponding to the inclination of the main diagonal concrete joint strut, shear resistance starts to degrade. In many cases, however, the axial load at peak displacement does not immediately drop as discussed in detail in Chapter 6. Substantial axial load from the upper column must be transferred across the joint shear failure surface. Experimental observation of joint axial failure, Sec. 8.3, suggests transferring this axial load by shear-friction across the shear failure plane. Several shear-friction models are available; however, the classical shear-friction model adopted by ACI 318-08 [1] and used by Elwood and Moehle [39] for shear-critical columns is used here.

Figure 8.15 shows the free body diagram of the upper block of the beam-column joint subassembly after shear failure. The critical crack angle can be calculated using the strut-and-tie model developed in Chapter 5 for joint shear strength. The axial failure is evident to take place during the downward loading of beam. Some simplifying assumptions will be made next.

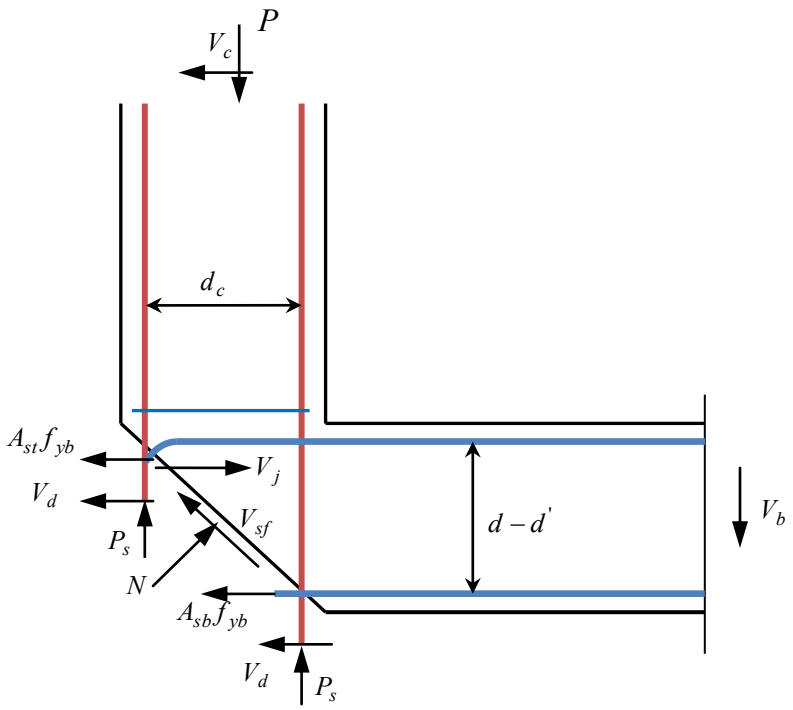

Figure 8.15 Free body diagram for beam-column joint at the onset of axial failure

Since the beam shear force $V_{b,a}$ and joint shear force $V_{j,a}$ at axial failure are not always insignificant (Fig. 8.11) like the case of columns (Elwood and Moehle [39]), they cannot be neglected in formulating the equilibrium equations. The dowel action provided by the

longitudinal column and beam reinforcement will be implicitly included in the shear friction resistance $V_{sf;}$ hence they will not appear in the equilibrium equations. The total axial capacity of column reinforcement bars is denoted ΣP_s. The beam longitudinal reinforcement will act as shear-friction reinforcement holding the lower concrete block (the column) from separation. At the axial failure, the force in both top and bottom longitudinal beam bars will be tensile within the joint regardless the sense of the force within beam span.

The top beam longitudinal reinforcement appears to be less efficient in resisting shear friction since it experiences bond failure at earlier stage. More importantly, the portion of the top beam bars holding the lower concrete block is usually the hook tail which is very poorly embedded and bonded to concrete at late stages of loading because of cover spalling or detachment. Accordingly, the resistance of top beam bars will not be included in the equilibrium equations.

Based on the abovementioned simplifying assumptions, the equilibrium equations in the horizontal and vertical directions can be respectively written as:

$$N \sin\theta + V_j = V_{sf} \cos\theta + A_{sb} f_{yb} + \Sigma . V_d \tag{8.6}$$

$$P + V_b = N \cos\theta + V_{sf} \sin\theta + \Sigma . P_s \tag{8.7}$$

The proposed model assumes that joint axial capacity is primarily dependent on shear-friction mechanism. Column longitudinal axial capacity is considered secondary to shear-friction mechanism, which is triggered only after shear-friction failure. The calculation of axial capacity of column bars presented in Section 8.3 shows that this capacity is relatively small. Even if a portion of axial load is supported by column bars immediately before axial failure, suggesting a concurrent collective mechanism, this portion is insignificant as suggested by Elwood and Moehle [39] and will be shown shortly. Accordingly, this quantity will not be included in the equations presented next.

8.6.1.2 EFFECTIVE COEFFICIENT OF FRICTION

The classical shear-friction model assumes that shear friction resistance across the shear failure plane is a function of an effective coefficient of friction μ, which is related to the shear-friction capacity by the compression force N normal force to the shear failure plane as:

$$V_{sf} = \mu_{sf} N \tag{8.8}$$

The effective shear friction coefficient will be estimated from fitting test data for the joints used in the axial failure dataset. Substituting Eq. 8.11 into Eq. 8.9 and 8.10 and manipulating to obtain an expression the effective shear-friction coefficient gives:

$$\mu_{sf} = \frac{(P + V_{b,a})\tan\theta + (V_{j,a} - A_{sb}f_{yb})}{(P + V_{b,a}) - (V_{j,a} - A_{sb}f_{yb})\tan\theta} \tag{8.9}$$

The coefficient of friction using Eq. 8.12 is plotted in Fig. 8.16 against the drift ratio at axial failure for the joint database. Some friction coefficient values at very large drift were meaninglessly negative. Thus, a minimum value of μ of 0.01 is used. A general inverse proportionality between coefficient of friction and drift ratio at axial failure can be observed. This relation is intuitive since it reflects concrete roughness deterioration at the shear-friction plane with larger drifts. A linear fit, however, does not seem reasonable. Thus, a power fit is proposed between coefficient of friction and drift ratio at axial failure as:

$$\left(\frac{\Delta}{L}\right)_{axial} = 0.031\mu_{sf}^{-0.25} \tag{8.10}$$

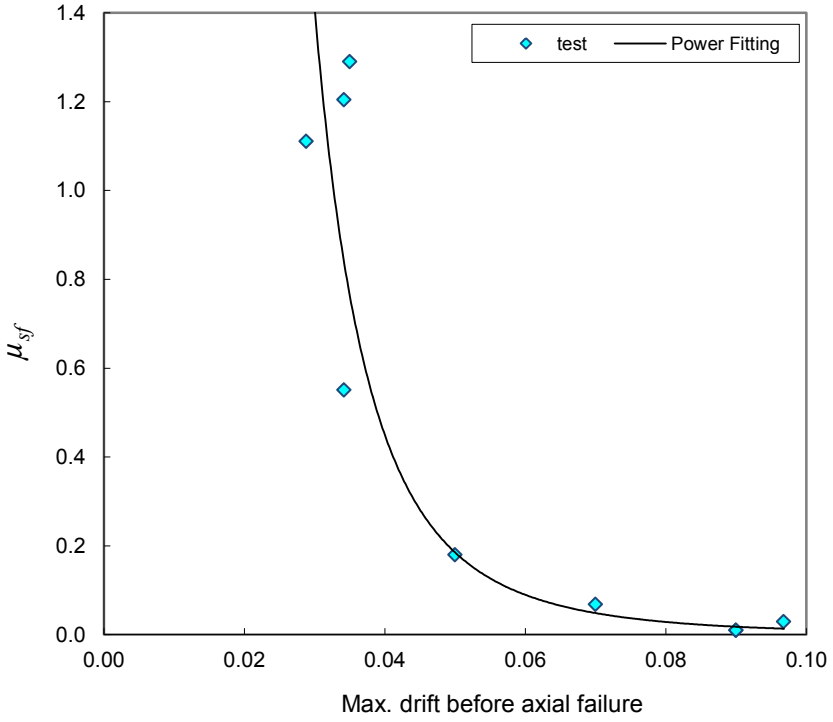

Figure 8.16 Relation between effective coefficient of friction and drift at axial failure

Another relation similar to that in Fig. 8.16 for the effective coefficient of friction including the effect of axial capacity of column longitudinal bars was found to be almost identical to Fig. 8.16 indicating insensitivity to column bar capacity before axial failure and confirming the progressive nature of axial failure mechanism. That is the shear-friction capacity is governing the joint axial capacity, whose failure transfers the axial load to column bars that immediately deform and experience axial failure. The joint axial capacity can be then expressed as:

$$P = \left[A_{sb} f_{yb} - V_{j,a}\right] \frac{(1 + \mu_{sf} \tan\theta)}{\tan\theta - \mu_{sf}} - V_{b,a} \tag{8.11}$$

The drift ratio capacity at axial failure can be expressed as:

$$\left(\frac{\Delta}{L}\right)_{axial} = 0.031 \left\{ \frac{(P + V_{b,a}) \tan\theta + (V_{j,a} - A_{sb} f_{yb})}{(P + V_{b,a}) - (V_{j,a} - A_{sb} f_{yb}) \tan\theta} \right\}^{-0.25} \tag{8.12}$$

This model requires knowing the joint shear and beam shear forces at axial failure. This is a challenging task since no clear correlation can be found that fits all joints in the dataset between drift ratio at axial failure and ratio of shear forces at axial failure to those at peak joint shear strength. However, a clear linear trend can be seen for the subset (previous joint tests) with more than two loading cycles per displacement step, and a different linear proportionality for the NEES joint subset as seen in Fig. 8.11 and Fig 8.12. Here we adopt the trend observed for the NEES joints.

The following expression can be used to estimate joint shear strength and beam shear strength at axial failure in relation to axial failure load and to their counterparts at peak joint shear strength:

$$V_{j,a} = \left(1.1 \frac{P}{f_c' A_j} - 0.03\right) . V_j = \chi_a V_j \tag{8.13}$$

$$V_{b,a} = \left(1.1 \frac{P}{f_c' A_j} - 0.03\right) . V_b = \chi_a V_b \tag{8.14}$$

or related to maximum drift reached before axial failure

$$\left(\frac{\Delta}{L}\right)_{axial} = 0.25 \left(\frac{V_{j,a}}{V_j}\right) + 0.15 \tag{8.15}$$

where χ_a is equal or greater than zero. The joint shear force V_j and beam shear force V_b at peak joint shear strength can be estimated using the shear strength strut-and-tie model developed in Chapter 5 as:

$$V_j = \gamma_{j,STM} \cdot \sqrt{f_c'} A_j \tag{8.16}$$

$$V_b = \frac{1}{\frac{L - h_c/2}{jd_b} - \frac{L}{H}} = \chi V_j \tag{8.17}$$

Substituting Eq. 8.16 and 8.17 into Eq. 8.15 gives the final expression for drift capacity at axial failure:

$$\left(\frac{\Delta}{L}\right)_{axial} = 0.031\left\{\frac{(P + \chi\chi_a V_j)\tan\theta + (\chi_a V_j - A_{sb} f_{yb})}{(P + \chi\chi_a V_j) - (\chi_a V_j - A_{sb} f_{yb})\tan\theta}\right\}^{-0.25} \tag{8.18}$$

where

$$\left\{\frac{(P + \chi\chi_a V_j)\tan\theta + (\chi_a V_j - A_{sb} f_{yb})}{(P + \chi\chi_a V_j) - (\chi_a V_j - A_{sb} f_{yb})\tan\theta}\right\} \geq 0.01 \tag{8.19}$$

Substituting Eq. 8.13, 8.14 8.16 and 8.17 into Eq. 8.12 gives the joint axial capacity for a given drift ratio. More test data regarding axial failure of exterior and corner beam column joints is needed to refine and validate the expressions for lateral load capacity at axial failure.

8.6.2 Empirical Shear-Friction Capacity Model

The above theoretically based shear-friction model is plausible if enough knowledge on the residual joint shear capacity at axial failure can be confirmed. It also contains two empirical components, namely the estimation of effective shear-friction coefficient and the residual shear capacity at axial failure. The model is delivered finally in a rather lengthy expression. These factors motivated investigating the possibility of the presence of a trend between drift ratio and the axial failure load normalized by the influential parameters of the shear-friction phenomenon. The goal of this attempt was to develop a simpler empirical expression for quick estimation of drift capacity at axial failure eliminating the need for residual joint shear strength at axial failure.

To achieve this goal, a simple expression based on the linear trend observed in Fig. 8.17 for NEES joints and for previous joint tests (with no slab and more cycles per drift level) that experienced axial failure can be formed as:

For NEES Joints:

$$\left(\frac{\Delta}{L}\right)_{axial} = 0.15 - 0.27\left(\frac{P}{f_c' A_j}\right) \tag{8.20.a}$$

For Previous Joint Tests:

$$\left(\frac{\Delta}{L}\right)_{axial} = 0.11 - 0.28\left(\frac{P}{f_c' A_j}\right) \tag{8.20.b}$$

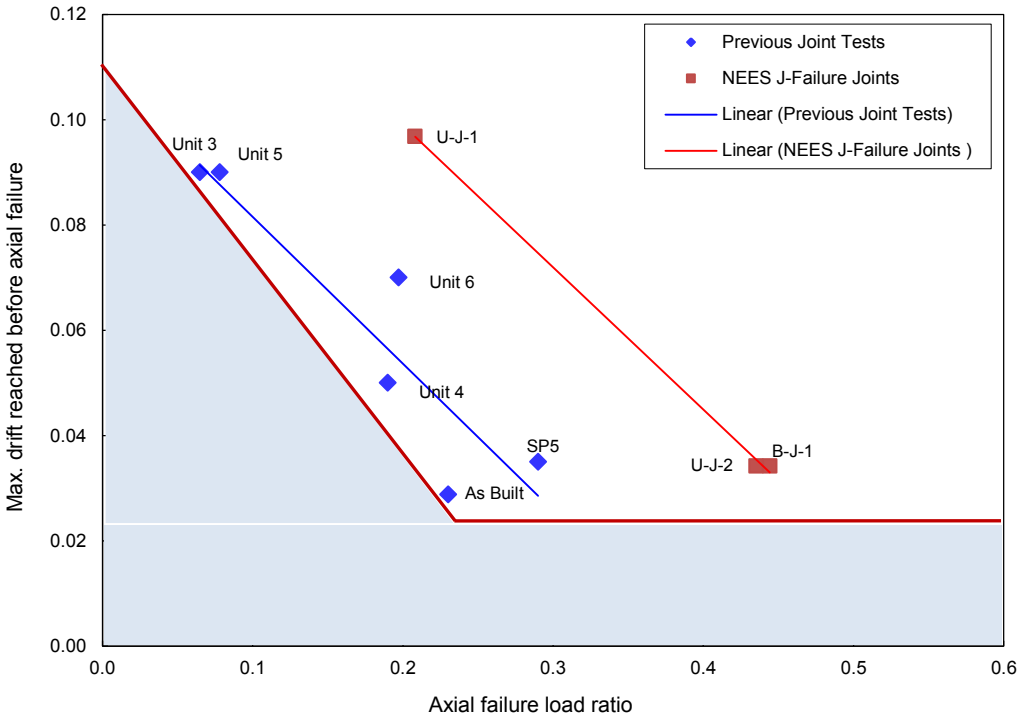

Figure 8.17 Linear trends of axial failure load-drift ratio relationship

Equation 8.20 is a generic empirical relation that can be used for preliminary purposes unless more test data is available to confirm it.

Another empirical expression can be developed based on shear friction influence parameters. Figure 8.18 shows the relationship between drift ratio at axial failure and the axial failure load normalized by beam bottom reinforcement strength (acting as shear friction reinforcement) and the critical angle of inclination of the crack, a key parameter in beam-column joint shear and axial capacity. The figure suggests an inverse proportionality similar to that noticed before between effective shear friction coefficient and drift capacity. This implies that a power based relationship can be fitted directly relating drift ratio and normalized axial load as:

$$\left(\frac{\Delta}{L}\right)_{Axial} = 0.057\left(\frac{P.\tan\theta}{A_{sb}f_{yb}}\right)^{-0.5} \tag{8.21}$$

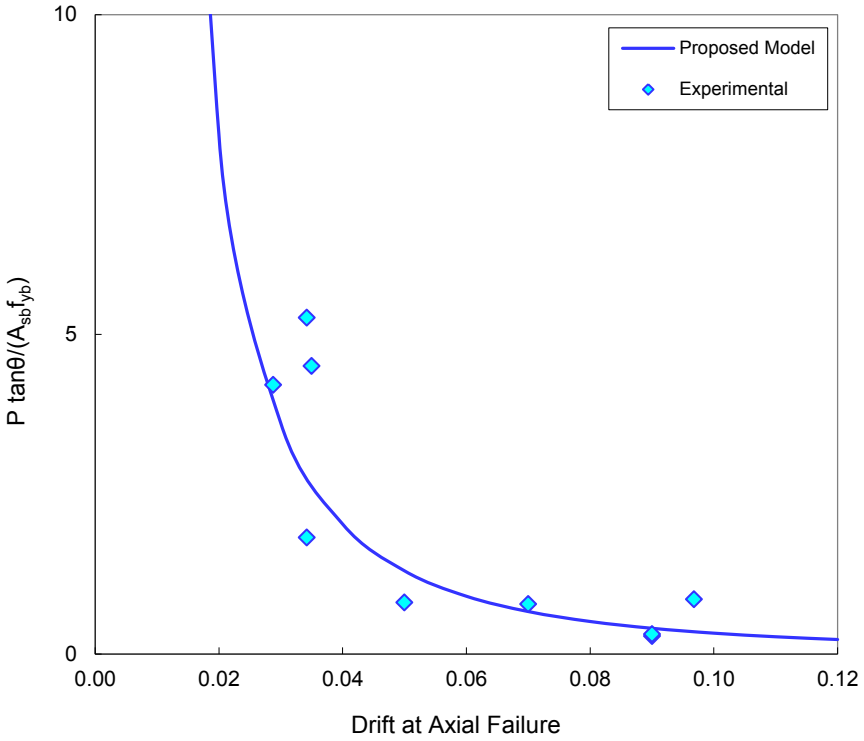

Figure 8.18 Proposed empirical model (Eq. 8.21) for drift capacity at axial failure

It was worthy also investigating the influence of other important parameters such as the concrete strength, joint effective area and column longitudinal reinforcement strength. These factors are common in axial capacity studies of columns. Figure 8.19 shows that expression 8.21 is relatively insensitive to concrete strength suggesting the validity of the shear-friction mechanism. Slight sensitivity and weaker correlations were noticed when axial load was normalized by column longitudinal reinforcement capacity as shown in Fig. 8.20.

This above discussion suggests the appropriateness of the empirical expression 8.21 for quick estimation of drift capacity at joint axial failure. It is important to notice that this expression is based on a rather small joint axial failure database. Thus, more joint axial failure tests are needed to further verify this relation. In addition, it is worth mentioning that this expression is suitable for J-Failure joints with any axial load ratio, BJ-Failure joints with small axial load ratio, and BJ-Failure with high axial load ratio when the flexural capacity of the beam is close to the direct J-Failure strut-and-tie model capacity. The case of high axial load on a joint in a subassembly where the beam flexural capacity is much smaller than the direct J-failure capacity is excluded from the application of this model for reasons mentioned earlier.

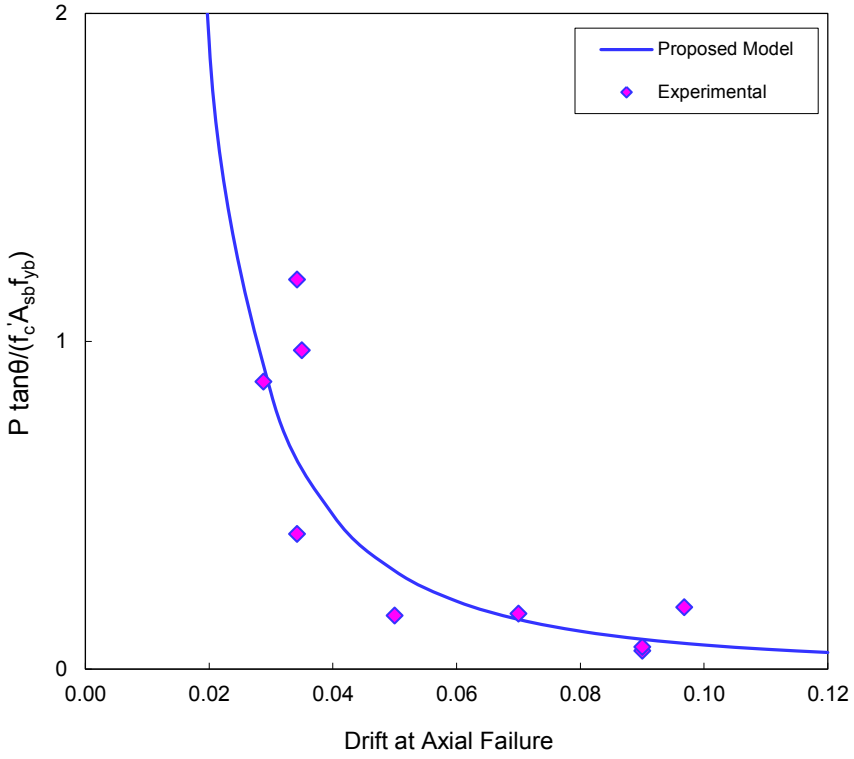

Figure 8.19 Proposed empirical model (Eq. 8.24) normalized by concrete strength

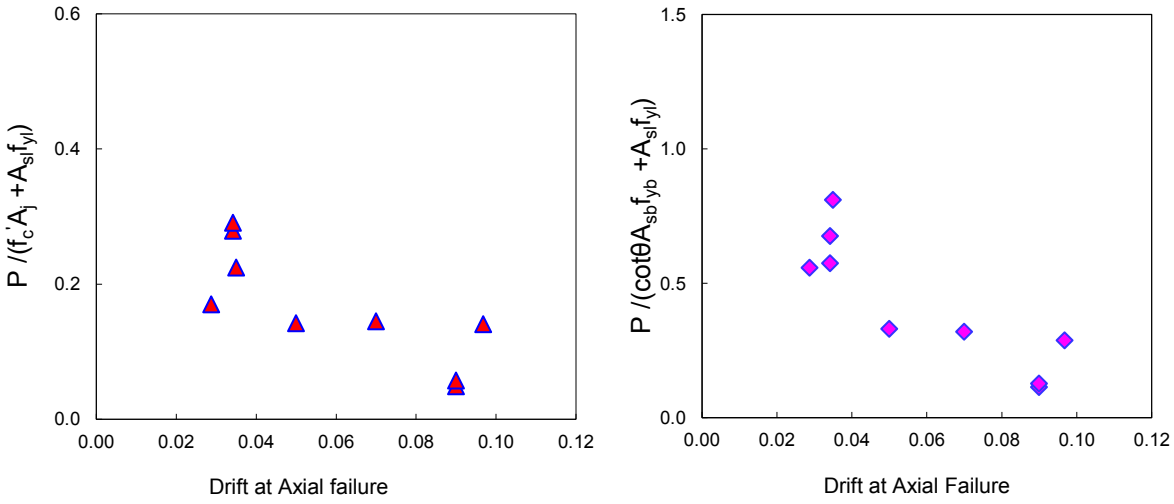

Figure 8.20 Effect of concrete strength and column steel strength on drift capacity at axial failure

8.6.3 Proposed Models Evaluation

Figure 8.21 presents the correlation of the experimental drift capacity at axial failure to the calculated one using the shear-friction model for axial capacity (Eq. 8.18). The average test to model drift ratio is 1.00 and the COV is 0.27. It is also worth mentioning that residual shear capacity at axial failure is based on the NEES joint results; which led to the drift for other tests loaded with greater number of displacement cycles to be overestimated by the model.

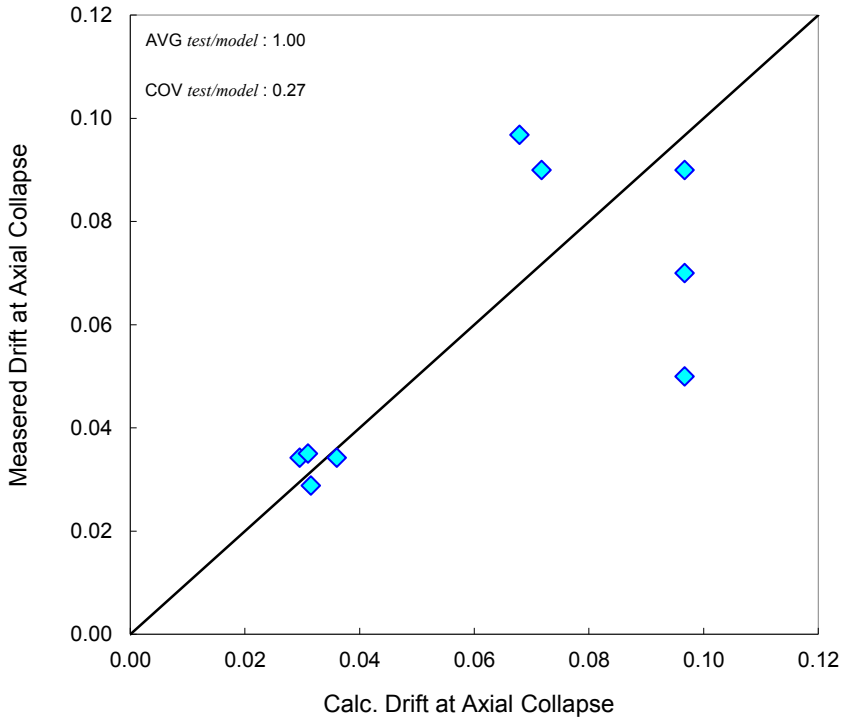

Figure 8.21 Correlation of the proposed axial capacity model (Eq. 8.18) to test results

The empirical axial capacity model proposed by Eq. 8.21 is evaluated against test results in Fig. 8.22. The ratio of test to model drift capacity as mean of 1.07 and COV of 0.26. Note that The calculated drift for specimen U-J-1 is underestimated by about 43%. Recall that the axial load for this test specimen dropped after onset of shear failure. It is plausible that the drift ratio would have been decreased had the axial load remained high.

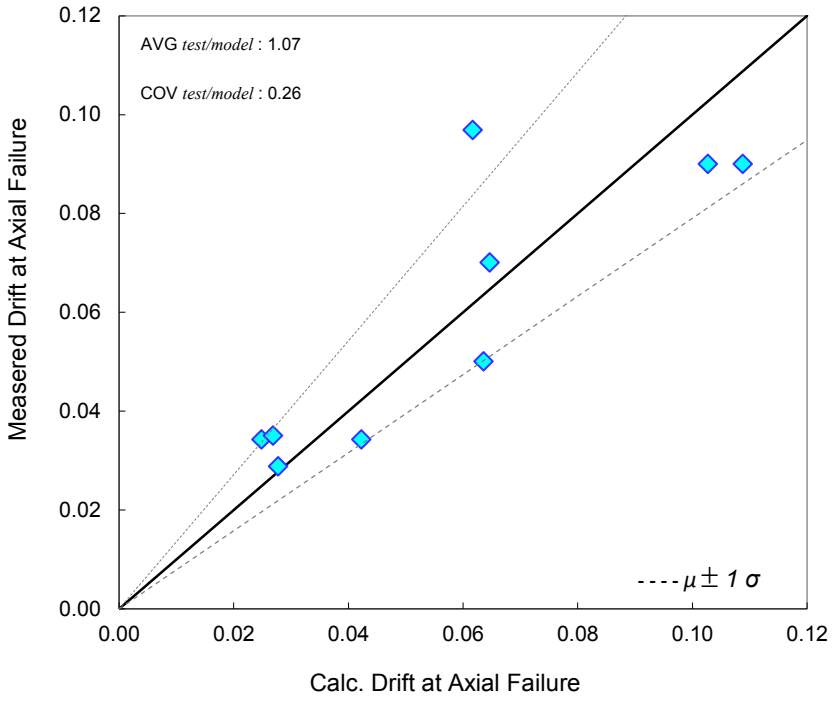

Figure 8.22 Correlation of the proposed axial capacity empirical model (Eq. 8.21) to test results

8.7 AXIAL COLLAPSE VULNERABILITY OF SHEAR DEFICIENT BUILDINGS

Past earthquake reconnaissance reported building failure and collapse in which joint damage was apparent along with other critical types of failure. A key question is whether joint failure triggered the collapse or whether instead joint failure was a consequence of some other triggering mechanism. To provide a preliminary answer to this question, a simple study was carried out to compare drift capacities of vulnerable columns and vulnerable beam-column joints.

8.7.1 Axial Failure Vulnerability: Parametric Study

A parametric study was carried out using the prototype frame building shown in Figure 8.24. 8.24). Joint deformation capacity was based on the empirical model reported previously (Eq. 8.24), while column deformation capacity was based on Elwood and Moehle [39]. Different building configurations, joint dimensions, and axial loads were explored to determine whether joint or column axial failure would be first to occur.

The main parameters in this parametric study reflect the design parameters of concern of the proposed joint empirical model (Eq. 8.24). These parameters are beam span to column height ratio, beam reinforcement ratio, beam to column depth ratio and column transverse reinforcement volumetric ratio. A matrix of 81 different combinations of design parameters such as joint dimensions, beam bottom longitudinal reinforcement and column transverse reinforcement ratio was developed. These 81 combinations shown in Table 8.2 are thought to cover wide spectrum of practical ranges of these design parameters. The mode of shear failure of all the joints considered in this parametric study is a J-Failure mode. The BJ-Failure mode was excluded since it has a very low probability of axial failure based on the results of the current investigation.

Table 8.2 Parametric study matrix

Beam Span *2L*	Column transverse reinforcement	Beam depth h_b= 18 in.			Beam depth h_b= 27 in.			Beam depth h_b= 40 in.		
		ρ_1	ρ_2	ρ_3	ρ_1	ρ_2	ρ_3	ρ_1	ρ_2	ρ_3
15 ft.	ρ_1'' =0.001	0.013	0..015	0.018	0.008	0.01	0.011	0.0057	0.0068	0.0079
	ρ_2''=0.0015	0.013	0..015	0.018	0.008	0.01	0.011	0.0057	0.0068	0.0079
	ρ_3''=0.002	0.013	0..015	0.018	0.008	0.01	0.011	0.0057	0.0068	0.0079
		h_b= 24 in.			h_b= 36 in.			h_b= 54 in.		
20 ft.	ρ_1'' =0.001	0.009	0.011	0.013	0.006	0.007	0.009	0.0047	0.0056	0.0066
	ρ_2''=0.0015	0.009	0.011	0.013	0.006	0.007	0.009	0.0047	0.0056	0.0066
	ρ_3''=0.002	0.009	0.011	0.013	0.006	0.007	0.009	0.0047	0.0056	0.0066
		h_b= 30 in.			h_b= 45 in.			h_b= 68 in.		
25ft.	ρ_1'' =0.001	0.007	0.0086	0.01	0.005	0.006	0.007	0.0044	0.0052	0.006
	ρ_2''=0.0015	0.007	0.0086	0.01	0.005	0.006	0.007	0.0044	0.0052	0.006
	ρ_3''=0.002	0.007	0.0086	0.01	0.005	0.006	0.007	0.0044	0.0052	0.006

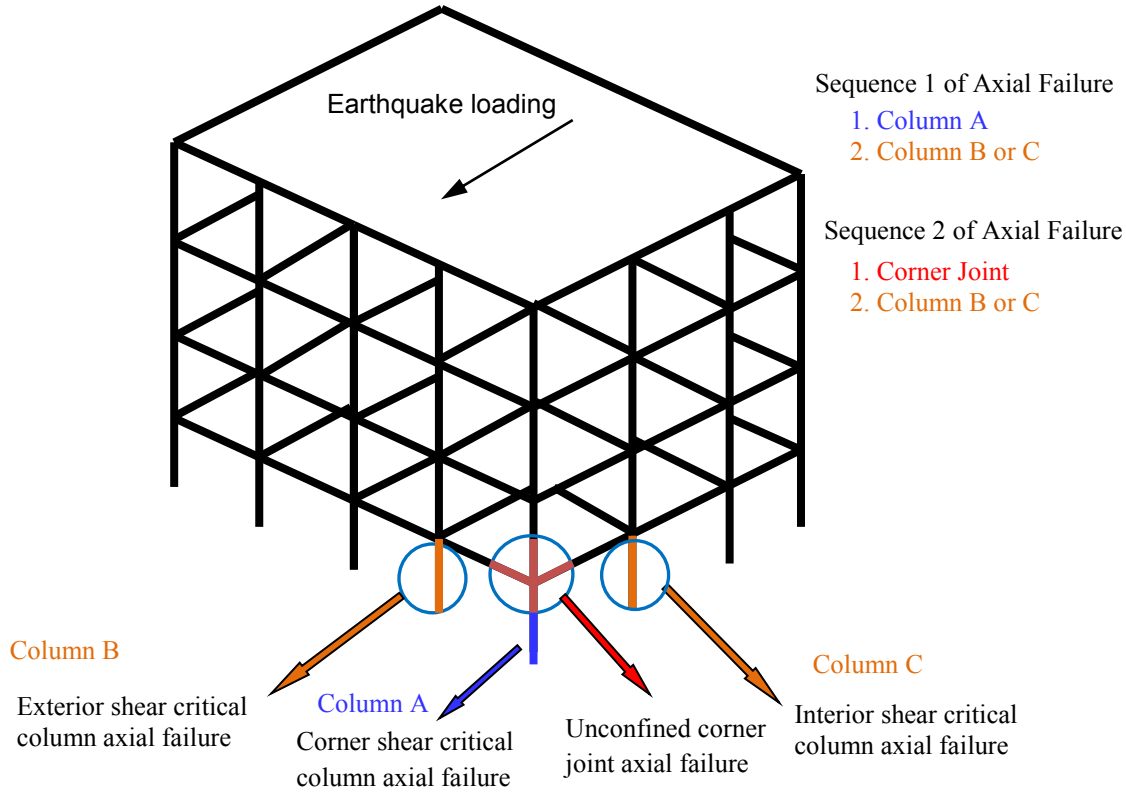

Figure 8.23 Axial failure vulnerability of shear critical joints and columns

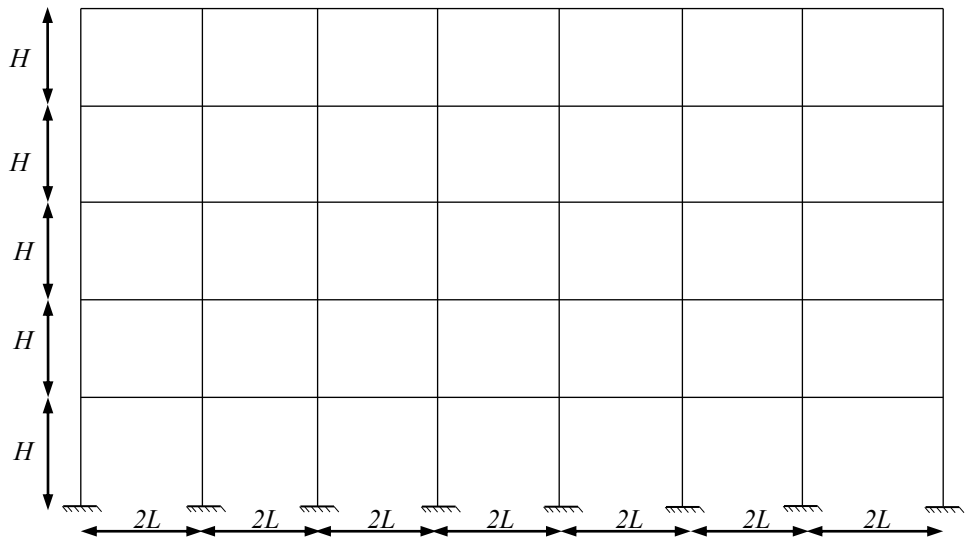

Figure 8.24 Fictitious frame for parametric study

Column height was fixed as 10 feet while column dimensions were fixed as 16x16 inches. Yield strengths f_{yc} and f_{yb} were chosen to be 50 ksi, consistent with older building construction and

concrete compressive strength f_c' was 4000 psi. Column hoop diameter was 0.375 inch, with a transverse reinforcement ratio varied by hoop spacing. Beam width was 16 inch.

The beam span to column height ratios *2L/H* of 1.5, 2 and 2.5 are selected to represent common frame configurations. In gravity building design, the beam depth is determined based on ultimate capacity and checked against deflection requirements. Alternatively, a minimum recommended depth to avoid deflection checks is recommended by ACI 318 [1]. Three beam depths were chosen for each beam span to column height ratio. The first beam depth was chosen based on these requirements for exterior spans. The second depth was arbitrary chosen as 1.5 times the first depth and similarly the third depth was chosen as 1.5 times the second beam depth.

Three different beam bottom reinforcement ratios were chosen. The first reinforcement ratio was chosen to correspond to the minimum reinforcement ratio to guarantee J-Failure mode, implicitly assuming equal top and bottom beam reinforcement. This ratio was checked against ACI 318 [1] minimum flexural reinforcement ratio and proved to be always higher than it. The second and third beam reinforcement ratios were arbitrarily amplified by the factors of 1.2 and 1.4 to cover the cases of high live loads.

It was decided to choose design parameters based on the above rationale rather than performing actual designs of the building for simplicity reasons. This allowed covering broader range of building configurations than would otherwise have been feasible. Finally this enabled focus on only joints sustaining J-Failure mode.

Three different column volumetric transverse reinforcement ratios ρ'' were used. The first is 0.002, which reflects a borderline shear critical column as indicated by ASCE 41 [11]. The other two ratios are 0.001 and 0.0015.

8.7.2 Analysis Results of Parametric Study

Figures 8.25 through 8.27 show the results of the parametric study, expressed in terms of axial load-drift ratio at axial failure. Red arrows indicate the point at which joint axial failure becomes more critical than column axial failure for the most critical configurations. It can be observed that generally column axial failure precedes joint axial failure for most design configurations. However, for critical shear-friction angle (or strut angle) higher than 2 (which reflects joint aspect ratio α_j of about 1.7) with relatively low beam reinforcement ratio (lower than 0.01), joint axial failure preceding column axial failure is evident. However, in many cases this occurred at a drift ratio larger than 3%, which might downplay axial failure importance since other modes of failure due to P-Δ effect on the columns might take place before joint axial failure. It is worth mentioning that a range of 1-2.5 is considered a practical range for joint aspect ratio α_j.

For the special joint aspect ratios higher than 2.5, which are also frequent in many buildings, the joint axial failure hazard preceding column axial failure appears to be high, especially with low beam reinforcement ratios and borderline shear critical columns.

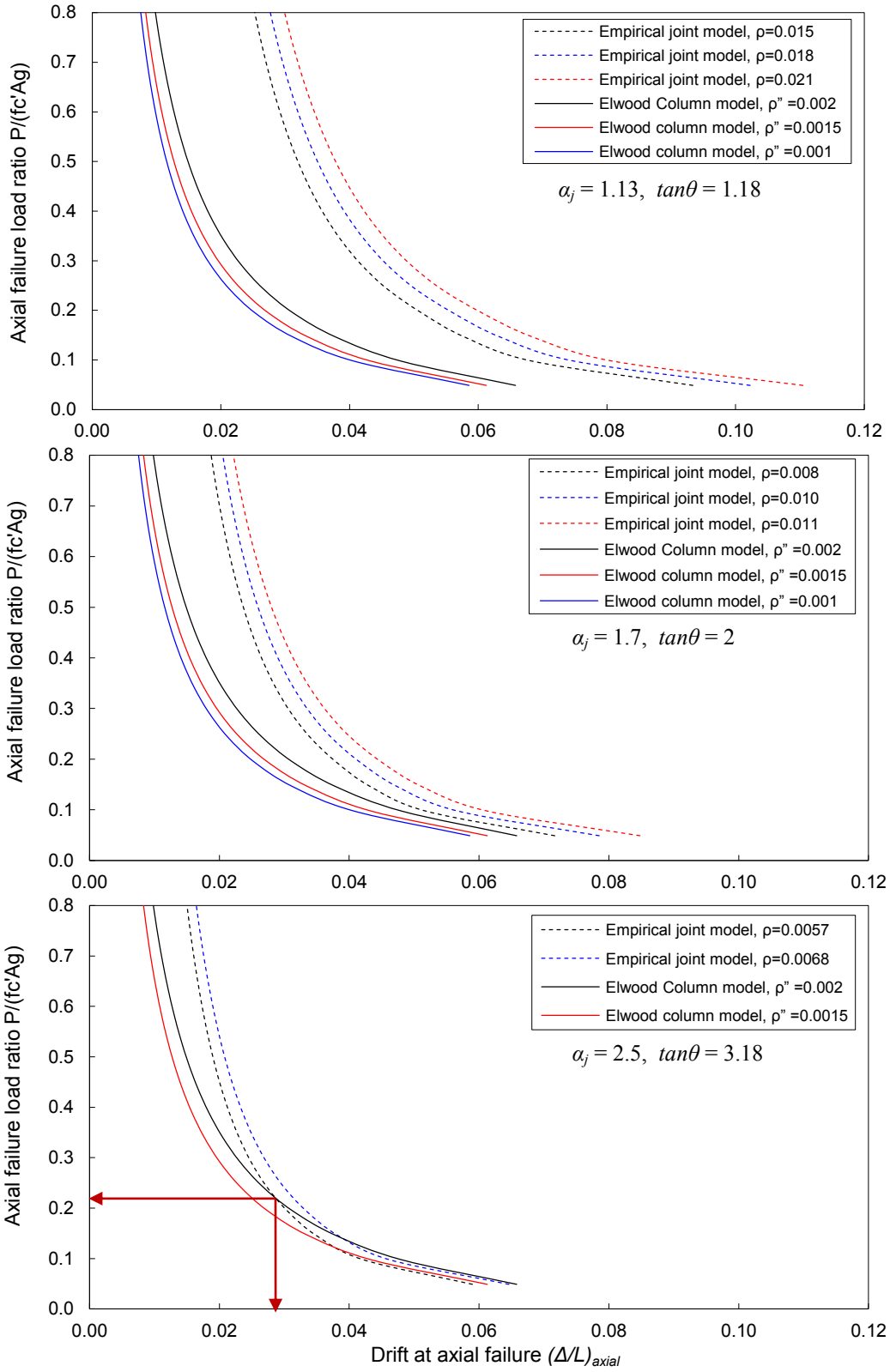

Figure 8.25 Axial failure vulnerability, *2L/H*=1.5

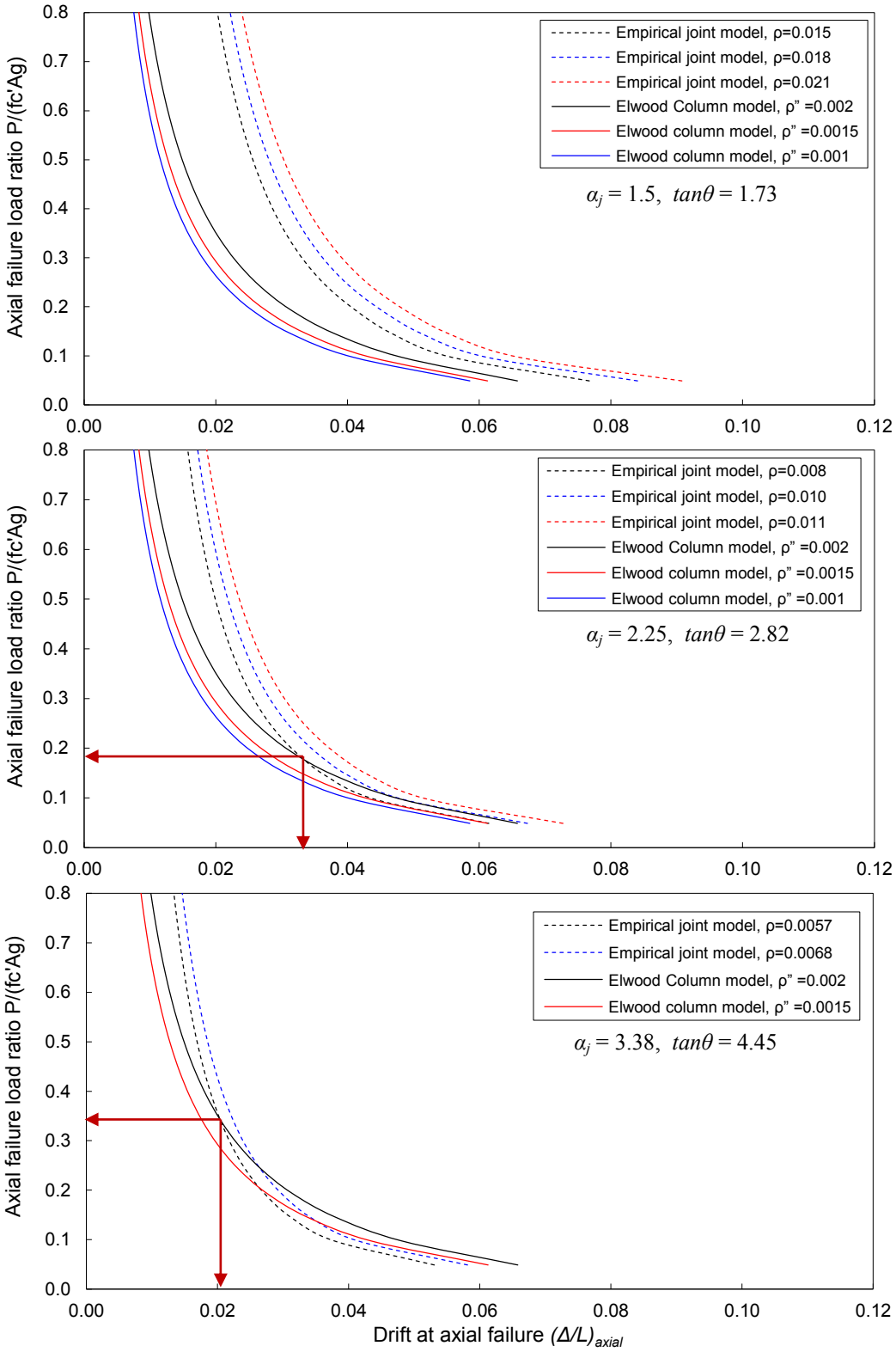

Figure 8.26 Axial failure vulnerability, *2L/H*=2

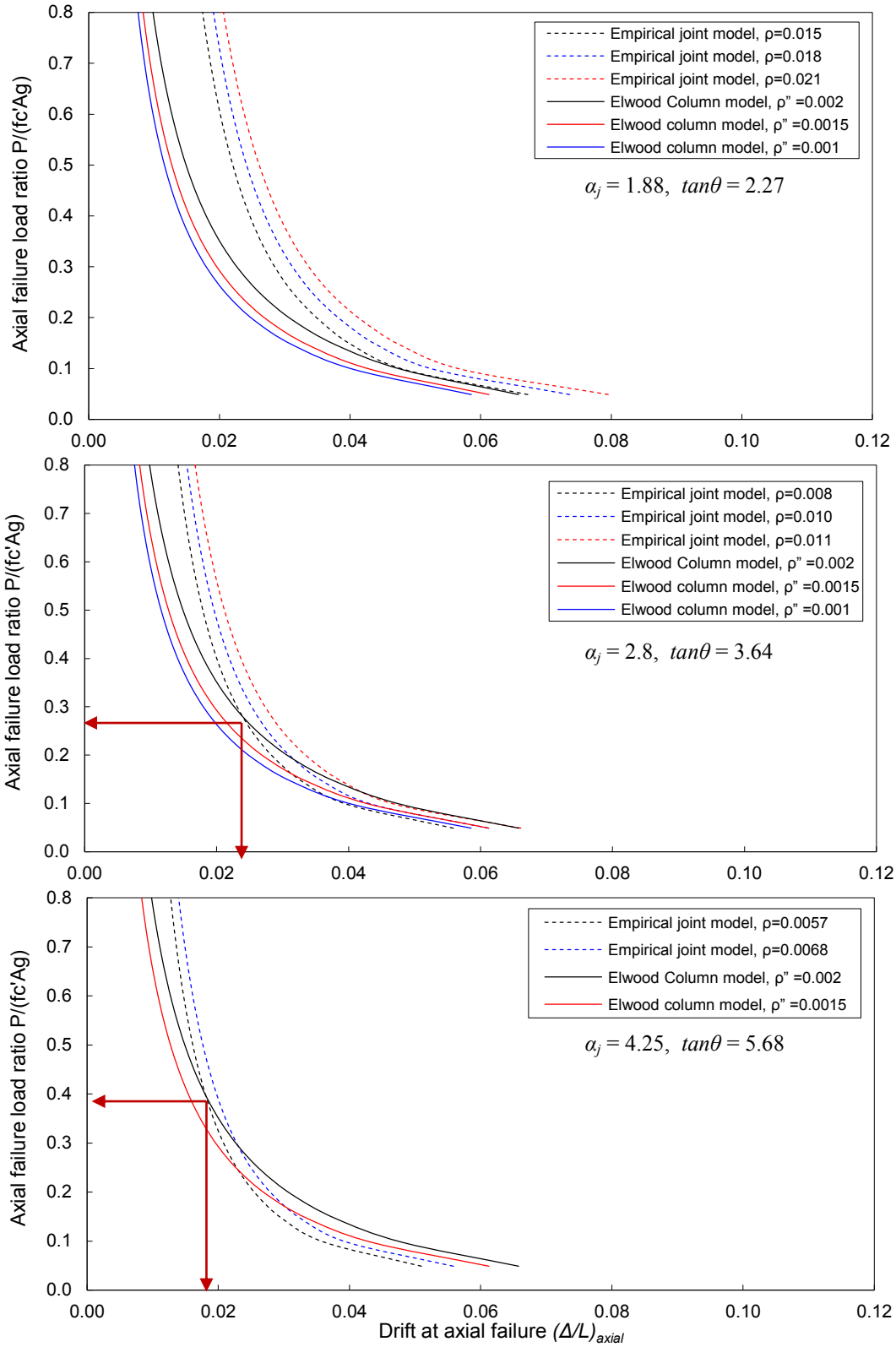

Figure 8.27 Axial failure vulnerability, *2L/H*=2.5

CHAPTER 9

ANALYTICAL BEAM-COLUMN JOINT MODEL FOR FINITE ELEMENT BUILDING SIMULATION

9.1 INTRODUCTION

This chapter develops a model for the cyclic stress-deformation behavior of exterior and corner unconfined beam-column joints for use in finite element numerical simulation of concrete frames of older-type buildings. The chapter briefly presents the available joint component models used for practical and research purposes. A new nonlinear backbone constitutive model for joint simulation also is proposed. The model is used to simulate the cyclic response of the test specimens of the current study presented in Chapter 7. Model calibration and validation using previous unconfined beam-column joint tests is also performed.

9.2 MODELING JOINT BEHAVIOR IN FINITE ELEMENT ANALYSIS

9.2.1 EXISTING PANEL ZONE JOINT MODELING TECHNIQUES

9.2.1.1 CONVENTIONAL CENTERLINE FRAME ANALYSIS

It has been accepted for long time in engineering practice to model the beam-column joints in concrete frame simulation as rigid joints. In one version of this the joint is treated as a completely rigid element having dimensions equal to those of the joint. Some analysts have recognized that such model overestimates stiffness and instead have used a model in which the beam and column flexibilities extend to the joint centerline, as shown in Fig. 9.1. Previous studies [23] have shown that the completely rigid joint model with finite dimensions overestimates stiffness and underestimates drift because of shearing deformations of the joint as well as slip of reinforcement from the joint. The latter model can overestimate or underestimate stiffness. In addition to underestimating drifts, this practice significantly overestimates the frame stiffness which affects the structural period and hence the attracted seismic forces. The experimental results of the current testing program, Chapter 7, showed that joint flexibility contributed significantly to overall story drift, especially in the nonlinear range. In some cases, the contribution of the beam-column joint flexibility to total drift reached 40%. This chapter

presents results of finite element simulations of several beam-column joint test subassemblies to explore analytical modeling requirements.

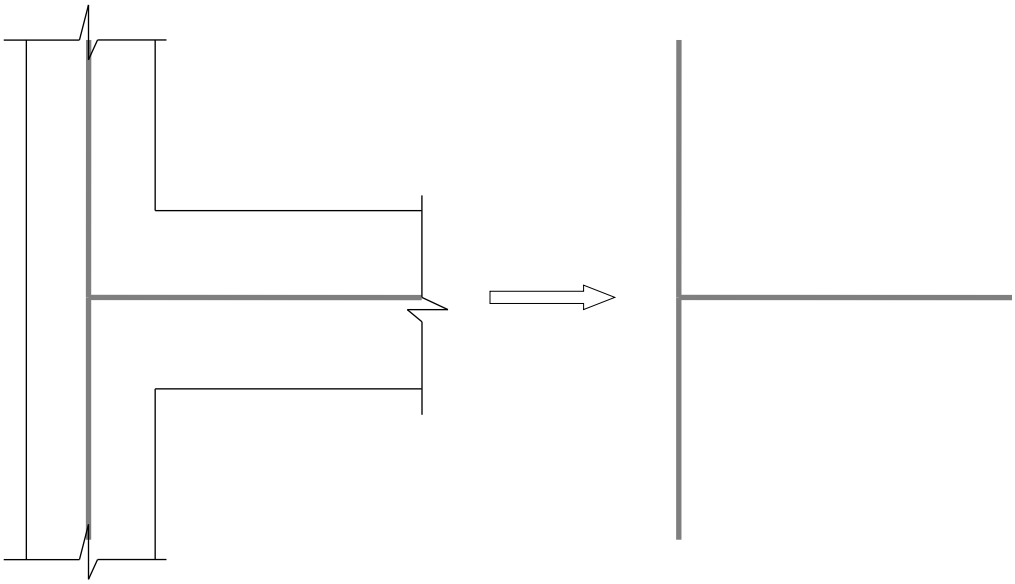

Figure 9.1 Centerline rigid joint model for concrete frame simulation

9.2.1.2 ASCE/SEI 41-06 JOINT MODEL

I. Conventional Rigid Panel Model for Linear Analysis

ASCE/SEI 41-06 [11] and ACI 369-R11 [3] suggest modeling beam-column joint in concrete frame linear analysis as a rigid panel. This is performed as depicted in Fig. 9.2 and elaborated in ASCE 41 as:

"The beam-column joint in monolithic construction shall be represented as a stiff or rigid zone having horizontal dimensions equal to the column cross-sectional dimensions and vertical dimension equal to the beam depth"

It is worth mentioning that although ASCE 41 and ACI 369-R11 ignore joint shear deformations, they account for beam bar slip rotation by suggesting reduced flexural beam stiffness.

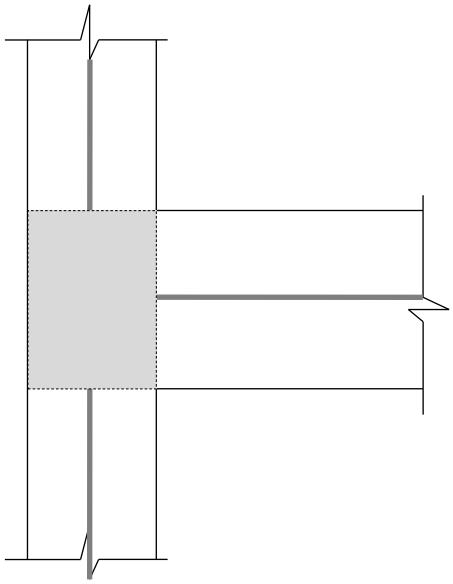

Figure 9.2 Recommended rigid joint model for linear concrete frame simulation, ASCE 41 [11]

II. Joint Model for nonlinear Analysis

ASCE 41 suggests a backbone curve, Fig. 9.3 and Table 9.1, for joint shear strain modeling in nonlinear static and dynamic analyses. However, approaches to implement this model are not described. The ASCE 41 recommended values for joint shear strength coefficient and plastic shear strain for joint modeling are shown in Fig. 9.3 and Table 9.1.

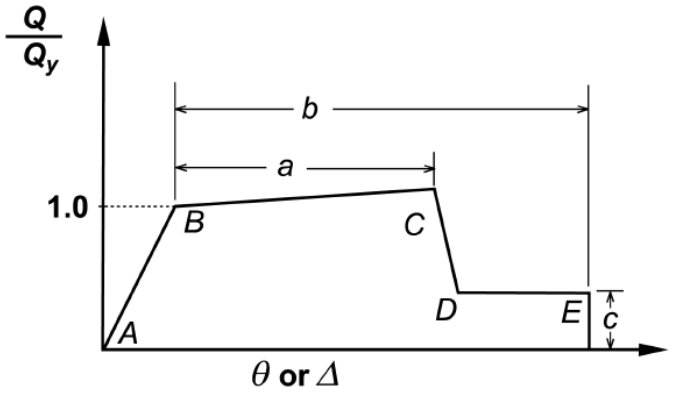

Figure 9.3 Recommended joint strength-shear deformation backbone curve for unconfined beam-column joint nonlinear modeling, ASCE 41 [11] and ACI 369 [3]

Table 9.1 Nonlinear joint modeling parameters, ASCE 41 [11] and ACI 369 [3]

Conditions			Modeling parameters*			Acceptance criteria*†				
			Plastic rotations angle, radians		Residual strength ratio	Plastic rotations angle, radians				
						Performance level				
							Component type			
							Primary		Secondary	
			a	b	c	IO	LS	CP	LS	CP
Condition i. Interior joints (Note: for classification of joints, refer to Fig. 4.2)										
$\frac{P}{A_g f_c'}$ ‡	Transverse reinforcement§	$\frac{V}{V_n}$ ‖								
≤ 0.1	C	≤ 1.2	0.015	0.03	0.2	0.0	0.0	0.0	0.02	0.03
≤ 0.1	C	≥ 1.5	0.015	0.03	0.2	0.0	0.0	0.0	0.015	0.02
≥ 0.4	C	≤ 1.2	0.015	0.025	0.2	0.0	0.0	0.0	0.015	0.025
≥ 0.4	C	≥ 1.5	0.015	0.2	0.2	0.0	0.0	0.0	0.015	0.02
≤ 0.1	NC	≤ 1.2	0.005	0.2	0.2	0.0	0.0	0.0	0.015	0.02
≤ 0.1	NC	≥ 1.5	0.005	0.015	0.2	0.0	0.0	0.0	0.01	0.015
≥ 0.4	NC	≤ 1.2	0.005	0.015	0.2	0.0	0.0	0.0	0.01	0.015
≥ 0.4	NC	≥ 1.5	0.005	0.015	0.2	0.0	0.0	0.0	0.01	0.015
Condition ii. Other joints (Note: for classification for joints, refer to Fig. 4.2)										
$\frac{P}{A_g f_c'}$ ‡	Transverse reinforcement§	$\frac{V}{V_n}$ ‖								
≤ 0.1	C	≤ 1.2	0.01	0.02	0.2	0.0	0.0	0.0	0.015	0.02
≤ 0.1	C	≥ 1.5	0.01	0.015	0.2	0.0	0.0	0.0	0.01	0.015
≥ 0.4	C	≤ 1.2	0.01	0.02	0.2	0.0	0.0	0.0	0.015	0.02
≥ 0.4	C	≥ 1.5	0.01	0.015	0.2	0.0	0.0	0.0	0.01	0.015
≤ 0.1	NC	≤ 1.2	0.005	0.01	0.2	0.0	0.0	0.0	0.0075	0.01
≤ 0.1	NC	≥ 1.5	0.005	0.01	0.2	0.0	0.0	0.0	0.0075	0.01
≥ 0.4	NC	≤ 1.2	0.0	0.0075	0.0	0.0	0.0	0.0	0.005	0.0075
≥ 0.4	NC	≥ 1.5	0.0	0.0075	0.0	0.0	0.0	0.0	0.005	0.0075

Figure 9.4 shows the experimental joint shear stress-strain backbone curves compared to the nonlinear joint model backbone curves of ASCE 41 for specimens U-J-2 and U-J-1 of the current experimental program. It is clear that ASCE 41 is quite conservative in terms of estimating joint shear strength and plastic shear deformations. The same backbone curves will be implemented in a cyclic model for comparison with cyclic test data in a subsequent section.

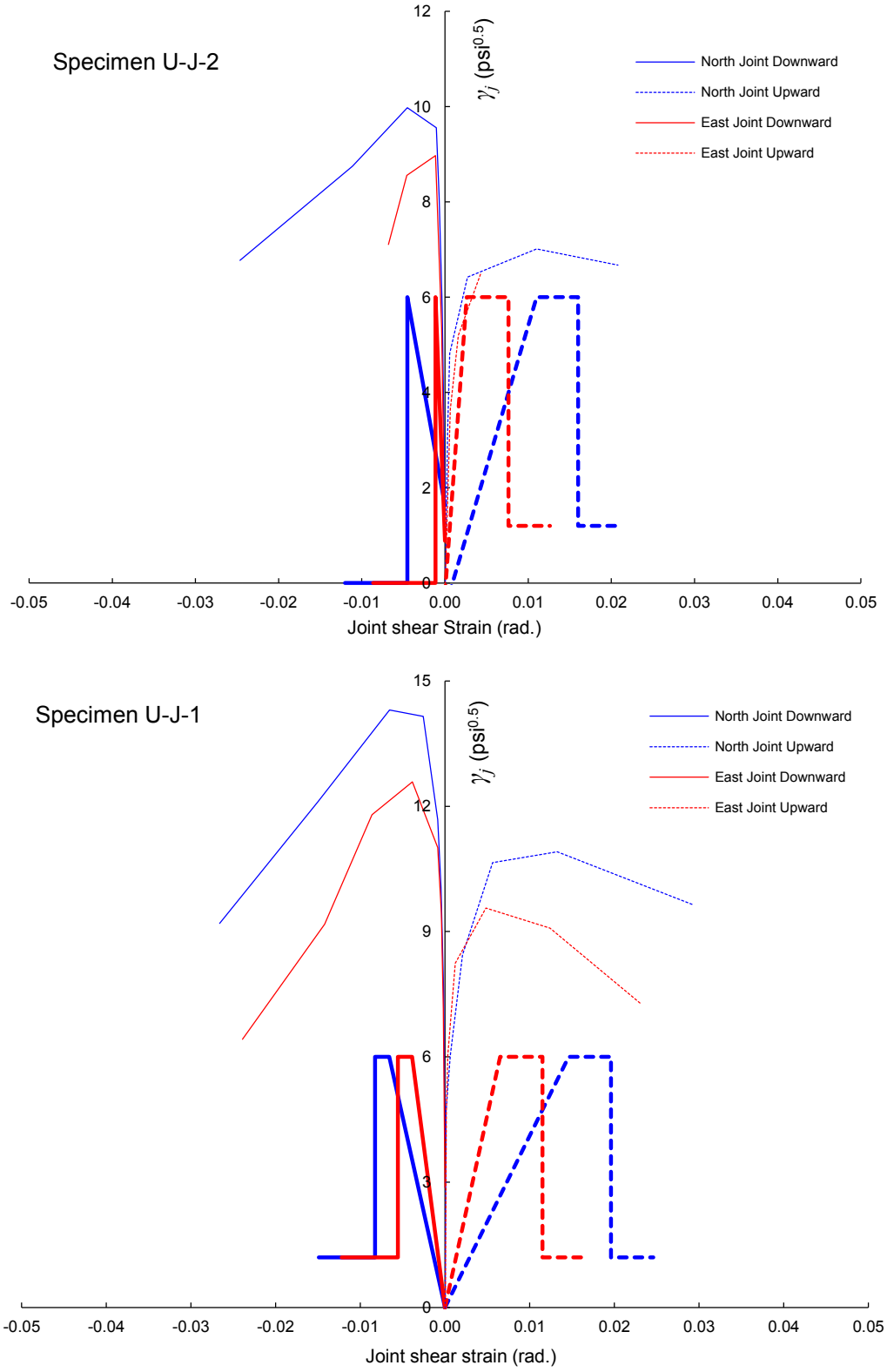

Figure 9.4 Comparison between test and ASCE 41 nonlinear modeling backbone curve parameters (heavy lines: ASCE 41 backbone curves, light lines: experimental backbone curves)

9.2.1.3 ASCE/SEI 41-06 SUPPLEMENT- ACI 369-R11 JOINT MODEL

The existing buildings beam-column joint provisions of ASCE/SEI 41 supplement and ACI 369 suggest that joint panel dimensions must be modeled to account for joint flexibility to avoid the frame stiffness overestimation and drift underestimation that results from ASCE 41 provisions. ASCE 41 supplement and ACI 369 take into account joint shear deformation by extending beam or column flexibility into the joint in the analytical model as shown in Fig. 9.5 (ASCE 41 [11]).

The ASCE 41 and ACI 369 method is based on the experimental results of Beres et al. [17], Leon and Jirsa [84], and Walker [154] that show that joint stiffness depends on the relative flexural beam and column strengths. As ASCE 41 recommends and as depicted in Fig. 9.5:

"*If the sum of nominal column flexural strengths (M_{nc}) is greater than 1.2 times the sum of nominal beam flexural strengths (M_{nb}), the recommended model considers the beam flexibility to extend to the joint centerline (for normal joint dimensions) with the column modeled as rigid within the joint. If the column-to-beam strength ratio is less than 0.8, the recommended model has rigid beam end zones with the column flexibility extending to the joint centerline (Figure 9.1b). Between these limits, half of the end zones of both beam and column elements are modeled as rigid within the joint extents (Figure 9.1c)*".

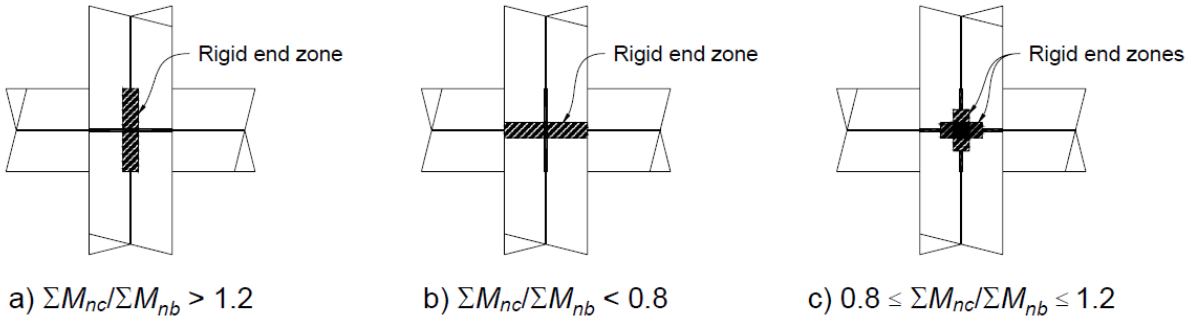

Figure 9.5 Rigid end zones for beam-column joint modeling. (ΣM_{nc}, ΣM_{nb} = sums of the nominal flexural strengths of the columns and beams, respectively, at the face of the joints.), ASCE/SEI 41[11]

However, ASCE 41 and ACI 369 still recommend a sole joint shear strength coefficient value of 6 for unconfined exterior or corner beam-column joints.

9.2.1.4 ROTATIONAL SPRING WITH RIGID LINKS JOINT MODEL (SCISSORS MODEL)

As discussed in Chapter 3, many panel zone joint models have been proposed previously (see Fig. 9.6). Some may be unsuitable for older concrete building assessment, either because they were developed and calibrated for confined beam-column joints or because they are very complicated to implement. One of these models that may be suitable, designated the scissors model (Figure 9.6.1), is a relatively simple model composed of a rotational spring with rigid links that span the joint dimensions. The model is a simplification of a model developed by Krawinkler [163] for steel panel zones. This model was first suggested by Alath and Kunnath [5]. The scissors model was also tested by Theiss [142], Celik and Ellingwood [23], and Favvata et al. [42], for interior and exterior unconfined beam-column joints under the effect of cyclic and dynamic loading, and by Burak [162] for confined beam-column joints under cyclic loading. Their analyses yielded promising results. To investigate the appropriateness of this model for unconfined corner beam-column joints under the effect of high axial compression and tension loads, a proposed extension of the model is presented in the next section. Finite element analyses using the proposed model are conducted and presented subsequently in this chapter.

The drawbacks of the scissors model include the inability to model the true kinematics of the joint. This is illustrated in Figure 9.7.

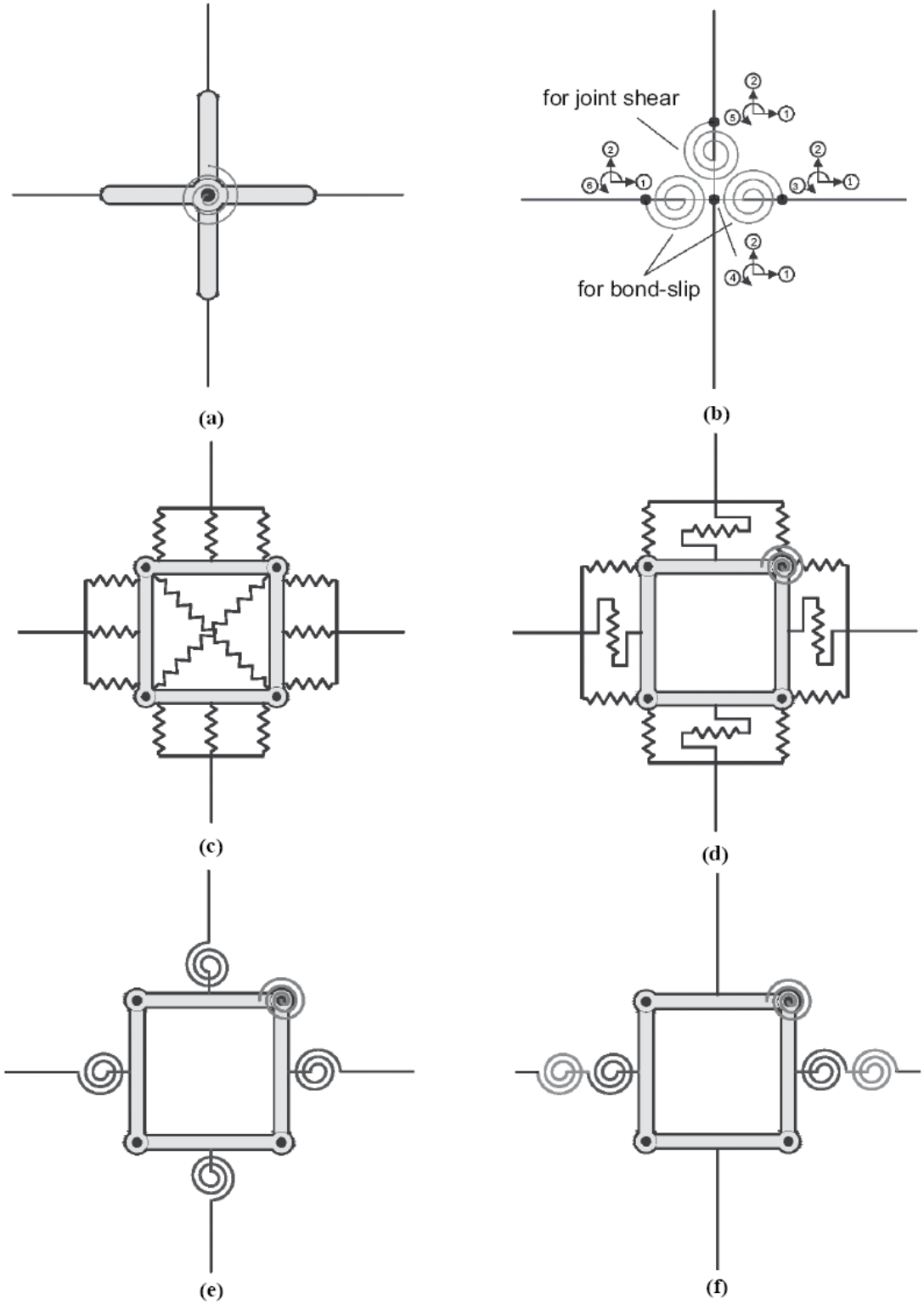

Figure 9.6 Existing beam-column joint panel models: (a) Alath and Kunnath [5], (b) Biddah and Ghobarah [18], (c) Youssef and Ghobarah [157], (d) Lowes and Altoontash [87], (e) Altoontash [8], and (f) Shin and LaFave [140]. After Celik and Ellingwood [23]

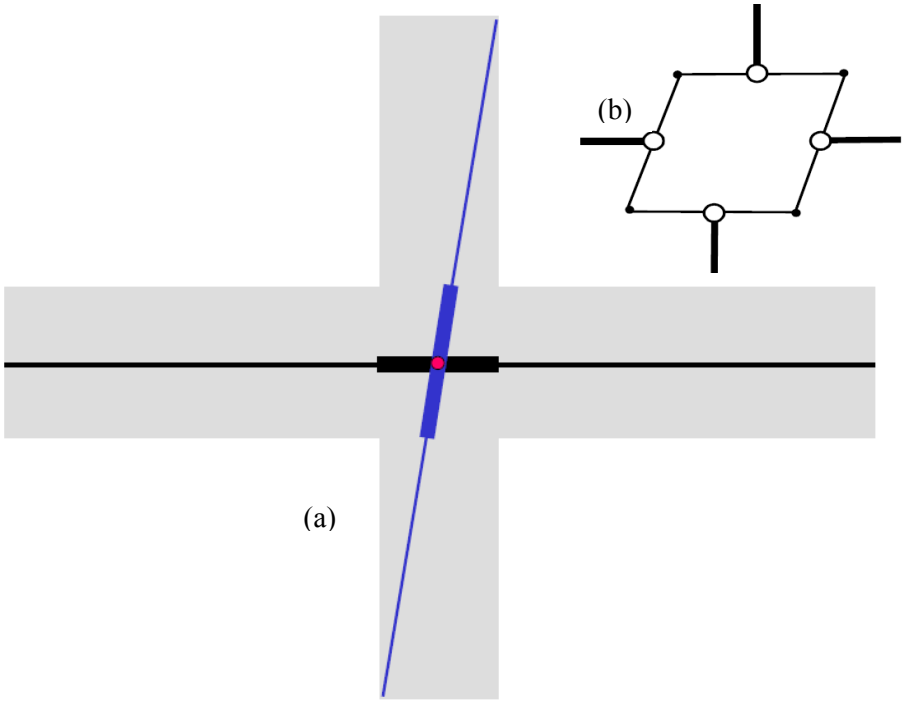

Figure 9.7 Scissors joint model: (a) Model kinematics, FEMA 451 [45],
(b) Drawback of missing joint translation, Theiss [142]

9.2.2 PROPOSED JOINT SPRING MODEL

The proposed joint panel zone model is a scissors model as described previously (Fig. 9.8). The element is implemented through defining duplicate nodes, node A (master) and node B (slave), with the same coordinates at the center of the joint (intersection of beam and column centerlines). After defining the two nodes, the element connectivity is set such that node A is connected to the column rigid link and node B is connected to the beam rigid link. Next, a zero length rotational spring is used to connect the two nodes so that the column rigid link is connected to one end of the spring while the beam rigid link is connected to the other. The degrees of freedom at the two central nodes are defined to permit only relative rotation between the two nodes through the constitutive model of the rotational spring which incorporates shear deformation of the joint (Fig. 9.8c).

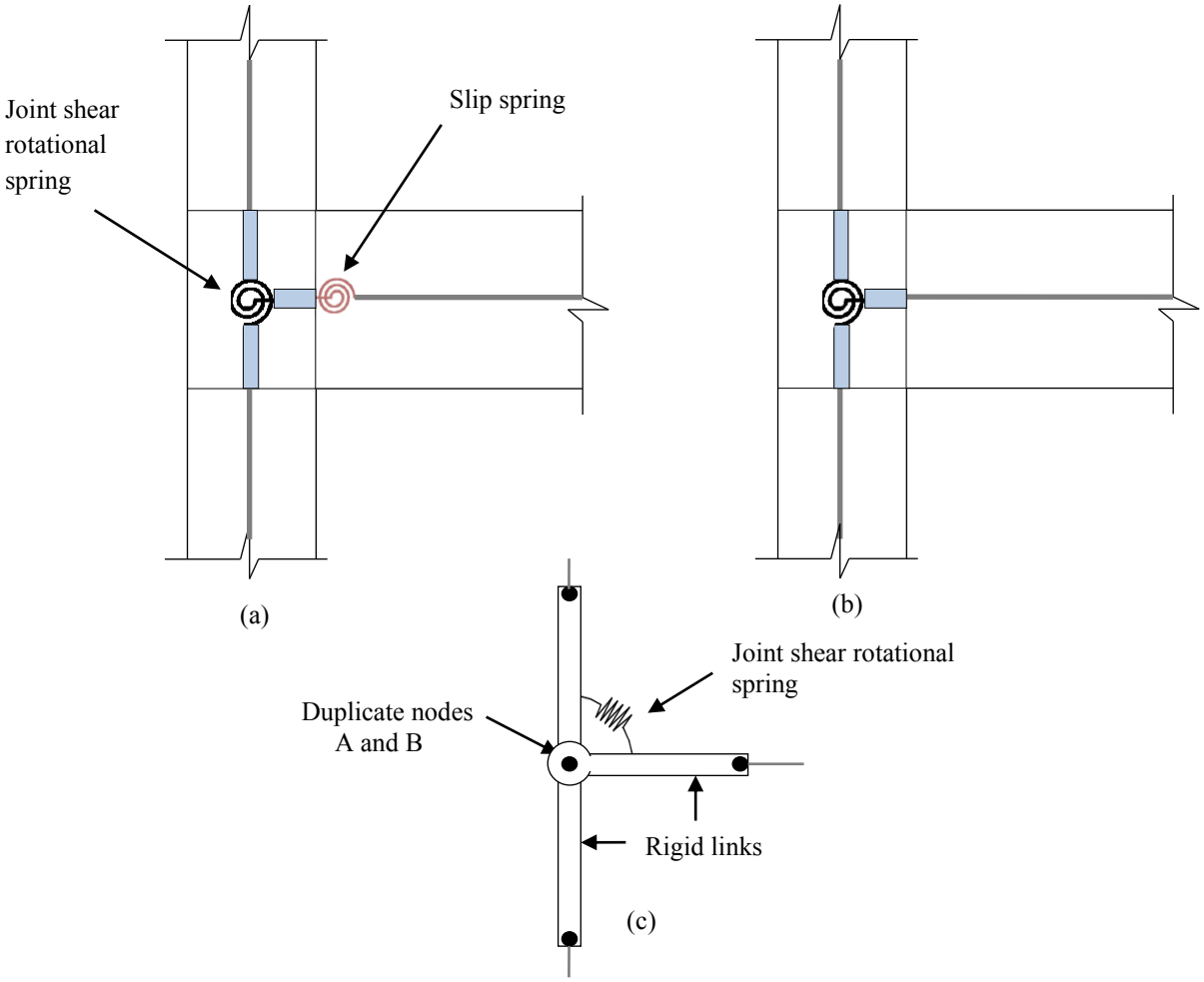

Figure 9.8 Proposed scissors model: (a) Explicit slip modeling, (b) Implicit slip modeling, (c) Slaving nodes

9.2.2.1 PROPOSED SHEAR STRESS-STRAIN BACKBONE CURVES

The material constitutive model of the rotational spring element is defined through moment-rotation backbone curves presented in Fig. 9.9. The backbone curve is a quad-linear curve that resembles the experimental joint shear stress-strain envelopes for unconfined joints. The moment transferred through the rotational spring M_j is related to the joint shear stress τ_j through:

$$M_j = \tau_j A_j \frac{L}{\frac{L - h_c/2}{jd_b} - \frac{L}{H}} \tag{9.1}$$

where L is the length from beam inflection point to the column centerline, which can be approximated as half beam centerline span. The parameter j is the effective beam lever arm ratio, which can be approximated as 0.875 for J-Failure joints and 0.9 for BJ-Failure joints. The column height H is measured between column inflection points, which can be approximated by story height. The moment can be also related to joint shear stress coefficient by:

$$M_j = \gamma_j A_j \sqrt{f_c'} \frac{L}{\frac{L - h_c/2}{jd_b} - \frac{L}{H}} \tag{9.2}$$

The rotation of the spring can be defined in two ways. One way is to consider the joint panel rotation as solely the joint shear strain, which can be expressed as:

$$\theta_j = \gamma_s \tag{9.3}$$

In this case, the joint rotation resulting from beam bar slip is explicitly defined by a separate zero length rotational slip spring element attached between the beam-joint interface section and the end of the beam rigid link. This option is denoted option "A" in this chapter. The other assumption is to include the joint rotation due to beam bar slip in expression 9.3 for joint rotation by adding it to the joint shear strain as:

$$\theta_j = \gamma_s + \theta_{slip} \tag{9.4}$$

In this case there will be no need for a separate slip spring for the beam. This might impose the same slip rotation on the beam and the column. This option will be denoted option "B" in this chapter, refer to Fig. 9.8. Both options A and B will be investigated to find out if there is any advantage for one of them over the other. Equations 9.1 through 9.4 can be used to switch between joint shear stress-strain/rotation constitutive model and moment-rotation constitutive models. The proposed constitutive backbone model is presented in terms of joint shear stress-strain/rotation in order to relate to simplified expressions for "*modulus of shear rigidity*" of joint panel zone. Hence, shear stresses, shear strains and shear moduli are the key input parameters of the model. The proposed backbone curve characteristic points (point 1 through point 4) are described and quantified in the following paragraphs.

Point 1: Cracking Strength

The limit state damage level that point 1 represents is the hairline joint cracking. In the development of the modified compression field theory (Vecchio and Collins [151]), the cracking shear strain of a plain concrete shear panel was found to be 0.00012. It is well established that cracking strain is invariant in unconfined and confined joints. However, observed cracking shear strains during unconfined beam-column joint tests [23] are in the strain range from 0.0001 to 0.0013, which is much higher than that of plain concrete shear panels. Apparently the state of stress in beam-column joints does not resemble that in plain shear panels.

An alternate way of calculating joint shear cracking strain based on the cracking stress expression developed by Uzumeri [150] for beam-column joints including the effect of axial load is:

$$\frac{\tau_{j-1}}{\sqrt{f_c'}} = 3.5\sqrt{1+0.002\frac{P}{A_j}} \qquad \leq 0.6\frac{\tau_{j-3}}{\sqrt{f_c'}} \tag{9.5}$$

According to Eq. 9.5, an upper limit of 60% of the peak joint shear stress is set on the cracking stress. This limit was fit from experimental results of beam-column joint tests in the database of Chapter 5 and the experimental results of Chapter 7.

Based on the experimental results of the current study along with other joint tests in the literature presented in Chapter 5, the slope of the initial segment of the shear-stress strain backbone curve, which represents the joint shear modulus of rigidity G_{01} was found to be 50% the theoretical elastic shear rigidity of concrete.

$$G_{01} = 0.5G_c \tag{9.6}$$

Where G_c is the theoretical shear modulus of rigidity:

$$G_c = \frac{E_c}{0.2(1+\nu)} \tag{9.7}$$

where ν=0.20 is concrete Poisson's ratio. This lower apparent cracking shear modulus might be attributable to the joint micro-cracking, although this has not been definitively established. The proposed cracking shear modulus value of $0.5G_c$ is consistent with the observation of Anderson et al. [9]. Based on the cracking stress and shear modulus suggested above, the cracking strain can be calculated as:

$$\gamma_{s-1} = \frac{\tau_{j-1}}{G_{01}} \tag{9.8}$$

The above expressions for cracking point apply for upward and downward loading backbone curves.

Point 2: Pre-Peak "Yielding" Strength

For J-Failure mode, the limit state damage level reflected by point 2 is denoted "pre-peak" level. At this level main diagonal crack is widened and additional secondary diagonal cracks develop. For BJ-Failure mode, the limit state that point 2 represents is the yielding of the beam.

The secant joint shear modulus of rigidity at point 2, G_{02}, for downward loading direction can be approximated by $0.1G_c$, and the shear strain at this point is 0.002. The corresponding values for upward loading direction are $0.1G_c$ and 0.0025, respectively. These values were obtained based on average fitting of the current and previous test results for unconfined beam-column joints. Based on secant shear modulus and shear strain at point 2, the shear stress is calculated. For BJ failure mode downward loading under axial load higher than $0.3f_c'A_j$ the joint shear strains corresponding to points 1, 2, and 3 are negligible. Shear strain at point 2 can be taken as 0.0002 based on test results. The model equations at point to can be expressed as:

For Downward Loading (J-Failure)

$$G_{02} = 0.1G_c \tag{9.9}$$

$$\gamma_{s-2} = 0.002 \tag{9.10}$$

$$\tau_{j-2} = \gamma_{s-2}G_{02} \quad \geq 0.9\tau_{j-3} \tag{9.11}$$

For Downward Loading (BJ-Failure with High Axial Load)

$$\tau_{j-2} = 0.9\tau_{j-3} \tag{9.12}$$

$$\gamma_{s-2} = 0.0002 \tag{9.13}$$

For Upward Loading

$$G_{02} = 0.1G_c \tag{9.14}$$

$$\gamma_{s-2} = 0.0025 \tag{9.15}$$

$$\tau_{j-2} = \gamma_{s-2}G_{02} \quad \geq 0.9\tau_{j-3} \tag{9.16}$$

A lower limit of 90% of the peak joint shear stress is set for the shear stress at point 2 based on the minimum test results observed.

Point 3: Peak Shear Strength

The maximum joint shear stress can be obtained from joint shear strength coefficient calculated using the strut-and-tie model or the empirical shear strength model proposed in Chapter 5 for J-Failure mode as:

$$\tau_{j-3} = \gamma_{STM}G_{03} \tag{9.17}$$

The secant joint shear modulus G_{03} corresponding to point 3 can be calculated using the following expressions:

For Downward Loading (J-Failure)

$$G_{03} = \left(0.14 - \frac{3}{80}\alpha_j\right)G_c \qquad \text{For} \qquad \frac{P}{f_c^{'}A_j} \geq 0.3 \tag{9.18}$$

$$G_{03} = \left(0.175 - \frac{3}{40}\alpha_j\right)G_c \qquad \text{For} \qquad \frac{P}{f_c^{'}A_j} < 0.3 \tag{9.19}$$

For Downward Loading (BJ-Failure)

$$\gamma_{s-3} = 0.0002 \qquad \text{For} \qquad \frac{P}{f_c^{'}A_j} \geq 0.3 \tag{9.20}$$

For Upward Loading

$$G_{03} = 0.03G_c \qquad \text{For J-Failure mode} \tag{9.21}$$

$$G_{03} = 0.02G_c \qquad \text{For BJ-Failure mode} \tag{9.22}$$

where α_j is the joint aspect ratio h_b/h_c. Finally the joint shear strain at point 3 can be calculated as:

$$\gamma_{s-3} = \frac{\tau_{j-3}}{G_{03}} \tag{9.23}$$

For the BJ-Failure mode, the joint shear stress coefficient corresponding to beam strain-hardening capacity can be used to calculate the shear stress at point 3. This can be approximated as 1.10 times the joint shear stress coefficient corresponding to actual beam yield or 1.25 times that corresponding to nominal flexural capacity, thus:

$$\tau_{j-3} = 1.10\tau_{j-2} \tag{9.24}$$

The 10% stress increase represents an average strain-hardening ratio from steel tensile tests while the 25% increase reflects the collective strain hardening and overstrength to nominal yield stress. It is noteworthy that τ_{j-2} for BJ-Failure mode is calculated based on actual beam yield capacity.

Point 4: Post-Peak (Residual /Axial Failure) Strength

Downward Loading Backbone Curve

The post-peak strength can be expressed as the residual shear strength corresponding to the maximum drift reached prior to axial failure in the case of high axial load larger than $0.3f_c'A_j$ or to very large shear deformations and severe joint distress that correspond to large story drifts that may lead to dynamic instability collapse of a concrete frame in the case of axial loads below $0.3f_c'A_j$. In both cases, a shear stress of 70% the peak joint shear strength was found to be representative based on the test results of the current investigation for axial failure joints along with previous test results for the database in Chapter 5 for no-axial failure cases. To continue the analysis until reaching axial failure, it is recommended to extrapolate between point 3 and point 4 of the backbone curve to terminate the analysis at 50% peak shear stress. Thus, the shear stress at point 4 can be expressed as:

$$\tau_{j-4} = 0.7\tau_{j-3} \tag{9.25}$$

The "shear strain" at point 4 can be expressed as:

$$\gamma_{s-4} = \gamma_{s-3} + 0.02 \qquad \text{For} \quad \frac{P}{f_c'A_j} > 0.3 \tag{9.26}$$

$$\gamma_{s-4} = \gamma_{s-3} + 0.025 \qquad \text{For} \quad \frac{P}{f_c'A_j} \le 0.3 \tag{9.27}$$

It is emphasized here that the shear stress given by Equation 9.25 and "shear strains" given by Equation 9.26 correspond to a point immediately prior to axial failure of the joint or to a very large drift of the building.

Upward Loading Backbone Curve

For the upward loading, corresponding to tension overturning action on column, the following equations describe point 4 backbone curve parameters:

$$\tau_{j-4} = 0.8\tau_{j-3} \tag{9.28}$$

$$\gamma_{s-4} = 0.03 \tag{9.29}$$

When contrasting downward and upward loading equations presented above for point 4, it can be observed that for upward loading, the descending branch of the backbone curve is flatter than that of downward loading, which reflects lower strength degradation due to the lower compressive axial loads or the presence of tensile axial load. This also reflects the higher joint

shear strains (due to wider joint cracking) under the effect of small axial compressive or tensile loads. The implication of this observation is a higher interstory drift ratio for upward loading compared to downward loading. This is the reason a 20% strength reduction limit was selected for upward loading to represent severe joint damage and large drift that may correspond to dynamic instability compared to a 30% reduction for the downward loading.

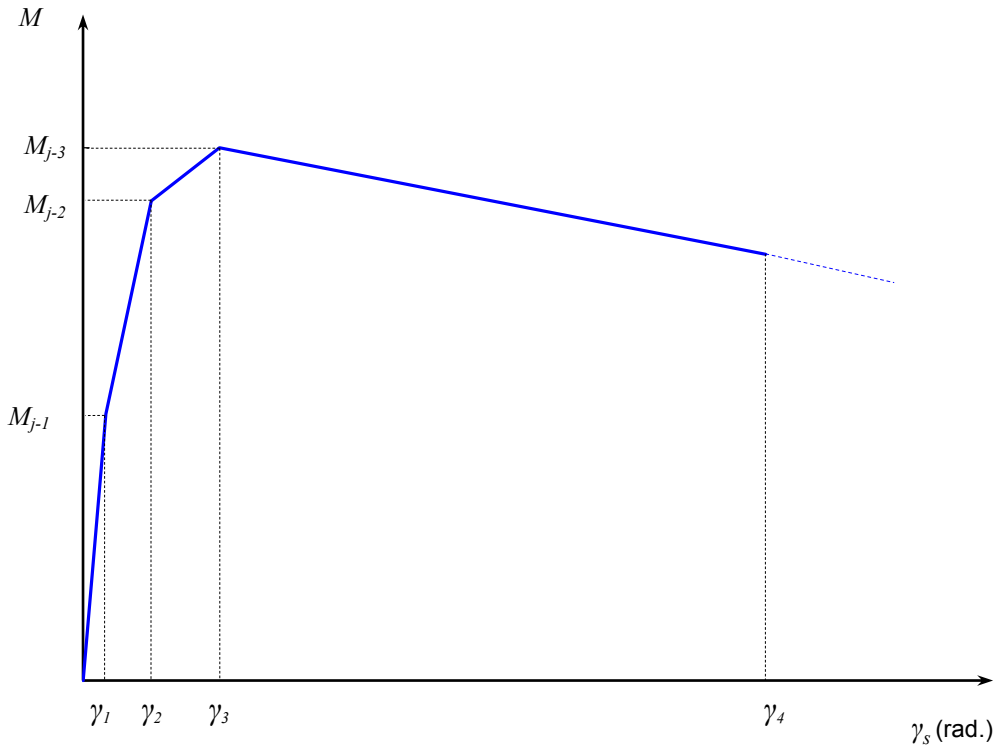

Figure 9.9.a Proposed moment-rotation backbone curve for joint rotational spring model

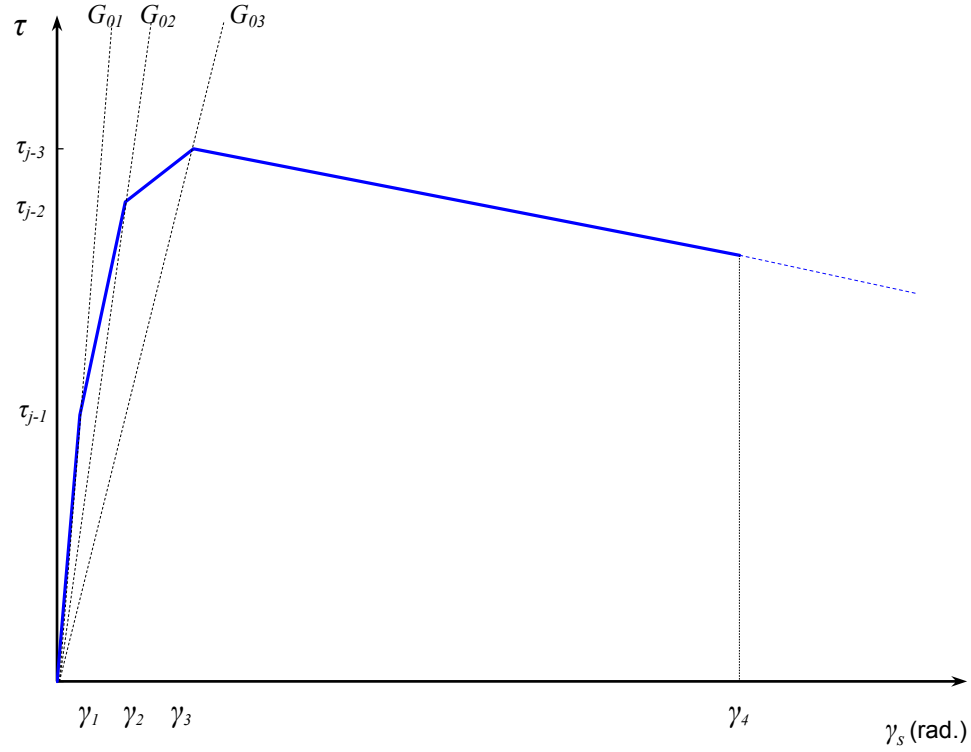

Figure 9.9.b Proposed shear stress-strain backbone curve for joint rotational spring model

9.2.2.2 BOND-SLIP MODELING

There are several techniques to represent bond-slip rotation in an analytical model of a beam-column joint. The most direct approach is to introduce a slip spring whose properties are either calibrated directly from tests or are calculated using a bond-slip model. An alternative is to scale the moment-shear strain (rotation) backbone to account for higher rotation resulting from slip; this method was used successfully by Celik and Ellingwood [23]. Yet another approach is to reduce the effective stiffness of beams and columns to account for slip deformation as recommended by ASCE/SEI 41 supplement 1 [11]. In the present study, the first approach is used with the slip spring properties calculated based on a bond-slip model. The specific approach is described next.

J-Failure Mode

In the case of joints that fail in J-Failure mode, the beams are essentially elastic. Thus, the steel stress is in the linear range, which enables the calculation of slip rotation corresponding to the joint shear capacity as:

$$\theta_{slip} = \frac{s_{slip}}{d_b - c} \tag{9.30}$$

where s_{slip} is bar slip and c is the compression zone height which can be approximated for elastic beam as $0.3d_b$, this leads to:

$$\theta_{slip} = \frac{s_{slip}}{0.7d_b} \tag{9.31}$$

The required reinforcement stress to be developed in the case of J-Failure mode is the steel stress f_s corresponding to peak joint shear strength. An elastic bond stress distribution can be assumed as shown in Fig. 9.1. The elastic stress f_s can be calculated as:

$$f_s = \frac{V_b.L_b}{0.875d_bA_{sb}} \tag{9.32}$$

where V_b is the beam shear corresponding to joint shear strength. The model adopted herein is the bilinear bond-slip model Lehman and Moehle [81] (Fig. 9.11), where average bond stresses over the entire elastic bar length are:

$$u = 12\sqrt{f_c'} \tag{9.33}$$

The required bar length within the joint region to develop the stress f_s is:

$$l_{ds} = \frac{\phi_b f_s}{4u} \tag{9.34}$$

Scott [135] suggested that the development length of beam bars in unconfined joints can be extended to the end of the tail of beam hook. Accordingly, the available bar length to develop stress f_s is:

$$l_s = l_{sb} + 0.5\pi R + l_{sc} \tag{9.35}$$

where l_{sb} is the length of the straight segment within the joint parallel to beam measured from the beam joint interface until the start of the bend. l_{sc} is the length of the straight segment of the bar within the joint parallel to column measured vertically from the end of the bend until the bar termination point. These quantities can be determined from column and beam depth, respectively. A standard ACI 318 hook radius can be used for R. If l_{ds} is shorter than l_s, Fig. 9.11 and Eq. 9.36 can be used to calculate the slip. If l_{ds} is longer than l_s, Fig. 9.11 and Equation 9.37 are used for slip calculations.

If $l_{ds} < l_s$

$$s_{slip} = \int_0^{l_{ds}} \varepsilon_s d_x = \frac{\phi_b f_s^2}{8uE_s} \tag{9.36}$$

If $l_{ds} > l_s$

$$s_{slip} = \int_0^{l_s} \varepsilon_s d_x = \left[\frac{l_{ds} - l_s}{l_{ds}} + 1\right].\frac{l_s f_s}{2E_s} \tag{9.37}$$

The slip rotation calculated according to Eq.31 is that corresponding to point 3 on the moment-rotation backbone curve for joint panel presented earlier. The slip-rotation corresponding to points 1 and 2 can be obtained by linear interpolation between zero shear stress and peak shear stress at point 3.

It remains to estimate the slip rotation corresponding to point 4 on the proposed backbone curve. It is hypnotized that slip in J-Failure mode is within the elastic range. Thus, once the joint reaches peak shear strength, the joint will start degrading and the steel stress demand from beam reinforcement starts to decrease since it did not reach yield. However, the current NEES joint tests show that slip continues to increase even after reaching joint shear capacity. This might be attributed to joint distress that worsens the bond conditions between beam bars and degrading joint concrete. No theoretical solution is available to quantify this effect. Thus, average values for slip rotations were approximated based on test results by Park [120] and the current experimental results for corner beam-column joints with J-Failure mode, expressed:

$$\theta_{slip-4} = 2\theta_{slip-3} \tag{9.38}$$

Where θ_{slip-3} is the slip rotation corresponding to peak joint shear strength (point 3 on the proposed backbone curve) calculated using Eq. 9.31.

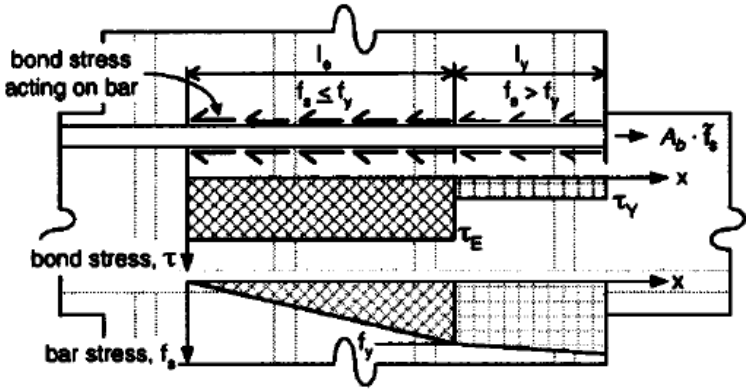

Figure 9.10 Lowes and Altoontash bond model [87].

BJ-Failure Mode

In the case of BJ-Failure mode, the beam bars yield before reaching the joint shear strength, which is the joint strength corresponding to beam strain-hardening capacity. According to Lehman and Moehle [81], this results in a reduced bond capacity of 6 √fc'. The bond-slip relationships in this case are adopted from Lowes and Altoontash [87] as:

$$l_e = \frac{\phi_b f_y}{4u_E} \tag{9.39}$$

If $l_e + l_y < l_s$:

$$s_{slip} = \int_0^{l_e} \frac{4}{\phi_b}\frac{u_E}{E_s} x dx + \int_{l_e}^{l_y+l_e} \frac{f_y}{E_s} + u_y \frac{4}{\phi_b}\frac{1}{E_h}(x - l_e)dx$$

$$= 2\frac{u_E}{E_s}\frac{l_e^2}{\phi_b} + \frac{f_y}{E_s} l_y + 2\frac{u_y}{E_h}\frac{l_y^2}{\phi_b} \tag{9.40}$$

Where

$$l_y = \frac{f_s - f_y}{u_y} \cdot \frac{A_b}{\pi\phi_b} \tag{9.41}$$

$$f_s = \frac{V_{by}.L_b}{0.9 d_b A_{sb}} \tag{9.42}$$

$$u_E = 12\sqrt{f_c'} \tag{9.43}$$

$$u_y = 6\sqrt{f_c'} \tag{9.44}$$

where f_s is the bar stress at joint-beam interface, which will be greater than yield stress in the BJ-Failure case since it corresponds to strain-hardening beam capacity (point 3 on the proposed backbone curve). E_h is the steel hardening modulus assuming a bilinear stress-strain response, u_E is the elastic bond strength, u_y is the inelastic bond strength, A_b is the nominal bar area, l_e and l_y are the lengths along the steel bar for which steel stress is less and greater than yield stress, respectively.

If the available bar length within the joint region is not sufficient to develop the yield stress to zero stress before reaching the end of the hooked portion; the slip relationship can be modified to:

If $l_e + l_y > l_s$

$$s_{slip} = \left[\frac{l_e - (l_s - l_y)}{l_e} + 1 \right] \frac{(l_s - l_y) f_y}{2E_s} + \frac{f_y}{E_s} l_y + 2 \frac{u_y}{E_h} \frac{l_y^2}{\phi_b} \tag{9.45}$$

Equation 9.31 can be then used to obtain the rotation corresponding to the calculated slip. The slip rotation calculated using Eq. 9.31 corresponds to point 3 on the moment-shear strain backbone curve proposed in Sec. 9.2.2.1. The slip rotation calculated based on yield using Eq. 9.39 can be considered corresponding to point 2 on the moment-rotation backbone curve. The slip rotation at point 1 on the proposed backbone curve can be obtained by linear interpolation from point 2 moment-slip rotation.

No simple analytical means is available to estimate the slip rotation corresponding to point 4 on the proposed backbone curve. Thus, average values for slip rotations obtained from test results by Park [1] and the current experimental results for corner beam-column joints with BJ-Failure mode were taken as:

$$\theta_{slip-4} = 1.5\theta_{slip-3} \tag{9.46}$$

where θ_{slip-3} is the slip rotation corresponding to peak joint shear strength (i.e., shear stress corresponding to beam strain-hardening capacity which is point 3 on the proposed backbone curve) calculated using Eq. 9.31.

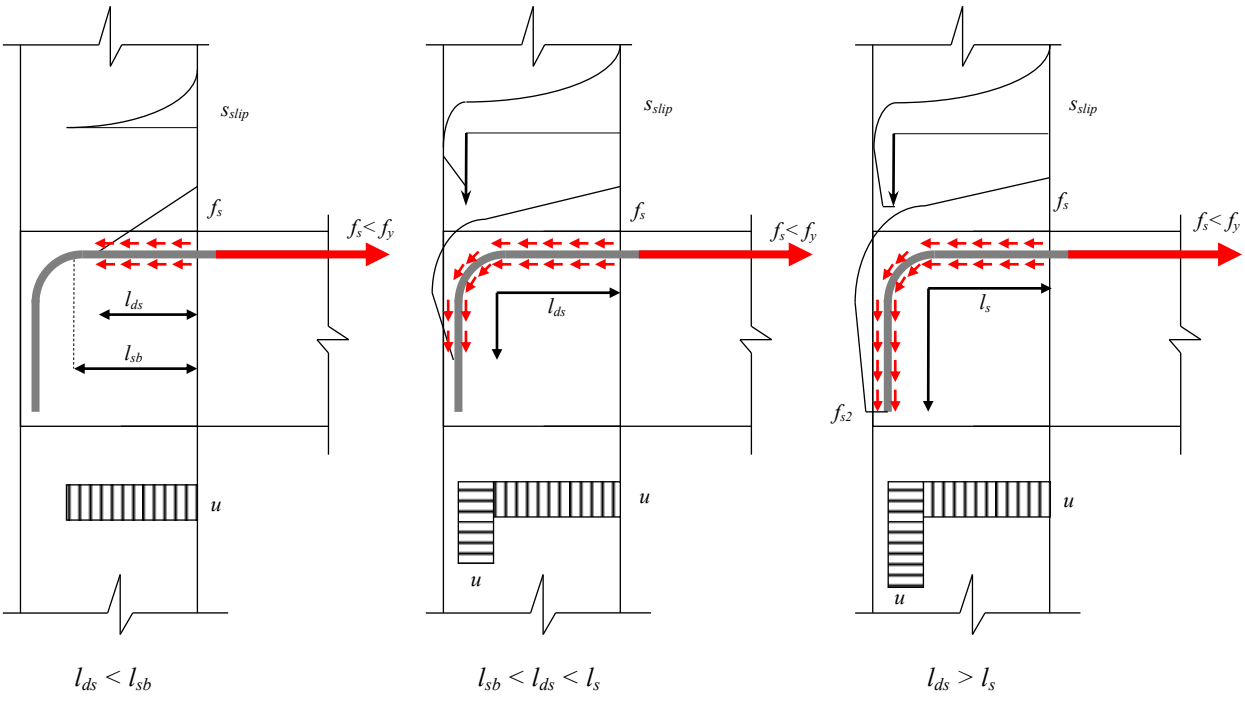

Figure 9.11.a Different cases of bond-slip parameters for J-Failure joints

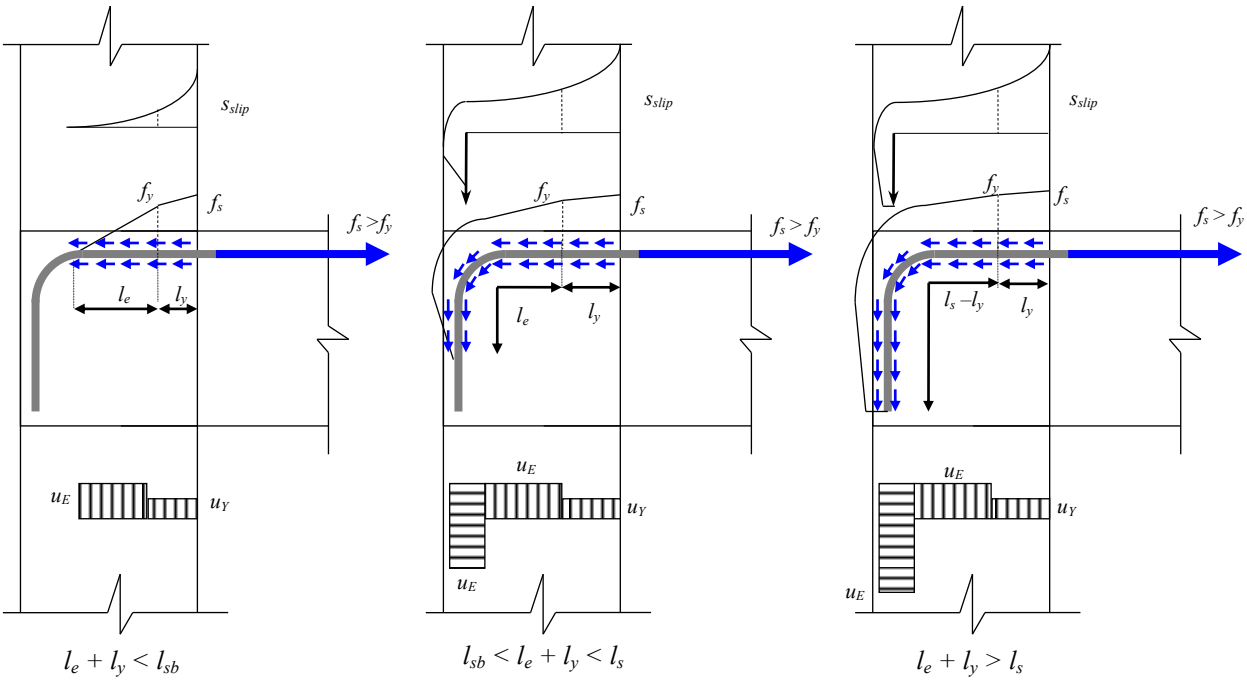

Figure 9.11.b Different cases of bond-slip parameters for BJ-Failure joints

9.2.2.3 JOINT ROTATIONAL SPRING HYSTERETIC MATERIAL MODEL

The one dimensional material model used to implement the proposed backbone curve for the joint constitutive model and to describe the hysteresis, pinching, energy dissipation, and cyclic degradation of the response is the *Pinching4* material model in OpenSees (Fig. 9.12), developed by Lowes et al. [88]. This model is particularly useful to represent the pinched hysteretic behavior of shear critical elements like unconfined-beam column joints.

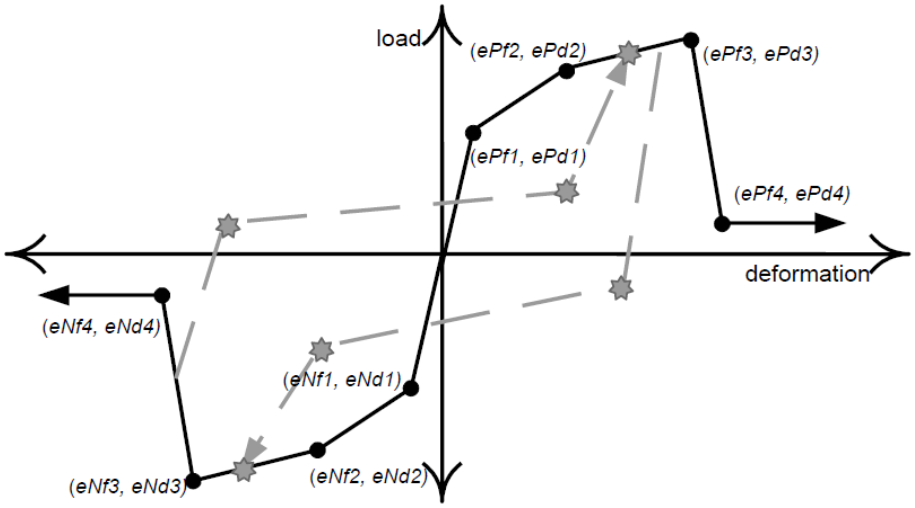

Figure 9.12 *Pinching4* OpenSees model, Lowes et al. [88], after Theiss [142].

The model parameters are defined in Table 9.2. The model has eight positive and negative envelope parameters. These parameters are calculated using the proposed backbone curves in Section 9.2.2.1. The model has different parameters to define pinching behavior (*rDispP to uForceN*), parameters to define unloading stiffness degradation (*K1 to KLim*), parameters to define reloading stiffness degradation (*D1 to DLim*), parameters to define strength degradation (*F1 to FLim*), and finally a parameter *gE* to define energy dissipation rule. The eight envelope parameters for the simulated specimens are shown in Table 9.4, while the values of the 22 parameters used to define cyclic response are presented in Table 9.3. It is worth mentioning that these 22 parameters were calibrated to be consistent with the proposed backbone curves in Section 9.2.2.1 and may not guarantee appropriate joint response if used with other models.

Table 9.2 *Pinching4* material model parameter definitions and *Tcl* command, [142]

uniaxialMaterial Pinching4 $matTag $ePf1 $ePd1 $ePf2 $ePd2 $ePf3 $ePd3 $ePf4 $ePd4 [$eNf1 $eNd1 $eNf2 $eNd2 $eNf3 $eNd3 $eNf4 $eNd4] $rDispP $rForceP $uForceP [$rDispN $rForceN $uForceN] $gK1 $gK2 $gK3 $gK4 $gKLim $gD1 $gD2 $gD3 $gD4 $gDLim $gF1 $gF2 $gF3 $gF4 $gFLim $gE $dmgType

$matTag	unique material object integer tag
$ePf1 $ePf2 $ePf3 $ePf4	floating point values defining force points on the positive response envelope
$ePd1 $ePd2 $ePd3 $ePd4	floating point values defining deformation points on the positive response envelope
$eNf1 $eNf2 $eNf3 $eNf4	floating point values defining force points on the negative response envelope (optional, default: negative of positive envelope values)
$eNd1 $eNd2 $eNd3 $eNd4	floating point values defining deformations points on the negative response envelope (optional, default: negative of positive envelope values)
$rDispP	floating point value defining the ratio of the deformation at which reloading occurs to the maximum historic deformation demand
$rForceP	floating point value defining the ratio of the force at which reloading begins to force corresponding to the maximum historic deformation demand
$uForceP	floating point value defining the ratio of strength developed upon unloading from negative load to the maximum strength developed under monotonic loading
$rDispN	floating point value defining the ratio of the deformation at which reloading occurs to the minimum historic deformation demand (optional, default: $rDispP)
$rForceN	floating point value defining the ratio of the force at which reloading begins to the force corresponding to the minimum historic deformation demand (optional, default: $rForceP)
$uForceN	floating point value defining the ratio of the strength developed upon unloading from a positive load to the minimum strength developed under monotonic loading (optional, default: $rForceP)
$gK1 $gK2 $gK3 $gK4 $gKLim	floating point values controlling cyclic degradation model for unloading stiffness degradation
$gD1 $gD2 $gD3 $gD4 $gDLim	floating point values controlling cyclic degradation model for reloading stiffness degradation
$gF1 $gF2 $gF3 $gF4 $gFLim	floating point values controlling cyclic degradation model for strength degradation
$gE	floating point value used to define maximum energy dissipation under cyclic loading. Total energy dissipation capacity is defined as this factor multiplied by the energy dissipated under monotonic loading.
$dmgType	string to indicate type of damage (option: "cycle", "energy")

Table 9.3 *Pinching4* material model parameter

Parameter Type	Parameter ID	Stevens[163]	Theiss[142]	Proposed
Pinching Parameters	*rDispP*	0.25	0.11	0.15
	rForceP	0.15	0.25	0.35
	uForceP	0.00	-0.10	-0.10
	rDispN	-0.25	-0.11	0.15
	rForceN	-0.15	-0.25	0.15
	uForceN	0.00	-0.10	-0.40
Unloading Stiffness Degradation Parameters	*gK1*	1.30	0.42	0.50
	gK2	0.00	0.35	0.20
	gK3	0.24	0.20	0.10
	gK4	0.00	0.028	-0.40
	gKLim	0.89	0.99	0.99
Reloading Stiffness Degradation Parameters	*gD1*	0.12	0.046	0.10
	gD2	0.00	0.005	0.40
	gD3	0.23	1.34	1.00
	gD4	0.00	0.00	0.50
	gDLim	0.95	0.99	0.99
Strength Degradation Parameters	*gF1*	1.11	1.00	0.05
	gF2	0.00	0.00	0.02
	gF3	0.32	2.00	1.00
	gF4	0	0.00	0.05
	gFLim	0.13	0.99	0.99
Energy Dissipation	*gE*	10.0	2.00	10.00
	dmgType	energy	energy	energy

Table 9.4 Backbone curve parameters for simulated specimens, Option A

Loading Direction	Backbone Parameters	Proposed Backbones				ASCE 41 Backbones			
		U-J-1	U-J-2	U-BJ-1	SP4[1]	U-J-1	U-J-2	U-BJ-1	SP4[1]
Upward Loading	*ePf1*	1616	2770	1469	2557	1500	2000	1075	1850
	ePd1	0.00041	0.00035	0.00026	0.00035	0.0113	0.0055	0.00105	0.005
	ePf2	3196	4156	2421	4179	1990	3952	2150	3715
	ePd2	0.0025	0.0025	0.0025	0.0025	0.015	0.011	0.0021	0.01
	ePf3	3552	4617	2690	4644	1990	3952	2150	3715
	ePd3	0.015	0.00984	0.0158	0.0105	0.02	0.016	0.015	0.015
	ePf4	2131	2770	2152	1857	398	790	430	620
	ePd4	0.065	0.06	0.03	0.0855	0.025	0.021	0.02	0.02
Downward Loading	*eNf1*	-1898	-3631	-1625	-2842	-898	-1819	-991	-1770
	eNd1	-0.0005	-0.0005	-0.0001	-0.0004	-.0033	-.0023	-0.0001	-0.005
	eNf2	-3850	-5447	-2438	-4581	-1795	-3638	-1982	-3551
	eNd2	-0.002	-0.002	-0.0002	-0.002	-.0066	-.0045	-0.0002	-0.01
	eNf3	-4278	-6052	-2709	-5090	-1795	3638	-1982	-3551
	eNd3	-0.006	-0.0056	-0.0002	-0.0073	-.0083	-.0045	-0.0002	-0.014
	eNf4	-1711	-2420	-2709	-2036	359	0	0	-592
	eNd4	-0.056	-0.0456	-0.01	-0.082	-0.015	-0.012	-0.0077	-0.02

9.2.2.4 BOND-SLIP ROTATIONAL SPRING MATERIAL MODEL

The calculated slip rotation θ_{slip} based on the analytical method presented in Sec. 9.2.2.2 can be used explicitly in a zero length rotational spring model based an explicit backbone constitutive curve, denoted previously as Option A. In this case, the uniaxial *Hysteretic Material* in OpenSees framework can be used to define the backbone curve (Fig. 9.13).

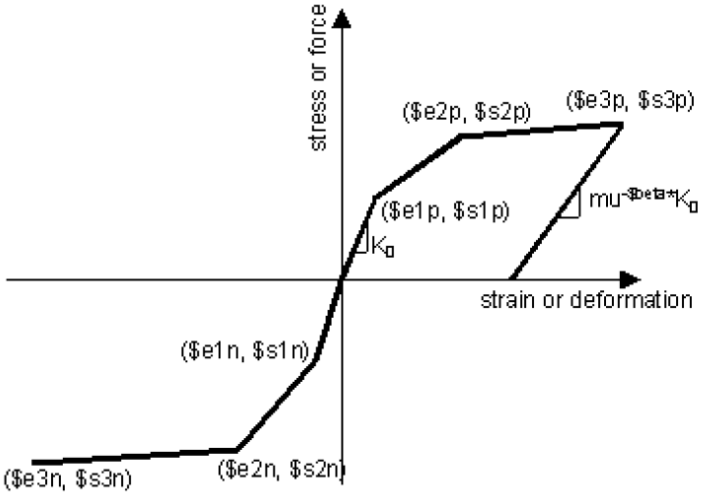

Figure 9.13 Hysteretic material model, OpenSees [108].

In Option B, θ_{slip} is added to the shear strains of the proposed backbone curve in Sec. 9.2.2.1. Accordingly, the total joint rotation of the scissors spring can be estimated as:

$$\theta_{j-1} = \gamma_{s-1} + \frac{M_{j-1}}{M_{j-3}}\theta_{slip-3} \qquad \text{For J-Failure mode} \tag{9.47}$$

$$\theta_{j-1} = \gamma_{s-1} + \frac{M_{j-1}}{M_{j-2}}\theta_{slip-2} \qquad \text{For BJ-Failure mode} \tag{9.48}$$

$$\theta_{j-2} = \gamma_{s-2} + \theta_{slip-2} \tag{9.49}$$

$$\theta_{j-3} = \gamma_{s-3} + \theta_{slip-3} \tag{9.50}$$

$$\theta_{j-4} = \gamma_{s-4} + \theta_{slip-4} \tag{9.51}$$

Thus, the *Pinching4* material model used for moment-joint shear strain backbone, including the same cyclic stiffness strength degradation parameters, is also used in Option B to represent the cyclic and backbone behavior of bond-slip rotation.

9.3 SIMULATION OF BEAM-COLUMN JOINT SUB-ASSEMBLAGES

9.3.1 MODEL GEOMETRY

The finite element model geometry used to simulate the test beam-column joint sub assemblage is shown in Fig. 9.14. Simulations were conducted for test specimens U-J-1, U-J-2, U-BJ-1 of the current test program, SP2 and SP4 from test phase I [120], BS-L and BS-L-600 reported by Wong [155], and Unit 5 and Unit 6 reported by Pantelides et al. [116].

The actual test boundary conditions were modeled in OpenSees 2.2.2 platform as follows; axial column shortening was permitted through a top vertical roller, beam and column end rotation was permitted through moment releases, and a beam end roller was used so that beam longitudinal translation was not restrained. Figure 9.14 shows the boundary conditions used in simulation.

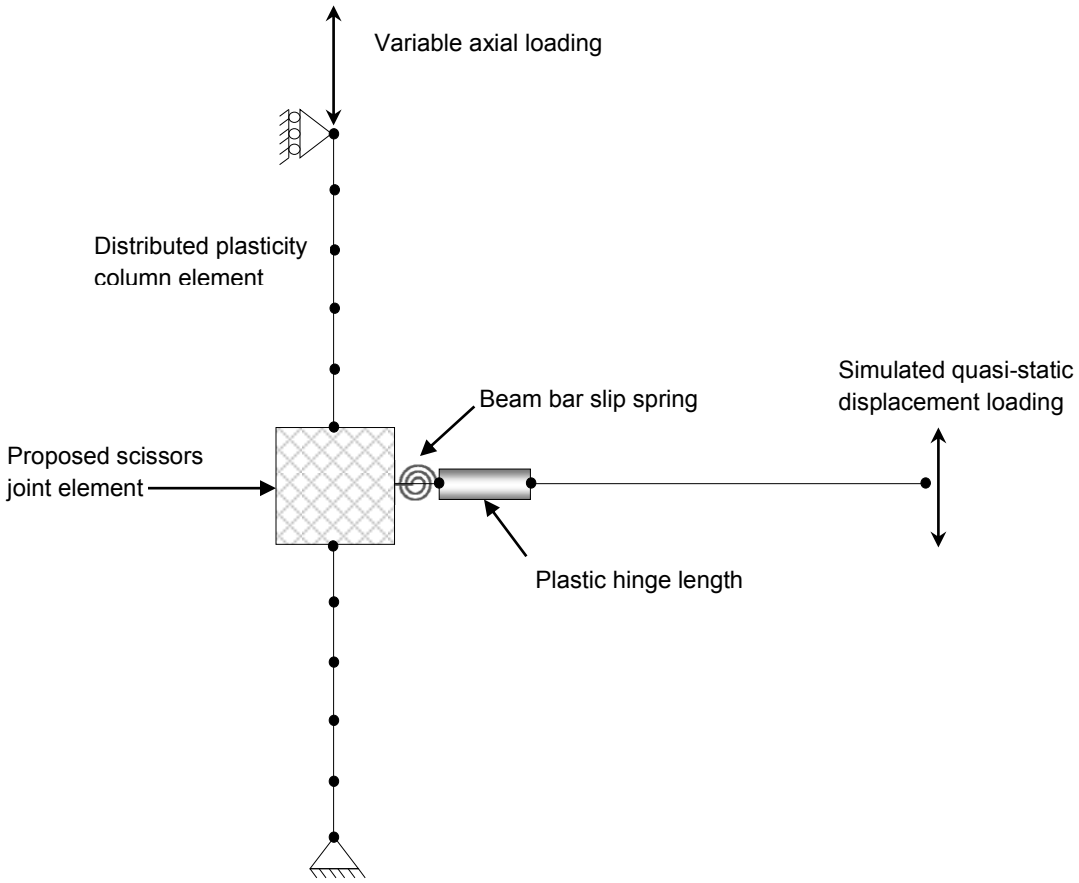

Figure 9.14.a NEES GC beam-column joint test simulation model, Option A

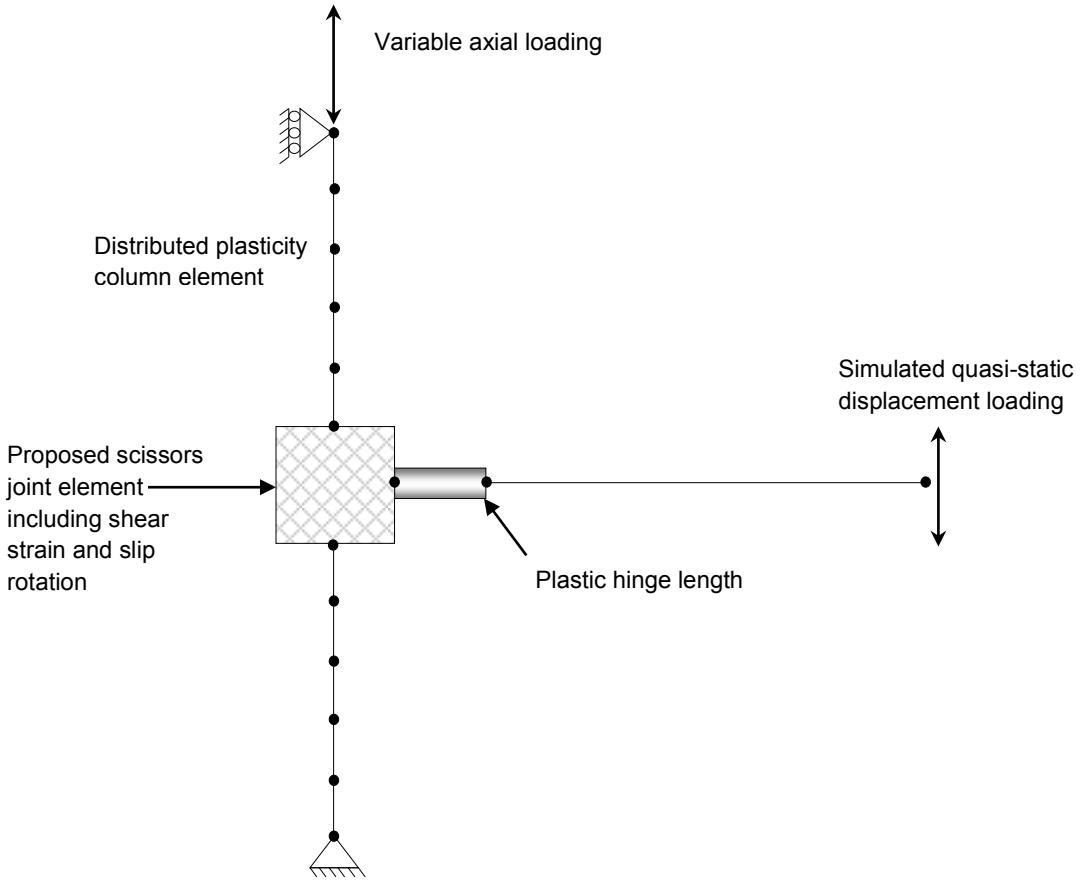

Figure 9.14.b NEES GC beam-column joint test simulation model, Option B

9.3.2 MATERIAL SIMULATION PARAMETERS

Uniaxial stress-strain concrete and steel materials were used to model the specimens at the section level. *Concrete02* material (Yassin [156]) was used to model concrete behavior. This material model defines the uniaxial response of concrete in compression and tension. The model features linear tension softening to represent inelastic tension action.

The unconfined concrete parameters used for cover concrete were those experimentally obtained at test date for specimen sub-assemblages (Chapter 6). Concrete strain at maximum strength was assumed as -0.002. The maximum tensile stress was taken from cylinder test results.

Since significant ductility enhancement is provided by confinement, a modification to the *Concrete02* unconfined properties was used to account for this enhancement. Thus, this modification was implemented by using confined concrete model by Kent and Park [70] for the core concrete.

Steel02 material model was used to model the uniaxial cyclic behavior of reinforcing steel. The model uses a bilinear backbone, and the Menegotto-Pinto model for loading and unloading rules. Monotonic steel properties are based on reported materials tests.

9.3.3 BEAM AND COLUMN SIMULATION PARAMETERS

Column Section Level
The column section was discretized as fiber section using 1 in. mesh. To predict axial load-moment interaction of the fiber section, one-dimensional material model for steel and concrete was used. The core confined concrete and the cover unconfined were defined using *Concrete02* material described before. *Steel02* was used to model reinforcement steel bars in the section using the as-built locations observed after specimen testing of the current test program.

Column Member Level
The columns were modeled on the member level using an inelastic fiber element (distributed inelasticity model) along the column height, with four integration points within the field span. The reason for using fiber section along the column height although it is computationally demanding is to account for axial load variability due to overturning moment to capture any possible nonlinearity over the column height.

Beam Section Level
Beam sections were discretized as fiber section having 2 in. height and 1 in. width. The concrete was defined using *Concrete02* material described earlier. Reinforcing steel bars were modeled in the section using the as-built effective depth observed after specimen testing as noted in Table 6.5. Only slab reinforcement that are confirmed to have contributed to the shear stress demand during tests of the current study was included. *Steel02* material model described earlier was used to model steel reinforcement.

Beam Member Level
The beams were modeled using *beamWithHinges2* elements in OpenSees 2.2.2 framework. This element is a force-based elastic element along the beam length with all inelasticity concentrated at the beam ends. The advantage of this element over other concentrated plasticity elements is that these elements have only one inelastic section at each beam end where all the plasticity is lumped, while in *beamWithHinges2* element there are two inelastic sections spaced apart by the plastic hinge length at each beam end, which resembles the plastic hinge region length [142]. A plastic hinge length $0.5h_b$ was used.

9.3.4 COMPARISON OF SLIP ROTATION SIMULATION OPTIONS A AND B

Figure 9.15 shows comparisons of the simulation responses using Option A and Option B for modeling bond slip rotation. It can be observed that both options tend to yield similar responses with no major advantage for one option over the other. A similar observation was noted by Theiss [142]. However, Option A will be used in specimen simulations performed in the next section. This choice was made to enable comparison of the proposed model backbone curve and responses directly with other available models that explicitly incorporate the joint shear deformation separately from slip rotation.

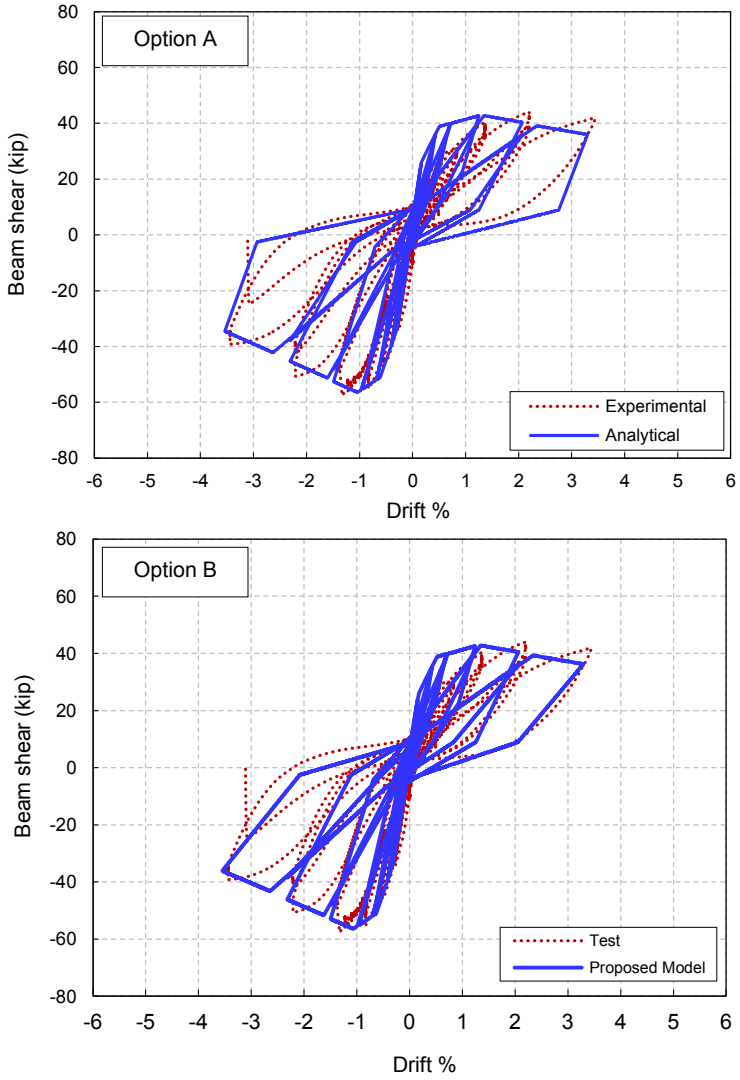

Figure 9.15 Simulation results for specimen U-J-2 using explicit and implicit slip rotation models

9.3.5 SIMULATION RESULTS USING PROPOSED JOINT MODEL

Figures 9.16 through 9.18 show the simulation results using the proposed scissors joint model with option A of bond slip rotation for specimens U-J-2, U-J-1 and U-BJ-1, respectively. The proposed model was able to capture the response of specimen U-J-2 when the joint is subjected to compression axial load successfully. However, it slightly overestimated the initial stiffness of the specimen when the overturning moment brings the joint into tension or small compression. This might be the result of two aspects. The first is the model simplification of initial stiffness of joint panel, $0.5G_c$, which could be slightly lower for tension cycle. The second aspect is that the proposed model assumed that the mode of failure is a J-Failure mode without accounting for slight beam yielding before joint failure. During specimen U-J-2 test, however, the exterior beam reinforcement bar slightly yielded prior to reaching peak joint shear strength while the interior bars remained elastic. This could have contributed additional unexpected flexibility to the test sub-assemblage in the tension cycle that was not completely captured by the model. The proposed model slightly underestimated the peak shear strength drift of the downward loading cycle. Finite element simulations generally produce slightly stiffer responses compared to "true" stiffness, which might partially explain the slight underestimation. The concrete micro-cracking in the elastic elements and the relative setup flexibility are not accounted for in the current finite element simulation since they could not be quantified reasonably. It is worth mentioning that it was not possible to predict the response of the last downward loading cycle that triggered axial failure (second cycle at -3.42% drift) since it would have needed a fatigue based analysis to be included in the simulation to force axial failure that occurs at a drift ratio not located on the shear-force-drift envelope.

As seen in Fig. 9.17, the proposed joint scissors model reproduced the cyclic response of specimen U-J-1 with reasonable accuracy. Similar to specimen U-J-1, the model slightly underestimated the peak shear strength drift in the downward loading direction. The simulated response in the upward loading direction was less accurate than that in the downward loading direction in terms of strength degradation envelope. This might be attributed to the calibration procedure followed for the proposed model, which did not account for the degrading axial tension force that took place during specimen U-J-1 testing.

Figure 9.18 shows the simulation response of specimen U-BJ-1 using the proposed joint model. The model was able to successfully predict the experimental response of the specimen.

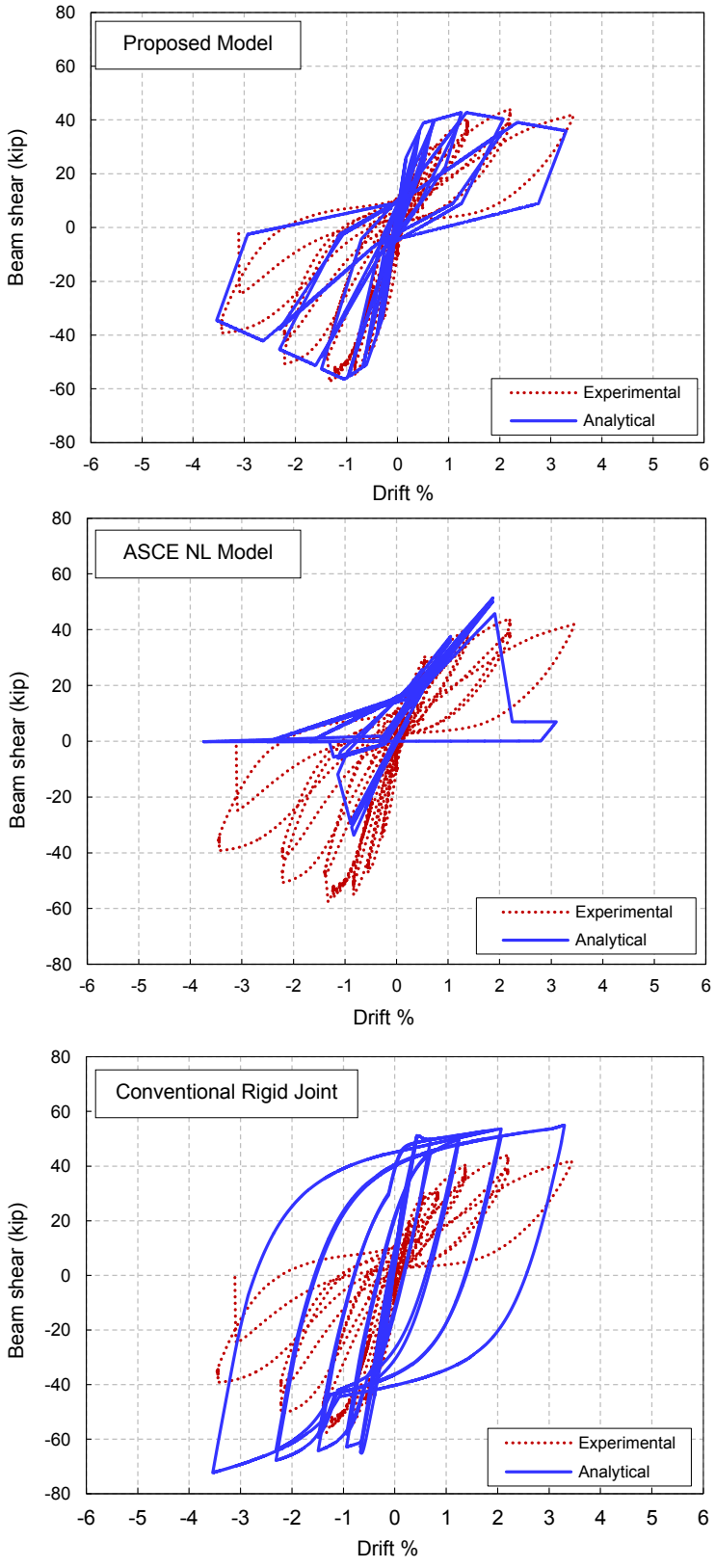

Figure 9.16 Simulation results of specimen U-J-2

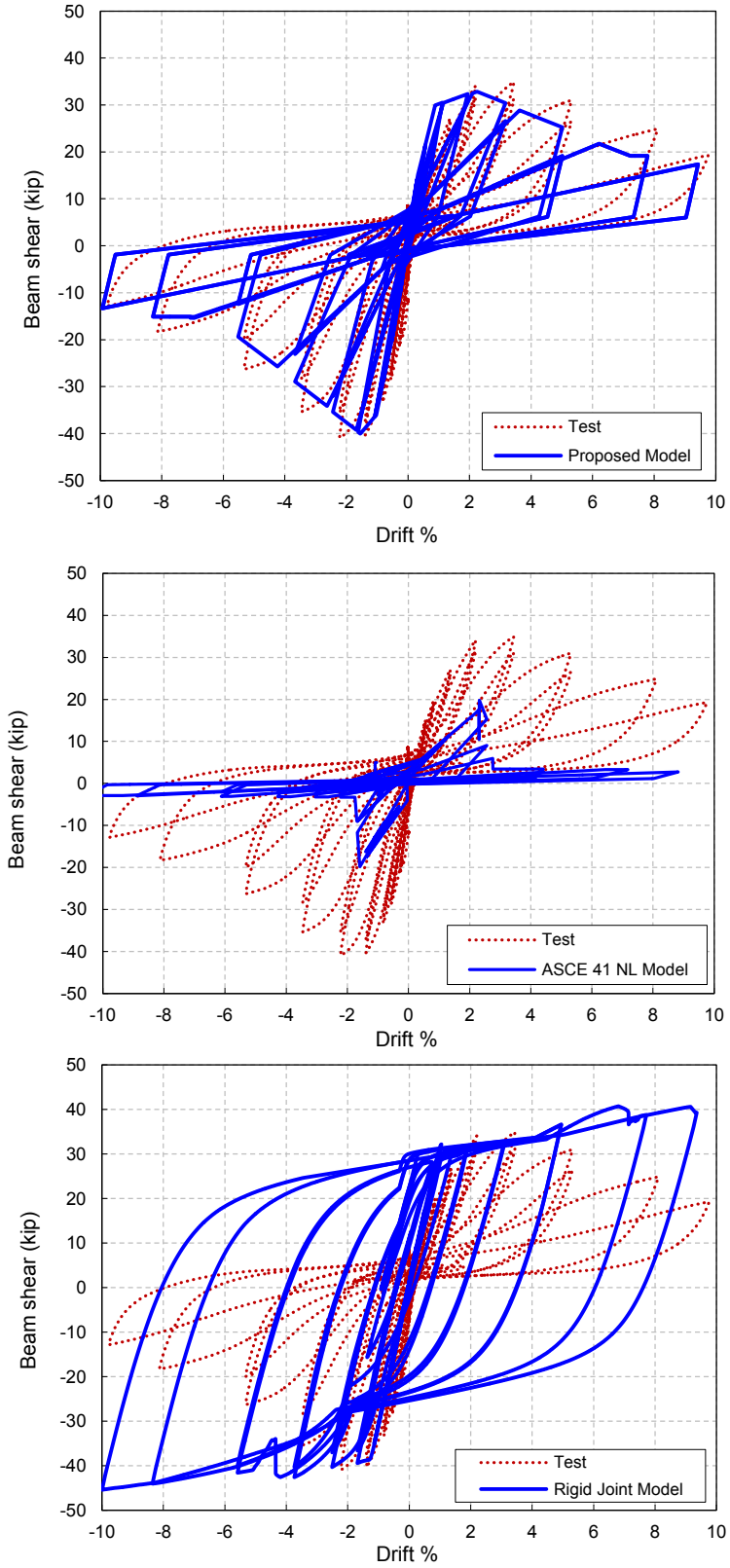

Figure 9.17 Simulation results of specimen U-J-1

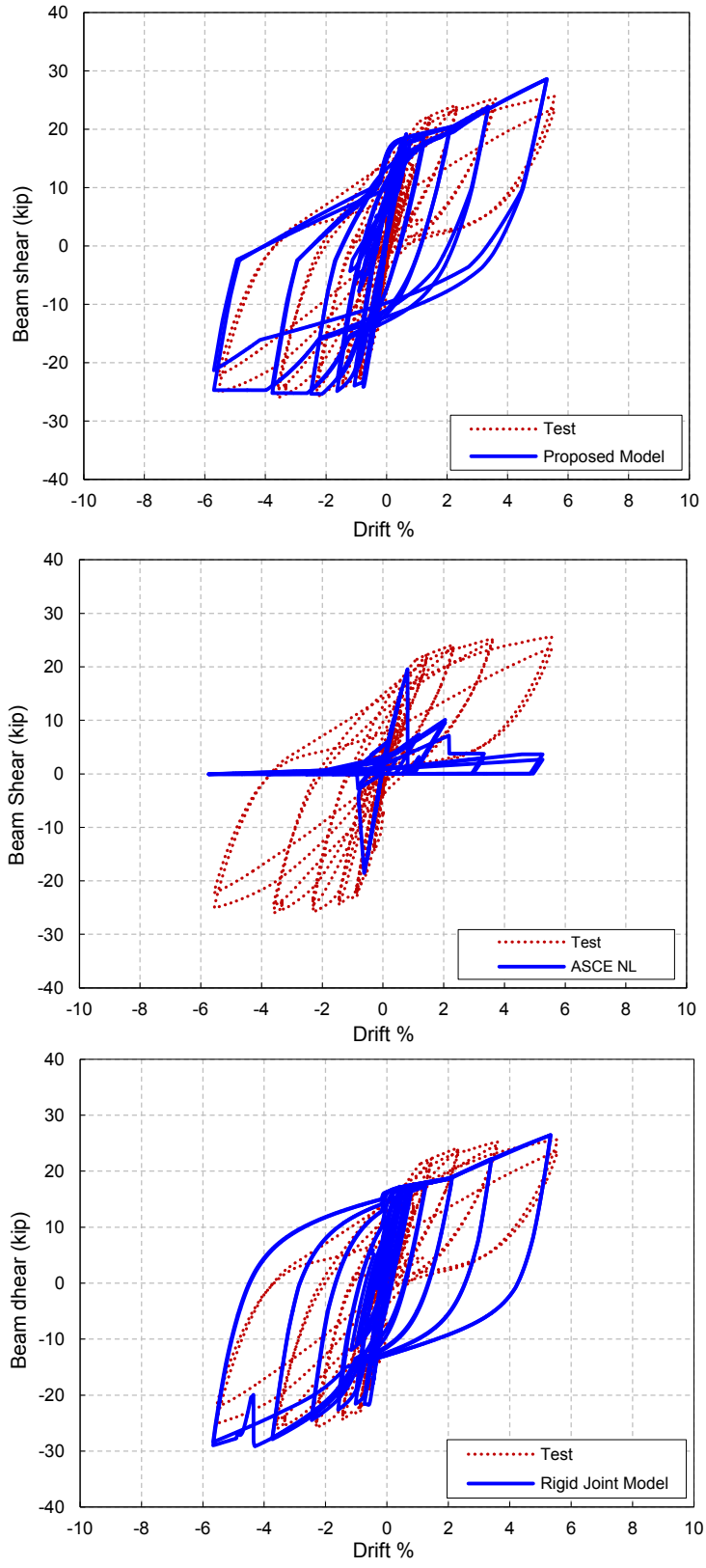

Figure 9.18 Simulation results of specimen U-BJ-1

9.3.6 SIMULATION RESPONSE USING CONVENTIONAL RIGID JOINT MODEL

Figures 9.16. 9.17 and 9.19 show the force-drift simulation response for specimen U-J-1 and U-J-2, and Phase 1_SP4 [120] using conventional centerline rigid joint assumption. It can be observed that the simulated response of all three specimens is dominated by beam flexural capacity whereas the experimental failure mode was J-Failure with no beam yielding. The simulated results deviate unacceptably from the measured behavior.

Figure 9.18 shows the force-drift simulation response for specimen U-BJ-1, which experienced experimental BJ-Failure mode, using conventional centerline joint assumption. The Figure shows that this assumption is capable of predicting the cyclic response of specimen U-BJ-1 with reasonable accuracy. This is expected the experimental response was dominated by beam flexural response until late stages of loading. However, this result should not be generalized to all BJ-Failure mode cases and should be limited to high axial loads (higher than 40% the column compression capacity). Recall that the post-yield profile in this specimen is substantially prolonged due to clamping effect of high axial load on the joint as explained in detail in Chapter 7. Thus, joint contribution to the total response was not negligible which explains the reasonable accuracy of conventional centerline analysis. A drawback of the rigid joint model is its lower accuracy for the upward loading direction where the joint is under tension or small compression and thus it contributes to the overall drift more significantly than it does for the downward compression cycle.

9.3.7 SIMULATION RESPONSE USING ASCE 41 NONLINEAR MODELING PROVISIONS

Figures 9.16. 9.17 and 9.19 show the force-drift simulation response for specimen U-J-1 and U-J-2, and Phase 1_SP4 using ASCE 41 nonlinear joint modeling strength and deformation provisions along with the ASCE 41 supplement semi-rigid joint model described earlier in Section 9.2. The results indicate that the ASCE 41 nonlinear modeling parameters can produce unacceptably inaccurate simulations. Post peak plastic deformations were underestimated. The calculated steep strength loss immediately following the peak joint shear strength does not resemble the test results. In addition, the peak shear strength coefficient suggested by ASCE 41 underestimates the actual strength.

9.3.8 MODEL VALIDATION AND CALIBRATION

To further investigate the appropriateness of the proposed joint model for unconfined joints, six additional unconfined exterior and corner beam-column joint tests were simulated using the proposed model, as described previously. The failure mode of specimens SP4, BS-L, BS-L600 and Unit 5 were J-Failure mode while there was some yielding in specimens SP2 and Unit 6 prior to reaching peak joint shear strength.

In general, the proposed model was able to simulate the test response of the six specimens with reasonable accuracy. The only calibration that took place was to accommodate the slight change

in joint shear strain corresponding to peak shear strength due to the change in joint aspect ratio. This was calibrated using specimen SP4 and was reflected in Eq. 9.18 and Eq. 9.19.

The model prediction of cyclic response of specimen SP4 was superior to the ASCE 41 linear and nonlinear modeling provisions as depicted in Fig. 9.19. The model prediction of the force-drift envelope, including peak drift-to-peak drift strength and stiffness degradation was better than its prediction of the strength and stiffness degradation within the same drift peak. This may suggest the need for a fatigue based expressions for future model development of strength and stiffness degradation parameters rather than using empirical fitting for *pinhing4* material model.

Figure 9.20 and Fig. 9.21 show comparisons between test and simulation responses of specimens BS-L and BS-L600 using the proposed joint scissors model. The model was able to predict the test response with reasonable accuracy. However, the proposed strut-and-tie model in Chapter 5, that was used to predict point 3 on the envelope curve, overestimated the peak shear strength of specimen BS-L by about 10%. This led to slight overestimation of the response envelope of specimen BS-L. The model prediction for specimen BS-L-600 was symmetric for both loading directions; however, the test response was unsymmetrical possibly due to special test conditions that led to lower strength and higher deformation in the negative loading direction.

The proposed model predicted response for specimen SP2 is shown in Fig. 9.22. It can be noticed that the model response was dominated before reaching peak joint strength by beam flexure. Afterwards, the predicted strength degradation was controlled by joint degradation envelope. This is consistent with experimental observations of specimen SP2, which had minor beam yielding (BJ-Failure) in both loading directions before reaching shear strength capacity of strut-and-tie model J-Failure mode. The mode was able to recognize that the beam flexural capacity corresponded to a lower strength than the J-Failure capacity input by the scissors model envelope and hence forced the beam yielding before joint degradation.

The simulation results of Unit 5 and Unit 6 is shown in Fig. 9.23. The model produced a generally stiffer response compared to the experimental one. However, the general model response is conservatively acceptable. It is worth mentioning that the model development and calibration relied mainly on corner joints with slab included, but the application to joints without slab also was successful.

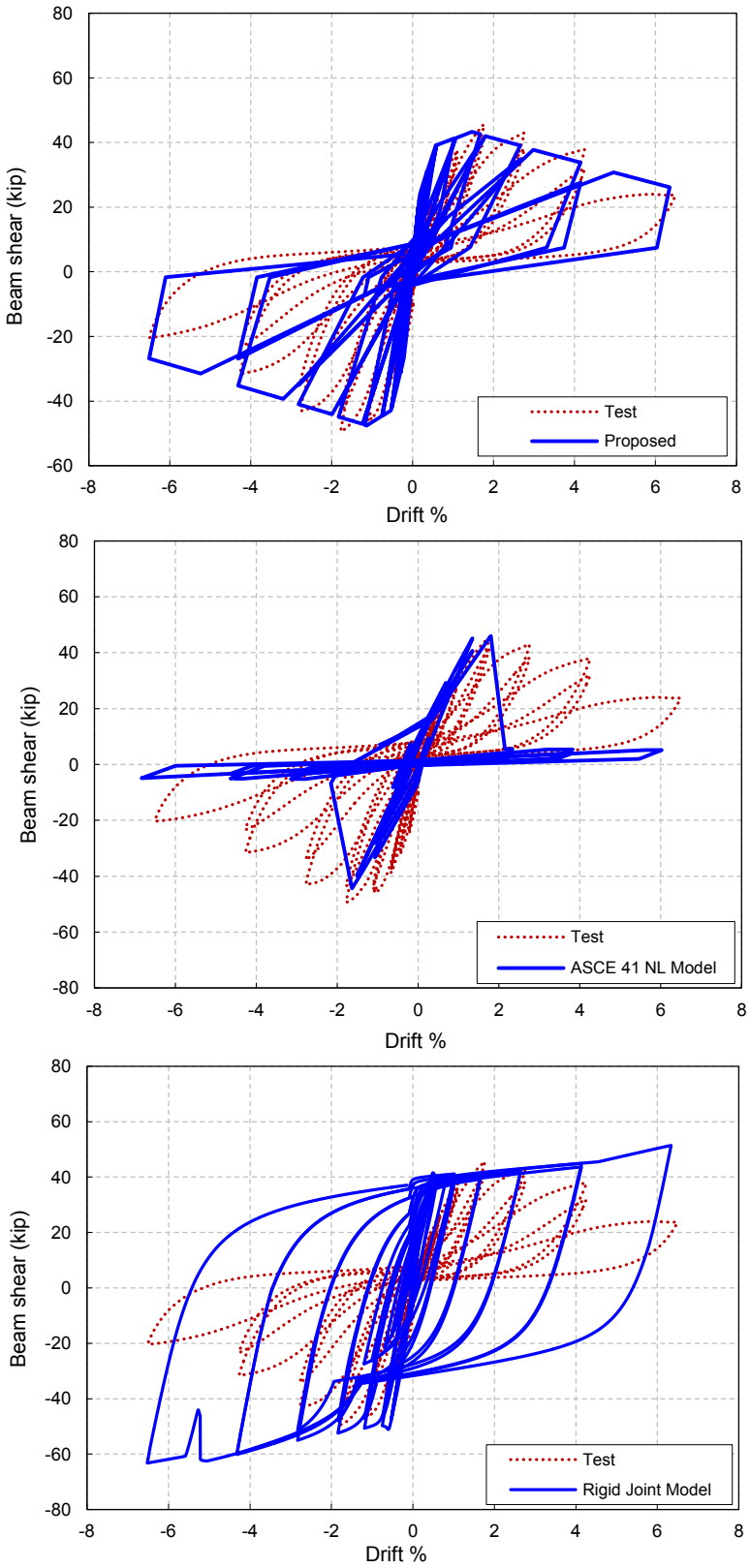

Figure 9.19 Simulation results of Park [120] specimen SP4

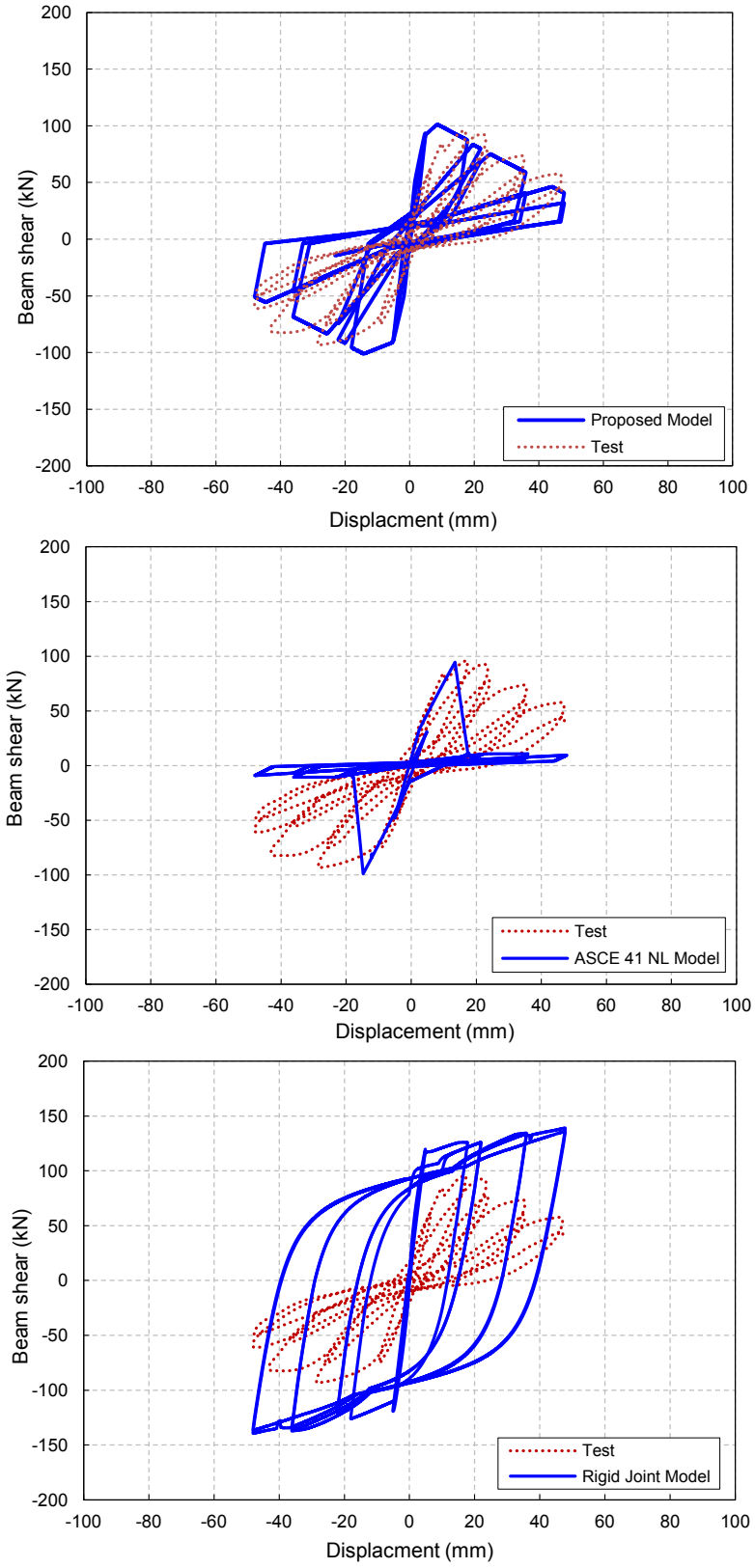

Figure 9.20 Simulation results of Wong [155] specimen BS-L

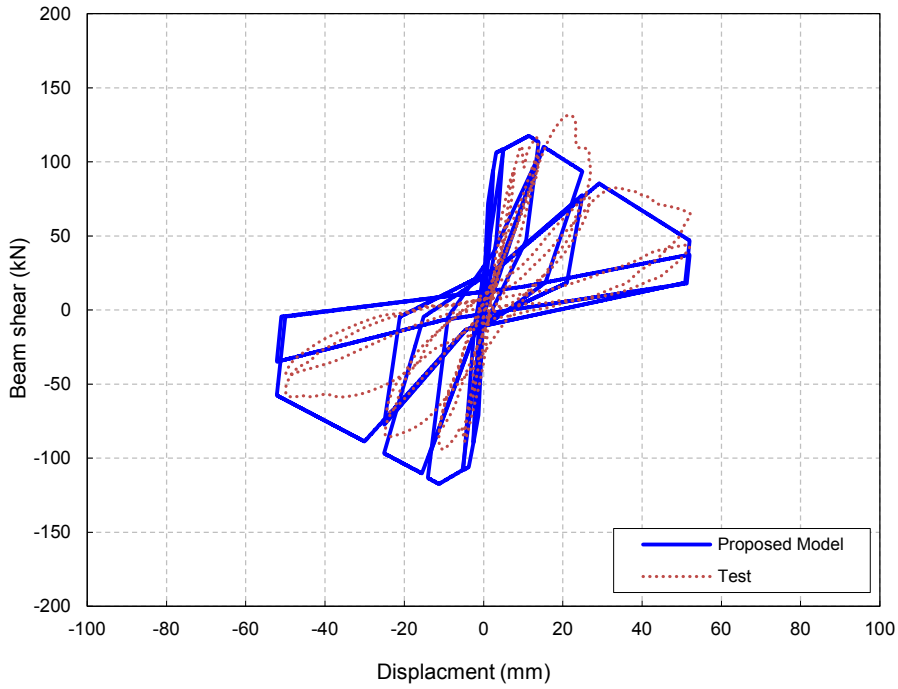

Figure 9.21 Simulation results of Wong [155] specimen B-S-L600

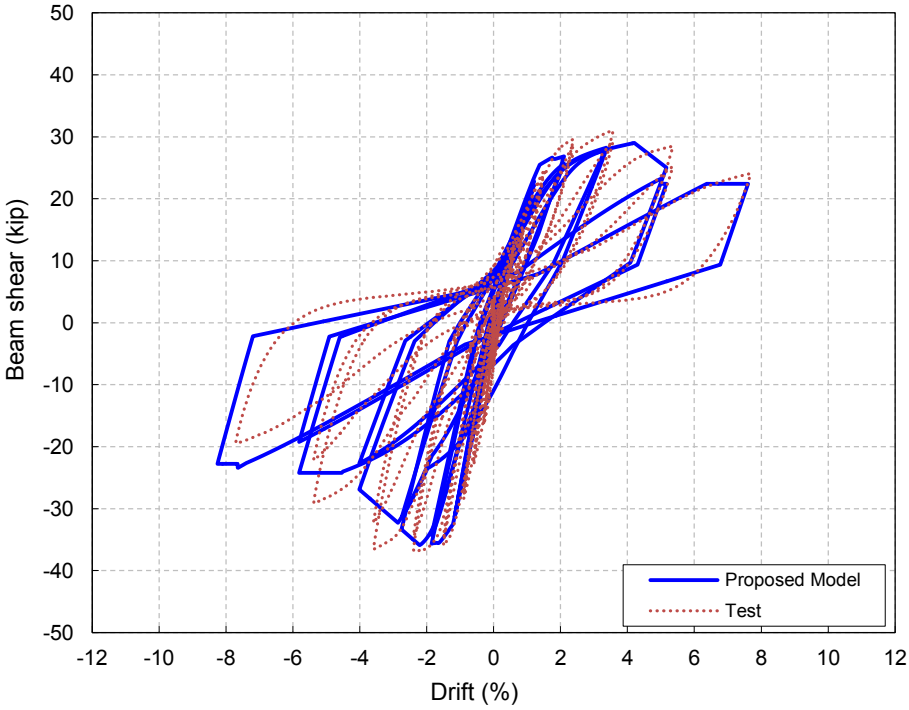

Figure 9.22 Simulation results of Park [120] specimen SP2

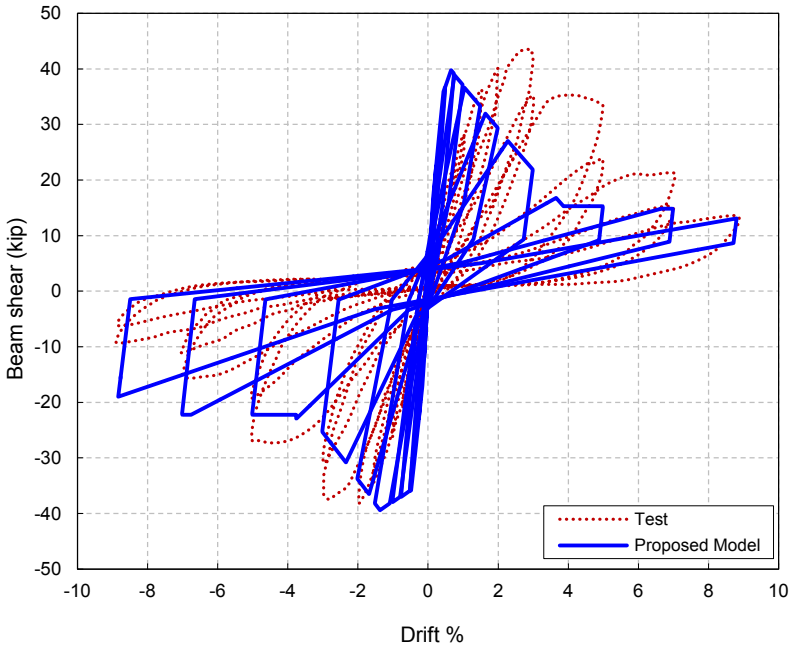

(a)

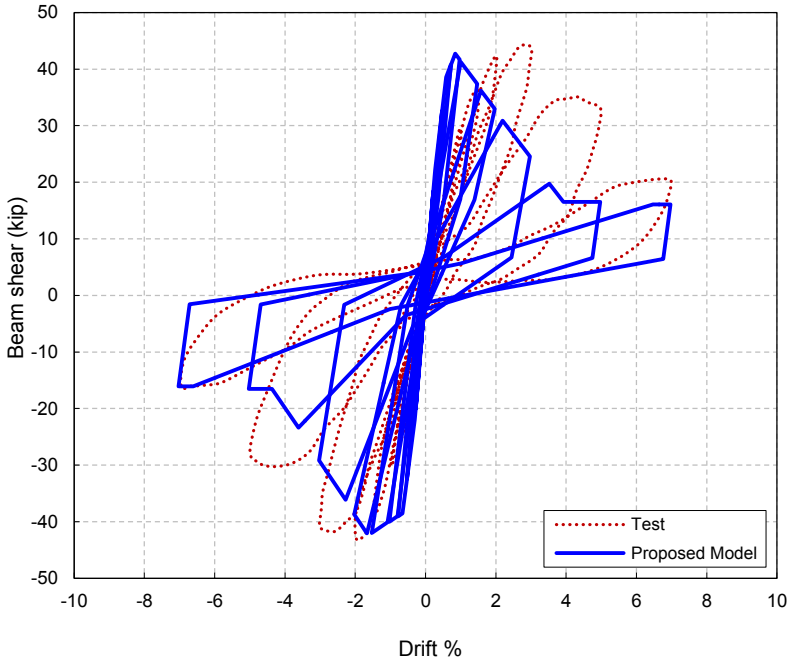

(b)

Figure 9.23 Simulation results of Pantelides et al. [116] specimens, (a) Unit 5, (b) Unit 6

CHAPTER 10

SUMMARY, CONCLUSIONS, AND RECOMMENDATIONS

10.1 SUMMARY

Beam-column joints in concrete buildings are key components to ensure structural integrity of building performance under seismic loading. Earthquake reconnaissance has reported the substantial damage that can result from inadequate beam-column joints. In some cases, failure of older-type corner joints appears to have led to building collapse.

Since the 1960s, many advances have been made to improve seismic performance of building components, including beam-column joints. New design and detailing approaches are expected to produce new construction that will perform satisfactorily during strong earthquake shaking.

Much less attention has been focused on beam-column joints of older construction that may be seismically vulnerable. Concrete buildings constructed prior to developing details for ductility in the 1970s normally lack joint transverse reinforcement. The available literature concerning the performance of such joints is relatively limited, but concerns about performance exist.

The current study aimed to improve understanding and assessment of seismic performance of unconfined exterior and corner beam-column joints in existing buildings. An extensive literature survey was performed, leading to development of a database of about a hundred tests. Study of the data enabled identification of the most important parameters and the effect of each parameter on the seismic performance.

The available analytical models and guidelines for strength and deformability assessment of unconfined joints were surveyed and evaluated. Upon identifying deficiencies in these models, new joint shear strength models, a bond capacity model, and axial capacity models designed and tailored specifically for unconfined beam-column joints were developed.

In the laboratory testing phase of the current study, four full-scale corner beam-column joint subassemblies, with slab included, were designed, built, instrumented, tested, and analyzed. The specimens were tested under unidirectional and bidirectional displacement-controlled quasi-static loading that incorporated varying axial loads that simulated overturning seismic moment effects. The axial loads varied between tension and high compression loads reaching about 50% of the

column axial capacity. The test parameters were axial load level, loading history, joint aspect ratio, and beam reinforcement ratio.

Based on the literature database investigation, the shear and axial capacity models developed and the test results of the current study, an analytical finite element component model was developed to represent the behavior of unconfined beam-column joints in computer numerical simulations of concrete frame buildings. Finally, a parametric study was conducted to assess the axial failure vulnerability of unconfined beam-column joints based on the developed shear and axial capacity models.

10.2 CONCLUSIONS AND RECOMMENDATIONS

Based on the results of the research work conducted and presented in this manuscript and within the range of parameters investigated and the limitations and the calibration datasets for the models developed, the key findings and outcomes of this investigation are summarized hereafter.

10.2.1 Joint Shear Strength Assessment

1. Pre-1970 construction can be vulnerable for joint shear failure. This vulnerability is well documented by test results and post-earthquake reconnaissance.

2. Several joint failure modes are identified. These modes were defined as J (joint shear failure before yielding of beams or columns), BJ (beam yielding before joint shear failure), CJ (column yielding before joint shear failure), S (slip of beam bottom reinforcement with straight anchorage), B and C failure modes (beam or column yielding without joint shear failure respectively).

3. In joints with strong beams, columns, and anchorages, J-type joint shear failure occurs in which strength is determined largely by the “true” capacity of the joint region. If beam or column yields prior to reaching the true capacity of the joint region, subsequent joint failure still is possible but in this case the joint shear strength is limited by the shear corresponding to the flexural strength of the beam or column, whichever is yielding.

4. Several existing joint shear strength models are not suitable for unconfined exterior and corner joints since they were primarily designed and calibrated using joints with transverse reinforcement.

5. A strut-and-tie model for J-Failure unconfined joint shear strength calculation was proposed. This model is based on the ACI 318-08 strut-and-tie modeling provisions interpreted and modified to suite beam-column joints. Effects of axial load level, joint aspect ratio, and bidirectional loading were included in this model. The model correlates well with test results for unconfined exterior and corner beam-column joints; (AVG test/model strength=1.03; COV=0.11).

6. An empirical model for quick estimation of shear strength of unconfined exterior and corner joint with J-Failure mode was proposed. The model accounts for axial load level, joint aspect ratio, and bidirectional loading. The model can estimate joint shear strength for preliminary analysis with reasonable accuracy; (AVG test/model strength=0.99; COV=0.13).

7. Expressions to relate shear strength degradation with displacement ductility were proposed to modify joint shear strength calculated using strut-and-tie or empirical models. Inclusion of a ductility parameter in the shear strength model yields slightly conservative model correlation to test results due to the conservative choice of the ductility parameter to reflect the uncertainty and variability of ductility calculations.

8. Current bond strength models are not suitable for estimating pull-out capacity of insufficiently embedded reinforcement in beam-column joints since they do not account accurately for axial load and confinement effects.

9. An empirical model for estimation of pull-out capacity of insufficiently embedded reinforcement in beam-column joints was proposed. The model accounts for axial load level, transverse beam confinement, and concrete slab effect. The model correlates to test results with reasonable accuracy (AVG test/model strength=0.94; COV=0.14).

10.2.2 Existing Buildings Assessment Documents ASCE/SEI 41-10 and ACI 369-11

1. The shear strength provisions of the existing building assessment documents ASCE/SEI 41/06 and ACI 369-R11 are overly conservative for unconfined exterior and corner joints. Their shear strength coefficient is approximately a lower bound for all possible strength values; with a level of conservatism that can reach 150%. This is because they do not account for mode of joint failure, joint aspect ratio, beam reinforcement ratio, axial load ratio and bidirectional loading conditions.

2. The plastic rotation (plastic shear strain) nonlinear modeling parameters of ASCE 41 are very conservative compared to test results, especially with high axial loads.

3. The nonlinear modeling recommendation for residual shear capacity is quite conservative, especially for high axial load cases. A zero residual shear capacity is specified by ASCE 41 for high axial loads in contrast with a 20% to 50% residual shear capacity at axial failure observed during the current experimental investigation.

4. ASCE 41 nonlinear modeling parameters for beam-column joints result in unrealistically severe strength degradation cyclic response. They also result in a major underestimation of post-peak drift capacity of unconfined joints.

5. Modeling the beam-column joint region as a rigid element significantly overestimates the stiffness of beam-column framing.

10.2.3 Effect of Key Test Parameters on Joint Performance Measures

10.2.3.1 AXIAL LOAD LEVEL

J-Failure

1. Axial loads higher than $0.2 f_c' A_j$ enhance joint shear strength. Increasing axial load from $0.15 f_c' A_j$ to $0.46 f_c' A_j$ enhanced joint shear strength by about 18.5% for joint aspect ratio of 1.67.

2. The axial load joint shear strength enhancement within the range of 0-0.2 $f_c' A_j$ is marginal. No general trend of axial load enhancement for joint shear strength within this range is evident.

3. Introducing small tensile axial load (3% the compression capacity) reduced joint shear strength by about 6.5% compared to the case of zero axial tension for the joint aspect ratio of 1.67.

4. The high compression axial load significantly accelerated post-peak strength degradation by about 24-37%.

5. Increasing axial load from $0.15 f_c' A_j$ to $0.46 f_c' A_j$ reduced drift capacity corresponding to peak shear strength by 25.5% for joint aspect ratio of 1.67. The high axial load reduced maximum drift reached by about 55%.

6. High axial loads increased brittleness of joint behavior. Increasing axial load from 0.15 $f_c' A_j$ to $0.46 f_c' A_j$ reduced ductility capacity by about 20% for joint aspect ratio of 1.67.

7. The high axial load increased initial and pre-peak effective stiffness. However, the post-peak effective stiffness was decreased due to high axial load.

8. High axial load decreases joint shear strain. This is due the reduction of principal tension stresses. It is also associated with smaller number and less smeared shear cracks compared to lower axial loads.

9. Joint shear deformation contribution to overall story drift ratio is very significant, especially in the nonlinear range. This contribution can reach 50% at about 3% drift.

BJ-Failure

1. The level of axial load does not affect joint shear strength in the case of BJ-Failure mode. This is attributed to the flexural controlled behavior due to beam yielding which determines the joint strength. A beam hinging action with no strength gain after strain

hardening is evident. Increasing axial load level from $0.12 f_c' A_j$ to $0.50 f_c' A_j$ did not affect peak strength of the subassembly for joint aspect ratio of 1.

2. High axial has a major beneficial effect in maintaining the peak shear strength in the post-peak regime and allowing much longer profile of strain hardening by the clamping action to the joint which delays its degradation. This allows full utilization of beam strain hardening plastic capacity by reaching very large beam plastic rotations and drifts (larger than 5%) with marginal joint cracking and negligible degradation in joint shear strength.

3. The high axial load clamping effect is evident to improve bond capacity between beam bars and concrete within the joint region. Increasing axial load from $0.12 f_c' A_j$ to $0.50 f_c' A_j$ significantly delayed joint cracking and shear stress deterioration by clamping action of beam bars in the joint that delayed yield stress penetration and bond strength degradation.

4. Increasing axial load from $0.12 f_c' A_j$ to $0.50 f_c' A_j$ did not affect drift capacity at peak strength for joint aspect ratio of 1. However, high axial loads significantly enhanced ductility capacity of beam-column joint sub assemblage. Increasing axial load from $0.12 f_c' A_j$ to $0.50 f_c' A_j$ doubled the ductility capacity of joints with aspect ratio of 1.

5. The higher axial load significantly reduced stiffness degradation after reaching peak joint shear strength and plastic strain hardening capacity. The reduction of stiffness degradation due to higher axial load at the same drift level was about 70% in average.

6. High axial load increases initial stiffness due to the added joint rigidity which led to less joint contribution to total drift.

7. High axial load helped significantly reduce joint shear strain at the same drift level compared to lower axial loads.

8. Joint contribution to overall story drift for joints undergoing high axial compression loads is negligible. However, this contribution is significantly exceeding 20% at 5% drift when the column is under tension or small compression.

10.2.3.2 BIDIRECTIONAL LOADING HISTORY

1. Shear strength along principal framing lines of a biaxially loaded joint was about 25% lower than that of uniaxially loaded joint for joint aspect ratio of 1 under compressive joint loading. However, biaxial shear strength along the biaxial lateral loading direction under compression loading was close to the shear strength of uniaxially loaded joints. This observation suggests that a circular (or perhaps elliptical) biaxial shear strength relation may be appropriate to approximate strength of biaxially loaded joints. The circular interaction envelope was more accurate when the joint is under compression than when it is under tension.

2. Drift ratio at peak shear strength was slightly reduced when applying the simultaneous biaxial loading for an unconfined corner joint experiencing J-Failure.

3. Joint shear cracking started earlier for the biaxially loaded joint compared to the uniaxially loaded ones.

4. Stiffness degradation under simultaneous biaxial loading was more pronounced than that under alternating uniaxial loading. Post-peak pinching is more evident under bidirectional loading.

5. The effective stiffness is lower for biaxially loaded joints. This is partially due to the lower stiffness of the column. In addition, the effective stiffness degradation within the same drift level is more pronounced in a bidirectionally loaded specimen.

6. Biaxial column flexural capacity should be checked independently from joint capacity and compared to beam overstrength flexural capacity to ensure beam hinging before column hinging under bidirectional earthquake loading.

10.2.3.3 JOINT ASPECT RATIO

1. Joint shear strength is significantly reduced by increasing joint aspect ratio due to steeper joint strut inclination. Increasing joint aspect ratio from 1 to 1.67 resulted in decreasing joint shear strength by about 36%.

2. The strut-tie-model and the empirical model proposed for joint shear strength are able to accurately represent the effect of joint aspect ratio.

3. Joint aspect ratio has negligible effect on post-peak joint shear strength degradation.

4. Joint aspect ratio effect on displacement ductility could not be firmly established. However, there is some evidence that higher aspect ratio might slightly decrease ductility.

5. Increasing joint aspect ratio increases joint shear strain for the same drift ratio. However, the overall joint rotation including beam bar slip decreased with increasing joint aspect ratio.

6. Increasing joint aspect ratio from 1 to 1.67 reduced drift ratio at peak shear strength by about 20% in the compression cycle and 35% in the tension cycle. The source of this reduction was not identified but it could be associated with lower beam bar slip rotation contribution to the drift.

7. Higher joint aspect ratio specimen is characterized by more rapid peak-to-peak effective beam stiffness degradation than that of smaller joint aspect ratio.

10.2.3.4 BEAM REINFORCEMENT RATIO / MODE OF JOINT SHEAR FAILURE

1. Joint shear strength is proportional to beam reinforcement within the BJ-Failure mode ratio until the threshold limit of J-Failure capacity is reached.

2. Within BJ-Failure, joint shear strength is essentially equal to shear stress demand from beam flexural strain hardening capacity up to the threshold limit of J-Failure direct shear strength of the joint.

3. Beyond the J-Failure shear strength capacity, increasing beam reinforcement has no appreciable effect on joint shear strength.

4. The long strain hardening post-peak profile of specimens with BJ-Failure, especially with high axial load, is distinctively different from the fast degrading post-peak profile of J-Failure ones. Much higher ductility of BJ-Failure mode under high axial loads is evident.

5. The effective stiffness degradation within the same drift ratio in J-Failure and BJ-Failure modes are similar until reaching joint shear capacity of the former, after which the J-Failure joints stiffness degrades much faster than that of BJ-Failure joints due to the significant joint cracking and pinching of the former as opposed to the ductile response with most nonlinearity is concentrated in flexural hinging in the latter.

10.2.4 Effect of Other Design Parameters on Joint Performance Measures

1. Based on the their negligible strains at peak shear strength during the current tests, the contribution of intermediate column reinforcement bars to joint shear strength was concluded to be negligible. This observation is contrary to the observation of some other previous tests.

2. The joint shear stress demand increases due to slab reinforcement contribution. Joint shear strength should be checked against demand from beam reinforcement and effective slab reinforcement collectively in deciding the mode of joint failure and in deciding the shear capacity of joints in BJ-Failure mode.

3. The effective width of slab in tension in the case of BJ-Failure mode can be conservatively taken as the beam width plus the transverse beam depth. However, the effective slab width in the case of J-Failure mode can be chosen as the beam width plus twice the transverse beam depth.

4. The presence of concrete slab created significant twisting moments and rotations in the beams. This effect is more pronounced in alternating bidirectional loading.

5. Joint shear strength is inversely proportional to displacement ductility input. However, previous test results show moderate correlation between these two parameters. A conservative shear strength degradation model based on this correlation was established.

6. Principal tension stress is not a good indicator to represent shear strength since it overestimated the axial load contribution. No generalized trend between principal tension stresses and drift ratio or displacement ductility was observed.

10.2.5 Joint Numerical Modeling for Finite Element Simulation

1. Rigid joint assumption for linear or nonlinear modeling of concrete frames is generally incorrect. Models using this approach did not correlate well with observed response of J-Failure beam-column joint test subassemblies.

2. For joints with BJ-Failure mode subjected to very high design axial loads (larger than $0.45\ f_c' A_j$), the rigid joint model produced results that resembled test cyclic response more reasonably. This is because the response in BJ-Failure mode associated with high axial loads is dominated by beam yielding with a high joint clamping action that delays joint degradation.

3. A cyclic constitutive model backbone curve was proposed for nonlinear modeling of shear parameters of unconfined beam-column joints in finite element building simulation. The proposed model incorporates the effect of axial load level, overturning seismic moment, joint aspect ratio, joint failure mode and the post-shear damage residual axial capacity.

4. The rotational spring with rigid links joint model (scissors model) associated with the proposed backbone curve was able to adequately model the cyclic response of beam-column joint subassemblies of current and previous tests.

10.2.6 Axial Capacity of Unconfined Beam-Column Joints

1. An inverse proportionality between axial load and maximum drift reached before axial failure is evident for joints failing in the J-Failure mode. Joints with very high axial loads (perhaps larger than $0.45\ f_c' A_j$) experiencing BJ-Failure mode may benefit from higher axial load, such that they do not follow the aforementioned inverse relation.

2. Although not isolated as an independent variable in this study, joints undergoing more rigorous loading history (for example, more cycles) generally had smaller drift at axial failure.

3. The axial failure of joints tested in the current study occurred at an axial joint strain of about 0.005 to 0.006.

4. Two distinct modes of joint axial failure were identified. One mode is characterized by column bar sway and concrete core damage within the joint region and is associated with low to medium design axial loads (lower than $0.3f_c'A_j$). The second mode is characterized by column bar buckling and concrete core damage and is associated with high design axial loads.

5. The main resisting mechanism that supports axial loads in a shear damaged joints is believed to be shear friction on the previously damaged shear failure plane. The buckling capacity of column reinforcement is believed to be a secondary mechanism to shear friction mechanism, which is triggered upon shear friction failure.

6. Unlike some cases of column axial failure, joint axial failure does not immediately follow joint shear failure. The ratio of drift at axial failure to drift at shear failure ranged from 2.5 to 3.3 for high axial loads, and from 3 to 5.5 for low axial load.

7. An "axial failure safe zone" was identified based on the current and previous tests with and without axial failure. Joint axial failure was not observed for drift ratio demand below 2.5%-3%. For drift ratios higher than 2.5%-3%, axial failure was observed especially with increasing drift, axial load, or both.

8. The residual joint shear capacity at axial failure ranged from 0.20-0.50 the peak joint shear strength. Higher values corresponded to higher axial load ratios, which are the conditions of greater interest.

9. Joint axial capacity models were proposed based on the shear friction concept. The models correlated well with available data, but the data set was relatively small, such that additional model calibration is warranted.

10. A parametric study to assess axial collapse vulnerability for different combinations of column and joint geometries and reinforcement representing different building configurations was conducted. The study was based on extrapolating the proposed axial capacity empirical model to different joint geometries. Results of the parametric study indicate that axial collapse due to unconfined beam-column joint axial failure preceding column axial failure is unlikely except for particular geometric configurations. For beam to column depth ratio higher than 2.5, axial failure of joint that may trigger progressive axial collapse if the columns in the building are borderline shear critical with transverse reinforcement ratio of 0.0015-0.002.

10.3 FUTURE RESEARCH WORK

1. Implement the developed joint models into finite element software and conduct nonlinear dynamic analyses to better understand the effect of joint flexibility and failure on overall building performance. Specific outcomes could be improved understanding of the role of joints in collapse of older concrete buildings and development of collapse fragility curves for loss estimation purposes.

2. Conduct more exterior and corner beam-column joint tests that are continued until axial failure to further verify the developed axial failure models. Parameters of interest could include the effect of loading history in terms of number of displacement cycles on shear and axial strength and drift capacity. They may also include testing joints with aspect ratios higher than 2 and testing the effect of beam and column reinforcement ratios on axial capacity of J-Failure joints. A hybrid simulation test could be performed to assess more realistic building performance in the event of shear and axial degradation of joint.

3. Quantify the effect of intermediate column reinforcement bars on joint performance through testing several percentages of this reinforcement and establish a model to reflect any possible effect on shear strength.

4. Implement the proposed joint scissors model with its backbone parameters reflecting shear and axial capacity into OpenSees platform source code for easier future building modeling using a single command.

5. Investigate current and new retrofit options including fiber reinforced polymers, epoxy injected reinforcement, and external steel plates for possible strengthening of shear deficient unconfined corner beam-column joints.

6. Perform a shaking table building frame test with high gravity and seismic axial load to investigate the collapse vulnerability associated with joint flexibility and failure, and to calibrate analytical models.

7. Present a rigorous analytical procedure to quantify the torsional effect due to slab presence along with design recommendation to include this effect in design codes.

8. Conduct corner beam-column joint cyclic tests to assess the effect of beam width and eccentricity on seismic performance of the unconfined joints.

9. Extend the shear strength models created in the current study to interior and knee unconfined joints.

REFERENCES

1. ACI 318-08 Committee, "*Building Code Requirements for Structural Concrete (ACI 318-08) and Commentary*", American Concrete Institute, Farmington Hills, Michigan, 2008.

2. ACI 352R-02, "*Recommendations for Design of Beam-Column Connections in Monolithic Reinforced Concrete Structures*", American Concrete Institute, Farmington Hills, Michigan, 2002.

3. ACI 369R-11, "*Guide for Seismic Rehabilitation of Existing Concrete Frame Buildings and Commentary*", American Concrete Institute, Farmington Hills, Michigan, 2011.

4. Akguzel, U., and Pampanin, S., *"Experimental Behavior of Exterior Beam-Column Joint Subassemblies Retrofitted Using GFRP Composites",* New Zealand Society of Earthquake Engineering Conference, 2007.

5. Alath, S., and Kunnath, S.K., "*Modeling Inelastic Shear Deformation in RC Beam-Column Joints*", Engineering Mechanics Proceedings of Tenth Conference, University of Colorado at Boulder, ASCE, Vol.2, 1995, pp 822-825.

6. Alire, D. A., "*Seismic Evaluation of Existing Unconfined RC Beam–Column Joints"*, MSc thesis, University of Washington, 2002.

7. Altoontash, A., and Deierlein, G.G., "*A Versatile Model for Beam-Column Joints"*, ASCE Structures Congress Proceedings, Seattle, Washington, 2003.

8. Altoontash, A., "*Simulation and damage models for performance assessment of reinforced concrete beam- column joints,*" PhD Dissertation, Department of Civil and Environmental Engineering, Stanford University, Stanford, California, 2004.

9. Anderson, M., Lehman, D., and Stanton, J., "*A Cyclic Shear Stress-Strain Model for Joints without Transverse Reinforcement"*, Engineering Structures, No. 30, 2008, pp. 941-954.

10. Antonopoulos, C.P., and Triantafillou, T.C., "*Experimental Investigation of FRP Strengthened RC Beam-Column Joints"*, ACSE Journal of Composites for Construction, V.7, No. 1, 2003, pp 39-49.

11. ASCE/SEI 41/06, "*Seismic Rehabilitation of Existing Buildings"*, American Society of Civil Engineers, Reston, Virginia, 2006.

12. Bakir, P.G., and Boduroğlu, H.M., "*A new design equation for predicting the joint shear strength of monotonically loaded exterior beam-column joints"*, Engineering Structures, No. 24, 2002, pp. 1105-1117.

13. Barnes, M., and Jigoral, S., "*Exterior Non-Ductile Beam Column Joints*", PEER/NEES-REU Research Report, University of California, Berkeley, August 2008.

14. Belarbi, A. and Hsu, T.T.C., "Constitutive Laws of Softened Concrete in Biaxial Tension Compression," ACI Structural Journal, Vol. 91, No. 4, August 1994, pp.465-474.

15. Bertero, V.V., Personal Communication, University of California, Berkeley, 2008

16. Beres, A., et al, "*Seismic Behavior of Reinforced Concrete Frame Structures with Non-ductile Details: Part 1-Summary of Experimental Findings of Full Scale Beam-Column Joint Tests*", Technical Report NCEER-92-0024, National Center for Earthquake Engineering Research (NCEER), State University of New York at Buffalo, NY, Sep 1992.

17. Beres, A., et al, "*Seismic Performance of Interior and Exterior Beam-to-Column Joints Related to Lightly Reinforced Concrete Frame Buildings*", Research Report No.92-7, Nov 1992, School of Civil and Environmental Engineering, Cornell University, Ithaca, NY.

18. Biddah, A., and Ghobarah, A., "*Modeling of Shear Deformation and Bond Slip in Reinforced Concrete Joints"*, Structural Engineering and Mechanics, V.**7**, No. 4, 1999, pp. 413–432.

19. Biddah, A., Ghobarah A., and Aziz T.S., *"Upgrading of Non-ductile Reinforced Concrete Frame Connections",* ASCE Journal of Structural Engineering, Vol. 123, No. 8, August, 1997.

20. Boduroglu, H., Zahertar P., and Ozdemir, P., *"An Experimental Study on Reinforced Concrete Beam-Column Joints",* Turkish Science and Technology Second Earthquake Symposium, Ankara, Turkey, November 1997.

21. Bolong, Z., and Yuzhou, C., *"Behavior of Exterior Reinforced Concrete Beam-Column Joints Subjected to Bi-Directional Cyclic Loading"*, ACI SP123-3, American Concrete Institute, Detroit, Michigan, 1991.

22. Bresler, B., "*Design Criteria for Reinforced Columns Under Axial Load and Biaxial Bending*", ACI Structural Journal, Vol. 57, No. 5, November 1960, pp.481-490.

23. Celik, O.C., and Ellingwood, B.R., "*Modeling beam-column joints in fragility assessment of gravity load designed reinforced concrete frames"*, Journal of Earthquake Engineering, Vol.12, No. 3, 2008, pp. 357-381.

24. Cheung, P.C., Paulay, T., and Park, R., *"New Zealand Tests on Full-Scale Reinforced Concrete Beam-Column-Slab Sub-assemblages Designed for Earthquake Resistance",* ACI SP123-1, American Concrete Institute, Detroit, Michigan, 1991.

25. Cheung, P.C., Paulay, T., and Park, R., *"Mechanisms of Slab Contributions in Beam-Column Sub-assemblages",* ACI SP123-10, American Concrete Institute, Detroit, Michigan, 1991.

26. Clyde, C., et al, "*Performance-Based Evaluation of Exterior Reinforced Concrete Building Joints for Seismic Excitation*", Technical Report PEER 2000-5, Pacific Earthquake Engineering Research Center (PEER), University of California, Berkeley, CA, July 2000.

27. Concrete Coalition, *Preliminary report to California Emergency Management Agency*, on the inventory of older buildings in California, 2010

28. Durrani, A.J., and Zerbe, H.E., " *Seismic Resistance of R/C Exterior Connections with Floor Slab*", Journal of Structural Engineering, American Society for Civil Engineers, Vol. 113, No. 8, 1987, pp.1850-64.

29. Earthquake Engineering Research Institute, introduction about earthquakes failures, http://www.eeri.org/earthquakes/earthquakes.html, December 1999.

30. Earthquake Engineering Research Institute, "*The Tehuacan, Mexico, Earthquake of June 15, 1999*", 1999a. EERI Special Earthquake Report, Sep. 1999. http://www.eeri.org/earthquakes/earthquakes.html

31. Earthquake Engineering Research Institute, "*The Chi-Chi, Taiwan Earthquake of September 21, 1999*", EERI Special Earthquake Report, 1999

32. Ehsani, M.R., and Wight, J.K. "*Exterior Reinforced Concrete Beam-to-Column Connections Subjected to Earthquake-Type Loading*". ACI Journal, 82(4), 1985, pp.492-499.

33. El-Amoury, T., and Ghobarah, A., "*Seismic Rehabilitation of Beam-Column Joints Using GFRP Sheets"*, Engineering Structures, V. 24, No. 11, 2002, pp. 1397-1407.

34. Eligehausen, R., et al, "*Three-dimensional Modeling of Poorly Detailed RC Frame Joints*", Annual Conference of the New Zealand Society of Earthquake Engineering, New Zealand, Paper No.23, 2006.

35. Elmorsi, M., Kianoush, R. M., and W.K. TsoCan. J. Civ.,"*Modeling Bond–Slip Deformations in Reinforced Concrete Beam–Column Joints*", 2000, pp490–505.

36. Elnashai, A.S., and Di Sarno, Luigi. "*Fundamentals of Earthquake Engineering*", John Wiley & Sons, Ltd., 2003.

37. Elwood, K. J., Matamoros, A. B., Wallace, J. W., Lehman, D. E., Heintz, J. A., Mitchell, A. D., Moore, M. A., Valley, M. T., Lowes, L. N., Comartin, C. D., and Moehle, J. P., "*Update to ASCE/SEI 41 Concrete Provisions*", Earthquake Spectra, Earthquake Engineering Research Institute, Volume 23, No. 3, August 2007, pp 493–523.

38. Elwood, K.J. and Eberhard, M.O., *"Effective Stiffness of Reinforced Concrete Columns*", Pacific Earthquake Engineering Research Center, Research Digest No. 2006-1

39. Elwood, K.J., and Moehle, J.P., "*Shake Table Tests and Analytical Studies on the Gravity Load Collapse of Reinforced Concrete Frames"*, PEER Report 2003/01, University of California, Berkeley, 2003.

40. Elwood, K.J., and Moehle, J.P., "*Evaluation of Existing Reinforced Concrete Columns"*, 13th World Conference on Earthquake Engineering Vancouver, B.C., Canada, August 1-6, 2004.

41. Engindeniz, M., "*Repair and Strengthening of Pre-1970 Reinforced Concrete Corner Beam-Column Joints Using CFRP Composites"*, PhD Thesis, Civil and Environmental Engineering Department, Georgia Institute of Technology, August 2008.

42. Favatta M., Izzuddin B.A., Karayannis, C.G., "*Modeling Exterior Beam-Column Joints for Seismic Analysis of RC Frame Structures*", Earthquake Engineering and Structural Dynamics, 37:1527-1548, 2008.

43. Filiatraut, A., and Lebrun, I., "*Seismic Rehabilitation of Reinforced Concrete Joints by Epoxy Pressure Injection Technique,*" ACI SP-160, American Concrete Institute, Farmington Hills, MI, 1996.

44. FEMA 356, "*Pre-standard and Commentary for the Seismic Rehabilitation of Buildings*", Federal Emergency Management Agency, Washington D.C., 2000.

45. FEMA 451, "*Structural Analysis for Performance-Based Earthquake Engineering*", Federal Emergency Management Agency, Washington D.C.

46. Fleury, F, Reynouard, J.-M., and Merabet, O., "*Multicomponent Model of Reinforced Concrete Joints for Cyclic Loading*" Journal of Engineering Mechanics, vol. 126, no. 8, August, 2000.

47. Ghobarah, A. and El-Amoury, T., "Seismic Rehabilitation of Deficient Exterior Concrete Frame Joints", ASCE Journal of Composites for Construction, Vol.9, No.5, 2005, pp. 408-416

48. Ghobarah, A. and Said, A., "*Seismic Rehabilitation of Beam Column Joints Using FRP Laminates*", Journal of Earthquake Engineering, Vol. 5, No. 1, 113-129, 2001.

49. Ghobarah, A., and Said, A., "*Shear strengthening of beam-column joints.*" Engineering Structures: The Journal of Earthquake, Wind and Ocean Engineering; 24(7), 2002, pp. 881-888.

50. Gokgoz, E., "*Experimental Research on Seismic Retrofitting of R/C Exterior Beam-Column-Slab Joints Upgraded with CFRP Sheets"*, M.Sc. Thesis, Graduate Program in Civil Engineering, Bogaziçi University, 2008.

51. Hakuto, S., Park, R. and Tanaka, H. "*Seismic load tests on interior and exterior beam-column joints with substandard reinforcing details*". ACI Structural Journal, Vol. 97, No. 1, 11-25, 2000.

52. Hachem, M.M., *"Seismic Performance of Circular Reinforced Concrete Bridge Columns under Bidirectional Earthquake Loading",* PhD Dissertation, Civil and Environmental Engineering Department, University of California, Berkeley, Fall 2002.

53. Hanson N. W., and Connor, H. W., "*Seismic Resistance of Reinforced Concrete Beam Column Joints*", Journal of the Structural Division, Proceedings of the American Society of Civil Engineers, Vol. 93, No. ST5, October 1967, pp. 533-560.

54. Hanson N. W., and Connor, H. W., "*Tests of Reinforced Concrete Beam-Column Joints Under Simulated Seismic Loading*", Research and Development Bulletin RD 012, Portland Cement Association, 1972.

55. Hassan, W. M., *"Behavior Of Biaxially And Uniaxially Loaded Short High Strength Concrete Columns Strengthened Using Fiber Reinforced Polymer Laminates",* M.Sc. Thesis, Cairo University, June 2004.

56. Hassan, W. M., *"Seismic Performance of Exterior and Corner Substandard Beam-Column Joints in Gravity Load Designed Reinforced Concrete Buildings",* CE 299 Research Report, University of California, Berkeley, August 2009.

57. Hassan, W. M., Park, S., Lopez, R.R., Mosalam, K. M., and Moehle, J. P., *"Seismic Response of Older-Type Reinforced Concrete Corner Joints",* Proceedings of the 9th U.S. National and 10th Canadian Conference on Earthquake Engineering, Toronto, Ontario, Canada, July 25-29, 2010.

58. Hassan, W. M., Park, S., Mosalam, K. M., Moehle, J. P., *"Seismic Performance of Corner Beam Column Joints without Transverse Reinforcement",* CMMI National Science Foundation Grantee Conference, NEES 7th Annual Meeting, Hawaii, June 2009.

59. Higazy, E. M., Elnashai, A. S., and Agbabian, M. S., "*Behavior of Beam-Column Conections Under Axial Column Tension*", Earthquake Spectra, Vol. 122, No. 5, May 1996.

60. Hillerborg, A., Modéer, M. and Petersson, P. E., *"Analysis of crack formation and crack growth in concrete by means of fracture mechanics and finite elements"* , Cement and Concrete Research, Vol.6, 1976, pp.773-782.

61. Hodhod, O.A., Hassan, W., Hilal, M.S., Bahnsawy, H., "*Strength And Ductility Of Biaxially Loaded High Strength RC Short Square Columns Wrapped With GFRP Jackets*", Structural Engineering and Mechanics, Vol. 20, No. 6, August 2005.

62. Hoffschild, T.E., Prion, H.G.L., and Cherry, S., "*Seismic Retrofit of Beam-to-Column Joints with Grouted Steel Tubes*", Proc. Tom Paulay Symposium on Recent Development in Lateral Force Transfer in Buildings, 1993, pp. 403-431.

63. Hsu, T. T. C., "Toward a Unified Nomenclature for Reinforced Concrete Theory," Journal of Structural Engineering, ASCE, V. 122, No. 3, Mar. 1996, pp. 275-283. Also, discussion by Y. L. Mo and author, V. 123,No. 12, Dec. 1997, pp. 1691-1693.

64. Hwang, S., and Lee, H. "*Analytical Model for Predicting Shear Strengths of Exterior Reinforced Concrete Beam-Column Joints for Seismic Resistance*". ACI Structural Journal, Vol. 96, No. 5, 846-858, 1999.

65. Hwang, S.J., Lee, H.J., Liao, T.F., Wang, K.C., and Tsai, H.H., "*Role of Hoops on Shear Strength of Reinforced Concrete Beam-Column Joints*", ACI Structural Journal, V. 102, No. 3, 2005, pp. 445-453.

66. Ibrahim H.H., and MacGregor, J.G., "*Modification of ACI Rectangular Stress Block for High-Strength Concrete*", ACI Structural Journal, Vol.94, S.5, 1997.

67. Karayannis, C. G. and Sirkelis, G. M., "*Strengthening and rehabilitation of RC beam–column joints using carbon-FRP jacketing and epoxy resin injection*", Earthquake Engineering and Structural Dynamics Earthquake, 11 February 2008, pp. 769–790.

68. Karayannis, C.G., Chalioris, C.E., and Sirkelis, G.M., "*Local Retrofit of Exterior RC Beam-Column Joints Using Thin RC Jackets: An Experimental Study"*, Earthquake Engineering and Structural Dynamics, V. 37, 2008, pp. 727-746.

69. Karayannis, C. G., Sirkelis, G. M., "*Effectiveness of RC Beam-Column Connections Strengthening Using Carbon-FRP Jackets*", 12th European Conference on Earthquake Engineering, Paper No. 549.

70. Kent, D. C., and Park, R., "*Flexural Members with Confined Concrete*," Journal of the Structural Division, ASCE, V. 97, No. ST 7, July 1971, 1969-1990.

71. Kim, J and LaFave, J. M. ,"*Joint Shear Behavior of Reinforced Concrete Beam-Column Connections subjected to Seismic Lateral Loading*" Department of Civil and Environmental Engineering University of NSEL Report Series Report No. NSEL-020 November 2009

72. Kim, J. and LaFave J. M., "*Probabilistic Joint Shear Strength Models for RC Beam-Column Connections*" ACI Structural Journal, 105(6), 2008, pp769-779.

73. Kim, J., and LaFave, J.M., "*Key Influence Parameters for the Joint Shear Behavior of Reinforced Concrete (RC) Beam-Column Connections"*, Engineering Structures, No. 29, 2007, pp. 2523-2539.

74. Kishida, S., and Kotaro, A. "*Mechanical Properties of Pre-Cast Prestressed Concrete Corner Beam-Column Joints Assembled by Post-Tensioning Tendons under 3-Directional Forces: Part1-Test Program and Results*", in press.

75. Krawinkler, H., *"Van Nuys Hotel Building Testbed Report: Exercising Seismic Performance Assessment",* PEER 2005/11, University of California, Berkeley, Oct. 2005.

76. Kurose, Y., "*Recent Studies on Reinforced Concrete Beam-Column Joints in Japan*", PMFSEL Report No. 87-8, University of Texas at Austin, 1987

77. Kurose, Y., Guimaraes, G. N., Liu, Z., Kreger, M. E., and Jirsa, J. O., "*Study of reinforced concrete beam-column joints under uniaxial and biaxial loading*", Report, No. 88-2, Department of Civil Engineering, University of Texas at Austin, Austin, TEX, 1988

78. Kurose, Y., Guimaraes, G. N., Zuhua, L., Kreger, M. E., and Jirsa, J. O., "*Evaluation Of Slab-Beam-Column Connections Subjected to Bi-Directional Loading*," Design of Beam-Column Joints for Seismic Resistance (SP123), American Concrete Institute, Detroit, MI, 1991, pp39-67.

79. Lee, J., Kim, J., and Oh., G., "*Strength deterioration of reinforced concrete beam column joints subjected to cyclic loading*", Engineering Structures 31, pp. 2070-2085, 2009.

80. Lee, J., Oh, G., Hwang, H., Kim, J., and Chang, M., "*Ductile Capacity of RC Beam-Column Assembles Subjected to Reversed Cyclic Loading*", First European Conference on Earthquake Engineering and Seismology, Geneva, Switzerland, pp. 1279, September 2006.

81. Lehman, D.E., and Moehle, J.P., "*Seismic Performance of Well-Confined Concrete Bridge Columns*", PEER Report 1998/01, University of California, Berkeley, 1998.

82. Lehman, D., ed., "*Performance Characterization of Non-Ductile Reinforced Concrete Frame Components*", Unpublished Technical Report PEER 2002, Pacific Earthquake Engineering Research Center (PEER), University of California, Berkeley, CA, 2002.

83. Lehman, D., Stanton, J., Anderson, M., Alire, D., and Walker, S., "*Seismic Performance of Older Beam-Column Joints*" 13th World Conference on Earthquake Engineering, Vancouver, Canada, 1464, 2004.

84. Leon, R., and Jirsa, J.O., *"Bidirectional Loading of RC Beam-Column Joints",* Earthquake Spectra, Vol. 2, No. 3, 1986, pp. 537-564.

85. Li, B., Pan, T., and Tran, C., "*Effects of Axial Compression Load and Eccentricity on Seismic Behavior of Non-seismically Detailed Interior Beam-Wide Column Joints*", Journal of Structural Engineering, Vol. 135, No. 7, July 1, 2009.

86. Longwell, J.E., *"A comparative Study of Biaxially Loaded Reinforced Concrete Beam-Column Joints",* M.Sc. Thesis, University of Texas at Austin, May 1980.

87. Lowes, L.N., and Altoontash, A., "*Modeling Reinforced-Concrete Beam-Column Joints Subjected to Cyclic Loading"*, ASCE Journal of Structural Engineering, V. 129, No. 12, 2003, pp. 1686-1697.

88. Lowes, L.N., Mitra, N., and Altoontash, A., "*A Beam-Column Joint Model for Simulating the Earthquake Response of Reinforced Concrete Frames"*, PEER Report 2003/10, University of California, Berkeley, 2004.

89. Lynn, A.C., "*Seismic Behavior of Existing Reinforced Concrete Building Columns*", PhD Dissertation, University of California, Berkeley, 2001

90. MacGregor, J.G., and Wight, R. "*Reinforced Concrete - Mechanics and Design*", Fourth Edition, Prentice Hall, Inc., Upper Saddle River, NJ, 2003.

91. Mahini, S.S., and Ronagh, H.R., *"A New Method for Improving Ductility in Existing RC Ordinary Moment Resisting Frames Using FRPS",* Asian Journal of Civil Engineering (Building and Housing), Vol. 8, No. 6, 2007, pp. 581-595.

92. Mander, J.B., Priestley, M.J.N., and Park, R., "*Theoretical Stress-Strain Model for Confined Concrete"*, ACSE Journal of Structural Engineering, V. 114, No. 8, 1988, pp. 1804- 1826.

93. Megget, L.M., "*Cyclic Behavior of Exterior Reinforced Concrete Beam-Column Joints*", Bulletin of the New Zealand National Society for Earthquake Engineering, Vol. 7, No. 1, 1974.

94. Meinheit, D.F., and Jirsa, J.O., "*The Shear Strength of Reinforced Concrete Beam-Column Joints*", CESRL Report No. 77-1, University of Texas at Austin, 1977.

95. Mitra, N., and Lowes, L.N., "*Evaluation, Calibration, and Verification of a Reinforced Concrete Beam-Column Joint Model*", ACSE Journal of Structural Engineering, V. 133, No. 1, 2007, pp. 105-120.

96. Moehle, J. P., "*State of research on seismic retrofit of concrete building structures in the US.*" US-Japan Symposium and Workshop on Seismic Retrofit of Concrete Structures - State of Research and Practice, 2000.

97. Moehle, J.P., "*Beam-Column Connections*", PowerPoint Presentation, NEES GC Project: Mitigation of Collapse Risk of Older Concrete Buildings, Pacific Earthquake Engineering Website, 2008.

98. Moehle, J.P., "*Existing Reinforced Concrete Building Construction: A Review of Practices and Vulnerabilities*", Structural Engineering Association of Northern California Fall Seminar, 1998.

99. Moehle, J.P., "*Collapse Assessment of Reinforced Concrete Structure",* Proceedings, International Symposium Honoring Shunsuke Otani on Performance-Based Engineering for Earthquake Resistant Reinforced Concrete Structures, University of Tokyo, Japan, 2003.

100. Moehle, J. P., "*Load-Deflection Calculations*", Graduate Course Lecture Notes, University of California, Berkeley, 2006, pp. 5-22:5-30.

101. Moehle, J. and Elwood, K., "*Collapse performance prediction for RC frame structures,*" Paper No. 154, Proceedings, 2003 Pacific Conference on Earthquake Engineering, Christchurch, New Zealand, 8pp.

102. Moehle, J., K. Elwood, and H. Sezen, "*Gravity Load Collapse of Building Frames during Earthquakes,*" ACI SP-197, Behavior and Design of Concrete Structures for Seismic Performance, American Concrete Institute, 2001.

103. Moehle, J. P., and Mahin, S. A., "*Observations on the Behavior of Reinforced Concrete Buildings during Earthquakes*," Earthquake-Resistant Concrete Structures—Inelastic Response and Design, SP-127, S. K. Ghosh, ed., American Concrete Institute, Farmington Hills, Mich., 1991, pp. 67-89.

104. Mosier, G. "*Seismic Assessment of Reinforced Concrete Beam-Column Joints*". MSc thesis, University of Washington, Seattle, 2000.

105. Mosalam, K. M., "*Behavior of Reinforced Concrete: Strut and Tie Models*", Graduate Course Lecture Notes, University of California, Berkeley, 2007, part 8.

106. National Information Service for Earthquake Engineering (NISEE), Pacific Earthquake Engineering Center, University of California, Berkeley, 2010.

107. NZS 3101:1995, "*Concrete structures standard (NZS 3101)*", Standard Association of New Zealand, Wellington, New Zealand, 1995.

108. OpenSees 2.2.2, "*Open System for Earthquake Simulation*", McKenna, F. and Fenves G. PEER, University of California, Berkeley. http://opensees.berkeley.edu, 2010.

109. Ortiz, I.R., "*Strut-and-Tie Modeling of Reinforce Concrete Short Beams and Beam-Column Joints*", PhD Dissertation, University of Westminster, 1993.

110. Pagni, C.A., "*Modeling of Structural Damage of Older Reinforced Concrete Components*", M.Sc. Thesis, University of Washington, 2003

111. Pampanin, S., Amaris, A., Akguzel, U. and Palermo, A., "*Experimental Investigation on High-Performance Jointed Ductile Connections for Precast Frames*", First European Conference on Earthquake Engineering and Seismology, Geneva, Switzerland, September 2006, Paper Number: 2038

112. Pampanin, S., et al, "*Modeling of Shear Hinge Mechanism in Poorly Detailed R.C. Beam Column Joints*", 12th European Conference on Earthquake Engineering, London, 2002.

113. Pampanin, S., et al, "*Seismic Behavior of R.C. Beam Column Joints Designed for Gravity Loads*", 12th European Conference on Earthquake Engineering, London, Paper No.726, 2002.

114. Pantazopoulou, S., and Bonacci, J., "*Consideration of Questions about beam-column joints",* ACI Structural Journal, V. 89, No. 1, 1992, pp. 27-37.

115. Pantazopoulou, S. J., and Moehle, J. P., "*Truss Model for 3-D Behavior of R.C. Exterior Connections*", Journal of Structural Engineering, American Society of Civil Engineers, Vol. 116, No. 2, Feb. 1990, pp. 298-315.

116. Pantelides, C., et al, "*Assessment of Reinforced Concrete Building Exterior Joints With Substandard Details*", Technical Report PEER 2002-18, Pacific Earthquake Engineering Research Center (PEER), University of California, Berkeley, CA, May 2002.

117. Parra-Montesinos, G., and Wight, J. K., "*Seismic Behavior, Strength and Retrofit of RC Column-to-Steel Beam Connections,*" Report No. UMCEE 00-09, Dept. of Civil and Environmental Engineering, University of Michigan, Ann Arbor, MI, April 2000.

118. Park R., and Paulay, T., "*Reinforced Concrete Structures*", John Wiley & Sons, First Edition, 1975, pp. 769.

119. Park, R., "*A Summary of Results of Simulated Seismic Load Tests on Reinforced Concrete Beam-Column Joints, Beams and Columns with Substandard Reinforcing Details*", Journal of Earthquake Engineering, Vol. 6, No. 2, pp.1-27, 2002.

120. Park, S., "*Experiential and Analytical Studies on Old Reinforced Concrete Buildings with Seismically Vulnerable Beam-Column Joints*". PhD Dissertation, University of California, Berkeley, December 2010.

121. Park, S., and Mosalam, K.M., "*Shear Strength Models of Exterior Beam-Column Joints without Transverse Reinforcement*". PEER Report 2009/106, University of California, Berkeley, 2009.

122. Parker, D.E., and Bullman, P.J.M., "*Shear Strength within Reinforced Concrete Beam-Column Joints*", The Structural Engineer, V. 75, No. 4, pp. 53-57, 1997.

123. Paulay, T., Park, R., and Priestley, M.J.N., "*Reinforced Concrete Beam-Column Joints under Seismic Actions*", ACI Journal, Vol. 75, No. 60, 1978, pp. 585-593.

124. Paulay, T., "*Seismic Behavior of Beam Column Joints in Reinforced Concrete Space Frames*", State of the Art Report, Proceedings of Ninth World Conference on Earthquake Engineering, Tokyo, Vol. VIII, August 1988, pp. 557-568.

125. Pessiki, S.P., Conley, C., Gergely, P., and White, R.N., "*Seismic Behavior of Lightly-Reinforced Concrete Column and Beam Column Joint Details*", NCEER-90-0014, National Center for Earthquake Engineering Research, State University of New York at Buffalo, 1990.

126. Priestley, M.J.N., "*Displacement-Based Seismic Assessment of Reinforced Concrete Buildings*", Journal of Earthquake Engineering, V. 1, No. 1, 1997, pp. 157-192.

127. Paulay, T., and Priestley, M. J. N., "*Seismic Design of Reinforced Concrete and Masonry Buildings*", John Wiley and Sons, 1992, 744 pp.

128. Priestley, M.J.N., "*Displacement-Based Seismic Assessment of Reinforced Concrete Buildings*", Journal of Earthquake Engineering, Vol. 1, No. 1, pp.157-192, 1997.

129. Priestley, M.J.N. and Hart, G., "*Royal Palm Resort, Guam, Seismic Behavior of As-Built and As-Designed Corner Joints"*, SEQAD Consulting Engineers, Solana Beach, CA, 1994.

130. Said, A.M., and Nehdi, M.L., "*Use of FRP for RC frames in seismic zones – Part I: Evaluation of FRP beam-column joint rehabilitation techniques."* Applied Composite Materials, 11(4), 2004, pp. 205-226.

131. Salim, I.B., *"The influence of Concrete Strengths of the Behavior of the External Beam-Column Joints",* M.Sc. Thesis, Universiti Teknologi Malaysia, May 2007.

132. Sanchez, V.M., Lloyd, B., Hassan, W.M., and Moehle J.P., "*Evaluation of Non-Ductile Reinforced Concrete Building Corner Joint Experiencing Early Column Failure*",

133. Sarsam, K.F., and Phipps, M.E., "*The Shear Design of In-situ Reinforced Beam-Column Joints Subjected to Monotonic Loading*", Magazine of Concrete Research, V. 37, No. 130, 1985, pp. 16-28.

134. Schlaich, J., and Schäfer, K., "*Design and detailing of structural concrete using strut-and-tie models*", The Structural Engineer, V. 69, No. 6, 1991, pp. 113-125.

135. Scott, R.H., "*The effects of detailing on RC beam/column connection behavior*", The Structural Engineer, V. 70, No. 18, 1992, pp. 318-324.

136. Scott, R.H., and Hamil, S.J., "*Connection Zone Strain in the Reinforced Concrete Beam Column Connections*". Proceedings of the 11th International Conference on Experimental Mechanics, Oxford, UK, 1998, pp. 65-69.

137. Sezen, H., "*Seismic Behavior and Modeling of Reinforced Concrete Building Columns*", PhD Dissertation, University of California, Berkeley, 2002.

138. Sezen, H., and Alemdar, F., "*Evaluation of FEMA 356 Models for Reinforced Concrete Columns and Beam-Column Joints*", Structures Congress 2007.

139. Soroushian, P. and Choi, k., *"Analytical Evaluation of Straight Bar Anchorage Design in Exterior Joints*", ACI Structural Journal, V. 88, No. 2, 1991.

140. Shin, M. and LaFave, J. M., "*Modeling Of Cyclic Joint Shear Deformation Contributions In RC Beam-Column Connections To Overall Frame Behavior*" Structural Engineering and Mechanics, 18(5), 2004, pp. 645-669.

141. Takhirov, S., "*Laser Scanning Technology for Damage Assessment After the Jan 12, 2010 Haiti Earthquake*" Quake Summit, NEES and PEER annual meeting, San Francisco, California, 2010.

142. Theiss, A.G., "*Modeling the Earthquake Response of Older Reinforced Concrete Beam-Column Building Joints*", M.Sc. Thesis, University of Washington, 2005.

143. Topcu, I., "*Experimental Research on Seismic Retrofitting of R/C Corner Beam-Column-Slab Joints Upgraded with CFRP Sheets*", MSc Thesis, Graduate Program in Civil Engineering, Bogaziçi University, 2008.

144. Le-Trung, K., Lee, K., Lee, J., Lee, D.H., and Woo, S., "*Experimental Study of RC beam-Column Joints Strengthened using CFRP Composites*", Composites Part B: Engineering, Vol. 4, No. 1, 2010, pp. 76-85.

145. Tsonos, A. G., "*Effectiveness of CFRP-Jackets and RC-Jackets in Post-Earthquake and Pre-Earthquake Retrofitting of Beam–Column Sub-assemblages*", Engineering Structures, Vol.30, 2008, pp. 777-793.

146. Tsonos, A.G. "*Cyclic Load Behavior of Reinforced Concrete Beam-Column Sub assemblages of Modern Structures*", ACI Structural Journal, V. 104, No. 4, 2007, pp. 468- 478.

147. Tsonos, A.G., and Papanikolaou K. V.*, "Post-Earthquake Repair and Strengthening of Reinforced Concrete Beam-Column Connections (Theoretical & Experimental Investigation)",* Bulletin of the New Zealand Society for Earthquake Engineering, Vol. 36, No. 2, June 2003.

148. Tsonos A. G. and Stylianidis K., "*Seismic Retrofit of Beam-to-Column Joints with High Strength Fiber Jackets*", European Earthquake Engineering, 16:56-72, 2002

149. Uang, C-M., et al. "*Ji-Ji Taiwan Earthquake of Sep.21, 1999: A Brief Reconnaissance Report*", Department of Structural Engineering, University of California, San Diego, 1999.

150. Uzumeri, S. M., "*Strength and Ductility of Cast-in-Place Beam Column Joints*", Reinforced Concrete Structures in Seismic Zones, SP-53, Hawkins, N. M., ed., American Concrete Institute, Detriot, Michigan., 1977, pp. 293-350.

151. Vecchio, F.J., and Collins, M.P., "*The Modified Compression-Field Theory of Reinforced Concrete Elements Subjected to Shear*", ACI Structural Journal, V. 83, No. 2, 1986, pp. 219-231.

152. Vollum, R.L., "*Design and Analysis of Exterior Beam Column Connections*", PhD Dissertation, Imperial College of Science Technology and Medicine-University of London, 1998.

153. Vollum, R.L. and Newman J.B., "*Strut and Tie Models for the Analysis/Design of External Beam-Column Joints*", Magazine of Concrete Research, Vol. 51, No. 6, 1999, pp. 415-425.

154. Walker, S.G., "*Seismic Performance of Existing RC Beam–Column Joints*", M.Sc. Thesis, University of Washington, 2001.

155. Wong, H.F., "*Shear Strength and Seismic Performance of Non-Seismically Designed Reinforced Concrete Beam-Column Joints*", PhD Dissertation, Department of Civil Engineering, The Hong Kong University of Science and Technology, August 2005.

156. Yassin, M. "*Nonlinear Analysis of Prestressed Concrete Structures under Monotonic and Cyclic Load,*" PhD Dissertation, University of California, Berkeley, 1994.

157. Youssef, M. and Ghobarah, A., "*Modeling of RC Beam-Column Joints and Structural Walls*," Journal of Earthquake Engineering, 5(1), 2001, pp93-111.

158. Zahertar, P., *"Experimental Results on Different Transverse Reinforcements in Beam-Column Joints",* M.S. Thesis, Istanbul Technical University.

159. Zerbe, H. E., and Durrani, A. J., "*Effect of Slab on Behavior of Exterior Beam-to-Column Connections*," Report No. 30, Rice University, Houston, Tex., Mar. 1985, 159 pp.

160. Zhang, L., and Jirsa, J.O., "*A Study of Shear Behavior of RC Beam-Column Joints"*, *PMFSEL Report* No. 82-1, University of Texas at Austin, 1982.

161. Vollum R. and Parker, D., "External Beam-Column Joints: Design to Eurocode 2," Magazine of Concrete Research, 2008, Vol. 60, No. 7, September 2008, pp. 511-521.

162. Burak, B. "*Analytical Verification of a Simplified Reinforced Concrete Joint Model,*" Proceedings of the 9th U.S. National and 10th Canadian Conference on Earthquake Engineering, Toronto, Ontario, Canada, July 25-29, 2010.

163. Stevens N.J., Uzumeri, S.M., and Collins, M.P., "*Reinforced-Concrete Subjected to Reverse-Cyclic Shear – Experiment and Constitutive Model.*" ACI Structural Journal, Vol. 88, No. 2, 1991, pp.135-146.

APPENDIX A

COLUMN STEEL STRAINS

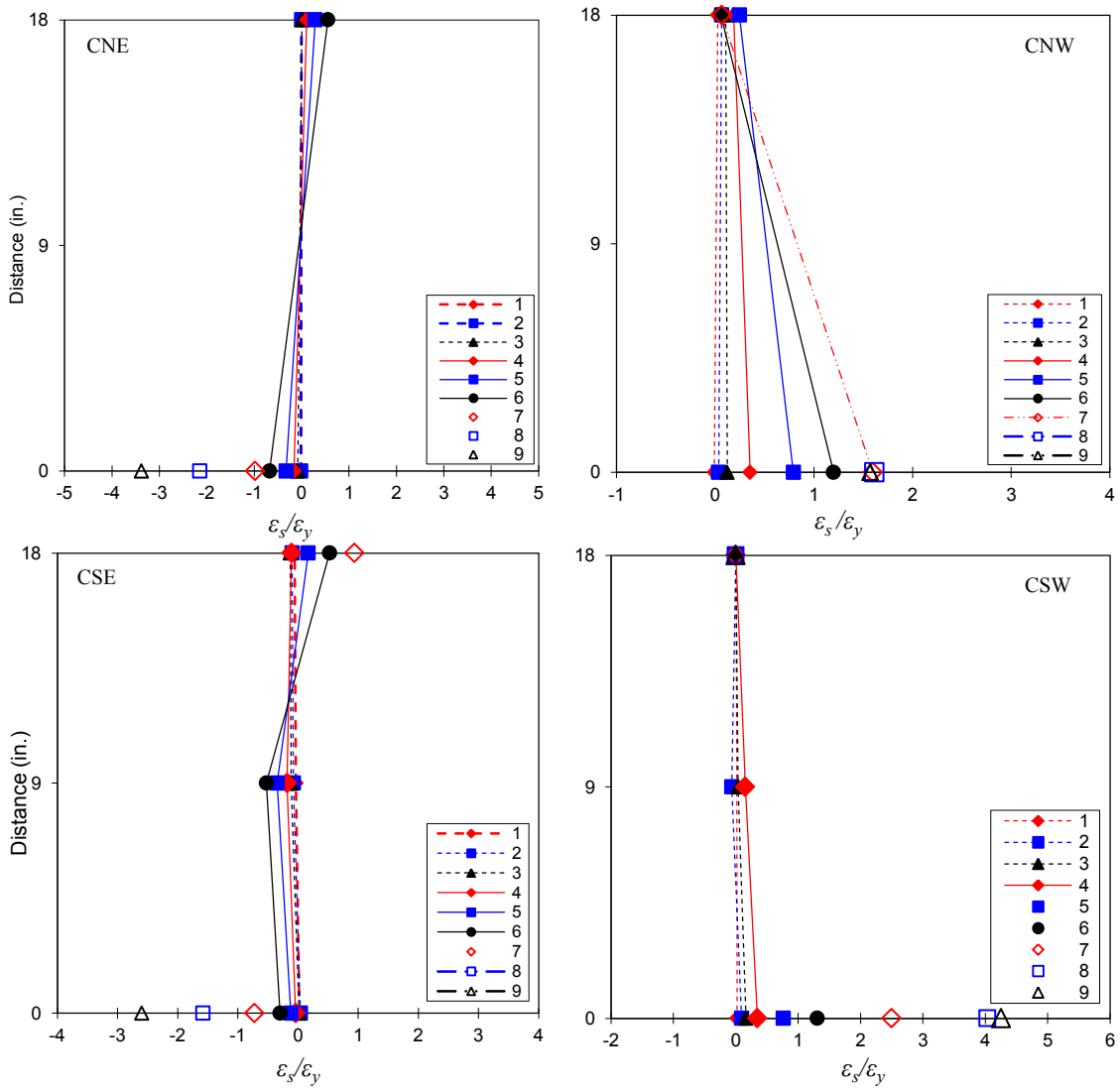

Figure A.1 Column reinforcement strain distribution during EW beam downward loading, specimen U-J-1

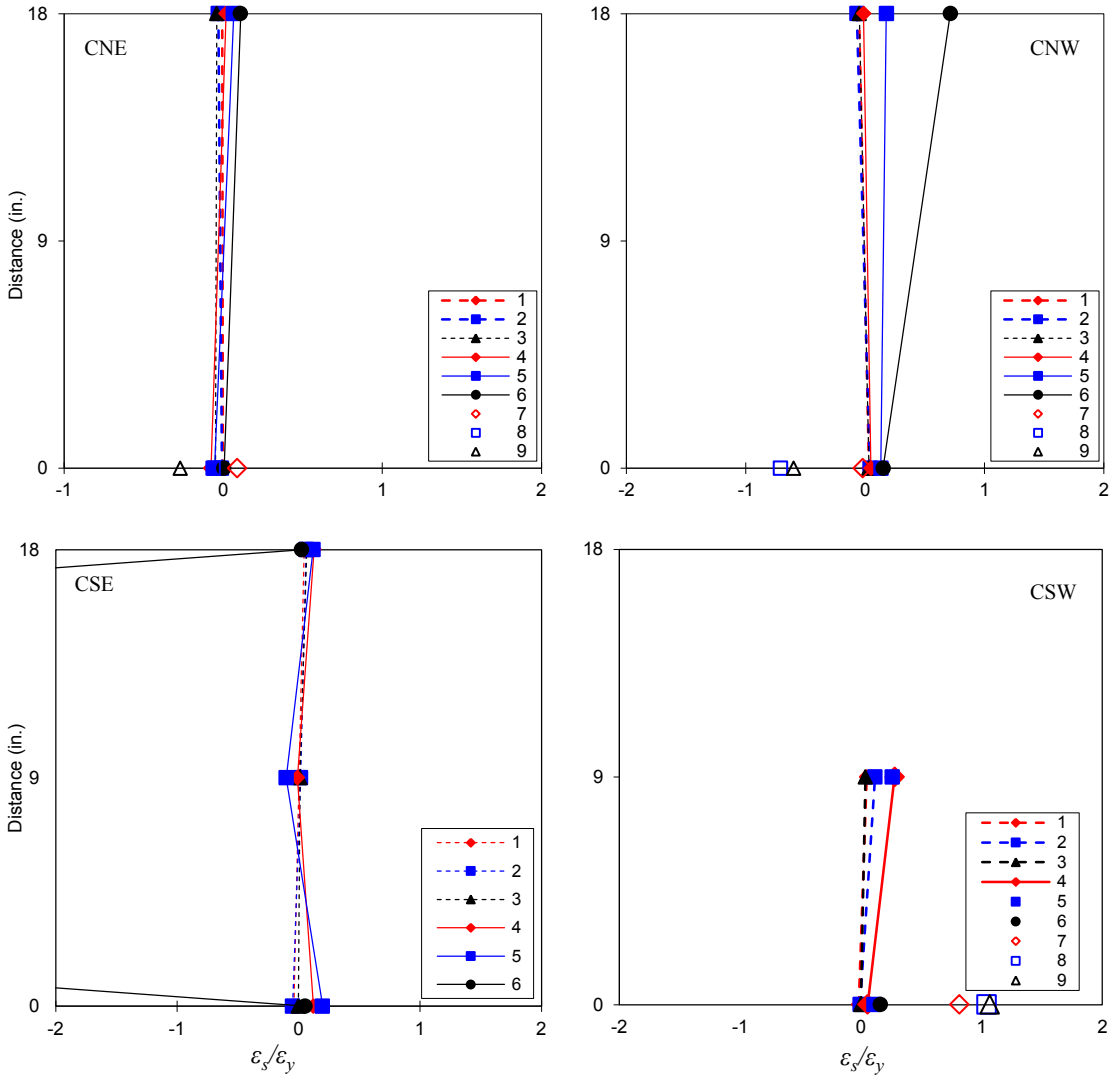

Figure A.2 Column reinforcement strain distribution during NS beam downward loading, specimen U-J-1

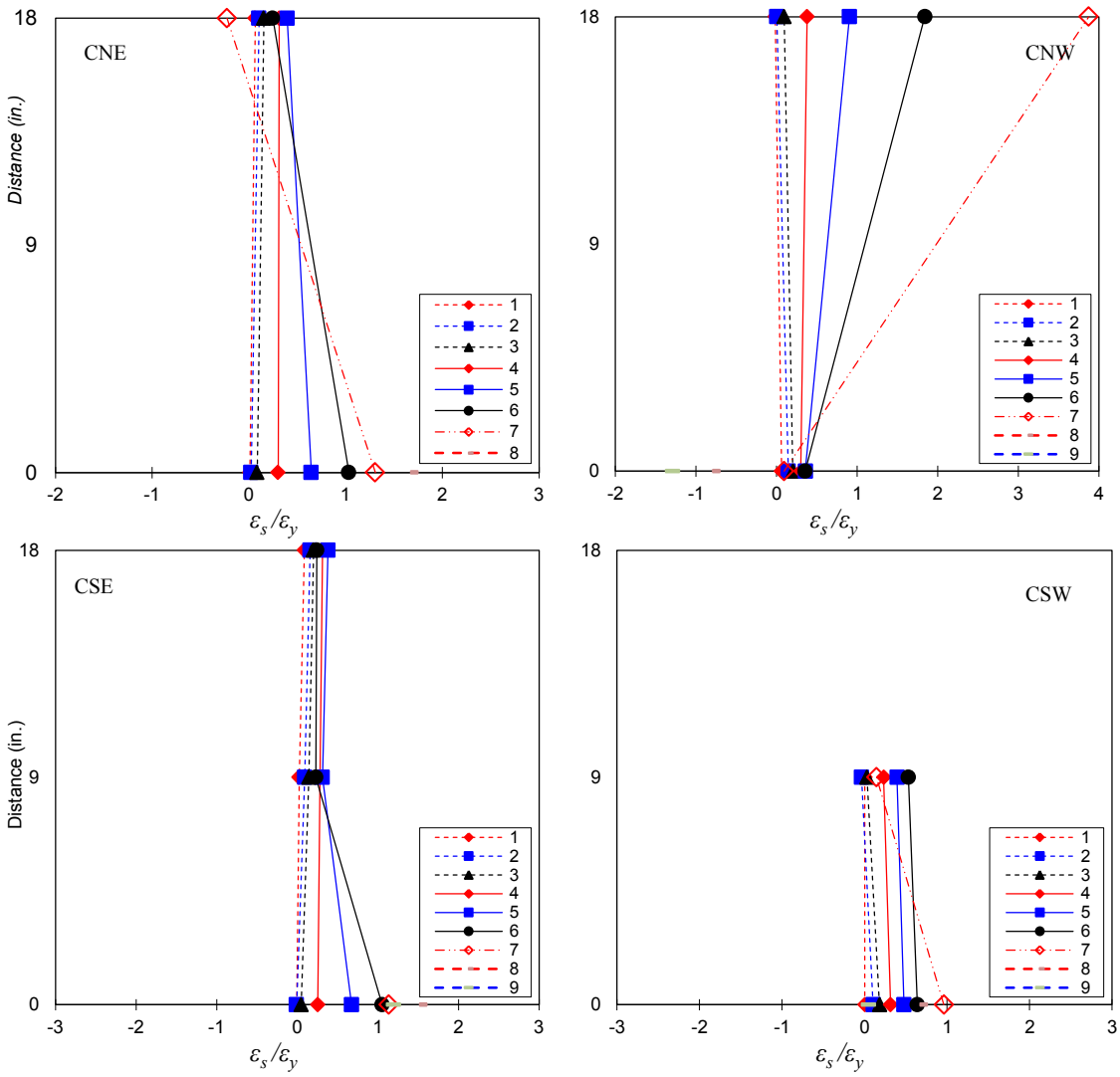

Figure A.3 Column reinforcement strain distribution during EW beam upward loading, specimen U-J-1

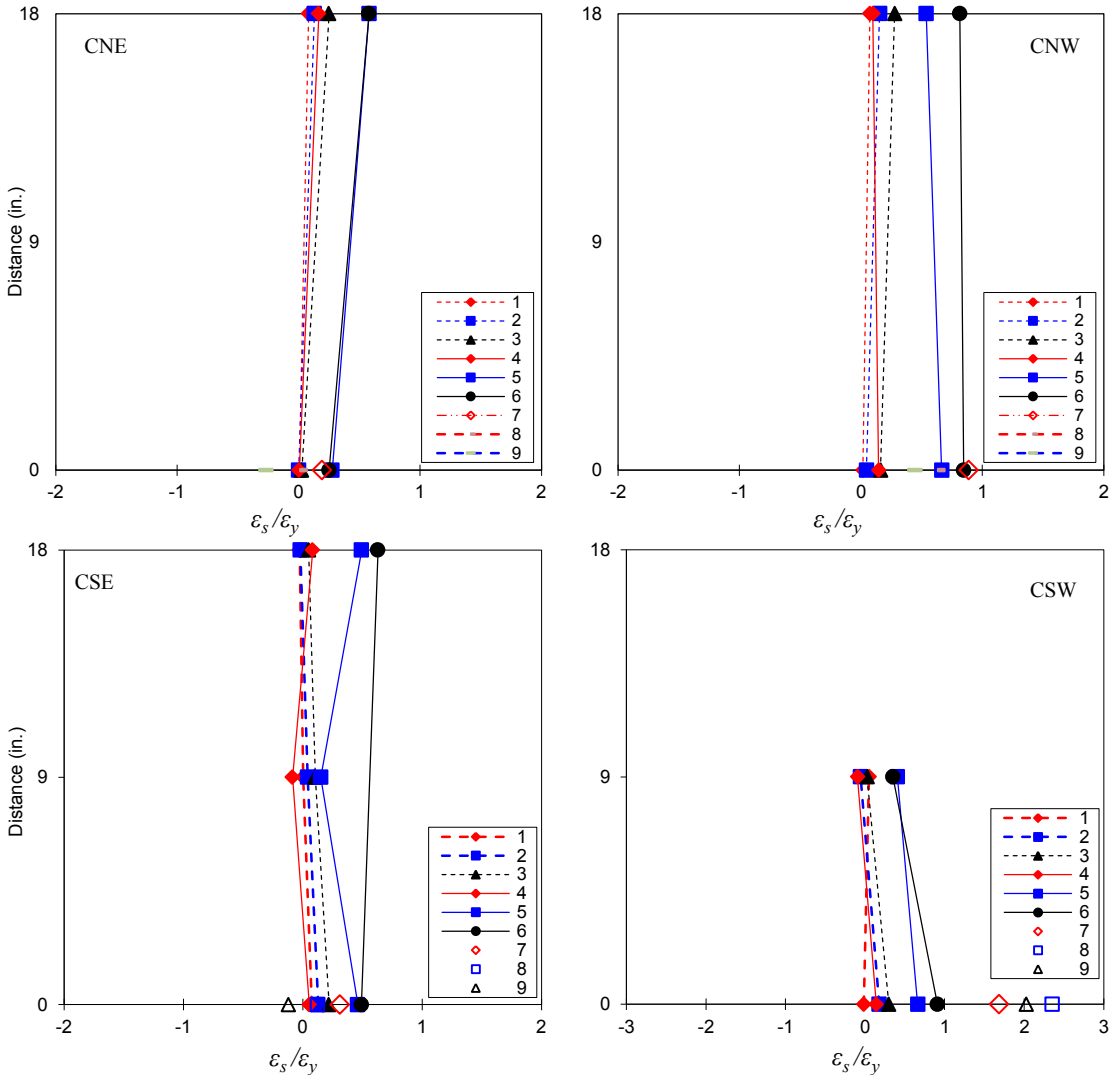

Figure A.4 Column reinforcement strain distribution during NS beam upward loading, specimen U-J-1

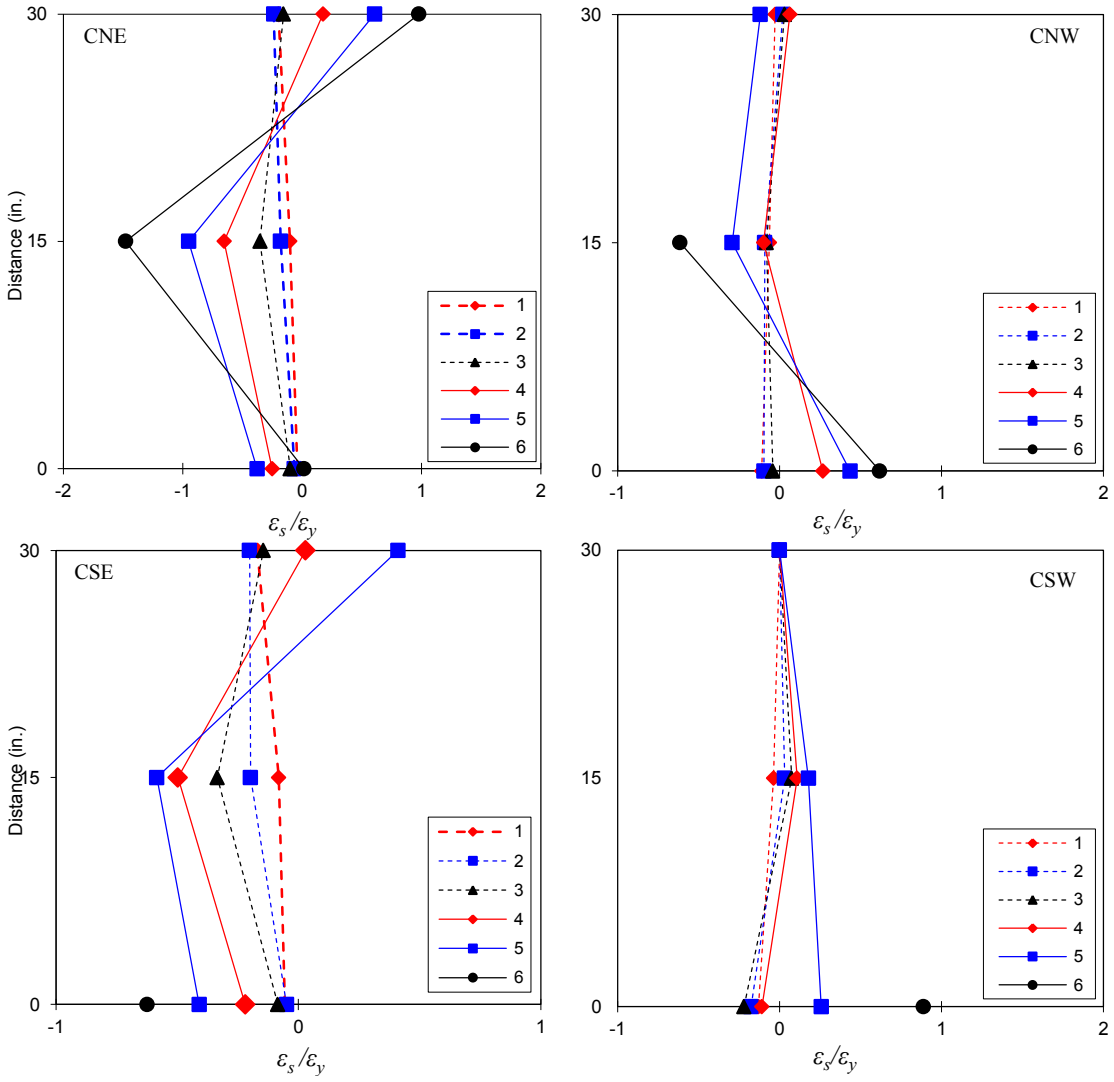

Figure A.5 Column reinforcement strain distribution during EW beam downward loading, specimen U-J-2

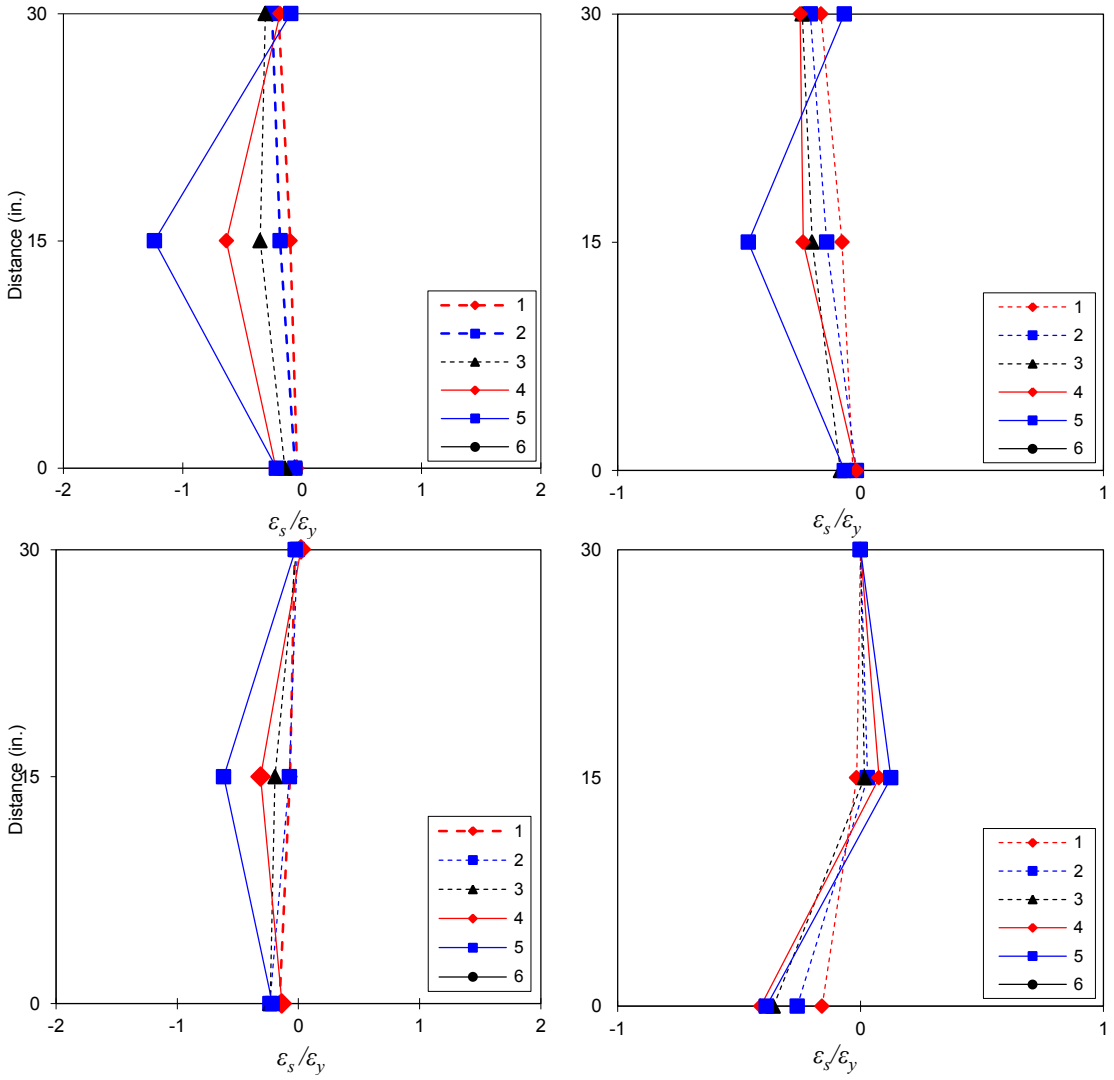

Figure A.6 Column reinforcement strain distribution during NS beam downward loading, specimen U-J-2

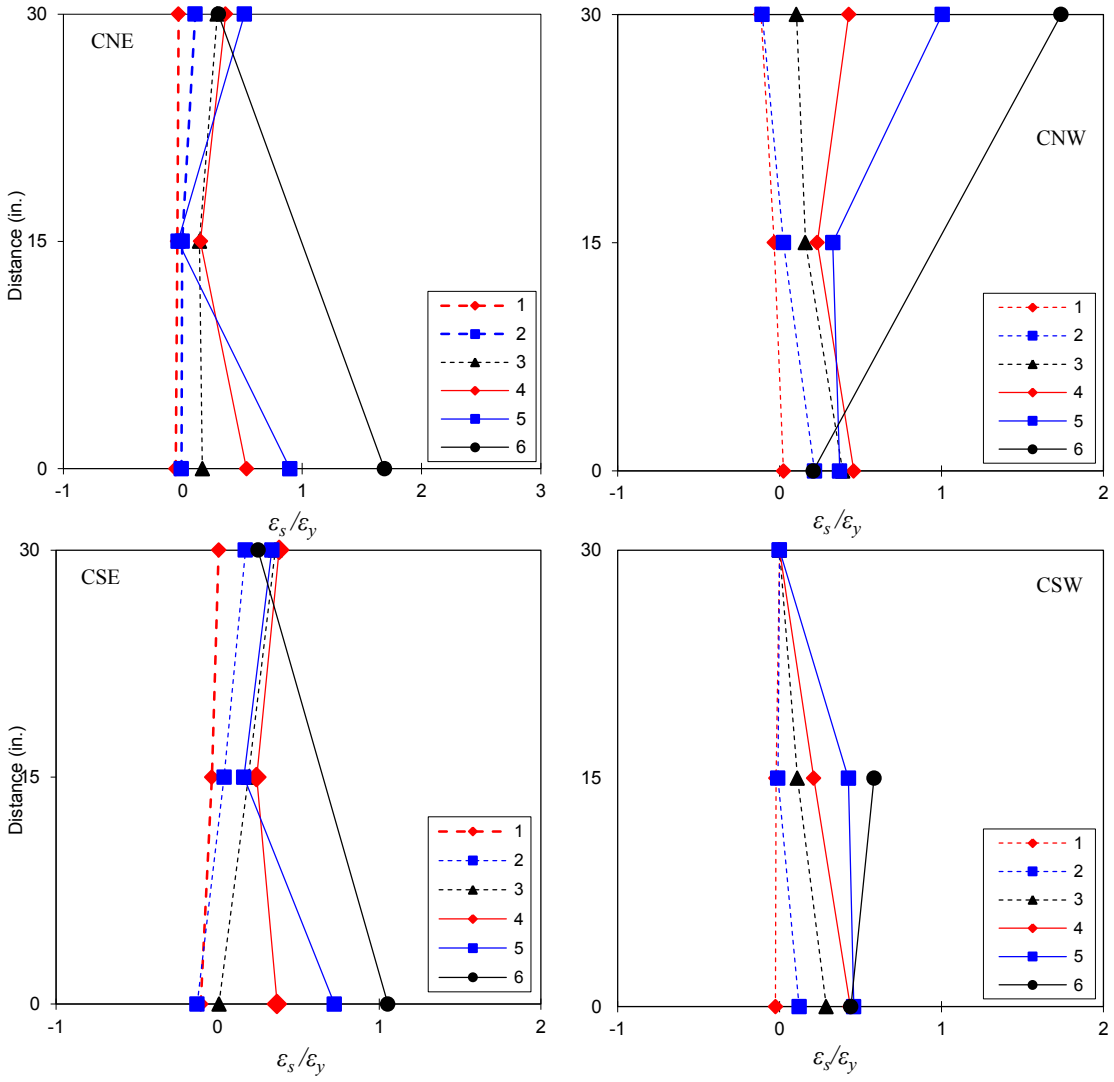

Figure A.7 Column reinforcement strain distribution during EW beam upward loading, specimen U-J-2

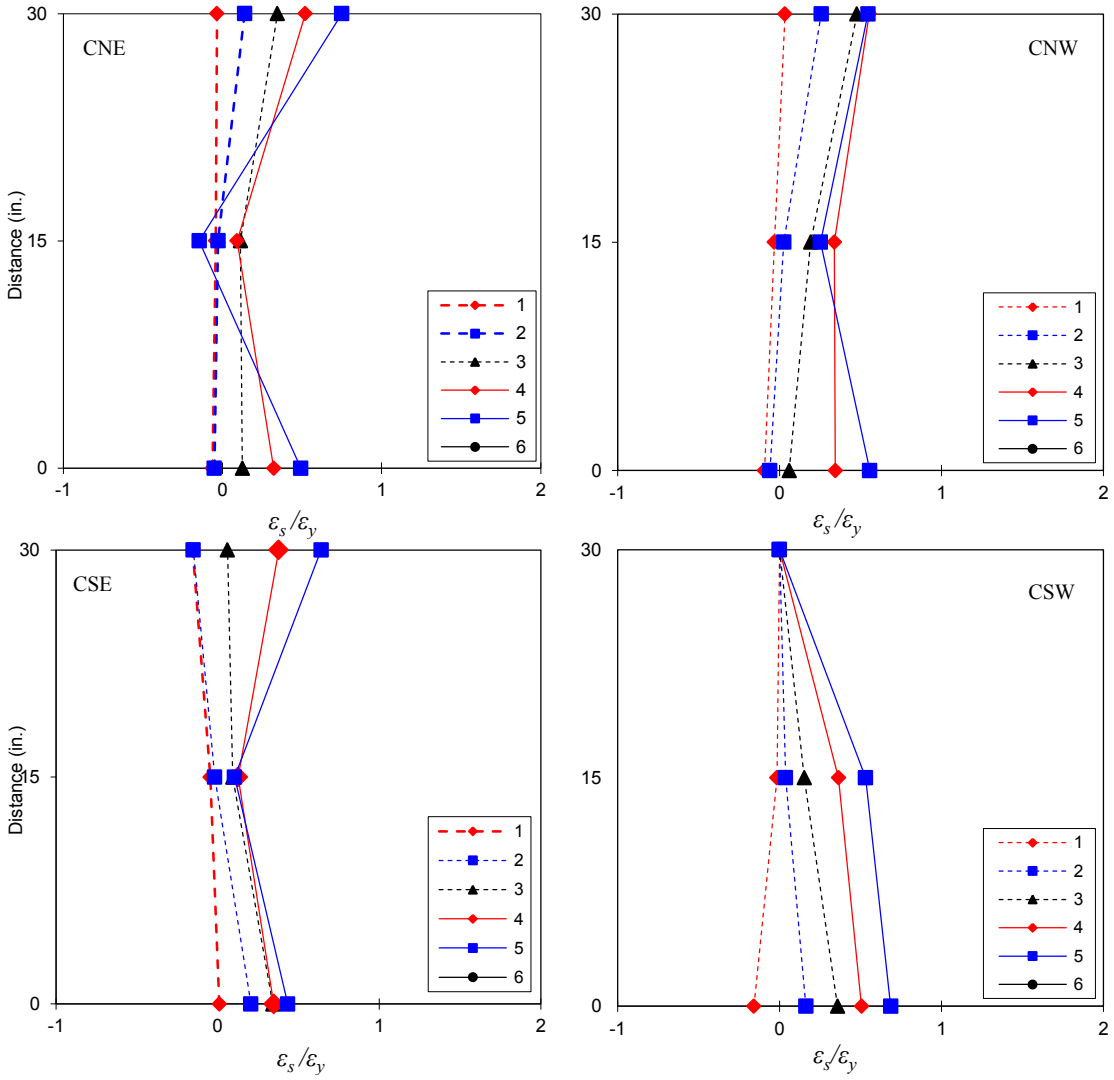

Figure A.8 Column reinforcement strain distribution during NS beam upward loading, specimen U-J-2

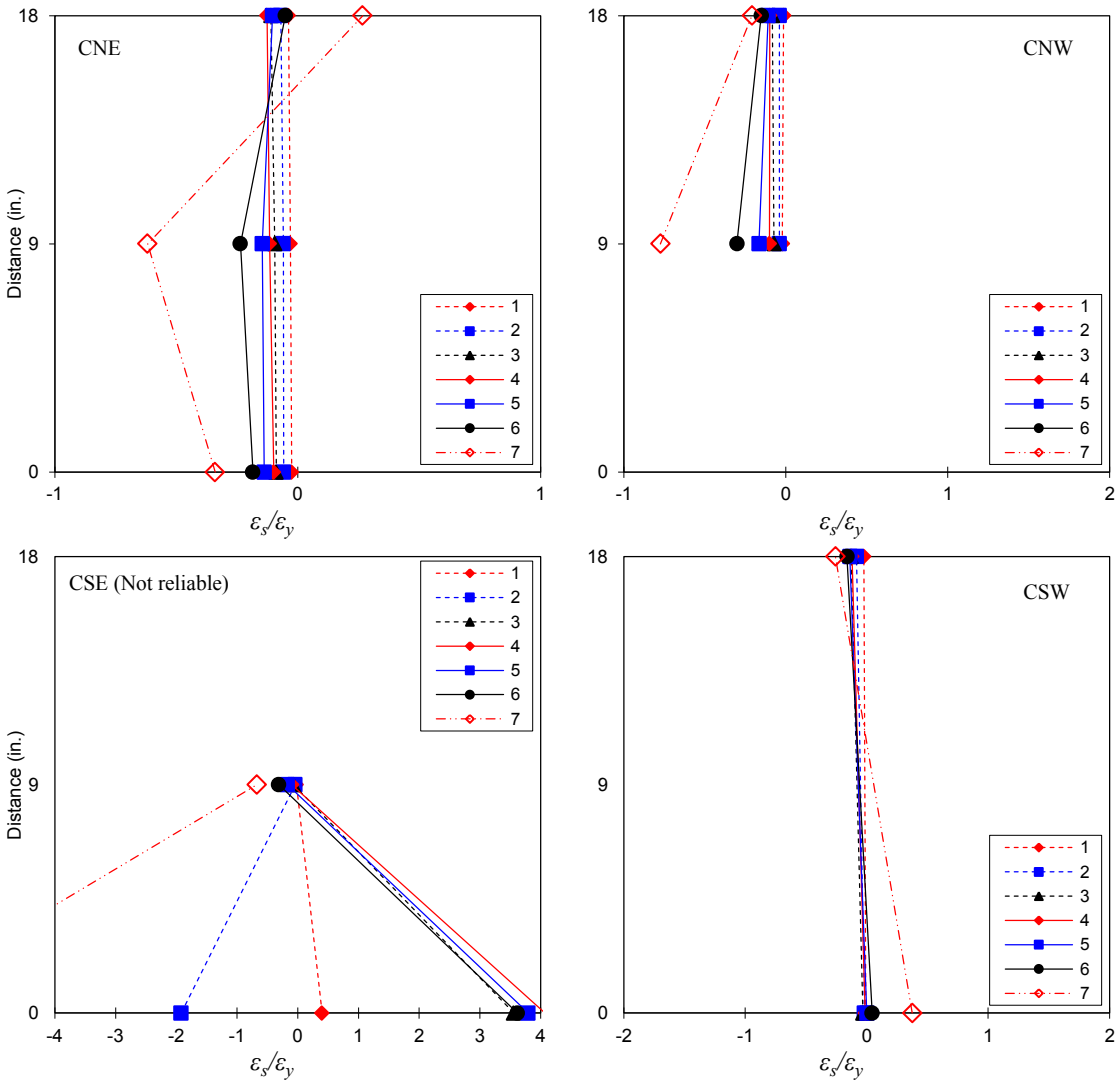

Figure A.9 Column reinforcement strain distribution during EW beam downward loading, specimen U-BJ-1

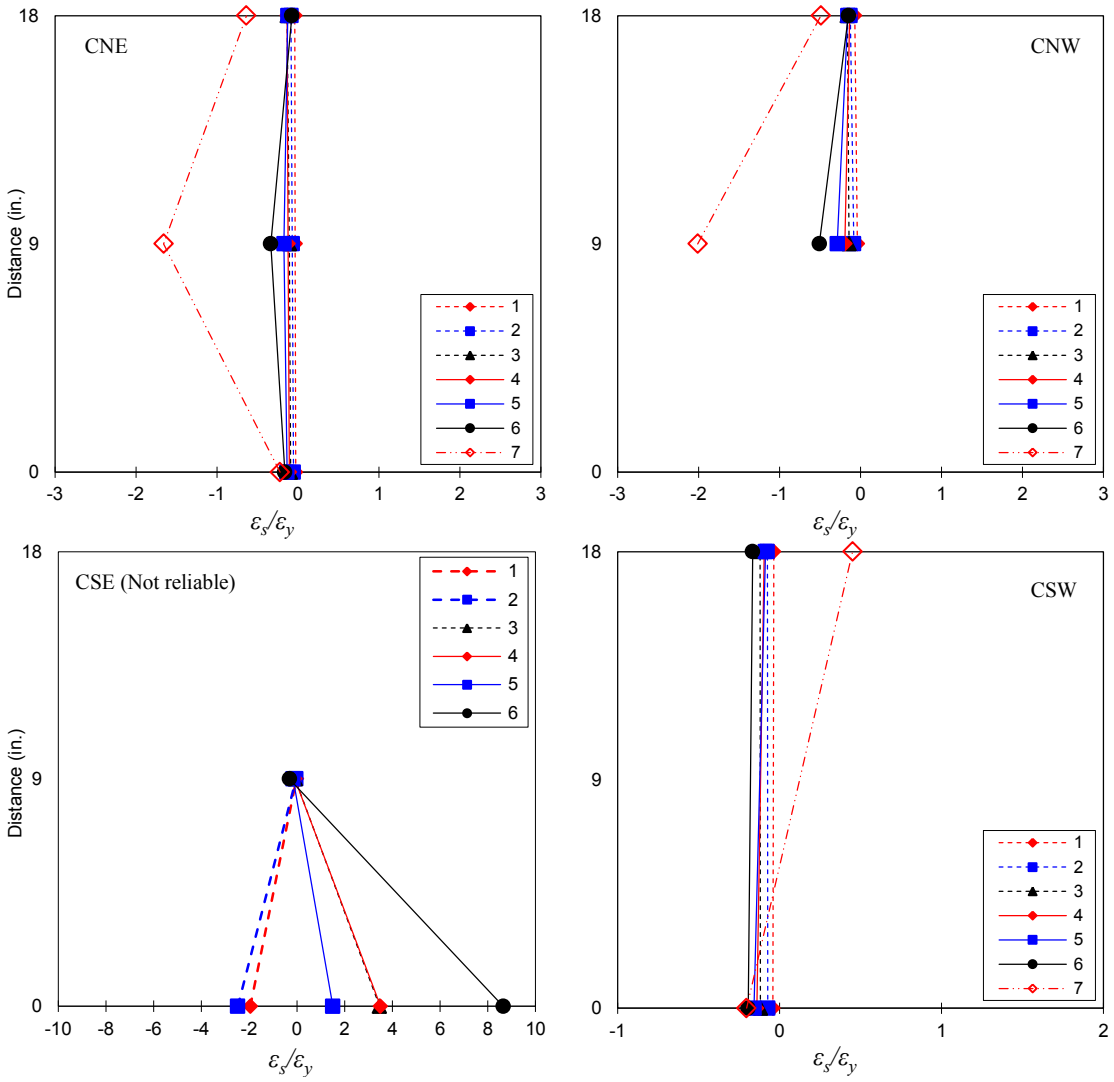

Figure A.10 Column reinforcement strain distribution during NS beam downward loading, specimen U-BJ-1

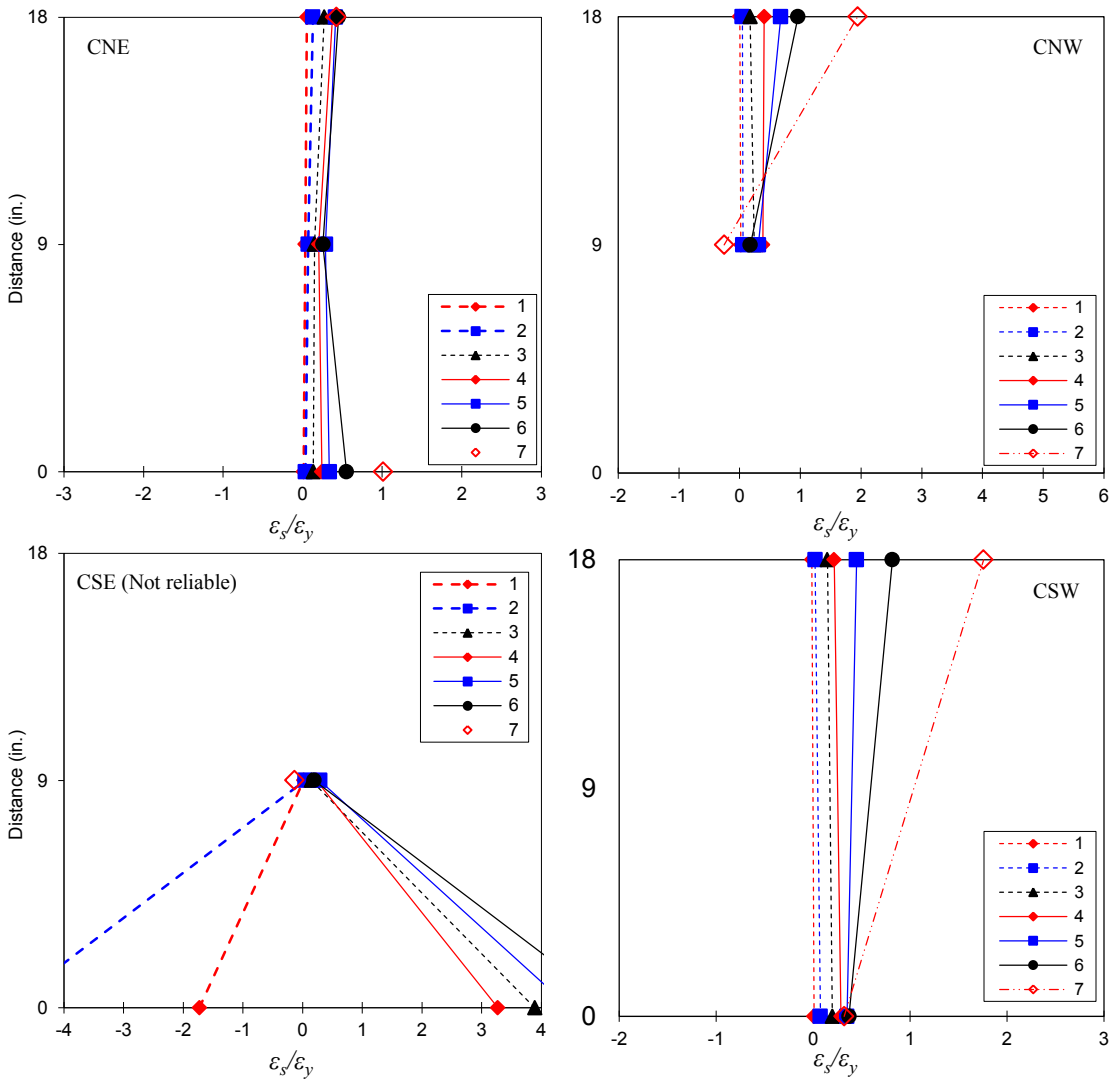

Figure A.11 Column reinforcement strain distribution during EW beam upward loading, specimen U-BJ-1

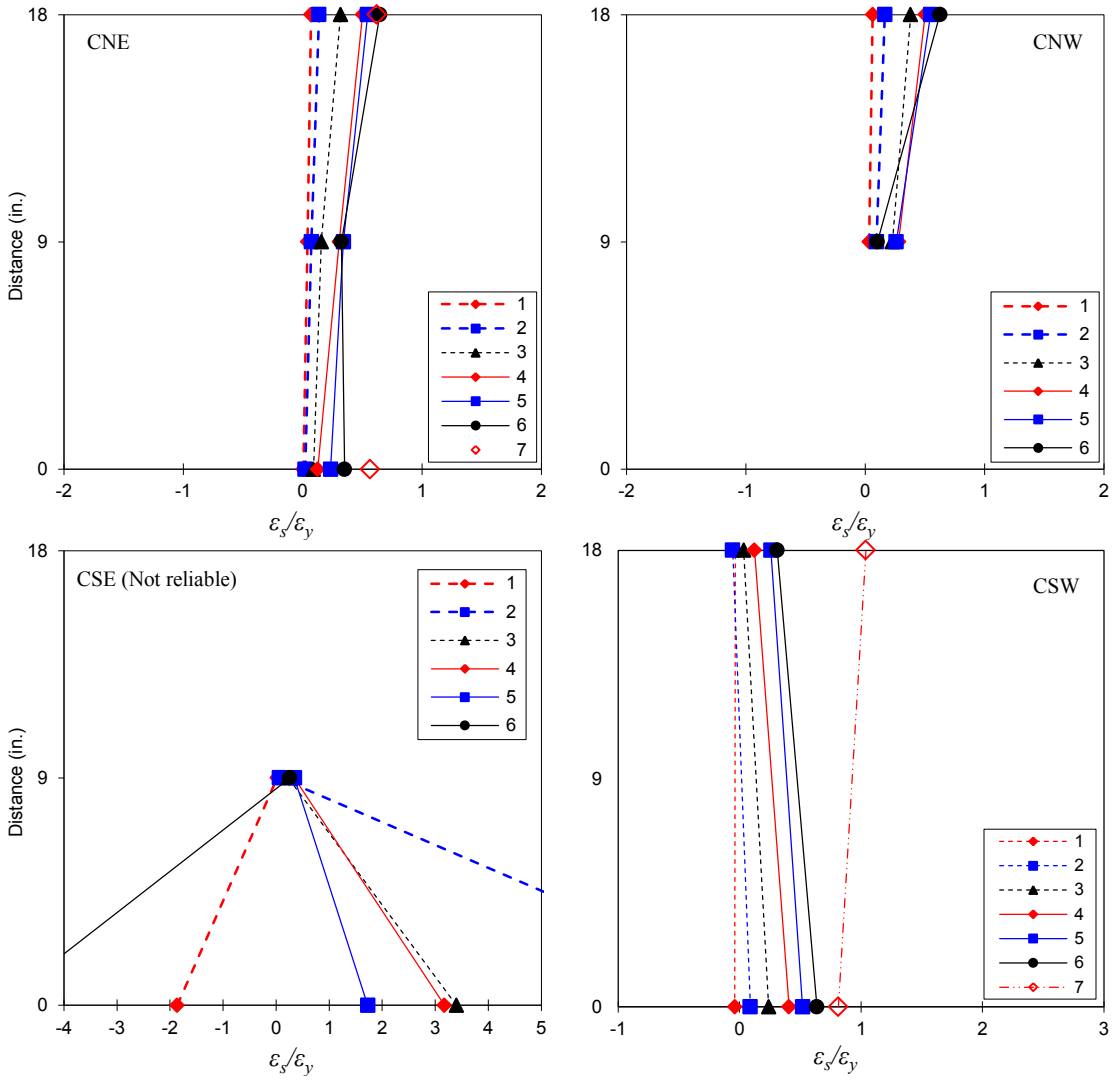

Figure A.12 Column reinforcement strain distribution during NS beam upward loading, specimen U-BJ-1

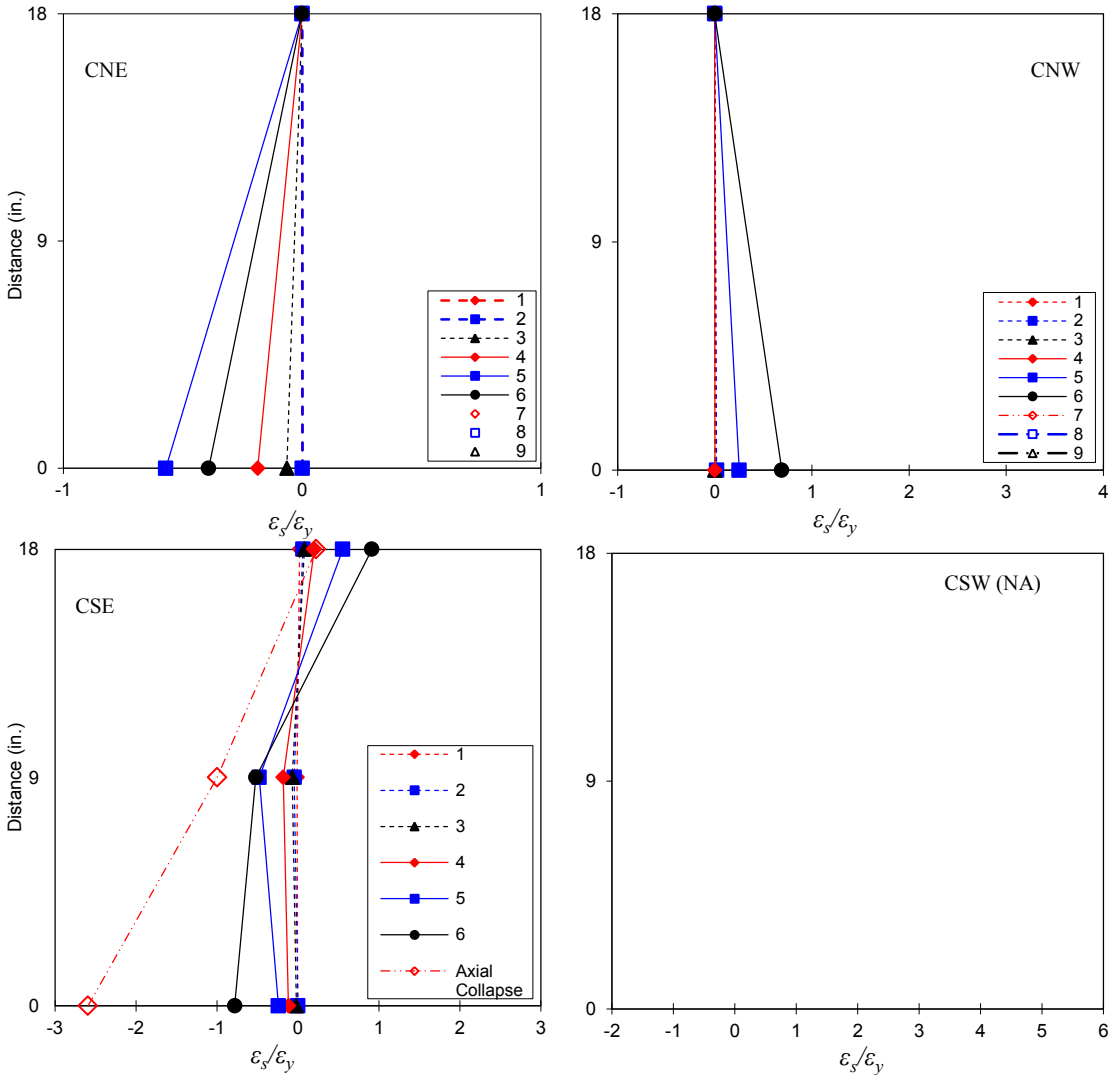

Figure A.13 Column reinforcement strain distribution during EW beam downward loading, specimen B-J-1

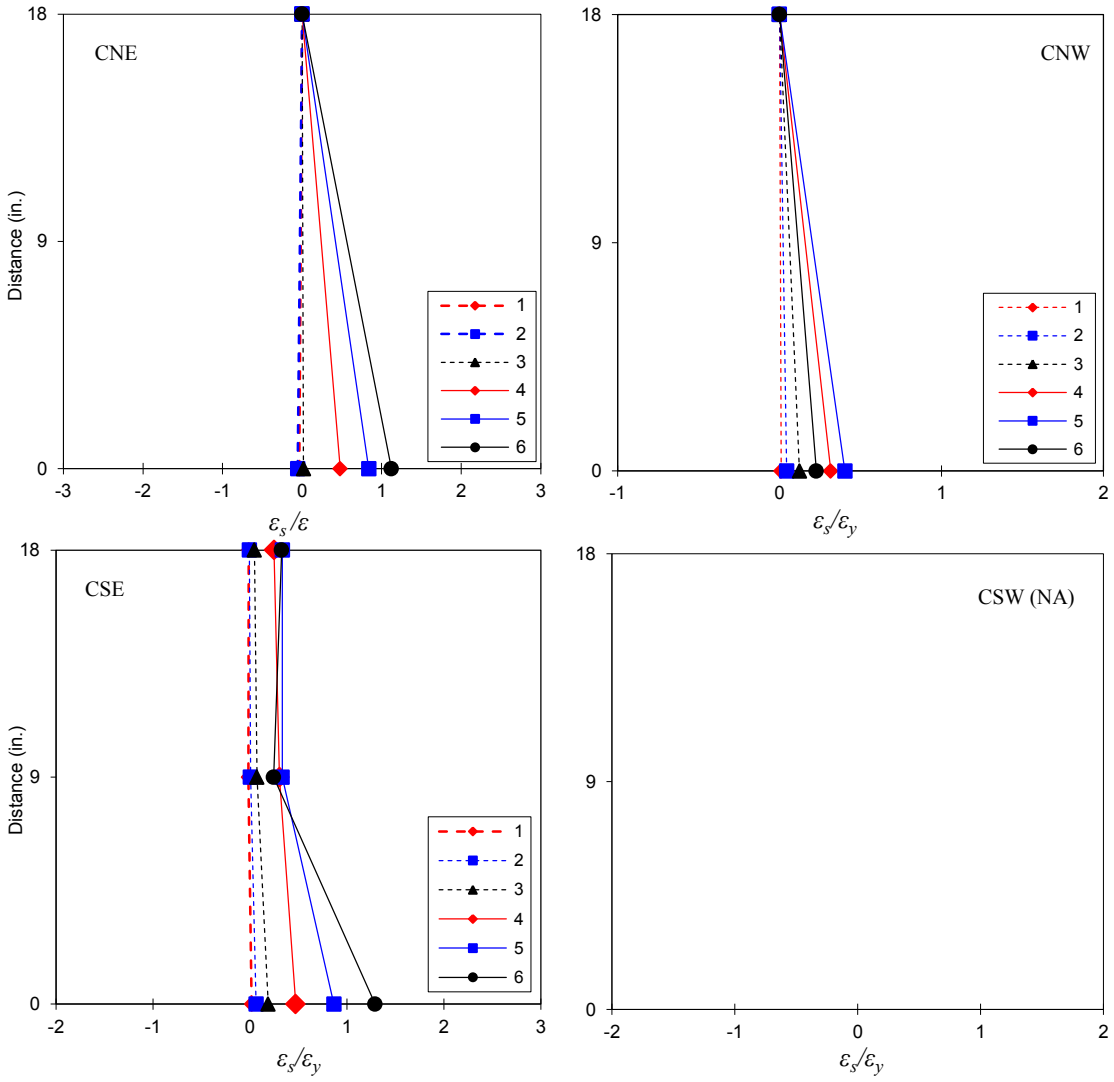

Figure A.14 Column reinforcement strain distribution during EW beam upward loading, specimen B-J-1

APPENDIX B

ADDITIONAL CHARTS AND TEST PICTURES

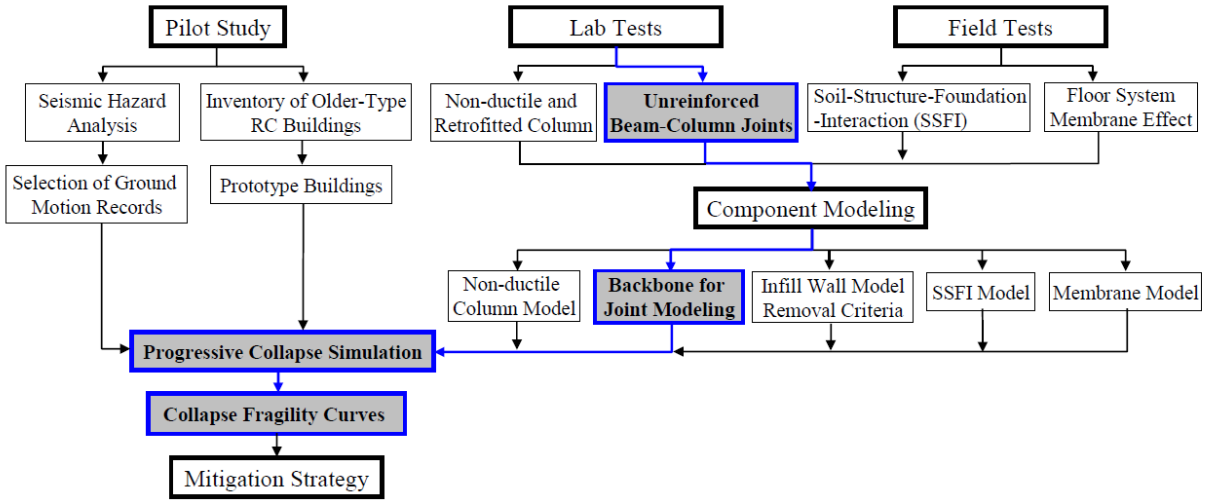

Figure B.1 NEES GC Project Research organization chart, Park [120]

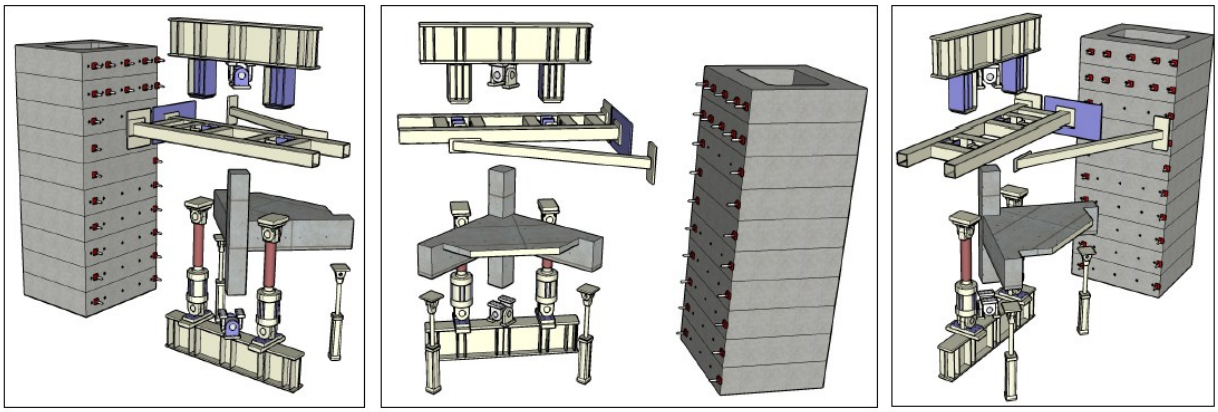

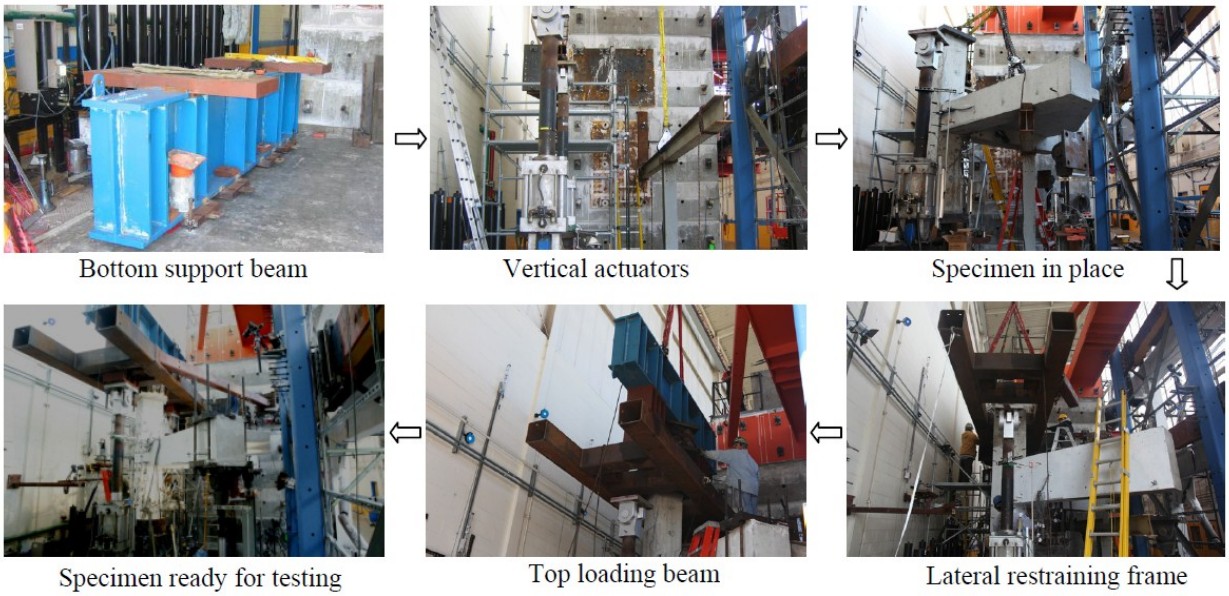

Figure B.2 NEES GC Project joint test setup assembling, Park [120]

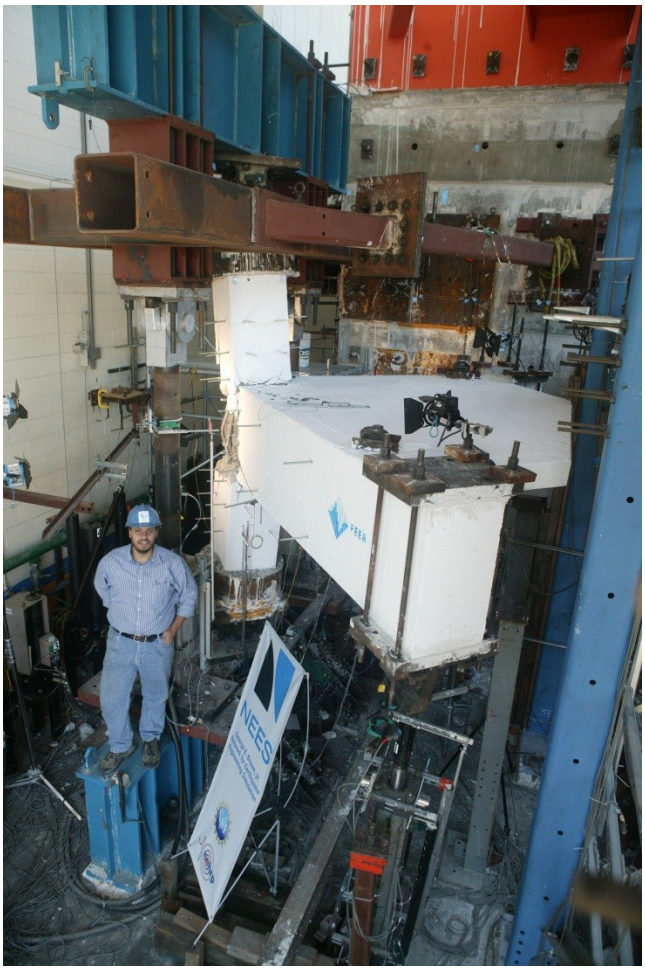

Figure B.3 Top view of collapsed specimen U-J-2

Figure B.4 Instrumented specimen U-BJ-1 before testing

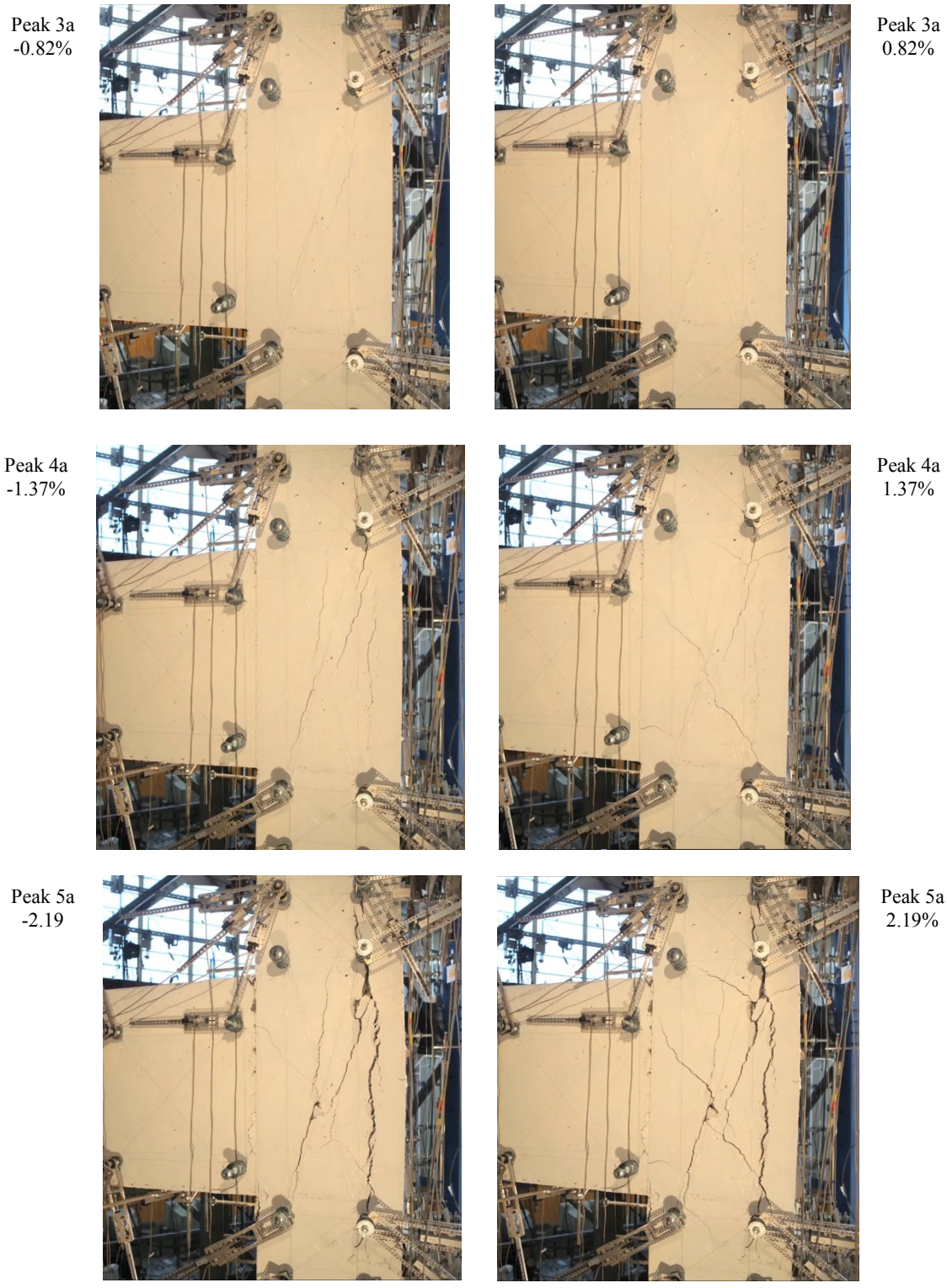

Figure B.5 East joint face distress and crack progression during NS beam loading first drift peaks (U-J-2)

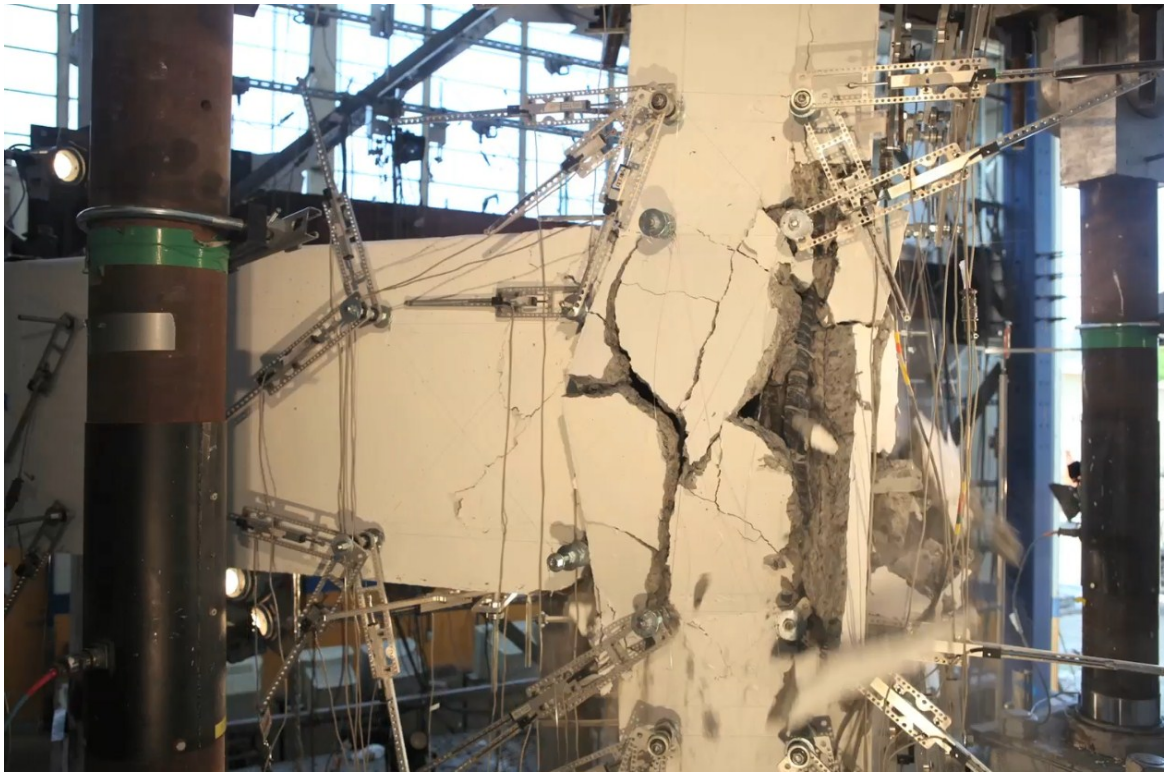

Figure B.6 East joint face during axial failure of specimen U-J-2

Figure B.7 East joint face instantly before axial failure of specimen U-J-1

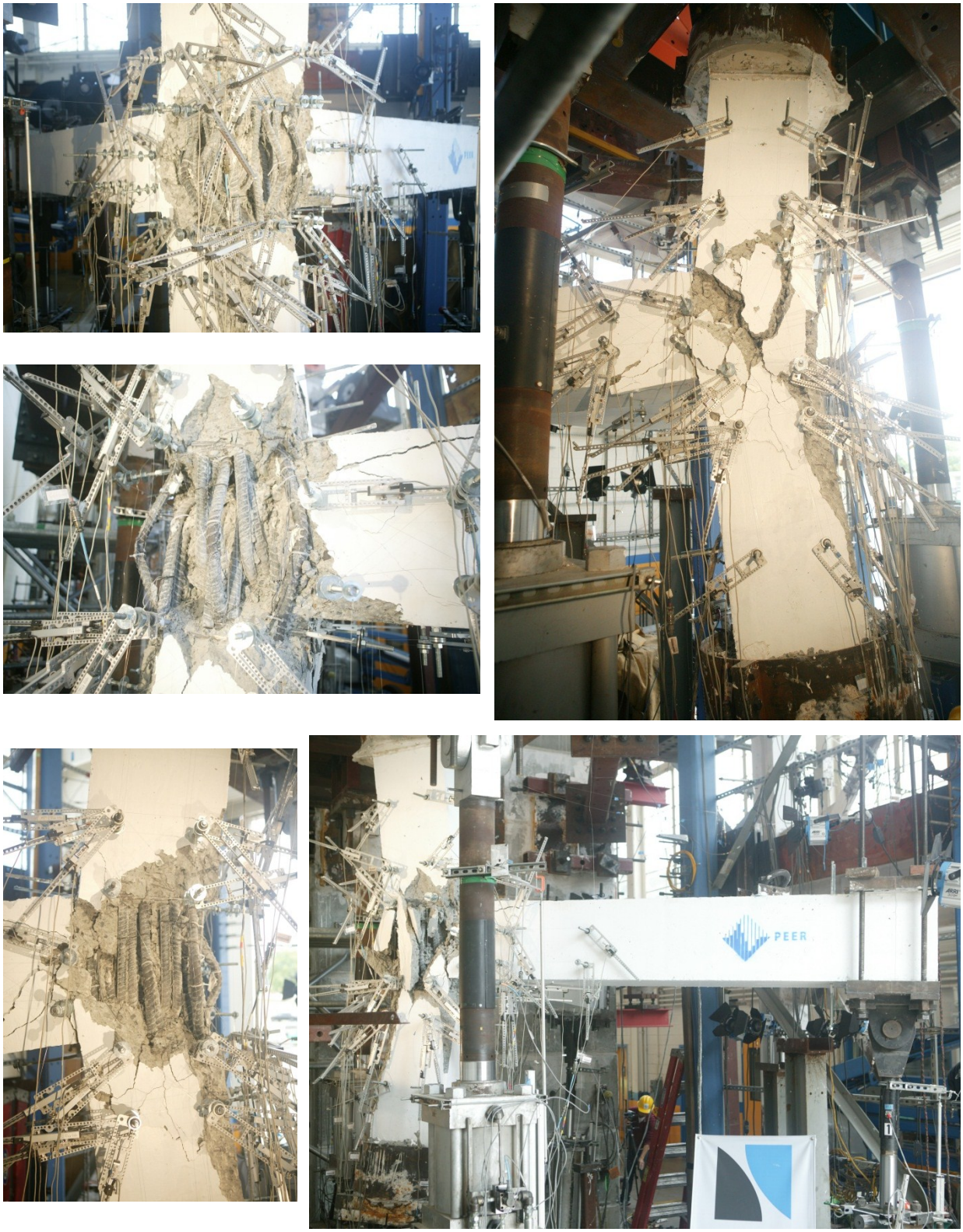

Figure B.8 Different views of axial collapse of specimen B-J-1